frontiers | Research Topics

Precise chemical application technology for horticultural crops

Edited by
Xiaolan Lv, Andreas Herbst and Jianli Song

Coordinated by
Xue Li

Published in
Frontiers in Plant Science

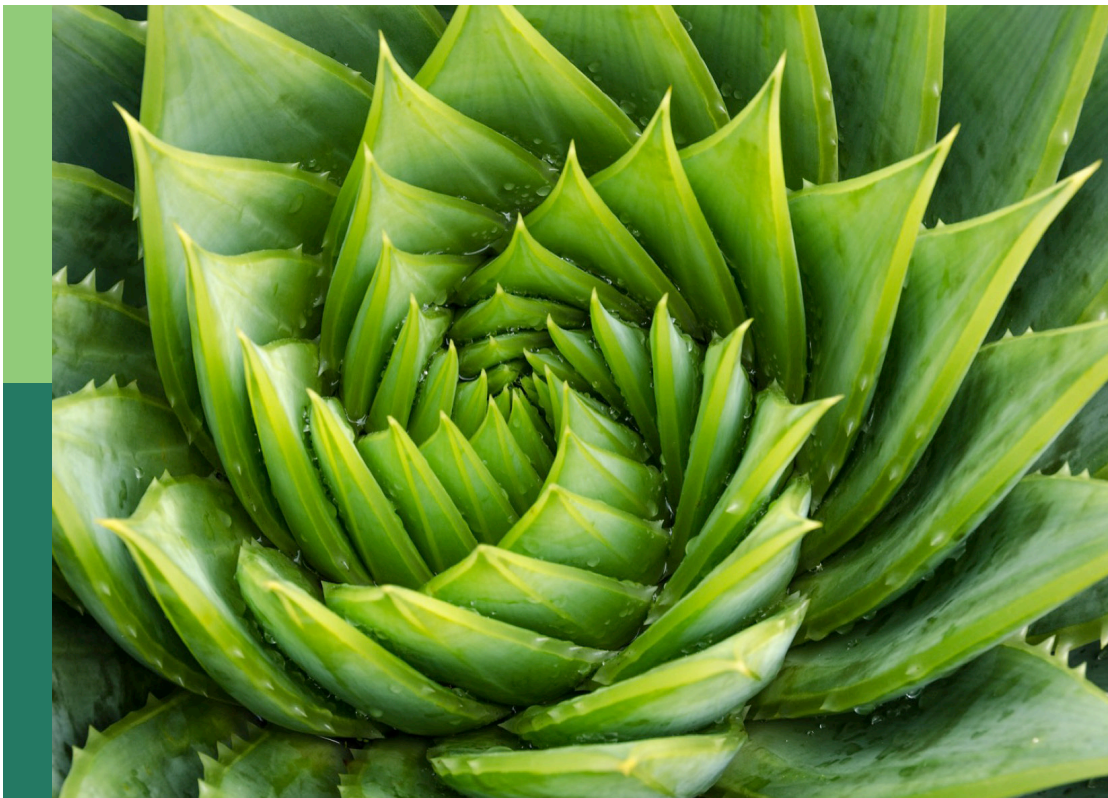

ISSN 1664-8714
ISBN 978-2-8325-4992-6
DOI 10.3389/978-2-8325-4992-6

About Frontiers

Frontiers is more than just an open access publisher of scholarly articles: it is a pioneering approach to the world of academia, radically improving the way scholarly research is managed. The grand vision of Frontiers is a world where all people have an equal opportunity to seek, share and generate knowledge. Frontiers provides immediate and permanent online open access to all its publications, but this alone is not enough to realize our grand goals.

Frontiers journal series

The Frontiers journal series is a multi-tier and interdisciplinary set of open-access, online journals, promising a paradigm shift from the current review, selection and dissemination processes in academic publishing. All Frontiers journals are driven by researchers for researchers; therefore, they constitute a service to the scholarly community. At the same time, the *Frontiers journal series* operates on a revolutionary invention, the tiered publishing system, initially addressing specific communities of scholars, and gradually climbing up to broader public understanding, thus serving the interests of the lay society, too.

Dedication to quality

Each Frontiers article is a landmark of the highest quality, thanks to genuinely collaborative interactions between authors and review editors, who include some of the world's best academicians. Research must be certified by peers before entering a stream of knowledge that may eventually reach the public - and shape society; therefore, Frontiers only applies the most rigorous and unbiased reviews. Frontiers revolutionizes research publishing by freely delivering the most outstanding research, evaluated with no bias from both the academic and social point of view. By applying the most advanced information technologies, Frontiers is catapulting scholarly publishing into a new generation.

What are Frontiers Research Topics?

Frontiers Research Topics are very popular trademarks of the *Frontiers journals series*: they are collections of at least ten articles, all centered on a particular subject. With their unique mix of varied contributions from Original Research to Review Articles, Frontiers Research Topics unify the most influential researchers, the latest key findings and historical advances in a hot research area.

Find out more on how to host your own Frontiers Research Topic or contribute to one as an author by contacting the Frontiers editorial office: frontiersin.org/about/contact

Precise chemical application technology for horticultural crops

Topic editors

Xiaolan Lv — Jiangsu Academy of Agricultural Sciences (JAAS), China

Andreas Herbst — Julius Kühn Institute (JKI) –Federal Research Centre for Cultivated Plants, Institute for Application Techniques in Plant Protection, Germany

Jianli Song — China Agricultural University, China

Topic coordinator

Xue Li — Jiangsu Academy of Agricultural Sciences (JAAS), China

Citation

Lv, X., Herbst, A., Song, J., Li, X., eds. (2024). *Precise chemical application technology for horticultural crops*. Lausanne: Frontiers Media SA.

doi: 10.3389/978-2-8325-4992-6

Table of contents

frontiers | Frontiers in Plant Science

TYPE Editorial
PUBLISHED 28 May 2024
DOI 10.3389/fpls.2024.1413941

OPEN ACCESS

EDITED AND REVIEWED BY
María R. Conesa,
Spanish National Research Council (CSIC), Spain

*CORRESPONDENCE
Xue Li
neigelee99@163.com
Xiaolan Lv
lxlanny@126.com

RECEIVED 08 April 2024
ACCEPTED 29 April 2024
PUBLISHED 28 May 2024

CITATION
Li X, Lv X, Herbst A, Song J, Xu T and Qi Y (2024) Editorial: Precise chemical application technology for horticultural crops. *Front. Plant Sci.* 15:1413941. doi: 10.3389/fpls.2024.1413941

Editorial: Precise chemical application technology for horticultural crops

Xue Li[1,2]*, Xiaolan Lv[1,2]*, Andreas Herbst[3], Jianli Song[4], Tao Xu[1,2] and Yannan Qi[1,2]

[1]Institute of Agricultural Facilities and Equipment, Jiangsu Academy of Agricultural Sciences, Nanjing, Jiangsu, China, [2]Key Laboratory of Horticultural Equipment, Ministry of Agriculture and Rural Affairs, Nanjing, China, [3]Application Techniques in Plant Protection, Julius Kühn Institute, Braunschweig, Germany, [4]College of Science, China Agricultural University, Beijing, China

KEYWORDS

chemical application, horticultural crops, plant protection, precision agriculture, spraying

Editorial on the Research Topic
Precise chemical application technology for horticultural crops

The field of plant chemical protection utilizes professional spraying machines to transport chemicals, such as pesticides and herbicides, to targeted sites for effective control of pests, diseases, and weeds in horticultural crop production (Wang et al., 2022). These practices play a crucial role in ensuring the provision of safe and abundant food, fruits, and vegetables for human consumption. However, conventional methods of applying plant chemicals suffer from issues such as excessive pesticide usage, low utilization rates, and high labor intensity due to outdated sprayers and single atomization technology (Abbas et al., 2020). To further advance modern agriculture, it is necessary to focus on efficient, precise, and intelligent application technologies and equipment for plant chemical protection. By incorporating smart chemical application technology with efficient equipment, significant reductions in pesticide usage can be achieved while mitigating environmental harm caused by chemicals and alleviating labor intensity (Talaviya et al., 2020). This approach facilitates sustainable development in disease and pest control of horticultural crops while ensuring food safety as well as maintaining crop yield and quality.

The published articles cover three main areas: target detection, variable-rate automated spraying systems, and autonomous trajectory planning and navigation. The primary goal of this Research Topic is to comprehensively study novel technologies for applying chemicals in horticultural crop cultivation. This focused examination will facilitate the exploration of innovative theories, advancements in technological solutions, and optimization of chemical applications for effective pest control, disease prevention, and weed management in horticultural crops.

Target detection

The precision targeting technology is essential for implementing precise variable-rate spraying. Before applying variable-rate spraying, agricultural machinery needs to accurately detect and acquire the target or application area, and then execute automatic spraying based on the severity of pests and diseases (Li et al., 2017). The essence of precision targeting technology lies in target detection. Currently, various methods such as infrared, ultrasonic, lidar, machine vision, spectral imaging, and multi-sensor fusion are employed for detecting targets (Partel et al., 2021).

Qiu et al. proposed a citrus disease classification model that incorporates data diversity, knowledge assistance, and modal fusion. The study utilized leaves from healthy plants as well as plants infected with 10 prevalent diseases to construct three datasets with white, natural, and mixed backgrounds. This approach aimed to enhance the adaptability of the model in real-world scenarios. Visual features of the leaves were extracted using convolutional networks of varying depths (VGG16, ResNet50, MobileNetV2, and ShuffleNetV2). Additionally, TextCNN and fastText were employed to extract textual features and semantic relationships. By integrating image and text information synergistically, a joint learning model for citrus disease features was developed. The results demonstrated that ShuffleNetV2 + TextCNN achieved an impressive classification accuracy of 98.33% on the mixed dataset – an improvement of 9.78% over single-image models and 21.11% over single-text models respectively. Furthermore, this model exhibited faster convergence rate, superior classification balance, and enhanced generalization capability compared to other methods available in literature; thus, providing a more reliable basis for decision-making regarding precise application of biological and chemical control strategies in citrus production.The dataset created by Lyu et al. consists of images capturing citrus psyllids in their natural habitats, and they proposed a lightweight detection model based on spatial channel interaction. Experimental results demonstrated that the YOLO-SCL model exhibits excellent accuracy in detecting citrus psyllids. Compared to the conventional YOLOv5s model, the YOLO-SCL model achieved a mAP@0.5 of 97.07% for citrus psyllids, surpassing the performance of the conventional YOLOv5s model by 1.18%. Furthermore, the number of parameters and computational requirements of the YOLO-SCL model are reduced by 14.25% and 2.52%, respectively, compared to those of the conventional YOLOv5s model. Additionally, through optimization using the black widow algorithm for hyperparameters, the mAP@0.5 score for citrus psyllid detection with the YOLO-SCL model improved to 97.18%, making it more suitable for detecting these pests in natural environments.

Variable-rate automated spraying systems

The variable-rate automated spraying technology for pesticides plays a vital role in achieving accurate pesticide application by gathering data on factors including pest severity, crop canopy morphology and density (Tumbo et al, 2007). This information is then integrated with operational parameters such as position, speed, and spray pressure to precisely target crops.

Xue et al. designed a variable spraying control system. The system employed a Kinect sensor to real-time detect the canopy volume of citrus trees and adjusted the duty cycle of solenoid valves by pulse width modulation to control the pesticide application. The experimental results indicated that the variable spraying control system demonstrated good consistency between the theoretical spray volume and the actual spray volume. Compared to constant-rate spraying, the droplets under the variable-rate mode based on canopy volume exhibited higher deposition density achieving the goal of reducing pesticide use with a maximum pesticide saving rate of 57.14%.

Autonomous trajectory planning and navigation

The autonomous navigation of agricultural machinery relies on machine vision, lidar, and satellite positioning techniques. Machine vision extracts reference data from ground oblique views and aerial global views. Lidar technology establishes the operational environment through SLAM methods. Satellite positioning transmits geographic information to enable navigation via wireless data transmission.

Traditional navigation methods based on GNSS and 2D LIDAR is unreliable in complex scenarios with little sensory information due to tree canopy occlusion. Xia et al. proposes a 3D LiDAR-based navigation method for trellis orchards. Using 3D LiDAR with a 3D SLAM algorithm, orchard point cloud information was collected and filtered using the PCL (point cloud library) to extract trellis point clouds as matching targets. In terms of positioning, the real-time position was determined through a reliable method of fusing multiple sensors for positioning, which involves transforming the RTK information into the initial position and doing a normal distribution transformation between the current frame point cloud and the scaffold reference point cloud to match the point cloud position. For path planning, the required vector map was manually planned in the orchard point cloud to specify the path of the roadway, and finally, navigation was achieved through pure path tracking. Field tests showed that the accuracy of the NDT SLAM method reached 5 cm in each rank with a coefficient of variation less than 2%. Additionally, the navigation system had a high positioning heading accuracy with a deviation within 1° and a standard deviation of less than 0.6° when moving along the path point cloud at a speed of 1.0 m/s in a Y-trellis pear orchard. The lateral positioning deviation was also controlled within 5 cm with a standard deviation of less than 2 cm. This navigation system has a high level of accuracy and can be customized to specific tasks, making it widely applicable in trellis orchards with autonomous navigation pesticide sprayers.

To address the issue of low-density canopy in greenhouse crops affecting the robustness and accuracy of simultaneous localization and mapping (SLAM) algorithms, Tan et al. proposed a map

construction and localization method based on spatial down sampling with multiline LiDAR using the Cartographer framework. Focusing on suspended tomato plants grown in greenhouses as the research subject, an adaptive filtering point cloud projection (AF-PCP) SLAM algorithm was developed. The results demonstrated that compared to the Cartographer algorithm, the AF-PCP SLAM algorithm increased the average mapping area of crop rows by 155.7%. The mean error and coefficient of variation for crop row length were 0.019 m and 0.217%, respectively. Additionally, the average maximum void length was measured at 0.124m while the average relative localization errors at speeds of 0.2 m/s, 0.4 m/s, and 0.6 m/s were found to be 0.026 m, 0.029 m, and 0.046 m respectively; all with standard deviations less than or equal to 0.06 m. The proposed algorithm reduced average localization error by approximately79 .9% when compared to track deduction algorithms. Thus, it can be concluded that even in low-density canopy environments within greenhouses, the AF-PCP SLAM algorithm is capable of precisely mapping and localizing robots.

Conclusion

The innovative advancement of chemical application technology for horticultural crops has resulted in reduced pesticide usage, improved operational efficiency, cost reduction, and risk mitigation associated with plant protection operations. We believe that this Research Topic will be a valuable resource for readers seeking to understand the latest advancements in chemical application technology for horticultural crops and their practical implications on precise spraying.

Author contributions

XL: Conceptualization, Data curation, Investigation, Writing – original draft, Writing – review & editing. XLL: Funding acquisition, Project administration, Writing – review & editing. AH: Writing – review & editing. JS: Validation, Writing – review & editing. TX: Validation, Writing – review & editing. YQ: Validation, Writing – review & editing.

Funding

The author(s) declare financial support was received for the research, authorship, and/or publication of this article. We acknowledge support from the “333” Youth Talent Foundation of Jiangsu Province [23212202] and Shandong Province key research and development project [2022SFGC0204].

Acknowledgments

The editors would like to thank the authors, reviewers, and Frontiers in Plant Science team, whose efforts contributed to the creation of this Research Topic.

Conflict of interest

The authors declare that the research was conducted in the absence of any commercial or financial relationships that could be construed as a potential conflict of interest.

Publisher’s note

References

Abbas, C. J., Huang, Y. Y., Liu, Y. S., Faheem, Y. C., Shahzad Noor, R., Ali Shaikh, S., Ali Solangi, K., et al (2020). Different sensor based intelligent spraying systems in Agriculture. *Sensors and Actuators A: Physical* 316, 112262. doi: 10.1016/j.sna.2020.112265

Li, L. L., He, X. K., Song, J. L., Wang, X. N., Jia, X. M., and Liu, C. H. (2017). Design and experiment of automatic profiling orchard sprayer based on variable air volume and flowrate. *Trans. CSAE* 33, 70–76. doi: 10.11975/j.issn.1002-6819.2017.01.009

Parter, V., Costa, L., and Ampatzidis, Y. (2021). Smart tree crop sprayer utilizing sensor fusion and artificial intelligence. *Comput. Electron. Agric.* 191, 106556. doi: 10.1016/j.compag.2021.106556

Tumbo, S. D., Salyani, M., Miller, W. M., Sweeb, R., and Buchanon, S. (2007). Evaluation of a variable rate controller for aldicarb application around buffer zones in citrus groves. *Comput. Electron. Agric.* 56, 147–160. doi: 10.1016/j.compag.2007.01.010

Talaviya, S. D., Shah, M., Patel, W. M., Yagnik, R., and Shah, S. (2020). Implementation of artificial intelligence in agriculture for optimisation of irrigation and application of pesticides and herbicides. *Artificial Intelligence in Agriculture* 4, 58–73. doi: 10.1016/j.aiia.2020.04.002

Wang, S. L., Li, X., Liu, Y. J., Lv, X. L., and Wang, W. (2022). Comparison of a new knapsack mist sprayer and three traditional sprayers for pesticide application in plastic tunnel greenhouse. *Phytoparasitica* 50, 177–190. doi: 10.1007/s12600-021-00947-3

frontiers | Frontiers in Plant Science

TYPE Original Research
PUBLISHED 19 April 2023
DOI 10.3389/fpls.2023.1168228

OPEN ACCESS

EDITED BY
Xiaolan Lv,
Jiangsu Academy of Agricultural Sciences (JAAS), China

REVIEWED BY
Shilin Wang,
Jiangsu Academy of Agricultural Sciences (JAAS), China
Xiaojing Yan,
Institute of Plant Protection (CAAS), China

*CORRESPONDENCE
Weicai Qin
qinweicai@caas.cn

SPECIALTY SECTION
This article was submitted to Sustainable and Intelligent Phytoprotection, a section of the journal Frontiers in Plant Science

RECEIVED 17 February 2023
ACCEPTED 22 March 2023
PUBLISHED 19 April 2023

CITATION
Qin W, Chen P and Wang B (2023) Productivity model and experiment of field crop spraying by plant protection unmanned aircraft.
Front. Plant Sci. 14:1168228.
doi: 10.3389/fpls.2023.1168228

Productivity model and experiment of field crop spraying by plant protection unmanned aircraft

Weicai Qin[1,2]*, Panyang Chen[3] and Baokun Wang[2]

[1]Suzhou Polytechnic Institute of Agriculture, Suzhou, China, [2]Nanjing Institute of Agricultural Mechanization, Ministry of Agriculture and Rural Affairs, Nanjing, China, [3]Nanjing Institute of Technology, Nanjing, China

Traditional agricultural production requires numerous human and material resources; however, agricultural production efficiency is low. The successful development of plant protection unmanned aerial vehicles (UAVs) has changed the operation mode of traditional agricultural production, saving human, material, and financial resources and significantly improving production efficiency. To summarize the process of improving the productivity of plant protection UAVs, this study established a productivity calculation model of UAVs based on the time composition of the UAV agricultural plant protection process, including spraying, turning, replenishment, and transfer times. The time required for the unmanned aircraft application process was counted through years of tracking the application process of eight different plant protection unmanned aircraft. Plot lengths of 100, 300, 500, 700, 1,000, 1,500, 2,000, 2,500, 3,000, and 3,500 m were established to calculate the theoretical productivity. The results showed that the productivity of different types of plant protection UAVs increased with an increase in plot length in the range of 100 to 1,500 m; however, when the plot length reached a certain value, the productivity growth rate slowed down or even decreased slightly. Simultaneously, based on the working area per 10,000 mu, the recommended plot length and the number of configured models for different models were recommended. If the plant protection UAV was distinguished by electric and oil power, the time utilization rate of electric plant protection UAVs was 72.7%, and the labor productivity was 56.4 mu/person·h. In contrast, the time utilization rate of the heavy load oil-powered plant protection unmanned aircraft was 86%, and the labor productivity was 63.5 mu/person ·h. This study can support plant protection UAV enterprises to optimize equipment efficiency, provide evaluation methods for the operation efficiency assessment of plant protection UAVs, provide a reference for the selection of plant protection UAVs, and provide a basis for field planning.

KEYWORDS

unmanned aerial vehicle, spraying pesticide, productivity, model, evaluation method

1 Introduction

The plant protection unmanned aerial vehicle (UAV) has several advantages compared with the ground boom sprayer, which include high operation efficiency, strong ability to handle emergencies, low operating cost, and labor intensity (Lou et al., 2017). Specifically, it solves the difficult problem of ground equipment and manual work in the late stage of crop growth. Furthermore, with the further implementation of China's land transfer policy, the scale of agricultural production has continued to expand (Xue and Lan, 2013; Feng and Yang, 2014), the cost of rural labor has continued to rise, and the demand for unmanned aerial vehicle application in agricultural plant protection has become increasingly strong (Kirk, 2003). Therefore, technical research, equipment development, and operation mode formulation of plant protection UAV spraying operations have become the research hotspots of scientific research units, enterprises, and promotion departments in plant protection machinery.

Recently, studies have reported considerable innovations in improving the quality and efficiency of plant protection unmanned aerial vehicle operations from spraying operation parameter matching, equipment performance optimization, and operation path planning (Zhang et al., 2021). Several studies have been conducted on the application of plant protection UAVs, such as operating speed (Kirk et al., 2001; Qin et al., 2014), spray volume and height (Lan et al., 2010), spray width (Zhu et al., 2019), droplet size (Qiu et al., 2013), natural wind speed (Chen et al., 2017a), and airflow field (Carlton, 1999; Chen et al., 2017b), on the influence of droplet deposition, establishing an advanced and specific spraying operation parameter model and its evaluation method (Zhang et al., 2015; Wang et al., 2016a).

Productivity improvement studies mainly focused on the path planning of pesticide application (Wang et al., 2016b), such as the accuracy and control of the route of plant protection unmanned aircraft based on the farmland environment (Ru et al., 2012; Yang et al., 2017), the development of an efficient matching algorithm for plant protection unmanned aircraft operations (Xu et al., 2017), the deployment and decision-making of the UAV flying defense team (Cao et al., 2019), and the monitoring technology of the pesticide application state of the plant protection unmanned aircraft (Xu et al., 2017; Yang et al., 2019).

Current studies mainly focus on improving the operation quality of plant protection UAVs and the reliability of spraying equipment, which provides much technical support for popularizing and applying plant protection UAVs. The productivity of plant protection UAVs is very important for farmland size planning and equipment configuration for intensive production; however, there are no relevant studies. Therefore, this study collected production data of plant protection UAVs from 2016 to 2020 to summarize the method of enhancing their production process. Furthermore, the study proposes the appropriate plot length and configuration quantity for each model under stable labor productivity, providing data support for applying plant protection UAVs.

2 Material and methods

2.1 Technical index of productivity

The technical indicators of plant protection unmanned aerial vehicle spraying operation productivity include hourly working time productivity, net spraying hourly productivity, shift time utilization, and labor productivity. Equations 1–4 (Qiao et al., 2016) are as follows:

$$W_b = \frac{U}{T_T} \tag{1}$$

$$W_s = \frac{U}{T_z} \tag{2}$$

$$\tau = \frac{T_z}{T_T} \cdot 100\,\% \tag{3}$$

$$G_j = \frac{W_b}{A_j} \tag{4}$$

where W_b is the actual hourly productivity, mu/h; U is the actual working area, mu; T_T is the flight time, h; W_S is the hourly productivity of net spraying, mu/h; T_Z is the net spraying time, h; τ is the time utilization, %; G_j is labor productivity, mu/person·h; and A_j is the number of crew members, people.

2.2 Job productivity model

2.2.1 Model basis

The productivity of plant protection unmanned aircraft was acquired according to GB/5667-2008 (Standardization Administration of China, 2008):

$$W = 0.36B \cdot v \cdot \tau \tag{5}$$

where W is the productivity, mu/h; B is the spraying amplitude of plant protection unmanned aircraft, m; v is the application speed, m/s; and τ is the time utilization rate, the ratio between the net application time and the total time during the application duration of plant protection UAV. Plant protection UAV pesticide application requires frequent take-off and landing, and the time utilization model is shown in Equation 6.

$$\tau = \frac{\sum T_{zi}}{\sum T_{Ti}} \tag{6}$$

where T_{zi} is the net spraying time when spraying the ith tank of spray liquid, s, and T_{Ti} is the total time for spraying the ith tank of spray liquid, s.

2.2.2 Total operation time model

The reliability of the plant protection UAV is not part of the content of this test, the scale of the test is large, and communication and coordination will cause time delays. Therefore, the total time of this test is the sum of the time of each operation sortie statistical spraying task. The spraying operation of the plant protection UAV includes preparation before the first operation (assembly, maintenance, and debugging), supply (maintenance, dosing,

refueling, or battery replacement), attitude adjustment before the operation (stabilizing the rotor speed and entering the flight trajectory), spraying, U-turn (acceleration and deceleration and U-turn), return and flameout (empty travel and rotor stop), and supply point transfer and other links. The total time model of its work is shown in Equation 7:

$$T_{Ti} = T_{fp} + \sum \ (T_{si} + T_{ami} + T_{ai} + T_{ri} + T_{toi} + T_{sui}) \quad (7)$$

where T_{fp} is the preparation time before the first operation, s; T_{si} is the total refill time at the ith tank of solution, s, including refilling, refueling, battery replacement, maintenance, and other time; T_{ami} is the adjustment time before the application operation at the ith tank of liquid, s, time from ignition to when spraying begins; $T_{ai}$is the net spray time when the ith tank is sprayed, s; T_{ri} is the turnaround time when the ith tank of medicine, s; $T_{toi}$is the return flameout time at the ith tank of medicine, s, from the end of spraying until the rotor stops rotating; and $T_{sui}$is the transfer time of the ith resupply point, s.

Research on the time composition and representation of plant protection unmanned aircraft production operations aims to improve the basic theory of production performance and testing methods, summarize the production performance testing methods of agricultural machinery, construct an unmanned aircraft production efficiency model, and propose processing solutions to improve the production performance of different unmanned aircraft platforms in response to their production data.

2.2.3 Replenishment time calculation model

The net spraying time is mainly affected by the maximum travel, replenishment times, and time the plant protection unmanned aircraft can operate with a full tank of spray liquid. Among them, the maximum stroke that can be operated with a full tank of spray liquid is related to the capacity of the tank, the operating speed, and the total flow of the nozzle. The model calculation is shown in Equation 8:

$$L_{max} = \frac{60Q \cdot v}{q} \quad (8)$$

where L_{max} is the maximum stroke that can be operated with a full tank of liquid, m; Q is the (maximum) spray liquid loading capacity, L; and q is the total flow rate of the nozzle, L/min. The flight path is planned with the fewest supply points and the fewest number of U-turns during spraying operations. For example, suppose the length of the plot is L, and the width of the plot is B_f; the number of operational trips of the plant protection UAVs to complete the application of a field is the ratio of the width of the field to the width of the spray operation, and combined, thus, the calculation is shown in Equation 9:

$$N_x = \left[\frac{B}{B_f}\right] \quad (9)$$

where B is the spraying working width, m; B_f is the width of the plot, m; and N_x is the number of operating strokes. The width of the plot should be designed as much as possible to be double the spray width of the plant protection unmanned aircraft to ensure that the spraying operation does not occur with heavy and missing spraying and spreading of empty strokes.

1) When $L_{max} \le 2L$, the replenishment points are

$$N_b = \left[\frac{2L}{L_{max}}\right] \quad (10)$$

The number of refills is $N_s = N_b \cdot \left[\frac{N_x}{2}\right] + \left[\frac{N_x[2L-(N_b-1)L_{max}]}{2L_{max}}\right]$.

2) When $L_{max} > 2L$, only one resupply point is set up on one side of the ground.

The number of refills is

$$N_s = \left[\frac{N_x}{\left[\frac{L_{max}}{2L}\right]}\right] \quad (11)$$

2.2.4 Productivity calculation model

To obtain the productivity model Equation 12 of plant protection unmanned aerial vehicle spraying operation, substitute Equations 6–11 into Equation 5:

$$W = 0.36Bv\frac{\sum_{i=1}^{N_a} T_{ai}}{T_{fp}+\sum_{i=1}^{N_a}(T_{si}+T_{ami}+T_{ai}+T_{toi})+\sum_{i=1}^{N_s} T_{ri}+\sum_{i=1}^{N_b} T_{sui}} \quad (12)$$

where $N_s$is the number of refills, N_{am} is the number of adjustments before application operations, N_{to} is the number of returns and flameouts and N_a is the number of spraying operations frame. $N_s = N_{am} = N_{to} = N_a$.The number of turns is $N_r = N_b(N_x - 1)$. Test statistics determine each time item in the formula, and the time data of each model are shown in Table 1.

2.3 Plant protection UAV

A total of eight types of plant protection unmanned aircraft with different power, atomization methods, and the number of rotors were selected for this test. As shown in Figure 1. The power included electric and oil power, and the rotors included single, four, six, and eight rotors. The weight was 8–30 kg. The basic parameters of the test plant protection UAVs are shown in Table 2.

2.4 Test conditions and methods

Eight adjacent plots were selected for allocation to each plant protection UAV, each 730 m in length, with CE20, P20, 4DE1000, HY-B-16L, MG-1S, LF-D10, 3WQF120-12, and AT-30 operating plots of 60.3, 51.7, 21.5, 21.5, 21.1, 19.1, 41.8, and 52.8 mu, respectively.

Based on continuous tracking of plant protection unmanned aircraft productivity tests for many years, Excel 2010 software was used to process data and draw curves, among which the key replenishment point calculation condition statement function was as follows:

IF(N_b = 1,CEILING(20/CEILING(L_{max}/(2 * L),1),1),((N_b − 1) * 10 + CEILING(20 *(2 * L − (N_b − 1) * L_{max})/(2 * L_{max}),1))).

10.3389/fpls.2023.1168228

TABLE 1 1 Time composition test data for each unit.

Model	Preparation time before application T_{fp}/s	Replenishment time T_s/s	Adjust time before spraying operation T_{am}/s	Net spray time T_a/s	Turnaround time T_t/s	Return, turn off time T_{to}/s	Supply point transfer time T_{su}/s
CE20	325	256	40	750	3	36	1,200
P20	350	345	30	600	2	32	1,200
AT-30	900	240	105	1,500	10	75	1,200
4DE1000	185	305	45	460	6.5	25	1,200
MG-1S	450	350	10	400	2	20	1,200
HY-B-16L	250	305	30	400	6	45	1,200
3WQF120-12	358	180	42	500	3	51	1,200
LF-D10	485	285	31	250	3.8	30	1,200

The test crews were professionals from each plant protection unmanned aircraft company, and each crew developed his/her operation plan according to the characteristics of his/her unmanned aircraft. In addition, each crew had a researcher responsible for recording the total effective operation time, the net spraying time, and the time consumption of each time item.

2.5 Data acquisition and recording

The total time consumption and net spraying time of the three plant protection operations were recorded and averaged as shown in Table 3. In addition, the technical indicators such as time utilization, hourly productivity, net spraying hourly productivity, and labor productivity were calculated according to Equations 1–4, respectively, according to the number of crew members and the actual operating area of each model. The calculation results are shown in Table 3.

The productivity test was conducted together with the efficacy test to facilitate the organization of the test. A fixed operating area was arranged for different units. So that the normal application operations are not affected, each operational sortie was used as a statistical unit to track and test various time items occurring during application operations of different models and to record the time consumed by each time item. Therefore, the data in Table 1 are a combination of years of test data for each time item with abnormal data exclusion, and the average of the time items of all sorties during the operation period is the test result, as shown in Table 1. The transfer time of the resupply point was set to 20 min because the crews of different types of plant protection UAVs were configured by the ability of one crew to complete the transfer at one time, and the article was calculated according to the transfer length of 600 m and the weight walking speed of 0.5 m/s.

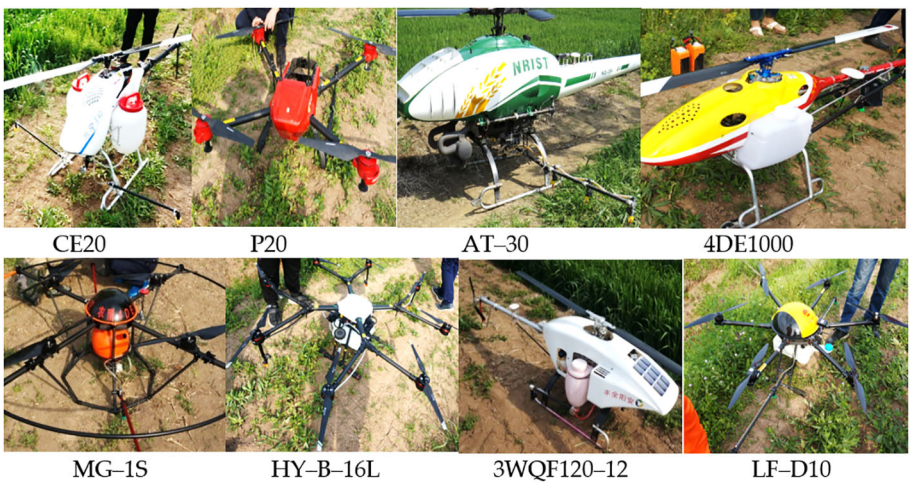

FIGURE 1
The UAVs used in testing. Note: the P20 is installed with four nozzles, but only two nozzles spray at a time. UAVs, unmanned aerial vehicles.

10.3389/fpls.2023.1168228

TABLE 2 Basic parameters of plant protection UAV participating in the test.

Model	Power type	Sprinkler type	Number of nozzles/piece	Nozzle flow/L/min	Tank capacity Q/L	Amplitude/m	Velocity/m/s	Single operation time/min
CE20	Electric single rotor	Hydraulic atomization	2	0.8	20	6	5	20
P20	Electric quadrotor	Centrifugal atomization	4 (2)	0.4	8	3	4	25
AT-30	Oil powered single rotor	Hydraulic atomization	6	0.25	30	8	5	20
4DE1000	Electric quadrotor	Hydraulic atomization	4	0.33	10	4.5	6	10
MG-1S	Electric octa-rotor	Hydraulic atomization	4	0.38	10	4	4	22
HY-B-16L	Electric single rotor	Hydraulic atomization	5	0.48	16	7	5	33
3WQF120-12	Oil powered single rotor	Hydraulic atomization	2	0.73	12	4	5	25
LF-D10	Electric hexacopter	Hydraulic atomization	4	0.6	10	4	4	15

UAVs, unmanned aerial vehicles.

3 Results and discussion

3.1 Comparative analysis of technical indicators of productivity of different models

As observed from Equation 2, the net spraying hourly productivity of plant protection UAVs is an important indicator of the inherent performance of plant protection unmanned aircraft, including spraying width, operating speed, and tank capacity. The actual hourly productivity of the impact indicators, in addition to the inherent performance of the equipment and time utilization, is also a key factor affecting the hourly productivity.

The test results in Table 3 completely verified the law, such as the AT30 plant protection UAV with a tank capacity of 30 L, a spraying width of 8 m, and an operating speed of 5 m/s. Therefore, the net spraying time of this model was the highest among all models, reaching 117.3 mu/h. In contrast, the LF-D10 plant protection UAV has a tank capacity of 10 L, a spraying width of 4 m, and an operating speed of 4 m/s; thus, the net spraying time of this model was the lowest among all models, only 42.4 mu/h. However, the complexity of the operations and the level of organizational proficiency of the different models lead to significant differences in time utilization, ranging from a minimum of 20% to a maximum of 45%, which was affected by time utilization AT30's actual hourly productivity of 26.4 mu/h, which was lower than CE20's actual hourly productivity of 30.15 mu/h. Furthermore, the labor productivity calculation model Equation 4 shows that the labor productivity is related to the actual hourly productivity and unit configuration labor; therefore, the labor productivity of P20 with a 2-labor unit configuration can reach up to 13.6 mu/person·h. In contrast,

TABLE 3 Productivity technical indicators of different types of plant protection UAVs.

Technical indicators	CE20	P20	4DE1000	HY-B-16L	MG-1S	LF-D10	3WQF120-12	AT-30
Working area/mu	60.300	51.700	21.500	21.500	21.100	19.100	41.800	52.800
Total time/h	2.000	1.900	1.030	0.880	1.100	1.100	2.500	2.000
Number of crew members/person	3	2	2	3	2	2	3	4
Net spray time/h	0.9	0.85	0.34	0.36	0.4	0.45	0.5	0.45
Time utilization/%	45	44.7	33	40.9	36.4	40.9	20	22.5
Actual hourly productivity, mu/h	30.150	27.211	20.874	24.432	19.182	17.364	16.720	26.400
Net spray hour productivity, mu/h	67.000	60.824	63.235	59.722	52.750	42.444	83.600	117.333
Labor productivity, mu/person·h	10.050	13.605	10.437	8.144	9.591	8.682	5.573	6.600

UAVs, unmanned aerial vehicles.

the actual labor productivity of AT30 was only 6.6 mu/person·h owing to the low time utilization and a large amount of labor allocated to the unit.

From the above analysis, the actual operational efficiency of plant protection unmanned aircraft application is affected by the inherent performance of the unit as well as closely related to the reasonable configuration of the unit's labor force, the level of organization and coordination of the crew, and the degree of operational proficiency (time utilization).

3.2 Analysis of the relationship between theoretical productivity and plot length

From the time consumption data of the plant protection unmanned aircraft in Table 1, the variation law of crew productivity and plot conditions can be derived according to the productivity model Equation 12. To study the effect of plot length on the productivity of each plant protection UAV, the width of the operating plot for each model in the study was calculated according to 20 operating strokes, and the plot lengths were calculated from 100, 300, 500, 700, 1,000, 1,500, 2,000, 2,500, 3,000, and 3,500 m. Combined with the data in Table 1 using Excel 2010 software to prepare the calculation program, the theoretical productivity of each model with the plot length variation law is shown in Figure 2.

Analysis of Figure 2 shows that the productivity of different models of plant protection UAVs increases with plot length on the 100–1,500-m interval, but the increase varies. When the block length reaches a certain value, the rate of increase in productivity slows down or even decreases slightly.

To derive the plot lengths corresponding to the maximum productivity of the different models, the curves in Figure 2 focused on the 100–1,500-m plot length interval to obtain the optimum plot lengths for the different models and their corresponding theoretical productivity, as shown in Table 4. Analysis of the data in Table 4 shows that the theoretical productivity of the plant protection unmanned aircraft can reach a maximum of 10.1 ha/h. The theoretical productivity of each model also varies greatly because

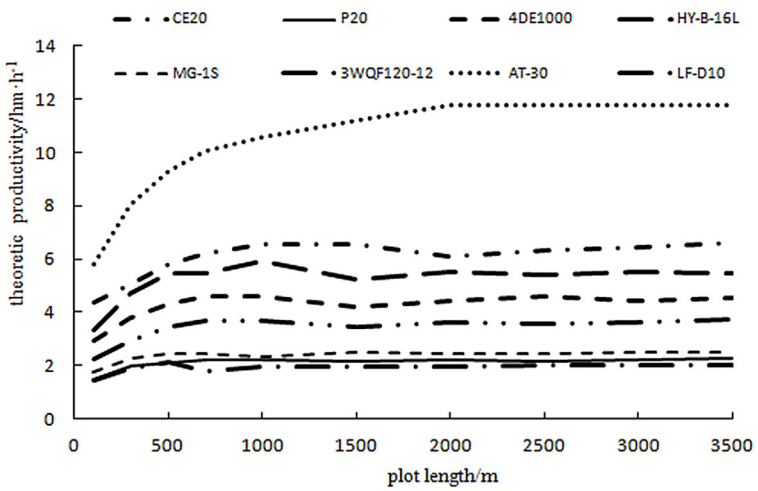

FIGURE 2
Curves of theoretical productivities at different plot lengths.

TABLE 4 Suitable plot lengths and the number of configurations for each model.

Model	Plot length/m	Theoretical productivity ha/h	Configuration quantity/rack·10,000 mu^{-1}
CE20	1,000–1,500	6.5	4
P20	700–1,000	2.2	9
AT-30	2,000–2,500	10.1	3
4DE1000	700–1,000	4.58	5
MG-1S	500–700	2.43	8
HY-B-16L	700–1,000	5.9	4
3WQF120-12	700–1,000	3.8	6
LF-D10	300–500	2.11	10

the theoretical productivity is related to the time of each statistical item in Table 1 and is more affected by key parameters such as spraying width, operating speed, and the tank capacity of the plant protection unmanned aircraft. However, theoretical productivity does not consider the differences in organizational coordination, staffing, and requirements of each model, and these parameters are important indicators of time utilization and labor productivity.

According to the operating area of 10,000 mu, the effective period of each pest control is calculated by 5 days, and each unit works 8 h/day; combined with the maintenance requirements of each model, Table 4 recommends the number of plant protection unmanned aircraft required for the operating area of 10,000 mu for different models.

3.3 Labor productivity improvement

From the model Equation 5, the productivity of plant protection UAVs is related to the spraying width, operating speed, and time utilization; the optimal spraying width and operating speed are determined for a specific plant protection UAV type to improve productivity only by the time utilization of the application operation. Model Equation 4 reveals that labor productivity is related to productivity and has an important relationship with the number of units configured; therefore, reducing the number of units is the most direct way to improve labor productivity.

As observed in Figure 3, with the advancement of the battery technology of electric UAVs and the reliability of oil-powered plant protection UAVs, the time utilization rate of electric plant protection UAVs increased from 43% in 2016 to 72.7% in 2020, and the labor productivity increased from 4.85 mu/person·h in 2016 to 56.4 mu/person·h in 2020. In contrast, the time utilization rate of oil-powered aircraft increased from 17.8% in 2016 to 86% in 2020, and labor productivity increased from 4.55 mu/person·h in 2016 to 63.5 mu/person·h in 2020. The reason for this is the high failure rate of the early oil-powered plant protection unmanned aircraft. The complex take-off and landing process leads to low efficiency, and with the reliability of the aircraft to improve the equipment control, and autonomous improvement, efficiency greatly improved.

4 Conclusion

1) This study determined the time composition of plant protection UAV application operations and established a mathematical model of the variation pattern of operational productivity and plot length.
2) The actual operational efficiency of plant protection UAV application is affected by the inherent performance of the crew and is closely related to the reasonable configuration of the crew's labor force, the level of organization and coordination of the crew, and the degree of operational proficiency (time utilization).
3) The optimal plot lengths of different types of plant protection UAVs and their corresponding theoretical productivity were obtained, and the number of UAVs required for each 10,000 mu of operating area was recommended.
4) As battery technology for electric UAVs and the reliability of oil-powered plant protection UAVs progressed, the time utilization of electric and oil-powered plant protection UAVs increased from 2016 to 2020.

The study conclusions obtained can support plant protection UAV enterprises to optimize equipment efficiency, provide evaluation methods for the operational efficiency assessment of plant protection UAVs, provide a reference for the selection of plant protection UAVs, and provide a basis for field planning.

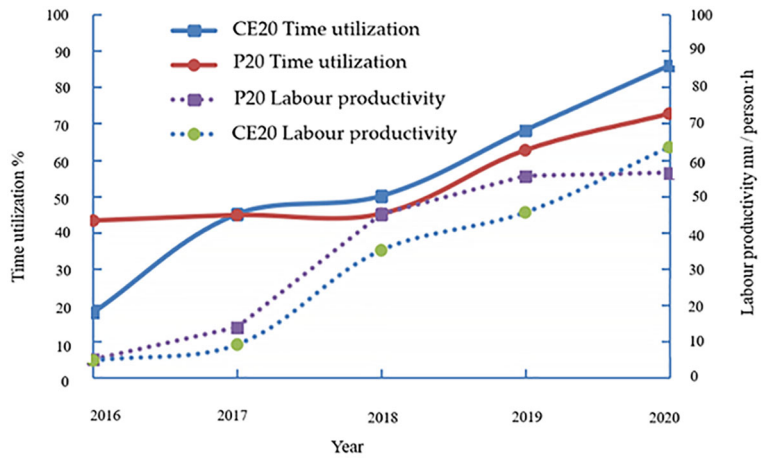

FIGURE 3
Production efficiency improvement.

Data availability statement

The original contributions presented in the study are included in the article/supplementary material. Further inquiries can be directed to the corresponding author.

Author contributions

WQ designed the study. WQ, PC, and BW performed most experiments. WQ analyzed the data and wrote the first draft of the manuscript. PC revised the manuscript. BW supervised the project and reviewed the manuscript. All authors contributed to the article and approved the submitted version.

Funding

This research was funded by the National Natural Science Foundation of China (Grant No. 31971804), Jiangsu Modern Agricultural Machinery Equipment and Technology Demonstration and Promotion Project (Grant No. NJ2022-17), Suzhou Agricultural Independent Innovation Project (SNG2022061), Suzhou Agricultural Vocational and Technical College Landmark Achievement Cultivation Project (CG[2022]02), and Natural Science Foundation of Jiangsu Province (Grant No. BK20191128).

Conflict of interest

The authors declare that the research was conducted in the absence of any commercial or financial relationships that could be construed as a potential conflict of interest.

Publisher's note

All claims expressed in this article are solely those of the authors and do not necessarily represent those of their affiliated organizations, or those of the publisher, the editors and the reviewers. Any product that may be evaluated in this article, or claim that may be made by its manufacturer, is not guaranteed or endorsed by the publisher.

References

Cao, G., Zhang, Q., Chen, C., Zhang, M., Zhang, J., and Huang, Y. (2019). Scheduling model of UAV plant protection team based on multi-objective optimization. *Trans. Chin. Soc Agric. Mach.* 50 (11), 92–101. doi: 10. 6041 /j.issn. 1000-1298. 2019. 11. 010

Carlton, J. B. (1999). Technique to reduce chemical usage and concomitant drift from aerial sprays: U. s. *Patent* 5, 975, 425, pp 08–15.

Chen, S., Lan, Y., Bradley, K. F., Jiyu, L. I., Aimin, L. I. U., and Yuedong, M. A. O. (2017a). Effect of wind field below rotor on distribution of aerial spraying droplet deposition by using multi-rotor UAV. *Trans. Chin. Soc Agric. Mach.* 48 (8), 105–113. doi: 10.6041/j.issn.1000-1298.2017.08.011

Chen, S., Lan, Y., Li, J., Xu, X., Wang, Z., and Peng, B. (2017b). Evaluation and test of effective spraying width of aerial spraying on plant protection UAV. *Trans. Chin. Soc Agric. Eng.* 33 (7), 82–0. doi: 10.11975/j.issn.1002-6819.2017.07.011

Feng, Y., and Yang, Q. (2014). Key research fields and basic directions of Chinese rural-land comprehensive consolidation in transitional period. *Trans. Chin. Soc Agric. Eng.* 30 (1), 175–182. doi: 10.3969/j.issn.1002-6819.2014.01.023

Kirk, I. W. (2003). "Electrostatic coalescence for aerial spray drift mitigation," in *National cotton council of America* (Nashville: Beltwide Cotton Conferences), 189–191.

Kirk, I. W., Hoffmann, W. C., and Carlton, J. B. (2001). Aerial electrostatic spray system performance. *Trans. ASAE* 44 (5), 1089–1092. doi: 10.13031/2013.6431

Lan, Y., Thomson, S. J., Huang, Y., Hoffmann, W. C., and Zhang, H. (2010). Current status and future directions of precision aerial application for site-specific crop management in the u. s. a. *Comput. Electron. Agric.* 74 (1), 34–38. doi: 10.1016/j.compag.2010.07.001

Lou, S. Y., Xue, X. Y., Gu, W., Cui, L. F., Xiao, H. T., and Tian, Z. (2017). Current status and trends of agricultural plant protection unmanned aerial vehicle. *J. Agric. Mech. Res.* 39 (12), 1–6. doi: 10.13427/j.cnki.njyi.2017.12.001

Qiao, J., Han, Z., Hong, K., Chen, H., Hao, Y., and Zhang, X. (2016). Variation of technology productivity of harvesting outfit along with site conditions. *Trans. Chin. Soc Agric. Eng.* 32 (7), 43–50. doi: 10.11975/j.issn.1002-6819.2016.07.006

Qin, W., Xue, X., Zhou, L., Zhang, S., Sun, Z., Kong, W., et al. (2014). Effects of spraying parameters of unmanned aerial vehicle on droplets deposition distribution of maize canopies. *Trans. Chin. Soc Agric. Eng.* 30 (5), 50–56. doi: 10.3969/j.issn.1002-6819.2014.05.007

Qiu, B., Wang, L., Cai, D., Wu, J., Ding, G., and Guan, X. (2013). Effects of flight altitude and speed of unmanned helicopter on spray deposition uniform. *Trans. Chin. Soc Agric. Eng.* 29 (24), 25–32. doi: 10.3969/j.issn.1002-6819.2013.24.004

Ru, Y., Jia, Z., Fan, Q., and Che, J. (2012). Remote control spraying system based on unmanned helicopter. *Trans. Chin. Soc Agric. Mach.* 43 (6), 47–52. doi: 10. 6041 /j. issn. 1000-1298. 2012. 06. 009

Standardization Administration of China. *GB/5667–2008 agricultural machinery production test methods*. Beijing: Standards Press of China, (2008).

Wang, C., He, X., Wang, X., Wang, Z., Pan, H., and He, Z. (2016a). Testing method of spatial pesticide spraying deposition quality balance for unmanned aerial vehicle. *Trans. Chin. Soc Agric. Eng.* 32 (11), 54–61. doi: 10.11975/j.issn.1002-6819.2016.11.008

Wang, C., He, X., Wang, X., Wang, Z., Wang, S., Li, L., et al. (2016b). Distribution characteristics of pesticide application droplets deposition of unmanned aerial vehicle based on testing method of spatial quality balance. *Trans. Chin. Soc Agric. Eng.* 32 (24), 89–97. doi: 10.11975/j.issn.1002-6819.2016.24.012

Xu, B., Chen, L., Xu, M., and Tan, Y. (2017). Path planning algorithm for plant protection UAVs in multiple operation areas. *Trans. Chin. Soc Agric. Mach.* 48 (2), 75–81. doi: 10.6041/j.issn.1000-1298.2017.02.010

Xue, X., and Lan, Y. (2013). Agricultural aviation applications in USA. *Trans. Chin. Soc Agric. Mach.* 44(5), 194–201. doi: 10. 6041/j.issn.1000-1298.2013.05.034

Yang, X., Xinyu, X., Zhu, S., Chun, C., Wei, G., Chen, C., et al. (2019). Online spraying quality assessment system of plant protection unmanned aerial vehicle based on android client. *Comput. Electron. Agric.* 166, 104938. doi: 10.1016/j.compag.2019.104938

Yang, Z., Zheng, L., Li, M., Yang, W., and Sun, H. (2017). Matching algorithm for plant protecting unmanned aerial vehicles and plant protecting jobs based on r-tree spatial index. *Trans. Chin. Soc Agric. Eng.* 33 (Supp.1), 92–98. doi: 10. 11975/j.issn.1002-6819.2017.z1.014

Zhang, M., Li, T., Luo, W., Pu, P., Wang, C., and Zhu, X. (2021). Quality of plant protection drone operations and their evaluation of the effectiveness of plant protection against corn borer. *China Plant Prot.* 41 (06), 66–69. doi: 10. 3969/j.issn.1672-6820.2021.06.013

Zhang, S., Xue, X., Qin, W., Sun, Z., Ding, S., and Zhou, L. (2015). Simulation and experimental verification of aerial spraying drift on n-3 unmanned spraying helicopter. *Trans. Chin. Soc Agric. Eng.* 31 (3), 87–93. doi: 10.3969/j.issn.1002-6819.2015.03.01

Zhu, H., Jiang, Y., Li, H., Li, J., and Zhang, H. (2019). Effects of application parameters on spray characteristics of multi-rotor UAV. *Int. J. Precis. Agric. Aviat.* 2 (1), 18–25. doi: 10.33440/j.ijpaa.20190201.0025

frontiers | Frontiers in Plant Science

TYPE Original Research
PUBLISHED 19 April 2023
DOI 10.3389/fpls.2023.1164200

OPEN ACCESS

EDITED BY
Xiaolan Lv,
Jiangsu Academy of Agricultural Sciences (JAAS), China

REVIEWED BY
Agnieszka Synowiec,
University of Agriculture in Krakow, Poland
Pei Wang,
Southwest University, China
Cui Longfei,
Ministry of Agriculture and Rural Affairs, China

*CORRESPONDENCE
Chen Gong
gcld2017@ujs.edu.cn
Can Kang
kangcan@ujs.edu.cn

SPECIALTY SECTION
This article was submitted to Sustainable and Intelligent Phytoprotection, a section of the journal Frontiers in Plant Science

RECEIVED 12 February 2023
ACCEPTED 27 March 2023
PUBLISHED 19 April 2023

CITATION
Gong C, Chen F and Kang C (2023) Theoretical and experimental studies on the oil-based emulsion spray.
Front. Plant Sci. 14:1164200.
doi: 10.3389/fpls.2023.1164200

Theoretical and experimental studies on the oil-based emulsion spray

Chen Gong[1]*, Fujun Chen[1] and Can Kang[2]*

[1]School of Agricultural Engineering, Jiangsu University, Zhenjiang, China, [2]School of Energy and Power Engineering, Jiangsu University, Zhenjiang, China

Oil-based emulsion is a common herbicide formulation in agricultural spray, and its atomization mechanism is different from that of water spray. In this paper, a theoretical model based on the characteristics of spray sheets was proposed to predict the spray droplet size for oil-based emulsion spray. An image processing method was used to measure droplet size distributions for different spray pressures and nozzle configurations, and the measured results were used to validate the theoretical model. The results show that oil-based emulsion spray is characterized by the web structure constituted by perforations. The liquid originally occupied by spray sheets eventually gathers in these web structures. The proposed theoretical model is based on the size of the nozzle exit, the angle of spray sheets, and the perforation number in the web structure, which are relatively easy to obtain. The theoretical droplet size is in inverse proportion to the square root of the perforation number in the web structure while in proportion to the square root of the area of the nozzle exit. The captured images of spray sheets and the measured droplet size distribution show consistency with the theoretical prediction. The difference between theoretical results and measured volumetric median diameter is less than 10% for different spray pressures and nozzles.

KEYWORDS

oil-based emulsion spray, theoretical model, sheet structure, image processing, nozzle configuration

1 Introduction

The flat-fan spray is a commonly used method to deliver agricultural chemicals and control weeds in agricultural production (Kalsing et al., 2018; Qin et al., 2021; Gong et al., 2022). The spray characteristics of the flat-fan nozzle have been widely studied; however, most of them are focused on experimental measurement of droplet characteristics (Ellis et al., 2021; Perine et al., 2021; Szarka et al., 2021). Theoretical research for the flat-fan spray, especially as agricultural chemicals are used, is limited.

Different from the cylindrical liquid jet, the fat-fan spray has a complex geometry that makes it difficult to find simplified assumptions (Lefebvre, 1989). Nonetheless, there have been some attempts to establish a theoretical model to describe the atomization process and

forecast the droplet size of the flat-fan spray (Kashani et al., 2018; Asgarian et al., 2020). For water spray, the most common theoretical model is termed the "wave model", which was first proposed by Fraser et al. (1962). This model has been widely studied and improved until recent years (Kooij et al., 2018; Post and Hewitt, 2018). The wave model has featured a wave-like structure, which is supposed to be caused by the velocity difference between gas and liquid at the interface (Shao et al., 2018). These wave-like structures are amplified by the Rayleigh–Taylor destabilization, and it introduces the thickness modulations of a liquid sheet (Kooij et al., 2018). It eventually leads to the breakup of the liquid sheet as the local thickness is thin enough. For water spray, the wave model is validated by good prediction of the droplet size (Post and Hewitt, 2018). However, the wave model may be not suitable, as agricultural chemicals are used. Many works indicated that the droplet characteristics of oil-based emulsion spray are significantly different from those of water spray even when the percentage of active ingredients of the chemical in the spraying liquid is only 0.1% (Lin et al., 2016; Carvalho et al., 2017).

Oil-based emulsion is a common herbicide formulation that has an obviously different atomization process from that associated with water spray (Gong et al., 2020; Gong et al., 2021). In general, the perforations in the liquid sheet are supposed to be the feature structure of an oil-based emulsion spray (Hilz, 2013; Vernay, 2015). It is argued that the generation of perforation has a close relationship with the characteristics of oil droplets in the oil-based emulsion solution (Hilz et al., 2012; Cryer and Altieri, 2017; Cryer et al., 2021). Once perforations are generated, they will expand due to the surface tension (Vernay et al., 2017). With the development of the perforations, they will eventually meet each other, and their borders will coalesce into ligaments (Li et al., 2021). The perforations are supposed to cause an early breakup of the liquid sheet; therefore, oil-based emulsions have larger droplet sizes compared with those of water spray (Carvalho et al., 2017; Alves et al., 2018). Meanwhile, perforations in the spray sheets can balance the pressure difference between the two sides of the liquid sheet; therefore, the amplitude of wave-like structures is suppressed (Gong et al., 2020). As a result, less loss of kinetic energy is caused by the flapping of the spray sheet, and spray droplets have higher velocity when compared with water spray (Cloeter et al., 2010; Hilz and Vermeer, 2013). Based on the review above, it can be concluded that oil-based emulsion spray has an obviously different atomization process and feature structure from those of water spray. Research related to oil-based emulsion spray is limited; as far as we know, only Altieri and their colleagues have made some attempts to establish a theoretical model to describe the atomization process (Altieri et al., 2014; Altieri and Cryer, 2018). Their models are based on the development of perforations; therefore, the position and diameter of the primary perforations are of vital importance. However, as indicated by Altieri and Cryer (2018), these parameters are difficult to obtain since the mechanism of perforation nucleation is unknown. Undoubtedly, these works provide inspiration for further research.

In this paper, a theoretical model based on web structure was proposed to predict the droplet size of an oil-based emulsion spray. The number of perforations in the web structure and spray droplet sizes of the primary breakup were measured based on image processing methods. The theoretical and experimental results were compared and discussed for different spray pressures and nozzle configurations.

2 Materials and methods

2.1 Capture of spray sheet

The physical information of spray sheets is the foundation of a theoretical model. Therefore, as shown in Figure 1A, an experimental system was built to capture the liquid sheet of oil-based emulsion spray. The oil-based emulsion solutions were prepared and stored in the pressure vessel and pressured by an air compressor. The oil-in-water emulsion solution was prepared with water and commercial butachlor (Jiangsu Lvlilai Co., Kunshan, Jiangsu, China). The main composition is as follows: 60% w/w butachlor, 15% w/w cyclohexanone (dissolvant), 9% w/w styrylphenyl polyoxyethylene ether (emulsifiers), and 6% w/w sodium alkylbenzene sulfonate (emulsifiers). The volumetric concentration of the commercial butachlor in the solution is 0.1%. The size distribution of oil droplets in an oil-based emulsion solution was measured using the Malvern particle size analyzer (type: Zetasizer Nano ZS90), and the result is shown in Figure 2. A pressure valve (SMC AR-3000, SMC China Co., China; accuracy of 0.02 MPa) was used to regulate the spray pressure. Three spray pressures, namely, 0.1, 0.3, and 0.5 MPa, were selected

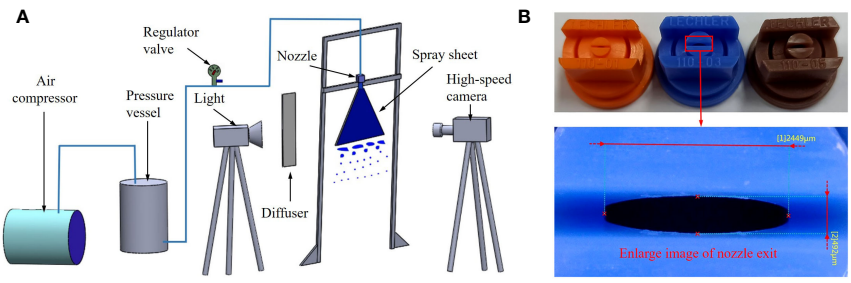

FIGURE 1
(A) Schematic view of experimental apparatus. **(B)** Nozzle image and enlarged image of nozzle exit.

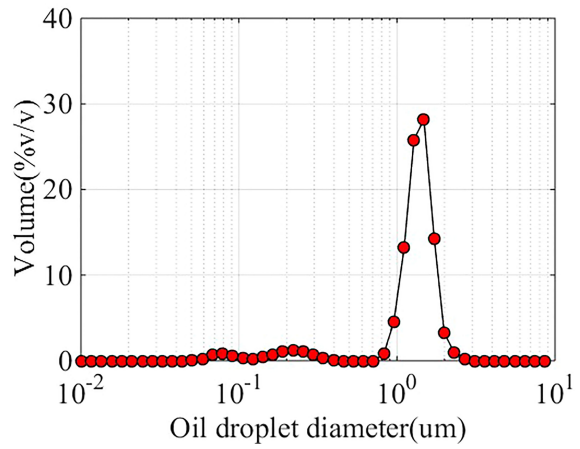

FIGURE 2
Size distribution of oil droplet in oil-based emulsion solution.

in the experiments. After the pressurized liquid passes through the nozzle, a spray is produced. Three standard flat-fan nozzles, ST-110-01, ST-110-03, and ST-110-05 (Lechler Inc., Germany), were used in the experiments. As shown in Figure 1B, the long diameter (N_L) and shorter diameter (N_s) If the discharge orifice of the nozzles were measured using a microscope (VHX-900F, Keyence Co., Japan) with a magnification factor of 50, and the measured results are listed in Table 1.

The spray sheets and droplets were captured using an Olympus i-Speed TR high-speed camera and a macro lens (Tokina Macro 100 F 2.8 D, Olympus Co., Japan). A backlit-imaging arrangement was adopted, and a diffuser was mounted between the light source and the spray sheets to ensure a uniform light distribution over the monitored plane. The exposure time of the camera was set to 2.16 μs, and the frame rate was set to 2,000 fps (frame per second). The resolution of the captured images was 1,280 × 1,024 pixels.

2.2 Measurement of spray sheet

A typical image of the sheet structure of an oil-based emulsion spray is presented in Figure 3. After the spray liquid leaves the nozzle exit, it first forms a flat-fan sheet, and then perforations are generated in the sheet. With the development of perforations, they contact each other and form a web-like structure. Eventually, these web structures break up into ligaments and droplets.

An image processing method was proposed to measure the perforation number in web structures. Images are constructed based on digital information representing image intensities. The digital information essentially reflects the morphological characteristics of the flow structures. In the spray image, the image intensities of the liquid and the background air are different. Based on this principle, the edges of web structures and air can be identified by processing the image intensities. As indicated in Figure 4A, at the radial distance where the web structure is located, a red line is plotted along the circular arc. The image intensities of the pixels on this red line were measured through a commercial image analysis code Image Pro Plus, and the results are plotted in Figure 4B. Due to reflection and refraction, the pixels of the liquid show low image intensities relative to those of the air. Therefore, as indicated in Figure 4, once the red line passes through an edge of the web structure, there will be a trough of wave on the curve of image intensity. Based on the commercial code MATLAB (Cai, 2020), a digital signal processing method was designed to count the number of wave troughs; therefore, perforation numbers in web structure can be obtained. Under the same experimental condition, 20 images were processed. The average result obtained based on these 20 images was obtained to determine the perforation number.

TABLE 1 Structural parameters of different nozzle exits.

	Long diameter N_L/μm	Short diameter N_s/μm
ST-110-01	1,450	242
ST-110-03	2,449	492
ST-110-05	2,944	695

2.3 Measurement of droplet size

Light transmittance of the oil-based emulsion solution is different from that of water; therefore, the droplet size measurement based on light diffusion or refraction may cause errors (Sijs et al., 2021). Here, we measure droplet sizes based on image processing. In order to measure the primary diameter of the spray droplet, the position of the sampling window is set as close as possible to the breakup position of the spray sheet. The size of the sampling window is 10 × 10 mm. A typical raw image within a sampling window is shown in Figure 5(1); spray droplets distribute in different depths of the field. The droplets that are not on the focal plane (indicated with blue arrows) should be filtered. In order to remove those noises, the initial raw image was enhanced using the Retinex algorithm, and then the Otsu algorithm was selected to determine the image intensity threshold and achieve a binarization image. After that, the binarization image was reversed, then the noise was filtered, and the image was padded. Eventually, the pre-processed image of spray droplets was obtained (Figure 5(6)). The boundary of the spray droplets was detected and extracted using the Bwlabel function, and then the droplets were measured with the Regionprops function (Cai, 2020). In order to ensure enough samples and reduce random error, multiple images of different times were processed and measured. In this paper, the number of samples (spray droplets) is more than 5,000 for each experimental condition.

3 Results and discussion

3.1 Theoretical model

Based on the image of the spray sheets shown in Figure 3, it is found that the web structures are the final structures prior to the

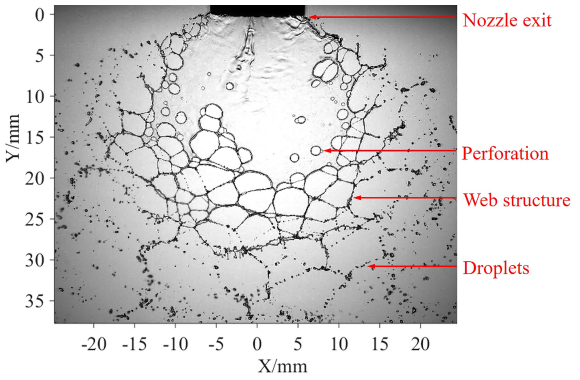

FIGURE 3
Sheet structure of oil-based emulsion spray.

breakup of the liquid sheet. Therefore, it can be inferred that all the liquid occupied by the sheet will finally gather at the edges of the web structures. Furthermore, the diameter of the edges determines the initial size of ligaments and droplets. We proposed a theoretical model that is based on web structure to forecast droplet sizes. The sheet structure is simplified and plotted in Figure 6. The point of intersection of the sheet edges is defined as the theoretical origin. The circles are used to represent the perforations, and the web structure region consists of multiple perforations with different diameters. The average position of the centers of these circles is indicated with a red dash curve, as shown in Figure 6.

The original liquid volume of the web structure region is defined as V_1,

$$V_1 = \bar{L}\,\bar{W}\,\bar{\tau}, \tag{1}$$

where $\bar{W}$, $\bar{L}$ and $\bar{\tau}$ denote the average width, the average length, and the average sheet thickness, respectively, of the web structure region.

Here, the arc length of the red dash curve was used to represent the average length of the web structure region and is expressed by the following:

$$\bar{L} = \frac{\pi X\theta}{180}, \tag{2}$$

where X represents the radial distance between the red dash curve and the theoretical origin. θ denotes the angle of the spray sheet.

The average diameter of the perforations was used to represent the average width of the web structure region:

$$\bar{W} = \frac{D_1 + D_2 \ldots + D_n}{N} \tag{3}$$

where D_1, $D_2 \ldots D_n$ denote the diameters of the perforations. N denotes the number of perforations.

The perforations are tangent; therefore,

$$D_1 + D_2 \ldots + D_n = \bar{L}. \tag{4}$$

The sheet thickness decreases as the sheet moves away from the nozzle. According to Altieri et al. (2014) and Fraser et al. (1962), there is a relationship between sheet thickness and radial distance:

$$\tau = \frac{\kappa}{X}, \tag{5}$$

where k is the spray parameter. It is related to the nozzle dimension and spray angle:

$$k = \frac{N_L \tau_n}{2\sin(\theta/2)}, \tag{6}$$

where N_L is the long diameter of the nozzle exit and τ_n is the sheet thickness at the nozzle exit, which is equal to the short diameter N_s if the nozzle exit.

Combining Eqs. 1–6 yields

$$V_1 = \frac{\pi X\theta}{180}\,\frac{\pi X\theta}{180N}\,\frac{N_L N_S}{2X\sin(\theta/2)} = \frac{\pi^2\theta^2 N_L N_S X}{64,800N\sin(\theta/2)}, \tag{7}$$

The liquid volume, V_2, in the edges of the web structures is defined as follows:

$$V_2 = \bar{S}L_s, \tag{8}$$

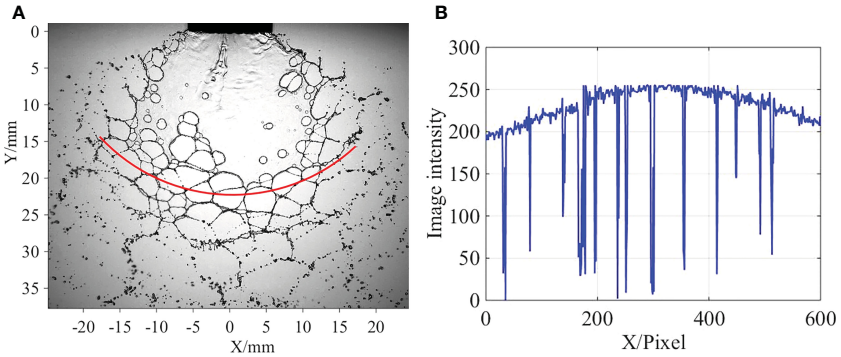

FIGURE 4
Measurement of perforation number in web structure. **(A)** Red line indicates the positions where image intensities of pixels were measured. **(B)** Variation of image intensity.

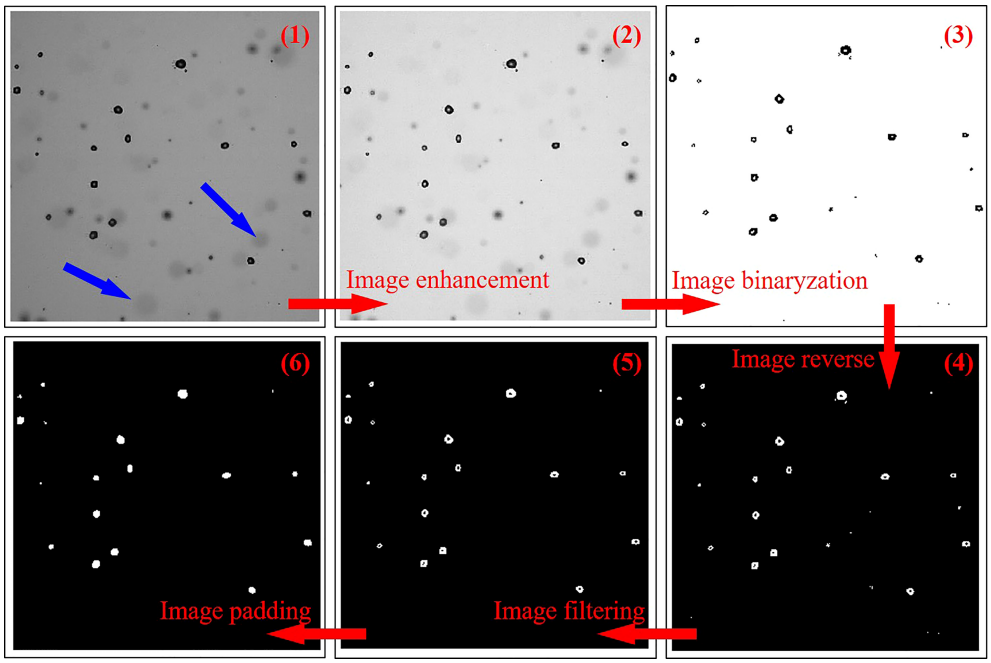

FIGURE 5
Image processing method.

where $\bar{S}$ denotes the average cross-section area of edges of the web structure and L_s denotes the total length of edges of the web structure.

Suppose the edges of the web structure have circular cross sections:

$$S = \pi R_s^2, \tag{9}$$

where R_s denotes the average radius of circular cross sections.

The total length of the edges of the web structures is equal to half the total perimeter of the perforations since two perforations share one edge.

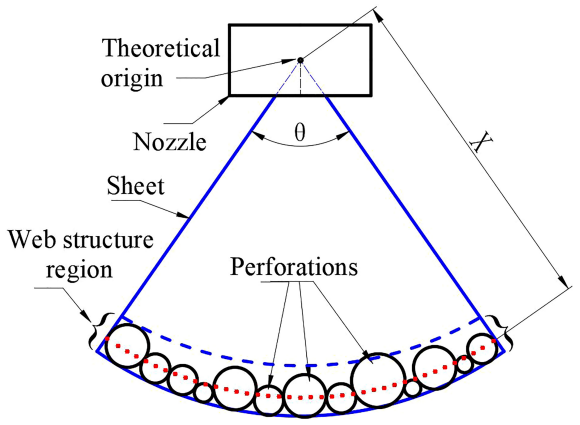

FIGURE 6
Theoretical schematic view of oil-based emulsion spray.

$$L_s = 0.5\pi(D_1 + D_2 \ldots + D_n). \tag{10}$$

Combining Eqs. 8–10 yields

$$V_2 = \pi R_s^2\, 0.5\pi(D_1 + D_2 \ldots + D_n) = 0.5\pi^2 R_s^2 \frac{\pi X\theta}{180}. \tag{11}$$

Assume that all the liquid that was originally contained in the perforations now resides in the edges of web structures. Based on mass conservation,

$$\rho V_1 = \rho \frac{\pi^2\theta^2 N_L N_S X}{64,800 N \sin(\theta/2)} = \rho 0.5\pi^2 R_s^2 \frac{\pi X\theta}{180} = \rho V_2, \tag{12}$$

where ρ denotes the density of spray liquid.

Based on Eq. 12, the diameter of the edge of the web structure can be calculated as follows:

$$D_s = 2R_s = 2\sqrt{\frac{\theta N_L N_S}{180\pi N \sin(\theta/2)}}. \tag{13}$$

The image of the spray sheets indicates that the diameter of the primary droplets has a similar size to the edge of the web structure. Therefore, D_s is used to characterize the primary diameter of spray droplets.

3.2 Comparison with experimental results

From Eq. 13, it can be deduced that the theoretical diameter is determined by the size of the nozzle exit, the angle of spray sheets, and the number of perforations in the web structure. These parameters have a close relationship with nozzle configuration and spray pressure. Therefore, the theoretical results for different

spray pressures and nozzle configurations were estimated and validated through measured results.

First, the effects of the spray pressure are discussed. Three typical spray sheets obtained at different spray pressures are presented in Figure 7. For the angle of the spray sheet, it increases with spray pressure; however, the increasing ratio decreases. After the spray liquid is ejected from the nozzle, the liquid sheet expands along a spanwise direction due to the configuration of the flat-fan nozzle exit. The higher the spray pressure, the higher the kinetic energy, and the larger the angle of the spray sheet. Meanwhile, limited by the nozzle configuration, the increase of the angle of the spray sheets attenuates as it attains a critical value. For the perforations in the web structure, the number increases, but the average size decreases with increasing spray pressure. It is proposed that the vortices and rollup motion may thus excite the movement of liquid at different positions, causing the oil droplets in the emulsion to interact with each other, and larger oil droplets are thereby produced (Gong et al., 2020). Large oil droplets are more likely to generate perforations (Cryer and Altieri, 2017); therefore, the number of perforations increases with spray pressure. Due to the increase in the perforation number, perforations come into contact much more easily. Consequently, the development of the perforations will be resisted by adjacent perforations. Therefore, the average size of the perforations in the web structure decreases.

Based on the measured angle of the spray sheets and the number of perforations in the web structure, the theoretical results are estimated and presented in Table 2. The theoretical values decrease with the spray pressure. Thin spray sheets and small perforations are responsible for the decrease in theoretical data. The liquid at the edges of the web structure is supposed to come from the liquid, which was originally contained in the perforations (Fraser et al., 1962). Alternatively, the area of the perforation and the thickness of local spray sheets where the perforation is located determine the size of the edges of the web structure. As shown in Figure 7, the average size of perforations decreases with spray pressure. Meanwhile, the area of the spray sheets increases with spray pressure; therefore, the thickness of the spray sheets decreases. The theoretical data are in accordance with the experimental results.

The spray droplet distributions measured with the developed image processing method are presented in Figure 8. With the increase of the spray pressure, the distribution of droplets moves from a large size zone to a smaller size zone. The volumetric droplet size metrics D_{V10}, D_{V50}, and D_{V90} also decrease with spray pressure. The theoretical results are close to the volumetric median diameter D_{V50}. The difference between theoretical results and the measured volumetric median diameters is less than 10% for different spray pressures. The volumetric median diameter D_{V50} is commonly used to characterize the general size of spray droplets in agriculture (Miranda-Fuentes et al., 2018). It is indicated that the theoretical model can well predict the droplet size of oil-based emulsion spray at different spray pressures.

Three typical spray sheets for different nozzle configurations are presented in Figure 9. The nozzle configuration has a significant effect on the spray sheet. Typically, for the ST-110-01 nozzle, the spray sheets break up earlier in both streamwise and spanwise directions. The spray sheets have no apparent boundary; therefore, the angle of the spray sheets was estimated based on the trajectory of spray droplets at the two edges of the spray sheet. Generally, the angles of the spray sheets discharged from the three nozzles have no significant difference. However, the area of spray sheets obviously increases with the size of the nozzle exit. The thickness of the primary spray sheets is determined by the size of the nozzle exit, and the spray sheets associated with the ST-110-01 nozzle have a

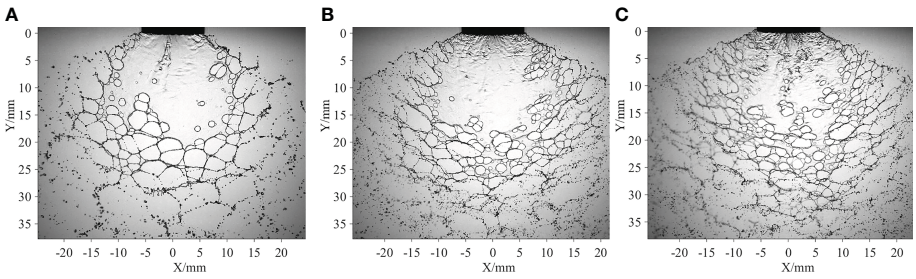

FIGURE 7
Spray sheets at different spray pressures. The spray sheets are produced by the ST-110-03 nozzle, and the volumetric concentration of the oil-based emulsion is 0.1%. **(A)** P=0.1 MPa **(B)** P=0.3 MPa **(C)** P=0.5 MPa.

TABLE 2 Theoretical results at different spray pressures.

Spray pressure (P/MPa)	Measured angle of the spray sheets (θ)	Measured number of perforations (N)	Estimated theoretical diameter (D_s/um)
0.1	119.68 ± 1.49	19.6 ± 1.90	237.80
0.3	127.10 ± 2.34	29.7 ± 2.45	195.63
0.5	129.84 ± 1.60	42.6 ± 4.21	164.15

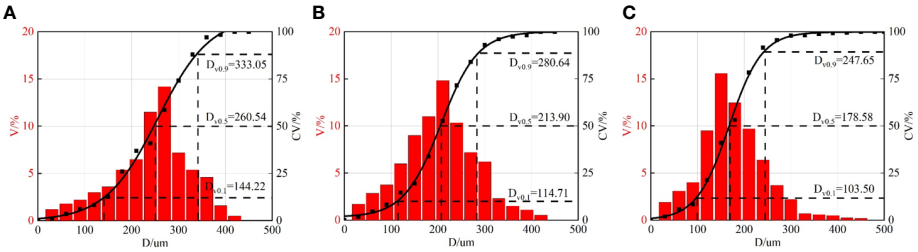

FIGURE 8
Droplet distributions at different spray pressures. V% denotes percentage of volume of droplets of different sizes. CV% denotes cumulative volume of droplets. **(A)** 0.1 MPa **(B)** 0.3 MPa **(C)** 0.5 MPa.

relatively small thickness. Therefore, the oil droplets in the spray liquid are much easier to reach the interface of spray sheets (Cryer and Altieri, 2017). As a result, the perforations are generated at the positions close to the nozzle exit. Accordingly, the spray sheets break up earlier, and the area is small. For the perforations in the web structure, the number increases with the size of the nozzle exit. A possible reason is that the flow rate increases with the size of the nozzle exit, more oil droplets are contained in the spray sheets, and the probability that oil droplets interact with each other and the formation of larger droplets is high. Large oil droplets are efficient in terms of causing perforations (Vernay, 2015). Accordingly, the spray sheets of the ST-110-05 nozzle involve more perforations.

The measured angle of the spray sheet, the number of perforations in the web structure, and the theoretical results for different nozzles are presented in Table 3. Theoretical values increase with the size of the nozzle exit. The diameter of ligaments is supposed to have a close relationship with the thickness of spray sheets at the position where the sheet breaks up. The sheet thickness is in proportion to the area of the nozzle exit while in inverse proportion to the radial distance (Altieri et al., 2014). From Figure 9, it can be inferred that the breakup length of the spray sheets of the ST-110-01 nozzle is about half of that of the ST-110-03 nozzle and one-third of that of the ST-110-05 nozzle. However, based on the measured results shown in Table 1, the area of the nozzle exit of the ST-110-03 nozzle is three times more than that of the ST-110-01 nozzle, while the area of the nozzle exit of the ST-110-05 nozzle is nearly six times that of the ST-110-01 nozzle. Therefore, the ST-110-05 nozzle has a larger theoretical diameter.

Similarly, the spray droplet distributions for different nozzles are measured and presented in Figure 10. In general, the experimental results are in accordance with the theoretical prediction. Furthermore, the theoretical results are close to the volumetric median diameters. The maximum difference between theoretical and experimental results is less than 10% for different nozzles. The difference might be due to the simplification of the spray structure. The structure of spray sheets varies with time; some simplifications are needed so as to establish a theoretical model. In our model, circles are used to represent the perforations, and spray droplets are assumed to have a spherical shape. In practice, perforations have complex structures, and some of the spray droplets are not spherical, and these reasons might bring some errors.

4 Conclusions

A theoretical model was proposed to predict the droplet size of oil-based emulsion spray. The droplet size distributions under different experimental conditions were measured with a developed image processing method, and the measured results were used to validate the theoretical model. Major conclusions drawn from the study are as follows:

1) The web structure constituted by perforations is the typical structure before the breakup of the liquid sheet of oil-based emulsion spray. The liquid originally occupying the sheet eventually gathers at the edges of the web structures. The

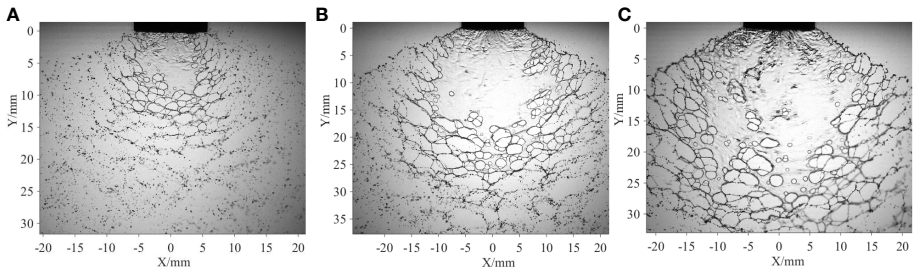

FIGURE 9
Spray sheets for different nozzles. The spray pressure is 0.3 MPa, and the volumetric concentration of the oil-based emulsion is 0.1%. **(A)** ST-110-01 **(B)** ST-110-03 **(C)** ST-110-05.

TABLE 3 Theoretical results at different nozzle configurations.

Nozzles	Measured angle of the spray sheets (θ)	Measured number of perforations (N)	Estimated theoretical diameter (D_s/um)
ST-110-01	121.69 ± 1.90	18.9 ± 1.65	135.31
ST-110-03	127.10 ± 2.34	29.7 ± 2.45	195.63
ST-110-05	126.25 ± 2.00	38.2 ± 3.02	231.63

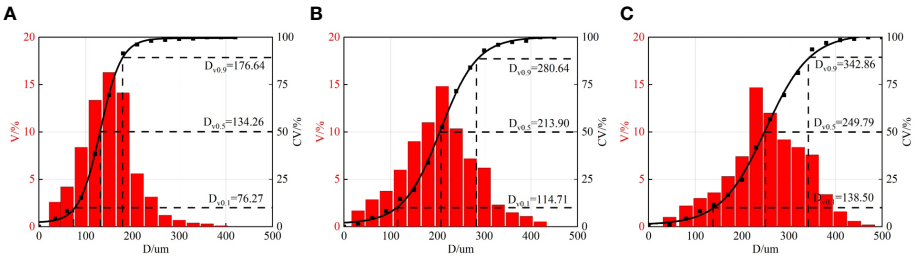

FIGURE 10
Droplet distributions for different nozzles. V% denotes percentage of volume of droplets of different sizes. CV% denotes cumulative volume of droplets. **(A)** ST-110-01 **(B)** ST-110-03 **(C)** ST-110-05.

dimension of the edges of the web structures determines the primary size of ligaments and droplets produced with the breakup of the spray sheet.

2) The proposed theoretical model is based on the size of the nozzle exit, the angle of the spray sheets, and the perforation number in the web structure. These parameters are relatively convenient to obtain by measuring the nozzle and the spray sheet. The theoretical model indicates that the droplet size is in proportion to the square root of the area of the nozzle exit while in inverse proportion to the square root of the perforation number in the web structure.

3) The experimentally captured images of spray sheets for different spray pressures and nozzles show that the theoretical results are well consistent with the experimental results under different experimental conditions. The theoretical results are close to the volumetric median diameter of the measured results. The difference between theoretical and experimental results is less than 10% for different spray pressures and nozzles.

Data availability statement

The original contributions presented in the study are included in the article/supplementary material. Further inquiries can be directed to the corresponding authors.

Author contributions

CG: Methodology, Writing-Original draft preparation. FC: Image processing. CK: Conceptualization, Writing-Review and Editing. All authors contributed to the article and approved the submitted version.

Acknowledgments

The authors gratefully acknowledge the financial support of the National Natural Science Foundation of China (No. 51905220), China Postdoctoral Science Foundation (Nos. 2019M661755 and 2020T130259), and Priority Academic Program Development of Jiangsu Higher Education Institutions (No. PAPD-2018-87).

Conflict of interest

The authors declare that the research was conducted in the absence of any commercial or financial relationships that could be construed as a potential conflict of interest.

Publisher's note

References

Altieri, A. L., and Cryer, S. A. (2018). Break-up of sprayed emulsions from flat-fan nozzles using a hole kinematics model. *Biosyst. Eng.* 169, 104–114. doi: 10.1016/j.biosystemseng.2018.02.006

Altieri, A., Cryer, S. A., and Acharya, L. (2014). Mechanisms, experiment, and theory of liquid sheet breakup and drop size from agricultural nozzles. *Atomization Sprays* 24 (8), 695–721. doi: 10.1615/AtomizSpr.2014008779

Alves, G. S., Kruger, G. R., and da Cunha, J. P. A. R. (2018). Spray drift and droplet spectrum from dicamba sprayed alone or mixed with adjuvants using air-induction nozzles. *Pesquisa Agropecuária Bras.* 53 (6), 693–702. doi: 10.1590/S0100-204X2018000600005

Asgarian, A., Heinrich, M., Schwarze, R., and Bussmann, M. (2020). Experiments and modeling of the breakup mechanisms of an attenuating liquid sheet. *Int. J. Multiphase Flow* 130, 103347. doi: 10.1016/j.ijmultiphaseflow.2020.103347

Cai, L. M. (2020). *MATLAB image processing theory, algorithm and case analysis* (Beijing: Tsinghua).

Carvalho, F. K., Antuniassi, U. R., Chechetto, R. G., Mota, A. A. B., de Jesus, M. G., and de Carvalho, L. R. (2017). Viscosity, surface tension and droplet size of sprays of different formulations of insecticides and fungicides. *Crop Prot.* 101, 19–23. doi: 10.1016/j.cropro.2017.07.014

Cloeter, M. D., Qin, K., Patil, P., and Smith, B. G. (2010). "Planar laser induced fluorescence (PLIF) flow visualization applied to agricultural spray nozzles with sheet disintegration; influence of an oil-in-water emulsion," in *ILASS-Americas 22nd Annual Conference on Liquid Atomization and Spray Systems*(Cincinnati, OH). Available at: http:// www.ilass.org/2/ConferencePapers/ILASS2010-161.PDF.

Cryer, S. A., and Altieri, A. L. (2017). Role of large inhomogeneities in initiating liquid sheet breakup in agricultural atomization. *Biosyst. Eng.* 163, 103–115. doi: 10.1016/j.biosystemseng.2017.08.020

Cryer, S. A., Altieri, A. L., Schmucker, A. L., and Day, K. M. (2021). Minimising atomisation drift potential by exploring the break-up of liquid sheets using multiphase methylated soybean and silicon oil emulsions. *Biosyst. Eng.* 202, 142–151. doi: 10.1016/j.biosystemseng.2020.12.004

Ellis, M. C. B., Lane, A. G., O'Sullivan, C. M., and Jones, S. (2021). Wind tunnel investigation of the ability of drift-reducing nozzles to provide mitigation measures for bystander exposure to pesticides. *Biosyst. Eng.* 202, 152–164. doi: 10.1016/j.biosystemseng.2020.12.008

Fraser, R. P., Eisenklam, P., Dombrowski, N., and Hasson, D. (1962). Drop generation from rapidly moving liquid sheets. *AIChE J.* 8, 672–680. doi: 10.1002/aic.690080522

Gong, C., Kang, C., Jia, W. D., Yang, W. T., and Wang, Y. L. (2020). The effect of spray structure of oil-based emulsion spray on the droplet characteristics. *Biosyst. Eng.* 198, 78–90. doi: 10.1016/j.biosystemseng.2020.08.001

Gong, C., Li, D. Y., and Kang, C. (2022). Visualization of the evolution of bubbles in the spray sheet discharged from the air-induction nozzle. *Pest Manage. Sci.* 78 (12), 5347–5357. doi: 10.1002/ps.6803

Gong, C., Li, D. Y., Kang, C., and Wang, Y. L. (2021). Visualisation of the evolution of perforations in oil-based emulsion sheets formed by flat-fan spray nozzles. *Biosyst. Eng.* 207, 68–80. doi: 10.1016/j.biosystemseng.2021.04.005

Hilz, E. (2013). *Atomization of dilute oil-in-water emulsions during application of crop protection products* (The Netherlands: Ph.D. dissertation, Wageningen University). Available at: https://edepot.wur.nl/258158.

Hilz, E., and Vermeer, A. W. P. (2013). Spray drift review: the extent to which a formulation can contribute to spray drift reduction. *Crop Prot.* 44, 75–83. doi: 10.1016/j.cropro.2012.10.020

Hilz, E., Vermeer, A. W. P., Stuart, M. A. C., and Leermakers, F. A. M. (2012). Mechanism of perforation based on spreading properties of emulsified oils. *Atomization Sprays* 22 (12), 1053–1075. doi: 10.1615/AtomizSpr.2013006728

Kalsing, A., Rossi, C. V. S., Lucio, F. R., Zobiole, L. H. S., da Cunha, L. C. V., and Minozzi, G. B. (2018). Effect of formulations and spray nozzles on 2,4-d spray drift under field conditions. *Weed Technology*. 32, 379–384. doi: 10.1017/wet.2018.18

Kashani, A., Parizi, H., and Mertins, K. H. (2018). Multi-step spray modelling of a flat-fan atomizer. *Comput. Electron. Agric.* 144, 58–70. doi: 10.1016/j.compag.2017.11.005

Kooij, S., Skis, R., Denn., M. M., Villermaux, E., and Bonn, D. (2018). What determines the drop size in sprays? *Physical review X* 8, 3, 031019–031013. doi: 10.1103/PhysRevX.8.031019

Lefebvre, A. H. (1989). *Atomization and sprays* (New York, NY: Hemisphere Publ).

Li, C., He, R. C., He, Z. L., Kumar, S. S., Fredericks, S. A., Hogan, C. J., et al. (2021). Spatially-resolved characterization of oil-in-water emulsion sprays. *Int. J. Multiphase Flow* 145), 103813. doi: 10.1016/j.ijmultiphaseflow.2021.103813

Lin, H., Zhou, H. P., Xu, L. Y., Zhu, H. P., and Huang, H. H. (2016). Effect of surfactant concentration on the spreading properties of pesticide droplets on eucalyptus leaves. *Biosyst. Eng.* 143, 42–49. doi: 10.1016/j.biosystemseng.2016.01.003

Miranda-Fuentes, A., Marucco, P., Gonzalez-Sanchez, E. J., Gil, E., Grella, M., and Balsari, P. (2018). Developing strategies to reduce spray drift in pneumatic spraying in vineyards: assessment of the parameters affecting droplet size in pneumatic spraying. *Sci. Total Environ.* 616, 805–815. doi: 10.1016/j.scitotenv.2017.10.242

Perine, J., Anderson, J. C., Kruger, G. R., Abi-Akar, F., and Overmyer, J. (2021). Effect of nozzle selection on deposition of thiamethoxam in actara (R) spray drift and implications for off-field risk assessment. *Sci. Total Environ.* 772. doi: 10.1016/j.scitotenv.2020.144808

Post, S. L., and Hewitt, A. J. (2018). Flat fan spray atomization model. *Trans. ASABE* 61 (4), 1249–1256. doi: 10.13031/trans.12572

Qin, Z. W., Wang, W. S., Dammer, K. H., Guo, L. F., and Cao, Z. (2021). Ag-YOLO: A real-time low-cost detector for precise spraying with case study of palms. *Front. Plant Sci.* 12. doi: 10.3389/fpls.2021.753603

Shao, C. X., Luo, K., Chai, M., and Fan, J. R. (2018). Sheet, ligament and droplet formation in swirling primary atomization. *AIP Adv.* 8, 045211. doi: 10.1063/1.5017162

Sijs, R., Kooij, S., Holterman, H. J., van de Zande, J., and Bonn, D. (2021). Drop size measurement techniques for sprays: Comparison of image analysis, phase Doppler particle analysis, and laser diffraction. *AIP Adv.* 11 (1), 015315. doi: 10.1063/5.0018667

Szarka, A. Z., Kruger, G. R., Golus, J., Rodgers, C., Perkins, D., and Brain, R. A. (2021). Spray drift deposition comparison of fluorimetry and analytical confirmation techniques. *Pest Manage. Sci.* 77, 4192–4199. doi: 10.1002/ps.6456

Vernay, C. (2015). *Destabilisation of liquid sheets of dilute emulsions* (France: Ph.D. dissertation, Université Montpellier). Available at: https://tel.archives-ouvertes.fr/tel-01254934.

Vernay, C., Ramos, L., Wurger, A., and Ligoure, C. (2017). Playing with emulsion formulation to control the perforation of a freely expanding liquid sheet. *Langmuir* 33 (14), 3458–3467. doi: 10.1021/acs.langmuir.7b00170

frontiers | Frontiers in Plant Science

TYPE Original Research
PUBLISHED 08 May 2023
DOI 10.3389/fpls.2023.1184244

OPEN ACCESS

EDITED BY
Xiaolan Lv,
Jiangsu Academy of Agricultural Sciences (JAAS), China

REVIEWED BY
Yang Yang,
Anhui Agricultural University, China
Wei Qiu,
Nanjing Agricultural University, China

*CORRESPONDENCE
Weidong Jia
jiaweidong@ujs.edu.cn

RECEIVED 11 March 2023
ACCEPTED 07 April 2023
PUBLISHED 08 May 2023

CITATION
Dai S, Ou M, Du W, Yang X, Dong X, Jiang L, Zhang T, Ding S and Jia W (2023) Effects of sprayer speed, spray distance, and nozzle arrangement angle on low-flow air-assisted spray deposition. *Front. Plant Sci.* 14:1184244. doi: 10.3389/fpls.2023.1184244

Effects of sprayer speed, spray distance, and nozzle arrangement angle on low-flow air-assisted spray deposition

Shiqun Dai[1], Mingxiong Ou[1], Wentao Du[1], Xuejun Yang[2], Xiang Dong[1], Li Jiang[1], Tie Zhang[2], Suming Ding[3] and Weidong Jia[1]*

[1]School of Agricultural Engineering, Jiangsu University, Zhenjiang, China, [2]Science Innovation Center, Chinese Academy of Agriculture Mechanization Sciences Group Co., Ltd., Beijing, China, [3]Nanjing Institute of Agricultural Mechanization, Ministry of Agriculture and Rural Affairs, Nanjing, China

Air-assisted spraying technology is widely used in orchard sprayers to disturb canopy leaves and force droplets into the plant canopy to reduce droplet drift and increase spray penetration. A low-flow air-assisted sprayer was developed based on a self-designed air-assisted nozzle. The effects of the sprayer speed, spray distance, and nozzle arrangement angle on the deposit coverage, spray penetration, and deposit distribution were investigated in a vineyard by means of orthogonal tests. The optimal working conditions for the low-flow air-assisted sprayer working in the vineyard were determined as a sprayer speed of 0.65m/s, a spray distance of 0.9m, and a nozzle arrangement angle of 20°. The deposit coverages of the proximal canopy and intermediate canopy were 23.67% and 14.52%, respectively. The spray penetration was 0.3574. The variation coefficients of the deposit coverage of the proximal canopy and intermediate canopy, which indicate the uniformity of the deposition distribution, were 8.56% and 12.33%, respectively.

KEYWORDS

air-assisted, sprayer speed, spray distance, nozzle arrangement angle, deposit coverage, spray penetration, deposit distribution

1 Introduction

Although great progress has been made in the development of plant protection machinery, pests and diseases continue to affect vineyards (Wise et al., 2010). The most effective and economical method of crop protection for pest and disease control in orchards remains the chemical control method (Gong et al., 2020). Pesticides are widely used in vineyards, but excessive pesticide spraying can lead to human damage and environmental pollution (Abd Kharim et al., 2019; Sinha et al., 2020). At the same time, the dense grape canopy reduces the effectiveness of pesticides to control pests and diseases inside the plant

(Simone et al., 2016). Therefore, vineyard sprayers have been selected for air-assisted droplet transport to and penetration of the canopy (Miranda-Fuentes et al., 2018).

Since the 1950s, axial fan airblast sprayers have been used in orchard plant protection (Fox et al., 2008). Axial fan airblast sprayers are widely used because of their strong auxiliary airflow and long range. With the change in the modern orchard planting pattern, for use in typical dwarf and semi-dwarf orchards, droplets of axial fan airblast sprayers are easily dispersed in the air, causing environmental pollution problems (Blanco et al., 2019). As a result, tower sprayers are beginning to be used in modern orchards. Studies have proven that droplet drift is more severe in axial fan sprayers compared to tower sprayers (Landers et al., 2017). Different types of sprayers have been developed in order to improve the effectiveness of the sprayers, such as multi-airway sprayers (Grella et al., 2020), multi-row sprayers (Pergher and Zucchiatti, 2018), or individual outlet sprayers (Miranda-Fuentes et al., 2018). To reduce pesticide use and improve pesticide deposition on grape leaves, an electrostatic sprayer using an innovative pneumatic electrostatic sprayer was developed (Simone and Emanuele, 2015).

During the operation of the orchard sprayer, the working parameters have a large influence on the deposition of droplets in the canopy (Sinha et al., 2020). Different liquid flow rates, air flow rates, forward speed, targeted and wind-oriented airflow adjustment, target height, and orientation can all affect the effectiveness of the sprayer (Devanand and Divaker, 2010; Ryszard et al., 2017; Salcedo et al., 2020). Choosing the right working conditions for the sprayer can effectively improve the quality of the sprayer's operation.

In this paper, a low-flow air-assisted sprayer for vineyards was designed based on a self-designed air-assisted nozzle to reduce the amount of pesticide spraying (Dai et al., 2022). In order to improve the quality of sprayer operation, an orthogonal test on three factors, namely, sprayer speed, spray distance, and the nozzle arrangement angle, was designed to determine the optimal working conditions of the sprayer. The data were also analyzed for the deposit coverage, spray penetration, and deposit distribution after the orthogonal tests, and the influence pattern between the three factors and each index was studied. We hope that the research results will provide some assistance in future air-assisted sprayer operations in vineyards.

2 Materials and methods

2.1 Sprayer characteristics

A low-flow air-assisted sprayer was developed as shown in Figure 1. The length, width, and height of the sprayer are 2.8m, 1.5m, and 2m, respectively. This low-flow air-assisted sprayer mainly consists of a travel system, an air-assisted system, and a spraying system. To be suitable for vineyards with soft soil, the travel system of the sprayer adopts 4WD dune buggy chassis by the China Jiangsu LINHAI Group, of which the Chassis power is 14.1kW. The air-assisted system mainly includes a Vortex blower to provide high-pressure airflow, a diesel engine to power the Vortex blower, ducts to fix the air-assisted nozzle, a splitter to divide the airflow evenly to both sides of the duct, and flexible ducts to guide the flow. The power rating of the Vortex blower (YASHIBA HG810-75CS9, China) is 7.5kW and the diesel engine power (BEILONG 2V95, China) is 9kW. The spraying system mainly consists of an electric water pump powered by a 12V battery, a 200L polyethylene tank, and air-assisted nozzles. The air-assisted nozzle is a self-designed low-flow nozzle (Dai et al., 2022). When the air pressure is 0.5bar and the liquid pressure is 0.7bar, the spray angle of the air-assisted nozzle is 18°, the volume flow rate is 0.21L/min, and the volume median diameter of the droplet is 35μm. There are 2 rows of air-assisted nozzles on both sides of the sprayer and there are 8 air-assisted nozzles in each row. The air-assisted nozzles can be arranged tilted downwards at an angle perpendicular to the duct. This angle was named the nozzle arrangement angle (Ferguson et al., 2016). Two linear actuators were used to facilitate the adjustment of the height of the nozzle and the distance from the nozzle to the vine canopy.

2.2 Field test site and canopy characterization

Field tests were conducted to study the effect of the low-flow air-assisted sprayer and to determine the optimal operating conditions in the field. Field tests were performed on 11-12th August 2021 in a research vineyard located in Yuquanying Farm, Ningxia Hui Autonomous Region, China (38.13° N, 105.96° E). During the tests, the weather was breezy without rain. The temperature in the field during the daytime was 20 to 24°C and the relative humidity was 46 ± 3%. Ten measurements of wind speed were taken using an anemometer (testo 416, Germany) at five-minute intervals. The maximum wind speed was 2.2m/s and the average wind speed was 1.3m/s.

The Merlot vines trained using the spur cordon system and the row spacing (D_0) of the research vineyard were about 3.5m (Otto et al., 2013). The height of the vine (H_0) and canopy (H) was about 2m and 1.8m, respectively, and the thickness of the canopy was

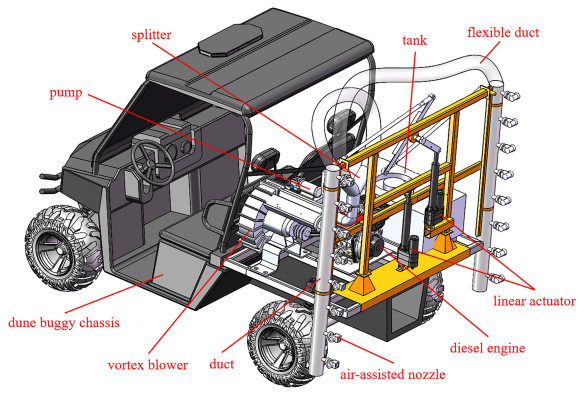

FIGURE 1
The low-flow air-assisted sprayer structure schematic.

about 0.8 to 1.2m. During the spray test phase, grapes were in the full leaf stage, and the leaf area index (*LAI*) was about 3.63. The model of the plant row volume (*PRV*) was used to calculate the *LAI* of the grape canopy (Sanchez-Hermosilla et al., 2013). Because the grape canopy thickness varied at each height, the canopy thickness at 1/6, 1/2, and 5/6 was taken to estimate the *PRV* in Figure 2A. The *LAI* and *PRV* were calculated as shown below.

$$LAI = PRV^{1.25} \times 3.5 \times 10^{-5} \quad (1)$$

$$PRV = \frac{10000H[(A_1 + A_2) + (M_1 + M_2) + (B_1 + B_2)]}{3D_0} \quad (2)$$

where H is the grape canopy height (m), A_1 and A_2 are the thickness of the canopy at 1/6 the height (m), B_1 and B_2 are the thickness of the canopy at 5/6 the height (m), M_1 and M_2 are the thickness of the canopy at 1/2 the height (m), and D is the distance between the rows (m).

2.3 Field test design

Regarding the sprayer's spraying operations, the deposit coverage on the leaves was significantly influenced by the sprayer speed (v), the nozzle arrangement angle (θ) and the spray distance (D) (Devanand and Divaker, 2010). The sprayer speed (v) is the sprayer's forward speed and three levels of sprayer speed (0.65m/s, 0.9m/s and 1.15m/s) are chosen referring to the speed of orchard sprayer (Simone et al., 2016). The spray distance (D) is the distance between the nozzles and grape canopy as shown in Figure 2B, and the appropriate spray distance levels (0.6m, 0.9m and 1.2m) are selected based on the wind attenuation performance of the air-assisted nozzle. The nozzle arrangement angle (θ) is the angle at which the spray nozzles are arranged tilted downwards at an angle perpendicular to the duct as shown in Figure 2C. Too large nozzle arrangement angle would increase the spray distance, however, too small nozzle arrangement angle will be due to errors and other reasons to make the results insignificant. Therefore, the choice of nozzle arrangement angle of 0°, 10° and 20°, respectively. To explore the effect of the sprayer speed, nozzle arrangement angle, and spray distance on the deposit coverage of spraying operations and find the optimal combination, orthogonal tests with three factors, each at three levels (Table 1), were designed and carried out, which generated nine different component ratios, and the details are shown in Table 2.

To prevent an inaccurate nozzle arrangement angle due to uneven ground in the test area, the sprayer passed through the test area several times to compact the ground into a specific track. The sprayer followed a specific track for spraying operations, and the distance between the nozzles and the grape canopy was controlled by adjusting the linear actuator. As the sprayer passed

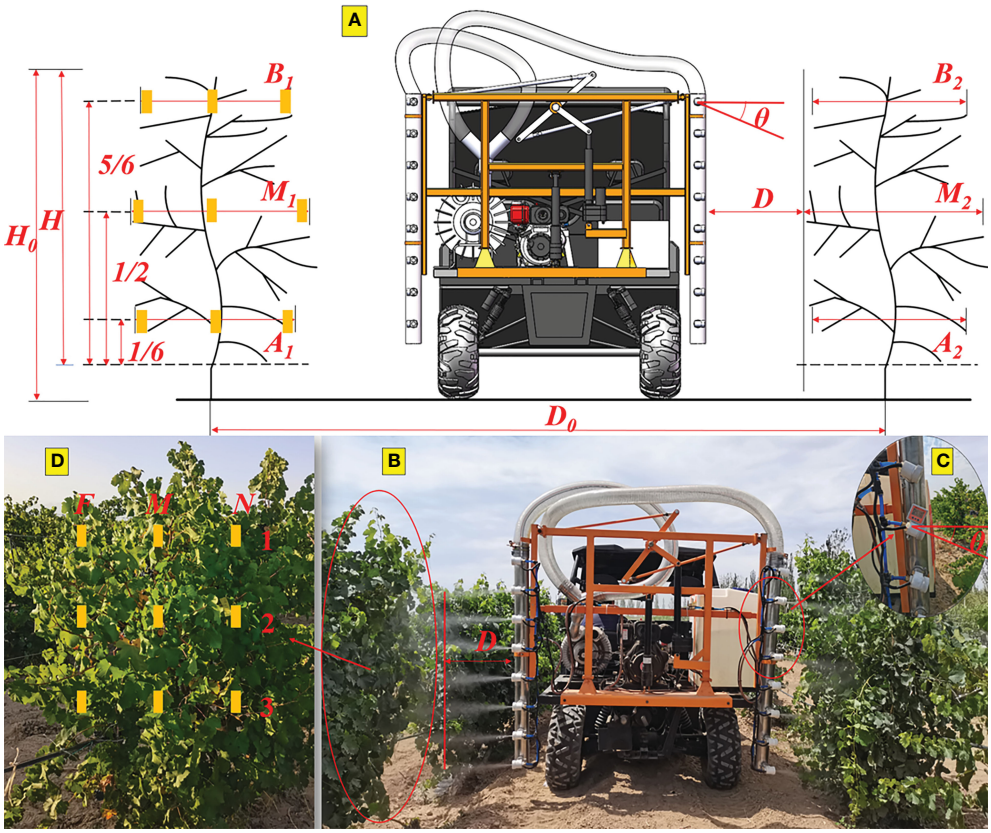

FIGURE 2
(A) Diagram of grape canopy and spraying operation; **(B)** graph of the sprayer in real time; **(C)** diagram of nozzle arrangement angle; **(D)** diagram of water-sensitive paper arrangement. Yellow marks represent water-sensitive papers.

TABLE 1 Factors and levels of the orthogonal experiment.

Treatment no.	A sprayer speed v (m/s)	B spray distance D (m)	C nozzle arrangement angle θ (°)
Level 1	0.65	0.6	0
Level 2	0.9	0.9	10
Level 3	1.15	1.2	20

TABLE 2 Schemes of the orthogonal experiment.

Treatment no.	A	B	Empty column	C
1	1	1	1	1
2	1	2	2	2
3	1	3	3	3
4	2	1	2	3
5	2	2	3	1
6	2	3	1	2
7	3	1	3	2
8	3	2	1	3
9	3	3	2	1

through the test area, the sprayer speed was controlled by feedback from the dashboard speed display to ensure that the speed was near the target speed.

During the sprayer spraying operation, the air pressure was 0.5 bar, the liquid pressure was 0.7 bar, and the volume flow rate was 3.36 L/min. The errors of the sprayer speed, spray distance, and nozzle arrangement angle were within ±0.05 m/s, ± 0.08 m, and ±5°, respectively.

Water-sensitive paper (26×76mm, Teejet, USA) was used to capture droplets sprayed by sprayers in these tests. According to the height of the grape canopy, water-sensitive papers were arranged in three layers, at 5/6, 1/2, and 1/6 height of the grape canopy, named layer 1, 2, and 3, respectively. According to the thickness of the grape canopy, water-sensitive papers were also arranged in three layers, at both sides and at the center of the grape canopy, named layer N, M, and F from near to far from the sprayer, respectively. For example, the water-sensitive paper, which was arranged at 1/2 height and on the far side of the grape canopy, was marked as F2. Nine sites per test were arranged, as shown in Figure 2D. After the test, the water-sensitive paper was left to dry completely, then marked and bagged for post-processing. Each test was repeated three times. The sprayer sprayed water in each test.

2.4 Field tests data analyses

In field trials, water-sensitive paper is widely used to assess the deposit coverage of droplets on leaves (Kosuke et al., 2012; Ömer and Ali, 2020). So, the leaves deposit coverage was studied in this paper (Victor et al., 2020). All water-sensitive papers were scanned by a scanner (M7628DNA, LENOVO) at 600 dpi to obtain 8-bit grayscale images. A software entitled "DepositScan", which was developed by the USDA-ARS Application Technology Research Unit, was used to obtain the leaves deposit coverage (Zhu et al., 2011).

In this paper, C_{ij} represented the deposit coverage of layer *ij* (*i*=N, M and F; *j*=1, 2 and 3). C_i included C_{i1}, C_{i2}, and C_{i3}. Because each test was repeated three times, C_i contained nine samples. In the data analysis, the two maximum and two minimum samples values were removed and the average of the remaining five samples was used as C_i. The deposit coverage of the whole grape canopy (C_W, %) was calculated as follows:

$$C_W = C_N + C_M + C_F \tag{3}$$

The spray penetration (*SP*) in the canopy was calculated as the ratio of the layer M deposit coverage (C_M, %) and the whole grape canopy deposit coverage (C_W, %) (Li et al., 2022):

$$SP = \frac{C_M}{C_W} \tag{4}$$

The deposit distribution is also an important indicator to evaluate the effectiveness of the sprayer operation, which can be described by the variation coefficient of the deposit coverage in the same canopy. The variation coefficient of the deposit coverage in layer I (CV_I) was studied as shown in Equation 5 (Liu et al., 2021):

$$CV_I = \frac{\sqrt{\sum_{j=1}^{n}(C_{Ij}^{`} - \overline{C_I})^2/(n-1)}}{\overline{C_I}} \times 100\,\% \tag{5}$$

where *I* represents *M* and *N*;$C_{Ij}^{`}$ represents the average of C_{Ij} in three replicate experiments, %; $\overline{C_I}$ is the average of nine C_I samples,

%; and n is the number of layers of the vertically oriented water-sensitive paper sites.

3 Results and discussion

3.1 Deposit coverage

The deposit coverage of the proximal canopy (C_N) and the deposit coverage of the intermediate canopy (C_M) were studied in Table 3 by processing data from orthogonal trials in the field. A higher deposit coverage indicates better results from the sprayer.

As shown in Table 3, for C_N, the maximum was 24.86% and the minimum was 7.70% among the nine sets of experiments in the orthogonal test, with a large difference. However, for C_M, the maximum value was 14.61% and the minimum was 2.70%. C_M is about half of C_N, or even smaller. There are two main reasons for this. First, droplets can be lost during transportation due to the drifting of the droplets caused by external factors (Grella et al., 2020; Rathnayake et al., 2021). Layer N was closer to the sprayer than layer M, and more droplets were adsorbed on the water-sensitive paper of layer N. Second, the water-sensitive papers of layer N were arranged on the surface of the canopy, and there was not much canopy obstruction between them and the sprayer; the water-sensitive paper of layer M was located in the center of the canopy, and the canopy leaves acted as an obstruction to the droplets (Duga et al., 2015), so fewer droplets penetrated the center of the canopy and were adsorbed on the water-sensitive paper of M.

For C_N and C_M, RB>RA>RC; this means that the indicator which had the largest impact was the spray distance, followed by the sprayer speed, and the indicator with the smallest impact was the nozzle arrangement angle. Based on the data from the range analysis in Table 3, the relationship between the effects of the three factors on C_N and C_M was plotted as shown in Figure 3. As shown in Figure 3, the sprayer speed and spray distance showed the same trend, with both C_N and C_M showing a decreasing trend as the sprayer speed and spray distance increased; Salyani obtained similar results in a wind-delivered spray test studying citrus trees (Salyani, 2000). Increasing the sprayer speed can produce airflow in opposite directions, leading to changes in the auxiliary airflow angles, which may also lead to droplet drift loss in complex airflow fields and

TABLE 3 Deposit coverage of the field orthogonal test.

Treatment no.	A	B	Empty column	C	C_N (%)	C_M (%)
1	1	1	1	1	24.86	14.61
2	1	2	2	2	22.22	13.33
3	1	3	3	3	14.39	6.35
4	2	1	2	3	22.00	11.98
5	2	2	3	1	20.53	7.42
6	2	3	1	2	8.26	3.78
7	3	1	3	2	13.24	7.72
8	3	2	1	3	14.35	7.44
9	3	3	2	1	7.70	2.70
$K1(C_N)$	61.47	60.10	47.46	53.09		
$K2(C_N)$	50.78	57.09	51.91	43.72		
$K3(C_N)$	35.29	30.35	48.16	50.74		
$k1(C_N)$	20.49	20.03	15.82	17.70		
$k2(C_N)$	16.93	19.03	17.30	14.57		
$k3(C_N)$	11.76	10.12	16.05	16.91		
$R(C_N)$	8.73	9.92	1.48	3.12		
$K1(C_M)$	34.29	34.32	25.84	24.73		
$K2(C_M)$	23.18	28.19	28.01	24.84		
$K3(C_M)$	17.87	12.83	21.49	25.78		
$k1(C_M)$	11.43	11.44	8.61	8.24		
$k2(C_M)$	7.73	9.40	9.34	8.28		
$k3(C_M)$	5.96	4.28	7.16	8.59		
$R(C_M)$	5.47	7.16	2.17	0.35		

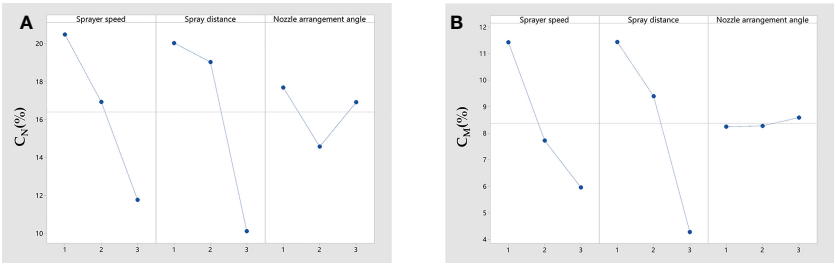

FIGURE 3
Range analysis of C_N **(A)** and C_M **(B)**.

affect the droplet deposition (Triloff, 2018). The nozzle arrangement angle had an insignificant pattern of influence on C_N and had a catalytic effect, but the impact was not significant on C_M. Foque's study of laurel spraying operations yielded similar conclusions (Foqué et al., 2012).

The optimal combination of C_N, which was determined according to the average values of the three factors at different levels, is indicated by B1A1C1, but there were differences in the optimal combination of C_M, which is indicated by B1A1C3.

3.2 Spray penetration

Spray penetration (*SP*) can effectively reflect the droplet's deposition in the canopy. The results of the field orthogonal test were processed according to the calculation formula of the spray penetration, as shown in the Table 4. The larger the value of the spray penetration, the better the droplet deposition in the canopy.

As shown in Table 4, the spray penetration was basically around 0.2~0.3, without much difference. This proves that the low-flow air-assisted sprayer operates with a better spray penetration. RA>RC>RB means that the sprayer speed had the greatest impact on the spray penetration, followed by the nozzle arrangement angle, and finally the spray distance, which had relatively little effect. Based on the data in Table 4, Figure 4 is drawn to show the relationship between the influence of each factor on the spray penetration. From Figure 4, it can be seen that the sprayer speed, spray distance, and nozzle arrangement angle had a clear pattern on the spray penetration. The difference is that the spray penetration decreased with the increase in the sprayer speed and spray distance, while the spray penetration increased with the increase in the nozzle arrangement angle.

TABLE 4 Spray penetration of the field orthogonal test.

Treatment no.	A	B	Empty column	C	SP
1	1	1	1	1	0.3388
2	1	2	2	2	0.3488
3	1	3	3	3	0.3340
4	2	1	2	3	0.3256
5	2	2	3	1	0.2581
6	2	3	1	2	0.2845
7	3	1	3	2	0.3177
8	3	2	1	3	0.3112
9	3	3	2	1	0.2348
K1	1.0215	0.9820	0.9345	0.8316	
K2	0.8682	0.9180	0.9092	0.9510	
K3	0.8636	0.8533	0.9097	0.9707	
k1	0.3405	0.3273	0.3115	0.2772	
k2	0.2894	0.3060	0.3031	0.3170	
k3	0.2879	0.2844	0.3032	0.3236	
R	0.0526	0.0429	0.0083	0.0464	

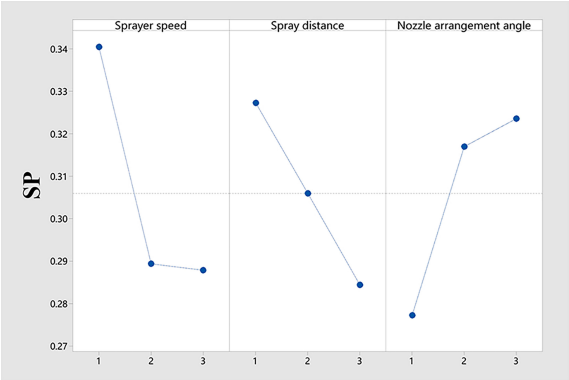

FIGURE 4
Range analysis of spray penetration.

The auxiliary airflow disturbed the canopy foliage and helped the droplets to enter the interior of the canopy, which was the main factor affecting the droplet penetration (Triloff, 2018; Bernat et al., 2022). An increase in the sprayer speed led to a decrease in the wind volume per unit canopy area, which was insufficient to disturb the blades to allow the droplets to enter the interior of the canopy, resulting in reduced penetration. After the auxiliary airflow was emitted from the nozzle, the airflow speed decreased rapidly against the increase in the spray distance (Gu et al., 2014). The increase in the spray distance led to a decrease in the velocity of the auxiliary airflow, which was insufficient to sufficiently disturb the canopy foliage, reducing penetration.

The nozzle arrangement angle had a significant impact on the spray penetration; within the test nozzle installation angle, the greater the angle, the better the spray penetration. Similar findings have been reported in previous studies (de Lima et al., 2018). The nozzle arrangement angle is the angle between the nozzle and the grape canopy. Therefore, changing the nozzle mounting angle and thus the angle of contact between the auxiliary airflow and the canopy may make it easier for the auxiliary airflow to disturb the canopy blades and facilitate the entry of droplets into the interior of the canopy. This is only a conjecture, and the exact reason for this requires further investigation. However, in the field of UAV research, the same principle may exist in the experimental study of pear orchards by changing the angle of the wing while changing the angle of the nozzle, which effectively improves the coverage inside the canopy (Qi et al., 2022).

The optimal combination determined according to the analysis of the influencing reasons of the three factors is A1C3B1.

3.3 Deposit distribution

The variation coefficients of the deposit coverage in layer M (CV_M) and in layer N(CV_N), which indicate the uniformity of the deposition distribution, are important parameters for evaluating the sprayer operation, and the same can be said for the spray penetration. The data of CV_M and $CV_N$from the field orthogonal trials are shown in Table 5. Smaller data means a better sprayer operation.

As shown in Table 5, it can be seen that RA>RB>RC, the three factors which influence CV_N in order of importance, are the sprayer speed, spray distance, and nozzle arrangement angle. According to the data in Table 5, the patterns of influence of each factor on CV_N is further elucidated in Figure 5A. The pattern of influence of the three factors on CV_N is more obvious. The effect of the sprayer speed on CV_N is positively correlated. High sprayer speeds can lead to a poor deposition distribution, resulting in an elevated CV_N, and this has been confirmed in previous studies (Planas et al., 1998; Devanand and Divaker, 2010). As mentioned earlier, a higher sprayer speed affects the droplet deposition; there is more uncertainty regarding this effect, which further affects the deposition uniformity. The effect of the spray distance on CV_N is negatively correlated. Contrary to the speed of the sprayer, a better deposition distribution was obtained for longer spray distances. This may be due to the fact that although longer spray distances lead to increased droplet drift, the inertial force of the droplets overcomes the external forces causing a drift at the spray distances tested, thus improving the droplet deposition uniformity. However, this conjecture needs to be corroborated by further experimental studies. Similarly, the increase in the nozzle installation angle also improved the uniformity of the mist distribution. Foque's experimental study of spraying on laurel trees improved the deposition distribution significantly by changing the spray direction (Foqué et al., 2012). Although the angle of change varies, it was confirmed that the angle has an effect on the uniformity of the deposition distribution.

Noted in Table 5, we found that the variation coefficient of the deposit coverage in layer N(CV_N) reached a maximum of 25.15% and a minimum of 6.24%, while the variation coefficient of the deposit coverage and in layer M(CV_M) reached a maximum of 44.59% and a minimum of 16.15%. Comparing the magnitude of the CV_N and CV_M values, CV_M was generally significantly larger than CV_N, indicating a difference of about twice. At the same time, regarding M, RB>RC>RA, which means that the spray distance had the greatest influence on CV_M, followed by the nozzle arrangement angle, and the sprayer speed had the least influence. The order of the magnitude of the effects of the three factors on the CV_M is different from that of the CV_N. Additionally, then, compared with the pattern of CV_N, the pattern of the influence of each factor on CV_M appears to be more chaotic and there is no regularity, as demonstrated in Figure 5B. Compared to CV_N, the above three differences exist in the study of CV_M. The main reason for these would be that the sampling site N is located at the edge of the grape canopy and sampling site M is located in the middle of the grape canopy. Uncertainties such as the leaf density of the canopy, porosity, and the growth direction of the leaves, which exist stochastically, greatly influence the attachment of the droplets (Duga et al., 2015).

The optimal combination of CV_N, which is determined according to the average values of the three factors at different

TABLE 5 CV_N and CV_M of the field orthogonal test.

Treatment no.	A	B	Empty column	C	CV_N (%)	CV_M (%)
1	1	1	1	1	15.23	30.56
2	1	2	2	2	11.76	16.15
3	1	3	3	3	6.24	33.36
4	2	1	2	3	19.58	29.06
5	2	2	3	1	18.84	28.21
6	2	3	1	2	10.18	33.08
7	3	1	3	2	25.15	20.59
8	3	2	1	3	16.10	19.77
9	3	3	2	1	23.69	44.59
$K1(CV_N)$	33.23	59.97	41.52	57.76		
$K2(CV_N)$	48.61	46.70	55.03	47.09		
$K3(CV_N)$	64.95	40.11	50.23	41.92		
$k1(CV_N)$	11.08	19.99	13.84	19.25		
$k2(CV_N)$	16.20	15.57	18.34	15.70		
$k3(CV_N)$	21.65	13.37	16.74	13.97		
$R(CV_N)$	10.57	6.62	4.50	5.28		
$K1(CV_M)$	80.07	80.21	83.40	103.36		
$K2(CV_M)$	90.36	64.13	89.81	69.82		
$K3(CV_M)$	84.94	111.03	82.16	82.19		
$k1(CV_M)$	26.69	26.74	27.80	34.45		
$k2(CV_M)$	30.12	21.38	29.94	23.27		
$k3(CV_M)$	28.31	37.01	27.39	27.40		
$R(CV_M)$	3.43	15.63	2.55	11.18		

levels, is A1B3C3, but the optimal combination of CV_M is B2C2A1.

3.4 Optimal working condition

During the data analysis of the orthogonal test, different indicators correspond to different optimal working conditions. An optimal working condition needs to be determined in the actual operation. A slower sprayer speed can obtain a higher deposit coverage and spray penetration, as well as a better deposition distribution uniformity, so a slower sprayer speed is the appropriate choice. The angle of the nozzle arrangement has a greater effect on the spray penetration and deposit distribution, and a smaller effect on the deposition coverage. A larger nozzle arrangement angle can increase the spray penetration and

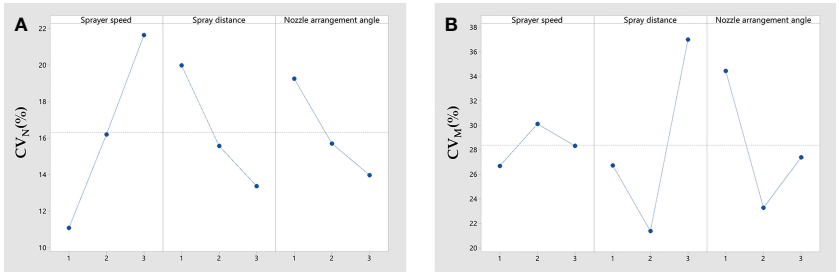

FIGURE 5
Range analysis of CV_N **(A)** and CV_M **(B)**.

improve the deposit distribution uniformity, so a larger nozzle arrangement angle is preferred. The spray distance contributes to the deposit coverage and spray penetration, but it reduces the deposit distribution uniformity, indicating a paradoxical combination. However, a suitable spray distance can reduce the uniformity of fog distribution in the middle of the canopy. So, we compromised by selecting the middle spray distance.

In summary, A1B2C3 was used as a low-flow air-assisted sprayer for field work conditions. A field test was conducted with this working condition to obtain the deposit coverage, spray penetration, and deposit distribution uniformity, as shown in Table 6.

4 Conclusion

A low-flow air-assisted sprayer was designed for use in a vineyard, and field trials were conducted using an orthogonal test with the sprayer speed, spray distance, and nozzle arrangement angle. The deposit coverage, spray penetration, and deposit distribution were studied in the orthogonal test.

The spray distance had the largest influence on the deposit coverage, followed by the sprayer speed, and finally, the nozzle arrangement angle had the smallest influence. The spray distance and sprayer speed had a large and negative effect on the deposit coverage, but the angle of the nozzle arrangement had a smaller effect on the deposit coverage. The order of influence on the spray penetration was sprayer speed, the nozzle mounting angle, and spray distance. The increase in the sprayer speed and spray distance reduced the spray penetration, but the nozzle arrangement angle promoted spray penetration. The effect pattern of the sprayer speed, spray distance, and nozzle arrangement angle on the deposit distribution of canopy layer N was obvious. The sprayer speed had the greatest effect, and a higher sprayer speed reduced the deposit distribution uniformity. The spray distance and nozzle arrangement angle had relatively small effects, but both improved the deposit distribution uniformity. For the middle canopy layer M, uncertainties such as the leaf density of the canopy, porosity, and the growth direction of the leaves, which exist stochastically, greatly influenced the attachment of the droplets. Therefore, there was no significant trend of the three factors on the deposition uniformity.

The optimal working condition of the low-flow air-assisted sprayer was determined to be sprayer speed 0.65m/s, spray distance 0.9m, and nozzle arrangement angle 20° by considering the effects of the sprayer speed, spraying distance, and nozzle arrangement angle on each index, and a field test was conducted. The deposit coverages of the proximal canopy (C_N) and intermediate canopy (C_M) were 23.67% and 14.52%, respectively. The spray penetration was 0.3574. The variation coefficients of the deposit coverage of the proximal canopy (CV_N) and intermediate canopy (CV_M), which indicate the uniformity of the deposition distribution, were 8.56% and 12.33%, respectively.

TABLE 6 Optimal working condition field test results.

Type	C_N (%)	C_M (%)	SP	CV_N (%)	CV_M (%)
A1B2C3	23.67	14.52	0.3574	8.56	12.33

Data availability statement

The original contributions presented in the study are included in the article/Supplementary Material. Further inquiries can be directed to the corresponding author.

Author contributions

The contribution of ShD is conceptualization, methodology, data curation, writing original draft and writing review and editing. The contribution of MO is methodology, writing review and editing, validation, and funding Support. The contribution of WD is data curation and methodology. The contributions of XY, XD, LJ, TZ, and SuD are methodology. The contribution of WJ is conceptualization, methodology, writing review and editing, validation, and funding Support. All authors contributed to the article and approved the submitted version.

Funding

Jiangsu Province and Education Ministry Co-sponsored Synergistic Innovation Center of Modern Agricultural Equipment (XTCX1003). This project provides financial support for the material aspects of this paper. The Ningxia Hui Autonomous Region science and technology key R&D project (2018BBF02020).The project finances the costs incurred for the production of the prototype.

Conflict of interest

Authors XY and TZ were employed by Chinese Academy of Agriculture Mechanization Sciences Group Co., Ltd.

The remaining authors declare that the research was conducted in the absence of any commercial or financial relationships that could be construed as a potential conflict of interest.

Publisher's note

References

Abd Kharim, M. N., Wayayok, A., Shariff, A. R. M., Abdullah, A. F., and Husin, E. M.. (2019). Droplet deposition density of organic liquid fertilizer at low altitude UAV aerial spraying in rice cultivation. *Comput. Electron. Agric.* 167. doi: 10.1016/j.compag.2019.105045

Bernat, S., Ramón, S., Paula, O., Marco, G., and Emilio, G. (2022). Use of ultrasound anemometers to study the influence of air currents generated by a sprayer with an electronic control airflow system on foliar coverage. *Effect Droplet Size Comput. Electron. Agric.* 202. doi: 10.1016/j.compag.2022.107381

Blanco, M. N., Fenske, R. A., Kasner, E. J., Yost, M. G., Seto, E., and Austin, E.. (2019). Real-time monitoring of spray drift from three different orchard sprayers. *Chemosphere: Environ. Toxicol. Risk Assess.* 222 (May), 46–55. doi: 10.1016/j.chemosphere.2019.01.092

Dai, S., Zhang, J., Jia, W., Ou, M., Zhou, H., Dong, X., et al. (2022). Experimental study on the droplet size and charge-to-Mass ratio of an air-assisted electrostatic nozzle. *Agriculture* 12, 889. doi: 10.3390/agriculture12060889

de Lima, J. I. D. S., Degrande, P. E., de Souza, C. M. A., and Viegas Neto, A. L.. (2018). Droplet distribution as a function of cotton interrow spacing and angles of sprayer displacement. *Engenharia Agricola.* 38 (6), 927–933. doi: 10.1590/1809-4430-eng.agric.v38n6p927-933/2018

Devanand, M., and Divaker, D. (2010). Effects of charging voltage, application speed, target height, and orientation upon charged spray deposition on leaf abaxial and adaxial surfaces. *Crop Prot.* 29 (2), 134–141. doi: 10.1016/j.cropro.2009.10.006

Duga, A. T., Ruysen, K., Dekeyser, D., Nuyttens, D., Bylemans, D., Nicolai, B. M., et al. (2015). Spray deposition profiles in pome fruit trees: effects of sprayer design, training system and tree canopy characteristics. *Crop Prot.* 67, 200–213. doi: 10.1016/j.cropro.2014.10.016

Ferguson, J. C., Hewitt, A. J., and O'Donnell, C. C. (2016). Pressure, droplet size classification, and nozzle arrangement effects on coverage and droplet number density using air-inclusion dual fan nozzles for pesticide applications. *Crop Prot.* 89, 231–238. doi: 10.1016/j.cropro.2016.07.032

Foqué, D., Pieters, J. G., and Nuyttens, D. (2012). Spray deposition and distribution in a bay laurel crop as affected by nozzle type, air assistance and spray direction when using vertical spray booms. *Crop Protection.* 41, 77–87. doi: 10.1016/j.cropro.2012.05.020

Fox, R. D., Derksen, R. C., Zhu, H., Brazee, R. D., and Svensson, S. A. A.. (2008). A history of air-blast sprayer development and future prospects. *Trans. ASABE* 51 (2), 405–410. doi: 10.13031/2013.24375

Gong, C., Kang, C., Jia, W. D., Yang, W., and Wang, Y.. (2020). The effect of spray structure of oil-based emulsion spray on the droplet characteristics. *Biosyst. Eng.* 19, 878–19890. doi: 10.1016/j.biosystemseng.2020.08.001

Grella, M., Miranda-Fuentes, A., Marucco, P., and Balsari, P.. (2020). Field assessment of a newly-designed pneumatic spout to contain spray drift in vineyards: evaluation of canopy distribution and off-target losses. *Pest Manage. Sci.* 76 (12), 4173–4191. doi: 10.13031/trans.57.10646

Gu, J., Zhu, H., Ding, W., and Wang, X. (2014). Characterization of air profiles impeded by plant canopies for a variable-rate air-assisted sprayer. *Trans. ASABE* 57 (5), 1307–1315. doi: 10.13031/trans.57.10646

Kosuke, N., Motoyuki, I., Shohji, T., and Shuichiro, H. (2012). Detection of water vapor in cathode gas diffusion layer of polymer electrolyte fuel cell using water sensitive paper. *J. Power Sources* 199, 155–160. doi: 10.1016/j.jpowsour.2011.10.026

Landers, A., Palleja Cabre, T., and Llorens, J. (2017). Technologies for the precise application of pesticides into vineyards. *J. Enol. Vitic.*

Li, T., Qi, P., Wang, Z., Xu, S., Huang, Z., Han, L., et al. (2022). Evaluation of the effects of airflow distribution patterns on deposit coverage and spray penetration in multi-unit air-assisted sprayer. *Agronomy* 12, 944. doi: 10.3390/agronomy12040944

Liu, X., Song, Q., Cui, H., Liu, Y., Liu, X., and Wu, M. (2021). Decoupling on influence of air droplets stress and canopy porosity change on deposition performance in air-assisted spray. *Trans. Chin. Soc. Agric. Machinery* 52 (8), 117–126,137. doi: 10.6041/j.issn.1000-1298.2021.08.011

Miranda-Fuentes, A., Marucco, P., González-Sánchez, E. J., Gil, E., Grella, M., and Balsari, P. (2018). Developing strategies to reduce spray drift in pneumatic spraying in vineyards: assessment of the parameters affecting droplet size in pneumatic spraying. *Sci. Total Environ.* 616–617, 805–815. doi: 10.1016/j.scitotenv.2017.10.242

Ömer, B.Ö., and Ali, B. (2020). Development and assessment of a novel imaging software for optimizing the spray parameters on water-sensitive papers. *Comput. Electron. Agric.* 168, 105104. doi: 10.1016/j.compag.2019.105104

Otto, S., Mori, N., Fornasiero, D., Veres, A., Tirello, P., Pozzebon, A., et al. (2013). Insecticide drift and its effect on kampimodromus aberrans (Oudemans) in an Italian vineyard-hedgerow system. *Biosyst. Eng.* 116 (4), 447–456. doi: 10.1016/j.biosystemseng.2013.10.007

Pergher, G., and Zucchiatti, N. (2018). Influence of canopy development in the vineyard on spray deposition from a tunnel sprayer. *Agric. Eng.* 49, 165–173. doi: 10.4081/jae.2018.801

Planas, S., Solanelles, F., Walklate, P., Miralles, A., Ade, G., Pezzi, F., et al. (1998). Advances on air-assisted spraying on the Mediterranean orchards (Fruit, wine & citrus). *Norges Landbrukshoegskole*.

Qi, P., He, X., Liu, Y., Ma, Y., Wu, Z., and Wang, J. (2022). Design and test of target-oriented profile modeling of unmanned aerial vehicle spraying. *Int. J. Agric. Biol. Eng.* 015 (003), 85–F0002. doi: 10.25165/j.ijabe.20221503.6753

Rathnayake, A. P., Khot, L. R., Hoheisel, G. A., Thistle, H. W., Teske, M. E., and Willett, M. J. (2021). Downwind spray drift assessment for airblast sprayer applications in a modern apple orchard system. *Trans. ASABE* 64 (2), 601–613. doi: 10.13031/trans.14324

Ryszard, H., Grzegorz, D., Waldemar, Ś., Artur, G., and Paweł, J. K.. (2017). Variable air assistance system for orchard sprayers; concept, design and preliminary testing. *Biosyst. Eng.* 163, 134–149. doi: 10.1016/j.biosystemseng.2017.09.004

Salcedo, R., Llop, J., Campos, J., Costas, M., Gallart, M., Ortega, P., et al. (2020). Evaluation of leaf deposit quality between electrostatic and conventional multi-row sprayers in a trellised vineyard. *Crop Prot.* 127. doi: 10.1016/j.cropro.2019.104964

Salyani, M. (2000). Optimization of deposition efficiency for airblast sprayers. *Trans. ASAE.* 43 (2), 247–253. doi: 10.13031/2013.2699

Sanchez-Hermosilla, J., Paez, F., Rincon, V. J., and Perez-Alonso, J.. (2013). Volume application rate adapted to the canopy size in greenhouse tomato crops. *Scientia Agricola* 70 (6), 390–396. doi: 10.1590/S0103-90162013000600003

Simone, P., and Emanuele, C. (2015). Spray deposition in "tendone" vineyards when using a pneumatic electrostatic sprayer. *Crop Prot.* 68, 1–611. doi: 10.1016/j.cropro.2014.11.006

Simone, P., Emanuele, C., and Giuseppe, M. (2016). Foliar spray deposition in a "tendone" vineyard as affected by airflow rate, volume rate and vegetative development. *Crop Prot.* 91, 34–48. doi: 10.1016/j.cropro.2016.09.009

Sinha, R., Ranjan, R., Khot, L. R., Hoheisel, G. A., and Grieshop, M. J. (2020). Comparison of within canopy deposition for a solid set canopy delivery system (SSCDS) and an axial-fan airblast sprayer in a vineyard. *Crop Prot.* 132. doi: 10.1016/j.cropro.2020.105124

Triloff, P. (2018). A case study-canopy adapted dosing and spray application in 3D crops. *Dose Expr. Workshop. Assoc. Appl. Biol.*, 6–7.

Victor, J. R., Marco, G., Paolo, M., Leandro, E. A., Julian, S. H., and Paolo, B. (2020). Spray performance assessment of a remote-controlled vehicle prototype for pesticide application in greenhouse tomato crops. *Sci. Total Environ.* 726, 138509. doi: 10.1016/j.scitotenv.2020.138509

Wise, J. C., Jenkins, P. E., Schilder, A. M. C., Vandervoort, C., and Isaacs, R.. (2010). Sprayer type and water volume influence pesticide deposition and control of insect pests and diseases in juice grapes. *Crop Prot.* 29 (4), 378–385. doi: 10.1016/j.cropro.2009.11.014

Zhu, H., Masoud, S., and Robert, D. F. (2011). A portable scanning system for evaluation of spray deposit distribution. *Comput. Electron. Agric.* 76 (1), 38–43. doi: 10.1016/j.compag.2011.01.003

frontiers | Frontiers in Plant Science

TYPE Original Research
PUBLISHED 10 May 2023
DOI 10.3389/fpls.2023.1175939

OPEN ACCESS

EDITED BY
Xiaolan Lv,
Jiangsu Academy of Agricultural Sciences (JAAS), China

REVIEWED BY
Dong Xiaoya,
Jiangsu University, China
Longzhe Quan,
Anhui Agricultural University, China

*CORRESPONDENCE
Weicai Qin
qinweicai@caas.cn

RECEIVED 28 February 2023
ACCEPTED 07 April 2023
PUBLISHED 10 May 2023

CITATION
Qin W, Chen X and Chen P (2023) "H" sprayer effect on liquid deposition on cucumber leaves and powdery mildew prevention in the shed.
Front. Plant Sci. 14:1175939.
doi: 10.3389/fpls.2023.1175939

"H" sprayer effect on liquid deposition on cucumber leaves and powdery mildew prevention in the shed

Weicai Qin[1]*, Xuan Chen[2] and Panyang Chen[2]

[1]Suzhou Polytechnic Institute of Agriculture, Suzhou, China, [2]Nanjing Institute of Technology, Nanjing, China

To clarify the effect of droplet size on solution deposition and powdery mildew control on greenhouse cucumber leaves, the effect of volume median droplet diameter (VMD) on solution deposition and maximum retention, as well as the effect of flusilazole on powdery mildew control on cucumber, was determined using the stem and leaf spray method. The VMD of the typical fan nozzles (F110-01, F110-015, F110-02, F110-03) of the selected US Tee jet production differs by approximately 90 μm. The results showed that the deposition of flusilazole solution on cucumber leaves decreased as the VMD of the droplets increased and that the deposition of the solution in the treatments with VMD of 120, 172, and 210 μm decreased by 22.02%, 10.37%, and 46. 97%, respectively, compared to that observed with treatment with 151 μm VMD. The deposition of the solution on cucumber leaves showed the highest deposition efficiency of 63.3% when the applied solution volume was 320 L/hm^2, and the maximum stable retention of the liquid on the leaves was 6.6 μl/cm^2. The control effects of different concentrations of flusilazole solution on cucumber powdery mildew differed significantly, and the best control effect was achieved at the dosage of 90 g/hm^2 of the active ingredient, which was 15%–25% higher than that observed at the dosage of 50 and 70 g/hm^2 of the active ingredient per hectare. A significant difference in the effect of droplet size on the control of cucumber powdery mildew was observed at any specific liquid concentration. Nozzle F110-01 showed the best control effect when the dosage of the active ingredient was 50 and 70 g/hm^2 per hectare, which did not differ significantly from that observed with nozzle F110-015 but differed significantly from those observed with nozzles F110-02 and F110-03. Hence, we concluded that the use of smaller droplets with VMD of 100–150 μm, i.e. the choice of F110-01 or F110-015 nozzles, for application on the leaf parts of cucumber in the greenhouse under conditions of high liquid concentration, can significantly improve the effective use of pharmaceuticals and the disease control effect.

KEYWORDS

H-Sprayer, fan nozzles, amount of deposition, shed, cucumber leaves, effectiveness of powdery mildew prevention

1 Introduction

Cucumber powdery mildew is an important disease caused by the monocotyledonous powdery mildew fungus, *Sphaerotheca fuliginea*, which is characterized by a short incubation period, frequent reinfestation ability, and high prevalence. The pathogen can infect cucumbers throughout the reproductive season (Hamza et al., 2015). Climatic conditions are the main factors influencing the occurrence of powdery mildew (Sarhan et al., 2020. Wu et al., 2022). Powdery mildew damage has increased with the development of protected vegetables. Currently, research on plant breeding for developing disease resistance and the spraying of pesticides are the two main ways of controlling this disease (Lv et al., 2016). The former is one of the popular methods used to prevent and control powdery mildew in many countries, and several disease-resistant varieties, such as Jin Za No. 1, have been developed (Tang, 2002). However, powdery mildew species may vary with countries or regions within the same country (Elad et al., 2021). In addition, the complexity and variability of the pathogen and the difficulty in identifying it accurately (Cerkauskas and Ferguson, 2014. Wang et al., 2021) render breeding for disease resistance challenging; this has hindered efforts to effectively address the occurrence of powdery mildew, which is controlled using pharmaceuticals.

As mentioned above, excessive use of pesticides can cause a certain amount of environmental pollution (Lan et al., 2018), and insufficient use can induce resistance (Tang et al., 2019. Elsharkawy et al., 2014). In addition to the selection of suitable agents, application techniques are equally important for the control of cucumber powdery mildew. In China, research on efficient application techniques for pest and disease control using different droplet sizes is limited, and easy-to-use spray quality standards are lacking, which makes blind operations common. In fact, the concentration of the liquid spray and the density of the droplets considerably affect the control of pests and diseases (Ye et al., 2022. Mao et al., 2022). Cui et al. (2010) investigated the effect of liquid application volume and droplet density on the control of wheat aphids, and the results showed that reducing the liquid application volume and increasing the liquid concentration did not only reduce the deposition volume but also considerably decreased the rate of pesticide loss; in addition, a certain density of the deposited imidacloprid droplet effectively controlled aphids in the wheat spike. Yang et al. (2012) studied the effect of nozzle type on droplet deposition and control of wheat aphids; to this end, they measured the performance of nozzles in terms of deposition volume, deposition uniformity, and ground loss rate to screen nozzles suitable for wheat field spraying. Hong et al. (2022) investigated the effect of UAV operating parameters on the spraying effect in a horsetail pine forest. Santos-Júnior et al. (2022) investigated the relationship between pesticide application rates on spray deposition, stink bug control, and soybean yield in soybean crops, and the results confirmed that pesticide sprays require a certain amount of droplet deposition and deposition density to be effective. Furthermore, as diseases caused by plant pathogens differ from damage caused by insect pests, different droplet sizes and application volumes are required (Eskandari and Sharifnabi, 2020).

Therefore, in this study, four typical fan nozzles with different apertures were used to investigate the effect of droplet size and the volume of different concentrations of pesticide on the control of powdery mildew on greenhouse cucumbers. Our observations will provide a basis for nozzle selection and the development of standards.

2 Material and methods

2.1 Materials

2.1.1 Test cucumber

The test plant variety was Jimei Fuxing.

2.1.2 Agents and instruments

The agents used are a 40% flusilazole emulsifier (Tianjin Sprela Pesticide Technology Development Co. Ltd. Tianjin, China) and a 1-g/L aqueous solution of rhodamine-B fluorescent tracer (Shanghai Qianduan Biological Co. Ltd. Shanghai, China). The instruments used include the following: an F95 fluorescence spectrophotometer (Shanghai Prismatic Technology Co. Ltd. Shanghai, China), a 2 cm in diameter hole puncher, a Spray Tec Fog Droplet Sizer (Shandong Necht Analytical Instruments Co. Ltd. Shangdong, China), and fan nozzles Tee jet F110-01, F110-015, F110-02, and F110-03.

2.1.3 Test equipment

The test apparatus was an "H" type sprayer, as shown in Figure 1; the pressure was adjustable, and a spray pressure of 0.3 MPa was used. The detailed parameters are shown in Table 1.

2.2 Methods

2.2.1. Nozzle selection and droplet size determination

Different models of fan nozzles, Tee jet F110-01, F110-015, F110-02, and F110-03, all with a 110° spray angle, were used. At a

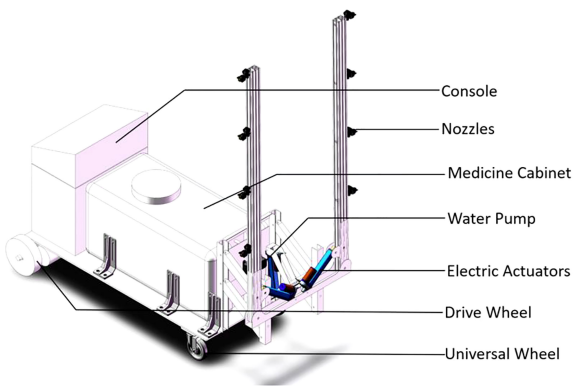

FIGURE 1
"H" type orbital stand crop sprayer. The sprayer was equipped with an adjustable pressure system and was operated at a spray pressure of 0.3 MPa to apply flusilazole for controlling powdery mildew on greenhouse cucumbers.

TABLE 1 Parameters of "H" type sprayer.

Parameter	Numerical value	Remark
Dimension (mm)	1,603 * 777 * 1,806 (bracket vertical)	Length * width * height
Maximum chemical load (L)	400	Maximum capacity of the tank
Number of nozzles (pc)	8	Self-loading with different numbers of nozzles
Working height	0.3–1.8 m	Can be set on demand
Nozzle flow	7 L/min	Fan-shaped nozzle

spray pressure of 0.3 MPa, the volume median diameter (VMD) of the droplets from different spray nozzles was measured using a Spray Tec Fog Droplet Sizer meter at a distance of 0.5 m from the spray nozzle. In total, 20–40,000 droplets were collected; the droplet VMD of the F110-01, F110-015, F110-02, and F110-03 spray nozzles were 120, 151, 172, and 210 μm, respectively. Single-nozzle flow rates of 390, 520, 820, and 1,200 ml/min, respectively, were used for the above spray nozzles.

2.2.2 Effect of droplet size on the amount of flusilazole deposited

The experiment was performed on greenhouse cucumbers at the experimental base of Suzhou Polytechnic Institute of Agriculture, with plant spacing of 30 cm and row spacing of 50 and 90 cm. Control of cucumber powdery mildew (*S. fuliginea* (Schlecht) Poll). The test was conducted when the cucumbers grew to the 10–12-leaf stage, and cucumbers with uniform growth and powdery mildew characteristics were selected for the test. Four different VMD nozzles were used for the test; each nozzle was used to spray a plot of 10 m^2, each plot was randomly arranged, and each treatment was repeated three times. Using tap water, prepare a mother solution of flusilazole with a concentration of 500 mg/L and a mother solution of rhodamine-B tracer with a mass fraction of 1%. In a 1:1 volume ratio, mix the rhodamine-B tracer mother solution and the flusilazole mother solution to prepare a mixed mother solution. The mixed mother solution was then used to prepare a medicine solution for spray treatment with a flusilazole concentration of 50 mg/L, and the spraying time was adjusted according to the flow rate of the nozzle such that the applied liquid volume of each treatment was 450 L/hm^2 and the effective dose of flusilazole was 22.5 g/hm^2. The spray pressure of the sprayer was set to 0.3 MPa. Five cucumber seedlings were randomly selected from each treatment after spraying, and each cucumber was marked from top to bottom by counting the second, fourth, seventh, and ninth leaves, which were used to measure the amount of flusilazole deposited per unit leaf area and calculate the average value. The spraying process is shown in Figure 2.

After the spray treatment, five holes were punched on the marked leaves using a hole puncher, placed in a self-sealing bag, brought back to the room, and eluted with 30 ml deionized water for 20 min. The absorbance value was measured after placing the eluate into a clean test tube at 572 nm. The amount of rhodamine-B in the eluate can be calculated from the standard curve of rhodamine-B. In this way, the amount of deposition of the spray liquid solution on the unit area can be calculated (Xue et al., 2014).The equation for calculating the amount deposited is as follows:

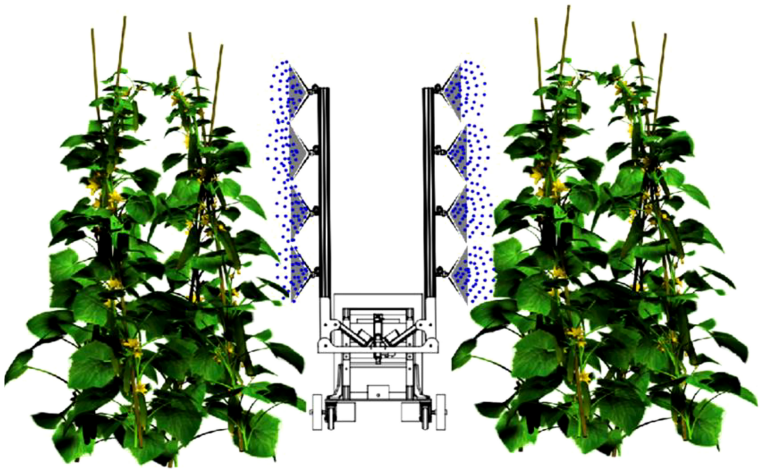

FIGURE 2
Diagram showing the spraying process used in the experiment, which was conducted on greenhouse cucumbers at the experimental base of Suzhou Polytechnic Institute of Agriculture. The experiment aimed to test the efficacy of four different VMD nozzles for controlling cucumber powdery mildew.

$$\beta_{dep} = \frac{(\rho_{smpl} - \rho_{blk}) \times F_{cal} \times V_{dii}}{\rho_{spray} \times A_{col}}$$

where β_{dep} is the amount of mist droplet deposition in micrograms per square centimeter; ρ_{smpl} is the fluorometer reading of the sample sampler; ρ_{blk} is the fluorometer reading of the blank sampler (sampler + dilution water); F_{cal} is the calibration factor (equal to the logarithm of the recovery rate) in micrograms per liter; V_{dii} is the amount of diluent (e.g., tap water or deionized water) in which the tracer from the sampler is dissolved in liters; ρ_{spray} is the concentration of the tracer in the spray solution in grams per liter; and A_{col} is the area of the sampler in square centimeters.

2.2.3 Maximum stable retention of flusilazole solution on cucumber leaves

The experiment was performed on greenhouse cucumbers at the experimental base of Suzhou Polytechnic Institute of Agriculture. The F110-015 spray nozzle was selected, and the spray pressure was 0.3 MPa. When the cucumber grew to the 10−12-leaf stage, 50 mg/L of flusilazole was sprayed at 110, 185, 320, 720, 950, and 1,100 L/hm^2 dosages. Five cucumber seedlings were selected for each treatment, and each treatment was repeated thrice to determine the amount of flusilazole deposited per unit leaf area. The method was the same as described in **Effect of droplet size on the amount of flusilazole deposited**. The amount deposited on the leaves and the deposition efficiency, as well as the maximum stable retention of the solution on the leaves, i.e., the amount deposited when the amount of solution applied increases until there is no more droplet flow on the leaves, were calculated. The deposition efficiency was calculated as follows:

$$DE = \frac{D}{A} \times 100\,\%$$

where D is the amount of flusilazole deposited on the leaves (mg/m^2) and A is the amount of flusilazole applied per unit area (mg/m^2).

In total, 10 Petri dishes of 10-cm diameter were used for each treatment to collect the solution on the ground. The amount of solution applied per unit area is the ratio of the amount of solution collected to the area of the Petri dish.

2.2.4 Effect of flusilazole solution on the control of cucumber powdery mildew

The experiment was conducted on greenhouse cucumbers at the experimental base of the Suzhou Polytechnic Institute of Agriculture. F110-01, F110-015, F110-02, and F110-03 spray nozzles were selected, corresponding to dosages of 110, 185, 320, and 500 L/hm^2, respectively. The active ingredient dosages of flusilazole were 50, 70, and 90 g/hm^2; 12 groups of treatments, one plot per treatment, and 10 m^2 per plot were used; each plot was arranged randomly, and each treatment was repeated thrice. When cucumbers grew to the 10–12-leaf stage, the whole plant was sprayed with 50 mg/L of flusilazole, and blank control (CK) was set without spraying the pesticide. At the beginning of the disease, flusilazole was applied thrice at an interval of 7 days. Four random samples were taken from each plot, and all the leaves of the two plants were surveyed at each point. Grading was performed based on the area of the diseased spot on each leaf as a percentage of the whole leaf area. The significance of the control effect was determined based on Duncan's new repeated difference (DMRT) method. Cucumber powdery mildew grading standard is as follows: grade 0: no disease spot; grade 1: disease spot area accounted for less than 5% of the whole leaf area; grade 3: accounted for 6%~10% of the whole leaf area; grade 5: accounted for 11%~20% of the whole leaf area; grade 7: accounted for 21%~40% of the whole leaf area; and grade 9: accounted for more than 40% of the whole leaf area. Disease development was investigated 10 days after administering the third dose, and the disease index and control effect (%) were calculated.

$$\mathrm{DI} = \frac{\sum_i N_i \times W_i}{\mathrm{T} \times 9} \times 100$$

where DI is the disease index, N_i is the number of leaves at level I, W_i is the relative level value of leaf level i (a decimal number between 0 and 1), T is the total number of leaves surveyed (a positive integer), and 9 is a constant, indicating the total number of leaf levels.

$$E = \frac{\mathrm{lc} - \mathrm{lp}}{\mathrm{lc}} \times 100$$

where E is the effect of control (%), lc is the index of disease in the blank control area, representing the index of disease without any treatment, and lp is the index of disease in the treated area, representing the index of disease after specific treatment.

2.3 Data analysis

The SPSS 20.0 software was used for statistical analysis, and the Student–Newman–Keuls (SNK) method was applied to test the significance of differences. The analysis of variance (ANOVA) method was used to compare the differences between groups, and the SNK test was used for a two-way comparison between groups; $p < 0.05$ was considered significant.

3 Results

3.1 Effect of droplet size on the deposition of flusilazole solution on cucumber leaves

Droplet size is one of the most important parameters in spraying technology, and mastering the spray droplet size distribution is important for accurately controlling the spraying process (Kang et al., 2021). Droplets drift easily if their size is too small (less than 50 μm in diameter), whereas too large droplets (more than 450 μm in diameter) cannot penetrate the crop canopy. To solve this problem, Xu et al. (2015) proposed using larger droplets (narrow droplet spectrum with diameters larger than 140 μm) to overcome the drift and increase deposition.

The amount of flusilazole solution deposited on cucumber leaves using different VMD mist droplet treatments differed

significantly (Figure 3). The deposition of flusilazole solution was higher for treatment with droplets of 151 µm VMD and decreased with increasing VMD; compared to that observed with treatment with 151 µm VMD droplets, the deposition of flusilazole solution on cucumber leaves decreased by 22.02%, 10.37%, and 46.97% for 120, 172, and 210 µm VMD droplets, respectively.

3.2 Maximum stable retention of flusilazole solution on cucumber leaves

The amount of flusilazole deposited on cucumber leaves varied with the amount of applied solution when treated with 50 mg/L of flusilazole solution (Figure 4). The deposition of flusilazole on cucumber leaves increased with the application rate when the latter was less than 720 L/hm^2 and reached a larger value of 6.6 µl/cm^2 when the application rate was 720 L/hm^2.

The deposition on the leaves did not increase but rather decreased when the applied liquid volume exceeded 720 L/hm^2. This indicated that the maximum stable retention of 50 mg/L of flusilazole solution on cucumber leaves was approximately 5.32 µl/cm^2. A comparison of the amounts of flusilazole solution applied and deposited on cucumber leaves revealed that the deposition efficiency of flusilazole solution on cucumber leaves was relatively high when the amount of solution applied was less than 320 L/hm^2, with about 63.3% of the flusilazole solution being deposited on cucumber leaves; when the amount of solution applied exceeded 320 L/hm^2, the deposition efficiency decreased until the amount of solution applied exceeded 720 L/hm^2, the deposition efficiency was 58.3%; following which it dropped sharply, the deposition efficiency was 37.6% after treatment with 1100 L/hm^2 of the applied solution.

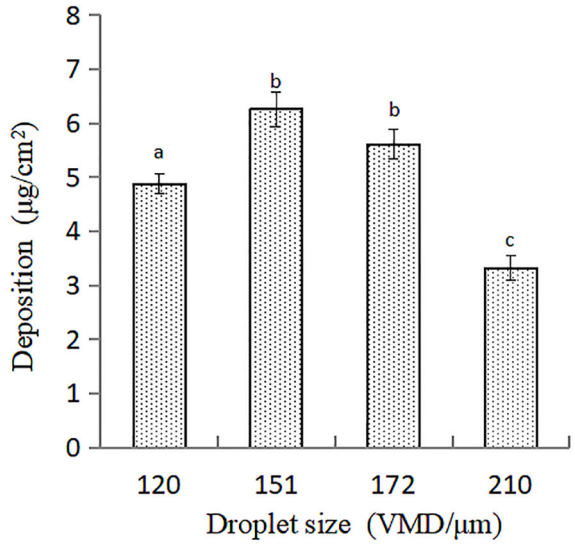

FIGURE 3
Deposition of flusilazole solution on cucumber leaves treated with different droplet sizes. The deposition was expressed as a volume of 50 mg/L flusilazole solution per cm^2 of cucumber leaves. The spray volume used in each treatment was 450 L/hm^2.

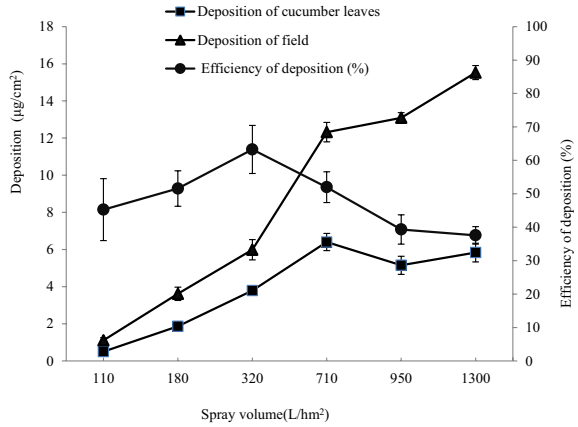

FIGURE 4
Maximum retention of flusilazole solution on cucumber leaves. The deposition was expressed as a volume of 50 mg/L flusilazole solution per cm^2 of cucumber leaves. VMD of droplets was 151 µm.

The deposition of field refers to the amount of pesticide solution that falls on plant leaves during the application process but is not absorbed and settles on the soil or ground below. According to the table data, it can be observed that as the amount of pesticide solution applied increases, the deposition of field also shows a gradually increasing trend. Within the range of pesticide solution applied, from 110 to 950, the deposition of field increased from 1.109 to 13.093, nearly 12 times. This means that at high levels of pesticide application, plants are unable to absorb all of the pesticides, leading to an increase in the amount of pesticide lost to the field and soil. Therefore, when applying pesticides, it is important to use appropriate amounts to reduce unnecessary drug loss and minimize environmental pollution risks.

3.3 Effect of flusilazole solution on the control of cucumber powdery mildew

Next, we compared the control effects of four fan spray nozzles, F110-01, F110-015, F110-02, and F110-03, with different pesticide dosages (active ingredient dosages of 50, 70, and 90 g/hm^2) on mildew control. As shown in Table 2, using the same nozzle, an overall increasing trend in the control effect was observed as the amount of active ingredient applied increased. When the active ingredient dosage was 90 g/hm^2, the lowest disease index of 2.25 was observed with the F110-01 nozzle, and its control effect was 89.48%, which was higher than the control effects of F110-015, F110-02, and F110-03. The control effects of F110-015, F110-02, and F110-03 were 87.61%, 86.06%, and 83.42%, respectively, which did not differ significantly; when the dosages of the active ingredient were 70 and 50 g/hm^2, the control effect obtained upon using the F110-01 nozzle was 80.38% and 70.03%, respectively. The control effects of F110-015, F110-02, and F110-03 were higher than those of F110-015, F110-02, and F110-03. A significant difference was observed in the control effect of liquid concentration on cucumber powdery mildew; the disease index was significantly

10.3389/fpls.2023.1175939

TABLE 2 Protective effect of flusilazole on cucumber powdery mildew (CPM).

Fungicides	Nozzles types	Dosage (g/hm^2)	Disease index	Control efficiency (%; mean ± SD)
Flusilazole emulsion (40%)	F110-01	50	6.4 ± 0.21 bcde	70.03 ± 1.0 cd
		70	4.19 ± 0.28 efgh	80.38 ± 1.29 fg
		90	2.25 ± 0.10 h	89.48 ± 0.49 i
	F110-015	50	6.77 ± 0.38 bcd	68.32 ± 1.78 c
		70	5.43 ± 0.26 cdef	74.57 ± 1.22 de
		90	2.65 ± 0.12 gh	87.61 ± 0.58 hi
	F110-02	50	7.25 ± 05 bc	66.06 ± 2.34 c
		70	4.67 ± 0.45 defg	78.14 ± 2.09 ef
		90	2.98 ± 0.46 gh	86.06 ± 0.21 hi
	F110-03	50	8.1 ± 0.17 b	62.07 ± 0.78 b
		70	5.63 ± 0.3 cdef	73.64 ± 1.42 de
		90	3.54 ± 0.19 fgh	83.42 ± 0.89 gh
Blank control		–	21.37 ± 1.72 a	0.0 ± 0.0 a

The data in the table show mean ± SD. Data followed by different small letters in the same column differ significantly among different treatments at $p < 0.05$ level by Student–Newman–Keuls test.

reduced at the active ingredient dosage of 90 g/hm^2. The best control effect was 15%–25% higher than that observed with the active ingredient dosages of 50 and 70 g/hm^2; the type of spray nozzle significantly affected the control effect. The control effect of F110-01 was the best at the same concentration, followed by those of F110-015, F110-02, and F110-03 (Table 2).

Table 3 shows that the effects of nozzle type and the amount of available active ingredient per hectare on the population were highly significant, with *p*-values less than 0.001. Furthermore, with the same type of nozzle, the control effect increased with the amount of active ingredient per hectare; considering nozzle F110-01 as an example, we observed a significant difference in the control effect with the amount of active ingredient; the control effect was 70.03%, 80.38%, and 89.48% with 50, 70, and 90 g/hm^2 of active ingredient, respectively. As shown in Table 2, the type of nozzle significantly affected the control effect. At the same concentration, F110-01 showed the best control effect, followed by F110-01.5, F110-02, and F110-02.5.

4 Discussion

Although research on pesticide application technology in China has increased and the quality of the application equipment has been gradually improved, atomization of liquid chemicals, target plant collisions, and deposition of liquid on the target plants complicate the spray transfer process. Droplet movement to the blade surface (excluding needle leaves) due to kinetic energy, surface energy, and electrostatic energy and blade contact angle at the droplet-leaf interface jointly determine the droplet impact at the interface after adhesion, bounce, and spray (Williams et al., 2008). However, related basic research on the spraying technology still needs to be improved (Roisman et al., 2006). Some studies have shown that the angle of mist flow affects the deposition of pesticide solutions on target plants and that 20°–40° or 60° mist flow angles are best for the deposition of solutions on simulated upright targets (Dhalin et al., 2008).

As the cucumber leaf surface has many ridges, the critical surface tension value is relatively low, and its adhesive tension is 6.2 mN/m; hence, the mist droplets are easily lost (Feng et al., 2022). The size of the pesticide droplets deposited on the cucumber leaves considerably affects their effectiveness; coarse droplets formed during movement under the influence of gravity are relatively large, while bouncing off droplets from leaves after collision leads to considerable loss (Song et al., 2019).

Under conditions where personnel control the uniformity of spraying speed, such as high-capacity coarse fog spraying as well as liquid flow spraying, the spraying of large droplets evidently increases the amount of liquid applied; however, changing the pattern of pesticide use by small-scale individual farmers in China is difficult. The results of this study show that the effective use rate decreases significantly as the VMD of the spray droplets increases and the volume of the applied liquid increases. Spray quality depends largely on the spray nozzle; different pesticide atomization methods can produce droplets of varying sizes; however, for a particular organism or part of the organism, only a certain droplet size can be captured to produce an effective toxic effect. This was discovered in the 1950s, and after extensive research, it was gradually accepted and recognized by researchers (Mount, 1970; Johnstone, 1971; Harburguer et al., 2012). Studies have shown that the optimum particle size is 10–50 μm for flying pests, 30–150 μm for cotton bollworms, 30–150 μm for treating diseases, and 100–300 μm for weeds.

In this study, the amount of flusilazole deposited on cucumber leaves increased with increasing spray volume when the spray volume was less than 720 L/hm^2, reaching a maximum of

TABLE 3 Inspection of effects among subjects.

Origin	Type III sums of squares	Df	Average square	F	Sig
Calibration model	3,536.742[a]	11	321.522	38.337	< 0.001
Intercept distance	285,177.501	1	285,177.501	34,003.204	< 0.001
Nozzle types	324.103	3	108.034	12.881	< 0.001
Active ingredient dosage	3,165.129	2	1,582.564	188.697	< 0.001
Error	301.924	36	8.387		
Total	289,016.167	48			
Total number of corrections	3,838.666	47			

Dependent variable: effectiveness of control.
[a]R^2 = 0.921 (adjustment of R^2 = 0.897).

6.6 μl/cm^2 at 720 L/hm^2. However, when the spray volume exceeded 720 L/hm^2, the amount deposited on the leaves no longer increased but decreased. As a rule, the higher the spray volume, the greater the deposition will be. This is because more spray volume causes more liquid or particulate matter to fall on the target surface, increasing the amount of surface deposition. However, an increase in spray volume does not always increase the amount of deposition linearly. When the spray volume is very high, saturation may occur and the surface cannot absorb any more liquid or particulate matter, at which point increasing the spray volume will not increase the amount of deposition. Therefore, the spray volume should be controlled within an appropriate range to ensure optimum deposition of flusilazole solution on the leaves.

In addition, there was an overall trend toward increasing control effectiveness with increasing dosages of active ingredients. At the same dosage, sprayers with smaller droplet VMD had better control, while the lowest disease index and best control were achieved with F110-01 sprayers. There was also a significant difference in the control of cucumber powdery mildew due to the concentration of the solution. At an active ingredient dosage of 90 g/hm^2, the disease index was significantly lower, and the control effect was the best, being 15%–25% higher than at 50 and 70 g/hm^2. The type of spray nozzle also had a significant effect on the control effect. At the same concentration, F110-01 had the best control effect, followed by F110-015, F110-02, and, worst of all, F110-03. Therefore, for the control of powdery mildew, we can consider using the F110-01 nozzle with small droplet VMD and applying it at an active ingredient dosage of 90 g/hm^2 per hectare to obtain the best control effect. At the same time, attention to the adjustment of the concentration of the liquid and the rational use of the spray nozzles are also important measures to improve the control effect.

5 Conclusion

In this study, the flusilazole water emulsion was applied to cucumber leaves at a uniform 45° angle to minimize the impact of the droplets on the leaf surface and thereby reduce the amount of solution lost *via* droplet bouncing. The deposition of flusilazole solution on greenhouse-grown cucumber leaves decreased with increasing VMD of the droplets (Figure 4), and the use of small droplets with a VMD of about 160–200 μm facilitated the deposition of the solution on cucumber leaves. Based on the results of a large number of experiments conducted using the blown mist method, we concluded that the deposition efficiency of the drug may be more desirable if the VMD of the mist droplets is further reduced, which requires further investigation.

The deposition efficiency of flusilazole solution on cucumber leaves was relatively high when the volume of the applied solution was less than 320 L/hm^2; about 63.3% of the flusilazole solution was deposited on cucumber leaves, and a small amount was deposited on leaf stems, but nearly one-third of the solution was still lost to the soil; the deposition efficiency decreased further when the applied liquid volume exceeded 320 L/hm^2. The deposition efficiency was 58.3% when the applied liquid volume exceeded 720 L/hm^2, following which it decreased sharply to 37.6% when treated with an applied liquid volume of 1,100 L/hm^2. This is similar to the observation of Lu et al. (2010), who observed that leaf retention started to increase rapidly with increasing application rate; after reaching the attrition point, the application rate further increased, while the retention rate decreased and gradually tended to a stable value, which was the maximum stable retention rate, indicating that the retention rate of leaf solution would not increase when the application rate exceeded the attrition point. During the cultivation of cucumber, the recommended amount of solution applied often reaches or even exceeds 720 L/hm^2, resulting in low efficiency of liquid deposition, which is an important reason for the unsatisfactory control effect.

We observed a significant difference in the effect of the concentration of the solution on the control of cucumber powdery mildew, with the best effect observed at 90 g/hm^2 of the active ingredient, which was 15%–25% more effective than those at 50 and 70 g/hm^2 of the active ingredient per hectare. For a specific concentration of the liquid, a significant difference was observed in the effect of droplet size on the control of cucumber powdery mildew. When the amount of active ingredient was 50 and 70 g/hm^2 per hectare, nozzle F110-01 showed the best control effect, which did not differ significantly from that observed with nozzle F110-015 but differed significantly from those observed with nozzles F110-02 and F110-03. This may be because the fine or medium particle size droplets were blocked less by the crop leaves, which is more conducive for the penetration of the droplets into the crop

canopy; as a result, the droplets are deposited in the inner layer of the crop, achieving a better control effect. According to the results of this study, the use of smaller droplets with a VMD of 100–150 μm for application to the upper part of the leaves of cucumber in greenhouses, i.e., the use of F110-01 or F110-015 nozzles, can significantly improve the effective use of pharmaceuticals and the disease control effect.

We have only analyzed the effect of the spray hole diameter of different fan nozzles in this study; in the future, cone nozzles or other types of fan nozzles should be tested to reduce the amount of liquid applied and enhance the scientific use of drugs.

Data availability statement

The original contributions presented in the study are included in the article/supplementary material. Further inquiries can be directed to the corresponding author.

Author contributions

WQ, XC, and PC: Investigation, Writing-Original draft preparation. XC: Investigation. WQ: Conceptualization, Supervision, Writing- Reviewing and Editing. All authors contributed to the article and approved the submitted version.

Funding

This research was funded by the National Natural Science Foundation of China (Grant No. 31971804), the Jiangsu Modern Agricultural Machinery Equipment and Technology Demonstration and Promotion Project (Grant No. NJ2022-17), the Suzhou Agricultural Vocational and Technical College Landmark Achievement Cultivation Project (CG[2022]02), the Suzhou Agricultural Independent Innovation Project (SNG2022061), and the Natural Science Foundation of Jiangsu Province (Grant No. 19KJD460006).

Conflict of interest

The authors declare that the research was conducted in the absence of any commercial or financial relationships that could be construed as a potential conflict of interest.

Publisher's note

All claims expressed in this article are solely those of the authors and do not necessarily represent those of their affiliated organizations, or those of the publisher, the editors and the reviewers. Any product that may be evaluated in this article, or claim that may be made by its manufacturer, is not guaranteed or endorsed by the publisher.

References

Cerkauskas, R. F., and Ferguson, G. (2014). Management of powdery mildew *(Podosphaera xanthii)* on greenhouse cucumber in Ontario. *Can. J. Plant Pathol.* 36, 22–37. doi: 10.1080/07060661.2013.878754

Cui, L., Wang, J., Qin, W., Yin, J., and Yuan, H. (2010). Relationship between droplet density and field efficacy when applying imidacloprid 700WG against wheat aphids with knapsack mist-blower. *Chin. J. Pestic. Sci.* 12, 313–318. doi: 10.3969/j.issn.1008-7303.2010.03.14

Dhalin, D., Kathirvel, K., Job, T. V., and Manina, R. (2008). Effect of operating parameters and pesticide flow characteristics on performance of air assisted spraying. *Ama Agric. Mechanization Asia Afr. Latin America.* 39, 39–45.

Elad, Y., Barnea, D., Rav-David, D., and Yermiyahu, U. (2021). Nutrient status of cucumber plants affects powdery mildew *(Podosphaera xanthii)*. *Plants (Basel).* 10, 2216. doi: 10.3390/plants10102216

Elsharkawy, M. M., Kamel, S. M., and El-Khateeb, N. M. M. (2014). Biological control of powdery and downy mildews of cucumber under greenhouse conditions. *Egypt. J. Biol. Pest Control.* 24, 407–414.

Eskandari, S., and Sharifnabi, B. (2020). Foliar spray time affects the efficacy of applied manganese on enhancing cucumber resistance to *Podosphaera fuliginea*. *Sci. Hortic.* 261, 108780. doi: 10.1016/j.scienta.2019.108780

Feng, Y., Guo, X., and Li, Y. (2022). Effects of surface free energy of crops leaves and spry adjuvants on the wettability of pesticide solution on five crop leaves. *Chin. J. Pestic. Sci.* 24, 1466–1472. doi: 10.16801/j.issn.1008-7303.2022.0054

Hamza, A. M., Essa, T. A., Derbalah, A. S., and Mohamed, A. A. (2015). Performance of some fungicide alternatives for controlling powdery mildew on cucumber under greenhouse conditions. Egypt. *J. Biol. Pest Control.* 25, 631–637.

Harburguer, L., Seccacini, E., Licastro, S., Zerba, E., and Masuh, H. (2012). Droplet size and efficacy of an adulticide-larvicide ultralow-volume formulation on *Aedes aegypti* using different solvents and spray application methods. *Pest Manage. Sci.* 68, 137–141. doi: 10.1002/ps.2237

Hong, Y., Guo, B., Xu, C., Shen, C., Huang, J., and Zheng, S. (2022). Effects of UAV spray parameters on droplet deposition distribution and control efficiency in pinus massoniana forest. *For. Sci. Technol.* 591, 28–33. doi: 10.13456/j.cnki.lykt.2021.06.16.0002

Johnstone, D. R. (1971). "Selecting the optimum droplet size distribution for the application of low and ultra-low volume insecticide sprays on to cotton from aircraft," in *Cotton Insect Control Proceedings of the Cotton Insect Control Conference*. 131–149.

Kang, F., Wu, X., Wang, Y., Yongjun, Z., Shougen, L., and Chongchong, C. (2021). Research progress and prospect of pesticide droplet deposition characteristics. *Trans. Chin. Soc. Agric. Eng.* 37, 1–14.

Lan, M., Zhong, L., Zhang, L., and Zhang, L. (2018). Effects of different combinations of fertilization and agrochemical application on yield and cost-effectiveness of cucumber. *Agric. Biotechnol.* 7, 24–29. doi: 10.19759/j.cnki.2164-4993.2018.03.006

Lu, J, Jia, WD, Qiu, BJ, and Li, PP. (2010). Experiment on retention of spray liquid on cucumber leaves. *Trans. Chinese Soc. Agri. Mach.* 41 (4), 60–64 (in Chinese).

Lv, X., Wang, X., and Jia, B. (2016). Construction of cucumber powdery mildew early warning system in solar greenhouse based on internet of things. *Agric. Sci. Technol.* 17, 2873–2884. doi: 10.16175/j.cnki.1009-4229.2016.12.046

Mao, H., Wang, Y., Yang, N., Liu, Y., and Zhang, X. (2022). Effects of nutrient solution irrigation quantity and powdery mildew infection on the growth and physiological parameters of greenhouse cucumbers. *Int. J. Agric. Biol. Eng.* 15, 68–74. doi: 10.25165/j.ijabe.20221502.6838

Mount, G. A. (1970). Optimum droplet size for adult mosquito control with space sprays or aerosols of insecticides. *Mosq. News.* 30, 70–75.

Roisman, I. V., Horvat, K., and Tropea, C. (2006). Sprayimpact: rim transverse instability initiating fingering and splash, and description of a secondary spray. *Phys. Fluids.* 18, 102–124. doi: 10.1063/1.2364187

Santos-Júnior, JoséL. C., Raetano, C. G., de Carvalho, F. K., Ferreira-Filho, P. J., Guerreiro, J. C., Ferrari, S., et al. (2022). Effects of application rate on spray deposition, stink bug control, and yield in soybean crops. *Phytoparasitica.* 50, 191–200. doi: 10.1007/s12600-021-00954-4

Sarhan, E. A. D., Abd-Elsyed, M. H. F., and Ebrahiem, A. M. Y. (2020). Biological control of cucumber powdery mildew *(Podosphaera xanthii)* (Castagne) under greenhouse conditions. *Egypt. J. Biol. Pest Control.* 30, 1–7. doi: 10.1186/s41938-020-00267-4

Song, Y., Cao, C., Xu, B., Ran, G., Cao, L., Li, F., et al. (2019). Research progress on bouncing behavior and control technology of pesticide droplets at plant leaf surface. *Chin. J. Pestic. Sci.* 21, 895–907. doi: 10.16801/j.issn.1008-7303.2019.0110

Tang, R. (2002). *Study and screening on plant extracts against powdery mildew of cucumber* Vol. 7 (Hebei: Hebei Agricultural University).

Tang, J., Lun, H., Zhao, C., Yun, M., Ma, Y., and Wang, J. (2019). Effects of microbial pesticides on prevention and control of cucumber downy mildew. *Asian Agric. Res.* 11, 56–59. doi: 10.19601/j.cnki.issn1943-9903.2019.08.010

Wang, S., Yang, W., Jia, F., Zhang, L., Wang, J., and Yang, J. (2021). Selection of rotational agents for the control of cucumber powdery mildew. *China Plant Protection.* 41, 84–86.

Williams, P. A., English, R. J., Blanchard, R. L., Rose, S. A., Lyons, L., and Whitehead, M. (2008). The influence of the extensional of very low concentrations of high molecular mass water-soluble polymers on atomisation and droplet impact. *Pest Manage. Sci.* 64, 497–504. doi: 10.1002/ps.1523

Wu, Y., Hong, W., Zhang, Z., Wu, Y., and Miao, Q. (2022). Epidemic dynamic and prediction model of cucumber powdery mildew under protected cultivation. *Acta Agriculturae Zhejiangensis.* 34, 104–111. doi: 10.3969/j.issn. 1004-1524. 2022. 01. 13

Xu, D. J., Xu, G. C., Xu, X. L., and Gu, Z. Y. (2015). Effect of application volume droplet size, rice leaf incline angle and spray adjuvant on pesticide deposition. *Southwest China J. Agric. Sci.* 28, 2056–2062. doi: 10.16213/j.cnki.scjas.2015.05.038

Xue, X., Tu, K., Qin, W., Yubin, L., and Huihui, Z. (2014). Drift and deposition of ultra-low altitude and low volume application in paddy field. *Int. J. Agric. Biol.* 7, 23–28.

Yang, X., Zhou, J., He, X., and Herbst, A. (2012). Influences of nozzle types on pesticide deposition and insecticidal effect to wheat aphids. *Trans. Chin. Soc. Agric. Eng.* 28, 46–50. doi: 10.3969/j.issn.1002-6819.2012.07.008

Ye, D., Zhou, Y., Zhang, Y., Iqbal, C., and Yang, X. (2022). Research progress of insecticidal peptides: a review. *Chin. J. Pestic. Sci.* 24, 962–981. doi: 10.16801/j.issn.1008-7303.2022.0114

frontiers | Frontiers in Plant Science

TYPE Original Research
PUBLISHED 15 May 2023
DOI 10.3389/fpls.2023.1188981

OPEN ACCESS

EDITED BY
Xiaolan Lv,
Jiangsu Academy of Agricultural Sciences (JAAS), China

REVIEWED BY
Wei Qiu,
Nanjing Agricultural University, China
Bingbo Cui,
Jiangsu University, China
Qin Weicai,
Suzhou Polytechnic Institute of Agriculture, China

*CORRESPONDENCE
Hailong Li
lihailong183@163.com

†These authors share first authorship

RECEIVED 18 March 2023
ACCEPTED 14 April 2023
PUBLISHED 15 May 2023

CITATION
Quan L, Chen K, Chen T, Li H, Li W, Cheng T, Xia F, Lou Z, Geng T, Sun D and Jiang W (2023) Monitoring weed mechanical and chemical damage stress based on chlorophyll fluorescence imaging.
Front. Plant Sci. 14:1188981.
doi: 10.3389/fpls.2023.1188981

Monitoring weed mechanical and chemical damage stress based on chlorophyll fluorescence imaging

Longzhe Quan[1†], Keyong Chen[1†], Tianbao Chen[1], Hailong Li[1*], Wenchang Li[1], Tianyu Cheng[1], Fulin Xia[2], Zhaoxia Lou[2], Tianyu Geng[1], Deng Sun[2] and Wei Jiang[3]

[1]College of Engineering, Anhui Agricultural University, Hefei, Anhui, China, [2]College of Engineering, Northeast Agricultural University, Harbin, China, [3]College of Engineering, China Agricultural University, Beijing, China

Currently, mechanical and chemical damage is the main way to carry out weed control. The use of chlorophyll fluorescence (CF) technology to nondestructively monitor the stress physiological state of weeds is significant to reveal the damage mechanism of mechanical and chemical stresses as well as complex stresses. Under simulated real field environmental conditions, different species and leaf age weeds (Digitaria sanguinalis 2-5 leaf age, and Erigeron canadensis 5-10 leaf age) were subjected to experimental treatments for 1-7 days, and fluorescence parameters were measured every 24 h using a chlorophyll fluorometer. The aim of this study was to investigate the changes in CF parameters of different species of weeds (Digitaria sanguinalis, Erigeron canadensis) at their different stress sites under chemical, mechanical and their combined stresses. The results showed that when weeds (Digitaria sanguinalis and Erigeron canadensis) were chemically stressed in different parts, their leaf back parts were the most severely stressed after 7 days, with photosynthetic inhibition reaching R=75%. In contrast, mechanical stress differs from its changes, and after a period of its stress, each parameter recovers somewhat after 1 to 2 days of stress, with heavy mechanical stress R=11%. Complex stress had the most significant effect on CF parameters, mainly in the timing and efficiency of changes in Fv/Fm, Fq'/Fm', ETR, Rfd, NPQ and Y(NO), with R reaching 71%-73% after only 3-4 days of complex stress, and its changes in complex stress were basically consistent with the pattern of changes in its chemical stress. The results of the study will help to understand the effects of mechanical and chemical stresses and combined stresses on CF parameters of weeds and serve as a guide for efficient weed control operations and conducting weed control in the future.

KEYWORDS

weeds, mechanical stress, chemical stress, complex stress, chlorophyll fluorescence

Introduction

Weeds in agricultural fields have long been one of the major causes of crop yield reduction because they compete directly with crops in consuming resources such as soil nutrients and water (Mézière et al., 2015; Colbach et al., 2019; Sabzi et al., 2020), and weeds are so damaging and vigorous that nearly 10% of crop yield is lost each year due to weed damage alone. Weed control technology is a very important part of agricultural production, and its development can reduce the competition of weeds to crops and improve the efficiency of agricultural production, which is divided into four ways: chemical control, mechanical control, biological control and soil management. Currently, two main methods of abiotic stress, mechanical and chemical, have been used for weed control (Chicouene, 2007; Mulder and Doll, 2017; Merritt et al., 2020; Chang et al., 2021; Qu et al., 2021). Mechanical damage is mainly through external forces that destroy the photosystem II (PSII) donor side of its photosynthetic system (Delaney, 2008; Nishiyama and Murata, 2014), while chemical stresses vary in damage principles and effects depending on the mechanism of action of their herbicides and the site of damage (Harker and O'Sullivan, 2017; Alizade et al., 2021), and compound stresses cause more severe damage (Zhou et al., 2017; Ma et al., 2018). Differences in the location and mode of stress have led to uneven results in weed control. Therefore, different weed damage methods and sites may have different responses, and their damage mechanisms lead to different physiological changes. Accurate monitoring of the phenotypic change information of weeds caused by stress, easy and fast access to weed mortality information, and find the optimal solution for weed control, the lowest cost to reduce weed damage, in order to improve crop yield and quality.

Both destructive and non-destructive methods have been used to detect abiotic stresses and their responses in plants (Gorbe and Calatayud, 2012; Baba et al., 2016). Among these, chlorophyll fluorescence (CF) imaging is one of the most common non-destructive techniques that have been applied to detect abiotic stresses in a range of plants (Dayan and Zaccaro, 2012; Gorbe and Calatayud, 2012; Wang et al., 2018). CF parameters can provide information about the details of mechanical damage and the extent of plant damage due to stress and measure various chlorophyll fluorescence parameters and quenching effects (Harbinson et al., 2012; Li et al., 2017; Schutte et al., 2019; Hassannejad et al., 2020). The use of chlorophyll fluorescence monitoring is based on the theory that plant stress leads to physiological changes in photosynthesis and fluorescence properties of plants (Bolhar-Nordenkampf et al., 1989; He et al., 2018). Snel et al. (1998) assessed the effect of the herbicide linuron on photosynthesis in freshwater algae by using chlorophyll fluorescence to measure the efficiency of photosystem II electron flow (ETR) (Snel et al., 1998). Raji et al. (2016) studied the changes in photosynthetic parameters such as net photosynthetic rate (Pn) and stomatal conductance (gs) in plants such as taro and sweet potato using fluorescence under herbicide and drought stress (Raji et al., 2016). Agostinetto et al. (2016) showed that photosynthetic rate, chlorophyll content, stomatal conductance and transpiration rate of wheat plants were reduced under the herbicides metribuzin, metsulfuron and 2,4-D stresses (Agostinetto et al., 2016). The above many studies show that chlorophyll fluorescence technique can be a good way to monitor the physiological changes of green plants when they are subjected to chemical and other stresses.

Many scholars have used chlorophyll fluorescence imaging techniques to study the effects of mechanical and chemical stresses on weeds, such as herbicides, machinery, high temperature, salinity, and drought (Hogewoning and Harbinson, 2007; Shin et al., 2020b; Lazarevic et al., 2021). Fuks et al. (1992) studied the photosynthetic performance of weeds using fluorescence of the oxidized PSII primary quinone receptor QA to determine if alterations in the 32-kD protein of photosystem PSII altered resistance to triazine herbicides (Fuks et al., 1992). Under herbicide stress, the chlorophyll content and photosynthetic capacity of weeds were reduced and the photochemical composition of the measured fluorescence quenching was altered. Linn et al. (2020) used chlorophyll fluorometry to measure weeds in the field after herbicide treatment and assessment of herbicide sensitivity (Linn et al., 2020) and determined that the fluorescence parameter Fv/Fm could be a strong indicator for evaluating weed sensitivity to herbicides. Fedotov et al. (2016) used fluorescence spectroscopy to monitor the effects of stress caused by mechanical damage in turfgrass and showed that the fluorescence ratio can be considered a reliable feature of plant stress status (Fedotov et al., 2016). Mechanical damage causes damage to the donor side of PSII, resulting in the production of large amounts of reactive oxygen species (ROS) in plants such as weeds, and excessive accumulation of ROS in plants (Choudhury et al., 2016), induces aldehyde formation and increases photosynthetic efficiency in response to stress by increasing the number of reaction centers per unit area (Wojtaszek, 1997; Maresca et al., 2020). These studies highlight the potential and effectiveness of using chlorophyll fluorescence for monitoring weeds subjected to herbicide versus mechanical stress.

At present, many researches are based on one factor of weed damage as the evaluation of weed control standard, but weeds are not affected by a single factor when they are under stress, such as species, damage mode and degree, damage site and application dose, etc. Considering many factors and observing the change pattern after stress, it is significant to reveal the damage mechanism of mechanical and chemical stress, and also can provide a strong theoretical basis for the related weed control technology. Therefore, the aim of this study was to investigate the changes in CF parameters and physiological response patterns of different species of weeds (Digitaria sanguinalis and Erigeron canadensis) at their different stress sites and levels under chemical, mechanical and their combined stresses.

Materials and methods

Plant material and damage conditions

Through the preliminary review of data and actual research, this study selected typical weeds in East China, where crops are biannual, tillage is frequent, and there are many weed species,

making prevention and control difficult. Therefore, according to the morphological classification of weeds, the experiments selected the most representative weeds of the region, Erigeron canadensis (Broadleaf family) and Digitaria sanguinalis (Gramineae family), as the sample weeds to carry out relevant studies (Chism and Bingham, 2017; Kelly and Coats, 2017; He et al., 2023). Maize is the main food crop in the region, and weed control in maize farmland is especially important, whose stalk weed control period is mostly the 3-5 leaf stage of maize. During this period, the field is mostly 5-10 leaves age and the plant height is mostly 2-5 cm; Digitaria sanguinalis is mostly 2-5 leaves age and the plant height is mostly 1-3 cm, so we only collected weeds randomly before the 5 leaves stage of maize.

In this experiment, wild weeds were transplanted into individual standard square pots (10cmx10cmx8cm) in the wild using a field transplanting method (Hazrati et al., 2016), and total transplanting about 300 plants. The transplanted weeds were placed in a shaded position for slow transition, and then the weeds were placed in daylight conditions to simulate the real field natural environment, and the weed samples are shown in (Figure 1). Treatment divisions included leaf surface chemical stress HD1; leaf back chemical stress HD2; leaf heart chemical stress HD3; stem chemical stress HD4; light mechanical stress MD1; severe mechanical stress MD2; light mechanical complex stress MD1-HD; and severe mechanical complex stress MD2-HD.

Preparation of stress samples and fluorescence image acquisition

Weed plants in good growth condition under daylight conditions will be damaged under natural environment after a slowing period of days. Prior to damage experiments on weeds, a chlorophyll fluorescence imager was used for predictive quantities, and for chlorophyll fluorescence imaging, a mobile chlorophyll fluorescence imaging system, PlantExplorer^{XS} (Pheno Vation, China), which is a mobile chlorophyll fluorescence measurement system specifically designed for field, greenhouse, climate chamber, and laboratory scenarios that can be moved, and set the average pixel value<0.75 for Fv/Fm images of weed plants were screened out to ensure that the experimental weeds were healthy weed plants before they underwent damage (Dong et al., 2020). At present, precision-to-rake application technology has become a trend in weed chemical control (Quan et al., 2022), and for its needs, herbicides were selected from the widely used and broad-spectrum tactile inactivating glufosinate ($C_5H_{15}N_2O_4P$) (Krausz et al., 2017; Tharp et al., 2017; Takano and Dayan, 2020), which has a wide herbicidal spectrum, low toxicity, high activity and good environmental compatibility. The general difference in chemical damage is mostly a distinction of site or dose (Tharp et al., 2017; Ali et al., 2020), so the dose used in the study was proportioned according to the actual local spraying situation, and the recommended dose was about 2500 g a.i./hm^2, the dosage of single plant agent is 10ml and applied to different parts of the leaf surface, leaf back, leaf heart and stem of the weed respectively (Figures 2A, B) (Mehmood et al., 2018). The difference in mechanical damage is mostly the distinction of damage mode and degree and the damage area is generally stem and leaf, so the mechanical damage was uniformly done by scratching the leaf with a blade to simulate the damage caused by field weeds due to weeding machinery operations, the degree of damage is divided by the area of the damaged leaf area and the number of scratches, the damage area ≤ 30% and the number of damaged leaf scratches for 1-2 for light damage, damage area ≥ 50% and the number of damaged leaf scratches for 3-4 for severe damage (Figures 2A, B) (Vitta and Quintanilla, 2017), complex stress is treated by simultaneous mechanical and chemical stresses. The experiment was divided into two main parts: a single-factor mechanical or chemical damage stress test and a compound factor mechanical and chemical damage stress test.

Chlorophyll fluorescence images were collected at 9:00 a.m. daily, and the damage treatment was performed in groups of three plants on the same site, averaged, monitored for 7 days and cycled (Figure 2C) and analyzed (Figure 2D). The Fv/Fm parameter is the

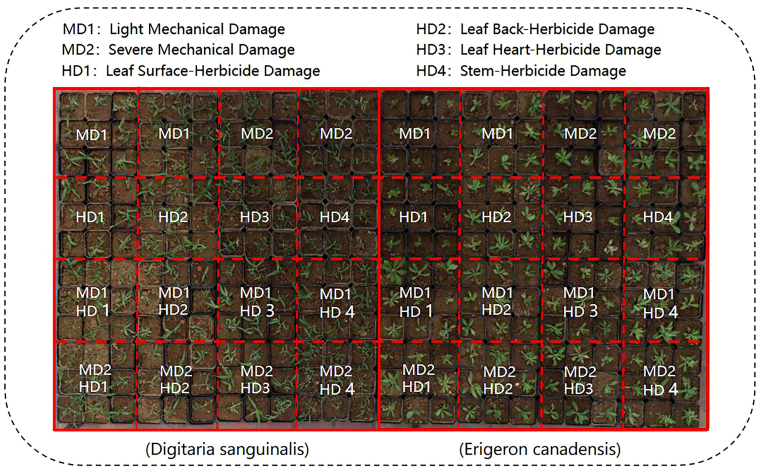

FIGURE 1
Visible visual appearance of the two weed samples collected.

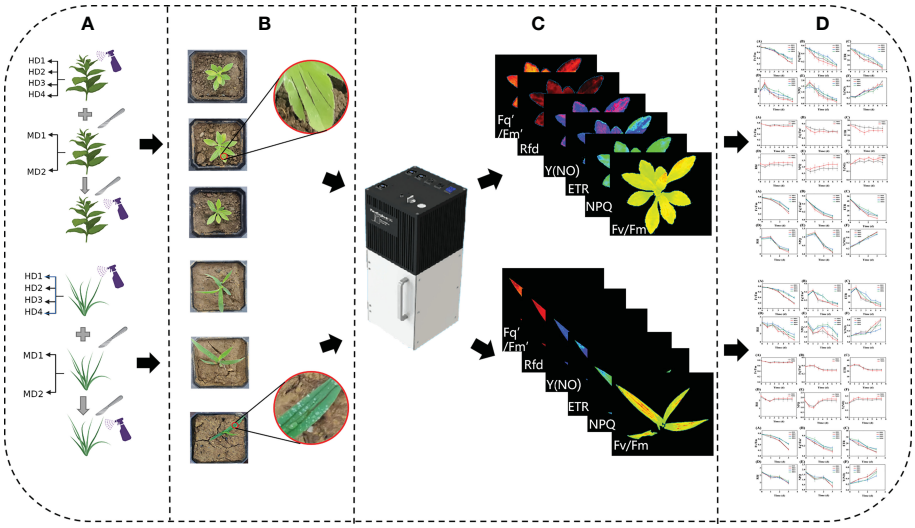

FIGURE 2
Experimental processing flow chart, **(A)** shows different stress treatments; **(B)** RGB images of sample weeds after treatment; **(C)** acquisition of fluorescence images; **(D)** data analysis.

most visual representation of the changes in photosynthetic capacity of plants, and the obtained Fv/Fm values were used to calculate their photosynthetic inhibition rate according to the following equation

$$R = \frac{(N - T)}{(N)} \times 100\,\%$$

R——Photosynthetic inhibition rate;
T——The average photosynthesis of weeds after duress;
N——The average photosynthesis of control weeds;

Selection of chlorophyll fluorescence parameters

For the selection of chlorophyll fluorescence parameters, CF parameters on the upper surface of all leaves of intact weed plants were obtained after measurement using chlorophyll fluorescence imaging, said CF parameters were measured independently after every 24 h at the onset of stress, fluorescence collection yielded a total of 14 fluorescence parameters, in this study, Fv/Fm, Fq'/Fm', ETR, Rfd, NPQ, and Y(NO) (Perez-Bueno et al., 2019; Ali et al., 2020; Shin et al., 2020a; Wang et al., 2021). And these parameters can clearly express the information about the changes in the photosynthetic system when the weed is stressed, the details of the six CF parameters evaluated are shown in (Table 1).

Statistical analysis

The results of CF fluorescence parameters were averaged over 3 biological replicate experiments. Statistical analysis was performed using SPSS software (Ver. 20; SPSS). Statistical differences between the means of the two groups were analyzed using analysis of variance (ANOVA) and Duncan's multiple polar difference test, $P<0.05$. The treatment protocols and their interactions were analyzed using a mixed model one-way ANOVA, $P<0.05$. The effects of treatments included (leaf surface chemical stress, HD1; leaf back chemical stress, HD2; leaf heart chemical stress, HD3; stem chemical stress, HD4; light mechanical stress, MD1; severe

TABLE 1 The chlorophyll fluorescence parameters used in this study.

Parameter	Formula	Description
Fv/Fm	(Fm - Fo)/Fm	Maximum quantum yield of PSII photochemistry measured in the dark-adapted state
Fq'/Fm'	(F'm - F'o)/F'm	Exciton transfer efficiency from antenna pigments to the reaction center of photosystem II in the light-adapted state
ETR	Fm– (Fm× PPFD × 0.5)	Electronic transmission rate in PSII
NPQ	(Fm - F'm)/F'm	Non photochemical quenching of maximum fluorescence
Rfd	(Fm - Fs)/Fs	Ratio of fluorescence decline
Y(NO)	1/[NPQ+ 1 + qL(Fm/Fo -1)]	Quantum yield of non-regulated energy dissipation in PSII

mechanical stress, MD2; light mechanical complex stress MD1-HD; severe mechanical complex stress MD2-HD), and time (0d-7d; for repeated measurements).

Results

Chlorophyll fluorescence imaging is a new technique for plant phenotyping that has been used to study the physiological and morphological response of weeds to chemical and mechanical stresses. Phenotypic characteristics were assessed at the onset of stress treatment (0d) and at the longest continuous time of weed decay (1d to 7d) after treatment onset. Pseudo-color images showing the effects of chemical, mechanical and combined stress on selected parameters Fv/Fm are shown in (Figure 3).

Effect of chemical stress on different parts of two weeds on CF parameters

The images of the effects of chemical stress treatment on Fv/Fm in Erigeron canadensis and Digitaria sanguinalis after 0-7 days are shown in (Figures 3A–D). From the site of chemical stress effect, the most obvious degree of change was monitored under chemical stress treatment in the leaf surface (HD1) and leaf back (HD2), and the back of the leaf was the most rapidly affected by chemical stress in comparison with the two. All CF parameters, except Y(NO), decreased during herbicide stress at different sites, with the most pronounced decreasing trend under leaf back treatment (Figures 4A, 5A). The most significant stress changes were obtained from Fv/Fm monitoring during 3 to 4 days under chemical stress treatment in Erigeron canadensis and Digitaria sanguinalis, and the direct cause of the decrease in photosynthetic rate was related to the mechanism of action of glufosinate (Richardson et al., 2007). Fv/Fm, the maximum quantum yield of PSII, the Fv/Fm parameters of Erigeron canadensis and Digitaria sanguinalis decreased insignificantly from day 0 to 1. In (Figure 4A), Fv/Fm changed significantly in different parts of the treatment from day 3, and the stress decrease in the back part of the leaf changed significantly, and the most obvious Fv/Fm value in the back part of the leaf decreased less than 0.2 after 7 days, and the photosynthetic inhibition rate R=75%. Fq′/Fm′, which is the effective quantum yield of PSII, (Figures 4A, 5A) also decreased after different site stress treatments, and the trend of change was distinguished clearly, with a higher decrease than that of Fv/Fm. ETR, the electron transport rate of chlorophyll fluorescence in PSII, showed a similar trend to Fq'/Fm' in different sites experimentally treated for stress, with Fq'/Fm' and ETR showing a significant increase from 0 to 1 day after treatment, decreasing fastest from 1 to 2 days, and becoming relatively slow after 2 days. Rfd, an important parameter indicating the attenuation of chlorophyll fluorescence, also showed similar trends to NPQ on different sites of experimental treatments of stress. NPQ is a very important non-chemical quenching parameter, and in (Figure 4E) Erigeron canadensis NPQ shows a transient increase during 0-1 days at the beginning of the stress. it shows a gradual decrease during 1-7 days, especially the stress change is most obvious in the back part of the leaf treatment, it is interesting to note that in Digitaria sanguinalis the changes in Rfd, NPQ from day 0-1 are reversed. Y(NO) indicates the components of the effectiveness of the photoprotective mechanism, and all other non-photoprotective components except heat diffusion, which are shown in (Figures 4F, 5F) to decrease to a certain extent in 0 to 1 day after stress treatment in different parts of Erigeron canadensis and Digitaria sanguinalis, and show a significant change of increase in the subsequent time, The results showed significant differences in all CF parameters.

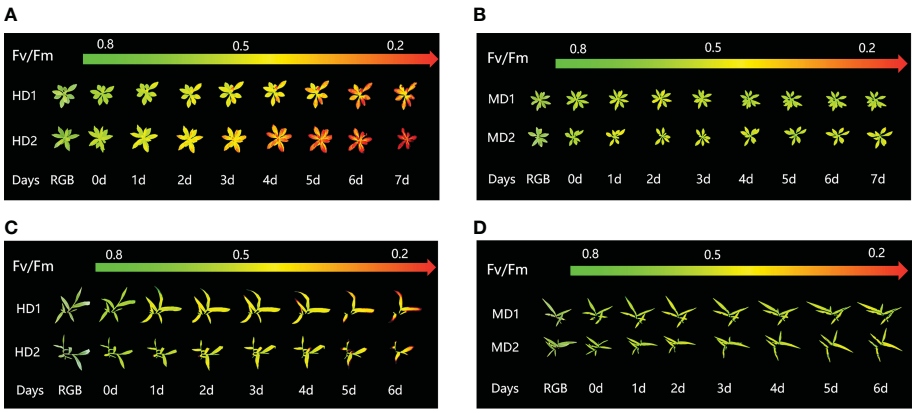

FIGURE 3
Fluorescence images of Fv/Fm parameters were captured daily during the experimental period, and the changes of Fv/Fm parameters images of Erigeron canadensis and Digitaria sanguinalis under different parts of Erigeron canadensis and Digitaria sanguinalis with different stresses were monitored continuously. **(A, B)** shows the image changes of Fv/Fm parameters in different parts of Erigeron canadensis with different levels of mechanical stress, and **(C, D)** shows the image changes of Fv/Fm parameters in different parts of Digitaria sanguinalis with different levels of mechanical stress.

10.3389/fpls.2023.1188981

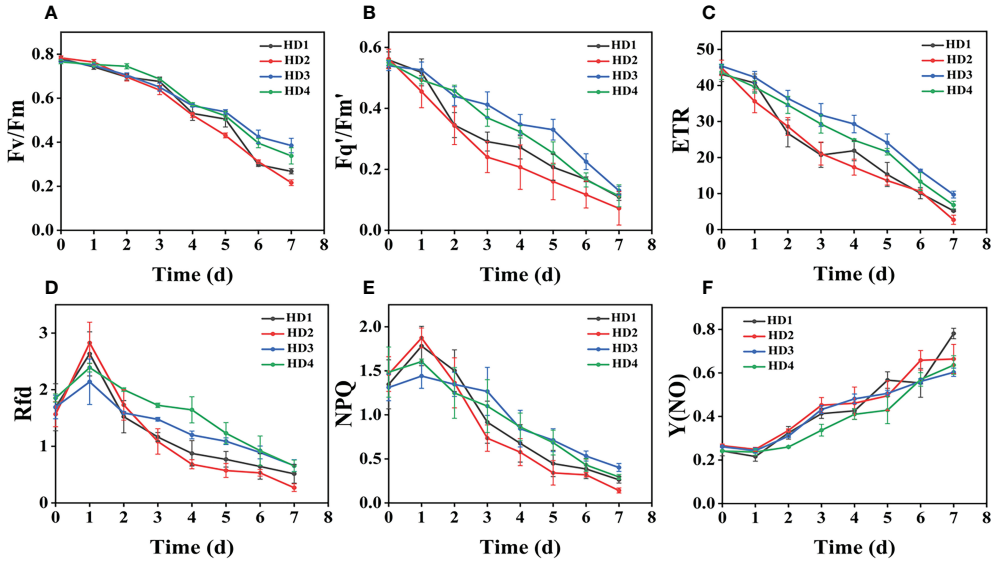

FIGURE 4
Fluorescence curves of each parameter of CF obtained by capturing each day during the experiment, **(A–F)** shows the variation of each CF parameter of Erigeron canadensis with treatment time under chemical stress treatment at different sites. Each plot point represents the mean ± SD of three biological replicate determinations. Refer (Table 1) for the description of each parameter.

Effect of different levels of mechanical damage acting on two weeds on CF parameters

From (Figures 3B, D), we can see the image changes of the effect on Fv/Fm between Erigeron canadensis and Digitaria sanguinalis after 0-7 days of mild (MD1) and severe (MD2) mechanical damage treatments. The CF parameters in (Figures 6A–F, 7A–F) were influenced by different degrees of mechanical damage. Among the light and heavy mechanical damage conditions, heavy mechanical damage had the greatest effect on all CF parameters. Among all CF parameters, the variation of Erigeron canadensis and Digitaria sanguinalis parameters were basically the same except for Fq'/Fm' and ETR. In (Figures 6A, 7A), Fv/Fm showed a decreasing change from 0 to 2 days, and a slow increase from 2 to 7 days, and a more stable fluctuation in a certain range, and R=11% for severe

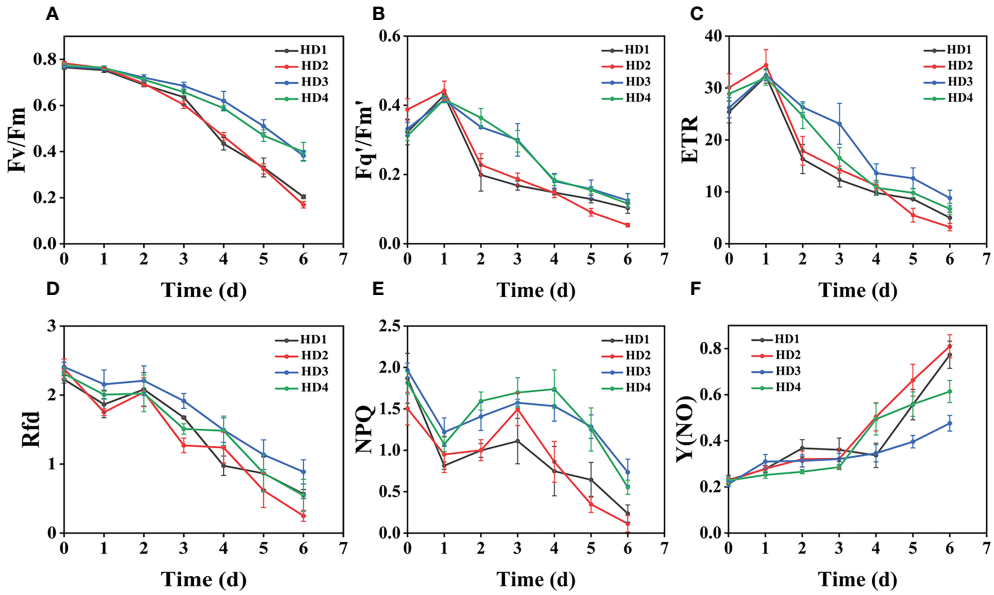

FIGURE 5
Fluorescence curves of each parameter of CF obtained by capturing each day during the experiment, **(A–F)** shows the variation of each CF parameter of Digitaria sanguinalis with treatment time under chemical stress treatment at different sites. Each plot point represents the mean ± SD of three biological replicate determinations. Refer (Table 1) for the description of each parameter.

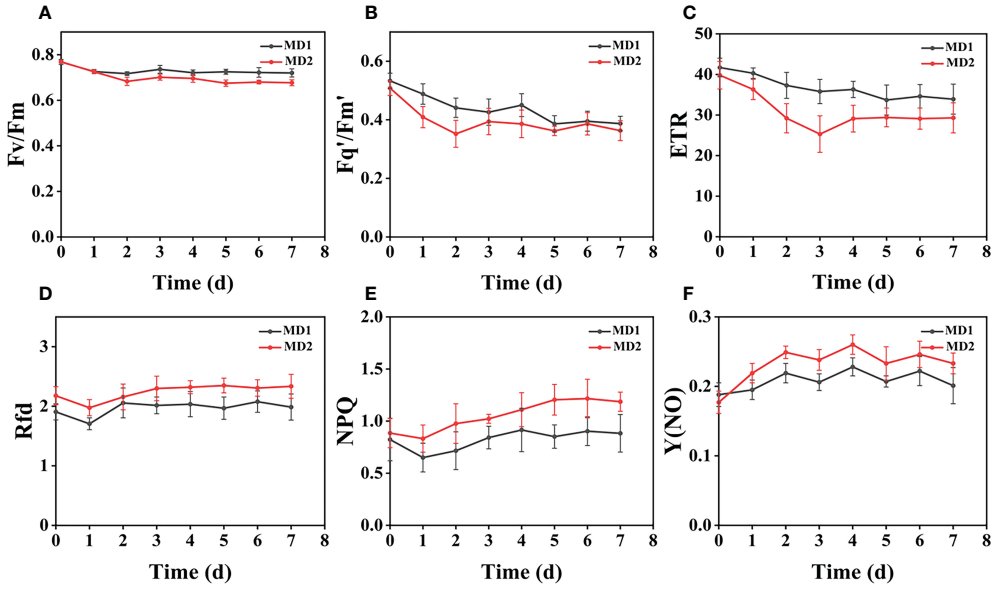

FIGURE 6
The fluorescence curves of each CF parameter were obtained by capturing each day during the experiment, and **(A–F)** are the changes of each CF parameter of Erigeron canadensis with treatment time under different levels of mechanical stress treatment. Each plot point represents the mean ± SD of three biological replicate determinations. Refer (Table 1) for the description of each parameter.

mechanical stress. The changes observed in Fq'/Fm' and ETR during mechanical stress in (Figure 6) show similar trends to the changes in Fv/Fm, and the results after stabilization were somewhat lower compared to the initial ones, with the difference that ETR showed a decreasing trend from 0 to 3 days and lasted longer compared to Fv/Fm. The changes of NPQ and Rfd parameters are approximately the same, both decrease rapidly from 0 to 1 day due to mechanical damage, slowly return to stability from 1 to 7 days, and the stable results are elevated compared to the initial ones. Y (NO) in (Figures 6F, 7F) increases when subjected to mechanical damage and stabilizes within a certain range of fluctuation after 2 days after the damage.

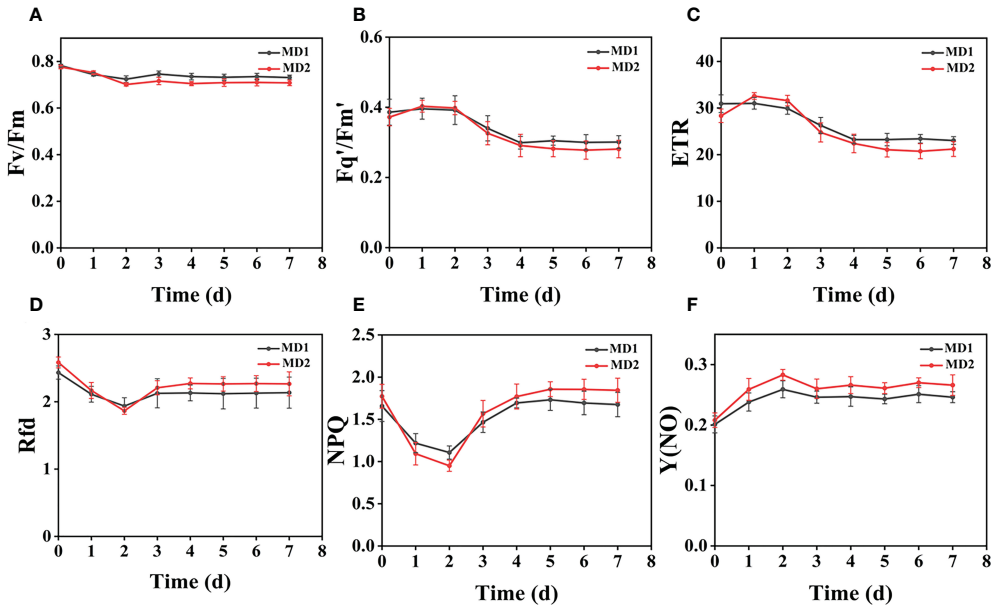

FIGURE 7
The fluorescence curves of each CF parameter were obtained by capturing each day during the experiment, and **(A–F)** are the changes of each CF parameter of Digitaria sanguinalis with treatment time under different levels of mechanical stress treatment. Each plot point represents the mean ± SD of three biological replicate determinations. Refer (Table 1) for the description of each parameter.

10.3389/fpls.2023.1188981

Effect of compound damage stress on CF parameters by acting on different parts of two weeds

(Figures 8A–D) shows the image changes of the effect of compound damage stress on Fv/Fm after the treatment of four different parts of light and heavy mechanical and chemical stresses, and the more severe the compound stress, the more obvious the changes of spatial heterogeneity (Figures 8B, D). The weed mortality status resulting from 3 days of heavy mechanical complex stress and 4 days of light mechanical complex stress in (Figures 8A, C) is the same and the change pattern is almost the same (Figures 9A, 10A). The most significant changes in Fv/Fm for both light and heavy mechanical complex stresses of Erigeron canadensis and Digitaria sanguinalis were observed after 2 days, and Fv/Fm reached the status of chemical stress treatment for 7 days with R=71%-73% at 3-4 days of complex stress treatment. The changes of Fq'/Fm' and ETR in (Figures 9B, C) are particularly pronounced from 0 to 1 day after the composite stress broke the cuticle hindrance, and the changes of Fq'/Fm' and ETR in (Figures 10B, C) in Digitaria sanguinalis also decreased from 0 to 1 day compared with the corresponding parameters of chemical stress in (Figures 5B, C). Erigeron canadensis and Digitaria sanguinalis Rfd and NPQ showed significant changes in compound stress than single stress, and the compound stress Y (NO) did not show a decreasing trend in 0-1 days of treatment, unlike the changes in chemical stress.

Discussion

Effect of chemical stress on different parts of two weeds on CF parameters

Chemical stress is a very important abiotic stress that will have a good effect on weed growth control and extermination, but the same application to different parts of the weed performance is also different. From (Figures 3A, C) leaf back (HD2), it can be observed that there is a change in area when the treatment proceeds to day 5-6, which is due to the cotyledons having a surface representation of stress, cotyledons wilting, chlorophyll disappearing, and Digitaria sanguinalis approaching a state of death more quickly than Erigeron canadensis when subjected to chemical stress, probably because of the very dense tomentum growing on the leaves of Erigeron canadensis, making it less accessible to the drug solution (Yu et al., 2009). The Fv/Fm parameters of Erigeron canadensis and Digitaria sanguinalis decreased insignificantly from 0 to 1 day, probably due to the obstruction of cuticle (Richardson et al., 2007; Kamtsikakis et al., 2021). The decrease in Fv/Fm values with time in this experiment indicates that photoinhibition of leaves occurred under herbicide glufosinate stress. Fv/Fm in (Figure 4A) changed significantly from day 3 onwards for different parts of the treatment, with significant changes in the decline of stress in the back part of the leaf, but in actual production, spraying the foliage is easier to achieve than the back part of the leaf (Figures 5B, C). Variation of Fq'/Fm' and ETR

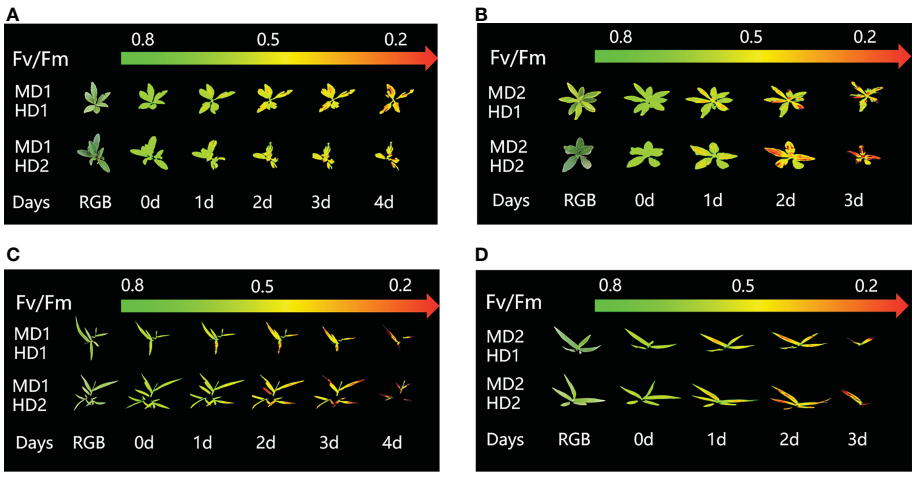

FIGURE 8
Fluorescence images of Fv/Fm parameters were captured daily during the experimental period, and the changes of Fv/Fm parameter images of Erigeron canadensis and Digitaria sanguinalis under the compound stress mode of chemical damage and different mechanical degree of damage at different parts of Erigeron canadensis and Digitaria sanguinalis during the continuous monitoring period. **(A, B)** shows the image changes of Fv/Fm parameters for light and heavy mechanical compound stresses in Erigeron canadensis, and **(C, D)** shows the image changes of Fv/Fm parameters for light and heavy mechanical compound stresses in Digitaria sanguinalis.

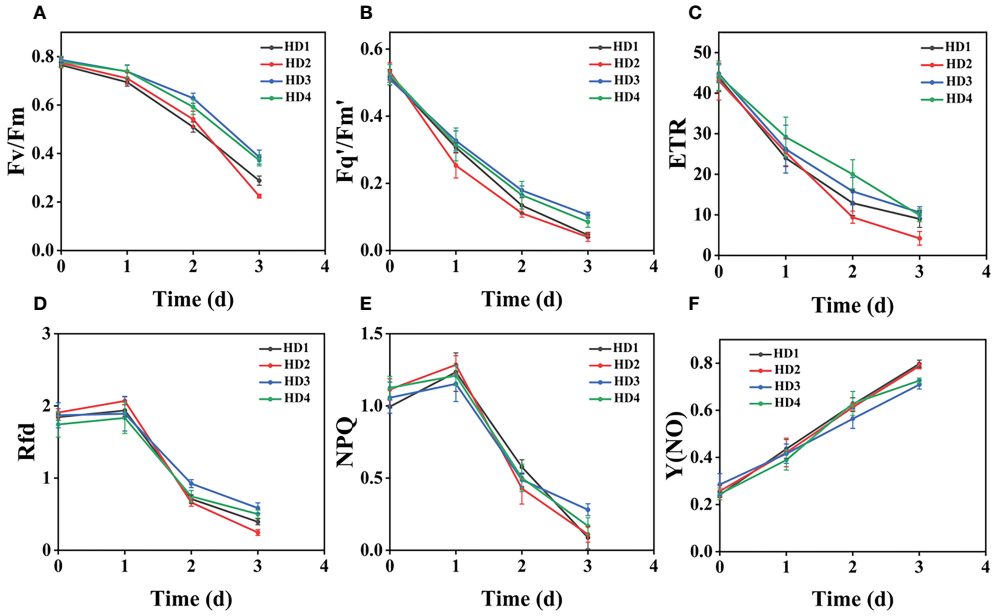

FIGURE 9
Fluorescence curves of each parameter of CF obtained by capturing each day during the experiment, **(A–F)** are the changes of each CF parameter of Erigeron canadensis with treatment time under f heavy mechanical complex stress treatment. Each plot point represents the mean ± SD of three biological replicate determinations. Refer (Table 1) for the description of each parameter.

parameters of Digitaria sanguinalis with respect to those corresponding to Erigeron canadensis in (Figures 4B, C). The Fq'/Fm' of Erigeron canadensis and Digitaria sanguinalis were the operational efficiency of PSII photochemistry, while the ETR parameters were also related to photochemistry, and the changes of both were different, probably due to different weed species and different sensitivity to glufosinate.

The variation of Rfd is closely related to the non-photochemical quenching of NPQ, which explains why the variation of Rfd is similar to that of NPQ. In (Figures 4D, E) Rfd and NPQ, however,

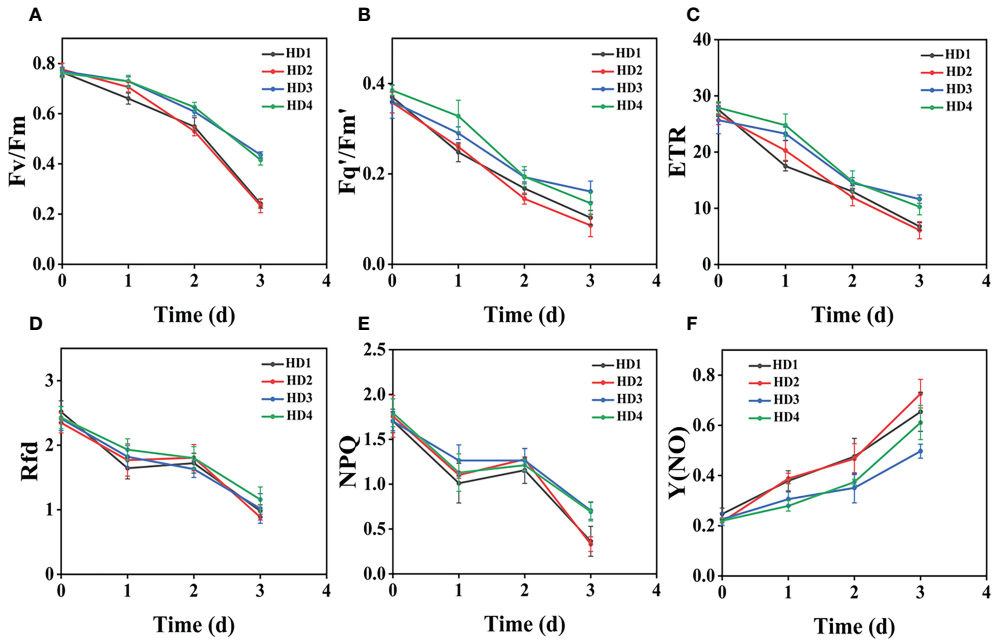

FIGURE 10
Fluorescence curves of each parameter of CF obtained by capturing each day during the experiment, **(A–F)** are the changes of each CF parameter of Digitaria sanguinalis with treatment time under f heavy mechanical complex stress treatment. Each plot point represents the mean ± SD of three biological replicate determinations. Refer (Table 1) for the description of each parameter.

showed a decreasing and then increasing trend from 0 to 2 days, which showed opposite changes to the parameters corresponding to the Erigeron canadensis. The trend of rising and then decreasing NPQ in Erigeron canadensis is due to the generation of photoinhibition (Lu et al., 2003). The rising trend of NPQ in the early stage indicates that the excess light energy absorbed by the antenna pigments in the PSII center is consumed by initiating the NPQ pathway to protect the activity of photosynthetic organs from damage or reduce the degree of damage, which likewise reflects that non-photochemical quenching is an important mechanism that can protect photosynthesis from proceeding smoothly. However, the NPQ tends to decrease with more severe chemical stress, which may be due to the blockage of the thermal dissipation mechanism due to severe chemical stress to the extent that excess light energy cannot be efficiently dissipated through non-photochemical quenching pathways (Chmeliov et al., 2019; Wilson and Ruban, 2020), the reduced heat dissipation capacity, the limitation of CO_2 assimilation and the imbalance of photochemical activity in photosystem II are factors that lead to energy overexcitation and subsequent photoinhibition (Song et al., 2015; Vodeneev et al., 2018; Chmeliov et al., 2019). The changes in NPQ in the pre-Digitaria sanguinalis period were the opposite of those in Erigeron canadensis, which may be due to insufficient light energy absorption by the antenna pigments in the PSII center, or may be due to the different stress responses to chemical stress caused by different weed species. The increase in Y(NO) levels under chemical stress conditions implies that the weeds were subjected to extreme stress during the experiment, indicating that the leaves developed invisible drug damage such as impaired photosynthetic electron transfer and reduced reaction center activity under herbicide stress, and that NPQ was also reduced under extreme stress conditions (Brugger et al., 2017; Tietz et al., 2017). Overall, chemical stress is highly destructive to the photosynthetic system of weeds, with significant effects on all CF parameters.

Effect of different levels of mechanical damage on CF parameters of two weeds

Mechanical damage is one of the most common forms of stress in weeds and induces multiple response mechanisms, which are also reflected in chlorophyll fluorescence when weeds are subjected to mechanical stress, and all parameters monitored respond when subjected to mechanical stress. The greater the degree of mechanical damage, the more pronounced the degree of change in weed fluorescence, and mechanical stress can damage weed leaves, possibly due to damage to chloroplast membranes and structures, increased chlorophyllase activity, and excessive accumulation of reactive oxygen species (ROS) due to weed resistance production after stress (Mhamdi and Van Breusegem, 2018; Mittler et al., 2022; Yan et al., 2023). It affects the photosynthesis of the weed for a period of time, leading to the impairment of the PSII community side, so that photosynthetic electron transfer is affected, which also explains the decrease of Fv/Fm, Fq'/Fm', and ETR in Erigeron canadensis from 0 to 3 days before mechanical stress.

Light and heavy mechanical damage can have different effects on the change of Fq'/Fm' and ETR in Digitaria sanguinalis, and in (Figures 3B, D) it can be observed that there is a significant change in color for heavy mechanical damage (MD2). In (Figures 7B, C), the Fq'/Fm' and ETR of Digitaria sanguinalis first increased and then decreased, which may indicate that the stress response of Digitaria sanguinalis leaves to compensate for the lack of light energy absorption due to damaged antenna pigments by increasing the efficiency of the PSII active reaction center while mechanical damage stress occurred (Appenroth et al., 2001). The different changes in Fq'/Fm' and ETR between Erigeron canadensis and Digitaria sanguinalis may be due to the different weed species and sensitivity to glufosinate, and also indicate that Erigeron canadensis are more sensitive to glufosinate and glufosinate is more effective on Erigeron canadensis (Steckel et al., 2017). The stabilized values were slightly lower than the initial ones, indicating that mechanical damage stress caused damage or inhibition of antennal pigments, resulting in a reduction of energy absorbed by antennal pigments and energy captured by reaction centers, and that this damage was permanent.

Rfd and NPQ parameters increased photosynthetic efficiency and decreased light energy consumption by non-photochemical quenching when subjected to mechanical stress, which explains why Rfd and NPQ decreased from 0 to 1 day. Since mechanical damage was always present, photosynthetic rate decreased with time and thermal consumption of light energy through non-photochemical quenching pathway increased, so Rfd and NPQ increased but did not change significantly in the subsequent period. Y(NO) increased significantly from 0 to 2 days, indicating that the weed was under the most severe stress during this period. The mechanical damage damaged the PSII community side, resulting in photochemical energy conversion and protective regulatory mechanisms (such as thermal diffusion) were not sufficient to completely consume the light energy absorbed by the weed, and after 2 days, the photosynthesis and physiology of the Erigeron canadensis gradually recovered to reach equilibrium and remained relatively stable, so Y(NO) also tended to stabilize. In conclusion, mechanical stress will destroy the internal physiological structure of weeds and affect the normal work of photosynthetic system, and each CF parameter will fluctuate, but after 2 days each CF parameter will have some recovery.

Comparative analysis of the effects of mechanical and chemical stresses on CF parameters of two weeds

The most obvious difference between chemical stress and mechanical stress is that chemical stress is irreversible in killing weeds. Regardless of the location where chemical stress acts, chemical stress affects the weed's individual life by disrupting its physiological patterns and preventing its growth. In contrast, mechanical stress limits weeds by the degree of damage to weeds by weeding machinery, which may be able to stop weed growth to a certain extent, but when the degree of mechanical damage is not

sufficient, weeds will still come back. The changes of the two stresses were more obvious by fluorescence parameters, and the R=75% in the back part of the leaf of chemical stress was much greater than the R=11% of heavy mechanical stress.

Fv/Fm responded to the potential maximum photosynthetic capacity of the weed, and the persistent and significant decrease in Fv/Fm of chemically stressed weeds indicated that the damage to the photosynthetic capacity of the weed by chemical stress was irreversible. The degree of variation in the corresponding Fq'/Fm', ETR, Rfd, and NPQ parameters all responded to the greater damage to the weed by chemical stress, and weed mechanical and chemical stresses behaved differently in the 0-1 day stress response to these four parameters, with chemical stress stresses being obvious, while the stresses exhibited by mechanical stresses were not. This may be due to the mechanical stress directly damage the physiological structure of the leaf, the damage is serious and rapid, fluorescence interval of 24 h monitoring, may be the next monitoring, mechanical stress stress response to manifest the effect has passed, resulting in fluorescence monitoring cannot be monitored or monitoring the effect is not obvious (Liu et al., 2019; Shetty et al., 2019; Li et al., 2020). The continuous increase in the Y(NO) parameter is an indication that the weed is under extreme stress. In contrast to the changes in the fluorescence parameters of mechanical stress, the weeds only changed significantly in the initial 1-2 days of stress, and the parameters hardly changed after the physiological changes of the weeds stabilized.

Effect of complex damage stress on CF parameters by acting on different parts of two weeds

(Figures 8A–D) shows the image changes of the effect of compound damage stress on Fv/Fm after the treatment of four different sites of light and heavy mechanical and chemical stress, the underlying cause of spatial heterogeneity of weeds on CF images is leaf loss of greenness, due to the accelerated degradation of chlorophyll and proteins after weeds are subjected to compound stress, the degradation of biomolecules in plants leads to the release of ROS, and ROS on The oxidative damage produced by the plant includes the accelerated production of ethylene, the main hormone that induces cellular senescence, which leads to the yellowing of leaves (Dubois et al., 2018; Katayose et al., 2021).

Fv/Fm in (Figure 9A) and (Figure 10A) reached the status of chemical stress treatment in (Figure 4A) and (Figure 5A) for 7 days with R=71%~73% at 3 days of compound stress treatment, indicating that mechanical stress accelerated the rate of action of chemical stress after breaking this obstructive layer of weed leaf cuticle and greatly accelerated the time of weed death (Figure 9A). The most significant changes in Fv/Fm were observed after 2 days for heavy mechanical complex stresses of Erigeron canadensis and Digitaria sanguinalis, which means that although mechanical damage broke the physical defense of leaves, only a small portion of glufosinate acted directly on cells, and most of it still needed to be transported in xylem to act on cells, inhibiting glutamine (GS) production and reducing photosynthetic yield, a process that takes time (Figures 9B, C). The changes in Fq'/Fm' and ETR of Erigeron canadensis were especially obvious from 0 to 1 days after the composite stress broke the cuticle hindrance, which was due to the inhibition of photosynthesis by the direct entry of glufosinate into the leaf cells where the action occurred, reducing the efficiency of PSII photochemical operation and the photosynthetic electron transfer (Figures 10B, C). Digitaria sanguinalis Fq'/Fm', ETR compared to the corresponding parameter changes of chemical stress in (Figures 5B, C) at 0 to 1 day also decreased, this is because the stress response of the weed will be somewhat to resist the stress when it is suddenly damaged by such a large stress, due to the extreme, permanent and irreversible damage caused by the complex stress to the internal physiology and structure of the weed, the physiological defense mechanism of the weed is far from sufficient to resist the damage of the complex stress (Figures 9D–F) is similar to the variation of (Figures 4D–F) and (Figures 10D–F) is similar to the variation of (Figure 5D-F), which may be due to the fact that their corresponding species are the same. Erigeron canadensis and Digitaria sanguinalis Rfd and NPQ showed significant changes under compound stress than single stress, suggesting that Erigeron canadensis and Digitaria sanguinalis were subjected to severe stress resulting in imbalance of PSII photochemical activity, energy overexcitation and photoinhibition, and leading to photooxidative damage with high production of reactive oxygen species (ROS) in chloroplasts (Ivanov and Khorobrykh, 2003; Ksas et al., 2015). Complex stress Y(NO) did not show a decreasing trend from 0 to 1 day of treatment, unlike the changes in chemical stress. Y(NO) showed a significant increase from the first day, indicating that the weed initiated a photoprotective mechanism on the first day of complex stress and that more and more light energy was dissipated by thermal diffusion with chlorophyll degradation. The sustained changes in Y(NO) of Erigeron canadensis under compound stress were faster, indicating that the heat diffusion ability of Erigeron canadensis was better than that of Digitaria sanguinalis, which also implied that Erigeron canadensis was more sensitive to glufosinate than Digitaria sanguinalis.

Comparative analysis of the effects of complex stress and single stress on CF parameters of two weeds

Compared with single stress, compound stress not only disrupted the physiological pattern of weeds but also directly damaged the leaf structure of weeds, broke the obstruction of weed cuticle layer, made glufosinate enter into weeds faster, and combined with ATP and occupied the reaction site of GS, the synthesis of GS was blocked, and photosynthesis was affected, which made the weeds die much more efficiently (Ulguim et al., 2019; Takano et al., 2020a; Takano et al., 2020b). It is evident from the time that the composite stress leads to the death of the weed in a far shorter time than when a single stress acts on the weed. As shown in (Figures 11A–F, 12A–F), it was observed from the experimentally obtained curves that the pattern of changes in weeds subjected to complex stress was consistent with that of the single chemical stress, which indicates that chemical stress damages weeds more severely compared to mechanical stress, therefore, compound stress should be dominated by chemical stress and supplemented by mechanical stress, and the heavy mechanical compound stress R increased by

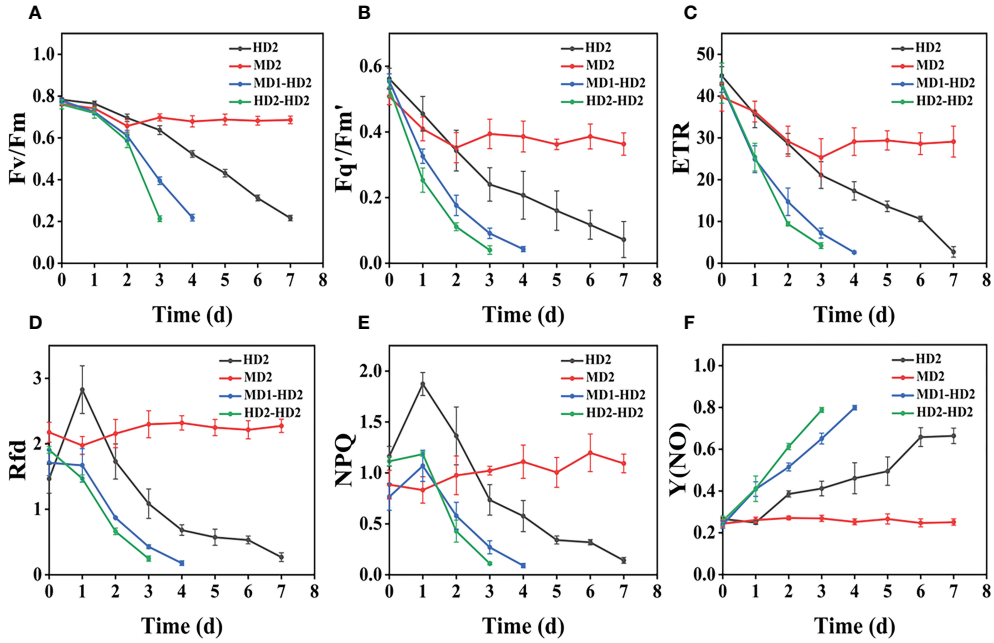

FIGURE 11
(A–F) Variation of each CF parameter with treatment time for different damage modalities (leaf abaxial chemical stress, heavy mechanical stress with light and heavy combined stress) in Erigeron canadensis. Each plot point represents the mean ± SD of three biological replicate determinations. Refer (Table 1) for the description of each parameter.

53% compared to chemical stress R. The Fv/Fm parameter is the most intuitive parameter to show the change of photosynthetic rate of the plant, and each parameter was approximately the same for Erigeron canadensis and Digitaria sanguinalis under different stresses. As shown in (Figures 13A–D), the error values of Fv/Fm of Erigeron canadensis were larger with longer stress time, indicating that the physiological changes of weeds under stress were stronger with increasing time. We found that in (Figures 13A–D), the error

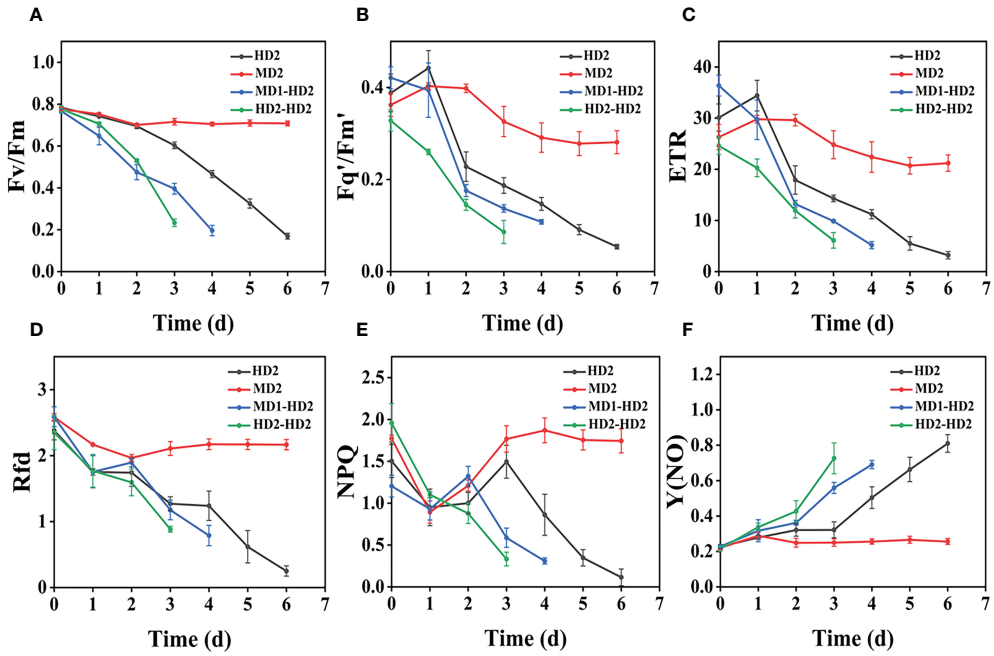

FIGURE 12
(A–F) Variation of each CF parameter with treatment time for different damage modalities (leaf abaxial chemical stress, heavy mechanical stress with light and heavy combined stress) in Digitaria sanguinalis. Each plot point represents the mean ± SD of three biological replicate determinations. Refer (Table 1) for the description of each parameter.

10.3389/fpls.2023.1188981

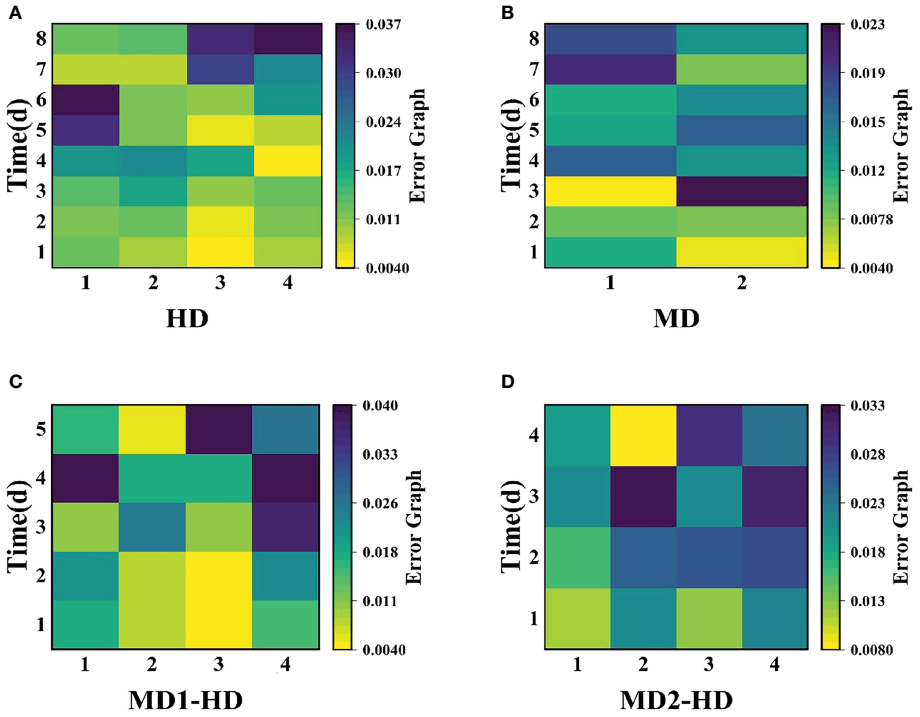

FIGURE 13
shows the variation of error diagrams of the Erigeron canadensis Fv/Fm at different parts with damage ways. **(A)** the variation of error diagrams of the flying canopy at different parts with chemical damage mode, **(B)** the variation of error diagrams of the Erigeron canadensis at different degrees with mechanical damage mode, **(C)** the variation of error diagrams of the Erigeron canadensis at light mechanical compound damage mode, **(D)** the variation of error diagrams of the Erigeron canadensis at severe mechanical compound damage mode.

values of the back part of the leaves under compound stress, however, all became smaller after 7 days of stress. The reason for this is that the back part of the leaves under compound stress is the most severely damaged part, and the longer the stress time is, the faster its chlorophyll disappears and the smaller its photosynthetic capacity becomes, so that it has almost no photosynthetic capacity, so its error values change less and less.

Conclusion

This study shows the potential of using CF images to monitor Erigeron canadensis and Digitaria sanguinalis when subjected to abiotic stresses (mechanical, chemical). The response of Erigeron canadensis and Digitaria sanguinalis to abiotic stresses was observed by monitoring the changes in the obtained CF parameters. These changes depended on the type, site and extent of the stressor. The most influential parameters were Fv/Fm, Fq'/Fm', ETR, Rfd, NPQ, and Y(NO), all of which decreased after the experimental treatment except for Y(NO). Fv/Fm is the most direct window indicating the change in photosynthetic quantum yield, Fv/Fm decreases continuously from the beginning, so chemical stress acts irreversibly on the weed, and chemical stress acts on different parts of the plant, and the maximum photosynthetic inhibition reaches R=75% in the back part of the leaf for Erigeron canadensis and Digitaria sanguinalis. The different levels of mechanical stress, heavy mechanical damage had a greater effect on Erigeron canadensis and Digitaria sanguinalis, with R=11% for heavy mechanical stress, and chemical stress had a significant effect on all parameters of CF compared to mechanical stress, which indicates that chemical stress is more severe than mechanical stress in photoinhibition of photosynthesis. The effect of compound stress on CF parameters was similar to that of chemical stress, but in time it was evident that heavy mechanical compound stress was going to be more severe damage stress on Erigeron canadensis and Digitaria sanguinalis, and the changes in CF parameters were especially obvious, and the compound stress reached 71%-73% of R after only 3-4 days. In summary, Fv/Fm, Fq'/Fm', ETR, Rfd, NPQ, and Y(NO) can be used as indicator parameters for detecting two abiotic stresses, and usually, the values of all their fluorescence parameters change when affected by stress, and chlorophyll content levels increase or decrease depending on the degree of stress. These results indicate that different types, sites and levels of stress have different effects on photosynthetic activity as well as fluorescence parameters, which will help to inform and guide the flexible design of mechanical weed control, the optimization of chemical weed control on rake spraying methods and the proposal of new weed control models.

Data availability statement

The raw data supporting the conclusions of this article will be made available by the authors, without undue reservation.

Author contributions

LQ and KC: Conception, methodology, software, formal analysis, investigation, writing-review and editing. HL: Conception, writing-review and editing, supervision and project management. TBC and WL: Fluorescence processing. TYC, FX, ZL and TG: Data collation, conceptualization and supervision. DS and WJ: Data collation. All authors have read and agreed to the published version of the manuscript.

Funding

This work was supported by the National Natural Science Foundation of China under the project (No. 52075092,32271998) and Anhui Agricultural University Intelligent Agricultural Equipment Research Institute Project (No.jz214102).

Conflict of interest

The authors declare that the research was conducted in the absence of any commercial or financial relationships that could be construed as a potential conflict of interest.

Publisher's note

References

Agostinetto, D., Perboni, L. T., Langaro, A. C., Gomes, J., Fraga, D. S., and Franco, J. J. (2016). Changes in photosynthesis and oxidative stress in wheat plants submmited to herbicides application. *Planta Daninha* 34 (1), 1–9. doi: 10.1590/s0100-83582016340100001

Ali, A., Xue, Q., Chen, S., Ren, Y., Fu, Q., Shao, W., et al. (2020). Herbicides act as restrictive factors in rice-watermelon rotation. *Scientia Hortic.* 261, 108974. doi: 10.1016/j.scienta.2019.108974

Alizade, S., Keshtkar, E., Mokhtassi-Bidgoli, A., Sasanfar, H., Streibig, J. C., and Bohren, C. (2021). Effect of drought stress on herbicide performance and photosynthetic activity of avena sterilis subsp. ludoviciana (winter wild oat) and hordeum spontaneum (wild barley). *Weed Res.* 61 (4), 288–297. doi: 10.1111/wre.12477

Appenroth, K. J., Stockel, J., Srivastava, A., and Strasser, R. J. (2001). Multiple effects of chromate on the photosynthetic apparatus of spirodela polyrhiza as probed by OJIP chlorophyll a fluorescence measurements. *Environ. Pollut.* 115 (1), 49–64. doi: 10.1016/s0269-7491(01)00091-4

Baba, W., Kalaji, H. M., Kompala-Baba, A., and Goltsev, V. (2016). Acclimatization of photosynthetic apparatus of tor grass (Brachypodium pinnatum) during expansion. *PLoS One* 11 (6), e0156201. doi: 10.1371/journal.pone.0156201

Bolhar-Nordenkampf, H. R., Long, S. P., Baker, N. R., Oquist, G., Schreiber, U., and Lechner, E. G. (1989). Chlorophyll fluorescence as a probe of the photosynthetic competence of leaves in the field: a review of current instrumentation. *Funct. Ecol.* 3 (4), 497–514. doi: 10.2307/2389624

Brugger, A., Kuska, M. T., and Mahlein, A.-K. (2017). Impact of compatible and incompatible barley–blumeria graminis f.sp. hordei interactions on chlorophyll fluorescence parameters. *J. Plant Dis. Protection.* 125, 177–186. doi: 10.1007/s41348-017-0129-1

Chang, C.-L., Xie, B.-X., and Chung, S.-C. (2021). Mechanical control with a deep learning method for precise weeding on a farm. *Agriculture* 11 (11), 1049. doi: 10.3390/agriculture11111049

Chicouene, D. (2007). Mechanical destruction of weeds. a review. *Agron. Sustain. Dev.* 27 (1), 19–27. doi: 10.1051/agro:2006012

Chism, W. J., and Bingham, S. W. (2017). Postemergence control of Large crabgrass (Digitaria sanguinalis) with herbicides. *Weed Sci.* 39 (1), 62–66. doi: 10.1017/s004317450005788x

Chmeliov, J., Gelzinis, A., Franckevicius, M., Tutkus, M., Saccon, F., Ruban, A. V., et al. (2019). Aggregation-related nonphotochemical quenching in the photosynthetic membrane. *J. Phys. Chem. Lett.* 10 (23), 7340–7346. doi: 10.1021/acs.jpclett.9b03100

Choudhury, F. K., Rivero, R. M., Blumwald, E., and Mittler, R. (2016). Reactive oxygen species, abiotic stress and stress combination. *Plant J.* 90 (5), 856–867. doi: 10.1111/tpj.13299

Colbach, N., Gardarin, A., and Moreau, D. (2019). The response of weed and crop species to shading: which parameters explain weed impacts on crop production? *Field Crops Res.* 238, 45–55. doi: 10.1016/j.fcr.2019.04.008

Dayan, F. E., and Zaccaro, M. (2012). Chlorophyll fluorescence as a marker for herbicide mechanisms of action. *Pesticide Biochem. Physiol.* 102 (3), 189–197. doi: 10.1016/j.pestbp.2012.01.005

Delaney, K. J. (2008). Injured and uninjured leaf photosynthetic responses after mechanical injury on nerium oleander leaves, and danaus plexippus herbivory on asclepias curassavica leaves. *Plant Ecol.* 199 (2), 187–200. doi: 10.1007/s11258-008-9423-0

Dong, Z., Men, Y., Liu, Z., Li, J., and Ji, J. (2020). Application of chlorophyll fluorescence imaging technique in analysis and detection of chilling injury of tomato seedlings. *Comput. Electron. Agric.* 168, 105109. doi: 10.1016/j.compag.2019.105109

Dubois, M., Van den Broeck, L., and Inze, D. (2018). The pivotal role of ethylene in plant growth. *Trends Plant Sci.* 23 (4), 311–323. doi: 10.1016/j.tplants.2018.01.003

Fedotov, Y., Bullo, O., Belov, M., and Gorodnichev, V. (2016). Experimental research of reliability of plant stress state detection by laser-induced fluorescence method. *Int. J. Optics* 2016, 1–6. doi: 10.1155/2016/4543094

Fuks, B., Eycken, F., and Lannoye, R. (1992). Tolerance of triazine-resistant and susceptible biotypes of three weeds to heat stress: a fluorescence study. *Weed Res.* 32 (1), 9–17. doi: 10.1111/j.1365-3180.1992.tb01857.x

Gorbe, E., and Calatayud, A. (2012). Applications of chlorophyll fluorescence imaging technique in horticultural research: a review. *Scientia Hortic.* 138, 24–35. doi: 10.1016/j.scienta.2012.02.002

Harbinson, J., Prinzenberg, A. E., Kruijer, W., and Aarts, M. G. (2012). High throughput screening with chlorophyll fluorescence imaging and its use in crop improvement. *Curr. Opin. Biotechnol.* 23 (2), 221–226. doi: 10.1016/j.copbio.2011.10.006

Harker, K. N., and O'Sullivan, P. A. (2017). Herbicide comparisons on quackgrass (Elytrigia repens) within different crop competition and tillage conditions. *Weed Sci.* 41 (1), 94–99. doi: 10.1017/s0043174500057647

Hassannejad, S., Lotfi, R., Ghafarbi, S. P., Oukarroum, A., Abbasi, A., Kalaji, H. M., et al. (2020). Early identification of herbicide modes of action by the use of chlorophyll fluorescence measurements. *Plants (Basel)* 9 (4), 529. doi: 10.3390/plants9040529

Hazrati, S., Tahmasebi-Sarvestani, Z., Modarres-Sanavy, S. A., Mokhtassi-Bidgoli, A., and Nicola, S. (2016). Effects of water stress and light intensity on chlorophyll fluorescence parameters and pigments of aloe vera l. *Plant Physiol. Biochem.* 106, 141–148. doi: 10.1016/j.plaphy.2016.04.046

He, C., Li, Y., Li, C., Wang, Y., Xu, Z., Zhong, S., et al. (2023). Photosynthetic capacity of erigeron canadensis l. may be more critical to its growth performance than photosynthetic area. *Biologia* doi: 10.1007/s11756-023-01317-6

He, L., Yu, L., Li, B., Du, N., and Guo, S. (2018). The effect of exogenous calcium on cucumber fruit quality, photosynthesis, chlorophyll fluorescence, and fast chlorophyll fluorescence during the fruiting period under hypoxic stress. *BMC Plant Biol.* 18 (1), 180. doi: 10.1186/s12870-018-1393-3

Hogewoning, S. W., and Harbinson, J. (2007). Insights on the development, kinetics, and variation of photoinhibition using chlorophyll fluorescence imaging of a chilled, variegated leaf. *J. Exp. Bot.* 58 (3), 453–463. doi: 10.1093/jxb/erl219

Ivanov, B., and Khorobrykh, S. (2003). Participation of photosynthetic electron transport in production and scavenging of reactive oxygen species. *Antioxid Redox Signal* 5 (1), 43–53. doi: 10.1089/152308603321223531

Kamtsikakis, A., Baales, J., Zeisler-Diehl, V. V., Vanhecke, D., Zoppe, J. O., Schreiber, L., et al. (2021). Asymmetric water transport in dense leaf cuticles and cuticle-inspired compositionally graded membranes. *Nat. Commun.* 12 (1), 1267. doi: 10.1038/s41467-021-21500-0

Katayose, A., Kanda, A., Kubo, Y., Takahashi, T., and Motose, H. (2021). Distinct functions of ethylene and ACC in the basal land plant marchantia polymorpha. *Plant Cell Physiol.* 62 (5), 858–871. doi: 10.1093/pcp/pcab042

Kelly, S. T., and Coats, G. E. (2017). Influence of fertilizer particle size on efficacy of dithiopyr, prodiamine, oryzalin, and oxadiazon for southern crabgrass (Digitaria ciliaris) control. *Weed Technol.* 13 (2), 385–389. doi: 10.1017/s0890037x00041907

Krausz, R. F., Kapusta, G., Matthews, J. L., Baldwin, J. L., and Maschoff, J. (2017). Evaluation of glufosinate-resistant corn (Zea mays) and glufosinate: efficacy on annual weeds. *Weed Technol.* 13 (4), 691–696. doi: 10.1017/s0890037x00042093

Ksas, B., Becuwe, N., Chevalier, A., and Havaux, M. (2015). Plant tolerance to excess light energy and photooxidative damage relies on plastoquinone biosynthesis. *Sci. Rep.* 5, 10919. doi: 10.1038/srep10919

Lazarevic, B., Satovic, Z., Nimac, A., Vidak, M., Gunjaca, J., Politeo, O., et al. (2021). Application of phenotyping methods in detection of drought and salinity stress in basil (Ocimum basilicum l.). *Front. Plant Sci.* 12. doi: 10.3389/fpls.2021.629441

Li, H., Wang, P., Weber, J. F., and Gerhards, R. (2017). Early identification of herbicide stress in soybean (Glycine max (L.) merr.) using chlorophyll fluorescence imaging technology. *Sensors (Basel)* 18 (1), 21. doi: 10.3390/s18010021

Li, J., Zhou, H., Zhang, Y., Li, Z., Yang, Y., and Guo, Y. (2020). The GSK3-like kinase BIN2 is a molecular switch between the salt stress response and growth recovery in arabidopsis thaliana. *Dev. Cell* 55 (3), 367–36+. doi: 10.1016/j.devcel.2020.08.005

Linn, A. I., Zeller, A. K., Pfündel, E. E., and Gerhards, R. (2020). Features and applications of a field imaging chlorophyll fluorometer to measure stress in agricultural plants. *Precis. Agric.* 22 (3), 947–963. doi: 10.1007/s11119-020-09767-7

Liu, X.-m., Wu, X.-l., Gao, W., Qu, J.-b., Chen, Q., Huang, C.-y., et al. (2019). Protective roles of trehalose in pleurotus pulmonarius during heat stress response. *J. Integr. Agric.* 18 (2), 428–437. doi: 10.1016/s2095-3119(18)62010-6

Lu, Q., Wen, X., Lu, C., Zhang, Q., and Kuang, T. (2003). Photoinhibition and photoprotection in senescent leaves of field-grown wheat plants. *Plant Physiol. Biochem.* 41 (8), 749–754. doi: 10.1016/s0981-9428(03)00098-6

Ma, B., Pu, R., Zhang, S., and Wu, L. (2018). Spectral identification of stress types for maize seedlings under single and combined stresses. *IEEE Access* 6, 13773–13782. doi: 10.1109/access.2018.2810084

Maresca, V., Lettieri, G., Sorbo, S., Piscopo, M., and Basile, A. (2020). Biological responses to cadmium stress in liverwort conocephalum conicum (Marchantiales). *Int. J. Mol. Sci.* 21 (18), 6485. doi: 10.3390/ijms21186485

Mehmood, A., Naeem, M., Khalid, F., Saeed, Y., Abbas, T., Jabran, K., et al. (2018). Identification of phytotoxins in different plant parts of brassica napus and their influence on mung bean. *Environ. Sci. Pollut. Res. Int.* 25 (18), 18071–18080. doi: 10.1007/s11356-018-2043-x

Merritt, L. H., Ferguson, J. C., Brown-Johnson, A. E., Reynolds, D. B., Tseng, T.-M., and Lowe, J. W. (2020). Reduced herbicide antagonism of grass weed control through spray application technique. *Agronomy* 10 (8), 1131. doi: 10.3390/agronomy10081131

Mézière, D., Petit, S., Granger, S., Biju-Duval, L., and Colbach, N. (2015). Developing a set of simulation-based indicators to assess harmfulness and contribution to biodiversity of weed communities in cropping systems. *Ecol. Indic.* 48, 157–170. doi: 10.1016/j.ecolind.2014.07.028

Mhamdi, A., and Van Breusegem, F. (2018). Reactive oxygen species in plant development. *Development* 145 (15), 164376. doi: 10.1242/dev.164376

Mittler, R., Zandalinas, S. I., Fichman, Y., and Van Breusegem, F. (2022). Reactive oxygen species signalling in plant stress responses. *Nat. Rev. Mol. Cell Biol.* 23 (10), 663–679. doi: 10.1038/s41580-022-00499-2

Mulder, T. A., and Doll, J. D. (2017). Integrating reduced herbicide use with mechanical weeding in corn (Zea mays). *Weed Technol.* 7 (2), 382–389. doi: 10.1017/s0890037x00027779

Nishiyama, Y., and Murata, N. (2014). Revised scheme for the mechanism of photoinhibition and its application to enhance the abiotic stress tolerance of the photosynthetic machinery. *Appl. Microbiol. Biotechnol.* 98 (21), 8777–8796. doi: 10.1007/s00253-014-6020-0

Perez-Bueno, M. L., Pineda, M., and Baron, M. (2019). Phenotyping plant responses to biotic stress by chlorophyll fluorescence imaging. *Front. Plant Sci.* 10. doi: 10.3389/fpls.2019.01135

Qu, R. Y., He, B., Yang, J. F., Lin, H. Y., Yang, W. C., Wu, Q. Y., et al. (2021). Where are the new herbicides? *Pest Manag Sci.* 77 (6), 2620–2625. doi: 10.1002/ps.6285

Quan, L., Jiang, W., Li, H., Li, H., Wang, Q., and Chen, L. (2022). Intelligent intra-row robotic weeding system combining deep learning technology with a targeted weeding mode. *Biosyst. Eng.* 216, 13–31. doi: 10.1016/j.biosystemseng.2022.01.019

Raji, S. N., Aparna, G. N., Mohanan, C. N., and Subhash, N. (2016). Proximal remote sensing of herbicide and drought stress in field grown colocasia and sweet potato plants by sunlight-induced chlorophyll fluorescence imaging. *J. Indian Soc. Remote Sens.* 45 (3), 463–475. doi: 10.1007/s12524-016-0612-3

Richardson, A., Wojciechowski, T., Franke, R., Schreiber, L., Kerstiens, G., Jarvis, M., et al. (2007). Cuticular permeance in relation to wax and cutin development along the growing barley (Hordeum vulgare) leaf. *Planta* 225 (6), 1471–1481. doi: 10.1007/s00425-006-0456-0

Sabzi, S., Abbaspour-Gilandeh, Y., and Arribas, J. I. (2020). An automatic visible-range video weed detection, segmentation and classification prototype in potato field. *Heliyon* 6 (5), e03685. doi: 10.1016/j.heliyon.2020.e03685

Schutte, B. J., Rashid, A., Wood, J. B., and Marquez, I. (2019). Colorimetric assay for detecting mechanical damage to weed seeds. *Weed Technol.* 34 (3), 454–460. doi: 10.1017/wet.2019.125

Shetty, P., Gitau, M. M., and Maroti, G. (2019). Salinity stress responses and adaptation mechanisms in eukaryotic green microalgae. *Cells* 8 (12), 1657. doi: 10.3390/cells8121657

Shin, Y. K., Bhandari, S. R., Cho, M. C., and Lee, J. G. (2020a). Evaluation of chlorophyll fluorescence parameters and proline content in tomato seedlings grown under different salt stress conditions. *Horticulture Environment Biotechnol.* 61 (3), 433–443. doi: 10.1007/s13580-020-00231-z

Shin, Y. K., Bhandari, S. R., Jo, J. S., Song, J. W., Cho, M. C., Yang, E. Y., et al. (2020b). Response to salt stress in lettuce: changes in chlorophyll fluorescence parameters, phytochemical contents, and antioxidant activities. *Agronomy* 10 (11), 1627. doi: 10.3390/agronomy10111627

Snel, J. F. H., Vos, J. H., Gylstra, R., and Brock, T. C. M. (1998). <Jan F.H. snel.pdf>. *Aquat. Ecol.* 32 (2), 113–123. doi: 10.1023/a:1009971930626

Song, X., Zhou, G., Xu, Z., Lv, X., and Wang, Y. (2015). Detection of photosynthetic performance of stipa bungeana seedlings under climatic change using chlorophyll fluorescence imaging. *Front. Plant Sci.* 6. doi: 10.3389/fpls.2015.01254

Steckel, G. J., Hart, S. E., and Wax, L. M. (2017). Absorption and translocation of glufosinate on four weed species. *Weed Sci.* 45 (3), 378–381. doi: 10.1017/s0043174500093012

Takano, H. K., Beffa, R., Preston, C., Westra, P., and Dayan, F. E. (2020a). Glufosinate enhances the activity of protoporphyrinogen oxidase inhibitors. *Weed Sci.* 68 (4), 324–332. doi: 10.1017/wsc.2020.39

Takano, H. K., Beffa, R., Preston, C., Westra, P., and Dayan, F. E. (2020b). A novel insight into the mode of action of glufosinate: how reactive oxygen species are formed. *Photosynthesis Res.* 144 (3), 361–372. doi: 10.1007/s11120-020-00749-4

Takano, H. K., and Dayan, F. E. (2020). Glufosinate-ammonium: a review of the current state of knowledge. *Pest Manag Sci.* 76 (12), 3911–3925. doi: 10.1002/ps.5965

Tharp, B. E., Schabenberger, O., and Kells, J. J. (2017). Response of annual weed species to glufosinate and glyphosate. *Weed Technol.* 13 (3), 542–547. doi: 10.1017/s0890037x00046170

Tietz, S., Hall, C. C., Cruz, J. A., and Kramer, D. M. (2017). NPQ((T)) : a chlorophyll fluorescence parameter for rapid estimation and imaging of non-photochemical quenching of excitons in photosystem-II-associated antenna complexes. *Plant Cell Environ.* 40 (8), 1243–1255. doi: 10.1111/pce.12924

Ulguim, A., Agostinetto, D., Vargas, L., Silva, J., Schneider, T., and Silva, B. (2019). Mixture of glufosinate and atrazine for ryegrass (lolium multiflorum lam.) control and its effect on seeds' quality. *Rev. Facultad Nacional Agronomía Medellín* 72 (1), 8655–8661. doi: 10.15446/rfnam.v72n1.69093

Vitta, J. I., and Quintanilla, C. F. (2017). Canopy measurements as predictors of weed-crop competition. *Weed Sci.* 44 (3), 511–516. doi: 10.1017/s0043174500094261

Vodeneev, V., Mudrilov, M., Akinchits, E., Balalaeva, I., and Sukhov, V. (2018). Parameters of electrical signals and photosynthetic responses induced by them in pea seedlings depend on the nature of stimulus. *Funct. Plant Biol.* 45 (2), 160–170. doi: 10.1071/FP16342

Wang, X., Li, Y., Wei, S., Pan, L., Miao, J., Lin, Y., et al. (2021). Toxicity evaluation of butyl acrylate on the photosynthetic pigments, chlorophyll fluorescence parameters, and oxygen evolution activity of phaeodactylum tricornutum and platymonas subcordiformis. *Environ. Sci. Pollut. Res. Int.* 28 (43), 60954–60967. doi: 10.1007/s11356-021-15070-3

Wang, H., Qian, X., Zhang, L., Xu, S., Li, H., Xia, X., et al. (2018). A method of high throughput monitoring crop physiology using chlorophyll fluorescence and multispectral imaging. *Front. Plant Sci.* 9. doi: 10.3389/fpls.2018.00407

Wilson, S., and Ruban, A. V. (2020). Rethinking the influence of chloroplast movements on non-photochemical quenching and photoprotection. *Plant Physiol.* 183 (3), 1213–1223. doi: 10.1104/pp.20.00549

Wojtaszek, P. (1997). Mechanisms for the generation of reactive oxygen species in plant defence response. *Acta Physiologiae Plantarum* 19 (4), 581–589. doi: 10.1007/s11738-997-0057-y

Yan, J., Zou, Y., Zhang, F., Zhang, S., Huang, X., and Benoit, G. (2023). Growth, ROS accumulation site, and photosynthesis inhibition mechanism of chlorella vulgaris by triclosan. *Environ. Sci. pollut. Res. Int.* 30 (5), 12125–12137. doi: 10.1007/s11356-022-23009-5

Yu, Y., Zhu, H., Frantz, J. M., Reding, M. E., Chan, K. C., and Ozkan, H. E. (2009). Evaporation and coverage area of pesticide droplets on hairy and waxy leaves. *Biosyst. Eng.* 104 (3), 324–334. doi: 10.1016/j.biosystemseng.2009.08.006

Zhou, R., Yu, X., Ottosen, C. O., Rosenqvist, E., Zhao, L., Wang, Y., et al. (2017). Drought stress had a predominant effect over heat stress on three tomato cultivars subjected to combined stress. *BMC Plant Biol.* 17 (1), 24. doi: 10.1186/s12870-017-0974-x

frontiers | Frontiers in Plant Science

TYPE Original Research
PUBLISHED 08 June 2023
DOI 10.3389/fpls.2023.1183387

OPEN ACCESS

EDITED BY
Andreas Herbst,
Julius Kühn Institute (JKI) –Federal Research Centre for Cultivated Plants, Germany

REVIEWED BY
Changling Wang,
China Agricultural University, China
Prashant Kaushik,
Yokohama Ueki, Japan

*CORRESPONDENCE
Chen Gong
gcld2017@ujs.edu.cn

RECEIVED 10 March 2023
ACCEPTED 16 May 2023
PUBLISHED 08 June 2023

CITATION
Gong C, Chen F, Cui B, Wang A, Zhang Z, Zhou Z and Liu Y (2023) Droplet spatial distribution of oil-based emulsion spray. *Front. Plant Sci.* 14:1183387. doi: 10.3389/fpls.2023.1183387

Droplet spatial distribution of oil-based emulsion spray

Chen Gong[1*], Fujun Chen[1], Bingbo Cui[1], Aichen Wang[1], Zhao Zhang[2], Zhenjiang Zhou[3] and Yufei Liu[3]

[1]School of Agricultural Engineering, Jiangsu University, Zhenjiang, China, [2]College of Information and Electrical Engineering, China Agricultural University, Beijing, China, [3]College of Biosystems Engineering and Food Science, Zhejiang University, Hangzhou, Zhejiang, China

Introduction: Oil-based emulsion solution is a common pesticide formulation in agricultural spraying, and its spray characteristics are different from that of water spraying. The well understanding of its spray characteristics is the theoretical basis to improve the pesticide spraying technology. The objective of the present study is to deepen the understanding of the spray characteristics of oil-based emulsion.

Method: In this paper, the spatial distribution characteristics of spray droplets of oil-based emulsion were captured visually using the high-speed photomicrography. On the basis of image processing method, the droplet size and distribution density of spray droplets at different spatial locations were analyzed quantitatively. The effects of nozzle configuration and emulsion concentration on spray structures and droplet spatial distribution were discussed.

Results: Oil-based emulsion produced a special perforation atomization mechanism compared with water spray, which led to the increase of spray droplet size and distribution density. Nozzle configuration had a significant effect on oil-based emulsion spray, with the nozzle changed from ST110-01 to ST110-03 and ST110-05; the sheet lengths increased to 18 and 28 mm, respectively, whereas the volumetric median diameters increased to 51.19% and 76.00%, respectively. With emulsion concentration increased from 0.02% to 0.1% and 0.5%, the volumetric median diameters increased to 5.17% and 14.56%, respectively.

Discussion: The spray droplet size of oil-based emulsion spray can be scaled by the equivalent diameter of discharge orifice of nozzles. The products of volumetric median diameters and corresponding surface tensions were nearly constant for the oil-based emulsion spray of different emulsion concentrations. It is expected that this research could provide theoretical support for improving the spraying technology of oil-based emulsion and increasing the utilization of pesticide.

KEYWORDS

oil-based emulsion spray, sheet structure, droplets distribution, nozzle configuration, emulsion concentration

1 Introduction

Oil-based emulsion, as one of common formulation for plant protection, is widely used in agricultural spraying (Li et al., 2022; Liu et al., 2022). The oil-based emulsion spray was supposed to have a same atomization mechanism with water spray over a period of time. However, in recent years, many research studies indicated that oil-based emulsion spray has a significantly different spray characteristics compared with water, and it causes a different droplet size distribution that plays a key role in agricultural application (Gong et al., 2020; Gong et al., 2021; Gaillard et al., 2022). Water spray has been widely studied in both experiments (Lewis et al., 2016; Kooij et al., 2018; Gong et al., 2020; Gong et al., 2022) and theories (Post and Hewitt, 2018; Qin et al., 2018); however, the work related to oil-based emulsion spray is limited.

For water spray, it is pointed out that its atomization process can be generally divided into two steps: the development of ripple structure on the spray sheet that leads to the formation of ligaments (Altieri et al., 2014; Qin et al., 2018; Li et al., 2021), followed by the fracture of ligaments and the formation of droplets due to interface instability (Qin et al., 2018). These include Rayleigh–Taylor instability (liquid sheet to ligament) and Rayleigh instability (ligament to droplet) mechanisms (Makhnenko et al., 2021). The spray droplets also undergo a series of spatial evolutionary processes before reaching the target (Lewis et al., 2016). Scholars had studied the droplet size distribution in terms of spray pressure, nozzle type, and spray space locations by methods such as numerical simulation (Musiu et al., 2019) and mathematical modeling (Dwomoh et al., 2020; Chen and Ashgriz, 2022; He et al., 2022). The result indicated that an increase in working pressure caused an increase in droplet pulverization regardless of the type of nozzle. In different spray pressure and orifice diameter values, the droplet volume percentage that presents a normal distribution, according to the mathematical model, can well predict the droplet size distribution.

For oil-based emulsion spray, the oil-phase particles lead to the generation of perforations in the spray sheet and the different breakup mechanism (Qin et al., 2010; Makhnenko et al., 2021). The development of perforations causes the earlier breakup of spray sheet (Gong et al., 2020; Cryer et al., 2021; Li et al., 2021). Compared with water spray, the droplet of oil-based emulsion spray has a larger average size and a narrower size distribution (Qin et al., 2010; Vieira et al., 2018; Gong et al., 2020). The droplet size distributions of water spray are commonly studied by using laser diffraction (LD) and phase Doppler particle analyzer (PDPA) methods (Vernay et al., 2016; Vernay et al., 2017; Vieira et al., 2018; Sijs and Bonn, 2020; Li et al., 2021; Zhang and Xiong, 2021). The LD method is based on light diffraction, and it measures droplet size by Mie theory with complete or fuzzy approximation (ISO13320:2009) (De Cock et al., 2016). The PDPA method measures the size and velocity of droplets based on light scatter (Blaisot and Yon, 2015). These non-contact measurement techniques are based on optics diagnostics (Blaisot and Yon, 2015). However, for the emulsion spray, the transmittance of droplets is limited; therefore, the above methods are supposed to bring errors (Tuck et al., 1997; Hilz and Vermeer, 2013). The image processing method is more suitable for measuring those droplets that have relatively low transmittance (Zeng et al., 2015; Farzad et al., 2017; Patil et al., 2017). The droplet sizes in the spray image can be accurately measured on the basis of the edge gray intensity criterion (De Cock et al., 2016; Minov et al., 2016).

In this paper, the oil-based emulsion spray is focused, and its sheet structure and spray droplets of different spatial locations were captured using high-speed photomicrography technology. An image processing method was used to quantitatively measure the spatial distribution of the spray droplet size and distribution density. The relationship between spray sheet structure and spatial distribution of spray droplets was investigated. In addition, the effects of nozzle configuration and emulsion concentration on spray structures and droplet spatial distribution were discussed. It is pointed out that this research could help to deepen the understanding of the spray characteristics of oil-based emulsion and provide a theoretical support for improving the spraying technology of oil-based emulsion and increasing the utilization of pesticide.

2 Materials and methods

2.1 Experimental setup

The main experimental devices are shown in Figure 1A. The spray liquid was stored in the pressure vessel (the capacity of the vessel is 10 L) and was pressurized by an air compressor. A pressure regulator valve (SMC AR-3000, SMC China Co., Shanghai, China) was used to control the spray pressure, and its precision is 0.02 MPa. The spray pressure was set as 0.3 MPa. The nozzles are fixed on an adjustable bracket, which can move in the vertical direction. The precision of the movement is 1 mm. A high-speed camera (Olympus I Speed 3, Olympus Co., Shinjuku-ku, Tokyo, Japan) was used to capture the spray structures of different vertical positions. A light and a diffuser are used to produce a uniform backlight. As indicated in Figure 1B, three standard flat-fan spray nozzles—ST110-01, ST110-03, and ST110-05 (Lechler Inc., Metzingen Germany)—were used in the experiments. The long diameter (D_L) and short diameter (D_S) of the nozzle exit are measured using a microscope (VHX-900F, Keyence Co., Japan). As indicated in Figure 1B, the exit of the nozzles has elliptical structures, and it is not suitable to use long diameter or short diameter to characterize the size of nozzle exit. Therefore, the equivalent diameter (Duarte and Corradini, 2018) $D_E = \sqrt{D_L D_S}$ was used to characterize the size of nozzle exit. The detail results are presented in Table 1.

Both water and oil-based emulsions were used as the spray liquid in the experiments. The oil-based emulsion was prepared with pre-emergent herbicide butachlor (Jiangsu Lvlilai Co., Kunshan, Jiangsu, China) and water. The main composition of the herbicide butachlor was as follows: 6% w/w sodium alkylbenzenesulfonate (emulsifiers), 9% w/w Styrylphenyl polyoxyethylene ether (emulsifiers), 15% w/w cyclohexanone (solvent), and 60% w/w (butachlor). The size distribution of oil droplets in oil-based emulsion solution in the experiment was measured using the Malvern particle size analyzer (type: Zetasizer Nano ZS90), as shown in Figure 1C. Some research studies indicated that oil-based emulsion has a significant effect on the

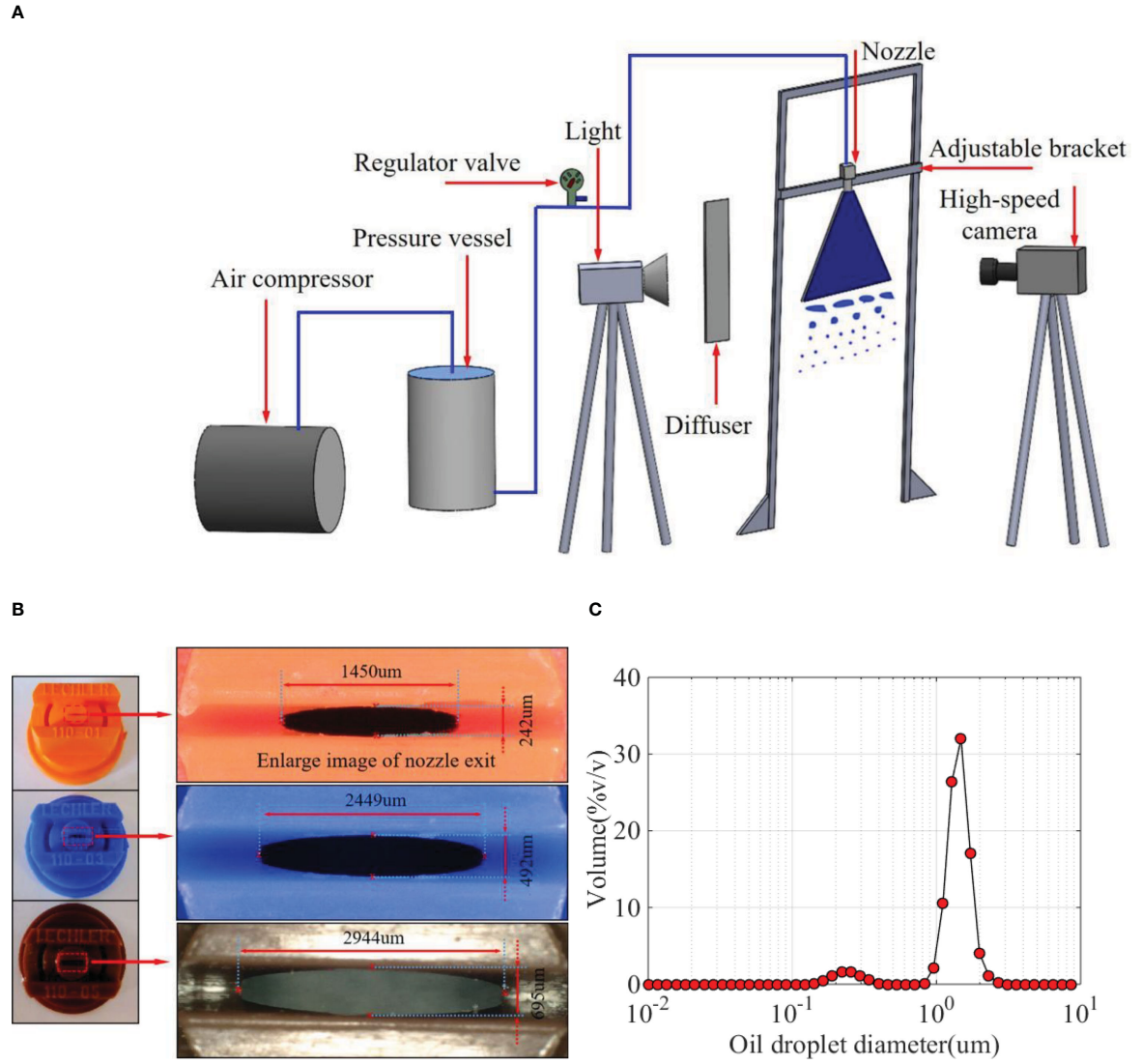

FIGURE 1
Spray experimental setup. **(A)** Experimental setup and **(B)** nozzles and discharge orifices. **(C)** Size distribution of oil droplets in oil-based emulsion solution.

spray droplet size as the emulsion concentration is in the range of 0.05%–0.6% (Dexter, 2001; Vernay, 2015). Therefore, the emulsion volume concentrations of 0.02%, 0.1%, and 0.5% were selected in the experiments to evaluate the effect of emulsion concentration on the spatial distribution of spray droplets. The static surface tension of different spray medium was measured using a contact angle measurement system (KSV CAM101, KSV Instruments, Ltd., Helsinki, Finland). The experimental conditions were indoor, and the room temperature was 23°C–25°C. Six groups of experiments were designed. Groups 1 and 2 were used to discuss the difference between water and oil-based emulsion sprays. Groups 2 to 4 were used to evaluate the effect of emulsion concentrations on the oil-based emulsion spray. Group 2, 5, and 6 were used to evaluate the effect of nozzle configuration on the oil-based emulsion spray. The parameters of different experimental conditions are listed in Table 2.

TABLE 1 The structural parameters of the nozzle exit.

Nozzle	Long diameter D_L/μm	Short diameter D_S/μm	Equivalent diameter D_E/μm
ST-110-01	1450	242	592.37
ST-110-03	2449	492	1097.68
ST-110-05	2944	695	1430.41

TABLE 2 Experiment conditions.

Test number	Nozzle	Pressure P (MPa)	Concentration	Surface tension σ (N m^{-1})
1	ST110-03	0.3	0	0.070
2	ST110-03	0.3	0.1%	0.041
3	ST110-03	0.3	0.02%	0.050
4	ST110-03	0.3	0.5%	0.032
5	ST110-01	0.3	0.1%	0.041
6	ST110-05	0.3	0.1%	0.041

2.2 Capture of spray structures

As indicated in Figure 2, the center point of the nozzle exit was defined as the origin of all coordinates; the right horizontal direction (spanwise direction) was set as the X direction; the vertically downward direction (streamwise direction) was set as the Y direction, and Z direction was perpendicular to the XOY plane. The images of spray along different Y distances were captured to analyze the spatial evolution of spray structures. Take Figure 2 for example, the first image ① captured near the nozzle exit (as indicated with dash rectangle). Then, the second image ② was captured downstream with an interval of 25 mm (as indicated with solid rectangle). This process was repeated 10 times, which means that the spray structure in the range of 0~250 mm was captured. In the X direction, similar processes were used, and the distance interval is set as 10 mm.

To capture the transient spray structure, the exposure time of the high-speed camera was set as 2.16 μs. The frame rate was set to 2,000 fps (frames per second); therefore, the time interval between adjacent images is 0.5 ms. Under this condition, the resolution of image is 1,280 × 1,024 pixels. A ruler was used to measure the length of each nozzle before the experiment. A Commercial Image analysis software IPP (Image Pro Plus, Meyer Instruments, Inc., Houston, TX, USA) was used to measure the pixel length of the nozzle in the spray image. The ratio of the two measured length was defined as the scale factor SF (SF = length/pixel length).

2.3 Measurement of droplet size distribution

For water spray, the LD instrument and PDPA are commonly used methods to measure the droplet size distributions (Vieira et al., 2018; Sijs and Bonn, 2020). However, the oil-based emulsion solution is opaque, and the transmittance of its spray droplets is limited; therefore, the above methods are supposed to bring errors. The image processing method is more suitable for measuring those droplets that have relatively low transmittance (Zeng et al., 2015; Farzad et al., 2017; Patil et al., 2017).

In this paper, droplet sizes were measured on the basis of image processing. A typical image processing process was shown in Figure 3. The size of the captured sampling window was 10 × 10 mm. The raw image in Figure 3A was first enhanced on the basis of "Retinex" theory (Cai, 2020) to highlight the edge intensity gradient between the background and the target spray droplet. Then, the Otsu algorithm (Ostu, 1979) was used to determine the segmentation threshold, and the binary image was obtained (Figure 3C). After that, the image was inverted (Figure 3D), and

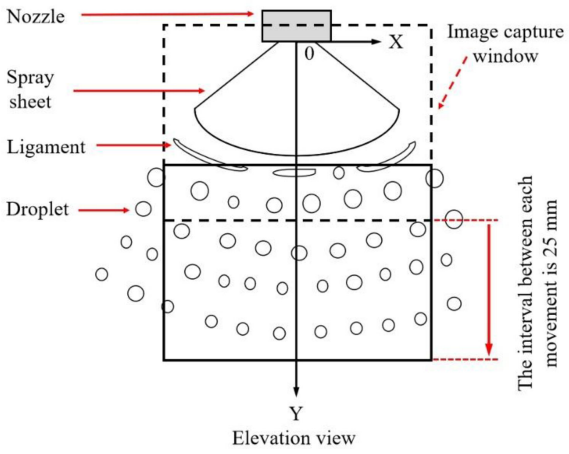

FIGURE 2
Diagram of spray coordinate and image capture window.

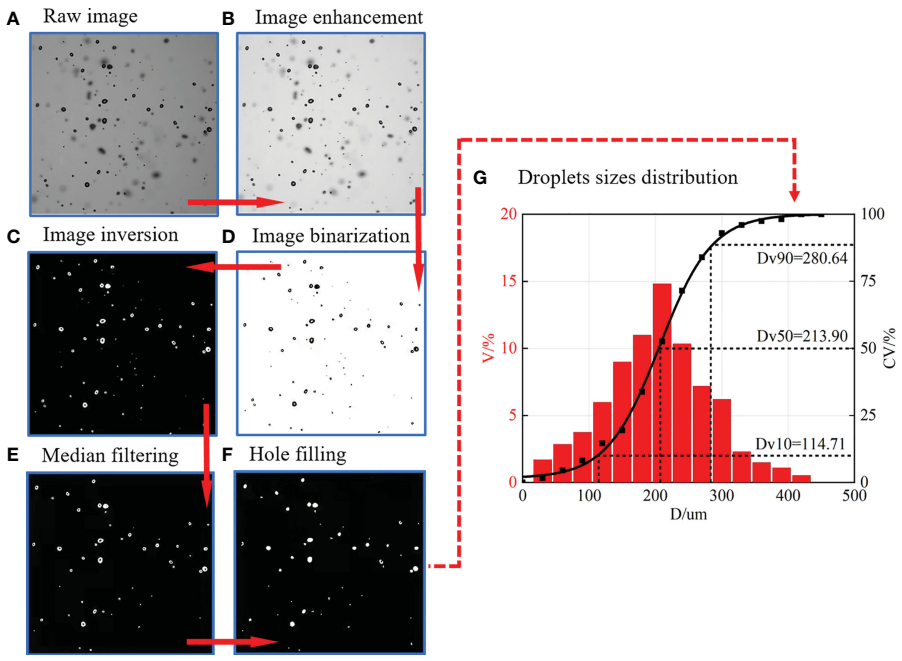

FIGURE 3
The methods of image processing and droplet size distribution measurement. **(A)** Raw image. **(B)** Image enhancement. **(C)** Image inversion. **(D)** Image binarization. **(E)** Median filtering. **(F)** Hole filling. **(G)** Droplets sizes distribution. V% denotes the volume percentage, CV% denotes the cumulative volume percentage.

the median filtering (Zhou et al., 2015) was used to remove noise. Finally, the imfill function (Zhou et al., 2015) was used to fill the "holes" within the droplets in Figure 3E. After image pre-processing, the "Bwlabel" function and "Regionprops" function (MATLAB, MathWorks Corporation, Natick, MA, USA) were used to detect and measure the spray droplets in Figure 3F. Next, an image batch processing code was independently developed on the basis of the commercial code MATLAB to calculate the volume size distribution of droplets. To reduce random error and ensure the enough samples, the numbers of images that are under the same experimental condition are processed and measured. In this paper, at least 100 images and 5,000 droplets were processed and measured for each experimental condition. One of the final results is presented in Figure 3G; the D_V10, D_V50, and D_V90, which represent the diameter with cumulative volume less than 10%, 50%, and 90%, are commonly used to characterize droplet size in agricultural (ANSI/ASABE, 2020).

3 Results and discussion

3.1 Comparison between water and oil-based emulsion spray

The spray sheets of water and oil-based emulsion are compared in Figures 4A, B. In the elevation view, for the water spray (the left half in Figure 4A), the liquid sheet has a relatively intact surface, with some "ripples" structures (marked by blue circle) on it. These ripples causes the breakup of the liquid sheet and the formation of the ligaments and droplets. As indicated in Figure 4A, this breakup regime causes both large and small droplets. For the oil-based emulsion (the right half in Figure 4A), it has a relatively shorter sheet length compared with water spray. Most notably, there are some perforations on the liquid sheet of oil-based emulsion spray. These perforations finally contact with each other to form web-like structure (marked by red circle) and breakup into droplets. The droplets generated by this breakup regime have a relatively uniform size distribution. In the side view, the water spray (the left half in Figure 4B) has a wave-like structure; on the contrary, the oil-based emulsion spray (the right half in Figure 4B) has no obviously fluctuation structures. As a result, the droplets of water spray distribute in a broad range in the Z direction.

The spray droplets of different Y positions are presented in Figures 4C, D. First, as indicated in phase ① in Figure 4C, the spray droplets have relatively bigger average size, and there are some droplets out of the focal plane for water spray. With the increase of flow direction distance, as shown in phases ② and ③ in Figure 4C, the average size of spray droplets obviously decreases; meanwhile, the number of droplets in the focal plane decreases. For emulsion spray (Figure 4D), it follows similar trend as water spray; however, the number of droplets that out of the focal plane is relatively smaller.

On the basis of the comparison above, it can be found that water spray is featured by wave-like structure, whereas the oil-based emulsion is featured by perforations. Different sheet structures cause different breakup regimes, and it supposes to produce different droplets distribution. Here, the quantitative information of droplet distribution of water and oil-based emulsion spray is discussed. Along the axis of symmetry, the volumetric median diameter (D_V50) and distribution density (droplet number in the focal plane) of spray droplets at different streamwise distances are

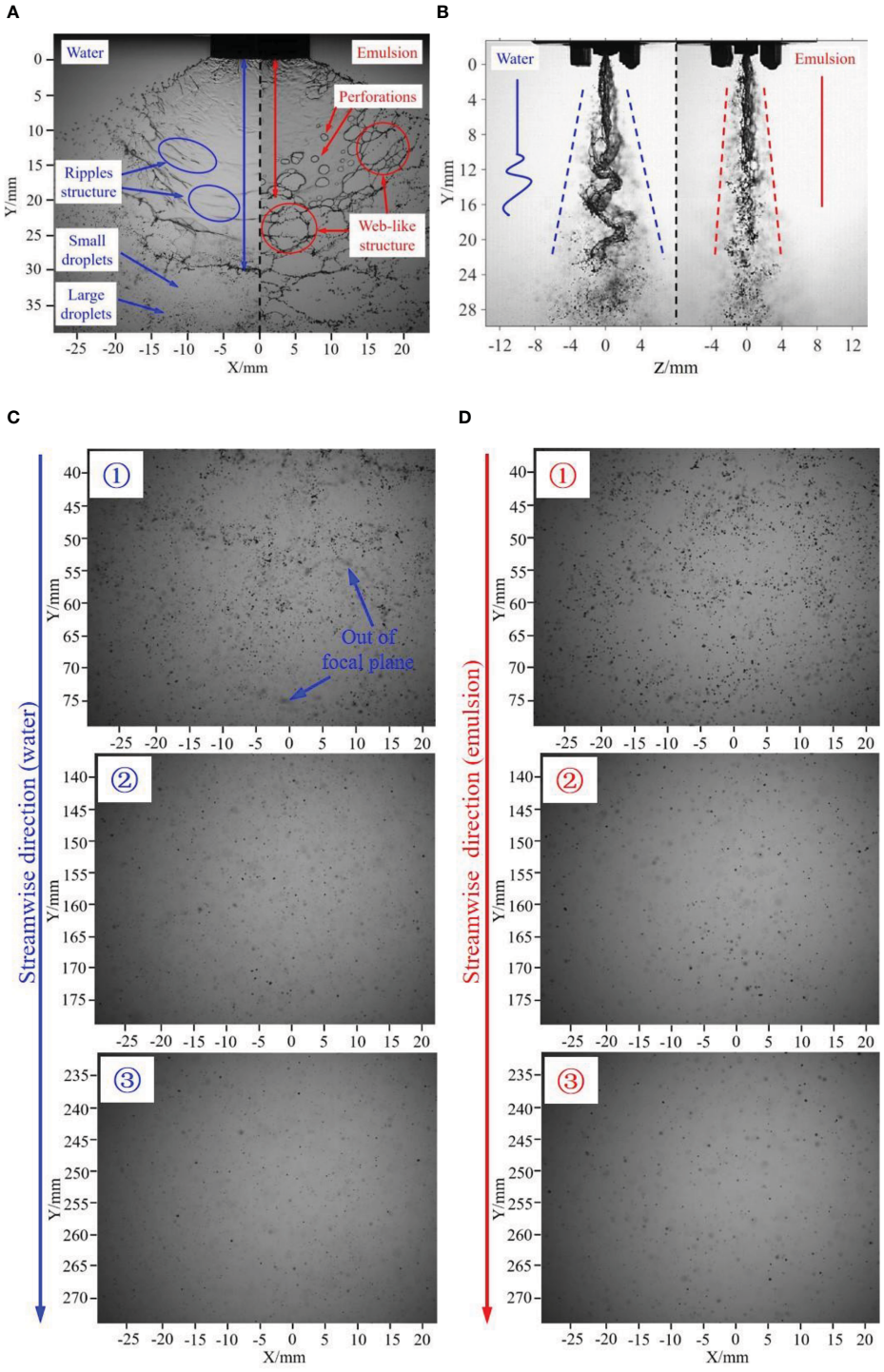

FIGURE 4
Comparison of water and emulsion spray. **(A)** Elevation view of water and emulsion spray sheet. **(B)** Side view of water and emulsion spray sheet. **(C)** Droplets images of water spray at different flow direction distances. **(D)** Droplets images of oil-based emulsion spray at different flow direction distances. The nozzle is ST110-03, spray pressure is 0.3 MPa, and the concentration of emulsion is 0.1%.

measured and compared in Figures 5A, B. As indicated in Figure 5A, for both water and oil-based emulsion spray, the droplet size decreases with the streamwise distance. The droplet sizes of oil-based emulsion spray are bigger than that of water spray at each positions. Meanwhile, measured results show that the size difference between water and oil-based emulsion spray decreases with the streamwise distance. For the distribution density of spray droplets, as shown in Figure 5B, in the range of 50~100 mm, both water and oil-based emulsion spray are dramatically decrease with streamwise distance. After Y = 200 mm, the distribution density changes little with streamwise distance, and the water and oil-based emulsion has no significant difference.

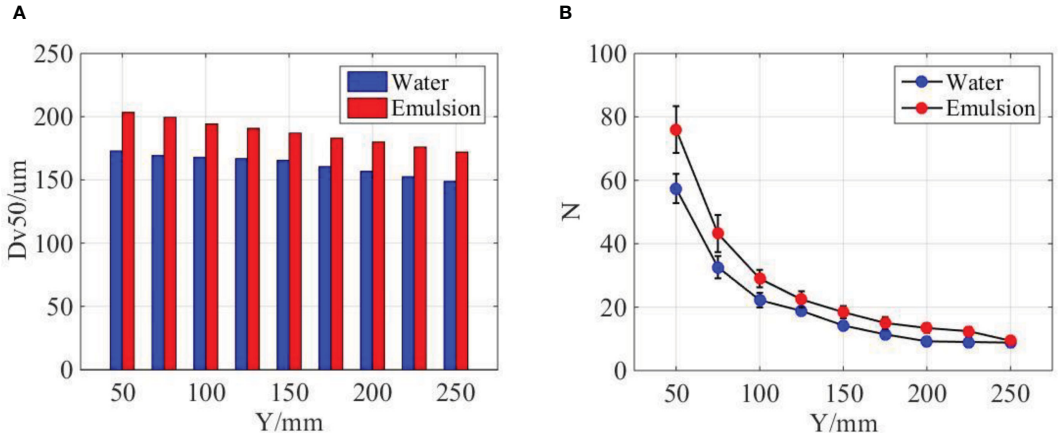

FIGURE 5
Comparison of water and emulsion spray. **(A)** The volumetric median diameter (D_V50) of spray droplets at different streamwise distances. **(B)** The distribution density of spray droplets at different streamwise distances. The ST110-03 nozzle was used, the spray pressure is 0.3MPa, and the concentration of emulsion is 0.1%.

The droplet size and distribution at different spanwise distances are measured and compared in Figures 6A, B. As indicated in Figure 6A, the size of water and oil-based emulsion spray follows a similar distribution, and the droplet size in middle position is smaller than lateral positions. At the same streamwise position, the droplet size of oil-based emulsion spray is larger than water spray. Meanwhile, the size difference between middle and lateral positions of oil-based emulsion spray is smaller than that of water spray. As for distribution density, as shown in Figure 6B, the droplet number in middle position is obviously larger than lateral positions. However, this difference will reduce with the increase of streamwise distance. When the streamwise distance increases to 250 mm, the distribution of water and oil-based emulsion spray has no significant different.

On the basis of the comparison above, it can be concluded that the volumetric median diameter of oil-based emulsion spray is bigger than water spray in both streamwise and spanwise direction positions. Oil-based emulsion spray also has a larger distribution density; however, the difference decreases with the increase of streamwise distance. From Figure 4A, it is know that the sheet length of oil-based emulsion spray is smaller than of water spray. The longer sheet length corresponds to the thinner sheet thickness under the same volume of flow. The thinner sheet is supposed to produce smaller droplets. This explains why water spray has a relatively smaller droplets sizes compared with oil-based emulsion spray. As indicated in Figure 4B, water spray has a wave-like motion in the Z direction. This fluctuation gives a kinetic energy in the Z direction for the droplet of water spray. As a result, water droplets distribute in a broad range in the Z direction and less droplets on the focal plane compared with oil-based emulsion spray. During the falling of the spray droplets, its kinetic energy decreases due to the resist of ambient air. Therefore, the difference between water and oil-based emulsion spray is reduced.

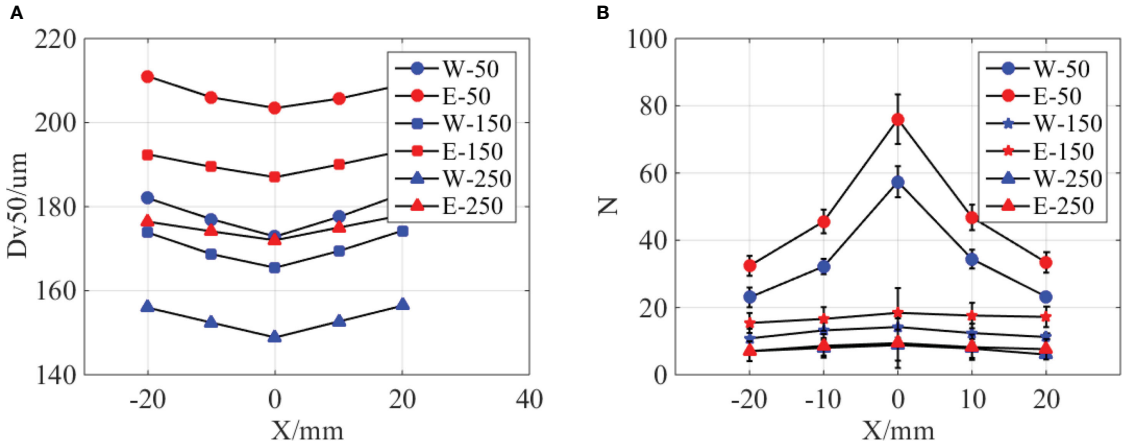

FIGURE 6
Comparison of water and emulsion spray. **(A)** The volumetric median diameter of spray droplets at different spanwise distances. "W-50" denotes water spray, and the position is 50 mm down below the nozzle exit. "E" denotes oil-based emulsion spray. **(B)** The distribution density of spray droplets at different spanwise distances. The ST110-03 nozzle was used, the spray pressure is 0.3MPa, and the concentration of emulsion is 0.1%.

3.2 Effect of nozzle configuration on the droplet distribution of emulsion spray

Different nozzles are commonly used to modify the droplet size distribution. In this part, the effect of nozzle configuration on the droplet distribution of emulsion spray was discussed. First, the images of sheet structures and spray droplets of different nozzles are compared in Figure 7. As shown in the first line, nozzle configuration has a significant effect on the sheet structures. The sheet length is approximately 7 mm as the nozzle ST110-01 was used. With the nozzle changes from ST110-01 to ST110-03 and ST110-05, the sheet lengths increase to 18 and 28, mm respectively. Meanwhile, the sheet areas are obviously increased. For all the three spray sheets, there are some perforations on them, which indicate that nozzle configurations do not change the breakup regime. As shown in the second and third lines, the droplets generated by the three nozzles have different size, and the droplet of nozzle ST110-05 has bigger size at all the streamwise positions. For the oil-based emulsion spray, the perforations cause the breakup of the liquid sheet. For nozzle ST110-01, the position that perforation generation is closer to the nozzle exit. Therefore, it has a shorter sheet length and smaller sheet area. As shown in Figure 1B, the discharge orifice of nozzle ST110-05 has a bigger size, and it supposed to produce thicker spray sheet. The generation position of perforations is far from the nozzle exit; as a result, it has a longer sheet length and larger sheet area.

More quantitative information of spray droplets is presented in Figure 8. First, as indicated in Figure 8A, with the increase of streamwise distance, the droplets sizes are gradually decrease for all the three nozzles. The nozzle configuration does not change the evolution patterns but has a significant effect on the droplet size. As the nozzle type is changed from ST110-01 to ST110-03 and ST110-05, the D_V50 increases to 51.19% and 76.00%, respectively. Different nozzles have different exit sizes (as shown in Figure 1B); therefore, we try to nondimensionalize the droplet sizes by using equivalent diameter of nozzle exits, as indicated in Figure 8B. Interestingly, we found that the data of different nozzles tend to coincide. It is indicated that the droplet size of oil-based emulsion spray can be scaled by the size of nozzle exit. A possible reason responsible for this interesting finding is that the size of spray droplets was determined by the thickness of spray sheet, which was controlled by the size of nozzle

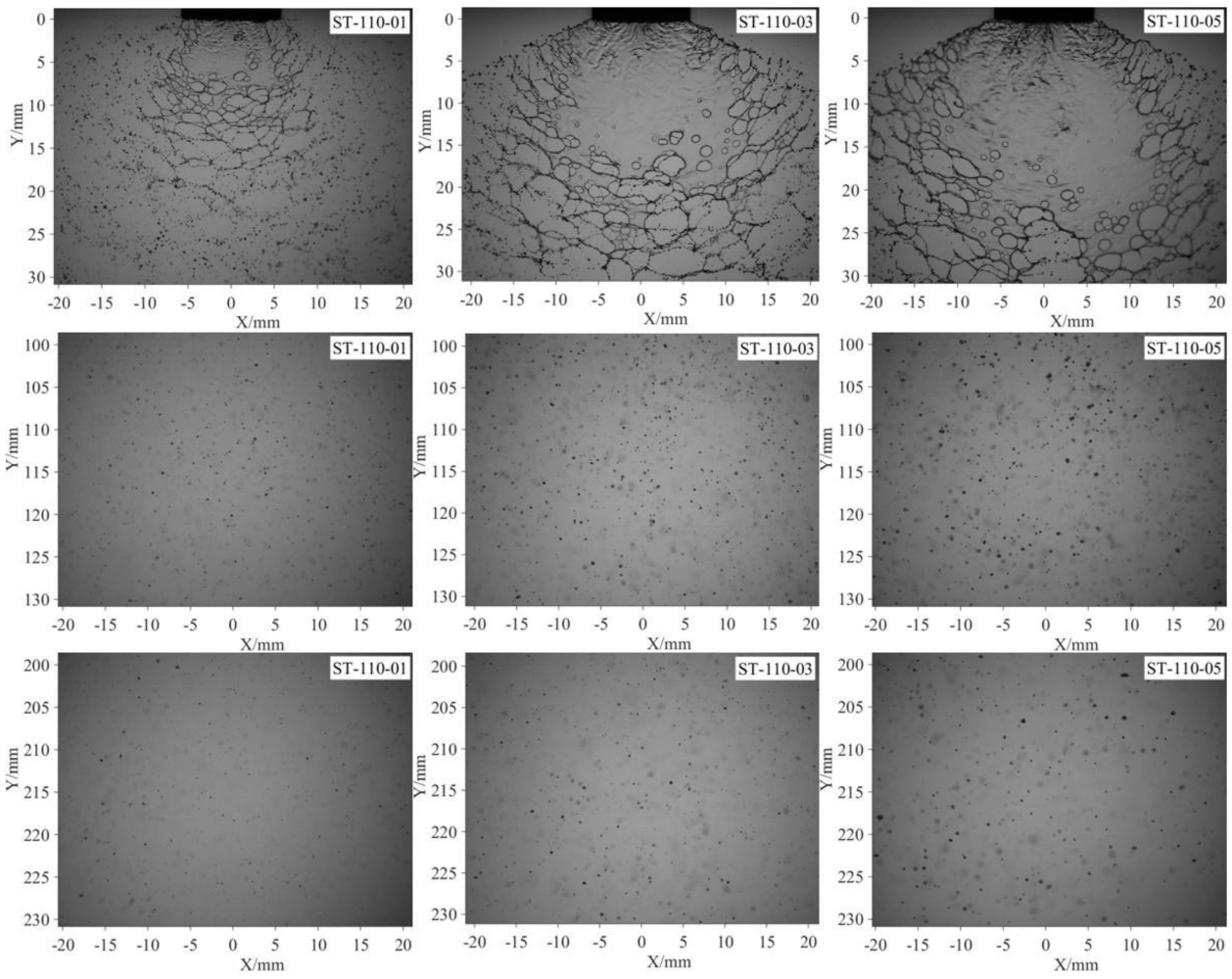

FIGURE 7
Spray images of different nozzle configurations. All the images are captured under the same pressure (0.3 MPa). The concentration of the oil-based emulsion is 0.1%.

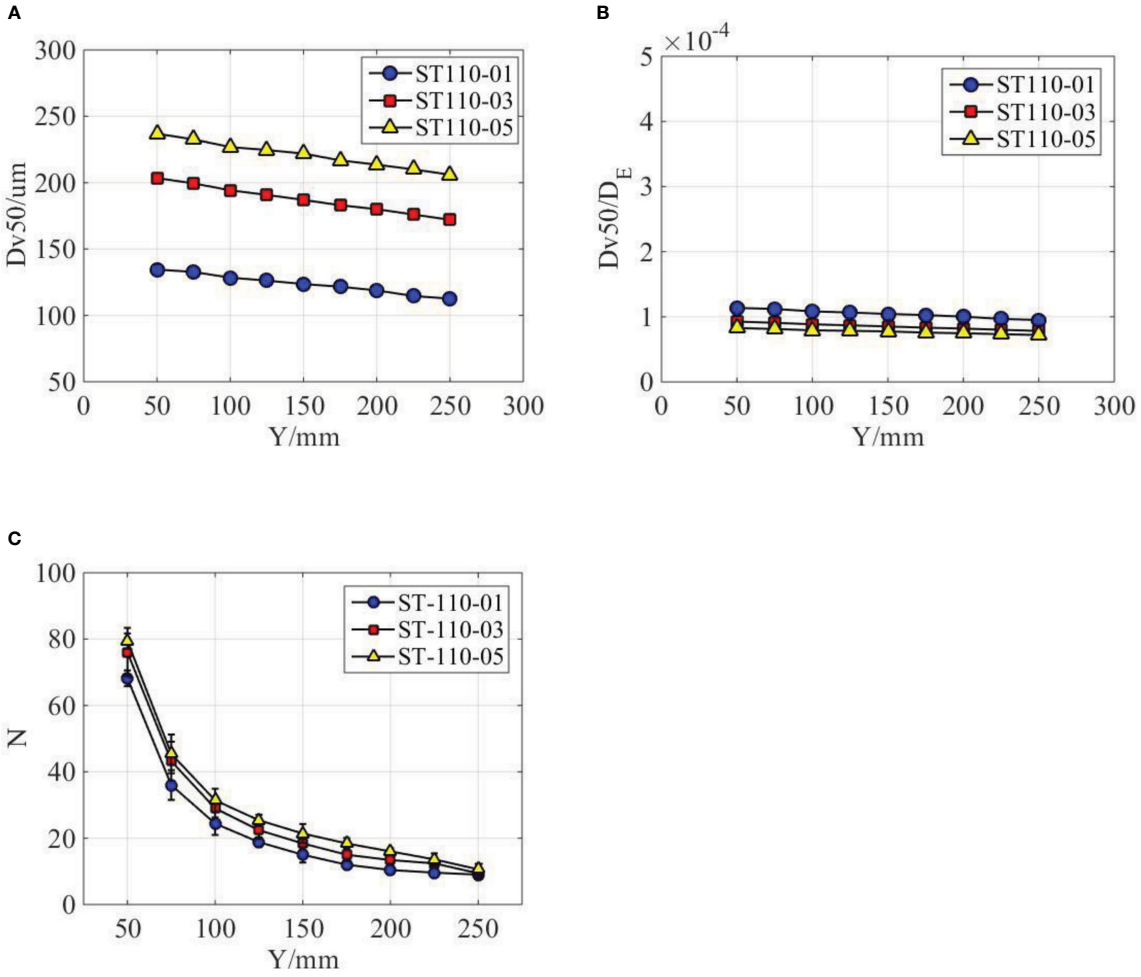

FIGURE 8
Droplet distribution characteristics at different nozzle configurations. **(A)** The effect of nozzle configurations on the volumetric median diameter. **(B)** Fitting curves of different nozzle configurations. **(C)** The effect of nozzle configurations on the droplet distribution density.

exit. For the nozzles used in this paper, the volumetric median diameter is approximately 1/10,000th of the equivalent diameter of nozzle exit. For the distribution density of spray droplets, as shown in Figure 8C, it is slightly increased with the nozzle type changes from ST110-01 to ST110-03 and ST110-05. Clearly, nozzle configuration has little effect on the distribution density of spray droplets.

3.3 Effect of emulsion concentration on the droplet distribution of emulsion spray

The spray images of different emulsion concentrations are compared in Figure 9. As indicated in the first line, with the increase of emulsion concentration, the number of perforations on the spray sheet is obviously increased. The development of the perforations forms web-structure and causes the breakup of liquid sheet. As a result, the sheet of higher emulsion concentration has a shorter length and smaller area. As indicated in the second and third lines, the droplet distributions have no significant different. Clearly, the effect emulsion concentration on the spray droplets is limited compared with nozzle configurations.

The droplet size and distribution of different emulsion concentrations were measured and compared in Figure 10. As indicated in Figure 10A, the volumetric median diameters generally increased with the increase of emulsion concentration. It increases by 5.17% as the emulsion concentration increases from 0.02% to 0.1%. However, when the emulsion concentration increases from 0.1% to 0.5%, the volumetric median diameters increased by 9.39%. The volumetric median diameters gradually decreased with the increase of axial distance for all the three emulsion concentrations. However, the decrease rate for emulsion concentration of 0.5% is relatively smaller. With the increase of emulsion concentration, the surface tension of the spray liquid decrease. If the product of volumetric median diameter and corresponding surface tension was used, we found that the data of different emulsion concentrations tend to coincide, as shown in Figure 10B. A possible reason responsible for this phenomenon is that the droplets sizes can be modified by the surface tension of spray liquid. Some existing references (Hilz and Vermeer, 2013) indeed verified that the size of spray droplets was inversely proportional to surface tension of spray liquid. From Table 2, it can be found that surface tension decreased with the increase of emulsion concentration. The droplet distribution density

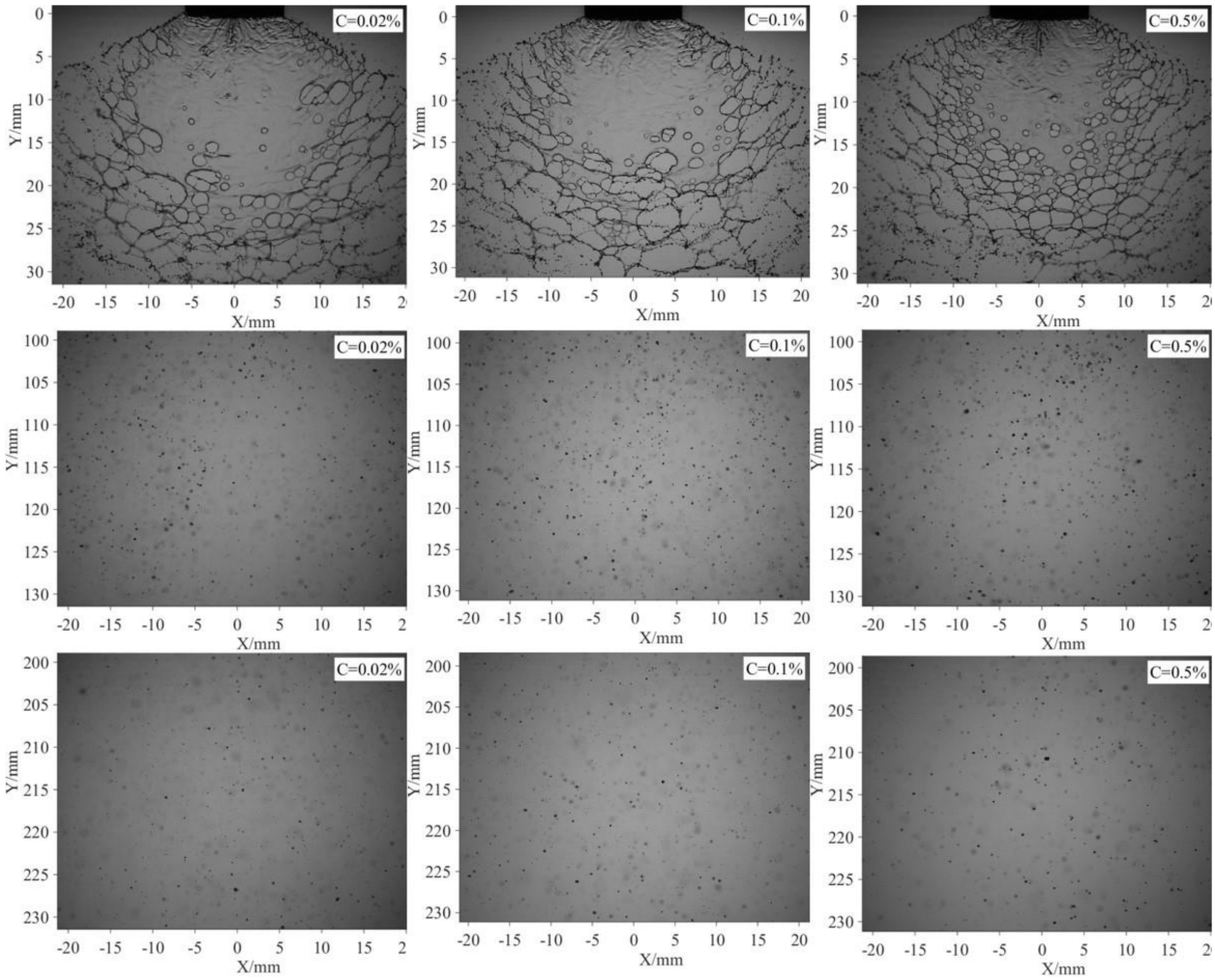

FIGURE 9
Spray images of different emulsion concentrations. All the images are captured under the same pressure (0.3 MPa) and same nozzle (ST-110-03).

of different emulsion concentrations is presented in Figure 10C. The droplet number generally increased with the emulsion concentrations; however, the difference of three emulsion concentrations is limited.

4 Conclusions

In this paper, the spatial sheet structure and droplet distribution of oil-based emulsion spray are captured and measured. The effect of nozzle configuration and emulsion concentration of the sheet structure and droplet distribution were discussed. Major conclusions drawn from the study are as follows.

Oil-based emulsion spray has a significantly different atomization mechanism compare water spray. Water spray is featured by wave atomization mechanism, whereas the oil-based emulsion spray is featured by perforation atomization mechanism. With the presence of holes, the spray sheet breaks earlier; therefore, the droplet size is larger than that of the water spray in both streamwise and spanwise direction. Because of the wave-like fluctuation of water spray, water droplets disperse in a broad range compared with oil-based emulsion spray. This spatial distribution difference between water and oil-based emulsion spray will reduce due to the resist of ambient air.

Nozzle configuration does not change the atomization mechanism of oil-based emulsion spray; however, it has a significant effect on the spray droplet size. The nozzle with a larger discharge orifice produces longer sheet length, larger sheet area, and bigger droplets. Interestingly, we found that the spray droplet size can be scaled by the equivalent diameter of discharge orifice of nozzles. For the nozzles used in this paper, the volumetric median diameter is approximately 1/10,000th of the equivalent diameter. The effect of nozzle configuration on the spatial distribution of the spray droplets is limited.

The typical structure, perforations, is sensitive to the variation of emulsion concentration. With the increase of emulsion concentration, the number of perforation on the spray sheet increased; as a result, sheet length and area decreased. The effect of emulsion concentration on the droplet size is limited compared

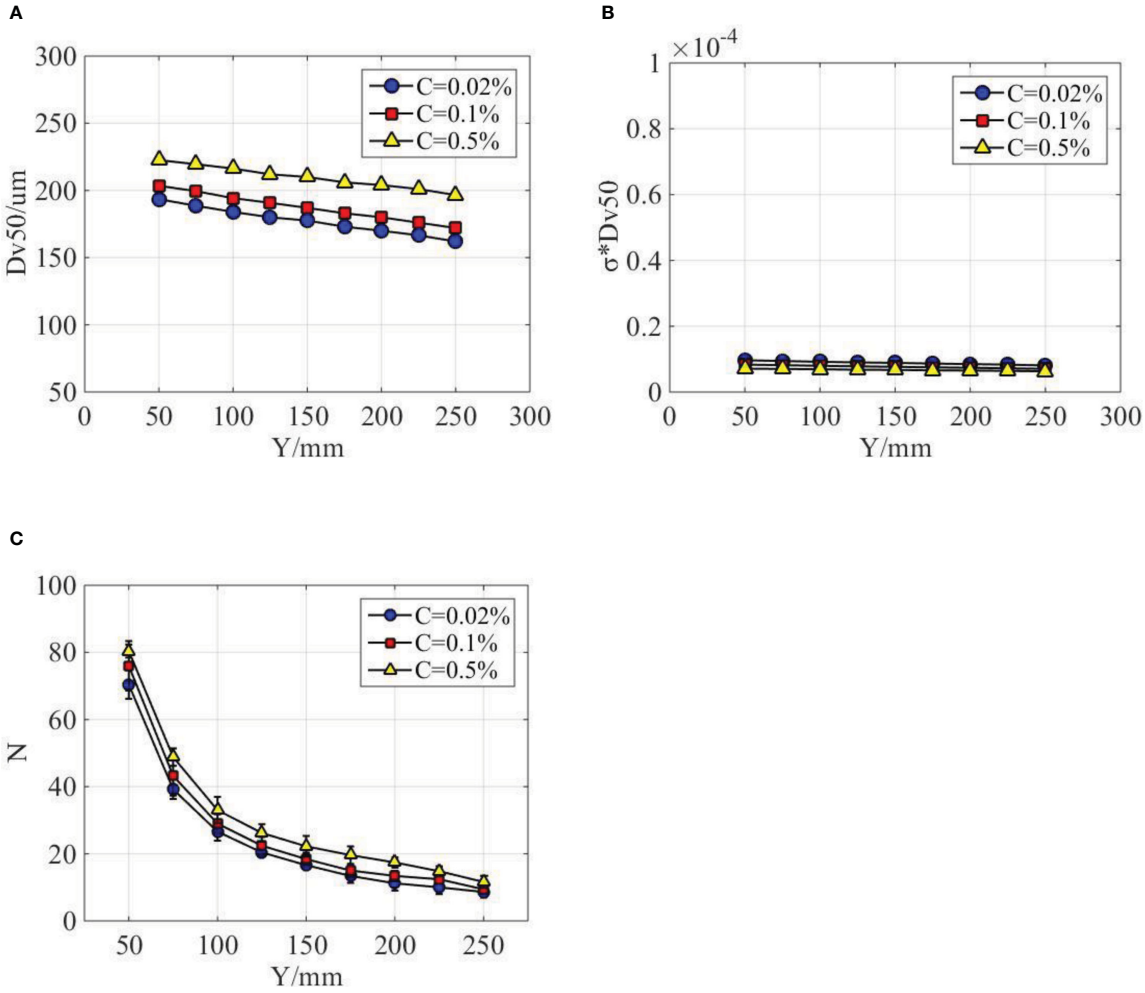

FIGURE 10
Droplet distribution characteristics at different emulsion concentrations. **(A)** The effect of emulsion concentrations on the volumetric median diameter. **(B)** Fitting curves of different emulsion concentrations. **(C)** The effect of emulsion concentrations on the droplet distribution density.

with nozzle configuration. If the product of volumetric median diameter and corresponding surface tension was used, then it is found that data of different emulsion concentrations tend to coincide.

Data availability statement

The original contributions presented in the study are included in the article/supplementary material. Further inquiries can be directed to the corresponding author.

Author contributions

CG: Methodology, Conceptualization; FC: Writing-Original draft preparation; BC: Capture of spray images; AW: Image processing; ZZ: Statistical analysis of the results; ZJZ: Writing Review and Editing; LY: Revised and Editing. All authors contributed to the article and approved the submitted version.

Funding

The authors gratefully acknowledge the financial support of the National Natural Science Foundation of China (No. 51905220) and the Jiangsu Province and Education Ministry Co-sponsored Synergistic Innovation Center of Modern Agricultural Equipment (XTCX2009 and XTCX2010).

Conflict of interest

The authors declare that the research was conducted in the absence of any commercial or financial relationships that could be construed as a potential conflict of interest.

Publisher's note

References

Altieri, A., Cryer, S. A., and Acharya, L. (2014). Mechanisms, experiment, and theory of liquid sheet breakup and drop size from agricultural nozzles. *Atomization. Spray.* 24, 695–721. doi: 10.1615/AtomizSpr.2014008779

ANSI/ASABE (2020). "Spray nozzle classification by droplet spectra. American society of agricultural and biological engineers. spray nozzle classification by droplet spectra," in *ASABE standard S572.1* (St. Joseph, MO, USA: American Society of Agricultural and Biological Engineers).

Blaisot, J. B., and Yon, J. (2015). Droplet size and morphology characterization for dense sprays by image processing: application to the diesel spray. *Exp. Fluids.* 39, 977–994. doi: 10.1007/s00348-005-0026-4

Cai, L. M. (2020). MATLAB image processing theory, algorithm and case analysis. (Beijing: Tsinghua).

Chen, S. Y., and Ashgriz, N. (2022). Droplet size distribution in swirl nozzles. *Int. J. Multiphas. Flow.* 156, 104219. doi: 10.1016/j.ijmultiphaseflow.2022.104219

Cryer, S. A., Altieri, A. L., Schmucker, A. L., and Day, K. M. (2021). Minimising atomisation drift potential by exploring the break-up of liquid sheets using multiphase methylated soybean and silicon oil emulsions. *Biosyst. Eng.* 202, 142–151. doi: 10.1016/j.biosystemseng.2020.12.004

De Cock, N., Massinon, M., Nuyttens, D., Dekeyser, D., and Lebeau, F. (2016). Measurements of reference ISO nozzles by high-speed imaging. *Crop Prot.* 89, 105–115. doi: 10.1016/j.cropro.2016.07.016

Dexter, R. (2001). The effect of fluid properties on the spray quality from a flat fan nozzle. *ASTM Special Tech. Publication.* 1400, 27–43. doi: 10.1520/STP10432S

Duarte, J. P., and Corradini, M. L. (2018). Hydraulic and heated equivalent diameters used in heat transfer correlations. *Nucl. Technol.* 201 (1), 99–102. doi: 10.1080/00295450.2017.1389594

Dwomoh, F. A., Yuan, S. Q., Li, H., Zhu, X. Y., Liu, J. P., Mensah, R., et al. (2020). Analysis of water droplet distribution in wind for the fluidic sprinkler. *Water* 12, 3320. doi: 10.3390/w12123320

Farzad, R., Puttinger, S., Pirker, S., and Schneiderbauer, S. (2017). Investigation of droplet size distribution for liquid-liquid emulsions in Taylor-couette flows. *J. Disper. Sci. Technol.* 39, 250–258. doi: 10.1080/01932691.2017.1312431

Gaillard, A., Sijs, R., and Bonn, D. (2022). What determines the drop size in sprays of polymer solutions? *J. Non-Newton. Fluid.* 305, 104813. doi: 10.1016/j.jnnfm.2022.104813

Gong, C., Kang, C., Jia, W. D., Yang, W. T., and Wang, Y. L. (2020). The effect of spray structure of oil-based emulsion spray on the droplet characteristics. *Biosyst. Eng.* 198, 78–90. doi: 10.1016/j.biosystemseng.2020.08.001

Gong, C., Li, D. Y., and Kang, C. (2022). Visualization of the evolution of bubbles in the spray sheet discharged from the air-induction nozzle. *Pest. Manage. Sci.* 78, 1850–1860. doi: 10.1002/ps.6803

Gong, C., Li, D. Y., Kang, C., and Wang, Y. L. (2021). Visualisation of the evolution of perforations in oil-based emulsion sheets formed by flat-fan spray nozzles. *Biosys. Eng.* 207, 68–80. doi: 10.1016/j.biosystemseng.2021.04.005

He, Y., Wu, J. J., Fu, H. L., Sun, Z. Y., Fang, H., and Wang, W. (2022). Quantitative analysis of droplet size distribution in plant protection spray based on machine learning method. *Water* 14, 175. doi: 10.3390/w14020175

Hilz, E., and Vermeer, A. W. P. (2013). Spray drift review: the extent to which a formulation can contribute to spray drift reduction. *Crop Prot.* 44, 75–83. doi: 10.1016/j.cropro.2012.10.020

Kooij, S., Sijs, R., Denn, M. M., Villermaux, E., and Bonn, D. (2018). What determines the drop size in sprays? *Phys. Rev. X.* 8, 31019. doi: 10.1103/physrevx.8.031019

Lewis, R. W., Evans, R. A., Malic, N., Saito, K., and Cameron, N. R. (2016). Polymeric drift control adjuvants for agricultural spraying. *Macromol. Chem. Phys.* 217, 2223–2242. doi: 10.1002/macp.201600139

Li, C., He, R. C., He, Z. L., Kumar, S. S., Fredericks, S. A., Hogan, C. J., et al. (2021). Spatially-resolved characterization of oil-in-water emulsion sprays. *Int. J. Multiphas. Flow.* 145, 103813. doi: 10.1016/j.ijmultiphaseflow.2021.103813

Li, L. L., Hu, Z. H., Liu, Q. J., Yi, T. C., Han, P., Zhang, R. R., et al. (2022). Effect of flight velocity on droplet deposition and drift of combined pesticides sprayed using an unmanned aerial vehicle sprayer in a peach orchard. *Front. Plant Sci.* 13. doi: 10.3389/fpls.2022.981494

Liu, Y. P., Xiao, Q. G., Han, X. Q., Zeeshan, M., and Fang, Z. H. (2022). Effect of aerial application of adjuvants on pepper defoliant droplet deposition and efficacy of defoliation sprayed by unmanned aerial vehicles. *Front. Plant Sci.* 13. doi: 10.3389/fpls.2022.917462

Makhnenko, I., Alonzi, E. R., Fredericks, S. A., Colby, C. M., and Dutcher, C. S. (2021). A review of liquid sheet breakup: perspectives from agricultural sprays. *J. Aerosol. Sci.* 157, 105805. doi: 10.1016/j.jaerosci.2021.105805

Minov, S. V., Cointault, F., Vangeyte, J., Pieters, J. G., and Nuyttens, D. (2016). Spray droplet characterization from a single nozzle by high speed image analysis using an in-focus droplet criterion. *Sensors* 16, 218. doi: 10.3390/s16020218

Musiu, E. ,. M., Qi, L. J., and Wu, Y. L. (2019). Evaluation of droplets size distribution and velocity pattern using computational fluid dynamics modelling. *Comput. Electron. Agr.* 164, 104886. doi: 10.1016/j.compag.2019.104886

Ostu, N. (1979). A threshold selection method from graylevel histograms. *IEEE Transactions on Systems, Man and Cybernetics* 9, 62-66. doi: 10.1109/TSMC.1979.4310076

Patil, A. V., Marti, X. S., Tetlie, P., and Johansen, S. T. (2017). Development of an advanced imaging technique for dynamic emulsion stability. *Chem. Eng. J.* 322, 90–101. doi: 10.1016/j.cej.2017.02.156

Post, S. L., and Hewitt, A. J. (2018). Flat-fan spray atomization model. *T. ASABE.* 61, 1249–1256. doi: 10.13031/trans.12572

Qin, K. D., Tank, H., Wilson, S., Downer, B., and Liu, L. (2010). Controlling droplet-size distribution using oil emulsions in agricultural sprays. *Atomization. Spray.* 20, 227–239. doi: 10.1615/atomizspr.v20.i3.40

Qin, L. Z., Yi, R., and Yang, L. J. (2018). Theoretical breakup model in the planar liquid sheets exposed to high-speed gas and droplet size prediction. *Int. J. Multiphas. Flow.* 98, 158–167. doi: 10.1016/j.ijmultiphaseflow.2017.09.010

Sijs, R., and Bonn, D. (2020). The effect of adjuvants on spray droplet size from hydraulic nozzles. *Pest. Manage. Sci.* 76, 3487–3494. doi: 10.1002/ps.5742

Tuck, C. R., Ellis, M. C. B., and Miller, P. C. H. (1997). Techniques for measurement of droplet size and velocity distributions in agricultural sprays. *Crop Prot.* 16, 619–628. doi: 10.1016/s0261-2194(97)00053-7

Vernay, C. (2015). *Destabilisation of liquid sheets of dilute emulsions* (France: Universite Montpellier). Available at: https://tel.archives-ouvertes.fr/tel-01254934.

Vernay, C., Ramos, L., Douzals, J. P., Goyal, R., Castaing, J. C., and Ligoure, C. (2016). Drop impact experiment as a model experiment to investigate the role of oil-in-water emulsions in controlling the drop size distribution of an agricultural spray. *Atomization. Spray.* 26, 827–851. doi: 10.1615/AtomizSpr.2015013630

Vernay, C., Ramos, L., Würger, A., and Ligoure, C. (2017). Playing with emulsion formulation to control the perforation of a freely expanding liquid sheet. *Langmuir* 33, 3458–3467. doi: 10.1021/acs.langmuir.7b00170

Vieira, B. C., Alves, G. S., Carvalho, F. K., da Cunha, J. P. A. R., Antuniassi, U. R., and Kruger, G. R. (2018). Influence of airspeed and adjuvants on droplet size distribution in aerial applications of glyphosate. *Appl. Eng. Agric.* 34, 507–513. doi: 10.13031/aea.12587

Zeng, L. L., Zhang, Y., Bukirwa, C., Li, W. S., and Yang, Y. Q. (2015). Study of mean diameter and drop size distribution of emulsion drops in a modified rotating disc contactor for an emulsion liquid membrane system. *Rsc. Adv.* 5, 89959–89970. doi: 10.1039/c5ra16267j

Zhang, X. G., and Xiong, L. X. (2021). Effect of adjuvants on the spray droplet size of pesticide dilute emulsion. *Colloid. Surface. A.* 619, 126557. doi: 10.1016/j.colsurfa.2021.126557

Zhou, W., Hu, J. R., Feng, M. L., Yang, B., and Cai, X. S. (2015). Study on imaging method for measuring droplet size in large sprays. *Particuology* 22, 100–106. doi: 10.1016/j.partic.2014.12.003

frontiers | Frontiers in Plant Science

TYPE Original Research
PUBLISHED 26 June 2023
DOI 10.3389/fpls.2023.1207742

OPEN ACCESS

EDITED BY
Chuanlei Zhang,
Tianjin University of Science and Technology, China

REVIEWED BY
Bingbo Cui,
Jiangsu University, China
Siniša Mitrić,
University of Banja Luka, Bosnia and Herzegovina

*CORRESPONDENCE
Xiaohui Lei
leixiaohui.2008@163.com
Xiaolan Lyu
lxlanny@126.com

RECEIVED 18 April 2023
ACCEPTED 07 June 2023
PUBLISHED 26 June 2023

CITATION
Xia Y, Lei X, Pan J, Chen L, Zhang Z and Lyu X (2023) Research on orchard navigation method based on fusion of 3D SLAM and point cloud positioning. *Front. Plant Sci.* 14:1207742. doi: 10.3389/fpls.2023.1207742

Research on orchard navigation method based on fusion of 3D SLAM and point cloud positioning

Ye Xia[1,2,3], Xiaohui Lei[1,2]*, Jian Pan[1,2], LuWei Chen[1,2], Zhen Zhang[1,2] and Xiaolan Lyu[1,2]*

[1]Institute of Agricultural Facilities and Equipment, Jiangsu Academy of Agricultural Sciences, Nanjing, China, [2]Key Laboratory of Modern Horticultural Equipment, Ministry of Agriculture and Rural Affairs, Nanjing, China, [3]School of Agricultural Engineering, Jiangsu University, Zhenjiang, China

Accurate navigation is crucial in the construction of intelligent orchards, and the need for vehicle navigation accuracy becomes even more important as production is refined. However, traditional navigation methods based on global navigation satellite system (GNSS) and 2D light detection and ranging (LiDAR) can be unreliable in complex scenarios with little sensory information due to tree canopy occlusion. To solve these issues, this paper proposes a 3D LiDAR-based navigation method for trellis orchards. With the use of 3D LiDAR with a 3D simultaneous localization and mapping (SLAM) algorithm, orchard point cloud information is collected and filtered using the Point Cloud Library (PCL) to extract trellis point clouds as matching targets. In terms of positioning, the real-time position is determined through a reliable method of fusing multiple sensors for positioning, which involves transforming the real-time kinematics (RTK) information into the initial position and doing a normal distribution transformation between the current frame point cloud and the scaffold reference point cloud to match the point cloud position. For path planning, the required vector map is manually planned in the orchard point cloud to specify the path of the roadway, and finally, navigation is achieved through pure path tracking. Field tests have shown that the accuracy of the normal distributions transform (NDT) SLAM method can reach 5 cm in each rank with a coefficient of variation that is less than 2%. Additionally, the navigation system has a high positioning heading accuracy with a deviation within 1° and a standard deviation of less than 0.6° when moving along the path point cloud at a speed of 1.0 m/s in a Y-trellis pear orchard. The lateral positioning deviation was also controlled within 5 cm with a standard deviation of less than 2 cm. This navigation system has a high level of accuracy and can be customized to specific tasks, making it widely applicable in trellis orchards with autonomous navigation pesticide sprayers.

KEYWORDS

orchard, robot, autonomous navigation, vector map, LiDAR, SLAM

1 Introduction

As a labor-intensive industry (Lyu et al., 2020), fruit production relies heavily on manual labor for its production process. With today's increasing labor costs and population pressure, traditional production methods are unsustainable. In order to overcome these problems, many studies have been devoted to the use of orchard robots to replace manual labor, and devices such as automated orchard picking robots (Wang X. et al., 2023; Wang Y. et al., 2023) and mobile orchard applications and fertilization robots (Yayan et al., 2015; Gao et al., 2020) have emerged. How to achieve accurate and efficient autonomous navigation in a complex orchard environment by determining its own position through various sensors is the focus of all orchard operation robots. Early autonomous navigation devices in orchards were mainly based on physical tracks (Keicher and Seufert, 2000; Yayan et al., 2015) with global navigation satellite system (GNSS) (Ryu et al., 2016; Yin et al., 2018). Bakker et al. (2011) developed a real-time kinematics–Differential Global Positioning System (RTK-DGPS) automatic navigation platform for sugar beet fields, which can achieve centimeter-level navigation accuracy. Bin et al. (2017) designed an orchard sprayer based on the BeiDou satellite navigation system, which was tested to have an average positioning accuracy of 0.03 m at 2 km/h operating conditions. Some orchards may pose a challenge for GNSS-based navigation devices as agricultural robots often work under the plant canopy. This can result in satellite signals being blocked and not reaching GNSS receivers, as highlighted by Li et al. (2009) and Niewola (2020). Therefore, many researchers have started to replace GNSS as the main sensor for navigation with light detection and ranging (LiDAR) for orchard navigation tasks. Bayar et al. (2015) completed the localization and steering control of orchard vehicles between rows of fruit trees using LiDAR, which is applicable to most orchards and has reliable localization accuracy. Zhang et al. (2020) obtained the trunk position by using 2D LiDAR acquisition and filtering, then fitted the navigation path using least squares, and finally used an improved tracking controller to achieve autonomous navigation. Li et al. (2022) constructed a raster map for the jujube orchard by LiDAR with the 2D simultaneous localization and mapping (SLAM) method and used DWA+A* to plan the path for navigation. Wang et al. (2022) constructed a map by 3D LiDAR for environment sensing while fusing multi-source information with millimeter-wave radar for obstacle avoidance. The navigation test shows its positioning accuracy within 15 cm.

Computer vision techniques also play an important role in the navigation of agricultural machinery. Visual navigation usually uses monocular and binocular cameras with the Hough transform (Hough and Paul, 1962; Winterhalter et al., 2018), least squares (Cui et al., 2015; Mao et al., 2019), and other methods to extract paths. With the rise of image deep learning processing techniques in recent years, many researchers have started to use deep learning processing orchard environment information and fit navigation lines to control vehicles traveling through the orchard. Cao et al. (2022) segmented farm crops based on residual networks and fitted the navigation paths by the least squares method, and their crop row detection accuracy reached 90.9%. Yang et al. (2022) fitted the navigation paths of orchard hard surfaces by training a semantic segmentation network based on SegNet (Badrinarayanan et al., 2017) and UNet (Ronneberger et al., 2015), and their path recognition rate reached 92%. Opiyo et al. (2021) obtained the navigation paths by extracting the texture features of fruit trees and roads, and their lateral accuracy is at the centimeter level.

With the standardized orchard development, trellis orchards are more adapted to mechanized operation. Due to the interference of the trellis and dense canopy, the GNSS signal is unstable, and the positioning method relying on GNSS alone is not reliable. The navigation method of extracting trunk position information by laser filtering is prone to failure due to missing path information at orchard corners. The navigation method of constructing raster maps by LiDAR tends to lose its own position due to the similarity of information between orchard rows. The visual extraction filter is too dependent on the light conditions, which is unsuitable for some working conditions that require night operation. In addition, today's orchard navigation tasks are more focused on the synergy of multiple tasks, and more intuitive orchard maps are needed to arrange various tasks. Traditional navigation methods mainly construct two-dimensional maps with little information and poor readability. It cannot reflect more effective orchard point cloud information, so a more intuitive way to construct orchard maps is urgently needed to match various mechanical operations. To address these problems, this paper proposes a trellis orchard navigation method based on 3D SLAM technology to construct maps and fuse RTK and LiDAR sensors for redundant positioning. The method uses normal distributions transform (NDT) mapping (Biber and Straßer, 2003) to construct 3D point clouds of orchards and extracts trellis feature points as reference point clouds by straight pass filtering, voxel filtering, outlier filtering, etc. The coordinates provided by RTK are transformed into the initial values of the position in real time and introduced into NDT matching for point cloud matching. Finally, the vector map (Darweesh et al., 2017) of the orchard is constructed in the form of manual planning by marking the paths in the constructed 3D point cloud map of the orchard to adapt to the navigation of various orchards with different scales and usage requirements.

2 Materials and methods

2.1 Orchard conditions

The trial site was located in the pear orchard of Jiangsu Academy of Agricultural Sciences, which was constructed using a standard Y-trellis with fruit trees spaced 6.0 m apart in rows, 3.0 m apart in columns, and an average height of 3 m. The trial was conducted in November 2022. Figures 1A, B show the aerial view of the orchard and the trellis, respectively.

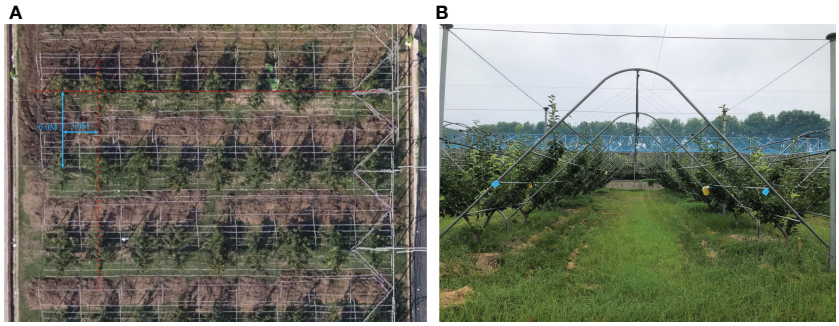

FIGURE 1
Test fields. **(A)** Aerial view of the orchard. **(B)** Y-trellis for orchard.

2.2 Hardware system

The study uses Songling Scout 2.0 robot as the motion chassis, which has four-wheel drive capability and uses differential speed for steering. For robot control, the target line and angular speed were received from the host computer via CAN bus and output to the motor for bottom control via STM32. The main technical parameters of the robot chassis are shown in Table 1. The navigation system was equipped with a 16-line LiDAR (C16, Leishen Intelligent System Co., Ltd., Shenzhen, China) and a nine-axis inertial measurement unit (IMU) (HFI-A9, HandsFree, Shenzhen, China). It was mounted on a metal bracket at 0.2 m in the X-axis direction and 0.25 m in the Z-axis direction with the center of the robot chassis as the origin of the coordinate system. GNSS (T3-B, QFRTK, Shenzhen, China) equipment was magnetically mounted to the front and rear center of the vehicle chassis to provide differential position information and record real-time trajectories. The laptop was used as a control terminal for various sensors. The laptop consisted of an Intel Core i7-12700 h CPU with 16 GB of DDR5 RAM. Ubuntu Linux 18.04LTS was installed on the computer, together with the Robot Operating System (ROS). The Laptop communicates with the STM32 in the chassis via usb2can with CAN signal output speed information. Figure 2 shows the complete system hardware platform.

TABLE 1 Main parameters of Scout 2.0 robot.

Name	Value
Dimensions (L × W × H), m	0.93 × 0.7 × 0.35
Wheelbase, mm	498
Tread, mm Top speed, m/s	582 1.5
Motor rated voltage Minimum ground clearance, mm Maximum grade, ° Maximum load, kg	24V DC 135 30 50

2.3 3D SLAM-based map construction method

NDT was proposed by Biber and Straßer, 2003. The idea of NDT can be summarized as filtering the input point cloud in each frame and then stitching it with the previous frame by matching the computed bit pose to build a map. NDT mapping first divides the single-frame point cloud scanned by 3D LiDAR into cubes with certain voxel dimensions to reduce the data complexity and introduce an initial set of positional parameters. Formula 1 represents the point cloud intensity of each cube. Then, the probability density is calculated from Formula 2 for all point clouds within the cube. Then, a set of discrete point clouds is expressed directly and approximately in the form of probability density functions, which are smooth and continuously derivable. Each probability density function can be considered as an approximation of a local surface, which not only describes the location of the surface in space but also contains information about the orientation and smoothness of the surface.

$$\Sigma = \frac{1}{m}\sum_{k=1}^{m}(\vec{y}_k - \vec{\mu})(\vec{y}_k - \vec{\mu})^T \tag{1}$$

$$f(\vec{x}) = \frac{1}{(2\pi)^{\frac{3}{2}}\sqrt{|\Sigma|}} e^{\frac{-(\vec{x}-\vec{\mu})^T\Sigma^{-1}(\vec{x}-\vec{\mu})}{2}} \tag{2}$$

where $\overrightarrow{y}_k$ k=1,…,m are the positions of the reference scan points contained in the cube.

After the transformation of the input point cloud in one frame was completed in this way, the NDT SLAM will update the point cloud in the global map. According to Formula 3, when the point cloud information was input in the next frame, for the point cloud $X = \{\vec{X}_1, \ldots, \vec{X}_n\}$, there exists a set of transformation matrices $T(\vec{p}, \vec{x})$. For a given probability density function of the scanned point cloud, the bit pose $\vec{p}$ that makes the best match between the two frames was the solution of the maximum likelihood function, which was also the minimal value of its negative logarithm, as shown in Formula 4.

$$\Psi = \prod_{k=1}^{n} p(T(\overrightarrow{p}, \overrightarrow{x}_k)) \tag{3}$$

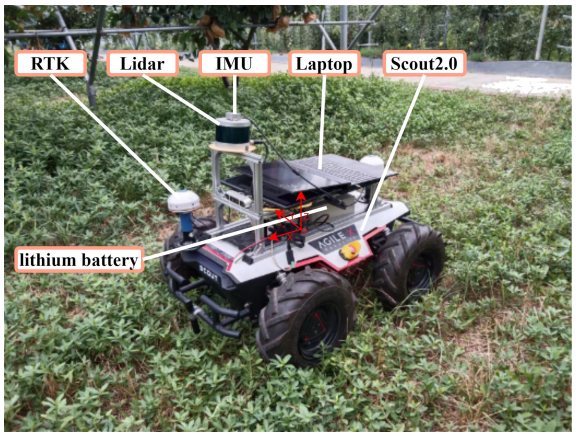

FIGURE 2
Photograph of the mobile platform.

$$-\log \Psi = -\sum_{k=1}^{n} \log(p(T(\vec{p}, \vec{x}_k))) \quad (4)$$

For Formula 4, the optimal solution was obtained by Newton's optimization iteration as the best matching poses, and then the point cloud of each LiDAR scan frame was updated in the global map with the result of the matching poses. This process was repeated to overlay the point clouds to finally obtain the global map. The flowchart of the NDT mapping algorithm is shown in Figure 3.

There are several advantages to using the NDT method for environment construction in an orchard environment. First, it can adjust the map resolution and reduce the data volume by voxelizing the point cloud, which has a good downsampling effect on the information of all kinds of branches and leaves noise in the orchard. Second, the method has higher adaptability to subtle changes in the environment. When there is a change in the fruit trees within a divided voxel, the probability density description method can effectively reduce the error caused by subtle changes in the point cloud matching.

2.4 GNSS fusion NDT point cloud matching based on localization method

The NDT matching approach to localization is also based on the above-mentioned principle of great likelihood estimation for positional computation. By continuously comparing the input point cloud with the already recorded point cloud in each frame, the position corresponding to each frame is continuously output. However, this approach needs to give the initial value of the locus pose during the point cloud matching calculation, and the approximate solution of the locus pose is used to obtain the optimal result faster by subsequent Newtonian iterative optimization. If completely relying on NDT positioning, the system can only set the initial value of the positional pose once at the beginning, which will lead to positioning failure and no automatic correction. When the initial value is set incorrectly or the subsequent matching cannot obtain the result, the vehicle position falls into robot abduction. In order to solve this problem, the best method is to continuously provide the NDT with the initial position value and recalculate it through external data when the NDT fails. Considering that the orchard is outdoors, it is suitable to introduce GNSS information with high position positioning accuracy and convert the longitude and latitude data provided by

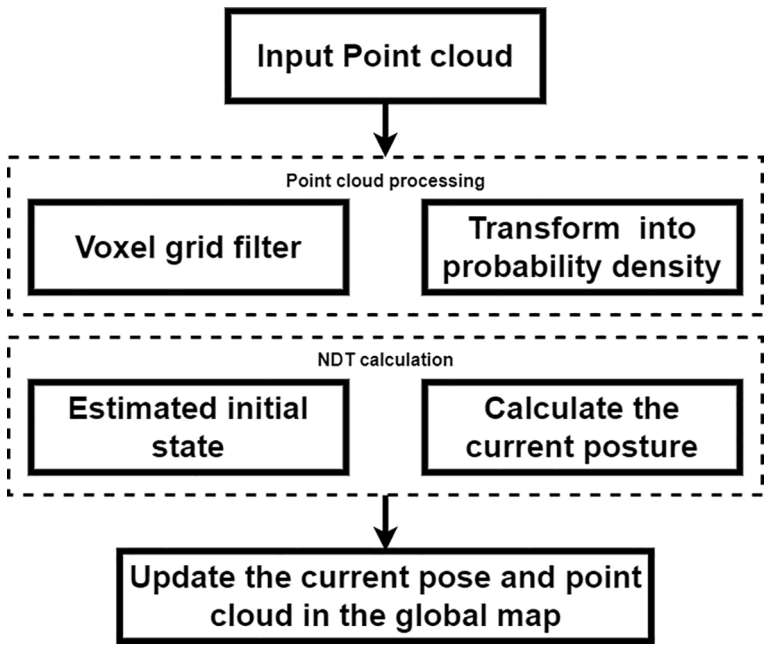

FIGURE 3
NDT mapping. NDT, normal distributions transform.

GNSS into the initial position parameters of the vehicle and use them as iterative initial values for NDT position calculation, which changes the positioning method from single sensor work to multi-sensor fusion positioning.

For the specific practice of converting RTK latitude and longitude information to vehicle position, this paper proposes a conversion procedure to convert it in real time, and its pseudo-code is shown in Figure 4. The program first records the latitude and longitude of the origin of the point cloud map and aligns the world coordinate system with it. Then, the relative latitude and longitude are obtained by subtracting the original world coordinate of the map from the input GNSS. Finally, the relative coordinate information is transformed into the map coordinate system in real time.

Considering the large variety of fruit trees, the timeliness and reliability of the point cloud generated by NDT mapping are poor, and the efficiency of the solution will be affected by a large amount of data in the subsequent point cloud matching. The trellis is a fixed and not easily deformed marker in the orchard, and it is the most ideal reference point cloud for alignment. The research uses the Point Cloud Library (PCL) to filter and extract it as the reference point cloud for NDT pose calculation. The specific flow of the point cloud processing and positioning method is shown in Figure 5. The input point cloud is first voxel filtered to reduce the overall data volume of the point cloud, then the lower height point cloud is cut in the form of straight pass filtering to retain the fruit tree and trellis point clouds, and finally, the redundant point clouds within the two trellises are cut by rows in the form of outlier filtering with straight pass filtering to retain the trellis point cloud alone. After the scaffold reference point cloud has been processed, the height of the input LiDAR point cloud is controlled to maximize the proportion of the input scaffold point cloud among all input point clouds, and the RTK-supplied positional information is used as the initial value for the NDT iterative algorithm to match the scaffold reference point cloud with the LiDAR input point cloud. The NDT first constructs a transformation matrix T containing six degrees of freedom according to the initial value of the pose and projects the input LiDAR point cloud into the reference point cloud coordinate system via the transformation matrix T. The algorithm calculates the matching score by comparing the position distribution of each cell of the input point cloud in the reference point cloud and superimposing the cells generated from the two sets of point clouds. When the matching score is less than the pre-defined matching threshold, the alignment parameter T is calculated by iterative Newtonian optimization to make the matching score meet the requirement, and the result is the position of the input point cloud. When the matching score does not meet the predetermined threshold, the positioning is judged to be lost. At this time, the positioning process is restarted, and the initial position information is recalculated from the previously obtained RTK coordinate information. The NDT calculation process is repeated to obtain the vehicle position information.

2.5 Vector map navigation path generation and tracing method

The task of mapping driveable paths in a 3D point cloud map is usually performed by means of high-precision vector maps in the field of autonomous driving. A vector map consists of point elements, lane elements, line elements, pole elements, surface elements, and so on. The lane information is generated by manually or automatically marking the position of each element in the point cloud. The complete vector map in the autonomous driving domain also has elements such as stop lines, traffic lights, and footpaths. Fruit trees are regularly arranged, which provides good conditions for map vectorization. Therefore, this paper uses a manually annotated vector map to plan the driving rules and only takes the four elements of the point node lane to form the basic elements of the navigation path. Each point element has its own ID number and coordinates position in a vector map, and the specific location of each point can be marked in the point cloud map. When a path is specified, the point element in the lane is converted into a node element. The node element defines the points on the driveable lane in the point cloud, and the location information of the lane elements can be defined by the node. The dtlane element is a point element that complements the lane shape information, including the directional angle between points and the curvature radius of the steering path. Lane elements are sequentially connected by node elements to build lanes and define the center of the driving route. These four elements are recorded in tabular form with their respective attributes and finally published separately in the point

Algorithm 1 Converting longitude and latitude into initial value of posture

```
Input:    nmea_date
Output:   geo_xyz, geo_head
While:    (nmea_date in):
    For time stamp in time line Do
        Time ← nmea_time
        lat  ← nmea_latitude - map_latitude
        lon  ← nmea_longitude - map_longitude
        h    ← nmea_height
        geo_llh ← (lat, lon, h)
        geo_xyz←WGS-84_trans_World(geo_llh)
        geo_head←Coordinate align(nmea_head , world_coordinate)
        ros_publish(geo_xyz , geo_head)
    End For
End While
```

FIGURE 4
Pseudo code for conversion.

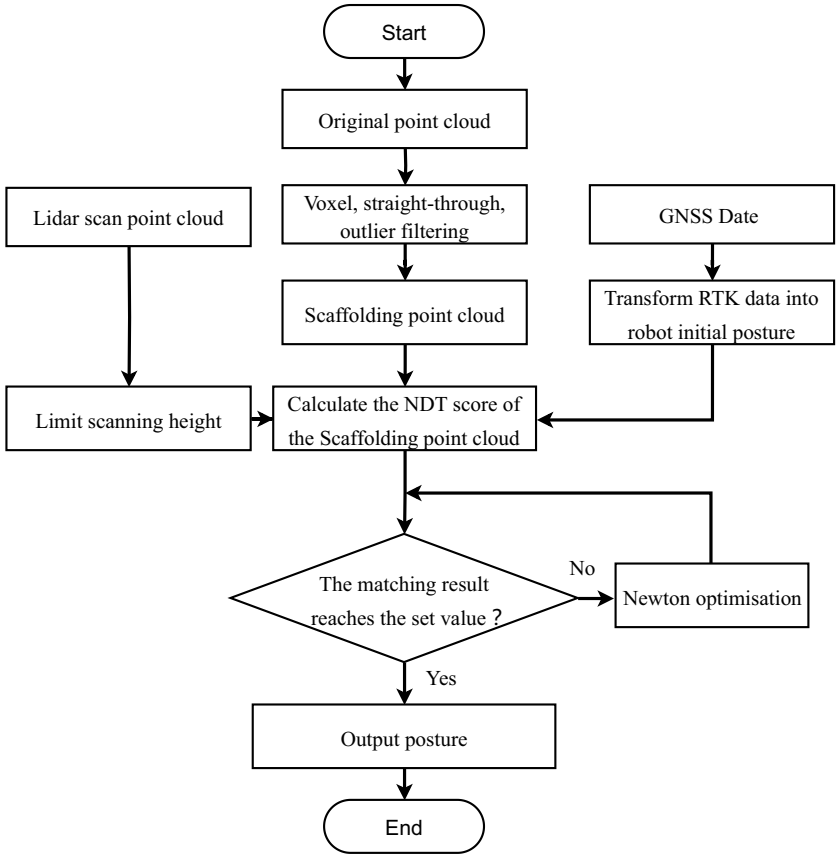

FIGURE 5
Flowchart of RTK fusion NDT location algorithm. RTK, real-time kinematics; NDT, normal distributions transform.

cloud map through the ROS system. Unity 3D Maptool plug-in is used to carry out manual vector map annotation in the orchard point cloud. The planned path is shown in Figure 6. The navigable path in the orchard is constructed by adding a point element and connecting each point to lane element. The same method is used to construct and transform road edges. The U-shaped line is taken as the fruit tree inter-row steering route, and the driving route map is built with three rows of fruit trees as the main object. Among them, the pink dotted line is the calibrated navigation route, the blue solid line is the prescribed form range, and the green part is the orchard point cloud. They are used to assist in labeling the driving line of a vector map to precisely locate the position of each element.

When the trajectory is generated, the final task of the navigation vehicle is to follow the trajectory. The planned trajectory in the orchard is relatively simple, and the mobile robot is a wire-controlled chassis satisfying the differential kinematic model, which can directly receive the linear and angular velocity commands sent from the ROS to achieve trajectory tracking. The kinematic model of the four-wheel chassis during tracing is modeled in Figure 7. Refer to pure path tracking (Coulter,1992). For the target trajectory M, a pre-sighting point C is selected on the reference path to be tracked, which is at a distance L_d from the vehicle's center of mass position, and the rear wheel center of the vehicle can be driven along a certain turning radius R to reach this point.

In triangle OAC, AC and OC satisfy the sine rule, and because angle OCA is complementary to angle CAB, Formula 5 can be obtained by using the sine rule.

$$\frac{L_d}{\sin(2\alpha)} = \frac{R}{\sin(\frac{\pi}{2} - \alpha)} \tag{5}$$

where L_d is the chord of the steering curvature arc, α is the heading angle at point A, and R is the radius of the steering curvature circle.

By simplifying Formula 5, the expression for the radius of curvature in terms of turning can be obtained, which is given by Formula 6.

$$R = \frac{L_d}{2\sin\alpha} \tag{6}$$

In order to determine the heading angle at each position during tracking, assume that the vehicle travels from point A to point B. Because β is complementary to angle OBA, and angle OBA is complementary to angle AOB, the expression for the heading angle β can be obtained in triangle AOB using trigonometric relationships, which is given by Formula 7.

$$\beta = \arctan\frac{L}{R} \tag{7}$$

where β is the heading angle and L is the distance from the center of the vehicle to the next position.

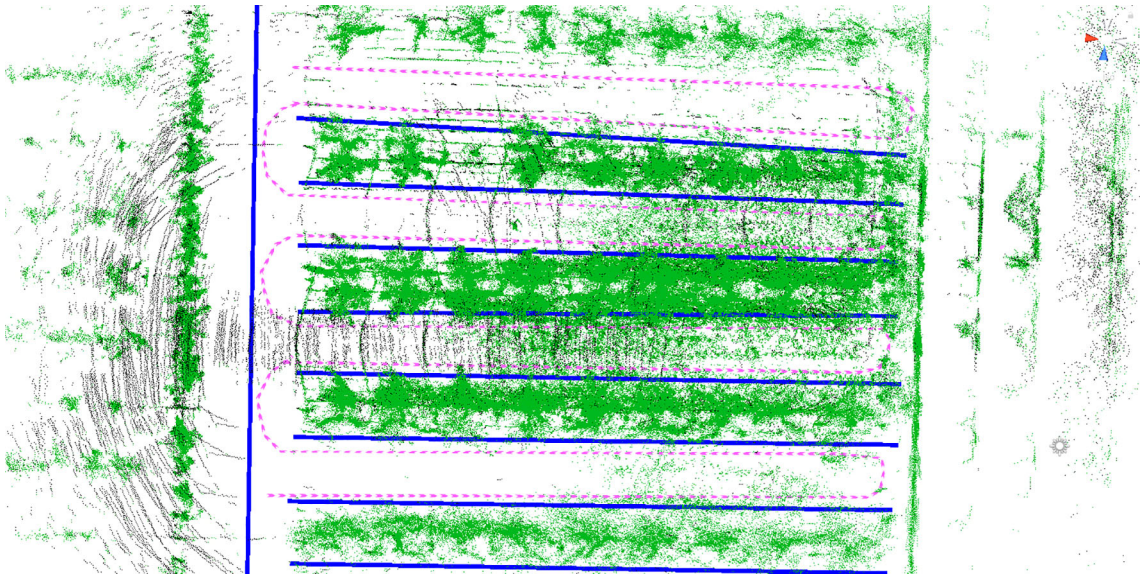

FIGURE 6
Vector map with manually labeled paths. The green part of the figure is the orchard point cloud, the pink route is the driving path, and the blue line is the driving boundary.

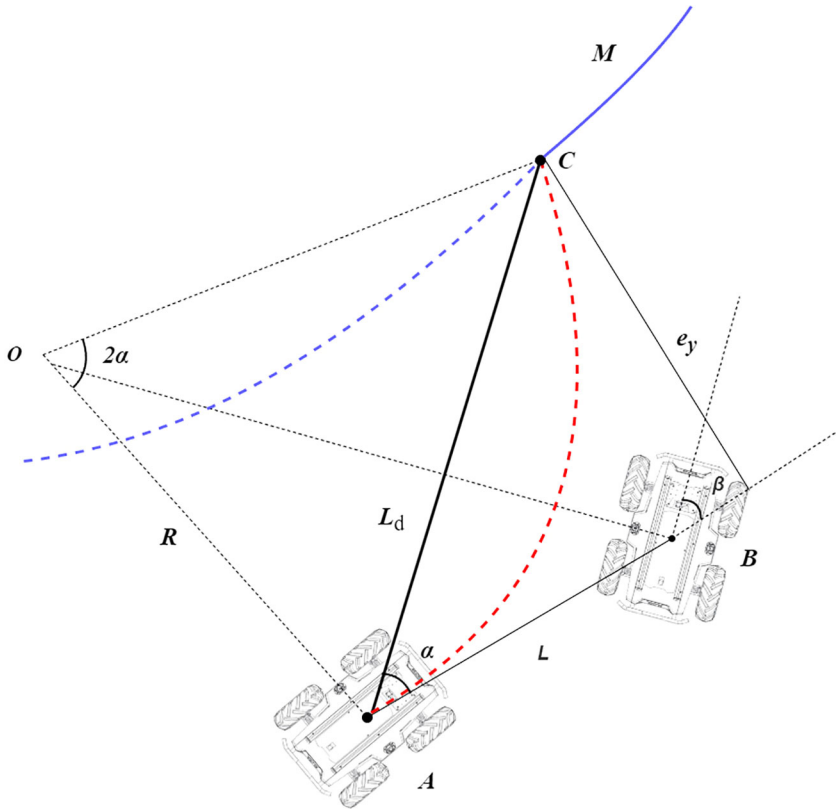

FIGURE 7
Pure pursuit model. Point *A* in the figure represents the current position, *C* represents the lookahead point position, and *B* represents the position of the vehicle during turning. The blue curve *M* represents the planned path, and the red curve *AC* represents the turning path. α is the heading angle at point *A*, β is the heading angle at point *B*, *L* is the distance from the center of the vehicle to the next position, L_d is the chord of the steering curvature arc, and e_y is the error in the lateral direction between the rear wheel center position and the lookahead point.

By substituting Formula 6 into Formula 7, a further simplified expression for the turning angle can be obtained, which is given by Formula 8.

$$\beta = \arctan\frac{2L\sin\alpha}{L_d} \tag{8}$$

The lateral error e_y is defined as the error in the lateral direction between the rear wheel center position and the lookahead point. In triangle ABC, the expression for the forward distance L_d can be obtained using the sine rule, which is given by Formula 9.

$$L_d = \frac{e_y}{\sin\alpha} \tag{9}$$

where e_y is the error between the rear wheel center position and the pre-sighting point in the lateral direction.

By substituting Formula 9 into Formula 8, the final expression for the heading angle can be obtained, which is given by Formula 10.

$$\beta = \arctan\left(\frac{2Le_y}{{L_d}^2}\right) \tag{10}$$

During the motion at each moment, the turning angle is relatively small. Therefore, Formula 10 can be simplified to the form of Formula 11, which leads to the final heading angle control model.

$$\beta = \frac{2L}{{L_d}^2}e_y \tag{11}$$

3 Results and discussions

3.1 NDT mapping trials

The NDT mapping test was conducted in a pear orchard. After connecting the hardware, the NDT mapping process was opened in ROS. The mobile platform was remotely controlled to move along the rows of trees and steered in a U-shaped trajectory at the end of each row. The final point cloud map of three rows of fruit trees is shown in Figure 8A. The point cloud of the orchard is very complex, it is unreliable to use the NDT-generated map as a reference map directly, and the original point cloud map needs to be processed using point cloud filtering to eliminate noise and compress map data. For the collected point clouds of Y-trellis orchards, the generated original point clouds were first retained 70% by downsampling to reduce the data volume. Then, the smaller dense point clouds were combined by voxel filtering and outlier filtering to reduce the overall resolution. The results are shown in Figure 8B, where the overall number of point clouds was effectively reduced. Three columns of fruit trees were selected as the test object, and the extra columns of fruit trees were removed by conditional direct-pass filtering, as in Figure 8C. Considering that the orchard has the characteristics of a trellis, it was chosen as a retained point cloud. In this way, the cluttered point cloud of the whole orchard can be preserved as a trellis point cloud, and it can be used as a high-precision map for positioning. The final processed localization point cloud is shown in Figure 8D, where the noisy and changeable canopy point clouds were filtered.

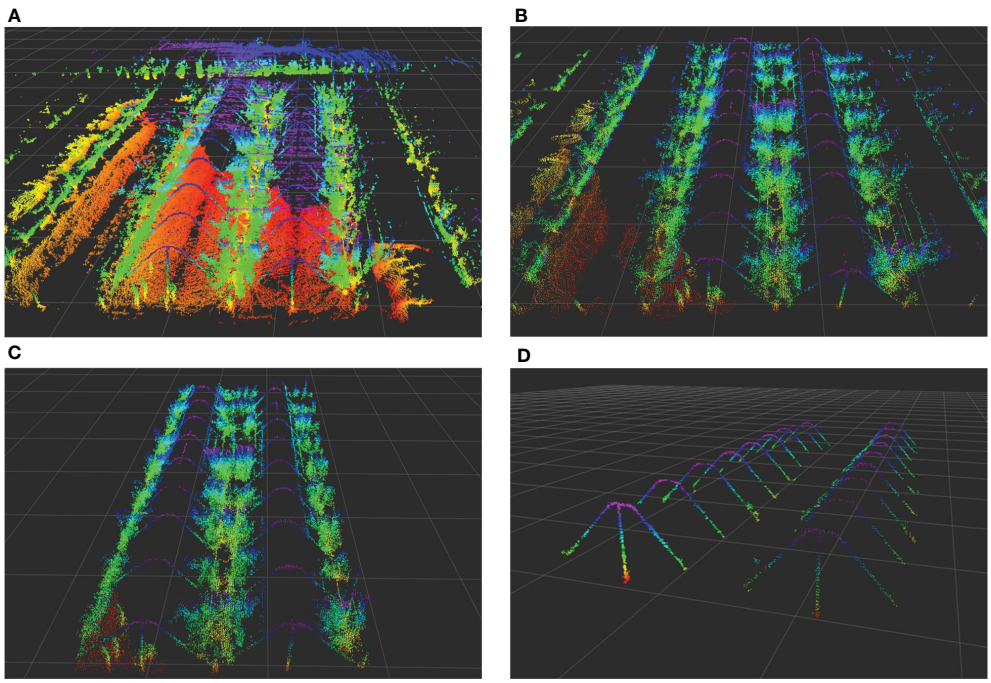

FIGURE 8
Orchard point cloud map processing method. **(A)** Original point cloud map. **(B)** Voxel filtering point cloud. **(C)** Pass-through filtering point cloud. **(D)** The trellis point cloud.

After the trellis point clouds were processed, the relative position of each point cloud was measured in RVIZ using the measure plugin and compared with the real distance of the orchard to verify the accuracy of the mapping. Figure 9A shows the initial point cloud obtained in RVIZ, where the red curve is the movement trajectory of the vehicle. The mapping effect test method is shown in Figure 9B, where the trellis structure was divided into two rows. In an ideal situation, the horizontal distance between the trellis is 3 m, and the vertical distance between the vertical vertices is 6 m.

The results of the point cloud distance measurement tests in RVIZ are shown in Table 2. The maximum and minimum absolute errors of the point cloud in each row were 8 and 3 cm, respectively. The average measured value of the distance between rows was 3.02 cm, with an average standard deviation of 0.059 cm. The maximum and minimum absolute errors between reference points in each column were 11 and 8 cm, respectively. The average measurement of the inter-column distance was 5.975 cm with a standard deviation of 0.096 cm. The average error between rows and columns were within 3 cm, and the accuracy level meets the requirements of subsequent NDT matching localization. In order to understand the consistency of the point cloud measurements between rows and columns, the coefficient of variation (CV) was used to compare the three ABC data sets to verify the dispersion errors. The average CV of the three data sets was less than 2%, and the errors in both column and row directions were stable, which means that NDT mapping is reliable as a method for large-scale orchards. Compared to the application of extended Kalman filter (EKF)–SLAM in orchards (Wu, 2019), the accuracy level of NDT mapping is not much different from that of EKF–SLAM because this type of SLAM method determines the location of each point cloud by randomly scattering particles and calculating their distribution probability density, which is essentially similar to the probabilistic estimation method of NDT. However, NDT mapping uses 3D gridding to calculate probabilities, and the resulting orchard map was more informative and intuitive, which has the advantage of better map readability. Compared to the use of Cartographer in orchards (Xiong, 2021), this method has higher accuracy and is more advantageous in terms of mapping speed, as Cartographer needs to continuously optimize the already generated map, while this method only needs to overlay point clouds based on position.

3.2 Fixed-point navigation test

The fixed-point navigation test was conducted to verify whether the GNSS with NDT point cloud matching in the orchard could achieve the desired accuracy. The test site is shown in Figure 10A, and the specific test plan is shown in Figure 10B. The intersection points of navigation paths were selected, and the column-wise trellis was selected as the reference point. The measured distances between the bottom of the scaffold in the point cloud map and each reference point were taken as the true value 0 for localization. The vehicle was controlled to pass through points M1, M2, …, M14 in the order, and the distance to the reference point was measured when it reaches each point to obtain the lateral deviation. For heading positioning, the heading of the navigation track was taken as the true value 0. Since the path generated by the vector map was actually constructed in the form of points, the Angle between the two points adjacent to the measurement position and the due east direction was selected as the ideal course Angle, and the course deviation during its movement was recorded by the on-board IMU. The speed of the vehicle was set at 1.0 m/s and the lateral, heading deviations were recorded as absolute values. Meanwhile, in order to compare the effect of NDT point cloud matching positioning more clearly, three methods of GNSS positioning, NDT matching positioning, and GNSS fusion NDT positioning were selected for the above positioning tests. The lateral and heading errors of the three methods at 14 reference points were recorded, and the results of the box line plot are shown in Figure 11.

When the vehicle speed was 1.0 m/s, the average lateral deviation of RTK positioning was less than 3 cm, and the SD was less than 2 cm, while the average heading deviation was less than 3.5°, and the SD was less than 1°. Compared with that of the other two positioning methods, the lateral accuracy of RTK positioning was the highest and the data stability was strong, but compared with the point cloud matching-based positioning method, it was more susceptible to lateral and heading deviations due to obstruction in the orchard. The average lateral deviation of the NDT point cloud matching method was less than 5 cm, and the SD was less than 2 cm, while the average heading deviation was within 1°, and the SD was less than 0.6°. This positioning method was better in terms of lateral and heading accuracy, but during long-time operation, it can be interfered with by similar point cloud scenes and lead to

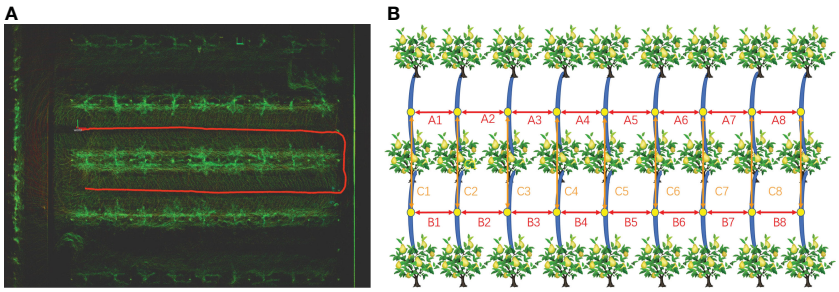

FIGURE 9
Orchard point cloud mapping test. **(A)** Initial orchard point cloud and data collection trajectory in RVIZ. **(B)** Mapping effect test schematic. A1 to A8 and B1 to B8 are the relative horizontal distances between the trellis, and C1 to C8 are the vertical relative distances between the vertical vertices.

10.3389/fpls.2023.1207742

TABLE 2 Reference point cloud relative distance measurement results.

No	Scaffold sampling point distance measurements (m)								Mean	Standard deviation	CV
	1	2	3	4	5	6	7	8			
Line A	A1	A2	A3	A4	A5	A6	A7	A8	3.015	0.064	0.021
	3.07	2.92	3.05	3.07	3.06	2.93	2.97	3.05			
Line B	B1	B2	B3	B4	B5	B6	B7	B8	3.026	0.054	0.018
	3.08	3.05	3.06	3.03	2.92	3.04	2.97	3.06			
Line C	C1	C2	C3	C4	C5	C6	C7	C8	5.975	0.096	0.016
	5.91	5.91	5.90	6.11	6.08	5.89	5.92	6.08			
Total											0.018

positioning failure. It can be inferred that relying solely on NDT positional estimation as a navigation method is not stable. The GNSS fusion NDT positioning was comparable in accuracy performance to the NDT-only positioning method, with an average lateral deviation of less than 5 cm and an SD of less than 2 cm. The average heading deviation was within 1° and an SD of less than 0.6°, in accordance with its positioning theory. However, it is re-positioned by GNSS when NDT matching fails, and the method lasts longer in operation than pure RTK positioning. It can still rely on aligned trellis point clouds to maintain accurate positioning under some heavily shaded fruit tree canopies. It also provides a more stable heading position by means of point cloud matching and correcting deviations in the heading by numerous key point clouds, which can be more effective in tasks requiring high orientation accuracy. At the same time, the redundant positioning approach by combining two positioning information is more fault tolerant in real-life positioning tasks than relying on one sensor alone for positioning.

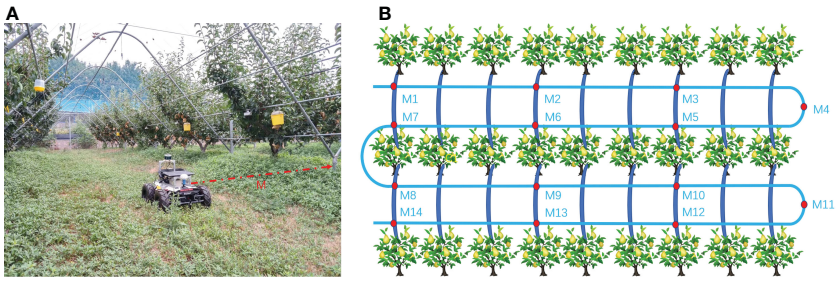

FIGURE 10
Fixed-point navigation tests. **(A)** Reference point distance measurement. **(B)** Schematic diagram of a fixed-point navigation test. M1 to M14 are measuring points on navigation path, and M is the distance between the tree column and the vehicle center.

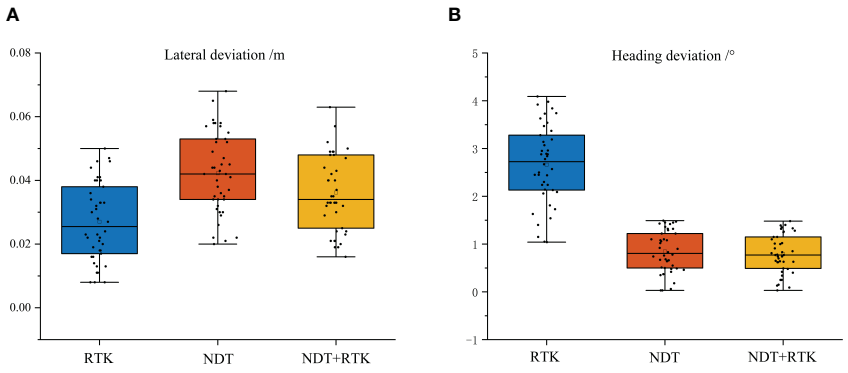

FIGURE 11
Fixed-point navigation test results. **(A)** Lateral deviation results. **(B)** Heading deviation results. The top and bottom horizontal lines are the maximum and minimum values, respectively. Three-quarters of the experimental error data points are in the box.

3.3 Navigation effect test

Figures 12A–F show different navigation positions when the speed was 1 m/s; the yellow path is the planning path, and the white line is the motion control line of pure path tracking planning. It was found that the planning line keeps changing with the path curvature, and the curvature was larger when navigating in a straight line and smaller when curving. Meanwhile, during the actual operation, the navigation effect changes significantly when different speeds were used for navigation. In order to explore the influence of different speeds on navigation accuracy, three driving speeds of 0.5, 1.0, and 1.5 m/s were selected, and the driving trajectories under each speed were recorded by RTK. The driving trajectories are shown in Figure 12G; the black curve is the planned path, and the round dots, stars, and triangular scatter points are the vehicle tracing paths under the three driving speeds. At the speed of

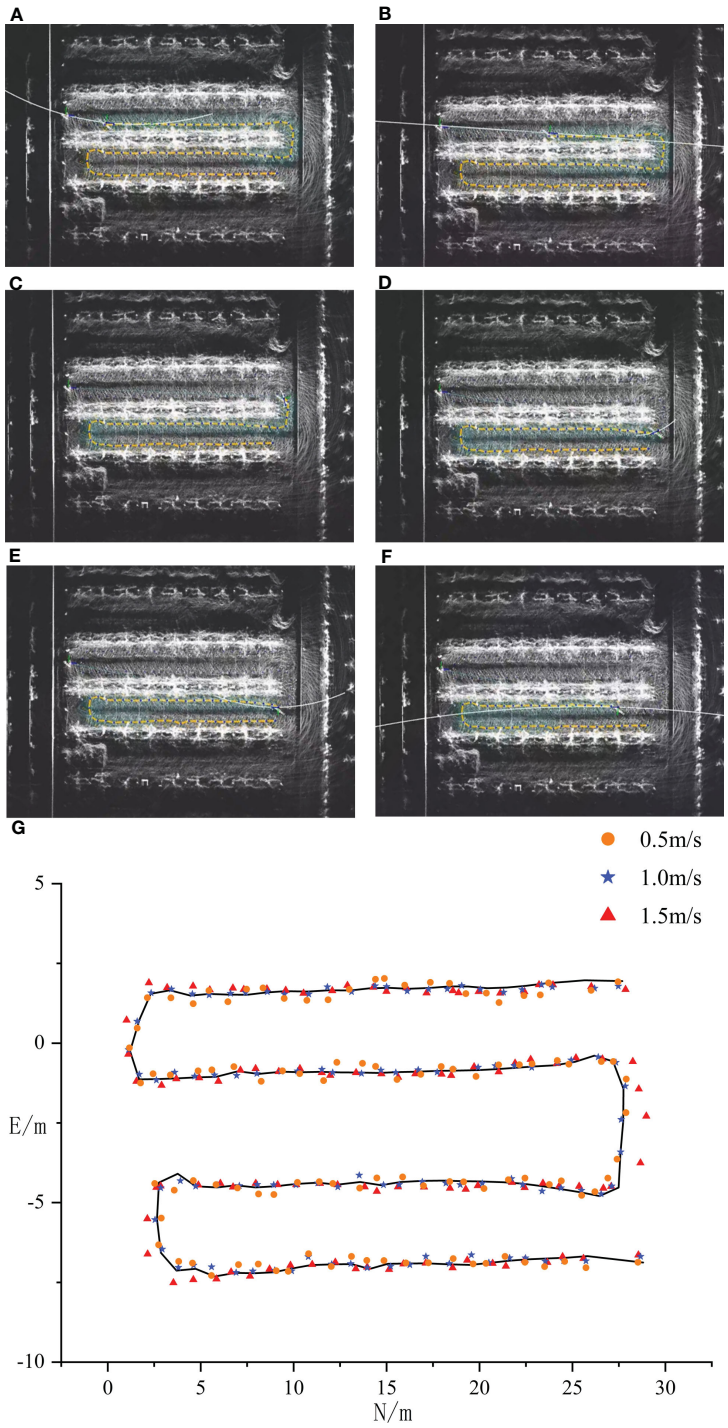

FIGURE 12
Navigation tests at different speeds. **(A–G)** The control line planning under straight and curved roads.

0.5 m/s, the maximum and minimum positioning errors of the tracing path were 13 and 3 cm, respectively, and the overall average error of the sampling points was 8 cm. At the speed of 1.0 m/s, the maximum and minimum errors of the tracing path were 6 and 1 cm, respectively, and the overall average error of the sampling points was 3.5 cm. At the speed of 1.5 m/s, the maximum and minimum errors of the tracing path were 15 and 5 cm, respectively, and the overall average error of the sampling point was 7 cm. When the speed was too slow, the heading adjustment of the navigation system was very frequent, and the tracing was incoherent. After it was combined with the pure path tracking, it can be found that the front view distance of the controller becomes smaller when the speed was too small, and the heading angle adjustment was large. At the same time, it can be found that the front view distance becomes longer when the speed was faster, and the tracking effect was stable in the straight trajectory, but the steering curvature was larger when passing through curves, resulting in a large radius through the curves. If the response lag of each sensor on the control platform was too fast, it will affect the navigation effect. When the vehicle was running at 1.0 m/s, the best tracing effect was achieved, as the speed setting affects the front view distance and thus changes the steering curvature. The best steering speed should be set according to the tree spacing. Based on the test, the best driving speed is 1.0 m/s, and the best forward-looking distance is 5.5 m.

4 Conclusion

Conducting various agronomic processes with an orchard autopilot platform is important for reducing human work time and improving operational accuracy in orchard production. Unlike scenarios in open environments such as field harvesting, the navigation system of an autonomous driving platform in an orchard environment is more difficult in terms of complex canopy handling and unstructured ground travel. In order to make the navigation in the orchard more suitable for continuous inter-row navigation and obstruction environment, this study used a four-wheel differential robot as the platform, constructed the environment using NDT Mapping's 3D SLAM method, and processed it with the PCL for the Y-shaped trellis environment. At the same time, the problem of easy loss of positioning in complex scenes in orchards was solved by GNSS fusion NDT point cloud matching for positioning. The results showed that the accuracy of NDT mapping was 10 cm. The positioning accuracy reached 5 cm in the lateral direction and 1° in the aerial direction. During the practical tests, the method was able to perform continuous navigation in the orchard, but there were problems such as the large amount of point cloud processing, which caused the chassis motion control to stutter, and the controller forward-looking distance parameters could not be applied to different scale scenarios.

In future research, we plan to explore a point cloud localization method that is less computationally intensive to suit devices with lower computing power and reduce system latency. To address the issue of control algorithms, controllers with variable parameters or control methods such as Model Predictive Control (MPC) and Linear Quadratic Regulator (LQR) should be used to improve the stability of navigation control, enabling autonomous navigation of orchard vehicles in a cost-effective, efficient, and accurate manner.

Data availability statement

The original contributions presented in the study are included in the article/Supplementary Material. Further inquiries can be directed to the corresponding authors.

Author contributions

XLL and XHL conceived the ideas and provided project funding support. YX wrote the paper and conducted the tests and equipment debugging. XHL reviewed the paper and suggestions. YX and XHL performed the experiments and processed the data with the assistance of JP, LC, and ZZ. Assistance includes moving equipment, recording test data, and preparing test materials. All authors contributed to the article and approved the submitted version.

Funding

This research was funded by the National Natural Science Foundation of China (32201680), China Agriculture Research System of MOF and MARA (CARS-28-21), Jiangsu Modern Agricultural Machinery Equipment and Technology Demonstration Extension Fund (NJ2022-14), Jiangsu Agricultural Science and Technology Innovation Fund (CX(21)2025), National Science and Technology Development Program of China (NK2022160104), Jiangsu Policy-guided Plans (BX2019016), and Wuxi Science and Technology Development Fund (N20221003).

Acknowledgments

We would like to thank Xiaogang Li, Qingsong Yang, and Zhonghua Wang (Institute of Pomology, Jiangsu Academy of Agricultural Science) for their help during the navigation test.

Conflict of interest

The authors declare that the research was conducted in the absence of any commercial or financial relationships that could be construed as a potential conflict of interest.

Publisher's note

Supplementary material

The Supplementary Material for this article can be found online at: https://www.frontiersin.org/articles/10.3389/fpls.2023.1207742/full#supplementary-material

References

Badrinarayanan, V., Kendall, A., and Cipolla, R. (2017). Segnet: a deep convolutional encoder-decoder architecture for image segmentation. *IEEE Trans. Pattern Anal. Mach. Intell.* 39, 2481–2495. doi: 10.1109/TPAMI.2016.2644615

Bakker, T., Van Asselt, K., Bontsema, J., Müller, J., and Van Straten, G. (2011). Autonomous navigation using a robot platform in a sugar beet field. *Biosyst. Eng.* 109, 357–368. doi: 10.1016/j.biosystemseng.2011.05.001

Bayar, G., Bergerman, M., Koku, A. B., and Ilhan Konukseven, E. (2015). Localization and control of an autonomous orchard vehicle. *Comput. Electron. Agric.* 115, 118–128. doi: 10.1016/j.compag.2015.05.015

Biber, P., and Straßer, W. (2003). "The normal distributions transform: a new approach to laser scan matching," in *Proceedings2002, 003 IEEE/RSJ international conference on intelligent robots and systems (IROS2002, 003)(Cat. no. 03CH37453)* (IEEE), 3, 2743–2748. doi: 10.1109/IROS.2003.1249285

Bin, X., Junxiong, Z., Feng, Q., Zhiqi, F., Dashuai, W., and Wei, L. (2017). Navigation control system for orchard spraying machine based on beidou navigation satellite system. *Nongye Jixie Xuebao/Transact. Chin. Soc. Agric. Machinery* 48, 45–50. doi: 10.6041 /j.issn.1000-1298.2017.02.006

Cao, M., Tang, F., Ji, P., and Ma, F. (2022). Improved real-time semantic segmentation network model for crop vision navigation line detection. *Front. Plant Sci.* 13. doi: 10.3389/fpls.2022.898131

Coulter, R. C. (1992). *"Implementation of the pure pursuit path tracking algorithm"* (Carnegie-Mellon UNIV Pittsburgh PA Robotics INST).

Cui, Y., Qiao, Z., Zou, X., and Wang, B. (2015). "Study on the method of visual navigation baseline identification and extraction of agricultural machinery," in *2015 6th IEEE international conference on software engineering and service science (ICSESS)* (IEEE), 766–769. doi: 10.1109/ICSESS.2015.7339169

Darweesh, H., Takeuchi, E., Takeda, K., Ninomiya, Y., Sujiwo, A., Morales, L. Y., et al. (2017). Open source integrated planner for autonomous navigation in highly dynamic environments. *J. Robotics Mechatronics* 29, 668–684. doi: 10.20965/jrm.2017.p0668

Gao, G., Xiao, K., and Jia, Y. (2020). A spraying path planning algorithm based on colour-depth fusion segmentation in peach orchards. *Comput. Electron. Agric.* 173, 105412. doi: 10.1016/j.compag.2020.105412

Hough, P., and Paul, C. (1962). *US Patent no. 3,069,654* (Washington, DC: US Patent and Trademark Office).

Keicher, R., and Seufert, H. (2000). Automatic guidance for agricultural vehicles in Europe. *Comput. Electron. Agric.* 25, 169–194. doi: 10.1016/S0168-1699(99)00062-9

Li,, M., Imou,, K., Wakabayashi,, K., and Ykoyama,, S, and . (2009). Review of research on agricultural vehicle autonomous guidance. *Int. J. Agric. Biol. Eng.* 2 (3), 1–16. doi: 10.3965/j.issn.1934-6344.2009.03.001-016

Li, Y., Li, J., Zhou, W., Yao, Q., Nie, J., and Qi, X. (2022). Robot path planning navigation for dense planting red jujube orchards based on the joint improved a* and DWA algorithms under laser SLAM. *Agriculture* 12, 1445. doi: 10.3390/agriculture12091445

Lyu, H.-K., Yun, S., and Choi, B. (2020). Machine learning feature extraction based on binary pixel quantification using low-resolution images for application of unmanned ground vehicles in apple orchards. *Agronomy* 10, 1926. doi: 10.3390/agronomy10121926

Mao, J., Cao, Z., Wang, H., Zhang, B., Guo, Z., and Niu, W. (2019). "Agricultural robot navigation path recognition based on k-means algorithm for large-scale image segmentation," in *2019 14th IEEE conference on industrial electronics and applications (ICIEA)* (IEEE), 1233–1237. doi: 10.1109/ICIEA.2019.8834296

Niewola, A. (2020). Mobile robot 6-d localization using 3-d Gaussian mixture maps in GPS-denied environments. *IEEE Intelligent Syst.* 37, 79–88. doi: 10.1109/MIS.2020.3046138

Opiyo, S., Okinda, C., Zhou, J., Mwangi, E., and Makange, N. (2021). Medial axis-based machine-vision system for orchard robot navigation. *Comput. Electron. Agric.* 185, 106153. doi: 10.1016/j.compag.2021.106153

Ronneberger, O., Fischer, P., and Brox, T. (2015). "U-Net: convolutional networks for biomedical image segmentation," in *Medical image computing and computer-assisted intervention–MICCAI2012, 015: 18th international conference* (Munich, Germany: Springer), 234–241. Proceedings, Part III 18.

Ryu, J. H., Gankhuyag, G., and Chong, K. T. (2016). Navigation system heading and position accuracy improvement through GPS and INS data fusion. *J. Sens.* 2012, 16. doi: 10.1155/2016/7942963

Wang, Y., He, Z., Cao, D., Ma, L., Li, K., Jia, L., et al. (2023). Coverage path planning for kiwifruit picking robots based on deep reinforcement learning. *Comput. Electron. Agric.* 205, 107593. doi: 10.1016/j.compag.2022.107593

Wang, X., Kang, H., Zhou, H., Au, W., Wang, M. Y., and Chen, C. (2023). Development and evaluation of a robust soft robotic gripper for apple harvesting. *Comput. Electron. Agric.* 204, 107552. doi: 10.1016/j.compag.2022.107552

Wang, S., Song, J., Qi, P., Yuan, C., Wu, H., Zhang, L., et al. (2022). Design and development of orchard autonomous navigation spray system. *Front. Plant Sci.* 13. doi: 10.3389/fpls.2022.960686

Winterhalter, W., Fleckenstein, F. V., Dornhege, C., and Burgard, W. (2018). Crop row detection on tiny plants with the pattern hough transform. *IEEE Robotics Automation Lett.* 3, 3394–3401. doi: 10.1109/LRA.2018.2852841

Wu, C. L. (2019). "Research of autonomous driving system of tractor based on multi-source information fusion in orchard," in *[dissertation/master's thesis]* ([NanJing]: Southeast University).

Xiong, C. C. (2021). "Research on SLAM navigation method of mobile operating platform for multi-span greenhouse," in *[dissertation/master's thesis]* ([Suzhou]: Soochow University).

Yang, Z., Ouyang, L., Zhang, Z., Duan, J., Yu, J., and Wang, H. (2022). Visual navigation path extraction of orchard hard pavement based on scanning method and neural network. *Comput. Electron. Agric.* 197, 106964. doi: 10.1016/j.compag.2022.106964

Yayan, U., Yucel, H., and Yazıcı, A. (2015). A low cost ultrasonic based positioning system for the indoor navigation of mobile robots. *J. Intelligent Robotic Syst.* 78, 541–552. doi: 10.1007/s10846-014-0060-7

Yin, X., Du, J., Noguchi, N., Yang, T., and Jin, C. (2018). Development of autonomous navigation system for rice transplanter. *Int. J. Agric. Biol. Eng.* 11, 89–94. doi: 10.25165/j.ijabe.20181106.3023

Zhang, S., Guo, C., Gao, Z., Sugirbay, A., Chen, J., and Chen, Y. (2020). Research on 2d laser automatic navigation control for standardized orchard. *Appl. Sci.* 10, 2763. doi: 10.3390/app10082763

frontiers | Frontiers in Plant Science

TYPE Original Research
PUBLISHED 04 July 2023
DOI 10.3389/fpls.2023.1211104

OPEN ACCESS

EDITED BY
Pei Wang,
Southwest University, China

REVIEWED BY
Wei Fu,
Hainan University, China
Aichen Wang,
Jiangsu University, China

*CORRESPONDENCE
Jianli Song
songjianli170@163.com

RECEIVED 24 April 2023
ACCEPTED 12 June 2023
PUBLISHED 04 July 2023

CITATION
Xu S, Wang X, Li C, Ran X, Zhong Y, Jin Y and Song J (2023) Effect of airflow angle on abaxial surface deposition in air-assisted spraying. *Front. Plant Sci.* 14:1211104. doi: 10.3389/fpls.2023.1211104

Effect of airflow angle on abaxial surface deposition in air-assisted spraying

Shaoqing Xu[1,2], Xiang Wang[2,3], Chao Li[4], Xiangkai Ran[1,2], Yuan Zhong[1,2], Ye Jin[1,2] and Jianli Song[1,2]*

[1]College of Science, China Agricultural University, Beijing, China, [2]Centre for Chemicals Application Technology, China Agricultural University, Beijing, China, [3]Sanya Institute of China Agricultural University, Sanya, China, [4]Weichai Lovol Intelligent Agricultural Technology Co., Ltd., Shandong, Weifang, China

Air-assisted sprayers are widely used in orchards for pest and disease control. However, air-assisted spray deposition on the abaxial surface of leaves is often limited. In this study, a method to achieve satisfactory spray deposition on the abaxial leaf surface and an assessment of factors that affect abaxial surface deposition were investigated. The effects of leaf angle, wind speed, platform velocity, and nozzle type were assessed. Abaxial surface coverage was significantly affected by leaf angle, wind speed, and nozzle type, of which the leaf angle had the strongest impact. The leaf angle largely determines the abaxial surface area exposed to the wind field. When the abaxial surface is situated leeward, deposition of droplets on the abaxial surface is difficult. Therefore, to improve abaxial surface exposure for field application, the exposure probability of the abaxial surface at different angles between the leaf and the airflow (α) was examined. The relationship was well represented by a logistic growth curve. The exposure probability exceeded 95% when the α value was greater than 5°. The latter finding was verified by conducting a field application in which the deposition efficiency on the abaxial surface (DEAS) was calculated. Adjustment of the airflow angle based on the theoretical value achieved DEAS of 49.9% and 109.3% in the middle and upper layers of the canopy, respectively, whereas the DEAS was less than 30% if the airflow angle was not adjusted. This is caused by the difference in the exposure probability of the back of the leaf. The results provide a reference for adjustment of the wind field of air-assisted sprayers in field applications.

KEYWORDS

air-assisted spray, abaxial surface, coverage, angle of airflow, exposure

1 Introduction

Air-assisted spraying is an efficient ground-based spray application technology recommended by the Food and Agriculture Organization of the United Nations (FAO, 2001). The auxiliary airflow may cause the leaves to turn over or oscillate. The spray droplets are directed by the airflow to penetrate the canopy, which improves the uniformity of spray distribution within the canopy (Burgio et al., 2016; Zhou et al., 2016). In addition,

disruption from natural wind flow and droplet drift are reduced by using a suitable airflow rate, and the pesticide utilization can be improved (Zhu et al., 2004).

For most types of fruit trees, the abaxial leaf surface has a greater number of stomata and a thinner cuticle than the adaxial surface (Toselli et al., 2009; Carr, 2013; Carr, 2014), and is the main site of pathogen infection (Washington et al., 1998; Churchill, 2011). Pests, such as red spider mites and whitefly, also tend to be more frequent on the abaxial leaf surface (Laurence et al., 1978). Therefore, adequate deposition of pesticides on the abaxial surface of leaves is required for effective pest control in fruit trees. However, deposition on the abaxial surface is often inadequate or uneven in air-assisted spraying. In addition, adjustment of the spray volume has little effect on deposition on the abaxial surface (Garcerá et al., 2020).

Airflow is another important factor affecting deposition. The state of leaves is changed when the airflow changes (Zhang et al., 2022). The reconfiguration and vibration of the leaf vary under different airflow characteristics (Jiang et al., 2021). Deposition can be affected by aerodynamic response speed (Li et al., 2021). Field application also showed that the adjustment of airflow influences droplet deposition between the medial and lateral parts of the canopy (Svensson et al., 2003; Pai et al., 2009). A computational fluid dynamics (CFD) simulation revealed that deposition on the abaxial leaf surface was strongly associated with the airflow angle (Wang et al., 2015). Therefore, airflow direction is an important factor that must be considered. In most orchard air-assisted sprayers, wind direction is varied mainly by adjusting the guide plate. A strong correlation between leaf droplet deposition in the vertical profile of the canopy and sprayer airflow direction has been reported (Duga et al., 2015). Furthermore, improved deposition is achieved by adjusting the angle of the air outlet (Celen, 2008; Pai et al., 2009; Grella et al., 2022).

Recommendation manuals and devices have been developed that allow rough adjustment of the airflow characteristics (TOPPS-Prowadis Project, 2014; Garcerá et al., 2017). However, these adjustments need to be based on specific canopy characteristics, such as canopy size and leaf density. Hence, the recommendations are not readily implemented in practical applications. In addition, there is currently a lack of guideline data for the improvement of deposition on the abaxial leaf surface during application. Therefore, in this study, factors that influence droplet deposition on the abaxial leaf surface were investigated. The effect of the angle between the leaf and airflow on exposure of the abaxial surface was examined, and the optimal angle was calculated. The findings provide a reference for the adjustment of air-assisted sprayers in practical applications.

2 Methods

2.1 Effect of parameters setting on deposition on the abaxial surface

A movable spray platform was used in the initial experiment (Figure 1). The platform was composed of an air-assisted spraying system and a crawler chassis. The air-assisted sprayer system

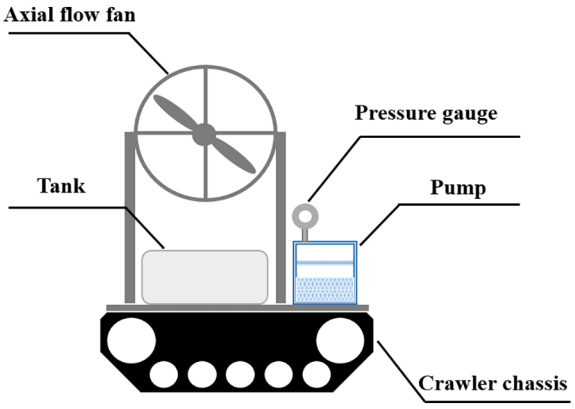

FIGURE 1
Schematic illustration of the movable spray platform used in the initial experiment.

comprised a 24 V power source, an axial fan (blade diameter 38 cm), a motor, a speed regulator, a pressure gauge, a centrifugal pump, and a nozzle. The motor speed was controlled by a speed regulator with an adjustable range from 1200 to 3600 rpm. The small tracked chassis was operated by remote control for constant speed movement.

An artificial leaf was used, which was made from a polyvinyl chloride sheet of 5 mm thickness. Unlike a real leaf, the artificial leaf would not deform in the wind field. Therefore, the angle between the artificial leaf and the direction of forward motion of the movable spray platform was fixed during the experiment. A double-headed clamp was used to fix the artificial leaf in position (Figure 2A). The artificial leaf was fixed at the same height as the center of the axial fan. The head of the clamp could be rotated to alter the angle between the leaf surface and the direction of forward motion. Seven artificial leaves were fixed on the test frame. The distance between each leaf was 0.2 m. The tested angles between the leaf surface and the direction of forward motion of the movable spray platform were 0°, 30°, 60°, 90°, 120°, 150°, and 180° (Figure 2B). Water-sensitive paper (WSP) was secured to the abaxial surface of the artificial leaf.

The horizontal distance between the axial fan and the artificial leaf was 1.0 m. The experimental parameters in each treatment group are summarized in Table 1. The rotation speed was 2700 or 3600 rpm. The forward speed of the movable spray platform was 0.8 or 1.2 m s^{-1}. The nozzle types used in the experiment were TR80-02 and TR80-005C hollow-cone nozzles (Lechler, Düsseldorf, Germany). The spray pressure was 3.0 bar. After spraying, the WSP was removed and scanned at 600 dpi resolution. Deposit Scan (National Institutes of Health, Bethesda, MD, USA) was used to determine the spray coverage for each artificial leaf. Each treatment group comprised three replications.

2.2 Effect of airflow angle on exposure of the abaxial surface

In this experiment, the probability of exposure of the abaxial surface to the airflow was evaluated. In addition, the minimum

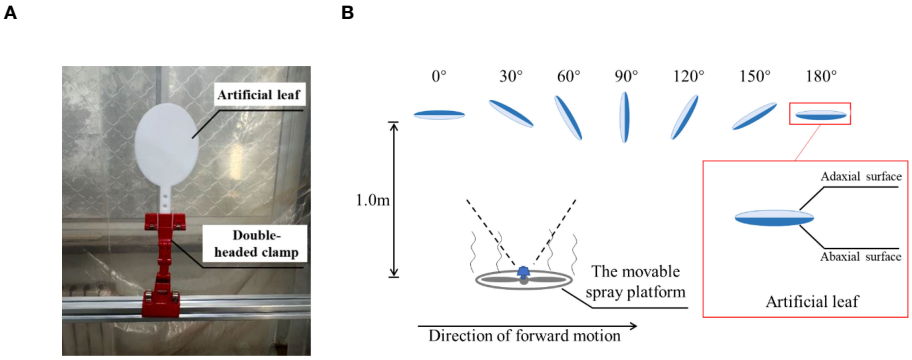

FIGURE 2
Experimental setup for spray deposition on the abaxial surface of an artificial leaf. **(A)** Method of securing the position of an artificial leaf. **(B)** The tested angles of an artificial leaf relative to the direction of forward motion.

angle between the leaf abaxial surface and the airflow for effective deposition was calculated. The leaf used in the experiment was from a citrus tree located at the China Agricultural University. To ensure the freshness of the leaves, the experiment was conducted within 10 min of their collection. The fan used was identical to that described in section 2.1. The direction of the axial fan was parallel to the ground.

The angle α between the leaf and the airflow direction was varied during the experiment (Figure 3). The α value was adjusted at 5° intervals from −40° to 40°. The leaf was fixed to an iron rod with clamps during the experiment. The leaf inclination angle was adjusted to the preset value with the aid of an angle-measuring instrument (ROK International Industry Co., Ltd., Shenzhen, China). The air-assisted spray platform used was identical to that described in section 2.1. The rotation speed was set to 3600 rpm. The fan was maintained at the same height as the center of the leaf. The horizontal distance between the fan and the leaf was 1.0 m. The velocity of the platform was 1.2 m s^{-1}. A Gopro Hero 7 digital camera (Gopro, Inc., San Mateo, CA, USA) was used to record the oscillation of the leaf. Thirty repetitions were performed for each α value.

The leaf oscillation in the recorded video was observed and scored. If the abaxial surface was exposed to the wind field (Figure 4B), the result was recorded as 1; if the abaxial surface was not exposed to the wind field (Figure 4A), it was recorded as 0. The probability of abaxial surface exposure to the wind field was calculated for each α. The probability (as the dependent variable on the *y*-axis) for each α (as the independent variable on the *x*-axis) was plotted. In addition, a growth curve function (Equation 1) was fitted to the data:

$$y = \frac{a}{1 + e^{-k(x-x_c)}} \quad (1)$$

where x is the angle between the fan and the leaf, y is the probability of abaxial surface exposure, and a, k, and x_c are constants.

2.3 Spray coverage with different airflow angles in field application

A field experiment was conducted to verify the applicability of the findings of the experiment described in section 2.2. The spraying equipment used was basically identical to the movable spray platform described in section 2.1. The difference was that the number of spray units was increased to three. Each spray unit was fixed to the connecting rod by adjustable fasteners at an angle adjustable from −20° to 20°. The distance between the center of adjacent fans was 0.5 m.

The experiment was conducted in a citrus orchard greenhouse in the Xiao Tangshan Agricultural Demonstration Park, Beijing, China. The spacing between rows of citrus trees was 2.8 m. The average height of the trees was 1.7 m. Three trees were selected for the experiment. The leaf angles in the upper, middle, and lower vertical layers of the canopy were measured. Thirty leaves in each layer were measured. The leaf angle was defined as the angle between the abaxial surface and the horizontal plane. The mean

TABLE 1 Parameters for spray deposition on the abaxial surface of the artificial leaf.

Treatment group	Rotation speed of the fan (rpm)	Platform velocity (m s^{-1})	Outlet wind speed (m s^{-1})	Nozzle type
1	2700	0.8	8	TR80-02
2	3600	0.8	12	TR80-02
3	2700	1.2	8	TR80-02
4	3600	1.2	12	TR80-02
5	3600	1.2	12	TR80-005C

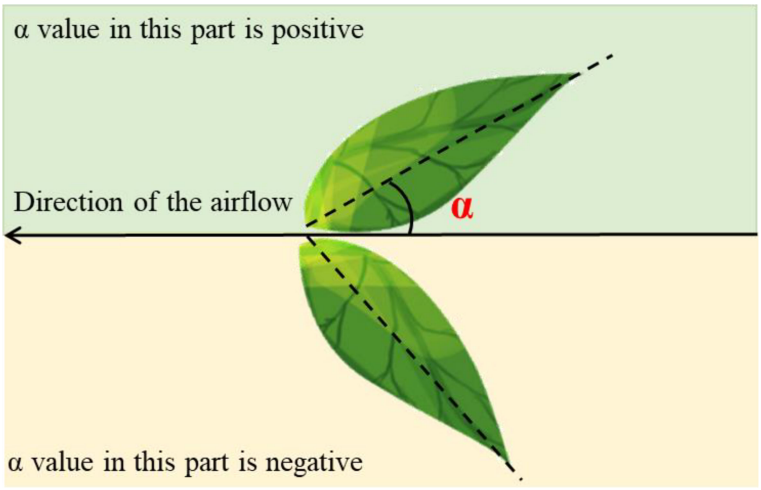

FIGURE 3
Schematic diagram illustrating the angle α between a leaf and the airflow direction.

leaf angles were 16.5° in the upper layer, −10.2° in the middle layer, and −43° in the lower layer. The angles of the fans were adjusted according to the conclusions from the experiment described in section 2.2 (Table 2). However, the angle of the lower fan in treatment group 1 could not be adjusted to the preset value because of the structure of the fan. Therefore, an angle of 20° was used. Fans in the control (treatment group 2) were set parallel to the horizontal plane.

Three citrus trees located on the spraying route were selected. The canopy of each tree was divided into 15 areas for measurement of spray distribution (Figure 5A) in accordance with the guidelines in ISO 22522:2007. The canopy was divided into three layers (upper [U], middle [M], and lower [L]) in the vertical profile and five sectors sequentially along the horizontal airflow direction (numbered 1 to 5). The layer nearest to the axial fan was termed the first layer and the layer farthest from the fan was the fifth layer. In each of the 15 areas of the canopy, three leaves were selected and WSP was secured to the adaxial and abaxial surfaces of each leaf. The distance between the sprayer and the tree row was 1.5 m. The nozzle used in the experiment was a TR80-02 hollow-cone nozzle (Lechler). The pressure was 5 bar and the velocity of the sprayer was 0.5 m s^{-1}. The rotation speed was 3600 rpm. To observe the effect of the airflow angle on spray deposition onto the leaf surfaces, only one side of the tree row was sprayed (Figure 5B). After spraying, the WSPs were collected and scanned at 600 dpi resolution. Deposit Scan was used to determine the spray coverage in each area of the canopy. Each treatment was repeated three times.

The deposition efficiency on the abaxial surface (DEAS) was used to express the ability for droplet deposition on the abaxial surface of the leaf, which was calculated using Equation 2:

$$DEAS\ (\%) = \frac{ABSC}{ADSC} \times 100 \tag{2}$$

where ABSC is spray coverage on the abaxial surface and ADSC is spray coverage on the adaxial surface.

Given that the airflow angle may affect droplet penetration, the penetration rate in each area of the canopy was calculated using Equation 3:

$$Penetration\ rate\ (\%) = \frac{C_i}{C_1} \times 100 \tag{3}$$

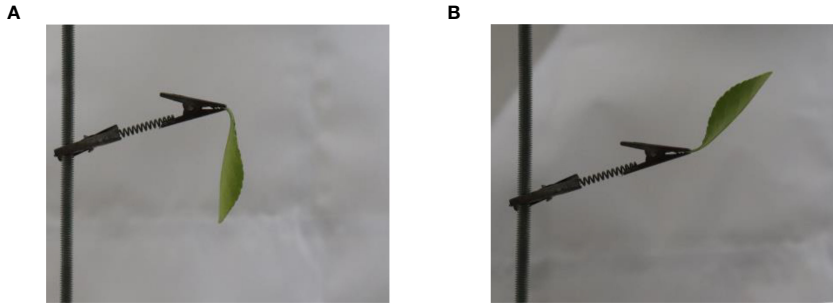

FIGURE 4
Two states of a leaf in the wind field. **(A)** The abaxial surface of the leaf is not exposed to the wind field. **(B)** The abaxial surface of the leaf is exposed to the wind field.

TABLE 2 Airflow angles applied in the field experiment.

Treatment group	Parameter	Canopy layer		
		Upper	Middle	Lower
1	Airflow angle (°)	−6.5	20.2	20
	α (°)	10	10	−23
2	Airflow angle (°)	0	0	0
	α (°)	16.5	−10.2	−43

The angle of the axial fan was adjusted relative to the horizontal plane (0°) to generate the specified airflow angle. α is the mean angle between the abaxial surface of a leaf (n = 30) and the airflow direction. Treatment group 2 (airflow angle = 0°) served as the control.

where C_1 is the spray coverage of the first layer and C_i is the spray coverage of layer *i*.

3 Results

3.1 Effect of parameters setting on spray deposition on the abaxial surface of an artificial leaf

The spray coverage on the abaxial surface of an artificial leaf, as influenced by four application parameters, is summarized in Table 3. The angle between the artificial leaf and the direction of forward motion of the movable spray platform significantly affected the coverage. At an angle between 0° and 90°, spray coverage on the abaxial surface was less than 2% in all treatments. In these cases, the abaxial surface was situated leeward, making droplet deposition difficult. Nevertheless, a small number of droplets were deposited on the abaxial surface. At an angle exceeding 90°, a significant increase in spray coverage on the abaxial surface was observed. In group 2, for example, the coverage was 1.6%, 18.7%, 34.1%, and 49.8% at 90°, 120°, 150°, and 180°, respectively, and at these angles, the differences in coverage were statistically significant ($P \leq 0.05$). Similar patterns were observed for the other treatments. The abaxial surface was directly exposed to the wind field at an angle greater than 90° and the degree of exposure increased gradually as the angle increased. These results indicated that deposition under air-assisted spraying was positively correlated with the degree of exposure to the wind field.

The effects of four application parameters on spray coverage were considered. Multi-factor ANOVA was used to analyze the effects of the included angle, the rotation speed of the fan, platform velocity, and nozzle type on spray coverage on the abaxial surface (Table 4). A significant effect was observed for the included angle, rotation speed of the fan, and nozzle type ($P \leq 0.05$). The included angle was observed to have the strongest significant effect on spray coverage (F-value = 54.8).

3.2 Effect of airflow angle on exposure of the abaxial surface

The probability of exposure of the leaf's abaxial surface under different α values is summarized in Table 5. At α< −25°, the abaxial surface was not exposed to spray droplets. With an increase in α, the degree of exposure gradually increased. At α ≥ 10°, the abaxial surface was entirely exposed to the wind field. The growth curve fitted to the data as well as the third-order derivative is shown in Figure 6. The curve was divided into three stages based on the positive and negative values of the third-order derivatives: α ≤ −17° (first stage), −17°< α ≤ −3° (second stage), and α > −3° (third stage). In the first stage, the leaves were located too low in the vertical profile of the canopy and were forced downwards by the wind field. Thus, the abaxial surface's probability of exposure was low (less than 22%). In the second stage, with an increase in α, the probability of exposure increased rapidly. At α > −3°, the rate of increase in the probability of exposure declined. In this stage, the probability of abaxial surface exposure was high (greater than 80%). Thus, it was

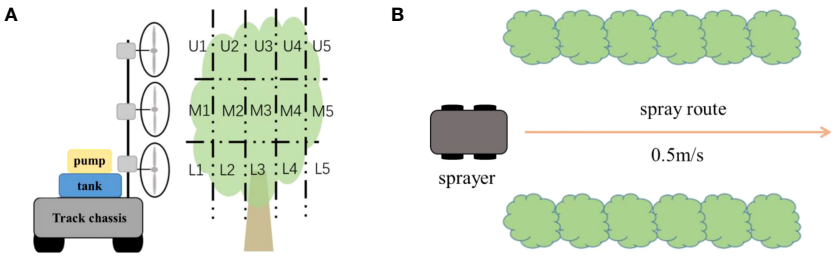

FIGURE 5
Schematic diagram of the experimental setup for the field application. **(A)** Division of the canopy of a citrus tree into horizontal and vertical layers. **(B)** The route used in the spray application.

TABLE 3 Spray coverage on the abaxial surface of an artificial leaf at different included angles.

Treatment group	Included angle (°)						
	0	30	60	90	120	150	180
1	0.9 ± 0.3 c	0.2 ± 0.1 c	0.4 ± 0.1 c	1.2 ± 0.6 c	10.3 ± 3.9 b	17.2 ± 5.4 ab	21.0 ± 6.6 a
2	1.0 ± 0.8 d	0.5 ± 0.1 d	0.3 ± 0.3 d	1.6 ± 0.8 d	18.7 ± 11.2 c	34.1 ± 13.2 b	49.8 ± 5.5 a
3	0.1 ± 0.1 d	0.2 ± 0.1 d	0.1 ± 0.1 d	0.6 ± 0.5 d	8.3 ± 3.1 c	16.5 ± 3.7 b	29.3 ± 2.9 a
4	0.2 ± 0.1 d	0.3 ± 0.2 d	0.1 ± 0.0 d	0.8 ± 0.2 d	19.0 ± 9.3 c	28.9 ± 5.0 ab	27.9 ± 4.9 a
5	0.1 ± 0.0 b	0.3 ± 0.2 b	0.1 ± 0.0 b	0.5 ± 0.4 b	8.0 ± 2.3 a	7.7 ± 0.7 a	11.9 ± 4.4 a

Values are the mean ± standard deviation (n = 3). Different lowercase letters within a column indicate a significant difference between means (one-way ANOVA; $p < 0.05$).

observed that the abaxial surface had a high probability of exposure to the airflow at an airflow angle slightly less than the leaf angle. The probability of abaxial surface exposure at $\alpha = 10°$ was greater than 98%. Therefore, an α value of 10° was chosen for the following field experiment.

3.3 Comparison of coverage under different α values

Spray coverage in the different canopy areas for the two treatments is summarized in Table 6. Paired-sample *t*-tests were performed to assess the treatment effects on spray coverage in the same canopy area. For the leaf adaxial surface, no significant differences were observed in all areas. However, for the abaxial surface, significant differences were observed in the middle layer ($P \leq 0.05$). Based on the conclusion from the experiment described in section 3.2, α affects the abaxial surface's probability of exposure. In the middle layer, α was 10° in group 1, which led to a high probability of abaxial surface exposure. In contrast, the α value in group 2 was −10.2° and the probability of abaxial surface exposure was less than 50%. This accounted for the difference in spray coverage on the abaxial surface between the two treatments. In addition, for the upper layer, α was always greater than 10° for the two treatments. Therefore, high spray coverage was consistently observed, with an average coverage of 10.3% and 16.7% in groups 1 and 2, respectively. For the lower layer, α was less than −20° in two treatments, which resulted in low spray coverage.

Differences in the DEAS were observed (Figure 7). In the lower layer, the two treatments showed low DEAS (25.0% in group 1 and 23.6% in group 2). In the middle layer, group 1 had a DEAS of 49.9%, whereas the DEAS of group 2 was 29.4%. High DEAS values were observed in the upper canopy layer (more than 100% for both treatments).

The penetration rates in the different areas of the canopy are summarized in Figure 8. As seen in the figure, both treatments showed high penetration rates (>75%) in the proximal portion of the canopy (layers 1 and 2). In the center of the canopy (layer 3), the penetration rates were higher than 50% in most areas. Area M3 in group 1 and L3 in group 2 had relatively low penetration rates of approximately 40%. The penetration rates decreased severely in the distal portion of the canopy (layers 4 and 5). In the middle layer, the penetration rates for all areas were less than 15%.

4 Discussion

Spray deposition on the leaf abaxial surface has been the focus of increasing research attention in recent years (Maski and Durairaj,

TABLE 4 Significance of the effects of application parameters on spray coverage on the abaxial surface of an artificial leaf.

Parameter	df	*F*	Significance
Included angle	6	54.8	*
Rotation speed of the fan	1	24.2	*
Platform velocity	1	2.6	–
Nozzle type	1	19.4	*

– $P > 0.05$, * $P \leq 0.05$.

TABLE 5 Probability of exposure of the abaxial leaf surface to spray deposition at different airflow angles (α).

α (°)	−40	−35	−30	−25	−20	−15	−10	−5	0	5	10	15	20	25	30	35	40
Number of leaves with deposition on abaxial surface	0	0	0	0	5	10	13	24	24	29	30	30	30	30	30	30	30
Exposure probability (%)	0	0	0	0	17	33	43	80	80	97	100	100	100	100	100	100	100

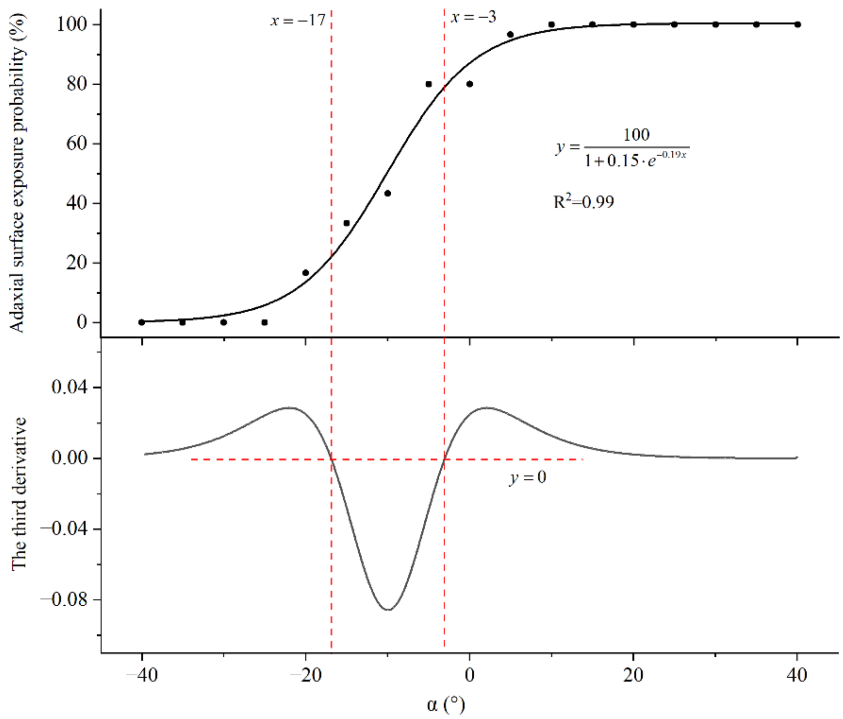

FIGURE 6
Fitted growth curve and the third-order derivative for the probability of exposure of the leaf's abaxial surface.

TABLE 6 Spray coverage on the adaxial and abaxial leaf surfaces in different canopy areas for the two treatments.

Canopy area		Adaxial surface of leaves				Abaxial surface of leaves			
		Group 1		Group 2		Group 1		Group 2	
Upper canopy	U1	14.4 ± 10.8	a	9.7 ± 6.9	a	16.7 ± 11.4	a	25.8 ± 11.2	a
	U2	10.3 ± 7.3		6.8 ± 3.7		17.0 ± 8.7		28.1 ± 6.7	
	U3	10.8 ± 6.7		8.3 ± 6.1		8.1 ± 9.9		22 ± 21.3	
	U4	6.8 ± 4.8		6.6 ± 4.6		7.4 ± 5.3		5.8 ± 6.2	
	U5	4.7 ± 2.4		6.8 ± 2.7		2.2 ± 2.8		2.0 ± 2.7	
	Average	9.4		7.6		10.3		16.7	
Middle canopy	M1	21.1 ± 12.8	a	23.2 ± 9.6	a	8.6 ± 8.8	a	6.7 ± 9.3	b
	M2	23.4 ± 10.4		18.6 ± 11.3		7.9 ± 3.5		4.7 ± 3.1	
	M3	4.8 ± 3.3		11.5 ± 10.5		6.9 ± 7.4		3.8 ± 6.8	
	M4	2.2 ± 1.5		2.5 ± 1.7		1.8 ± 2.5		1.9 ± 2.2	
	M5	2.4 ± 2.4		3.1 ± 1.6		1.7 ± 3.9		0.3 ± 0.3	
	Average	10.8		11.8		5.4		3.5	
Lower canopy	L1	23.5 ± 11.8	a	30.3 ± 12.2	a	3.8 ± 3.6	a	1.8 ± 1.4	a
	L2	19.7 ± 9.6		30.6 ± 8.6		3.2 ± 3.7		6 ± 8.3	
	L3	13.1 ± 7.1		6.7 ± 6.7		6.1 ± 5.8		6.5 ± 6.8	
	L4	12.5 ± 9.8		5.6 ± 5.1		3.3 ± 4.7		1.4 ± 1.0	
	L5	3.0 ± 1.6		2.2 ± 1.5		1.5 ± 2.3		2.0 ± 2.3	
	Average	14.4		15.1		3.6		3.6	

Values are the mean ± standard deviation (n = 3). Different lowercase letters within a column indicate a significant difference between means (pared-samples T test; $p < 0.05$).

2010; Owen-Smith et al., 2019; Jiang et al., 2023). Air-assisted spraying has been shown to achieve superior deposition on the abaxial surface of leaves in practical application (Christovam et al., 2010; Sinha et al., 2020; Xu et al., 2023). However, most previous studies have been conducted to test the performance of sprayers. The mechanism of deposition on the leaf's abaxial surface and the optimization of sprayer systems for field application are poorly investigated. In the present study, the patterns and efficiency of spray coverage were examined. Assessment of the effects of different application parameters revealed that the included angle, rotation speed of the fan, and nozzle type significantly influenced spray coverage on the leaf's abaxial surface, of which the included angle had the strongest effect (Table 4). When the target is situated leeward, deposition of droplets on the target is difficult. Although the airflow may move around a barrier to a certain extent (Greenspan, 2009), only a limited number of droplets will reach the abaxial surface of leaves in this manner. Therefore, it is necessary to investigate strategies to enhance the exposure of the abaxial surface of leaves to the wind field.

The effect of airflow on the leaf has been studied previously. Wu et al. (2021) defined two states of blade motion in the wind field. The critical wind speed when the leaf motion state changes is important. The wind deflection area of the leaf is affected by wind speed (Zhang et al., 2022). The reconfiguration, vibration, and wake characteristics of leaves were investigated by Jiang et al. (2021). With improvements in simulation technology, CFD has been used to simulate the motion and deformation of plant leaves in wind fields. The results suggest that the wind field angle of wind-delivered spray must be adjusted according to the stem and leaf angles (Yan et al., 2022). However, the relationship needs to be quantified by conducting additional research.

The present research explored the probability of exposure of the leaf's abaxial surface for different values of α. Guidance for the adjustment of the airflow angle was provided by fitting a growth curve. Airflow direction can be changed by adjustment of the deflector angle for most orchard air-assisted sprayers, although the degree of adjustment is relatively limited owing to the structure of the fan. Given that the airflows are derived from one axial fan, the interaction between the wind fields after splitting is negligible. However, for multi-head fan sprayers, the interaction between the fan units also needs to be considered. As the airflow is generated by different fans, the wind field of the adjacent fan units may be affected if the angle is adjusted excessively. In such a case, spray deposition will be unpredictable. In addition, the adjustable angle of the fan unit is often limited because of its structure. The fan unit may not be adjustable to the optimal angle when the leaf angle is extreme. In the present research, an α value of 5–10° was ideal when conditions enabled a combination of these factors. Based on the fitted curve, the probability of abaxial surface exposure was higher than 95% within this range. An α value of 10° was used in the field validation in the present study.

In the field application, differences in α led to changes in spray coverage of the abaxial surface. It is worth noting that the DEAS of the upper canopy layer was higher than 100% in both treatments. This may be because the canopy of the citrus trees was spindle-shaped. The density of the canopy in the upper layer was lower, and

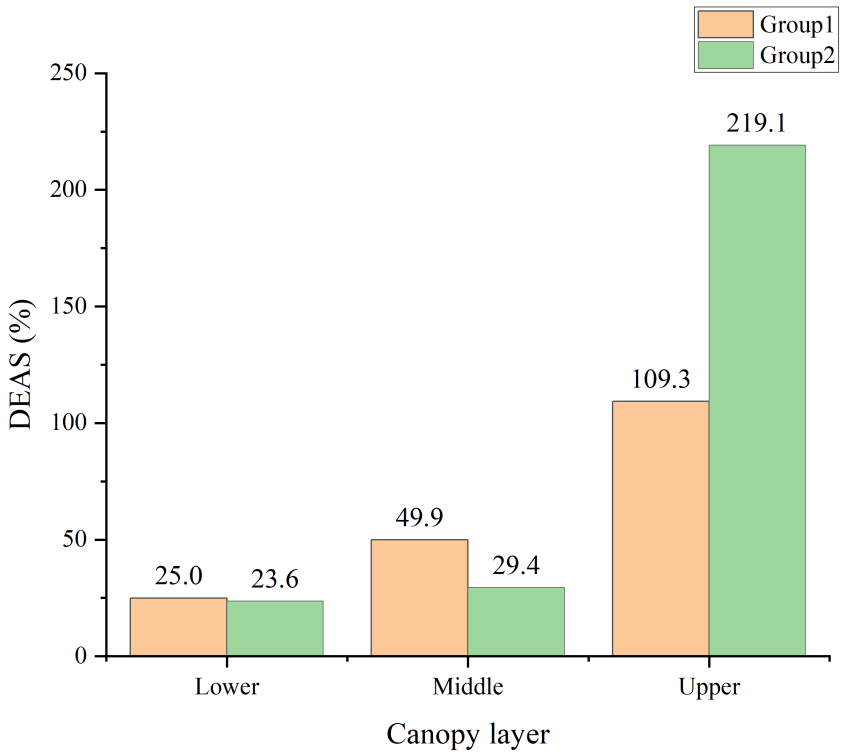

FIGURE 7
Spray deposition efficiency on the abaxial surface (DEAS) in different layers of the canopy under the two treatments.

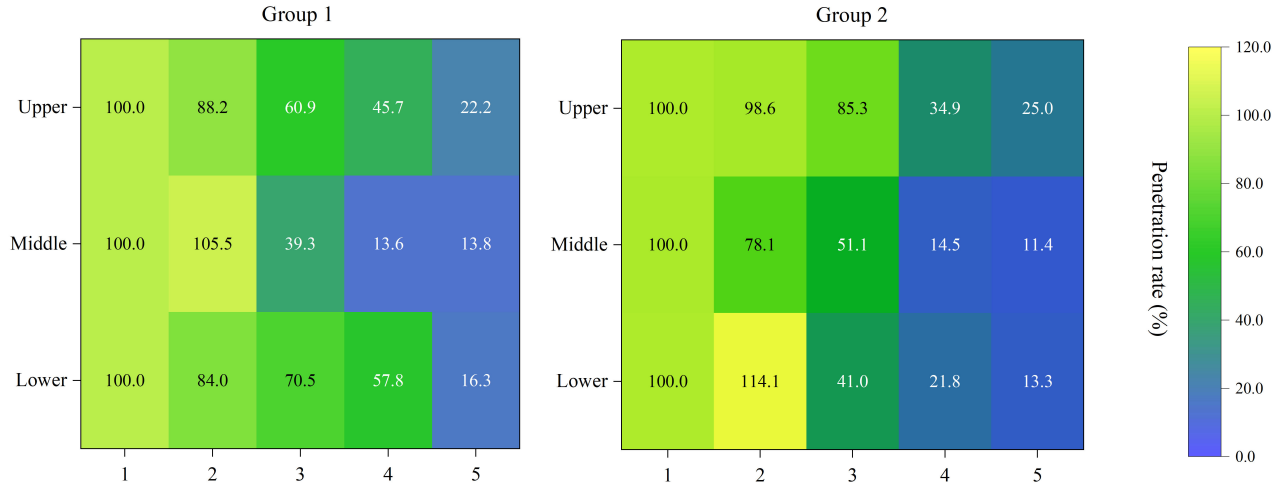

FIGURE 8
Spray penetration rate in different areas of the canopy under the two treatments.

thus the wind field and droplets would experience less resistance (Rossi et al., 1992). Therefore, the exposure of the abaxial surface in the upper layer was more similar to that of a single leaf. The α value was within a desirable range in both treatments (10° in group 1 and 15° in group 2). In terms of fog droplet penetration, it was found that an excellent deposition rate of the outer canopy may lead to a decrease in the deposition amount of the inner canopy (M3 in group 1 and L3 in group 2). This may be caused by excessive interception of droplets by the leaves of layers 1 and 2. Previous studies have shown that the penetration rate of droplets in the canopy is changed with the adjustment of the airflow angle (Pergher et al., 1997; Li et al., 2022). However, such change was not observed in the present field application. This may be associated with the canopy density of the citrus trees.

Many systems have been developed to guide the adjustment of sprayer parameters (Doruchowski et al., 2013; Doruchowski et al., 2014; Bahlol et al., 2020). Canopy features, such as tree row volume and leaf wall area, have been used to inform the adjustment of sprayer parameters (Sutton, 1988; Toews and Friessleben, 2012; Zhou et al., 2012; Miguez et al., 2019). However, such systems are aimed at improvement of pesticide utilization as well as reducing spray drift. There has been a lack of research attention on deposition on the abaxial surface of leaves. In the present study, the α value was used as a reference to guide the regulation of airflow. The only measurement required is that of the inclination angle of the leaf, which is easily determined for field application.

5 Conclusions

The angle α between the leaf and the airflow in an air-assisted spray system was observed to be an important factor affecting spray deposition on the abaxial leaf surface. Although a proportion of the droplets were deposited on the abaxial surface, the quantity was limited. To achieve improved abaxial surface deposition, the relationship between α and the abaxial leaf surface exposure probability was examined. The α value was positively correlated with the abaxial leaf surface exposure probability. The trend was in accordance with the fitted logistic growth curve. When the α value was greater than 5°, the probability of abaxial surface exposure was greater than 95%. The airflow angle adjustment was shown to be reliable in a field application. When the airflow angle was adjusted according to the theoretical value, spray coverage of the abaxial surface was significantly increased and higher DEAS was observed. In addition, the droplet penetration rate was not significantly affected by the adjustment of the airflow angle. These results provide a reference for adjustment of the wind field of air-assisted sprayers in field applications.

Data availability statement

The original contributions presented in this study are included in the article/supplementary material. Further inquiries can be directed to the corresponding author.

Author contributions

Conceptualization, JS. Methodology, JS and SX. Investigation, XW, YJ, and SX. Experimental platform construction, CL. Sources, JS. Data curation, XR and YZ. Writing—original draft preparation, SX. Writing—review and editing, SX, XW, and JS. Funding acquisition, JS. All authors contributed to the article and approved the submitted version.

Funding

This research was supported by The National Key Research and Development Plan: All-terrain “Twist + X” intelligent power machinery for hills and mountains (Grant No. 2022YFD2001302), as well as the administration of the Sanya Yazhou Bay Science and Technology City (Grant No. SYND-2022-23).

Conflict of interest

Author Chao Li was employed by Weichai Lovol Intelligent Agricultural Technology Co., Ltd.

The remaining authors declare that the research was conducted in the absence of any commercial or financial relationships that could be construed as a potential conflict of interest.

Publisher's note

References

Guidelines on minimum requirements for agricul_tural pesticide application equipment. Available at: https://www.fao.org/3/Y2765E/Y2765E00.htm.

Bahlol, H. Y., Chandel, A. K., Hoheisel, G. A., and Khot, L. R. (2020). The smart spray analytical system: developing understanding of output air-assist and spray patterns from orchard sprayers. *Crop Prot.* 127, 104977. doi: 10.1016/J.CROPRO.2019.104977

Burgio, G., Marchesini, E., Reggiani, N., Montepaone, G., Schiatti, P., and Sommaggio, D. (2016). Habitat management of organic vineyard in northern Italy: the role of cover plants management on arthropod functional biodiversity. *Bull. Entomol. Res.* 106, 759–768. doi: 10.1017/S0007485316000493

Carr, M. K. V. (2013). The water relations and irrigation requirements of macadamia (Macadamia SPP.): a review. *Exp. Agric.* 49, 74–90. doi: 10.1017/S0014479712000804

Carr, M. K. V. (2014). THE water relations and irrigation requirements of papaya (CARICA PAPAYA l.): a review. *Exp. Agric.* 50, 270–283. doi: 10.1017/S0014479713000380

Celen, I. H. (2008). Effect of angle of sprayer deflector on spray distribution in dwarf apple trees. *J. Agron.* 7, 206–208. doi: 10.3923/ja.2008.206.208

Christovam, R.S., Raetano, C. G., Aguiar, H. O.Jr., Dal-Pogetto, M. H. F. D. A., Prado, E. P., Gimenes, M. J., et al. (2010). Air-assistance in sleeve boom spray in the control of soybean rust. *Bragantia* 69, 231–238. doi: 10.1590/S0006-87052010000100029

Churchill, A. C. L. (2011). Mycosphaerella fijiensis, the black leaf streak pathogen of banana: progress towards understanding pathogen biology and detection, disease development, and the challenges of control. *Mol. Plant Pathol.* 12, 307–328. doi: 10.1111/j.1364-3703.2010.00672.x

Doruchowski, G., Balsari, P., Gil, E., Marucco, P., Roettele, M., and Wehmann, H. J. (2014). Environmentally optimised sprayer (EOS)–a software application for comprehensive assessment of environmental safety features of sprayers. *Sci. Total Environ.* 482–483, 201–207. doi: 10.1016/J.SCITOTENV.2014.02.112

Doruchowski, G., Roettele, M., Herbst, A., and Balsari, P. (2013). Drift evaluation tool to raise awareness and support training on the sustainable use of pesticides by drift mitigation. *Comput. Electron. Agric.* 97, 27–34. doi: 10.1016/J.COMPAG.2013.06.006

Duga, A. T., Ruysen, K., Dekeyser, D., Nuyttens, D., Bylemans, D., Nicolai, B. M., et al. (2015). Spray deposition profiles in pome fruit trees: effects of sprayer design, training system and tree canopy characteristics. *Crop Prot.* 67, 200–213. doi: 10.1016/j.cropro.2014.10.016

FAO. (2021). Guidelines on minimum requirements for agricul_tural pesticide application equipment[R]. Available at: https://www.fao.org/3/Y2765E/Y2765E00.htm

Garcerá, C., Fonte, A., Moltó, E., and Chueca, P. (2017). Sustainable use of pesticide applications in citrus: a support tool for volume rate adjustment. *Int. J. Environ. Res. Public Heal.* 14, 715. doi: 10.3390/IJERPH14070715

Garcerá, C., Vicent, A., and Chueca, P. (2020). Effect of spray volume, application timing and droplet size on spray distribution and control efficacy of different fungicides against circular leaf spot of persimmon caused by plurivorosphaerella nawae. *Crop Prot.* 130, 105072. doi: 10.1016/J.CROPRO.2019.105072

Greenspan, D. (2009). Computer studies of molecular air flow around a circular cylinder. *Comput. Math. Appl.* 58, 414–421. doi: 10.1016/J.CAMWA.2006.12.105

Grella, M., Marucco, P., Zwertvaegher, I., Gioelli, F., Bozzer, C., Biglia, A., et al. (2022). The effect of fan setting, air-conveyor orientation and nozzle configuration on airblast sprayer efficiency: insights relevant to trellised vineyards. *Crop Prot.* 155. doi: 10.1016/j.cropro.2022.105921

Jiang, H., Xin, D., and Zhang, H. (2021). Wind-tunnel study of the aerodynamic characteristics and mechanical response of the leaves of betula platyphylla sukaczev. *Biosyst. Eng.* 207, 162–176. doi: 10.1016/j.biosystemseng.2021.05.004

Jiang, Y., Yang, Z., Xu, X., Shen, D., Jiang, T., Xie, B., et al. (2023). Wetting and deposition characteristics of air-assisted spray droplet on large broad-leaved crop canopy. *Front. Plant Sci.* 14. doi: 10.3389/fpls.2023.1079703

Laurence, A. British Museum (Natural History), L. , Halsey, S. H. (1978). *Whitefly of the world; a systematic catalogue of the aleyrodidae (Homoptera) with host plant and natural enemy data.*

Li, J., Li, Z., Ma, Y., Cui, H., Yang, Z., and Lu, H. (2021). Effects of leaf response velocity on spray deposition with an air-assisted orchard sprayer. *Int. J. Agric. Biol. Eng.* 14, 123–132. doi: 10.25165/j.ijabe.20211401.5435

Li, T., Qi, P., Wang, Z., Xu, S., Huang, Z., Han, L., et al. (2022). Evaluation of the effects of airflow distribution patterns on deposit coverage and spray penetration in multi-unit air-assisted sprayer. *Agronomy* 12, 944. doi: 10.3390/agronomy12040944

Maski, D., and Durairaj, D. (2010). Effects of charging voltage, application speed, target height, and orientation upon charged spray deposition on leaf abaxial and adaxial surfaces. *Crop Prot.* 29, 134–141. doi: 10.1016/j.cropro.2009.10.006

Miguez, M., Deleon, R., Vicente, G., and Zoppolo, R. (2019). "Real time tree row volume estimation for efficient application of phytosanitary products in fruit trees," in *2019 IEEE International Symposium on Circuits and Systems (ISCAS)* (IEEE), Sapporo, Japan. pp. 1–3. doi: 10.1109/ISCAS.2019.8702561

Owen-Smith, P., Wise, J., and Grieshop, M. J. (2019). Season long pest management efficacy and spray characteristics of a solid set canopy delivery system in high density apples. *Insects* 10, 193. doi: 10.3390/insects10070193

Pai, N., Salyani, M., and Sweeb, R. D. (2009). Regulating airflow of orchard airblast sprayer based on tree foliage density. *Trans. ASABE* 52, 1423–1428. doi: 10.13031/2013.29122

Pergher, G., Gubiani, R., and Tonetto, G. (1997). Foliar deposition and pesticide losses from three air-assisted sprayers in a hedgerow vineyard. *Crop Prot.* 16, 25–33. doi: 10.1016/S0261-2194(96)00054-3

Rossi, F., Facini, O., Predieri, S., and Georgiadis, T. (1992). Relationships between canopy structure and wind speed pattern in a peach tree. *Acta Hortic.* 313, 157–164. doi: 10.17660/ActaHortic.1992.313.18

Sinha, R., Ranjan, R., Khot, L. R., Hoheisel, G. A., and Grieshop, M. J. (2020). Comparison of within canopy deposition for a solid set canopy delivery system (SSCDS) and an axial–fan airblast sprayer in a vineyard. *Crop Prot.* 132, 105124. doi: 10.1016/J.CROPRO.2020.105124

Sutton, T. B. (1988). Evaluation of the tree-Row-Volume model for full-season pesticide application on apples. *Plant Dis.* 72, 629. doi: 10.1094/PD-72-0629

Svensson, S. A., Brazee, R. D., Fox, R. D., and Williams, K. A. (2003). Air jet velocities in and beyond apple trees from a two-fan cross-flow sprayer. *Trans. ASAE* 46, 611–621. doi: 10.13031/2013.13587

Toews, R.-B., and Friessleben, R. (2012). Dose rate expression–need for harmonization and consequences of the leaf wall area approach. *Erwerbs-Obstbau* 54, 49–53. doi: 10.1007/s10341-012-0161-z

TOPPS-Prowadis Project (2014) *Best management practices to reduce spray drift*. Available at: http://www.topps-life.org/.

Toselli, M., Scudellari, D., Fernandez, V., and Abadia, J. (2009). Foliar nutrition of fruit trees. *Italus Hortus* 16, 45–54.

Wang, J., Qi, L., and Xia, Q. (2015). CFD simulation and validation of trajectory and deposition behavior of droplets around target affected by air flow field in greenhouse. *Trans. Chin. Soc Agric. Eng.* 31, 46–53. doi: 10.11975/j.issn.1002-6819.2015.11.007

Washington, J. R., Cruz, J., Lopez, F., and Fajardo, M. (1998). Infection studies of mycosphaerella fijiensis on banana and the control of black sigatoka with chlorothalonil. *Plant Dis.* 82, 1185–1190. doi: 10.1094/PDIS.1998.82.11.1185

Wu, S., Liu, J., Wang, J., Hao, D., and Wang, R. (2021). The motion of strawberry leaves in an air-assisted spray field and its influence on droplet deposition. *Trans. ASABE* 64, 83–93. doi: 10.13031/trans.14143

Xu, S., Feng, Y., Han, L., Ran, X., Zhong, Y., Jin, Y., et al. (2023). Evaluation of the wind field and deposition effect of a novel air-assisted strawberry sprayer. *Agriculture* 13, 230. doi: 10.3390/agriculture13020230

Yan, C., Niu, C., Ma, S., Tan, H., and Xu, L. (2022). CFD models as a tool to analyze the deformation behavior of grape leaves under an air-assisted sprayer. *Comput. Electron. Agric.* 198, 107112. doi: 10.1016/j.compag.2022.107112

Zhang, C., Zhou, H., Xu, L., Ru, Y., Ju, H., and Chen, Q. (2022). Measurement of morphological changes of pear leaves in airflow based on high-speed photography. *Front. Plant Sci.* 13. doi: 10.3389/FPLS.2022.900427/BIBTEX

Zhou, L., Ling, Z., XinYu, X., WeiMin, D., Zhu, S., QingQing, Z., et al. (2016). Design and experiment of 3WQ-400 double air-assisted electrostatic orchard sprayer. *Trans. Chin. Soc Agric. Eng.* 32, 45–53. doi: 10.11975/j.issn.1002-6819.2016.16.007

Zhou, J., He, X., and Landers, A. J. (2012). Dosage adjustment for pesticide application in vineyards. *Trans. ASABE* 55, 2043–2049. doi: 10.13031/2013.42490

Zhu, H., Derksen, R. C., Krause, C. R., Brazee, R. D., Fox, R. D., and Ozkan, H.E. (2004). Spray deposition in taxus and air velocity profile for a fiveport, air-assist sprayer. *ASABE*. doi: 10.13031/2013.17054

frontiers | Frontiers in Plant Science

TYPE Original Research
PUBLISHED 17 August 2023
DOI 10.3389/fpls.2023.1220878

OPEN ACCESS

EDITED BY
Jianli Song,
China Agricultural University, China

REVIEWED BY
Changling Wang,
China Agricultural University, China
Longlong Li,
Beijing Academy of Agricultural and Forestry Sciences, China

*CORRESPONDENCE
Pei Wang
peiwang@swu.edu.cn

RECEIVED 11 May 2023
ACCEPTED 18 July 2023
PUBLISHED 17 August 2023

CITATION
Wang P, Xu C, Li C, Wang L, Niu Q and Li H (2023) Investigation of factors enhancing droplets spreading on leaves with burrs. *Front. Plant Sci.* 14:1220878. doi: 10.3389/fpls.2023.1220878

Investigation of factors enhancing droplets spreading on leaves with burrs

Pei Wang[1,2]*, Chengrui Xu[1], Chengsong Li[1,3], Lihong Wang[1], Qi Niu[1] and Hui Li[1]

[1]College of Engineering and Technology, Key Laboratory of Agricultural Equipment for Hilly and Mountain Areas, Southwest University, Chongqing, China, [2]Interdisciplinary Research Center for Agriculture Green Development in Yangtze River Basin, College of Resources and Environment, Southwest University, Chongqing, China, [3]National Citrus Engineering Research Center, Chinese Academy of Agricultural Sciences & Southwest University, Chongqing, China

Introduction: Spread effect is one of the aspects on deposition quality evaluation of pesticide droplets. It could be affected by many factors such as the microstructure of the target plant leaf surface, physical features of the droplets, and the concentration of spray additives.

Methods: In this study, using a high-speed photography system, 2.3% glyphosate ammonium salt solution with different concentration of the additive was applied to investigate the impact process of single droplet deposition on the plant leaf surface with burrs. Effect of droplet sizes and velocities on spreading area and dynamic deposition procedure was analyzed using image processing programs.

Results: The diffusion factor in the process of droplet spreading was changed over time. The occurrence of bubbles in the droplets was observed in the results. With the bubble generation, the droplet diameter expands and a better diffusion effect is obtained. As a result, better spreading effect was obtained as the droplet diameter was expanded with the generation of bubbles. The significant effects of each physical property of droplets on droplet spreading and the interaction effects between the influencing factors were analyzed. A significant correlation was found between additive concentration, droplet impact velocity, droplet diameters and droplet spreading area. All interactions of concentration:velocity, concentration:diameter, velocity:diameter, and concentration:velocity:diameter had a significant effect on the spreading area of droplets. The study of the factors influencing the process of pesticide droplet impact on the leaf surface contributes to the efficient use of pesticides. Thus, the consumption of pesticides and the resulting impact on the environment can be reduced.

KEYWORDS

droplets, high-speed photography, spread area, impact velocity, weed leaves

1 Introduction

Pesticide application is one of the most effective and indispensable means to control pests during crop production, which mainly targets the stems and leaves of the plants (Song et al., 2019). However, environmental pollution and food safety risk issues in crop production could be attributed to the runoff of pesticides to the soil, atmosphere, and water, which could also result in over-residual of agrochemicals in crop products (Xia et al., 2022). Droplet loss to soil can be reduced by increasing the spread area and retention of droplets on plant foliage. The pesticide runoff could be reduced by enhancing droplet spread property to realize a better deposition effect, particularly on leaf surfaces with burrs.

During the deposition procedure, the phenomenon of droplet rebound, splashing, aggregation, and rolling off would occur as the surface of targets might not be effectively wetted (Xu et al., 2021). Droplet retention duration on leaves can affect the absorption of pesticide by insects or plants, leading to different pesticide efficacy (Bukovac et al., 2002; Dong et al., 2015; Krahmer et al., 2021). Microscopic kinetic studies on droplets have shown that the properties of the liquid had a significant influence on the behavior of the droplet when it hits solid objects (Yan et al., 2019). The physical properties of droplets include surface tension, viscosity, density, droplet particle size, impact velocity, and impact angle. Droplets of different surface tensions have different contact angles on crop leaves, thus affecting the adhesion properties of droplets (Kang et al., 2021). Previous studies have shown that the addition of reasonable additives to pesticide formulations could change the physicochemical properties of the solution, thereby improving the wetting deposition of the solution to the target (Appah et al., 2020; Huet et al., 2020; Zhang et al., 2020).

The addition of additives to the spray mixture could enhance the deposition, retention, diffusion, osmosis, and absorption of pesticide ingredients (Xu et al., 2011; Travlos et al., 2017; Li et al., 2019; Lee et al., 2021; Song et al., 2021). On the surface of hydrophilic plants, the droplet fragmentation is related to the leaf surface roughness of plants, while crushing possibility would reduce on the surfaces with polar chemicals of plants such as avocado and cabbage (Massinon et al., 2017).

The spread area and evaporation time of droplets on leaves would also be affected after the addition of additives (Lin et al., 2019). The hydrophilic leaf spread area and evaporation time of two sizes of droplets with and without additives were compared by experimental studies (de Oliveira et al., 2019). It was found that the retention of droplets on the leaf surface is related to the type of leaf surface and the physical and chemical properties of the spray. The above studies presented the effect of additives on droplet spreading and precipitation. However, the mechanism of these changing physical properties was not discussed.

Leaves with burrs are also more water repellent than leaves without trichomes, especially when the trichome density is greater than 1 per 25 mm^2 (Brewer et al., 1991). The hydrophobicity of the burr surface is related to the villous density, which prevents fluid from reaching the leaf surface, resulting in less retention of the liquid on the leaf surface during application (Xu et al., 2011). It is particularly important to study the impact behavior of pesticide droplets on the burr surface. There were fewer experiments that study the impact of droplets on burr surfaces. In this experimental study, glyphosate and patchouli thistle were used as experimental objects to study the impact behavior of pesticide droplets on the burr leaf surface.

This study investigated the difference in droplet impact behavior on the burr surface under different concentrations of silicone additives. The impact behavior of droplets was analyzed to investigate the effect of pesticide droplet physical properties on droplet spreading on the leaf surface of *Ageratum conyzoides* Linn, a weed species with burr leaves. In turn, optimization strategies for pesticide application parameters could be obtained in order to reduce the environmental pollution by agrochemicals.

2 Materials and methods

2.1 Test setup

A. conyzoides Linn was selected as the pesticide deposition object in this test. It is native to Central and South America and Mexico in North America, and is now widely distributed in tropical and subtropical regions of Asia (Okunade, 2002). During the test, the environmental conditions were controlled at a temperature of 25°C and a relative humidity of 20%. The plant leaves were cut into small blades with a size of 10 × 10 mm. The surface of the blades was wiped with a paper towel and placed on the blade holder. Figure 1 presents a schematic diagram of the test apparatus. The high-speed photography system (Model: Photron UX50, PHOTRON, Japan) was placed above the blade holder. An LED light source was placed opposite to the high-speed camera. Droplets in volumes of 0.10 µl, 0.15 µl, and 0.20 µl were generated with a pipette gun (Model: 7010101001, DLAB Scientific, Beijing, China, measurement range is 0.1–2.5 µl, minimum adjustable variable is 0.05 µl). The purpose of turning the knob of the transfer gun is to adjust to the proper droplet volume. Then, squeezing the knob of the pipette gun can generate drops of liquid. Droplets were released at heights of 15 cm, 20 cm, and 25 cm. The dynamic impact behavior of droplets hitting the blade and the spreading, bouncing, and balancing of droplets on the blade were recorded by using high-speed photography equipment under a focal length lens of 36 mm. The capture duration was set for 4 s, under a pixel resolution of 1,280 × 512 and a shutter frequency of 4,000 frames per second. The PFV4 (Model: Photron UX50, PHOTRON, Japan) and ImageJ (National Institutes of Health, USA) software were used to view and process the captured images after the shooting was completed.

2.2 Chemical preparation

In this study, droplets were generated from 2.3% glyphosate (a.i.: isopropylamine salt, provided by Hebei Zhongbao Green Crop Technology Co., Ltd.) solution mixed with silicone additives (Institute of Plant Protection, Chinese Academy of Agricultural Sciences, 99.9%) in several concentrations of 0%, 0.25%, 0.5%, and 0.75% (Table 1).

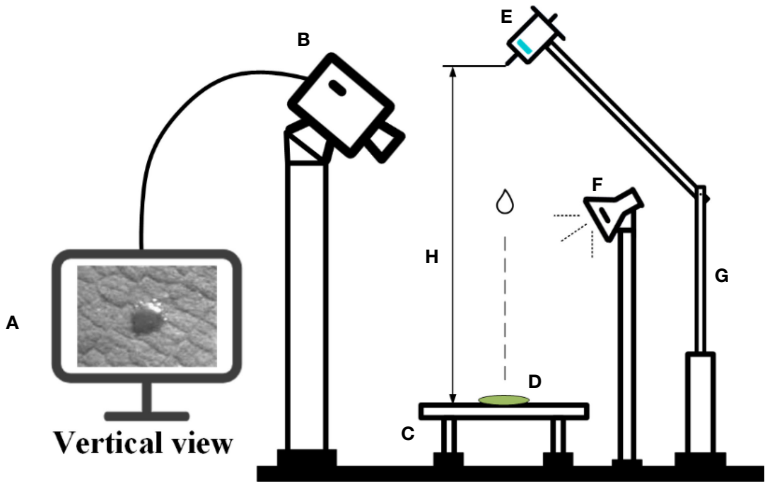

FIGURE 1
Schematic diagram of the test apparatus. **(A)** Computer + ImageJ software, **(B)** high-speed photography equipment, **(C)** blade holder, **(D)** leaf blade, **(E)** droplet generator pipette, **(F)** LED light source, **(G)** adjustable height holder, and **(H)** droplet release height.

TABLE 1 Preparation of droplet solutions. V_1 is the glyphosate volume and V_2 is the silicone volume.

Concentration	Glyphosate V_1 (μl)	Silicone V_2 (μl)	Water (ml)
0.25% silicone	200	25	10
0.50% silicone	175	50	10
0.75% silicone	150	75	10

2.3 Physical property evaluation

The physical properties of the droplet itself would greatly affect the spread of the droplet after impacting the blade. The surface tension and contact angle of the droplet would have a greater impact on the spread. Cassie and Baxter (1944) found a relationship between the angle of contact and the solid surface

$$\cos\theta_c = f\cos\theta - (1-f) \tag{1}$$

where f is the solid phase resolution of the solid surface, $f<1$; θ_c is an apparent contact angle.

It was possible to conclude from the equations that the droplet contact angle would be larger on the solid surface with a lower solid-phase resolution (f), which means that solid surfaces with a lower solid-phase resolution would have better hydrophobicity. Thus, the solid surface structure would affect the static contact angle of the droplet, which would further affect the spread and wetting of the droplet after impacting the surface. The lie-down method was applied to measure the static contact angle of the droplet on the solid surface. Leaves of *A. conyzoides* Linn used in the test were fixed on the stage. Eight-microliter droplets were spun out from a micropipette. Small droplets could be delivered to the tested leaf surface by adjusting the micropipette height to ensure that the droplet and plant foliage were just contacted. The measuring system (Kruss, model: DSA10030700, Hamburg, Germany) would correct the droplet shape and measure the contact angle on the leaf surface as shown in Figure 2. Each droplet was measured three times in the test and the results are shown in Table 2.

The surface tension of the droplets was measured using the suspension method. The shape of large droplets or bubbles was varied due to the competition between gravity and cohesion between liquid molecules. Gravitational forces tended to lengthen suspended droplets, while cohesive forces tended to produce compact, spherical droplets. The surface tension could be compared using capillary length by analyzing the equilibrium droplet shape (Figure 3). If the density of the fluid and the surrounding medium was known, the surface tension could be calculated. The specific principle is

$$2-\beta(z/b) = b/R + b\sin\Phi/x \tag{2}$$

$$\beta = (b\ \wedge\ 2\times\Delta\rho\times g)/\gamma = b^2/\alpha^2 \tag{3}$$

$$\alpha = \sqrt{(\gamma/(\Delta\rho\times g))} \tag{4}$$

where b is the radius of curvature at the low end of the suspension droplet; R is the radius of curvature of a point P(x,y) on the contour of the drop in the plane; Φ is the angle between the tangent line and the x axis at the point P(x,y) on the contour line; β is the shape factor of the droplet, which determines the shape of the droplets; $\Delta\rho$ is the density difference between the liquid direction and the surrounding gas phase; γ is the surface tension; and α is the capillary constant of the system.

The system software was used for the image processing in this test. The surface tension was measured by matching the suspension drop profile with the program. Surface tension was measured using the contact angle measuring instrument as described above. The surface tension of each droplet was measured three times during the test. The results are shown in Table 3.

10.3389/fpls.2023.1220878

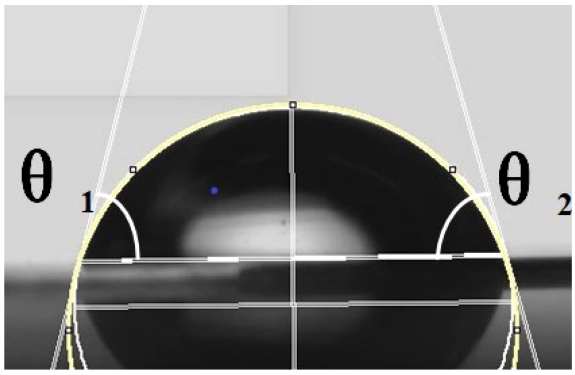

FIGURE 2
Schematic of contact angle measurement. The yellow line is the contour line of the droplet. The white lines on both sides are the tangent lines of the contact points between the droplet and the surface. θ1 and θ2 are the left and right contact angles, respectively.

3 Results

3.1 Spreading process

After the droplet affected the burr surface, there were four processes: movement, spreading and fragmentation, retraction, and balancing. No rebound behavior was observed in this test. Figure 4 shows the impact process on burr leaves of glyphosate droplets with 0.25%, 0.50%, and 0.75% silicone additives released at a height of 15 cm and with a diameter of 576 μm. The duration *t* was set as 0 ms when the droplet reached the leaf blade. The next image was recorded immediately after the contact of the droplet and leaf was defined as the beginning of spreading, when *t* = 0.25 ms (the minimum time interval between two shutters). Since 0.25 ms onwards, the droplets began to spread on the leaf surface. As shown in Figure 4, in the initial spread of droplet of glyphosate solution without additives, the edge of the deposition area was disturbed by the fine villi on the leaf surface. The surface tension was large, resulting in the spreading edge showing divergent spreading. This situation resulted in a splash of tiny droplets on impact. Test results in Table 3 show that droplet surface tension reduced when the silicone additive was mixed with the glyphosate solution. The low surface tension made the droplets less capable of maintaining the spherical shape.

Figure 4 shows that, at the beginning of the spreading process, the droplets with adjuvant could spread smoothly despite the disturbance from the burr on the leaf surface. A more regular circle was formed as the edge of the deposited area. Droplets spread to the maximum area approximately t = 1.00 ms. During the droplet spreading, the kinetic energy of the droplets was dissipated to overcome the viscosity and surface tension, which induced the establishment of a new droplet shape. Glyphosate solution droplets were subjected to excessive resistance in spreading due to their surface tension and the surface villi of the leaves, resulting in

TABLE 2 Measurement of static contact angles of glyphosate solutions with different concentrations of additives.

Additive concentration	Number of measurements	Measuring position and measured value (°)			Average (°)	Standard error
		θ_1	θ_2	mean		
	1	66.975	68.199	67.587		
0%	2	65.772	66.975	66.373	65.609	2.000772
	3	62.301	63.435	62.868		
	1	61.189	62.301	61.745		
0.25%	2	59.036	59.036	59.036	58.28	3.183449
	3	54.058	54.058	54.058		
	1	44.293	44.293	44.293		
0.50%	2	45.725	46.469	46.097	45.747	1.072882
	3	46.469	47.231	46.85		
	1	38.108	38.66	38.384		
0.75%	2	38.66	39.226	38.943	39.344	1.418781
	3	41.634	41.634	41.634		

10.3389/fpls.2023.1220878

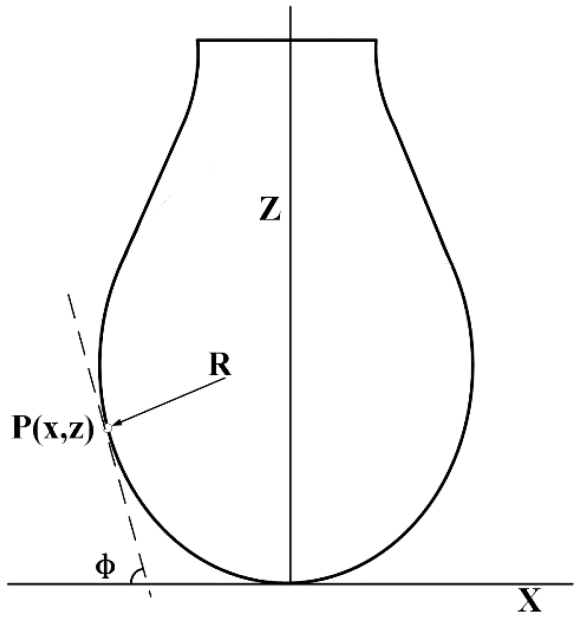

FIGURE 3
Schematic of surface tension measurement. *R* is the radius of curvature of a point P (*x*, *y*) on the contour of the drop in the plane; *Φ* is the angle between the tangent line and the *x* axis at the point P (*x*, *y*) on the contour line; Z and X correspond to the *X* and *Z* axes respectively.

incomplete spreading. During the spreading process, droplets with additives also spread more widely than the droplet of glyphosate-only solution.

The droplets shown in Figure 4 started to retract at $t = 1.25$ ms. The droplet retraction was affected by the surface tension of the droplets, the internal intermolecular forces, and the magnitude of the adsorption force on the droplet surface. The surface tension acting on the surface of the droplets prevented the droplets from spreading on the blade surface and thus caused the droplets to retract. It can be seen from Figure 4 that the retraction time of droplets with different additive concentrations was not the same. The retraction time of glyphosate solution with maximum surface tension was 1 ms, while the retraction time of the droplets with additive concentrations of 0.25%, 0.5%, and 0.75% was 2 ms, 1.25 ms, and 0.25 ms, respectively. It could be seen that the shape of the four droplets differed greatly after retraction. The degree of completion of the retraction was mainly affected by the surface tension and the surface structure of the blades. Droplets with 0.75% silicone had bubbles inside the droplet before impact. It also presented better spreading effect and shorter retraction time of droplets with 0.75% silicone.

TABLE 3 Measurement of surface tension of glyphosate solutions with different concentrations of additives.

Additive concentration	Number of measurements	Measured value (mN/m)	Average (mN/m)	Standard error
	1	43.746		
0	2	43.613	43.591	0.136428
	3	43.414		
	1	30.732		
0.25%	2	30.749	30.76	0.02798
	3	30.798		
	1	24.247		
0.50%	2	23.782	23.868	0.280654
	3	23.576		
	1	22.854		
0.75%	2	23.132	23.12	0.212459
	3	23.374		

10.3389/fpls.2023.1220878

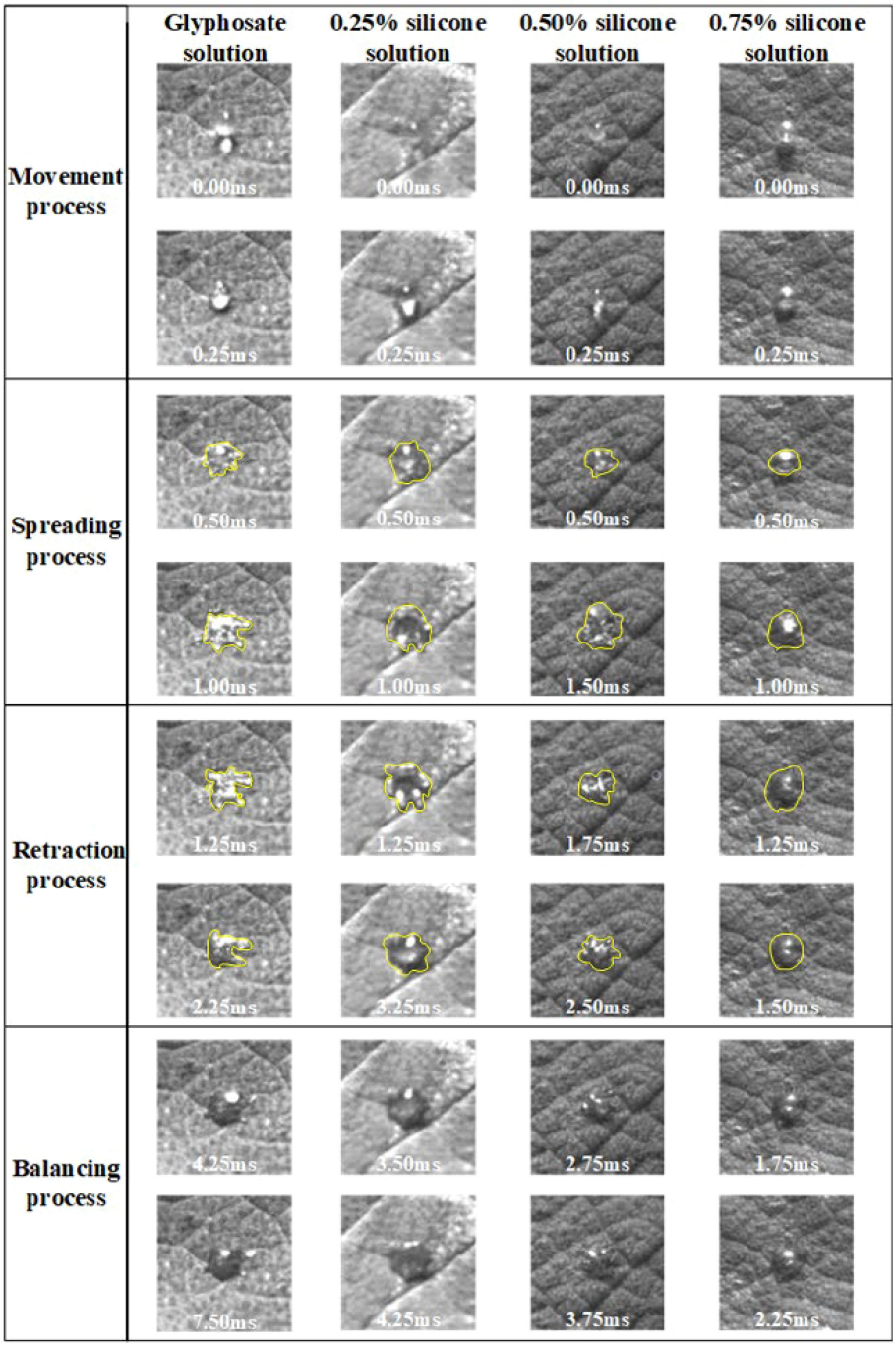

FIGURE 4
Spreading process of droplets after impacting the blade surface. The spreading process of droplets of 2.3% glyphosate solution with organosilicon additive concentrations of 0%, 0.25%, 0.50%, and 0.75%, respectively, with a velocity of 1.776 m/s and a diameter of 576 μm, impacted the leaf surface. Different categories of images have different scales.

3.2 Spread area

3.2.1 Relationship between spread area and droplet diameter

Figure 5 presents the results of the spread area of glyphosate solutions with different additive concentrations, different diameters, and different velocities. Figure 5A shows that the spread area of droplets with 0.25% silicone increased by 21.91% when the diameter increased from 576 μm to 660 μm. When the droplet diameter increased to 726 μm, the spread area of droplets increased by 41.17% and 15.81% compared with the spread area of droplets in diameters of 576 μm and 660 μm, respectively.

The spread area of droplets of the silicone additive at 1.776 m/s that affected the blade can be seen in Figure 5 for an additive concentration increase to 0.50% silicone additive. The spread area of droplets and droplet diameters could be seen to be positively

10.3389/fpls.2023.1220878

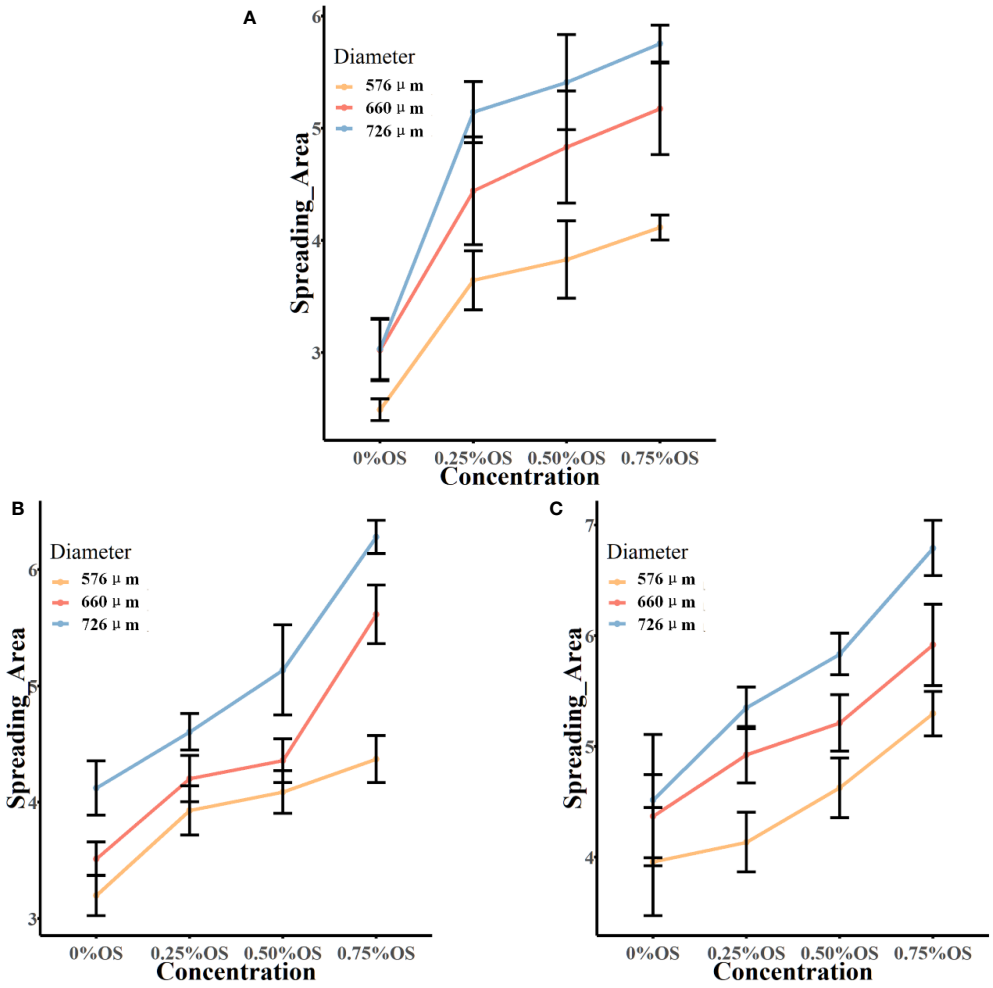

FIGURE 5
The spread area of the droplet impacting the burr surface. Panels **(A-C)** show the final spread area after impacting the leaf surface at a velocity of 1.776 m/s, 1.979 m/s, and 2.212 m/s, respectively. In the figure, the vertical coordinate is the spread area of droplets on the leaf surface; the horizontal coordinate is the solution of glyphosate with different concentrations of additives. OS, organic silicone. Spread area unit: mm^2.

correlated at three velocities. The spread area after the impact of 660-μm diameter at a velocity of 1.776 m/s increased by 26.23% compared with the spread area after the impact of 576 μm. The spread area increased by 41.32% after the droplet diameter increased to 726 μm and the spread area increased by 11.96% after the droplet diameter increased from 660 μm to 726 μm. At the rate of 1.979 m/s and 2.212 m/s, the glyphosate solution of 0.5% silicone additive was added, and the spread area of the droplets increased with the increase in diameter.

3.2.2 Relationship between spread area and additive concentration

As shown in Figure 5A, after adding 0.25% silicone additives, the droplets in all the three diameters presented a significant increase of the spread area after impacting the blade compared to the spread area of droplets without the addition of silicone additives. The addition of additives to the glyphosate solution could greatly increase the spread area of the droplets.

At a velocity of 1.776 m/s, the droplet diameter was 576 μm, and the spread area of the solution with 0.25% silicone additives was 46.36% higher than that of the solution without additives, which was a larger increase. With the increase of the concentration of the additives, the spread area of the silicone solution added to 0.5% was only 5.1% higher than that of the 0.25% silicone solution, and the 0.75% silicone solution was increased by 7.5% compared with the 0.5% silicone solution. It could be seen to increase the concentration of the additives, and the spread area of the droplet could also be increased. The same situation was also reflected in the droplets with droplet diameters of 660 μm and 726 μm. In droplets with a diameter of 660 μm, for each increase in silicone concentration of 0.25%, the growth of the spread area was 47%, 8.8%, and 7.0%, respectively. For each increase in silicone concentration of 0.25% of droplets with a diameter of 726 μm, the growth of the spread area was 69.73%, 5.2%, and 6.4%, respectively.

From Figure 5B, the spread area of droplets with a diameter of 576 μm increased by 22.87%, 4.1%, and 6.9%, respectively, with the concentration of the additive 0%–0.75% at a velocity of 1.979 m/s. The same situation was also observed for droplets of 660-μm and 726-μm diameters. It can be seen that at a velocity of 1.979 m/s, the spread area of the droplet increased with the increase of

the concentration of silicone additives. The spread area of the droplet after impacting the blade at a velocity of 2.212 m/s is shown in Figure 5C. At this velocity, it can also be seen that the droplet spread area is increasing with increasing concentration of silicone additives.

3.2.3 The relationship between spread area and velocity

The velocity of droplets impacting the leaf surface was controlled by releasing droplets at different heights in the experiment. Find the local acceleration of gravity and use the equation $v = \sqrt{2gh}$ to calculate the velocity of the droplet at impact, where v is the droplet falling velocity, g is the acceleration of local gravity, and h is the droplet release height. Table 4 shows the spread area of droplets at different velocities and the growth of droplet spread area when comparing different velocities. The spread area of glyphosate droplets without additives increased with increasing droplet impact velocity at three diameters. The same situation was observed in glyphosate solutions with 0.75% silicone additives. The impact velocity of 576-μm droplets was increased from 1.776 m/s to 2.212 m/s, and the growth of the spread area was 6.22%, 21.17%, and 28.71%. The droplet spread area of 660 μm and 726 μm was also continuously increased after the velocity increase. However, in glyphosate solutions with 0.25% and 0.50% silicones added, the effect of the increase in velocity on the droplet spread area was not clear.

3.2.4 Interpretation of the ANOVA results

3.2.4.1 Main effects

The ANOVA results presented sufficient statistical evidence that the concentration, velocity, and diameter could significantly affect the spread area of the droplets, as shown in Table 5. The *post-hoc* analyses showed that 0.75% of the concentration had the highest effect with a mean of 5.086587, while 2.212 m/s of velocity had the highest effect with a mean of 4.863929.

3.2.4.2 Interaction effect

The two-factor interaction between concentration and velocity reported a *p*-value of 0.0001702. This was less than alpha (0.05). Concluding with 95% statistical confidence, sufficient data existed to evidence that the interaction of concentration and velocity could affect the spread area of droplets. The *post-hoc* LSD test showed that the combination of 0.75% concentration and 2.212 m/s velocity led to the maximum spread area with a mean of 5.364571 mm², while the combination of 0% concentration and 1.776 m/s velocity showed a low effect on the droplet spreading with a mean of 2.953095 mm².

The two-factor interaction between velocity and diameter reported a *p*-value of 0.0486874. This was less than alpha (0.05). Concluding with 95% statistical confidence, it indicated that the combination of velocity and diameter had a significant effect on the spread area. *Post-hoc* analyses showed that 2.212 m/s:726 μm exhibited the highest effect with a mean of 5.245607, while 1.776 m/s:576 μm exhibited the lowest effect with a mean of 3.477071.

The two-factor interaction between concentration and diameter reported a *p*-value of 2.069e-06. This was less than alpha (0.05). Concluding with 95% statistical confidence, it indicated that the combination of concentration and diameter had a significant effect on the spread area. *Post-hoc* analyses showed that 0.75%:726 μm exhibited the highest effect with a mean of 5.783143, while 0%:576 μm exhibited the lowest effect with a mean of 3.217667.

The three-factor interaction of concentration:velocity:diameter reported a *p*-value of 3.038e-07. This was less than alpha (0.05). Concluding with 95% statistical confidence, there existed sufficient

TABLE 4 Droplet spread area. v1: 1.776 m/s; v2: 1.979 m/s; v3: 2.212 m/s.

Solution	Diameter	Spread area (mm^2)					
		Velocity			Percentage increase		
		v1	v2	v3	v2-v1	v3-v2	v3-v1
2.3% glyphosate	576 μm	2.489	3.197	3.958	28.45%	23.80%	59.02%
	660 μm	3.021	3.513	4.369	16.29%	24.37%	44.62%
	726 μm	3.030	4.121	4.514	36.01%	9.54%	48.98%
2.3% glyphosate + 0.25% organic silicone	576 μm	3.643	3.928	4.134	7.82%	5.24%	13.48%
	660 μm	4.441	4.202	4.924	-5.38%	17.18%	10.88%
	726 μm	5.143	4.605	5.348	-10.46%	16.13%	3.99%
2.3% glyphosate + 0.50% organic silicone	576 μm	3.828	4.088	4.626	6.79%	13.16%	20.85%
	660 μm	4.832	4.357	5.211	-9.83%	19.60%	7.84%
	726 μm	5.410	5.136	5.833	-5.06%	13.57%	7.82%
2.3% glyphosate + 0.75% organic silicone	576 μm	4.114	4.370	5.295	6.22%	21.17%	28.71%
	660 μm	5.172	5.615	5.916	8.57%	5.36%	14.39%
	726 μm	5.754	6.279	6.790	9.12%	8.14%	18.00%

TABLE 5 Analysis of variance table.

	Df	Sum	Mean_sq	*F*-value	Pr(>*F*)
Replicationvector	5	6.919	1.3838	6.6433	9.100e-06 ***
Fact.A	3	77.837	25.9458	124.5629	< 2.2e-16 ***
Fact.B	2	20.922	10.4609	50.2215	< 2.2e-16 ***
Fact.C	2	56.094	28.047	134.6507	< 2.2e-16 ***
Fact.A:Fact.B	6	5.853	0.9755	4.6831	0.0001702 ***
Fact.A:Fact.C	6	8.251	1.3752	6.602	2.069e-06 ***
Fact.B:Fact.C	4	2.026	0.5064	2.4312	0.0486874 *
Fact.A:Fact.B:Fact.C	12	12.424	1.0354	4.9706	3.038e-07 ***
Residuals	211	43.95	0.2083		

Replicationvector, repeat groups of measurements; Fact.A, concentration; Fact.B, velocity; Fact.C, diameter. $p < 0.05$: indicated by an asterisk "*". This indicates that the observed result is statistically significant at the significance level $\alpha = 0.05$.$p < 0.01$: indicated by two asterisks "**". This indicates that the observed result is highly significant at the significance level $\alpha = 0.01$. $p < 0.001$: ndicated by three asterisks "***". This indicates that the observed result is highly significant at a significance level of $\alpha = 0.001$.

statistical evidence to support the claim that the three-factor interaction of concentration, velocity, and diameter had a significant effect across all sets of combinations. *Post-hoc* analyses showed that 0.75%:1.979 m/s:726 µm exhibited the highest effect with a mean of 5.934429, while 0%:1.776 m/s:576 µm exhibited the lowest effect with a mean of 2.488571.

It could be seen from Figure 6 that the droplet with a velocity of 2.212 m/s has the best spreading effect at each diameter with the interaction of droplet diameter and velocity, in which the spread area of droplets with three velocities at all three droplet diameters has a positive trend. With the interaction of droplet additive concentration and velocity, the droplet with a velocity of 2.212 m/s has the best spreading effect at each additive concentration. Droplets with velocities of 1.979 m/s and 1.776 m/s had similar effects with the addition of additives. The spread area of the droplet at all three droplet velocities at all three additive concentrations showed a positive trend. The droplet with a diameter of 726 µm had the best spreading effect at the three additive concentrations with the interaction of droplet diameter and additive concentration. The droplet with a 576-µm diameter showed no growth trend at 0.5%–0.75% of the additive concentration. Droplets with 726-µm and 576-µm diameters showed a positive growth trend in the spread area at all three additive concentrations.

3.3 Spreading factors

To describe the impact phenomenon in more detail and accurately, the time evolution of the spreading factor (defined as spread factor, $\xi_t = D_t/D_0$, where D_0 is the initial diameter of the droplet before impact and D_t is the spreading diameter of the droplet impacting blade at time t) of the four solutions at different velocities and different diameters is shown in Figure 7. Figures 7A-C show the spreading process of the glyphosate solution without the addition of silicone additives at 576-µm, 660-µm, and 726-µm droplet diameters impacting the leaf surface, respectively. In Figure 7A, it can be seen that for the 576-µm-diameter droplets, the droplets of three velocities reached the maximum spread area at the time of 1.00 ms to 1.25 ms. The degree of undulation of the variation curve of the spreading factor of these droplets is relatively small at the three velocities. There was no significant increase or decrease in the spreading factor. However, the fluctuation of spreading factor variation for droplets with diameters of 660 µm and 726 µm was slightly higher than that for droplets with diameters of 576 µm.

Figures 7D-F show the ξ_t of the droplet in the glyphosate solution with 0.25% silicone added. It can be seen in Figure 7D that the ξ_t of the 1.776 m/s droplet was higher than that of the 1.979 m/s and 2.212 m/s droplet. The spreading factor of the droplet with a velocity of 1.979 m/s is higher than that of the droplet with a velocity of 2.212 m/s. Adding silicone additives to reduce the surface tension of the solution (Table 3), the droplets had difficulty maintaining their spherical shape after impacting the blade, which was conducive to spreading. The droplets without bubbles at low velocities had a better spreading factor ξ_t. In Figure 7E, the relationship of ξ_t of the droplets at the three velocities can be seen. Droplets impacting the blade at 1.979 m/s could achieve a good spreading process and the maximum spread area was reached at 1 ms, while droplets with velocities of 1.776 m/s and 2.212 m/s reached the maximum spread area at 1.75 ms and 2.00 ms, respectively. The droplet at a velocity of 1.979 m/s was relatively stable in the oscillation retraction stage, and the variation of ξ_t was small. The droplet of 1.979 m/s in Figure 7F also had a better spreading effect. Compared with the droplets with the other two velocities, the maximum spread area of the droplets with a velocity of 1.979 m/s was reached at approximately 1 ms, the ξ_t was higher, and the effect was better in the spreading process. The 2.212 m/s droplets had a small ξ_t value due to the generation of air bubbles. This was because before the droplet impacted the blade, there were obvious bubbles in the droplet, which resulted in no change in the mass of the droplet, but its volume increased (Figure 8). The droplets actually hit the blade as a liquid film during impact, and the liquid film breaks up to create a large spreading area. The appearance of air bubbles substantially increased the diameter of the

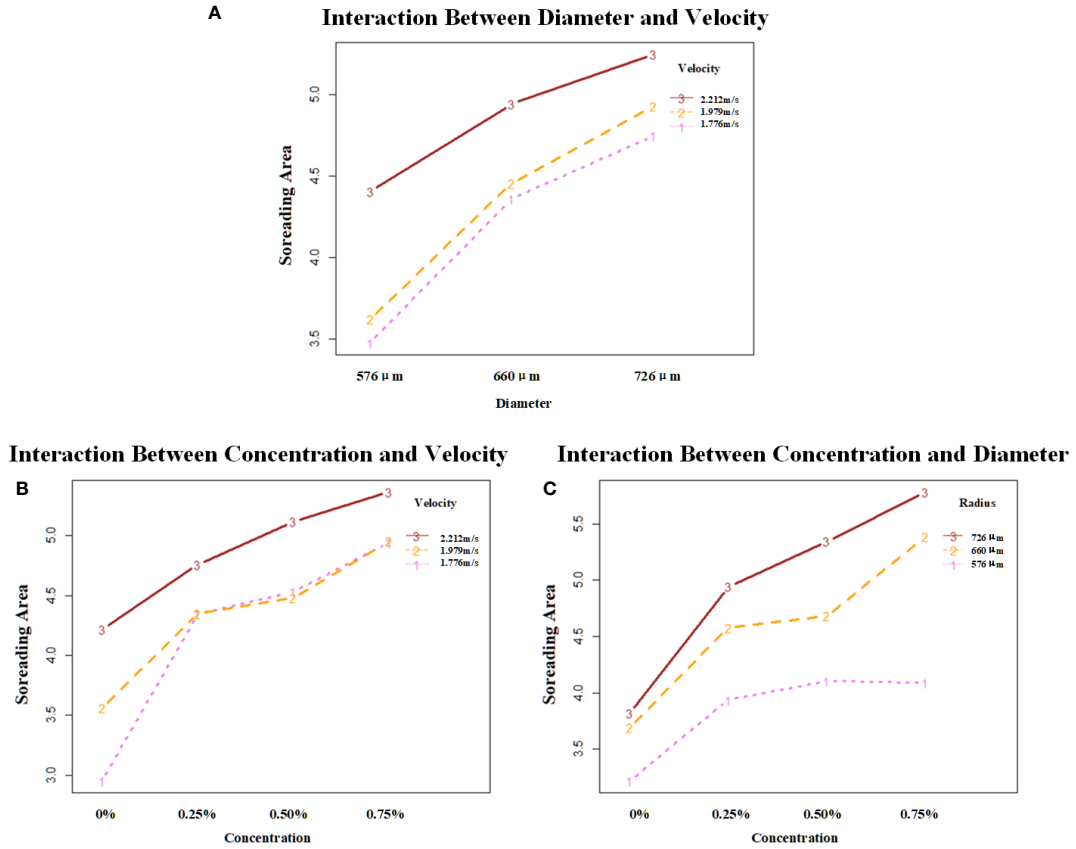

FIGURE 6
Analysis of the interaction effect between each of the two factors. **(A)** shows the interaction effect between diameter and velocity; **(B)** shows the interaction effect between concentration and velocity; **(C)** shows the interaction effect between concentration and diameter. The vertical coordinates are the mean values of spread area under different combinations of factors. Velocity unit: m/s; diameter unit: μm.

droplet, resulting in a smaller ξ_t. Through Figures 7D–F, it could be seen that the droplet of 2.212 m/s had a lower ξ_t during the spreading process, while the droplets of 1.776 m/s and 1.979 m/s with lower velocities had higher ξ_t during spreading.

From Figures 7G–I, the spreading factor ξ_t of the droplets with the concentration of 0.5% silicone additives was reduced compared with the addition of 0.25% silicone. The number of droplets with bubbles was found to increase significantly after the increase of additive concentration in the experiments. The same phenomenon was found in droplets of three diameters at 0.50% of the additive concentration. The droplets with a velocity of 1.979 m/s had a higher ξ_t than the droplets with the other two velocities and quickly reached the maximum spread area. The 1.979 m/s droplets of the three diameters reached the maximum spread area at 1.00 ms, 0.75 ms, and 1.00 ms, respectively. It was roughly 0.25 ms ahead of the droplets with 1.776 m/s and 2.212 m/s velocity. Comparative analysis of Figures 7G-I showed that in the three diameters, the spreading process ξ_t of the 576-μm-diameter droplet was higher, especially comparing the three diameters with a velocity of 2.212 m/s. The ξ_t value of the droplet was a decreasing trend with the elevation of the diameter. The other two velocity droplets had a similar trend but were not as pronounced as the high-velocity droplets. It can be seen from Figures 7J-L that only droplets with a diameter of 726 μm reached ξ_t above 3 at a velocity of 1.776 m/s.

4 Discussion

This study controlled the velocity of droplet impacting the leaf surface by adjusting the height of droplet release. Adding additives of different concentrations changed the surface tension of the droplets. A high-speed photographic system was used to observe the spreading process of droplets. The change of spread factor during the spreading process was analyzed, and the final spread area of different droplets was compared. Four stages of the droplet spreading procedure were observed. A similar phenomenon has been observed in the test on droplet impacting soybean foliage (burr surface) (Jia et al., 2013). During the spreading process, the droplets were spread many times, contracted, and finally stabilized. However, Jia's study focused on the retracting and broken state after the droplet hit the leaf surface. Studies have shown that the kinetic energy inside the droplets is different when droplets of different viscosities collide (Kumar et al., 2017). The variation of kinetic energy would greatly affect the behavior after the droplet impact, which corresponds to the result of this study. The same height as the released droplets would have the same kinetic energy. Surface tension and viscosity of droplets would vary after the addition of additives, resulting in a completely different impact behavior when droplets hit the blades. The droplets with low surface tension spread the maximum area in this study. It was observed that

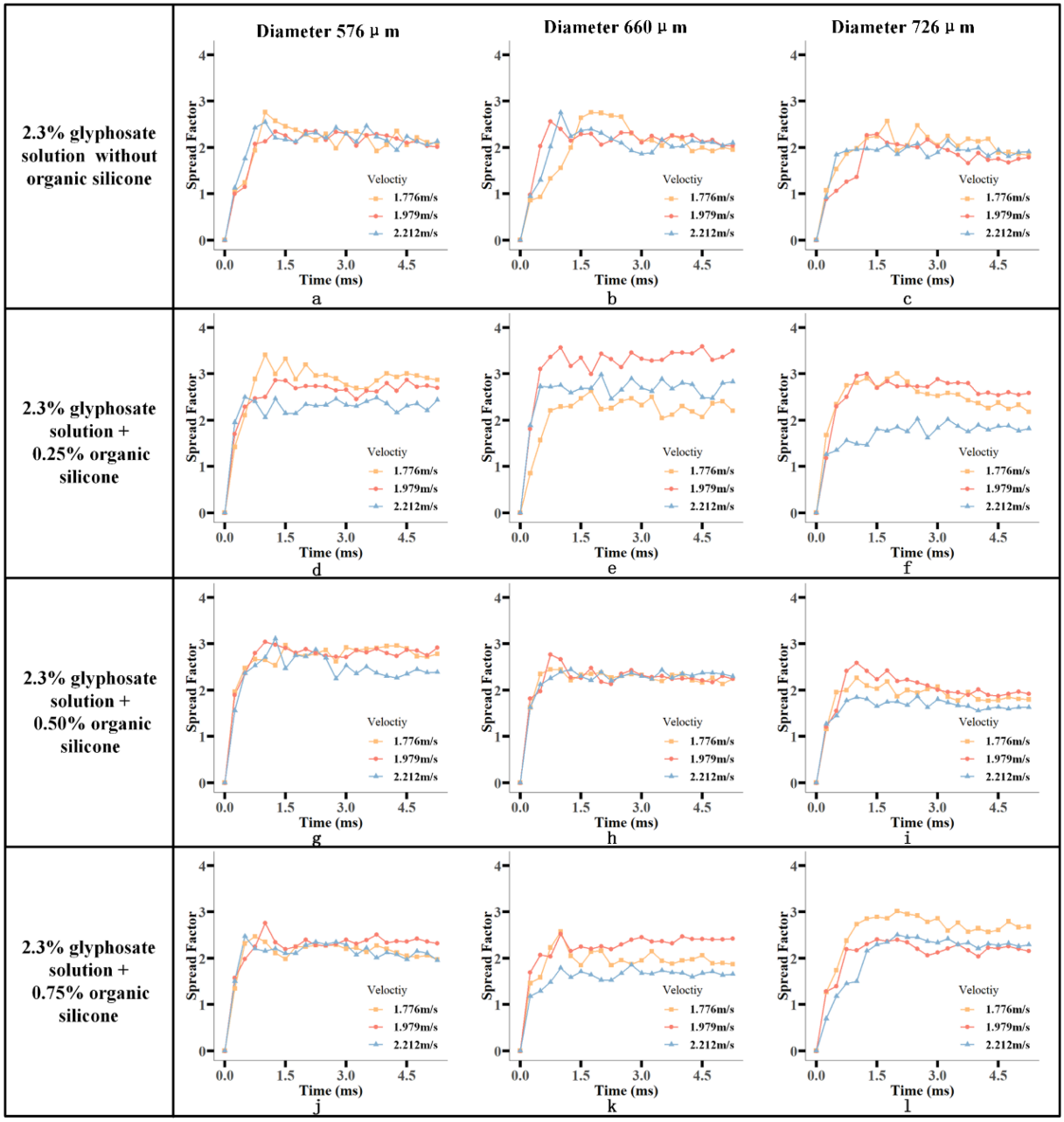

FIGURE 7
Variation of spreading factor (ξ_t) after the droplet affected the leaf surface. Evolution of the diffusion factor of droplets impacting the leaf surface over time for droplets of 2.3% glyphosate solution with organosilicon additive concentrations of 0%, 0.25%, 0.50%, and 0.75% at velocities of 1.776 m/s, 1.979 m/s, and 2.212 m/s and diameters of 576 μm, 660 μm, and 726 μm, respectively. The first to third columns are droplet spreading factors with diameters of 576 μm, 660 μm, and 726 μm, respectively. For ease of presentation each image is numbered from **(A-L)**.

the liquid spread and flowed from the middle to the surrounding area and formed a circle at the edge of the droplet. This phenomenon indicated that the liquid was less disturbed during flowing. The reason was that droplet surface tension was light, which helped maintain their original spherical shape easier. Thus, it was lightly affected by the burr of the blades. The surface tension during the spreading process was the resistance to the spreading of the droplets. The increasing concentration of silicone additives decreased the surface tension and contributed to lower obstruction of droplets in the spreading process. Different droplets behaved differently at each impact stage. When the droplet spread to the maximum area after impacting the blade, the kinetic energy of the droplet was converted to surface energy. Then, the surface tension of the droplets would cause retraction. Since no rebound occurs, the surface energy of the droplets was converted into viscous dissipation in contact with the leaf surface. More kinetic energy was converted into surface energy. For this reason, the retraction time was faster. The surface tension of droplets was reduced by the addition of silicone additives. The droplets were less hindered by surface tension during the spreading

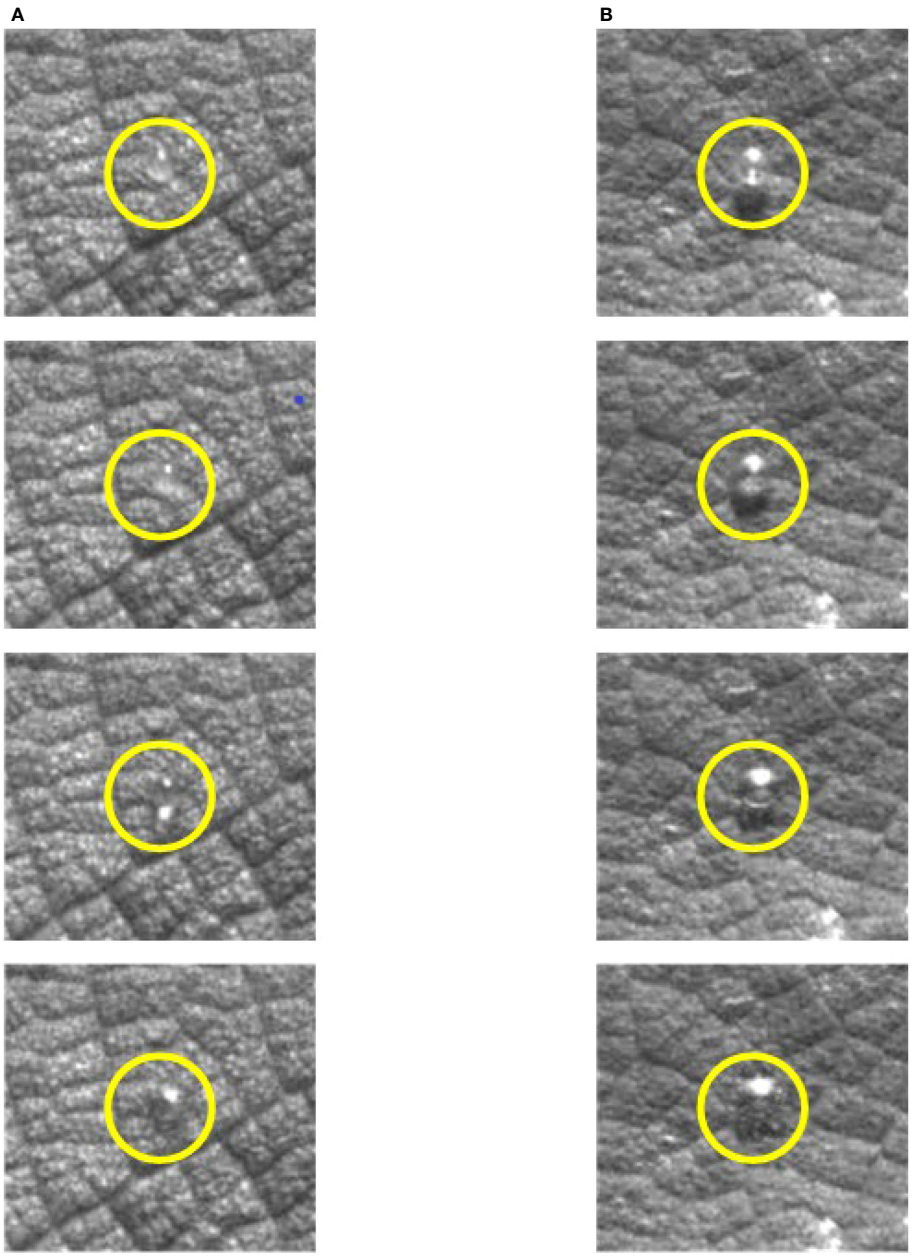

FIGURE 8
Comparison of droplets of the same mass with and without bubbles. **(A)** Droplets without bubbles. **(B)** Droplets with bubbles.

process of the maximum area. Thereby, the spread area was expanded. Thus, there would be more energy consumed by friction with the leaf surface, resulting in a progressively smaller retraction time. Finally, in the balancing process of the droplet, the surface energy of the droplet could be gradually converted into translation kinetic energy and oscillating kinetic energy. There was gradual stabilization of droplets on the leaf surface after gradual energy balance. Glyphosate solution droplets have more surface energy; thus, they required more energy conversion and a longer equilibrium time. This was proved by the equilibration times of the three droplets with the addition of silicone additives, which were 1.25 ms, 1 ms, and 0.5 ms, respectively.

This phenomenon could be attributed to the surface tension and viscosity of the droplets. Some experiments have found that lower surface tension promotes greater diffusion and dampens diffusion oscillations, while higher viscosity inhibits diffusion and retraction processes (Andrade et al., 2012). The spreading of droplets with different surface tensions was indeed observed in the experiment. Droplets with higher surface tension had shorter time to expand to the largest area. The study obtained similar conclusions by analyzing the differences between individual droplets from an energy perspective. By comparing and analyzing the final spread area of various droplets, the droplet spread area of glyphosate solution with additives was much higher than that of

droplets of glyphosate solution without additives. Some scholars have found that the addition of additives to pesticides can effectively improve the deposition properties of the liquid on the leaf surface of the target (Song et al., 2021). The same conclusion was found in Song's study. However, it mainly studied the effects of different kinds of additives on droplet deposition and did not study the effect of additive concentration and the physical properties of droplets on the deposition behavior of liquid droplets.

In this study, it was also found that the increase of additive concentration could increase the final spread area of the droplets. However, the effect of the improvement gradually declined. After comparing the effect of water droplets on glass and leaves with the addition of additives, it was found that the increase in additive concentration could reduce and eliminate the bounce or splash of water droplets, thus improving the diffusion area (Dong et al., 2015). The surfaces used in that experiment were all smooth surfaces, and no more studies were conducted on burrs. The reason for this phenomenon was that increasing the concentration of the additive reduced the surface tension and the contact angle of the droplet (Tables 2, 3), thereby increasing the wettability of the liquid. The effect of surface wettability on droplet kinetics has been studied. It was proposed that droplet diffusion was influenced by the wetting state of the surface (Abubakar et al., 2020). Therefore, increasing the contact angle of the surface would reduce the diffusion diameter of the droplet on the surface. The spreading time of droplets varied with the wetting state of the hydrophobic surface, resulting in the increase in droplet contact angle reducing the spreading time of droplets on the surface. The increase in the static contact angle of the droplet reduces the spreading ability of the droplet on the surface. In this way, droplets can easily form spheres and run off. It was found that increasing the concentration of the additive could lead to the increase of spread area of the droplets. In this study, the correlation between the spread area and the impact velocity of the droplet was found to be significantly positive when the droplet diameter of glyphosate solution was 576 μm. Jia et al. (2013) proposed that the higher the impact velocity of droplets, the greater the maximum spread area. It was similar to the results in this test. It has also been proposed by other scholars that increasing the diameter of the droplet increases the diameter of the wetted area on the impact surface (Abubakar et al., 2021). The same phenomenon was also observed in this test, in which the spread area of the droplet impact burr surface increased with the increase of droplet diameter.

By analyzing the spreading factor of droplets, it was found that the spreading factor of droplets gradually decreased with the increase of additive concentration. It was found that the number of droplets with bubbles increased after the addition of additives. The reason for the phenomenon of decreased spreading factor was the fact that the bubbles were generated from the liquid droplets. When generating droplets, the volume of the droplets increased when air entered the droplets. A bubble would be generated in the droplets, increasing the initial diameter of the droplets D_0. It was found that when the concentration of the additive increased, the surface tension of the droplets decreased and the number of droplets producing bubbles became larger, which led to a decrease in the spreading factor. For two droplets of the same mass, the droplet with bubbles could produce a larger spread area when it impacted the blade. This also verified the relationship between the spread area of droplets and the concentration of additives. The hydrodynamics of water droplets on surfaces with a different wettability was investigated, and it was found that droplets with a smaller diameter possess larger spreading factors (Khurana et al., 2019). In our test, it was observed that droplets with a lower velocity had larger diffusion factors. During the test, it was observed that larger droplets could easily form bubbles before impact, increasing the volume of droplets. As the droplet was pushed out of the mouth of the tube, the diameter of the area where the droplet was attached to the syringe gradually decreases. Then, after a small oscillation, the droplet would change to a flattened ellipsoidal shape. In this case, the droplet with a larger mass undergoes a greater shape change than the droplet with a lower mass. The change in droplet shape led to the increase in the contact area of the droplet with air and downward movement by gravity. This led to the increase in the possibility of air entering the droplet. The property of surface tension of such droplet tend to be minimized. The premise of air entering the droplet and forming bubbles was that the pressure generated by the gas inside the droplet and the pressure inside the droplet would be balanced between each other. According to the gas properties, the gas pressure was inversely related to the gas volume for the same mass of gas. Compared to droplets with a larger surface tension, droplets with a lighter surface tension would form larger bubbles inside the droplet.

5 Conclusion

In this work, the effect of droplets on the physicochemical properties of the impact burr surface was investigated. By observing the spreading process of droplets, various behaviors of droplets during impact were observed, including movement, spreading, retraction, and balance processes. By analyzing the physical properties, such as the surface tension of droplets and the energy conversion process of droplet diffusion, it was found that higher surface tension inhibits the diffusion process, reduces the retraction time of droplets, and increases the equilibrium time.

Impact velocity of droplet, droplet diameter, and additive concentration will positively affect the final spreading effect of droplets. ANOVA results presented that the additive concentration, droplet impact velocity, and droplet diameter had a significant correlation to the spread area of droplets. Concentration:velocity, concentration:diameter, velocity:diameter, and concentration:velocity:diameter interactions had a significant effect on the spread area of droplets. The spreading effect of droplets with a high concentration and high velocity was found to be better. It was also concluded that the droplets with a higher auxiliary concentration and larger diameter spread better. Velocity was also an important factor, but with a lower effect than the additive concentration and droplet diameter. The curve of surfactants reducing the surface tension of liquids shows a sharp drop and then levels off. This means that when applying pesticides, the addition of more additives can still have a better effect. However, choosing the best concentration in the application process can

significantly reduce droplet flow and spray drift, and also reduce the amount of surfactant. This study is relevant in guiding pesticide spraying.

Data availability statement

The original contributions presented in the study are included in the article/supplementary material. Further inquiries can be directed to the corresponding author.

Author contributions

PW, CL, LW, and HL contributed to conception and design of the study. PW provided the materials and instruments for the investigation. CX and PW organized the database. PW, CX, and QN performed the statistical analysis. CX wrote the first draft of the manuscript. PW, QN, and HL wrote sections of the manuscript. All authors contributed to manuscript revision, and read and approved the submitted version.

Funding

This research was funded by the National Natural Science Foundation of China, grant number 32001425 and 32201651; the Fundamental Research Funds for the Central Universities (SWU-KT22024); the Natural Science Foundation of Chongqing, China, grant numbers cstc2020jcyj-msxmX0414 and cstc2020jcyj-msxmX0459; and the Open Funding of the Key Laboratory of Modern Agricultural Equipment and Technology (Jiangsu University), grant numbers MAET202105.

Acknowledgments

The authors would like to thank Prof. Dr. Xinping Chen, Prof. Dr. Shouyong Xie, Dr. Dunyi Liu, Dr. Fanyi Liu, Mr. Linyun Chen, Ms. Yin Tang, and Mr. Shaolong Wang for technical support.

Conflict of interest

The authors declare that the research was conducted in the absence of any commercial or financial relationships that could be construed as a potential conflict of interest.

Publisher's note

References

Abubakar, A. A., Yilbas, B. S., A-Qahtani, M. H., Hassan, G., Yakubu, M., Bahatab, S., et al. (2021). Experimental and model studies of various size water droplet impacting on a hydrophobic surface. *J. Fluids Engineering-Transactions ASME.* 143 (6), 061402. doi: 10.1115/1.4049930

Abubakar, A. A., Yilbas, B. S., Hassan, G., Al-Qahtani, H., Ali, H., and Al-Sharafi, A. (2020). Droplet impacting on a hydrophobic surface: influence of surface wetting state on droplet behavior. *J. Fluids Engineering-Transactions ASME.* 142 (7), 071205. doi: 10.1115/1.4046559

Andrade, R., Skurtys, O., and Osorio, F. (2012). Experimental study of drop impacts and spreading on epicarps: effect of fluid properties. *J. Food Eng.* 109 (3), 430–437. doi: 10.1016/j.jfoodeng.2011.10.038

Appah, S., Jia, W., Ou, M., Wang, P., and Asante, E. A. (2020). Analysis of potential impaction and phytotoxicity of surfactant-plant surface interaction in pesticide application. *Crop Protection* 127, 104961. doi: 10.1016/j.cropro.2019.104961

Brewer, C. A., Smith, W. K., and Vogelmann, T. C. (1991). Functional interaction between leaf trichomes, leaf wettability and the optical-properties of water droplets. *Plant Cell Environment* 14 (9), 955–962. doi: 10.1111/j.1365-3040.1991.tb00965.x

Bukovac, M. J., Cooper, J. A., Whitmoyer, R. E., and Brazee, R. D. (2002). Spray application plays a determining role in performance of systemic compounds applied to the foliage of fruit plants. *Acta Horticulturae* 594, 65–75. doi: 10.17660/ActaHortic.2002.594.4

Cassie, A. B. D., and Baxter, S. (1944). Wettability of porous surfaces. *Trans. Faraday Society* 40, 546–551. doi: 10.1039/tf9444000546

de Oliveira, R. B., Precipito, L. M. B., Gandolfo, M. A., de Oliveira, J. V., and Lucio, F. R. (2019). Effect of droplet size and leaf surface on retention of 2,4-D formulations. *Crop Protection* 119, 97–101. doi: 10.1016/j.cropro.2019.01.015

Dong, X., Zhu, H. P., and Yang, X. J. (2015). Characterization of droplet impact and deposit formation on leaf surfaces. *Pest Manage. Sci.* 71 (2), 302–308. doi: 10.1002/ps.3806

Huet, O. D. Y., Massinon, M., De Cock, N., Forster, W. A., Zabkiewicz, J. A., Pethiyagoda, R., et al. (2020). Image analysis of shatter and pinning events on hard-to-wet leaf surfaces by drops containing surfactant. *Pest Manage. Sci.* 76 (10), 3477–3486. doi: 10.1002/ps.5796

Jia, W., Zhu, H., Dong, X., and Xue, F. (2013). Impact of spray droplet on soybean leaf surface. *Trans. Chin. Soc. Agric. Machinery* 44 (12), 87–93+113. doi: 10.6041/j.issn.1000-1298.2013.12.015.

Kang, F., Wu, X., Wang, Y., Zheng, Y., Li, S., and Cheng, C. (2021). Research progress and prospect of pesticide droplet deposition characteristics. *Trans. Chin. Soc. Agric. Eng.* 37 (20), 1–14. doi: 10.11975/j.issn.1002-6819.2021.20.001

Khurana, G., Sahoo, N., and Dhar, P. (2019). Phenomenology of droplet collision hydrodynamics on wetting and non-wetting spheres. *Phys. Fluids* 31 (7), 072003. doi: 10.1063/1.5103223

Krahmer, H., Walter, H., Jeschke, P., Haaf, K., Baur, P., and Evans, R. (2021). What makes a molecule a pre- or a post-herbicide - how valuable are physicochemical parameters for their design? *Pest Management Science* 77 (11), 4863–4873. doi: 10.1002/ps.6535

Kumar, S. S., Karn, A., Arndt, R. E. A., and Hong, J. R. (2017). Internal flow measurements of drop impacting a solid surface. *Experiments Fluids* 58 (3), 12. doi: 10.1007/s00348-016-2293-7

Lee, E., Chilukoti, H. K., and Muller-Plathe, F. (2021). Rebound suppression of a droplet impacting on a supersolvophobic surface by a small amount of polymer additives. *ACS Macro Letters* 10 (2), 192–196. doi: 10.1021/acsmacrolett.0c00808

Li, H., Travlos, I., Qi, L., Kanatas, P., and Wang, P. (2019). Optimization of herbicide use: study on spreading and evaporation characteristics of glyphosate-organic silicone mixture droplets on weed leaves. *Agronomy* 9 (9), 547. doi: 10.3390/agronomy9090547

Lin, J. L., Zhu, H., and Ling, P. (2019). Amendment of herbicide spray solutions with adjuvants to modify droplet spreading and fading characteristics on weeds. *Appl. Eng. Agricul.* 35 (5), 713–721. doi: 10.13031/aea.13339

Massinon, M., De Cock, N., Forster, W. A., Nairn, J. J., McCue, S. W., Zabkiewicz, J. A., et al. (2017). Spray droplet impaction outcomes for different plant species and spray formulations. *Crop Protection* 99, 65–75. doi: 10.1016/j.cropro.2017.05.003

Okunade, A. L. (2002). *Ageratum conyzoides* L. (Asteraceae). *Fitoterapia* 73 (1), 1–16. doi: 10.1016/s0367-326x(01)00364-1

Song, Y., Cao, C., Xu, B., Ran, G., Cao, L., Li, F., et al. (2019). Research progress on bouncing behavior and control technology of pesticide droplets at plant leaf surface. *Chin. J. Pesticide Sci.* 21 (Z1), 895–907. doi: 10.16801/j.issn.1008-7303.2019.0110

Song, Y., Huang, G., Zheng, L., Huang, Q., Cao, L., Zhao, P., et al. (2021). Polymer additives regulate the deposition behavior of pesticide droplets on target plants. *Polymer Testing* 93, 106958. doi: 10.1016/j.polymertesting.2020.106958

Travlos, I., Cheimona, N., and Bilalis, D. (2017). Glyphosate efficacy of different salt formulations and adjuvant additives on various weeds. *Agronomy* 7 (3), 60. doi: 10.3390/agronomy7030060

Xia, J., Latchininsky, A., Hadi, B., and Elkahky, M. (2022). Sustainable plant pest management through optimization and minimization. *Front. Agric. Sci. Eng.* 9 (1), 161–166. doi: 10.15302/j-fase-2021426

Xu, M., Li, X., Riseman, A., and Frostad, J. M. (2021). Quantifying the effect of extensional rheology on the retention of agricultural sprays. *Phys. Fluids* 33 (3), 032107. doi: 10.1063/5.0038391

Xu, L. Y., Zhu, H. P., Ozkan, H. E., Bagley, W. E., and Krause, C. R. (2011). Droplet evaporation and spread on waxy and hairy leaves associated with type and concentration of adjuvants. *Pest Manage. Sci.* 67 (7), 842–851. doi: 10.1002/ps.2122

Yan, X., Zhang, L., Sett, S., Feng, L., Zhao, C., Huang, Z., et al. (2019). Droplet jumping: effects of droplet size, surface structure, pinning, and liquid properties. *ACS Nano.* 13 (2), 1309–1323. doi: 10.1021/acsnano.8b06677

Zhang, Y., Liu, B., Huang, K., Wang, S., Quirino, R. L., Zhang, Z., et al. (2020). Eco-friendly castor oil-based delivery system with sustained pesticide release and enhanced retention. *ACS Appl. Mater. Interfaces* 12 (33), 37607–37618. doi: 10.1021/acsami.0c10620

frontiers | Frontiers in Plant Science

TYPE Original Research
PUBLISHED 08 September 2023
DOI 10.3389/fpls.2023.1250773

OPEN ACCESS

EDITED BY
Xiaolan Lv,
Jiangsu Academy of Agricultural Sciences (JAAS), China

REVIEWED BY
Baohua Zhang,
Nanjing Agricultural University, China
Bingbo Cui,
Jiangsu University, China

*CORRESPONDENCE
Changyuan Zhai
zhaicy@nercita.org.cn
Liping Chen
chenlp@nercita.org.cn

RECEIVED 30 June 2023
ACCEPTED 10 August 2023
PUBLISHED 08 September 2023

CITATION
Dou H, Zhai C, Zhang Y, Chen L, Gu C and Yang S (2023) Research on decoupled air speed and air volume adjustment methods for air-assisted spraying in orchards. *Front. Plant Sci.* 14:1250773. doi: 10.3389/fpls.2023.1250773

Research on decoupled air speed and air volume adjustment methods for air-assisted spraying in orchards

Hanjie Dou[1,2,3], Changyuan Zhai[1,2]*, Yanlong Zhang[1], Liping Chen[1,2]*, Chenchen Gu[1] and Shuo Yang[3]

[1]Intelligent Equipment Research Center, Beijing Academy of Agriculture and Forestry Sciences, Beijing, China, [2]National Engineering Research Center of Intelligent Equipment for Agriculture, Beijing, China, [3]National Engineering Research Center for Information Technology in Agriculture, Beijing, China

Different fruit tree canopies have different requirements for air speed and air volume. Due to the strong relationship between air speed and air volume, the decoupled control of air speed and air volume cannot be achieved using the existing sprayers. In this study, an innovative air-assisted sprayer that supports the independent adjustment of fan speed (0-2940 r/min) and air outlet area (1022.05-2248.51 cm^2) is developed, and the maximum air speed and air volume of the sprayer outlet are 45.98 m/s and 37239.94 m^3/h, respectively. An independent adjustment test of the fan speed and air outlet area was carried out. The results indicated that the fan speed and air outlet area have opposing adjustment effects on air speed and air volume; decoupled control of the outlet air speed and air volume can thus be achieved through combined control of the fan speed and air outlet area. A test was carried out on combined fan speed and air outlet area control. Two decoupled air speed and air volume adjustment models were established, one with a constant air speed and variable air volume and the other with a constant air volume and variable air speed. The test results show that the air volume adjustment model with constant air speed had a maximum mean error of 1.13%, and the air speed adjustment model with constant air volume had a maximum mean error of 1.67%. The results will provide theoretical and methodological support for the development of airflow adjustment systems for orchard air-assisted sprayer.

KEYWORDS

orchard, precision spraying, air speed, air volume, decoupled control

1 Introduction

The global fruit industry has become the third-largest agricultural planting industry after the grain and vegetable industries. By 2020, the area of orchards in China had reached 1.33×10^7 hm^2 (Zheng et al., 2020; Wei et al., 2023), ranking first in the world. Orchard pest control has long relied on chemical pesticides. According to statistics, 66-90% of fruit crops can be lost without pesticides (Mahmud et al., 2021b). The application rate of pesticides per unit area in China is considerably higher than the world average. Excessive application of pesticides not only wastes pesticides and causes environmental pollution but also greatly threatens the safety of agricultural products (Gil et al., 2014; Manandhar et al., 2020; Zheng and Xu, 2021). To improve the pesticide use efficiency, orchard precision spraying technology has gradually emerged in recent years. Orchard precision spraying refers to the target-oriented variable-rate application of pesticides through the online detection of the target characteristics and disease characteristics of orchards with sensor systems, the calculation of the pesticide dose and airflow requirements for air-assisted spraying according to the detected characteristics, and the variable adjustment of the pesticide dose and airflow supply (He, 2020).

Orchard air-assisted precision spraying requires on-demand pesticide dose control technology and on-demand airflow adjustment technology. Scholars worldwide have conducted considerable research regarding on-demand pesticide dose control, explored target orchard spraying control technology (Salcedo et al., 2021; Warneke et al., 2021; Dou et al., 2022) and developed variable adjustment models and methods (such as pipe and nozzle flow or the direct-injection flow of liquid pesticides) based on pressure, travel speed and pulse width modulation (PWM) to potentially solve the key theoretical and methodological problems of dose demand-based variable spraying control (Shen et al., 2017; Grella et al., 2022). However, there are few related studies of the on-demand control of airflow. Airflow includes three elements: air speed, air volume and airflow direction. For the current airflow adjustment devices, the airflow is mainly adjusted by changing the fan speed, the air inlet area, the air outlet area, the inclination angle of the deflector and the inclination angle of the air outlet (Zhai et al., 2018a). The fan speed, air inlet area, and air outlet area can be adjusted by changing the air speed and air volume at the air outlet. Professor Lander at Cornell University in the United States started research on airflow adjustment technology as early as 2010. By adding louvres at the air outlet of an air-assisted sprayer to change the airflow and integrating infrared target technology into the device, Landers (2010) and Khot et al. (2012) developed a sprayer that can control air speed and air volume according to the profile information of the fruit tree canopy and found that the use of air louvres resulted in a 30% increase in deposition and a 75% reduction in drift during trials in apple orchards. Qiu et al. (2016) adjusted the airflow by changing the fan speed to study the effects of airflow on deposition and drift. Hołownicki et al. (2017) designed a variable air volume system with a variable fan blade angle and fan speed and developed a target orchard sprayer with an adjustable air volume. Doruchowski et al. (2011a) ; Doruchowski et al. (2011b) successfully adjusted the air speed and air volume by changing the openings of the air inlet and outlet. Li et al. (2017) designed an orchard air-assisted sprayer for which the air volume can be adjusted according to an empirical parameter formula. Mahmud et al. (2021a); Mahmud et al. (2022) designed an orchard air-assisted sprayer with a variable air inlet area, used light detection and ranging (LiDAR) to obtain characteristic information from the fruit tree canopy, established an equation describing the relationship between the laser point cloud and the airflow demand, and realized online airflow adjustment. The inclination angles of the deflector and air outlet mainly influence the airflow direction, and Pai et al. (2009) successfully adjusted the outlet airflow direction by changing the inclination angle of the deflector. Osterman et al. (2013) designed a LiDAR-based orchard air-assisted sprayer with variable dimensions, and the position of the spray arm could be adjusted in real time according to the canopy feature information obtained by LiDAR; thus, the position of the air outlet of the bellows could be changed to achieve airflow adjustment at different canopy positions. Jiang et al. (2020) designed an air volume control system for an orchard multipipe air sprayer by installing a butterfly valve at each air outlet duct position to control the backflow ratio of the outlet air volume; they experimentally demonstrated that spraying with variable air volumes can improve canopy deposition by 17.3%, reduce deposition below the canopy and in gaps by 21.6% and 40.7%, respectively, and reduce airborne drift by 50.9%. Xu et al. (2013) and Zhai et al. (2018b) designed an orchard air-assisted sprayer with an adjustable spray height, and airflow adjustment was achieved by changing the inclination angle of the bellows.

In summary, most existing airflow adjustment devices only have a single adjustment mode, but due to the coupled relationship between the adjustment of air speed and air volume, these devices fail to provide independent adjustments for air speed and air volume. Different fruit trees require different combinations of air speed and air volume. In orchard air-assisted spraying, there are obvious differences in the canopy in different growth periods and for types of fruit trees. To improve the spray deposition in the canopy and reduce the spray drift in nontarget areas, differentiated canopies have different requirements for air speed and air volume at the sprayer outlet. For example, a canopy with dense branches and leaves but a small volume generally requires a high air speed and a low air volume, whereas a canopy with sparse branches and leaves but a large volume requires a low air speed and a high air volume. Therefore, the on-demand adjustment of airflow requires the decoupled control of air speed and air volume, which requires the online detection and calculation of the air speed and air volume demands of fruit trees to control the air supply actuator in real time and select the appropriate airflow, such that after the airflow loss in the conveying space, the pesticide can be delivered into the fruit tree canopy with the correct amount of airflow.

The objective of this study was to propose a method for the decoupled control of air speed and air volume at the sprayer outlet, and it could meet the air speed and air volume requirements of fruit trees with different combinations of canopy volume and branch/leaf density. Given that the independent adjustment of air speed and air volume cannot be achieved using the existing single-control-mode airflow adjustment devices, we designed an innovative airflow adjustment sprayer that supports the independent adjustment of

the fan speed and air outlet area. Based on this sprayer, we carried out airflow adjustment experiments and obtained the variation characteristics of air speed and air volume at the air outlet under two independent adjustment modes. Based on the opposing adjustment effects of fan speed and air outlet area on air speed and air volume, we proposed a method for the decoupled control of the outlet air speed and air volume of the bellows. This study will provide theoretical and methodological support for research on and the development of airflow adjustment sprayers for orchards.

2 Materials and methods

2.1 Design of an air-assisted sprayer for orchards

To realize the independent adjustment of fan speed and air outlet area and to facilitate subsequent research on methods for the decoupled control of air speed and air volume, an airflow adjustment sprayer was designed, as shown in Figure 1. The sprayer mainly consists of a fan speed adjustment device, an air outlet adjustment device, a spray system, LiDAR (LMS10100, SICK Ltd, Germany), a speed measuring device, a power system, a control system and a crawler chassis. The sprayer fan (CSF-660, Tianjin Cheng En Technology Co., Ltd, China) is an axial flow fan commonly used for orchard air-assisted spraying. The fan is connected to an AC motor (YE2-160M2-2, Tianjin Jin Rong Electromechanical Co., Ltd, China) by a belt, and the fan speed can be controlled from 0 to 2940 r/min by adjusting the motor speed. The back plate of the fan is connected to the air duct through six sliding bearings. The sliding bearings not only support the weight of the air duct but also allow relative movement between the bearing nut fixed on the air duct and the back plate. A linear actuator (12-150-50, Leicester Nuo (Dongtai) Transmission Machinery Manufacturing Co., Ltd, China) and a displacement sensor (KPM18, Shenzhen Milang Technology Co., Ltd, China) are installed between the back plate and the air duct. The movement of the linear actuator causes the sliding bearings to move, which in turn causes the air duct to move, such that the opening of the air outlet changes from 5 to 11 cm, corresponding to an air outlet area variation ranging from 1022.05 to 2248.51 cm^2. The spray system is used for pesticide application. To facilitate the subsequent on-demand control of the pesticide dose, a pressure regulation device and a PWM control solenoid valve (YCH41, Yuyao yongchuang solenoid valve co., ltd, China) are added to the system to support the adjustment of the system spraying pressure and single-nozzle flow. LiDAR can obtain information on fruit tree canopy features (position, volume, leaf area density, etc.) in real time to provide a basis for the online control of the airflow and pesticide dose. The control system is used to control the movement of the crawler chassis, the operation of the spraying system and the adjustment of the fan speed and air outlet area, thus ensuring the stable operation of the test platform in accordance with the control requirements.

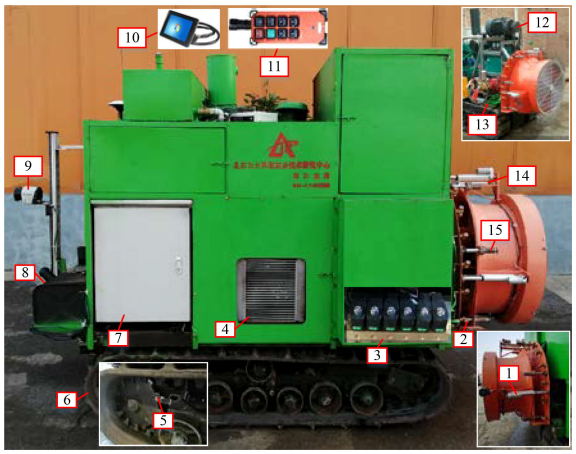

FIGURE 1
Orchard air-assisted sprayer that supports the independent adjustment of fan speed and air outlet area.

1. Linear actuator 2. Nozzle 3. Solenoid valve 4. Radiator 5. Speed sensor 6. Track chassis 7. Control cabinet 8. Fuel tank 9. LiDAR 10. PC 11. Remote control unit 12. Fan-driven motor 13. Spraying system 14. Displacement sensor 15. Slide bearing

2.2 Checking the airflow adjustment system

2.2.1 Fan speed adjustment

To accurately control the fan speed, it is necessary to clarify the relationship between the converter output frequency and fan speed. The converter output frequency was set to 15, 20, 25, 30, 35, 40 or 45 Hz, and the fan speed was measured with a noncontact laser induction tachometer (TM680, Mitutoyo, Japan) at the connection between the fan and the AC motor. The recorded data for the converter output frequency and fan speed were fitted to obtain the corresponding relationship equation, as shown in Figure 2. The maximum fan speed was 2923 r/min, the R^2 of the equation was 0.9998, and the linearity between the converter output frequency and the fan speed was good; thus, the control requirements were met.

2.2.2 Air outlet area adjustment

The fan outlet is a ring structure, and the air outlet area is equivalent to the sum of the areas of two rectangles and one arc. The air outlet area changes with the size of the opening, as shown in Figure 3. The air outlet area is calculated with Formula (1).

$$S_{OUT} = 2hl + \frac{\pi dal}{360} \quad (1)$$

where S_{OUT} is the air outlet area of the fan (cm^2), l is the size of the opening of the air outlet (cm), h is the height of the rectangular area of the air outlet (cm, set to 23.5 cm), d is the diameter of the arc area of the air outlet (cm, set to 90 cm), and a is the arc angle of the arc area of the air outlet (in degrees, set to 200.52°).

The air outlet adjustment device is controlled by three linear actuators, and the maximum moving speed is 80 mm/s. During the adjustment process, if the moving distances of the linear actuators are not synchronized, the air outlet will be inclined, which affects the distribution of air speed and air volume at the air outlet. Additionally, a

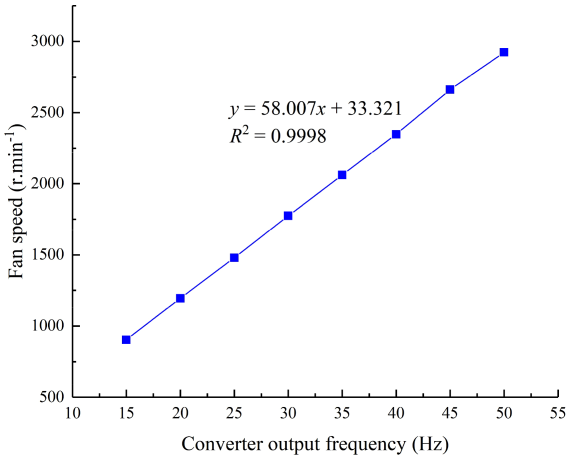

FIGURE 2
Relationship between the converter output frequency and fan speed.

large displacement deviation of the three linear actuators may cause deformation of the fan air duct or damage to the linear actuators. To reduce the synchronization error in the adjustment process, differential control is introduced to the control program, the displacements of the linear actuators are monitored in real time by the displacement sensor, and the deviation is corrected. The flow chart of air outlet area adjustment is shown in Figure 4. Due to the influence of the weight of the fan, the middle position of the fan is directed slightly downwards. When adjusting the system, the moving speed of the middle linear actuator is set to be 5 mm/s more than that of the linear actuators on the left and right sides. Overall, the adjustment error of the air outlet opening varies within the range of 5-8 mm.

2.3 Pneumatic conveying system adjustment test

2.3.1 Measurement of air speed at the fan outlet

Because the nozzles at the fan outlet are positioned at equal intervals, one air speed measurement point is set at each nozzle position at the fan outlet, and the centre of the air velocity transducer probe is located at the outermost edge of the nozzle. A soft blue ribbon of a certain length is used at each nozzle position to determine the airflow direction at that position (Hoheisel et al., 2021), and this information is used to measure the air speed at each nozzle position with an air velocity transducer (8455-300, TSI, USA), as shown in Figure 5. The air velocity transducer is characterized by a speed measurement range of 0-50 m/s, an airflow response time of 0.2 s, and a measurement error of ±2%.

2.3.2 Tests of the airflow variation characteristics

To obtain the airflow variation characteristics at the fan outlet during the independent control of fan speed and outlet area, a test of the airflow variation characteristics of the pneumatic conveying system under independent adjustment was designed. In the test of the independent adjustment of fan speed, the air outlet area was set to 2248.51 cm^2, the converter output frequency of the fan drive motor was set in the range of 15-50 Hz, and the fan speed was adjusted once every 5 Hz. In the test of the independent adjustment of the air outlet area, the air speed was set to 936 r/min, the linear actuator was set in the range of 5-11 cm, and the air outlet area was adjusted once every 1 cm. The air speed measurement method shown in Figure 5 was used to measure the air speeds at the 14 nozzle positions at the fan outlet. Each test was repeated three times, and the test data were recorded.

2.3.3 Tests of the combined control of fan speed and air outlet area

To achieve changes in the outlet air speed and air volume under the combined control of fan speed and outlet area, decoupled air speed and air volume adjustment models were established, and a test for the combined control of fan speed and air outlet area was designed. During the test, the fan speed and the outlet area were controlled with the airflow adjustment sprayer, and variations within the ranges shown in Table 1 were achieved. The air speed at the outlet was measured using the air speed measurement method shown in Figure 5. Each combination of parameters was tested three times, and a total of 49 tests were conducted to obtain 2058 air speed data points. The average value of the three test results at each nozzle position was used as the final air speed at that position. The average value of the air speed at each nozzle position was multiplied by the air outlet area to obtain the outlet air volume.

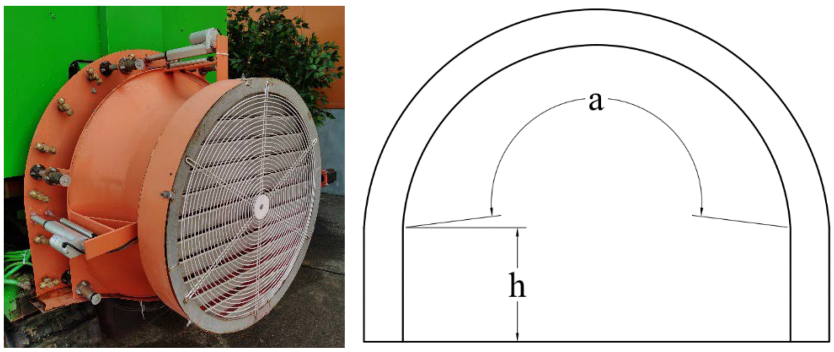

FIGURE 3
Schematic diagram of the air outlet area calculation.

10.3389/fpls.2023.1250773

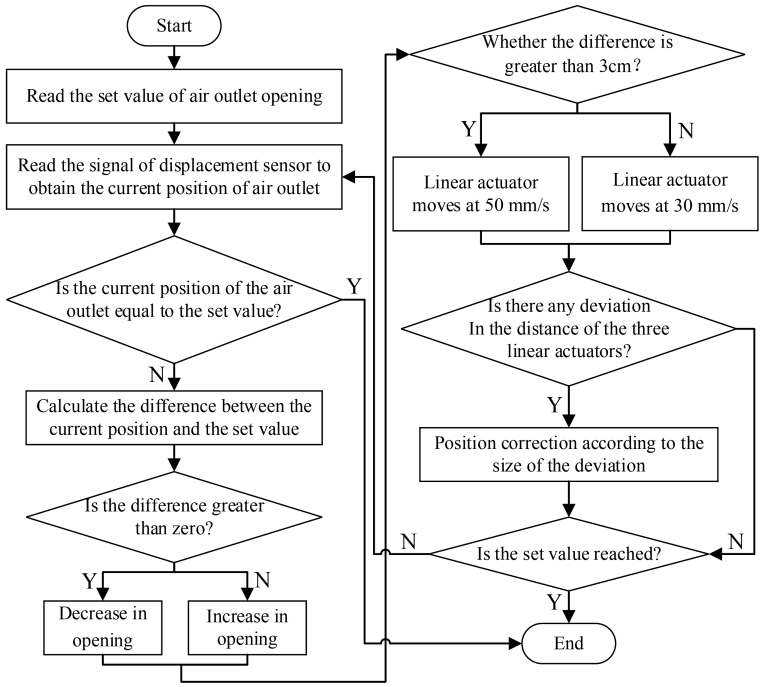

FIGURE 4
Flow chart of air outlet area adjustment.

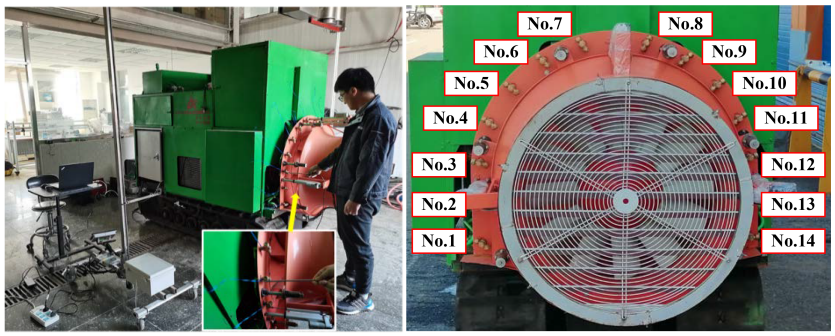

FIGURE 5
Air speed measurement for fan outlet **(A)** Measurement of air speed at the fan outlet **(B)** Nozzle number.

2.3.4 Verification tests of the decoupled air speed and air volume adjustment models

For the established air volume adjustment model with constant air speed and the air speed adjustment model with constant air volume, model verification tests were designed, and the test parameters are shown in Table 2. In the verification test of the air volume adjustment model with constant air speed, for each constant air speed value, five groups of air volume values were randomly selected within the allowable adjustment range of the air volume, and the fan speed and the air outlet area were calculated.

TABLE 1 Combined adjusted test parameters for the fan speed and air outlet area.

Adjusted parameters	Adjusted values						
Fan speed ($r.min^{-1}$)	904	1195	1480	1775	2062	2348	2662
Air outlet area (cm^2)	1022.05	1226.46	1430.87	1635.28	1839.69	2044.10	2248.51

TABLE 2 Parameters of the validation test for the decoupled air speed and air volume adjusment models.

Adjustment model	Constant values of the air speed ($m.s^{-1}$)	Values of the air volume ($m^3.h^{-1}$)				
Variable air volume with constant air speed	15.66	8200.00	9800.00	11000.00	12000.00	12500.00
	19.53	9000.00	10000.00	12000.00	14000.00	15000.00
	23.39	10000.00	13000.00	14000.00	16000.00	18000.00
	27.25	11000.00	13000.00	14000.00	16000.00	19000.00
	31.11	12000.00	13000.00	14000.00	16000.00	19000.00
	34.98	15000.00	18000.00	20000.00	24000.00	26000.00
	38.84	16000.00	19000.00	22000.00	24000.00	26000.00
Adjustment model	**Constant values of the air volume ($m^3.h^{-1}$)**	**Values of the air speed ($m.s^{-1}$)**				
Variable air speed with constant air volume	8012.50	13.00	14.00	16.00	18.00	21.00
	11325.00	16.00	17.00	19.00	21.00	23.00
	14637.50	20.00	22.00	25.00	30.00	35.00
	17950.00	24.00	26.00	30.00	34.00	40.00
	21262.50	27.00	29.00	31.00	33.00	35.00
	24575.00	31.00	33.00	35.00	37.00	39.00
	27887.50	35.00	36.00	37.00	38.00	39.00

The fan speed and the air outlet area were adjusted with the airflow adjustment sprayer. The outlet air speed under each combination of fan speed and air outlet area was measured and multiplied by the air outlet area at the corresponding position to obtain the air volume. The calculated air volume was compared with the actual measured air volume to obtain the adjustment error of the model under different combinations of parameter values. Using the same method, a verification test for the air speed adjustment model with a constant air volume was performed.

3 Results and analysis

3.1 The airflow variation characteristics of the pneumatic conveying system

Based on the outlet air speed and air volume data obtained in the test of the airflow variation characteristics of the pneumatic conveying system under the independent adjustment of fan speed and air outlet area, Origin software (OriginLab Corporation, USA) was used to generate plots of the changes in the outlet air speed and air volume during the independent adjustment of the fan speed and air outlet area, as shown in Figure 6.

Figure 6 demonstrates that the maximum air speed and air volume of the sprayer outlet are 45.98 m/s and 37239.94 m^3/h, respectively, and with increasing fan speed, the outlet air speed and air volume increase continuously. As the air outlet area increases, the outlet air speed continues to decrease, but the air volume continues to increase. The results indicate that changing the fan speed influences the outlet air speed and air volume in the same way, whereas changing the air outlet area effects the air speed and air volume in opposing ways. The decoupled method with constant air speed and variable air volume and the decoupled method with constant air volume and variable air speed can be achieved through the combined control of the fan speed and air outlet area to meet the air speed and air volume requirements for canopies of different fruit tree species in different growth periods.

3.2 Decoupled air speed and air volume adjustment model

3.2.1 The air volume adjustment model with constant air speed

Through an analysis of the test data for the combined control of fan speed and outlet area, the data for the sprayer outlet air speed under different combinations of fan speed and air outlet area were obtained, as shown in Table 3.

Origin software was used to process and analyse the obtained outlet air speed data and to fit the two-dimensional relationships between the outlet air speed and the fan speed and air outlet area, as shown in Figure 7.

Figure 7 indicates that under combined fan speed and air outlet area control, the changes in the outlet air speed correspond to constant air speeds, as indicated by the contours. For each contour line, the relationship between the fan speed and the air outlet area is approximately linear. As the air outlet area increases, the fan speed increases such that the two are directly proportional, and the slope of the contour line changes in different sections. A change in the air outlet area causes a change in the outlet air volume, thereby

10.3389/fpls.2023.1250773

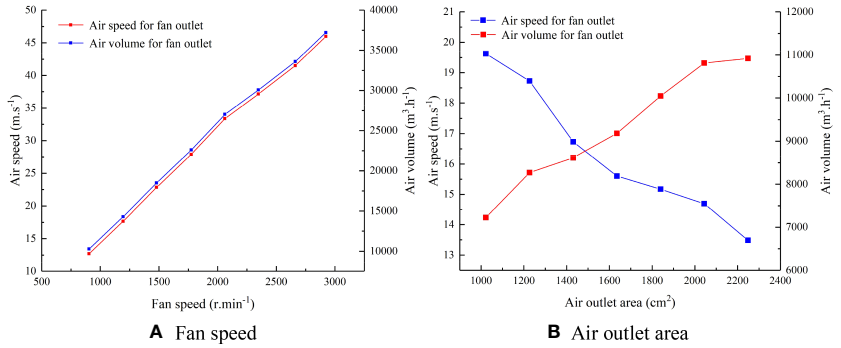

FIGURE 6
Air speed and air volume changes during the independent adjustment of the fan speed and air outlet area **(A)** Fan speed **(B)** Air outlet area.

realizing the control of the air volume at a constant air speed. The fan speed and outlet area data for the contour lines were extracted to obtain the mathematical relationships between the fan speed and the outlet area under different constant values of air speed. Based on these relationships, the mathematical equations for the fan speed and air outlet area in terms of air speed and air volume were obtained, as shown in Equation (2). The equation coefficients and R^2 values corresponding to different constant values of air speed are shown in Table 4.

$$\begin{cases} S_{OUT} = 2.778 \frac{AirVolume_{Bellow}}{AirSpeed_{Bellow}} \\ Speed_{Fan} = a_1 \frac{AirVolume_{Bellow}}{AirSpeed_{Bellow}} + a_2 \end{cases} \quad (2)$$

In the equations above, $AirVolume_{\mathrm{Bellow}}$ is the outlet air volume of the bellows (m^3/h), $AirSpeed_{\mathrm{Bellow}}$ is the outlet air speed of the bellows (m/s), S_{OUT} is the air outlet area (cm^2), $Speed_{\mathrm{Fan}}$ is the fan speed (r/min), and a_1 and a_2 are the coefficients of the fan speed and outlet air volume equations, respectively.

3.2.2 The air speed adjustment model with constant air volume

Based on the approach in subsection 3.2.1, the outlet air speed obtained for different combinations of fan speed and outlet area adjustment was multiplied by the air outlet area at the corresponding position to obtain the outlet air volume, as shown in Table 5.

The same data processing method as in Section 3.2.1 was used. Origin software was used to analyse the outlet air volume data and to fit the two-dimensional relationships between the outlet air volume and the fan speed and air outlet area, as shown in Figure 8.

Figure 8 demonstrates that under the combined fan speed and air outlet area control, increases in the fan speed and air outlet area lead to an increase in the outlet air volume, and contour lines corresponding to constant air volumes can be observed. For each contour line, as the air outlet area increases, the fan speed decreases, and the two are inversely proportional; along the same contour line, a higher fan speed and a smaller air outlet area produce a more gradual contour change. The data processing method in Section 3.2.1 was used to establish the equations for fan speed and air outlet area based on the air speed and air volume, as shown in Equation 3. The coefficients and R^2 values of the equations for different constant values of the air volume are shown in Table 6.

$$\begin{cases} S_{OUT} = 2.778 \frac{AirVolume_{Bellow}}{AirSpeed_{Bellow}} \\ Speed_{Fan} = c_1 \frac{AirVolume_{Bellow}}{AirSpeed_{Bellow}} + c_2 \end{cases} \quad (3)$$

where $AirVolume_{\mathrm{Bellow}}$ is the outlet air volume at the bellows (m^3/h), $AirSpeed_{\mathrm{Bellow}}$ is the outlet air speed at the bellows (m/s),

TABLE 3 Air speed change at the sprayer outlet achieved by adjusting the fan speed and air outlet area.

Fan speed (r.min^{-1})	Air speed at fan outlet (m.s^{-1})						
	Air outlet area (cm^2)						
	1022.05	1226.46	1430.87	1635.28	1839.69	2044.10	2248.51
904	13.02	12.91	12.89	12.65	12.36	12.03	11.89
1195	18.21	17.88	17.06	17.00	16.75	16.60	16.27
1480	23.35	23.01	22.34	21.97	21.26	20.94	20.68
1775	28.31	27.79	27.20	26.66	26.08	26.01	25.70
2062	34.53	33.37	31.90	31.72	30.70	30.65	30.64
2348	38.05	37.98	36.62	36.26	36.20	35.71	35.31
2662	42.62	42.02	40.92	40.31	40.18	39.52	38.51

10.3389/fpls.2023.1250773

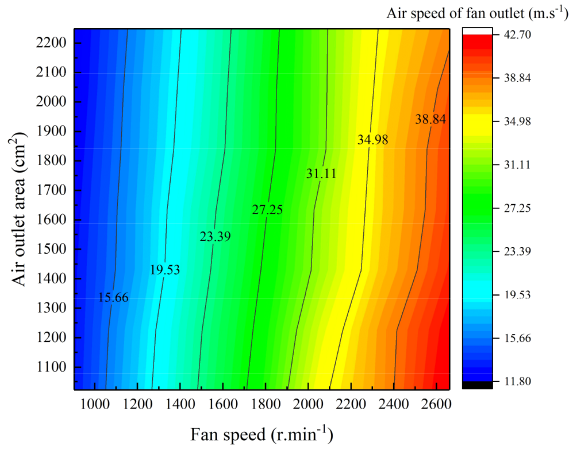

FIGURE 7
Air speed changes resulting from fan speed and air outlet area adjustments.

S_{OUT} is the air outlet area (cm^2), $Speed_{Fan}$ is the fan speed (r/min), and c_1 and c_2 are the coefficients of the fan speed and outlet air speed equations, respectively.

3.3 Verification of the control accuracy of the models

By analysing the verification test data for the decoupled air speed and air volume adjustment models, the control errors of the models under different combinations of fan speed and air outlet area were obtained, the average measurement error for each combination was determined, and the average measurement errors of all combinations were averaged to obtain the control error of each model, as shown in Table 7.

The air volume adjustment model with constant air speed displayed a maximum average error of 1.13% under different constant values of air speed. The air speed adjustment model with constant air volume control exhibited a maximum average error of 1.67% under different constant values of air volume. For the two control modes, the model control error was in the range of 0-2%. Therefore, the models were highly accurate.

4 Discussions

Most existing airflow adjustment sprayers only have a single adjustment mode, but due to the coupled relationship between the adjustments to air speed and air volume, these sprayers fail to achieve independent adjustment of air speed and air volume. The sprayer designed in this paper supports two control modes, fan speed and outlet area, which makes it possible to realize the decoupled control of air speed and air volume at the sprayer outlet. Based on the designed airflow adjustment sprayer, airflow adjustment experiments based on the independent adjustment of the fan speed and outlet area were carried out. The results showed that variable fan speed and variable outlet area had different control effects on the air speed and air volume at the sprayer outlet, and the

TABLE 4 Coefficients of the fan speed and air volume at the fan outlet and the corresponding R^2 values.

Parameters	Air speed of fan outlet ($m.s^{-1}$)						
	15.66	19.53	23.39	27.25	31.11	34.98	38.84
a_1	0.229	0.318	0.377	0.362	0.463	0.518	0.605
a_2	969.7	1153.3	1345.4	1587.8	1748.7	1930.2	2174.2
R^2	0.9825	0.9843	0.9798	0.9602	0.9244	0.9479	0.9573

TABLE 5 Air volume change at the fan outlet achieved by adjusting the fan speed and air outlet area.

Fan speed ($r.min^{-1}$)	Air volume at the fan outlet ($m^3.h^{-1}$)						
	Air outlet area (cm^2)						
	1022.05	1226.46	1430.87	1635.28	1839.69	2044.10	2248.51
904	4790.82	5698.20	6642.02	7444.54	8187.30	8851.01	9623.37
1195	6700.15	7893.53	8787.10	10007.91	11090.97	12217.64	13171.13
1480	8592.93	10157.30	11509.10	12935.44	14083.09	15409.24	16737.39
1775	10416.06	12270.63	14009.98	15693.50	17272.48	19140.13	20800.90
2062	12703.06	14733.71	16434.32	18674.01	20331.78	22554.07	24798.50
2348	13999.78	16767.25	18865.65	21345.45	23975.31	26274.45	28578.11
2662	15682.31	18554.80	21075.86	23731.37	26609.80	29083.92	31170.13

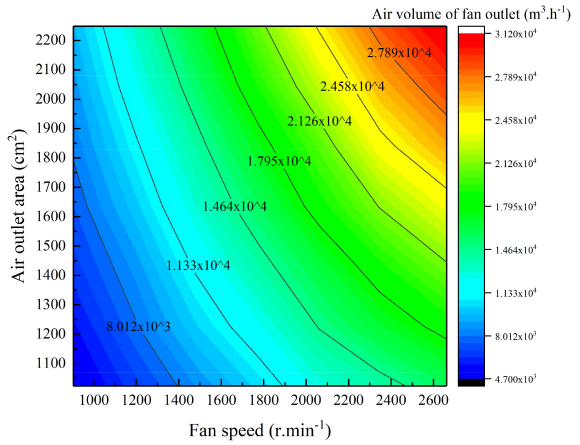

FIGURE 8
Air volume change resulting from fan speed and air outlet area adjustment.

decoupled control of the air speed and air volume was achieved through the combined control of the fan speed and outlet area; this approach provides a new research idea for the decoupled control of the air speed and air volume in orchard air-assisted spraying.

Through the combined control experiments, decoupled control models of air speed and air volume with constant air speed and variable air volume and with constant air volume and variable air speed were established. The control error of the two decoupled models was in the range of 0-2%, and the models displayed high control accuracy. However, due to the limitation of orchard spraying scenario for two decoupled models, the verification tests of the models were only carried out in the laboratory. The decoupled control models were for the subsequent research and development of the airflow online on-demand adjustment system based on orchard tree target characteristics (canopy volume, leaf area, etc.). The adjustment values of air speed and air volume are calculated according to the orchard tree target characteristics, and they are the values of air speed and air volume from generation to propagation to canopy position. However, the response delay of the airflow adjustment device itself, the propagation time of airflow from fan outlet to fruit tree canopy and the influence of natural wind on airflow propagation trajectory will have an impact on the control accuracy of airflow online on-demand adjustment system. In the future, orchard verification tests design for the decoupled control models, the above factors should be considered, and the decoupled control model of air speed and air volume proposed in this paper should be evaluated more reasonably combined with practical orchard spraying scenario.

The two decoupled models can meet the different requirements for air speed and air volume of the differentiated canopies. When the density of the fruit tree canopy does not change significantly but the canopy volume does change significantly, it is necessary to adjust the air volume at a constant air speed to achieve the best pesticide application. For example, during the period from germination to the first leaf stage for grapevines and standardized densely planted dwarf apple trees, the density of canopy branches and leaves does not change significantly, but the canopy volume changes considerably. However, when the volume of the fruit tree canopy does not change significantly but the density of the fruit tree canopy does change significantly, orchard air-assisted spraying requires a constant outlet air volume and a variable air speed. For example, the canopy contours of apple trees and peach trees are formed during the period from the complete growth of new leaves to the fruiting period; during the leaf growth period of apple trees and peach trees, the canopy volume changes little, but the canopy leaf area changes substantially. The decoupled control model provides a mathematical support for overcoming the key bottleneck of on-demand airflow control during air-assisted spraying and promoting the application of precision spraying technology for orchards. The research team has broken through the online detection models of tree canopy volume and leaf area (Gu et al., 2022; Wang et al., 2023), and the airflow online on-demand adjustment system based on orchard tree target characteristics will be developed in the future.

5 Conclusions

In this study, an innovative airflow adjustment sprayer that supports the independent adjustment of fan speed (0-2940 r/min) and air outlet area (1022.05-2248.51 cm^2) is developed, and the control ranges of the maximum air speed and air volume at the air outlet of the sprayer are 45.98 m/s and 37239.94 m^3/h, respectively. Based on the sprayer, independent control tests of fan speed and air outlet area were carried out. The results showed that changes in the fan speed and air outlet area have opposing effects on the air speed and air volume, and the decoupled control of the air speed and air volume can be achieved through the combined control of the fan speed and air outlet area, thus providing a new research concept for the decoupled control of the air speed and air volume at the sprayer outlet.

TABLE 6 Coefficients of the fan speed and air speed at the fan outlet and the corresponding R^2 values.

Parameters	Air volume at the fan outlet ($m^3.h^{-1}$)						
	8012.5	11325.0	14637.5	17950.0	21262.5	24575.0	27887.5
c_1	-1.724	-1.892	-2.499	-2.809	-2.835	-2.899	-3.398
c_2	1991.2	2494.2	3217.0	3733.9	4047.9	4370.9	5034.7
R^2	0.9820	0.9614	0.9440	0.9589	0.9679	0.9709	0.9960

TABLE 7 Model validation error in air volume adjustment for a constant air speed.

Variable air volume with constant air speed		Variable air speed with constant air volume	
Constant air speed ($m.s^{-1}$)	Average error (%)	Constant air volume ($m^3.h^{-1}$)	Average error (%)
15.66	1.13	8012.50	1.34
19.53	0.64	11325.00	1.02
23.39	0.57	14637.50	1.12
27.25	0.48	17950.00	1.22
31.11	0.33	21262.50	1.67
34.98	1.00	24575.00	0.50
38.84	0.38	27887.50	0.41

Decoupled airflow control tests were carried out by adjusting the fan speed and outlet area to control the air speed and air volume at the sprayer outlet in different ranges of combinations. Two decoupled air speed and air volume adjustment models (one with constant air speed and variable air volume and the other with constant air volume and variable air speed) were established by the contour line fitting of the outlet air speed and air volume data obtained for different combinations of fan speed and air outlet area. The model validation test results show that the air volume adjustment model with constant air speed had a maximum mean error of 1.13% and that the air speed adjustment model with constant air volume had a maximum mean error of 1.67%. The model with constant air speed and variable air volume is suitable for spraying scenarios in which the density of the fruit tree canopy does not change significantly but the canopy volume does change significantly, and the model with constant air volume and variable air speed is suitable for spraying scenarios in which the canopy volume does not change significantly but the density of the fruit tree canopy does change significantly. The results of this study provide theoretical and methodological support for research on and the development of airflow adjustment systems and sprayers for orchard air-assisted spraying.

Data availability statement

The original contributions presented in the study are included in the article/supplementary material. Further inquiries can be directed to the corresponding authors.

Author contributions

HD, CZ and LC: conceptualisation, validation, investigation and methodology. HD, SY and YZ: software and visualisation. HD, YZ and SY: formal analysis. HD, CZ and CG: data curation. GC and CZ: resources and supervision. HD and CZ: writing—original draft preparation. HD, CZ and LC: writing—review and editing and funding acquisition. CZ: project administration. All authors contributed to the article and approved the submitted version.

Funding

This work was financially supported by the National Key Research and Development Plan Project (grant number: 2022YFD2001402), the Natural Science Foundation of China (grant number: NSFC31971775), the Postdoctoral Science Foundation of Beijing Academy of Agriculture and Forestry Sciences (grant number: 323256) and the Outstanding Scientist Program of Beijing Academy of Agriculture and Forestry Sciences (grant number: jkzx202212).

Conflict of interest

The authors declare that the research was conducted in the absence of any commercial or financial relationships that could be construed as a potential conflict of interest.

The handling editor XL declared a past collaboration with the author CZ.

Publisher's note

References

Doruchowski, G., Balsari, P., Marucco, P., Zande, J., and Wenneker, M. (2011a). Crop Adapted Spray Application (CASA): precise and safe plant protection in fruit growing. *Aspects Appl. Biol.* 114, 129–136.

Doruchowski, G., Swiechowski, W., Godyn, A., and Holownicki, R. (2011b). Automatically controlled sprayer to implement spray drift reducing application strategies in orchards. *J. Fruit ornamental Plant Res.* 19 (1), 2011.

Dou, H. J., Zhai, C. Y., Wang, X., Zou, W., Li, Q., and Chen, L. P. (2022). Design and experiment of the orchard target variable spraying control system based on LiDAR. *Trans. CSAE* 38 (3), 11–21. doi: 10.11975/j.issn.1002-6819.2022.03.002

Gil, E., Arnó, J., Llorens, J., Sanz, R., Llop, J., Rosell-Polo, J. R., et al. (2014). Advanced technologies for the improvement of spray application techniques in Spanish viticulture: An overview. *Sensors* 14 (1), 691–708. doi: 10.3390/s140100691

Grella, M., Gioelli, F., Marucco, P., Zwertvaegher, I., Mozzanini, E., Mylonas, N., et al. (2022). Field assessment of a pulse width modulation (PWM) spray system applying different spray volumes: duty cycle and forward speed effects on vines spray coverage. *Precis. Agric.* 23 (1), 219–252. doi: 10.1007/s11119-021-09835-6

Gu, C., Zhao, C., Zou, W., Yang, S., Dou, H., and Zhai, C. (2022). Innovative leaf area detection models for orchard tree thick canopy based on LiDAR point cloud data. *Agriculture* 12 (8), 1241. doi: 10.3390/agriculture12081241

He, X. K. (2020). Research progress and developmental recommendations on precision spraying technology and equipment in China. *Smart Agric.* 2 (1), 133–146. doi: 10.12133/j.smartag.2020.2.1.201907-SA002

Hoheisel, G. A., Khot, L. R., and Castagnoli, S. (2021). *Six steps to calibrate and optimize airblast sprayers for orchards and vineyards* (USA: Washington State University). Available at: https://hdl.handle.net/2376/18323.

Hołownicki, R., Doruchowski, G., Świechowski, W., Godyń, A., and Konopacki, P. J. (2017). Variable air assistance system for orchard sprayers; concept, design and preliminary testing. *Biosyst. Eng.* 163, 134–149. doi: 10.1016/j.biosystemseng.2017.09.004

Jiang, H., Niu, C., Liu, L., Wang, D., Wang, J., and Mao, W. (2020). Design and experiment of air volume control system of orchard multi pipe air sprayer. *Trans. CSAM* 51, 298–307. doi: 10.6041/j.issn.1000-1298.2020.S2.035

Khot, L. R., Ehsani, R., Albrigo, G., Larbi, P. A., Landers, A., Campoy, J., et al. (2012). Air-assisted sprayer adapted for precision horticulture: Spray patterns and deposition assessments in small-sized citrus canopies. *Biosyst. Eng.* 113 (1), 76–85. doi: 10.1016/j.biosystemseng.2012.06.008

Landers, A. J. (2010). "Developments towards an automatic precision sprayer for fruit crop canopies," in *2010 pittsburgh, pennsylvania, june 20-june 23, 2010* (USA: American Society of Agricultural and Biological Engineers). doi: 10.13031/2013.29778

Li, L. L., He, X. K., Song, J. L., Wang, X. N., Jia, X. M., and Liu, C. H. (2017). Design and experiment of automatic profiling orchard sprayer based on variable air volume and flow rate. *Trans. CSAE* 33 (1), 70–76. doi: 10.11975/j.issn.1002-6819.2017.01.009

Mahmud, M. S., Zahid, A., He, L., Choi, D., Krawczyk, G., Zhu, H., et al. (2021a). Development of a LiDAR-guided section-based tree canopy density measurement system for precision spray applications. *Comput. Electron. Agric.* 182, 106053. doi: 10.1016/j.compag.2021.106053

Mahmud, M. S., Zahid, A., He, L., and Martin, P. (2021b). Opportunities and possibilities of developing an advanced precision spraying system for tree fruits. *Sensors* 21 (9), 3262. doi: 10.3390/s21093262

Mahmud, M. S., Zahid, A., He, L., Zhu, H., Choi, D., Krawczyk, G., et al. (2022). Development of an automatic airflow control system for precision sprayers based on tree canopy density. *J. ASABE* 65 (6), 1225–1240. doi: 10.13031/ja.14972

Manandhar, A., Zhu, H., Ozkan, E., and Shah, A. (2020). Techno-economic impacts of using a laser-guided variable-rate spraying system to retrofit conventional constant-rate sprayers. *Precis. Agric.* 21 (5), 1156–1171. doi: 10.1007/s11119-020-09712-8

Osterman, A., Godeša, T., Hočevar, M., Širok, B., and Stopar, M. (2013). Real-time positioning algorithm for variable-geometry air-assisted orchard sprayer. *Comput. Electron. Agric.* 98, 175–182. doi: 10.1016/j.compag.2013.08.013

Pai, N., Salyani, M., and Sweeb, R. D. (2009). Regulating airflow of orchard airblast sprayer based on tree foliage density. *Trans. ASABE* 52 (5), 1423–1428. doi: 10.13031/2013.29122

Qiu, W., Zhao, S., Ding, W., Sun, C., Lu, J., and Gu, J. (2016). Effects of fan speed on spray deposition and drift for targeting air-assisted sprayer in pear orchard. *Int. J. Agric. Biol. Eng.* 9 (4), 53–62. doi: 10.3965/j.ijabe.20160904.1938

Salcedo, R., Zhu, H., Ozkan, E., Falchieri, D., Zhang, Z., and Wei, Z. (2021). Reducing ground and airborne drift losses in young apple orchards with PWM-controlled spray systems. *Comput. Electron. Agric.* 189, 106389. doi: 10.1016/j.compag.2021.106389

Shen, Y., Zhu, H., Liu, H., Chen, Y., and Ozkan, E. (2017). Development of a laser-guided embedded-computercontrolled air-assisted precision sprayer. *Trans. ASABE* 60 (6), 1827–1838. doi: 10.13031/trans.12455

Wang, M., Dou, H., Sun, H., Zhai, C., Zhang, Y., and Yuan, F. (2023). Calculation method of canopy dynamic meshing division volumes for precision pesticide application in orchards based on lidar. *Agronomy* 13 (4), 1077. doi: 10.3390/agronomy13041077

Warneke, B. W., Zhu, H., Pscheidt, J. W., and Nackley, L. L. (2021). Canopy spray application technology in specialty crops: A slowly evolving landscape. *Pest Manage. Sci.* 77 (5), 2157–2164. doi: 10.1002/ps.6167

Wei, Z., Xue, X., Salcedo, R., Zhang, Z., Gil, E., Sun, Y., et al. (2023). Key Technologies for an orchard variable-rate sprayer: current status and future prospects. *Agronomy* 13 (1), 59. doi: 10.3390/agronomy13010059

Xu, S., Zhai, C., Zhu, R., Guo, J., Li, W., and Han, R. (2013). Design of an orchard air-assisted sprayer with adjustable spray height. *J. Northwest A F University-Natural Sci. Edition* 41 (11), 229–234.

Zhai, C., Xu, S., Long, J., Li, H., Zhang, B., and Zhu, R. (2018a). Optimization design of orchard air-assisted sprayer and mathematical model for spray height control. *J. Northwest A F University-Natural Sci. Edition* 46 (9), 148–154. doi: 10.13207/j.cnki.jnwafu.2018.09.019

Zhai, C., Zhao, C., Ning, W., Long, J., Wang, X., Weckler, P., et al. (2018b). Research progress on precision control methods of air-assisted spraying in orchards. *Trans. CSAE* 34 (10), 1–15. doi: 10.11975/j.issn.1002-6819.2018.10.001

Zheng, Y. J., Chen, B. T., Lyu, H. T., Kang, F., and Jiang, S. J. (2020). Research progress of orchard plant protection mechanization technology and equipment in China. *Trans. CSAE* 36, 110–124. doi: 10.11975/j.issn.1002-6819.2020.20.014

Zheng, J. Q., and Xu, Y. L. (2021). Development and prospect in environment-friendly pesticide sprayers. *Trans. CSAM* 52 (3), 1–16. doi: 10.6041/j.issn.1000-1298.2021.03.001

frontiers | Frontiers in Plant Science

TYPE Original Research
PUBLISHED 11 September 2023
DOI 10.3389/fpls.2023.1212818

OPEN ACCESS

EDITED BY
Lei Shu,
Nanjing Agricultural University, China

REVIEWED BY
Chong Cao,
Institute of Plant Protection (CAAS), China
Wei Fu,
Hainan University, China
Hafiz Sohaib Ahmed Saqib,
Fujian Agriculture and Forestry University, China
Guoxing Wu,
Yunnan Agricultural University, China
Ru Li,
Yunnan Agricultural University, China

*CORRESPONDENCE
Jianli Song
songjianli@cau.edu.cn
Zhenhua Zhang
zhangzhh@cau.edu.cn

RECEIVED 27 April 2023
ACCEPTED 21 August 2023
PUBLISHED 11 September 2023

CITATION
Liu Y, Wang G, Li Y, Zhang Z, Pang S, He X and Song J (2023) Spray losses study of two pesticides by UASS in integrated rice–crayfish farming system and acute toxicity evaluation on *Procambarus clarkii*. *Front. Plant Sci.* 14:1212818. doi: 10.3389/fpls.2023.1212818

Spray losses study of two pesticides by UASS in integrated rice–crayfish farming system and acute toxicity evaluation on *Procambarus clarkii*

Yang Liu[1,2], Guangyu Wang[1], Yuanyuan Li[3], Zhenhua Zhang[1,2]*, Sen Pang[1], Xiongkui He[1,2] and Jianli Song[1,2]*

[1]College of Science, China Agricultural University, Beijing, China, [2]College of Agricultural Unmanned Systems, China Agricultural University, Beijing, China, [3]College of Plant Protection, China Agricultural University, Beijing, China

Introduction: While the integrated rice-crayfish (*Procambarus clarkii*) farming system (IRCFS) is widely developing in China, the widespread use of Unmanned Aerial Spraying Systems (UASS) to protect rice from pests has led to potential pesticide risk for the crayfish in IRCFS. Therefore, it is crucial to examine UASS's spray deposition and drift in IRCFS.

Method: In this study, we used the oligonucleotide sequence-tracking / dot-blotting (OSTDB) method to trace pesticide spraying. We collected detailed data not only on spray loss in the paddy fields, but also on spray drift in the breeding ditches caused by upwind and downwind spray areas. Additionally, pesticide residues in the breeding ditches were measured using LC-MS/MS by collecting water samples after pesticide application.

Results: The data analysis indicated that the spray loss in the paddy field was significantly greater than that in the breeding ditches. The spray drift in the breeding ditches, caused by the upwind spray area, was seven times higher than that originating from the downwind spray area. Furthermore, the results also revealed that the bulk flow between the paddy fields and the breeding ditches contributed a substantial amount of pesticide residue to the water body in the breeding ditches. In addition, we investigated the acute toxicities of common insecticides using in paddy fields, including thiamethoxam (THI), chlorantraniliprole (CHI), THI·CHI-Mix and THI·CHI-WG.

Discussion: The results demonstrated that the spray losses and spray drift from UASS spray applications of these pesticides in IRCFS would not cause acute toxicity or death in crayfish. These findings provide important materials for establishing pesticide application standards and guiding the field testing of droplet deposition and drift in IRCFS.

KEYWORDS

integrated rice-crayfish farming system, unmanned aerial spraying systems, pesticide losses, spray drift, *Procambarus clarkii*, acute toxic effect

1 Introduction

Integrated rice–crayfish farming system (IRCFS), which refers to the simultaneous cultivation of rice and crayfish (*Procambarus clarkii*), has been intensively developed in China due to its extensive benefits (He et al., 2021; Mo et al., 2022; Wu et al., 2022; Yuan et al., 2022; Zhou et al., 2023; Yu et al., 2018a; Yu et al., 2018b). During the rice growing phase, crayfish live harmoniously in the paddy fields that are connected to breeding ditches and migrate back to these ditches during the field drying and rice harvesting periods (Yuan et al., 2021; Chen et al., 2022; Liu et al., 2022). This unique system not only improves the efficiency of water and soil resource utilization (Liu et al., 2022; Zhou et al., 2023; Hou et al., 2021a) but also significantly boosts the economic viability of rice cultivation (Gao et al., 2022; Wu et al., 2022; Xu et al., 2022; Zhang et al., 2022; Hou et al., 2021b).

While IRCFS can mitigate pests and disease (Li et al., 2022; Yu et al., 2022), chemical control remains crucial to prevent losses in rice yield. As wind and drift often carry the droplets to non-target areas (Hu et al., 2022), pesticide application raises environmental concerns since it would pose a potential risk to both the environment and crayfish. The advent of unmanned aerial spraying systems (UASS) has further increased this risk (Wang et al., 2018; Wang et al., 2022). Studies on its impact on IRCFS remain scarce. In IRCFS, breeding ditches hold a higher production value compared to paddy fields. Therefore, it is vital to examine the effects of pesticide spray conditions on IRCFS, such as pesticide residue and its origin in the breeding ditches. This is particularly important in light of the concurrent advancements in new spraying technologies and farming patterns. Compared to traditional water-sensitive paper, which is challenging to use in wet paddy field environments, and dye tracer methods that can easily lead to water field contamination, the new oligonucleotide sequence tracking/dot blotting (OSTDB) technology provides a straightforward way to accurately detect pesticide spray droplets on the surfaces of both targets and non-targets (Song et al., 2021; Zhang et al., 2021). This method will provide detailed information on the deposition distribution and drift of UASS in IRCFS.

With the development of IRCFS, there has been an increasing focus on studies about the acute toxicities of insecticides to non-target crayfish (Biever et al., 2003; Barbee and Stout, 2009; Mamun et al., 2009; Barbee et al., 2010; Yu et al., 2017; Zhu et al., 2022; Liao et al., 2023; Uçkun et al., 2021; Huang et al., 2022; Sun et al., 2022). Thiamethoxam (THI) and chlorantraniliprole (CHI) are two common insecticides that are used in paddy fields and have been widely registered as single-agent products (Mason et al., 2000; Hilton et al., 2016; Wei et al., 2019; Uçkun et al., 2021). In recent years, the blends of THI and CHI have become popular in IRCFS. Therefore, in reference to pesticide residue and its origin in the breeding ditches, it is urgent to evaluate the acute toxicity of mixing THI and CHI to crayfish in IRCFS.

In this study, we developed a risk assessment system to evaluate the impact of pesticide spray droplets on crayfish aquaculture within IRCFS. By employing the dual OSTDB strategy, we traced the origin of losses attributed to pesticide spray drift in both upwind and downwind areas. The pesticide residues of CHI and THI in breeding ditches were also examined. Furthermore, the acute toxicity of mixed THI and CHI to non-target crayfish was evaluated. These results provide crucial data for the safe application of pesticide in IRCFS and to pave the way for its further improvement.

2 Materials and methods

2.1 Experimental plots

The experiment was conducted in July 2019 in Qianjiang City, Hubei Province, China (112°44′ E, 30°17′ N). The test site employed a standard integrated rice–crayfish farming system (Figure 1D). A crayfish breeding ditch measuring 4 m in width and 1.5 m in depth was constructed around the paddy field. The marker labels the outlet of the paddy field, which is connected to the breeding ditch. The rice variety used in the experiment was Nanjing 5055, and the species of crayfish was *Procambarus clarkii*. The experiment began 7 days before rice heading. The predominant wind direction at the test site was northeast. In the experiment, a solution of 150 mL/ha of 40% chlorothalonil–thiamethoxam (Virtako, Syngenta, Switzerland) was selected. The solutions were also formulated with 0.1 μmol/L OST-probe-A and OST-probe-B, respectively.

2.2 Plant protection unmanned aerial vehicle

A four-rotor electric UASS with a spray tank volume of 10 L (P-20, Guangzhou XAG Technology Co., Ltd.) was used in the experiment for the spray applications in rice–crayfish fields Figure 1C. The performance indicators of the UASS are shown in Table 1. The

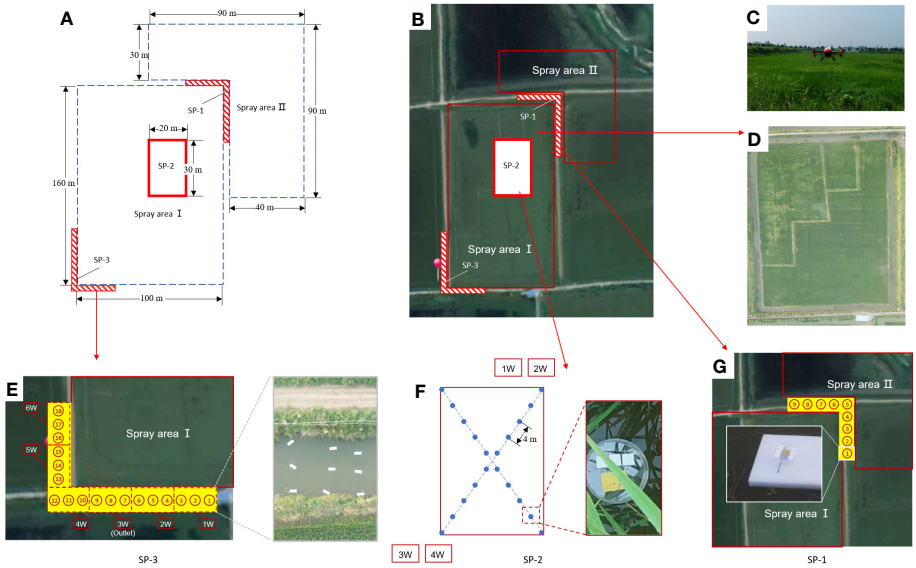

FIGURE 1
The paddy fields and breeding ditches of integrated rice-crayfish farming system and schematic diagram of the spray areas and the sampling positions. **(A)** Schematic diagram of the division of the spray areas and the sampling positions (SP); **(B)** Distribution of the spray areas and SP; **(C)** The P-20 conducted pesticide application in the experimental field; **(D)** Distribution of paddy fields and breeding ditches; **(E)** Sampling position 3 (SP-3) and on-site diagram of the droplet collectors; **(F)** Sampling position 2 (SP-2) and on-site diagram of the droplet collectors; **(G)** Sampling position 1 (SP-1) and on-site diagram of the droplet collector-NMCs.

P-20was equipped with high-speed centrifugal atomization nozzles and could implement the spray operation according to an automatically planned route. The spray parameters were set as follows: the flight height was set at 1.7 m above the ground, the spray width was set at 3.0 m, and the spray volume was set at 12 L/ha.

2.3 Dual-OST tracer strategy for spray drift assessment

An OSTDB-based tracing technology was used for pesticide mapping of spray droplet and drift. The oligonucleotide sequence tracking probes (OST probe) can achieve specific recognition through complementary base pairing. By mixing the OST probe into the spray tank with pesticides, the droplets containing the OST probe would be collected by nylon membrane collectors (NMCs) modified with complementary probe sequences. Those droplets would then be displayed on the NMCs through a post-processing procedure.

In this experiment, two spraying areas, spray area I (SA-I) and spray area-II (SA-II) were set up, which corresponded to the spray application with liquid containing OST probe-A and OST probe-B, respectively. Nylon membrane collector A (NMC-A) and nylon membrane collector B (NMC-B) were used as the droplet-collecting substrates to detect the spray drift from the two spraying areas on the same position.

2.4 Experimental design

The spray-treated area was divided into two parts, SA-I and SA-II, due to the northeast wind direction at the experimental site (Figure 1B). SA-I was 100 m × 160 m, while SA-II consisted of two paddy fields with spray areas of 90 m × 30 m and 40 m × 60 m, respectively (Figure 1A). A pesticide solution containing OST probe-A was sprayed in SA-I, while a pesticide solution containing OST probe-B was sprayed in SA-II.

Sampling position 1 (SP-1) was situated at the corner between SA-I and SA-II in order to investigate the spray drift caused by both SA-I and SA-II on the breeding ditches. Sampling position 2 (SP-2), located within a 20 m × 30 m area inside SA-I, aimed to detect the distribution of spray losses on the water surface of paddy fields within SA-I. Sampling position 3 (SP-3) was located in the breeding ditches in the downwind direction from SA-I, with the purpose of investigating the spray drift caused by SA-I on the breeding ditch.

TABLE 1 Main performance indicators of P-20.

Model	Maximum load (L)	Unfold fuselage size (mm × mm × mm)	Operating speed (m/s)	Flight height (m)	Effective spray width (m)	Spray droplet size (μm)
P-20	10	1,852 × 1,828 × 403	2–12	1–30	2–5	90–300

2.4.1 Spray drift of the breeding ditch in the upwind of SA-I

In the breeding ditch of SP-1, sampling points were set at intervals of 2 m, with nine sampling points totally in the ditch (Figure 1G). At each sampling point, sampling devices fixed on floating boards on the water surface were used to set up three pieces each of NMCs-A and NMCs-B. These were used to trace the spray droplet drift from SA-I and SA-II in the upwind, respectively.

2.4.2 Spray losses in SA-I paddy field

SP-2 was located in the interior region of SA-I paddy field, with 10 sampling points evenly distributed along the diagonal line, each approximately 4 m apart. At each sampling point, sampling devices, which were fixed on floating boards on the water surface, were used to set up three pieces of NMCs-A. These were used to detect the distribution of spray losses on the water surface of SA-I paddy field (Figure 1F).

2.4.3 Spray drift of the breeding ditch in the downwind of SA-I

The distribution of sampling points in SP-3 was the same as that in SP-1. As shown in Figure 1E, SP-3 was subdivided into 18 locations across six parts. The droplet collection devices were positioned at distances of 0.5, 2.0, and 3.5 m from the boundary of SA-I from SP3-1D to SP3-12D. In addition, six other collection devices were evenly distributed in the east–west ditch. At each sampling point, sampling devices fixed on floating boards on the water surface were used to position three pieces of NMCs-A. These were used to trace the spray droplet drift from SA-I in the downwind.

2.4.4 Water sample collection

Before the pesticide application, blank water samples were collected from the paddy field, with 12 random sampling points selected within the area.

Water samples were also collected from each point in SP-1, SP-2, and SP-3, following the blank water sample collecting procedure, at 1 h after the pesticide application.

At 1, 3, 4, 5, 7,10, 14, and 21 days after the pesticide application, subsequent collections of water samples were made in breeding ditches upwind of the paddy fields (WR-1), in breeding ditches downwind of the paddy fields (WR-2 and WR-3), and in the breeding ditch near the outlet (WR-O). For each water sample, approximately 400 mL was collected and stored at -20°C for analysis.

2.4.5 Measurement of meteorological conditions

A portable weather station "YG-BX" (Chenyun Technology Co., Ltd., China) was employed to monitor the relevant environmental conditions (wind speed, wind direction, temperature, and relative humidity) at a height of 1.0 m over the full duration of the trials. The weather station was positioned 10 m away from the UAV flight path in an open area without any vegetation.

2.5 Sample processing for NMCs

The NMC samples were treated using Song's method (Song et al., 2021). Then, the colored NMCs were scanned at a resolution of 600 dpi, and the grayscale values were measured by using ImageJ. The standard curve representing the relationship between grayscale value and droplet volume was established using droplets formed from the mother liquid of both OST probe-A and OST probe-B. The equation was as follows:

$$G_L = k_0 \times V_m$$

where k_0 is the coefficient relating the droplet volume to grayscale value and V_m is the volume of the OST-probe (μL).

Based on the grayscale values obtained from the samples, the spray drift or droplet loss per unit area was calculated as follows:

$$\beta_i = G_{Lsmpl}/(k_0 \times A_{col})$$

where β_i is the spray drift per unit area (μL/cm^2), G_{Lsmpl} is the grayscale value of the sample, and A_{col} is the collector area (cm^2).

2.6 Sample processing for water samples

In collecting water samples, two separate portions of 15.0 mL were transferred into individual centrifuge tubes. To each tube, 9.0 g of sodium chloride and 15.0 mL of acetonitrile were added. The mixture was then vortexed for 5 min and centrifuged at a speed of 2,800 rpm for another 5 min. From each centrifuge tube, 10 mL of the supernatant was extracted, resulting in a total of 20 mL, which was then transferred into a 50-mL vial. The vial was positioned on a rotary evaporator and evaporated until it reached dryness. Then, 1 mL of acetonitrile was added to the vial to thoroughly rinse the residue from the vial walls. The rinsed solution was filtered through a cellulose acetate filter with a pore size of 0.22 μm and then transferred to a sample vial for the following analysis.

2.7 LC–MS/MS analysis

The detection of CHI and THI was referred to the method (Rahul et al., 2020) and analyzed by LC-MS/MS. The test conditions of THI and CHI are shown in Supplementary Table S1. The parameters of mass spectrum for THI and CHI are shown in Supplementary Table S2.

2.8 Determination of LC_{50} values and application

Dose ranges of 3.0–14.0 mg/L of THI and 50.0–120.0 mg/L of CHI as well as 4.0–20.0 mg/L 40% CHI·THI (WG) and 8.0–40.0 mg/L CHI and THI (1:1) mixed dosages were used to determine the 96-h LC_{50} value.

The crayfish were sourced from Longwan Town, Qianjiang City, Hubei Province, China. For this study, glass aquariums with a capacity of 30 L with tubular shelters were used. The studies were conducted at room temperature (23°C ± 1°C) under natural daylight conditions (12-h dark/12-h light). Before applying the pesticide, the crayfish were acclimatized to the laboratory environment for a period of 7 days. Juvenile crayfish were used without regard to their gender. For standardization, crayfish weighing around 5.0 ± 1.0 g and with length of around 5.0 ± 1.0 cm were preferred. Test waters were maintained in the containers with static renewal every 24 h. Six groups were established for each treatment, five of which were exposed to pesticides, while one served as the non-pesticide-applied group (control). Each aquarium housed 10 crayfishes, and the study was replicated three times. Among the live subjects, those who became immobilized over time and exhibited signs of mortality were classified as dead. The count of deceased subjects was recorded at 24-, 48-, 72-, and 96-h intervals. The 96-h LC50 was determined using SPSS 24 probit analysis.

3 Results and discussion

3.1 Meteorological conditions

Table 2 shows the meteorological conditions for each spray. The meteorological parameters were in accordance with ISO24253-2 (2015) for field spray droplet deposition test requirements (wind speed, 0–3 m/s; temperature, 10°C–35°C).

3.2 Pesticide spray drift in breeding ditches upwind of paddy fields

The SP-1 was the breeding ditch located upwind of the SA-I paddy fields, as the wind direction was northeast at the time the pesticide application was conducted. Data on spray drift and pesticide residue in water samples were collected from nine locations (SP-1 to SP1-9). The spray drift ratio of droplets from SA-I and SA-II, obtained by UASS application using the dual-OST-probe tracer method (Figure 2), and the total spray drift were analyzed. The results indicated that the main source of spray drift in the breeding ditches upwind of the paddy fields originated from SA-I, which was closer to the ditch.

The average spray drift caused by SA-I was 0.0048 μL/cm^2, accounting for 4.0% of the theoretical droplet deposition volume (TDDV); the average spray drift caused by SA-II was 0.0007 μL/cm^2, accounting for 0.6% of TDDV. The total spray drift in the breeding ditches upwind of the paddy fields was 0.0055 μL/cm^2, accounting for 4.6% of TDDV. The coefficient of variation (CV) of the total spray drift in the breeding ditches upwind of the paddy fields was 0.46, indicating that the distribution of spray drift varies greatly at different locations within the ditch upwind of the paddy fields. This variation may be caused by real-time changes in wind speed during the application process, which alter the distribution of the droplets, or the flight parameters of the UASS may need optimization.

The average pesticide residue concentrations of THI and CHI on the water surface of the breeding ditch upwind of the paddy fields, caused by UASS spray application after 1 h, were 0.11 and 0.10 μg/L, respectively. The theoretical concentration of the pesticides was calculated based on the spray drift volume, assuming a diffusion rate of 50 cm/h in the water. As shown in Figure 3, this was compared with the pesticide residues detected on the water surface. The pesticide residues measured from the nine locations followed the same trend as the theoretical concentration, but all the data were lower than the theoretical value. The water flow causes the pesticides to move downstream to other areas within the ditch, and the rate of pesticide diffusion in the ditch exceeding the assumed 0.5 m/h may result in a lower proportion of pesticide in the water samples.

3.3 Pesticide spray drift in breeding ditches downwind of paddy fields

SP-3 was the breeding ditch located downwind of the SA-I paddy fields. Spray droplet drift volume and pesticide residues in water samples were collected from 18 locations in six areas. In this area, the influence of the distance between the breeding ditch and the SA-I on the spray drift in breeding ditches downwind of paddy fields was studied using the OSTDB tracing method. Droplet collection devices were placed at distances of 0.5, 2.0, and 3.5 m from the boundary of SA-I at SP3-1D to SP3-12D. The average spray drift at a distance of 0.5 m from the boundary of SA-I was 0.018 μL/cm^2, accounting for 14.8% of TDDV with a CV of 0.93. The average spray drift at a distance of 2.0 m from the boundary of SA-I was 0.009 μL/cm^2, accounting for 7.3% of TDDV with a CV of 0.63. The average spray drift at a distance of 3.5 m from the boundary of SA-I was 0.008 μL/cm^2, accounting for 6.4% of TDDV with a CV of 0.75 (Figure 4). Significant differences were observed in the spray drift between different positions of the breeding ditch and SA-I, which is similar to the distribution pattern observed in the upwind area. The droplet drift at SP3-1D to SP3-12D displayed a wave-like distribution pattern, akin to the spraying swath of the UASS, which may be related to the prolonged hovering time of the drone in the boundary area during flight direction changes.

TABLE 2 Meteorological parameter records.

Treatment	UV intensity (μW/cm^2)	Temperature (°C)	Humidity (%)	Wind speed (m/s)	Wind direction (°)
SA-I	3,332.8	34.4	56	1.13	45
SA-II	3,426.5	33.8	57	1.05	38

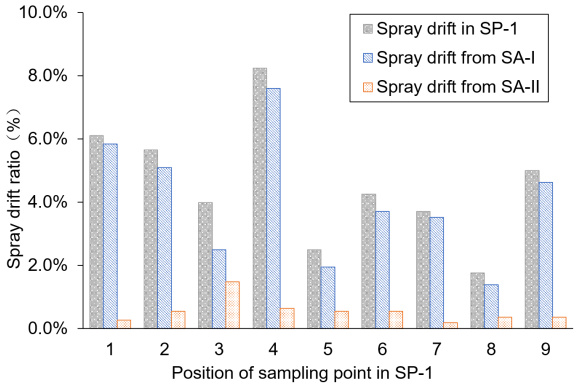

FIGURE 2
Spray drift distribution in the ditch upwind of the paddy field.

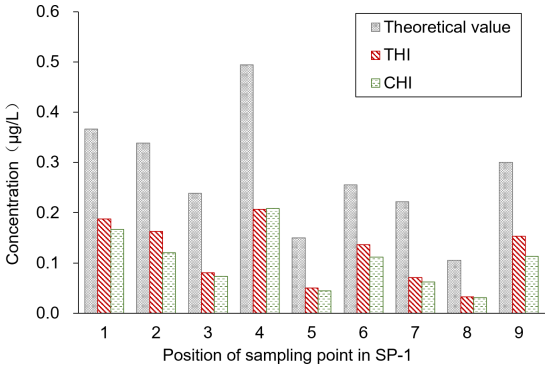

FIGURE 3
Pesticide residues in the ditch upwind of the paddy field.

The sampling position was segmented into six water sample collection areas, and the theoretical concentration of the pesticides was calculated based on the spray drift within these areas. Figure 5 presents a comparison of the pesticide residues detected on the water surface. Contrary to the results from the upwind area, the pesticide concentration detected in the water was higher than the theoretical concentration. The primary reason for this discrepancy is that SP3-3W acts as the outlet connecting the paddy field to the breeding ditch, allowing pesticide losses from the paddy field to flow into the breeding ditch. This flow results in increased pesticide residue in the water. Moreover, the pesticide concentration in the water gradually decreases from the outlet toward both sides. The average concentrations of THI and CHI pesticide residues on the water surface of the breeding ditch downwind of the paddy fields,

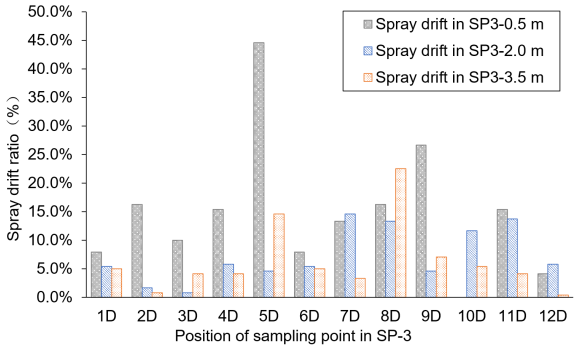

FIGURE 4
Spray drift distribution in the ditch downwind of the paddy field.

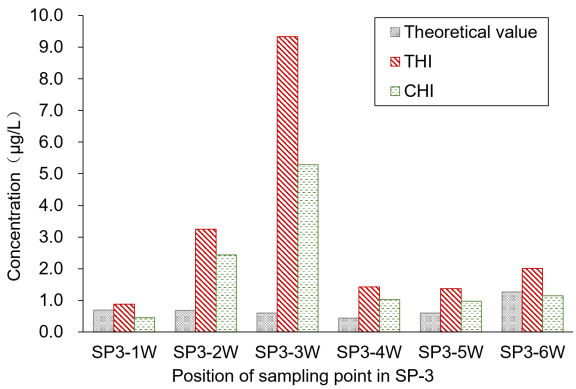

FIGURE 5
Spray drift distribution in the ditch downwind of the paddy field.

caused by UASS spray application after 1 h, were 3.05 and 1.88 μg/L, respectively. The significant difference in the residues of THI and CHI could be attributed to the varying solubility of the two pesticides in water. Despite the fact that crayfish are reared in rice paddies during the rice growing period, which could reduce the likelihood of pesticide exposure, there remains a potential risk of contact due to the circulation of water through the outlet.

3.4 Pesticide spray losses in paddy fields

In order to study the pesticide spray losses from UAS applications in paddy fields, the OSTDB tracing method was used. Data analysis from 16 sampling points revealed that the distribution of spray droplet losses on the water surface within the paddy field was not uniform. The average spray loss was 0.041 μL/cm^2, accounting for 34.5% of TDDV with a CV of 0.88 (Table 3). The sampling points were located in the water at the bottom of the rice canopy and were randomly distributed. Due to their location, the samplers were covered by the rice canopy. The density of the rice canopy affected the uniformity of spray droplet deposition, leading to differences in the distribution of loss on the water surface. Overall, the average pesticide spray losses were higher than those in breeding ditches. These dissolved pesticides in the water can enter the environment with the water flow, posing potential risks to crayfish.

The pesticide residues of THI and CHI on the water surface in spraying areas near the upwind boundary (SP2-1W and SP2-2W) and the spraying areas near the downwind boundary (SP2-3W and SP2-4W) in SA-I paddy field were tested 1 h after the pesticide application. As demonstrated in Table 4, the pesticide residues in SP2-1W and SP2-2W were higher than those in SP2-3W and SP2-4W. Given that SP2-3W and SP2-4W were closer to the outlet, the rapid flow at this point altered the distribution pattern of pesticide loss in the paddy field. This resulted in discrepancies between the pesticide residues in the water bodies and the theoretical concentration of the pesticides as tested by the OSTDB method.

3.5 Pesticide residues in water bodies over time of IRCFS

The experimental sites selected for sampling were located in breeding ditches upwind of the paddy fields (WR-1) and in breeding ditches downwind of the paddy fields (WR-2 and WR-3) as well as on the breeding ditch near the outlet (WR-O). Pesticide

TABLE 3 Pesticide losses on the water surface of the paddy fields.

Sampling position	Spray losses volume (μL/cm^2)	Spray losses ratio (%)	Sampling position	Spray losses volume (μL/cm^2)	Spray losses ratio (%)
2D-11	0.033 ± 0.002	27.2 ± 1.7	2D-21	0.028 ± 0.002	23.1 ± 1.8
2D-12	0.013 ± 0.003	11.1 ± 2.2	2D-22	0.134 ± 0.015	111.4 ± 12.3
2D-13	0.022 ± 0.002	18.3 ± 2.0	2D-23	0.020 ± 0.002	16.4 ± 1.7
2D-14	0.072 ± 0.002	59.7 ± 2.1	2D-24	0.013 ± 0.003	11.1 ± 2.4
2D-15	0.035 ± 0.003	29.4 ± 2.6	2D-25	0.109 ± 0.006	90.6 ± 5.1
2D-16	0.075 ± 0.004	62.8 ± 3.1	2D-26	0.042 ± 0.002	35.3 ± 1.7
2D-17	0.044 ± 0.002	36.7 ± 1.8	2D-27	0.011 ± 0.002	9.4 ± 1.6
2D-18	0.010 ± 0.005	8.0 ± 4.0	2D-28	0.001 ± 0.000	0.6 ± 0.0

TABLE 4 Pesticide residues on the water surface of the paddy fields.

Sampling position	Concentration of THI (μg/L)	Concentration of CHI (μg/L)
SP2-1W	2.77 ± 0.12	3.26 ± 0.20
SP2-2W	2.30 ± 003	3.14 ± 0.20
SP2-3W	0.05 ± 0.01	0.81 ± 0.06
SP2-4W	0.18 ± 0.02	0.69 ± 0.07

residues were detected 1, 3, 4, 5, 7, 10, 14, and 21 days after the pesticide application. As shown in Figures 6, 7, the pesticide residue at WR-O, as well as at sampling points WR-2 and WR-3 near the outlet, showed no significant differences. However, the pesticide residue at WR-1 was consistently lower than those in other areas. This can be attributed to the poor mobility of the water body, given that WR-1 is far away from the outlet.

The residues of THI and CHI in the water peaked on the 3rd day, after which they began to gradually decrease. After 21 days of pesticide application, the CHI residues remained detectable at 0.2 μg/L at sampling points located near the outlet. Among the four sampling points, WR-1 exhibited the lowest level of pesticide residue. This is presumably due to its distance from the outlet, limited water mobility, and its upwind location relative to the pesticide application, which aligns with the minimal drift loss observed in the outlet area during the course of the experiment.

3.6 Acute toxicity of THI and CHI to crayfish

In order to evaluate the toxic effects of UASS spray application on IRCFS, we further studied the acute toxicity of both THI and CHI as single components and in combination. We conducted a 96-h semi-static acute toxicity test on *P. clarkii* and calculated the lethal

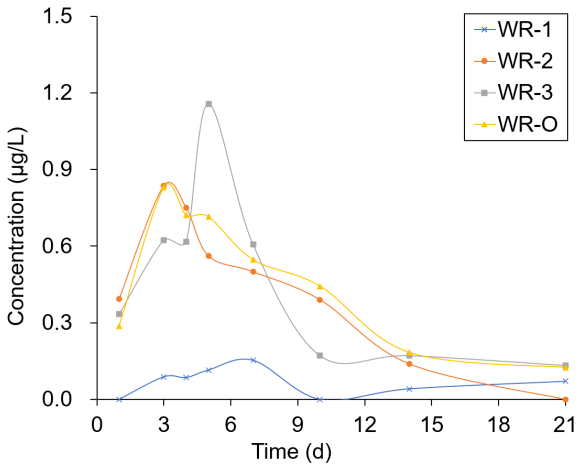

FIGURE 6
Pesticide residue distribution of THI in the paddy field within 21 days.

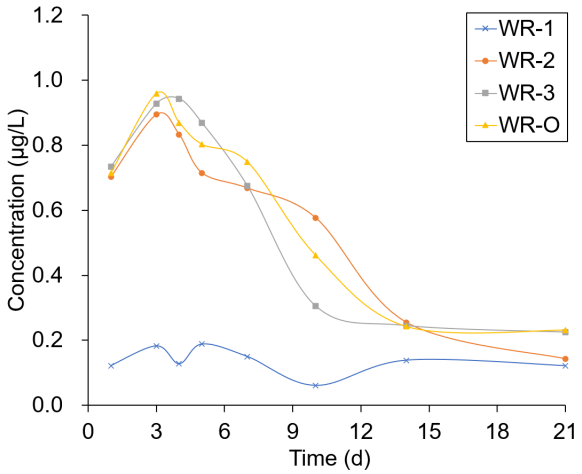

FIGURE 7
Pesticide residue distribution of CHI in the paddy field within 21 days.

concentration that causes 50% mortality (LC_{50}). Table 5 shows the acute toxicity of THI and CHI as single components, with THI demonstrating higher toxicity to juvenile crayfish than CHI. According to the toxicity evaluation criteria of the national standard GB/T 31270.21, the 96-h LC_{50} of THI and CHI on crayfish juveniles was 9.4 and 84.4 mg/L, respectively. This classifies THI as moderately toxic and CHI as less toxic. The relationship between exposure time and toxicity indicated that both THI and CHI exhibited time-dependent effects on the acute lethality of crayfish juveniles, suggesting that the acute toxicity of both insecticides to crayfish juveniles increased with prolonged exposure time.

The acute toxicity of THI and CHI as a 1:1 mixture (THI·CHI-Mix) and 40% THI·CHI water-dispersible granules (THI·CHI-WG) on crayfish is presented in Table 5. The toxicity of the THI·CHI-Mix was found to be lower than that of the THI·CHI-WG, with a 96-h LC_{50} of 14.6 mg/L, classifying it as less toxic. Conversely, the 96-h LC_{50} of THI·CHI-WG was 8.8 mg/L, marking it as moderately toxic. The combined toxicity effects were computed using the additivity index method, and the results are presented in Table 6. When CHI and THI were mixed in a 1:1 ratio, irrespective of whether it was a mixture of technical materials or a formulated mixture, the combined toxicity effects showed a synergistic action.

The highest concentrations of THI and CHI, detected in the paddy field and the breeding ditches following the UASS spray application, were 9.34 and 5.29 μg/L, respectively. Both of these concentrations were detected at the outlet sampling point. Fortunately, these concentrations were lower than the LC_{10} and LC_{50} values of THI·CHI-WG. Therefore, it is unlikely that the spray losses and spray drift from UASS spray application with these pesticides in IRCFS will cause acute toxicity and death in crayfish (*P. clarkii*).

TABLE 5 Acute toxicity and acute combined toxicity of THI and CHI to *P. clarkii*.

Pesticides	Exposure time (h)	LC_{10} (mg/L)	95% CI (mg/L)	LC_{50} (mg/L)	95% CI (mg/L)	Regression equation	R^2
THI	24	-	-	-	-	-	-
	48	5.0	1.1–7.1	25.7	15.2–399.9	$y = 3.1x - 4.3$	0.963
	72	2.2	0.2–3.9	16.3	10.9–78.8	$y = 2.5x - 3.0$	0.952
	96	1.5	0.2–2.9	9.4	7.1–15.7	$y = 2.8x - 2.7$	0.992
CHI	24	-	-	-	-	-	-
	48	72.1	14.2–93.1	226.5	141.3–130,122.1	$y = 4.4x - 10.4$	0.878
	72	35.8	0.77–54.9	161.4	113.2–3,276.7	$y = 3.4x - 7.4$	0.906
	96	32.9	14.3–44.9	84.4	72.3–101.8	$y = 5.4x - 10.3$	0.971
CHI·THI·WG	24	-	-	-	-	-	-
	48	4.0	1.4–6.0	15.9	12.7–23.3	$y = 3.6x - 4.4$	0.947
	72	2.8	0.9–4.5	11.8	9.2–15.4	$y = 3.5x - 3.8$	0.99
	96	2.5	1.0–3.9	8.8	6.8–10.9	$y = 4.1x - 3.8$	0.946
THI·CHI·Mix	24	10.7	4.7–14.3	38.0	13.9–47.7	$y = 4.0x - 6.3$	0.917
	48	9.2	5.7–11.7	23.2	19.7–29.5	$y = 5.5x - 7.5$	0.933
	72	7.6	4.7–9.8	18.7	16.0–22.4	$y = 5.6x - 7.2$	0.954
	96	5.8	3.2–7.7	14.6	12.3–17.1	$y = 5.5x - 6.4$	0.994

-, the number of deaths was low and did not correlate with concentration to calculate confidence intervals and regression equations.

TABLE 6 Acute combined effect of THI and CHI to *P. clarkii*.

Pesticides	Exposure time (h)	LC_{10} (mg/L)	S	AI	Joint toxicity evaluation
CHI·THI·WG	48	15.9	0.345	1.902	Synergy
	72	11.8	0.398	1.512	Synergy
	96	8.8	0.522	0.916	Synergy
THI·CHI·Mix	48	23.2	0.502	0.993	Synergy
	72	18.7	0.631	0.584	Synergy
	96	14.6	0.860	0.163	Synergy

4 Conclusion

In this study, a dual OSTDB method was employed to trace pesticide spray losses in IRCFS. Detailed information regarding the deposition distribution and spray drift of UASS was gathered. The average spray loss in the paddy field accounted for 34.5% of TDDV. The average spray drift in the breeding ditches, caused by upwind SA-I, was 4.0% of the TDDV, while that caused by downwind SA-II was 0.6%. The pesticide residues, measured by LC–MS/MS through the collection of water sample at the same location after pesticide application, displayed the same trend. The data analysis indicated that the spray loss in the paddy field was significantly greater than that in the breeding ditches. The spray drift in the breeding ditches, caused by the upwind spray area, was seven times higher than that originating from the downwind spray area. Furthermore, the results also revealed that the bulk flow between the paddy fields and the breeding ditches contributed a substantial amount of pesticide residue to the water body in the breeding ditches, even more so than the spray drift. A further study about the acute toxicity of THI and CHI to crayfish showed that the 96-h LC_{50} of THI, CHI, THI·CHI-Mix, and THI·CHI-WG on crayfish juveniles was 9.4, 84.4, 14.6, and 8.8 mg/L respectively. The highest concentrations of THI and CHI that were detected in the paddy field and the breeding ditches were lower than that of either THI·CHI-Mix or THI·CHI-WG. These results demonstrated that the spray losses and spray drift from the UASS spray application of these pesticides in IRCFS would not cause acute toxicity or death in crayfish. This interdisciplinary study on both pesticide losses and the acute toxicity of popular THI·CHI blend insecticide in IRCFS provided important materials for the establishment of pesticide application standards and guiding the field testing of droplet deposition and drift in IRCFS.

Data availability statement

The raw data supporting the conclusions of this article will be made available by the authors, without undue reservation.

Author contributions

JS and ZZ contributed to the conception of the study. YaL, JS, XH, and ZZ designed and directed the experiments. YaL and GW conducted the indoor experiments. YaL, GW, YuL, and SP performed the field trials. YaL and GW contributed significantly to analysis and manuscript preparation. YaL performed the data analyses and wrote the manuscript. YaL, SP, JS, XH, and ZZ helped perform the analysis with constructive discussions. All authors contributed to the article and approved the submitted version.

Funding

This study was supported by the earmarked fund for the China Agriculture Research System (CARS-28), the National Key Research and Development Plan of China (SQ2017YFNC040014), the National Natural Science Foundation of China (no. 31761133019), and the 2115 Talent Development Program of China Agricultural University.

Acknowledgments

We acknowledge the contributions of specific colleagues, institutions, or agencies that aided the efforts of the authors.

Conflict of interest

The authors declare that the research was conducted in the absence of any commercial or financial relationships that could be construed as a potential conflict of interest.

Publisher's note

Supplementary material

The Supplementary Material for this article can be found online at: https://www.frontiersin.org/articles/10.3389/fpls.2023.1212818/full#supplementary-material

References

Barbee, G. C., McClain, W. R., Lanka, S. K., and Stout, M. J. (2010). Acute toxicity of chlorantraniliprole to non-target crayfish (Procambarus clarkii) associated with rice–crayfish cropping systems. *Pest Manage. Sci.* 66 (9), 996–1001. doi: 10.1002/ps.1972

Barbee, G. C., and Stout, M. J. (2009). Comparative acute toxicity of neonicotinoid and pyrethroid insecticides to non-target crayfish (Procambarus clarkii) associated with rice-crayfish crop rotations. *Pest Manage. Sci.* 65 (11), 1250–1256. doi: 10.1002/ps.1817

Biever, R. C., Hoberg, J. R., Jacobson, B., Dionne, E., Sulaiman, M., and McCahon, P. (2003). ICON® rice seed treatment toxicity to crayfish (Procambarus clarkii) in experimental rice paddies. *Environ. Toxicol. Chem.* 22 (1), 167–174. doi: 10.1002/etc.5620220122

Chen, L., Xu, J., Wan, W., Xu, Z., Hu, R., Zhang, Y., et al. (2022). The microbiome structure of a rice-crayfish integrated breeding model and its association with crayfish growth and water quality. *Microbiol. Spectr.* 10 (2), e02204–e02221. doi: 10.1128/spectrum.02204-21

Gao, H., Li, Y., Zhou, Y., Guo, H., Chen, L., Yang, Q., et al. (2022). Influence of mechanical transplanting methods and planting geometry on grain yield and lodging resistance of indica rice taoyouxiangzhan under rice–crayfish rotation system. *Agron* 12 (5), 1029. doi: 10.3390/agronomy12051029

He, M., Liu, F., and Wang, F. (2021). Quantitative analysis of density dependent resource utilization, cannibalism, and competition of the red swamp crayfish (Procambarus clarkii) in rice-crayfish cocultures without supplementary food. *Aquaculture* 543, 736966. doi: 10.1016/j.aquaculture.2021.736966

Hilton, M. J., Jarvis, T. D., and Ricketts, D. C. (2016). The degradation rate of thiamethoxam in european field studies. *Pest Manage. Sci.* 72 (2), 388–397. doi: 10.1002/ps.4024

Hou, J., Styles, D., Cao, Y., and Ye, X. (2021a). The sustainability of rice-crayfish coculture systems: a mini review of evidence from Jianghan plain in China. *J. Sci. Food Agr* 101 (9), 3843–3853. doi: 10.1002/jsfa.11019

Hou, J., Wang, X., Xu, Q., Cao, Y., Zhang, D., and Zhu, J. (2021b). Rice-crayfish systems are not a panacea for sustaining cleaner food production. *Environ. Sci. pollut. R.* 28, 22913–22926. doi: 10.1007/s11356-021-12345-7

Hu, P., Zhang, R., Yang, J., and Chen, L. (2022). Development status and key technologies of plant protection UAVs in China: a review. *Drones.* 6 (11), 354. doi: 10.3390/drones6110354

Huang, X., Li, M., Huang, Y., Yang, H., Geng, Y., Ouyang, P., et al. (2022). Microbiome analysis reveals microecological advantages of emerging ditchless rice-crayfish co-culture mode. *Front. Microbiol.* 13, 892026. doi: 10.3389/fmicb.2022.892026

ISO24253-2 (2015). *Crop protection equipment - Spray deposition test for field crop - Part 2: Measurement in a crop*. ISO Central Secretariat: International Organization for Standardization.

Li, C., Huang, L., Zhang, Y., Guo, X., Cao, N., Yao, C., et al. (2022). Effects of triazole plant growth regulators on molting mechanism in Chinese mitten crab (*Eriocheir sinensis*). *Fish Shellfish Immunol.* 131, 646–653. doi: 10.1016/j.fsi.2022.10.059

Liao, M., Liang, Z., Wu, R., Xiao, J., Gao, Q., and Cao, H. (2023). Residue behavior of cyantraniliprole and its ecological effects on Procambarus clarkii associated with the rice–crayfish integrated system. *Pest Manage. Sci.* 79 (5), 1868–1875. doi: 10.1002/ps.7364

Liu, T., Li, C., Tan, W., Wang, J., Feng, J., Hu, Q., et al. (2022). Rice-crayfish co-culture reduces ammonia volatilization and increases rice nitrogen uptake in central China. *Agr. Ecosyst. Environ.* 330, 107869. doi: 10.1016/j.agee.2022.107869

Mamun, M. I. R., Park, J. H., Choi, J. H., Kim, H. K., Choi, W. J., Han, S. S., et al. (2009). Development and validation of a multiresidue method for determination of 82 pesticides in water using GC. *J. Sep. Sci.* 32 (4), 559–574. doi: 10.1002/jssc.200800606

Mason, G., Rancati, M., and Bosco, D. (2000). The effect of thiamethoxam, a second-generation neonicotinoid insecticide, in preventing transmission of tomato yellow leaf curl geminivirus (TYLCV) by the whitefly *Bemisia tabaci* (Gennadius). *Crop Prot.* 19 (7), 473–479. doi: 10.1016/S0261-2194(00)00042-9

Mo, A., Dang, Y., Wang, J., Liu, C., Yang, H., Zhai, Y., et al. (2022). Heavy metal residues, releases and food health risks between the two main crayfish culturing models: Rice-crayfish coculture system versus crayfish intensive culture system. *Environ. pollut.* 305, 119216. doi: 10.1016/j.envpol.2022.119216

Rahul, C., Harischandra, R., Pallavi, S., Rachappa, V., Pramesh, D., and Bheemanna, M. (2020). LC-ESI-MS/MS method for determination of chlorantraniliprole residue and its dissipation kinetics in pigeonpea. *Pest. Res. J.* 32 (1), 96–106. doi: 10.5958/2249-524X.2020.00013.8

Song, J., Liu, Y., He, X., Zhang, Z., Pang, S., Xu, S., et al. (2021). *Kit and method for simultaneously detecting droplet drift or deposition of multiple sprays, U.S. Patent US20210214777A1* (Washington, DC: U.S. Patent and Trademark Office).

Sun, Q., Khoshnevisan., B., Zhu, J., Wang, W., Liu, Y., Pan, J., et al. (2022). Comprehensive assessment of integrated rice-crayfish farming system as a new paradigm to air-water-food nexus sustainability. *J. Clean. Prod.* 377, 134247. doi: 10.1016/j.jclepro.2022.134247

Uçkun, M., Yoloğlu, E., Uçkun, A. A., and Öz, Ö.B. (2021). Acute toxicity of insecticide thiamethoxam to crayfish (Astacus leptodactylus): alterations in oxidative stress markers, ATPases and cholinesterase. *Acta Chim. Slov* 68 (3), 521–531. doi: 10.17344/acsi.2021.6823

Wang, X., He, X., Song, J., Wang, Z., Wang, C., Wang, S., et al. (2018). Drift potential of uav with adjuvants in aerial applications. *Int. J. Agric. Biol. Eng.* 11 (5), 54–58. doi: 10.25165/j.ijabe.20181105.3185

Wang, C., Liu, Y., Zhang, Z., Han, L., Li, Y., Zhang, H., et al. (2022). Spray performance evaluation of a six-rotor unmanned aerial vehicle sprayer for pesticide application using an orchard operation mode in apple orchards. *Pest Manage. Sci.* 6, 78. doi: 10.1002/ps.6875

Wei, Y., Yan, R., Zhou, Q., Qiao, L., Zhu, G., and Chen, M. (2019). Monitoring and mechanisms of chlorantraniliprole resistance in *Chilo suppressalis* (Lepidoptera: crambidae) in China. *J. Econ Entomol.* 112 (3), 1348–1353. doi: 10.1093/jee/toz001

Wu, Y., Li, Y., Niu, L., Zhang, W., Wang, L., and Zhang, H. (2022). Nutrient status of integrated rice-crayfish system impacts the microbial nitrogen-transformation processes in paddy fields and rice yields. *Sci. Total Environ.* 836, 155706. doi: 10.1016/j.scitotenv.2022.155706

Xu, Q., Peng, X., Guo, H., Che, Y., Dou, Z., Xing, Z., et al. (2022). Rice-crayfish coculture delivers more nutrition at a lower environmental cost. *Sustain. Prod. Consump.* 29, 14–24. doi: 10.1016/j.spc.2021.09.020

Yu, L., Li, C., Zhang, Y., Guo, X., Cao, N., Guo, S., et al. (2022). Residue monitoring of propiconazole in the rice crab co-culture field and its toxicity and bioaccumulation to eriocheir sinensis. *Front. Environ. Sci.* 10, 848348. doi: 10.3389/fenvs.2022.848348

Yu, J., Ren, Y., Xu, T., Li, W., Xiong, M., Zhang, T., et al. (2018a). Physicochemical water quality parameters in typical rice-crayfish integrated systems (RCIS) in China. *Int. J. Agr. Biol. Eng.* 11 (3), 54–60. doi: 10.25165/j.ijabe.20181103.3761

Yu, J., Xu, E. G., Li, W., Jin, S., Yuan, T., Liu, J., et al. (2018b). Acute toxicity of an emerging insecticide pymetrozine to Procambarus clarkii associated with rice-crayfish culture (RCIS). *Int. J. Environ. R. Pub. He* 15 (5), 984. doi: 10.3390/ijerph15050984

Yu, J., Xu, E. G., Ren, Y., Jin, S., Zhang, T., Liu, J., et al. (2017). Mixture toxicity of bensulfuron-methyl and acetochlor to red swamp crayfish (Procambarus clarkii): Behavioral, morphological and histological effects. *Int. J. Environ. R. Pub. He* 14 (12), 1466. doi: 10.3390/ijerph14121466

Yuan, P. L., Wang, J. P., Can, G. U. O., Guo, Z. Y., Yao, G. U. O., and Cao, C. G. (2022). Sustainability of the rice–crayfish farming model in waterlogged land: A case study in Qianjiang County, Hubei Province, China. *J. Integr. Agr* 21 (4), 1203–1214. doi: 10.1016/S2095-3119(21)63787-5

Yuan, P., Wang, J., Chen, S., Guo, Y., and Cao, C. (2021). Certified rice–crayfish as an alternative farming modality in waterlogged land in the Jianghan Plain region of China. *Agron. J.* 113 (6), 4568–4580. doi: 10.1002/agj2.20694

Zhang, Z., Du, L., Xiao, Z., Li, C., Wang, Z., Zhou, P., et al. (2022). Rice-crayfish farming increases soil organic carbon. *Agr. Ecosyst. Environ.* 329, 107857. doi: 10.1016/j.agee.2022.107857

Zhang, Z., Li, Z., Wu, X., Song, J., Liu, Y., Zhu, L., et al. (2021). *Kit and method for detecting droplet drift or deposition characteristics of spray, U.S. Patent US17/214,739* (Washington, DC: U.S. Patent and Trademark Office).

Zhou, Y., Harrison, M. T., Liu, K., Xiao, L., Zhu, J., Wang, M., et al. (2023). Field distribution characteristics and influencing factors of crayfish in rice-crayfish integrative system. *Aquaculture* 571, 739456. doi: 10.1016/j.aquaculture.2023.739456

Zhu, X., Ji, L., Cheng, M., Wei, H., Wang, Z., and Ning, K. (2022). Sustainability of the rice-crayfish co-culture aquaculture model: microbiome profiles based on multi-kingdom analyses. *Environ. Microbiome.* 17, 27. doi: 10.1186/s40793-022-00422-4

frontiers | Frontiers in Plant Science

TYPE Original Research
PUBLISHED 27 October 2023
DOI 10.3389/fpls.2023.1276833

OPEN ACCESS

EDITED BY
Xiaolan Lv,
Jiangsu Academy of Agricultural Sciences (JAAS), China

REVIEWED BY
Jianzhen Luo,
Guangdong Polytechnic Normal University, China
Parvathaneni Naga Srinivasu,
Prasad V. Potluri Siddhartha Institute of Technology, India

*CORRESPONDENCE
Zhen Li
lizhen@scau.edu.cn

RECEIVED 13 August 2023
ACCEPTED 09 October 2023
PUBLISHED 27 October 2023

CITATION
Lyu S, Zhou X, Li Z, Liu X, Chen Y and Zeng W (2023) YOLO-SCL: a lightweight detection model for citrus psyllid based on spatial channel interaction.
Front. Plant Sci. 14:1276833.
doi: 10.3389/fpls.2023.1276833

YOLO-SCL: a lightweight detection model for citrus psyllid based on spatial channel interaction

Shilei Lyu[1,2,3], Xu Zhou[1], Zhen Li[1,2,3]*, Xueya Liu[1], Yicong Chen[1] and Weibin Zeng[1]

[1]College of Electronic Engineering, College of Artificial Intelligence, South China Agricultural University, Guangzhou, China, [2]Pazhou Lab, Guangzhou, China, [3]Division of Citrus Machinery, China Agriculture Research System of MOF and MARA, Guangzhou, China

Efficient and accurate detection and providing early warning for citrus psyllids is crucial as they are the primary vector of citrus huanglongbing. In this study, we created a dataset comprising images of citrus psyllids in natural environments and proposed a lightweight detection model based on the spatial channel interaction. First, the YOLO-SCL model was based on the YOLOv5s architecture, which uses an efficient channel attention module to perform local channel attention on the inputs in the recursive gated convolutional modules to achieve a combination of global spatial and local channel interactions, improving the model's ability to express the features of the critical regions of small targets. Second, the lightweight design of the 21st layer C3 module in the neck network of the YOLO-SCL model and the small target feature information were retained to the maximum extent by deleting the two convolutional layers, whereas the number of parameters was reduced to improve the detection accuracy of the model. Third, with the detection accuracy of the YOLO-SCL model as the objective function, the black widow optimization algorithm was used to optimize the hyperparameters of the YOLO-SCL model, and the iterative mechanism of swarm intelligence was used to further improve the model performance. The experimental results showed that the YOLO-SCL model achieved a mAP@0.5 of 97.07% for citrus psyllids, which was 1.18% higher than that achieved using conventional YOLOv5s model. Meanwhile, the number of parameters and computation amount of the YOLO-SCL model are 6.92 M and 15.5 GFlops, respectively, which are 14.25% and 2.52% lower than those of the conventional YOLOv5s model. In addition, after using the black widow optimization algorithm to optimize the hyperparameters, the mAP@0.5 of the YOLO-SCL model for citrus psyllid improved to 97.18%, making it more suitable for the natural environments in which citrus psyllids are to be detected. The experimental results showed that the YOLO-SCL model has good detection accuracy for citrus psyllids, and the model was ported to the Jetson AGX Xavier edge computing platform, with an average processing time of 38.8 ms for a single-frame image and a power consumption of 16.85 W. This study provides a new technological solution for the safety of citrus production.

KEYWORDS

citrus psyllids, small target detection, YOLO, recursive gated convolution, lightweight, hyperparameter optimization

1 Introduction

Citrus is one of the most popular fruits in the world with numerous economic benefits (Liu et al., 2019). However, citrus huanglongbing (HLB) is a highly transmissible citrus disease that is difficult to prevent and control. HLB often leads to orchard yield reduction or even extinction, thereby affecting the safe citrus production. HLB is caused by the bast parasitic gram-negative bacterium Candidatus Liberibacter asiaticus (CLas) (Ma et al., 2022). HLB has a latent period, and its early yellowing symptoms are similar to fruit tree deficiencies (Jiao, 2016), making it difficult to diagnose accurately by hand. Currently, HLB is primarily diagnosed using polymerase chain reaction (PCR) detection technology (Bao et al., 2020; Wang et al., 2022b), but the low content and nonuniform distribution of CLas in plants lead to false-negative results of conventional PCR detection (Liang et al., 2018). Some studies have used near-infrared spectroscopy (Liu et al., 2016), hyperspectral remote sensing (Lan et al., 2019; Yang et al., 2021), and laser-induced breakdown spectroscopy (Yang et al., 2022) to diagnose HLB by analyzing the phenotype of the diseased plants and the degree of elemental uptake by the plants. However, these methods are complex, time-consuming, and difficult to meet large-scale management needs of orchards. Unlike the above studies, which are essentially based on HLB detection, this study explores the use of machine vision technology for detecting the primary vector of HLB, i.e., citrus psyllid, from the perspective of pest detection, which can provide early warning for orchard prevention and control.

In recent years, researchers have used machine vision technology to conduct a series of studies in the field of orchard pest detection. Wang et al. (Wang et al., 2021c) implemented the classification and localization of candidate bounding boxes in a real-time citrus-pest detection system, which can quickly detect red spiders and aphids with a detection accuracy of 91.0% and 89.0%, respectively, and an average processing speed as low as 286 ms for single-frame images. Shi et al. (Shi et al., 2023) proposed an adaptive spatial feature fusion-based lightweight detection model for citrus pests in the Papilionidae family. They integrated multiple optimization methods such as an adaptive spatial feature fusion module and an efficient channel attention mechanism into the YOLOX model, and achieved a higher than 95.76% mAP0.5 and an improvement in inference speed of 29 FPS over YOLOv7-x. Khanramaki et al. (Khanramaki et al., 2021) proposed a deep learning–based integrated classifier for detecting three citrus pests and achieved a 99.04% classification accuracy by developing an integrated classifier to detect citrus leafminer, sooty mold, and pulvinaria by considering the diversity of classification network level, feature level, and data level. Peng et al. (Peng et al., 2022) proposed a lychee pest detection model based on a lightweight convolutional neural network ShuffleNetV2 model, using the SimAM attention mechanism, Hardswish activation function, and migration learning method; the model detected 13 lychee pests, including Tessaratoma papillosa, with an accuracy of 84.9%. Ye et al. (Ye et al., 2021) proposed a multifeature fusion-based method for litchi pest detection, using the median filtering method for feature extraction of pests. The detection of three problems, namely, Tessaratoma papillosa, leaf rollers, and Pyrops candelaria, was achieved with a 95.35% accuracy by training the backpropagation network. Pang et al. (Pang et al., 2022) proposed an improved YOLOv4 target detection model that detected seven orchard insect pests, including Gryllotalpidae, with an average accuracy of 92.86% and a detection time of 12.22 ms for a single-frame image by optimizing the Nelder–Mead simplex algorithm and training method, as well as augmenting the training data. Li et al. (Li et al., 2023) proposed a pest detection model for passion fruit orchards based on the YOLOv5 model, employing the convolutional block attention module and mix-up data enhancement algorithm to detect 12 insect pests, including Bactrocera dorsalis Hendel, with an average accuracy of 96.51% and detection time of 7.7 ms. Zhang et al. (Zhang et al., 2022) proposed an orchard pest detection model that combines the YOLOv5 model and GhostNet and can detect seven orchard pests, such as chrysomelids, with a 1.5% increase in mAP0.5compared to YOLOv5.

In summary, machine vision technology has good feasibility in detecting orchard pests. However, the existing technology only excels in pest classification, and the presence of missed detections and false positives in the detection of pests, particularly for citrus psyllids, which have tiny bodies at the millimeter level and pose challenges to the effectiveness of target detection algorithms. To address this issue, this study developed a dataset of citrus psyllids in a natural environments and proposed a lightweight detection model based on spatial channel interaction(YOLO-SCL). The main research work includes:

(1) In the recursive gated convolutions (g_nConv), an efficient channel attention module is used for the feature maps after channel mixing to enhance the interactions between the local channels, achieve the interplay between global spatial interactions and local channel interactions, improve the feature representation of the model for critical regions, and enhance the contextual semantic information.
(2) The C3 module in the neck network is operated by deleting the convolutional layers to maximally retain the detailed feature information of the small targets and effectively improve the model detection performance.
(3) The black widow optimization algorithm (BWOA) is used to optimize hyperparameters of the YOLO-SCL model, making the optimized hyperparameters more suitable for the citrus psyllids detection task, as the optimal settings of the model hyperparameters are not always the same in different studies.

This study is outlined as follows: Section 2 presents the dataset construction; Section 3 introduces the design associated with the YOLO-SCL model; Section 4 outlines the BWOA algorithm utilized for optimizing hyperparameters of the YOLO-SCL model; Section 5 provides a detailed analysis of experimental results; and finally, in Section 6, we discuss and conclude our study.

2 Dataset description

2.1 Background

The experimental data for this study were mainly collected from the experimental base of the citrus orchard of South China Agricultural University (Guangzhou, Guangdong, China), and the collection period was from June to December 2022. Considering that the phototropic behavior of adult psyllids is remarkably affected by light intensity (Yuan et al., 2020), the collection periods were primarily selected from 10:00 to 11:30 and 14:30 to 16:00 under natural light environment on sunny days, and the shooting tools included a mirrorless interchangeable-lens camera (SONY Alpha 6400 APS-C) and a hand-held camera (Xiaomi Mi 9, Honor 30), and the shooting distance was 50–100 cm. The image resolutions were 900 × 900 pixels (Figure 1).

2.2 Citrus psyllid dataset construction

The adult citrus psyllids was approximately 3 mm long, and the resolution of the psyllids in the captured images was less than 32 × 32 pixels, which was classified as a tiny target according to the target definition of the MS COCO dataset (Gao et al., 2021). The constructed citrus psyllid dataset has 2660 original images. The annotated dataset was categorized into the training (2,128 images) and validation sets (532 images) at a ratio of 8:2. The dataset was expanded to 7,980 images by adding salt-pepper noise, adjusting brightness, photoflipping, and other data enhancement methods. The dataset was annotated using the Labelimg tool, with 11,043 adult psyllid targets.

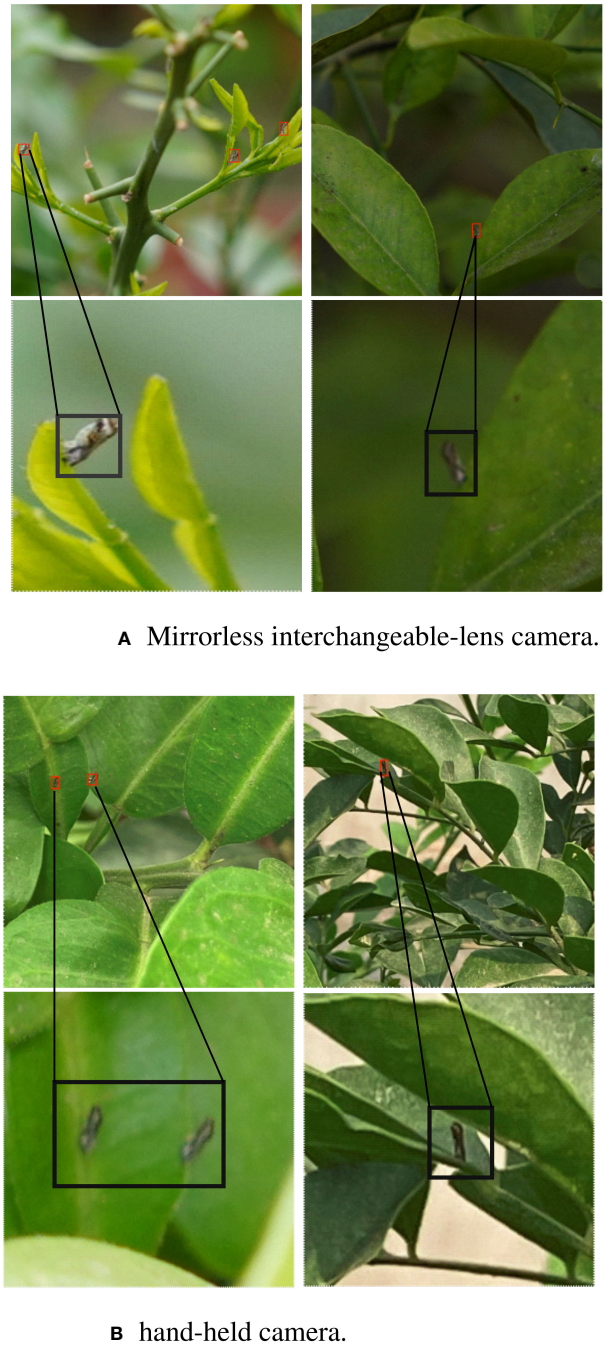

FIGURE 1
Example of citrus psyllid dataset. **(A)** Mirrorless interchangeable-lens camera. **(B)** hand-held camera.

3 Lightweight YOLO-SCL detection model design

Figure 2 shows the overall flow of the proposed lightweight YOLO-SCL detection model for citrus psyllids, using YOLOv5 as the baseline model. First, an improved (g_nConv) (19th layers) was added to the neck network to achieve long-distance modeling between features, improve feature representation in critical regions, and help the model resist complex background information. Second, the C3 module in the neck network was lightened to avoid too much loss of small target detail information while reducing the number of model parameters. Table 1 shows the specific parameters of the YOLO-SCL model.

3.1 Improved recursive gated convolutions based on spatial channel interactions

Transformer architecture was initially designed for natural language processing tasks (Vaswani et al., 2017). The vision transformer model (Dosovitskiy et al., 2020) was proposed to show that a vision model constructed only from transformer blocks and patch embedding layers can achieve performance comparable to those of convolutional neural networks. Unlike the convolutional kernel aggregation of the neighboring features approach, the visual transformer blends spatial elements using a multihead attention mechanism to achieve suitable modeling of spatial interactions in visual data. However, the quadratic complexity of the multihead self-attention mechanism remarkably limits its application, particularly in downstream tasks with high-resolution feature maps. The g_nConv (Rao et al., 2022) implements

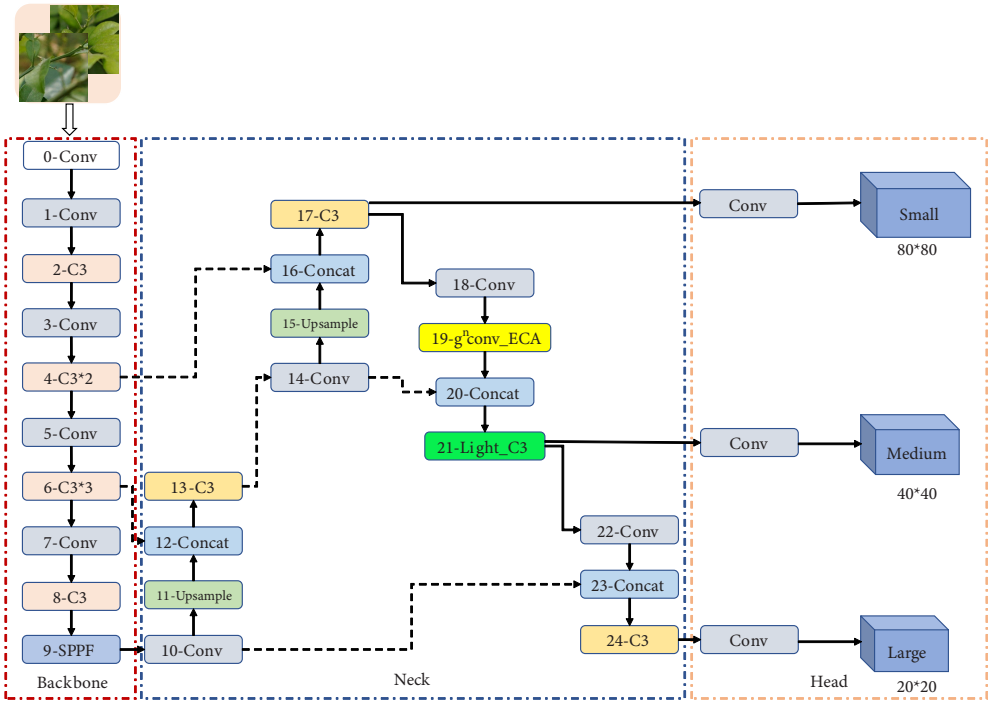

FIGURE 2
Schematic of citrus psyllid lightweight YOLO-SCL detection model.

spatial interactions using simple operations such as convolution and fully connected. Unlike the second-order interactions of the multiple attention mechanism, the g_nConv module implements spatial interactions in an arbitrary order (Figure 3). The g_nConv module enables the global spatial interaction through dot product operations, effectively overcoming the effect of complex backgrounds on target detection in citrus psyllids detection tasks. Therefore, in this study, we used the g_nConv module and modified it for long-range feature modeling and feature representation in critical regions.

The g_nConv module implements global spatial interaction of features to establish long-range dependencies, but only performs simple channel blending of the input feature maps, ignoring interchannel interaction. While the channel attention mechanism can effectively improve the performance and screening features of deep learning networks, this study uses the channel attention module to enhance the g_nConv module. Among the channel attention modules, the squeeze-and-excitation (SE) module (Hu et al., 2018) alters the feature dimensions, affecting the SE module's performance. In contrast, the efficient channel attention (ECA) module (Wang et al., 2020) is a highly efficient and lightweight local channel interaction strategy that is improved on the SE module. The ECA module avoids feature dimensionality reduction and uses some parameters to achieve a significant performance improvement. In this study, the ECA module was added to the g_nConv module (g_nConv ECA module) (Figure 4). Using the ECA module to perform local channel interaction on feature maps after channel blending in the g_nConv module improves the representation of the critical feature areas in the g_nConv module.

The improved recursive gated convolution (g_nConv ECA) module combines the global spatial and local channel interactions. The g_nConv ECA module inputs feature maps in the following steps:

(1) First, a set of features M_0 and N_i are obtained by channel blending through a linear projection layer.

$$\left[M_0^{HW\times C_0}, N_0^{HW\times C_0}, \ldots, N_{n-1}^{HW\times C_{n-1}}\right] = \psi_m(x) \tag{1}$$

(2) This set of features is then passed through the ECA module to obtain a new set of features M^+_0 and N^+_i.

$$\left[M_0^{+HW\times C_0}, N_0^{+HW\times C_0}, \ldots, N_{n-1}^{+HW\times C_{n-1}}\right] = ECA\left(\left[M_0^{HW\times C_0}, N_0^{HW\times C_0}, \ldots, N_{n-1}^{HW\times C_{n-1}}\right]\right) \tag{2}$$

(3) Gated convolution is performed recursively using the following equation,

$$M_{i+1} = DConv_i(N_i) \odot G_i(M_i)/S \tag{3}$$

$$G_i = \begin{cases} Identity, & i = 0 \\ Linear(C_{i-1}, C_i), & 1 \le i \le n-1 \end{cases} \tag{4}$$

where $DConv_i$ is a set of deep convolutional layers, G_i is the way of matching dimensions between different orders, and S is the scaling value to adjust the training stability. The formula for the ECA module in Eq. (2) is shown in Eq. (5).

$$\tilde{y} = \sigma(\varphi(y)) \otimes y \tag{5}$$

TABLE 1 YOLO-SCL model specific parameters table.

From	Params	Module	Arguments
-1	3520	Conv	[3, 32, 6, 2, 2]
-1	18560	Conv	[32, 64, 3, 2]
-1	18816	C3	[64, 64, 1]
-1	73984	Conv	[64, 128, 3, 2]
-1	115712	C3	[128, 128, 2]
-1	295424	Conv	[128, 256, 3, 2]
-1	625152	C3	[256, 256, 3]
-1	1180672	Conv	[256, 512, 3, 2]
-1	1182720	C3	[512, 512, 1]
-1	656896	SPPF	[512, 512, 5]
-1	131584	Conv	[512, 256, 1, 1]
-1	0	Upsample	–
[-1, 6]	0	Concat	[1]
-1	361984	C3	[512, 256, 1, False]
-1	33024	Conv	[256, 128, 1, 1]
-1	0	Upsample	–
[-1, 4]	0	Concat	[1]
-1	90880	C3	[256, 128, 1, False]
-1	147712	Conv	[128, 128, 3, 2]
-1	73059	g_nConv ECA	[128]
[-1, 14]	0	Concat	[1]
-1	132096	Light C3	[256, 256, False]
-1	590336	Conv	[256, 256, 3, 2]
[-1, 10]	0	Concat	[1]
-1	1182720	C3	[512, 512, 1, False]

where σ is the Sigmoid activation function, ϕ is a 1 × k one-dimensional convolution, and y is the input feature map.

3.2 C3 module lightweight design

The main role of the convolutional layer is to extract image features. An appropriate increase in the number of convolution operations for images containing large targets can obtain richer semantic information, whereas in images containing small targets, successive convolution operations may cause too much loss of detail information of some of the small targets, leading to unsatisfactory results of the task, whereas in images containing small targets, successive convolution operations may cause too much loss of detail information of some of the small targets, leading to unsatisfactory results of the task.

In images with small targets, successive convolution operations may cause too much loss of detailed information on some of the small targets, leading to unsatisfactory task results. The citrus psyllids accounts for a tiny proportion of the image pixels, resulting in the loss of some of its detailed feature information as the number of network layers increases. In the neck network of the YOLO-SCL model, the 17th, 21st, and 24th layer C3 modules detect small, medium, and large targets, respectively. Based on the deepening of layers, their degree of retaining the detailed feature information of small targets decreases sequentially. Therefore, to retain more feature information of small targets, this study improved the 21st layer C3 module in the neck network of the YOLO-SCL model by deleting convolutional layers. Figure 5 illustrates the C3 module before and after the improvement.

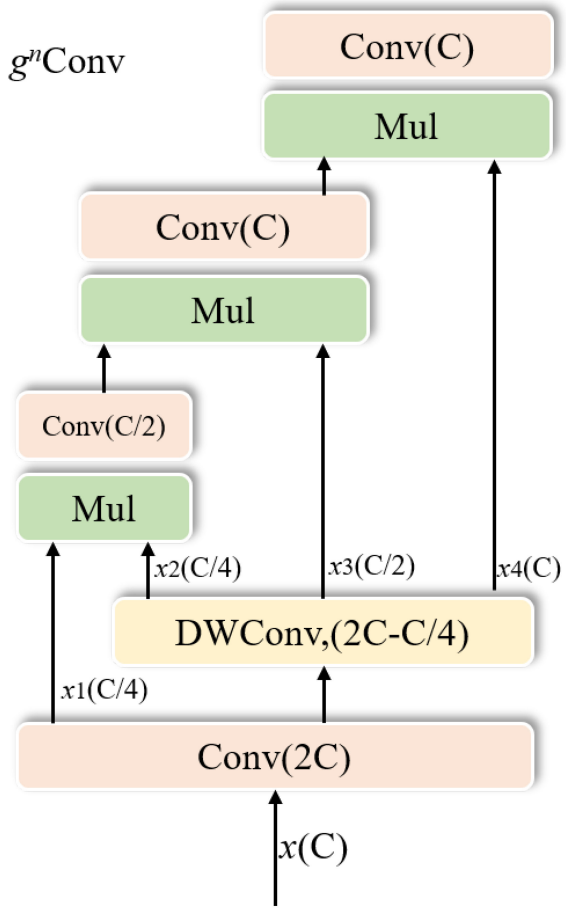

FIGURE 3
Recursive Gated Convolutions.

4 Hyperparameter optimization of the YOLO-SCL detection model

Considering the impact of hyperparameter settings on the performance of the detection model (Akay et al., 2022), this study adopts BWOA (F.Pena et al., 2020) to optimize the hyperparameters of the YOLO-SCL detection model. By leveraging the optimization iteration mechanism based on swarm intelligence, this study rapidly converged and obtained optimal

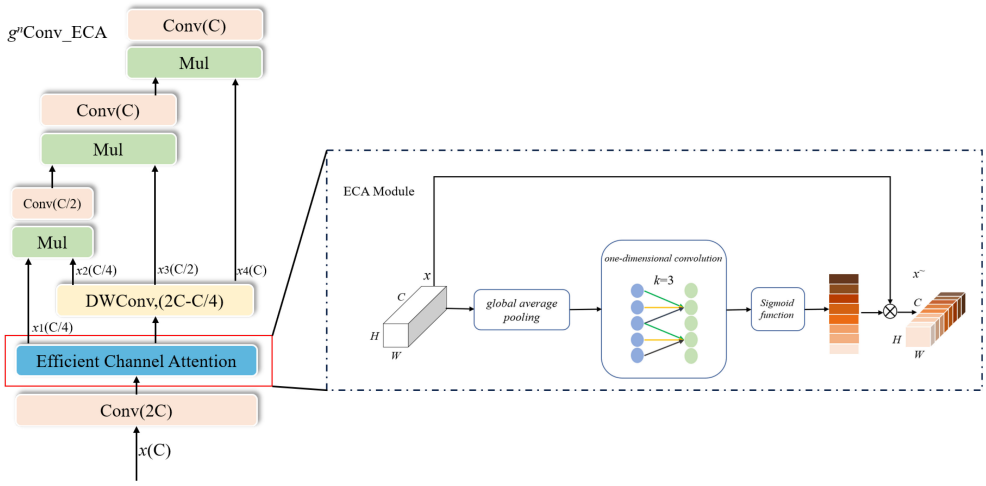

FIGURE 4
Improved Recursive Gated Convolutions based on spatial channel interaction.

hyperparameter combinations, thereby improving the performance of the model. This approach also addresses the issue of overreliance on experience in manual parameterization.

BWOA is inspired by the behavior of black widow spiders, and the algorithmic model mainly consists of in-web movement and pheromone control strategies for black widow spider groups. Figure 6 illustrates the movement strategy within the spider web, including both linear and spiral movement modes, which can be characterized by the formula shown in Eq. (6).

$$x_i(t+1) = \begin{cases} x_{gbest}(t) - m x_{r_1}(t), & if \ \ rand \le 0.3 \\ x_{gbest}(t) - \cos\ (2\pi\beta) x_i(t) \ in \quad other \quad case \end{cases} \tag{6}$$

where t is the current iteration number of the algorithm, x_i(t) is the ith spider individual, x_{gbest}(t) denotes the optimal spider individual of the current population, and x_{r1}(t) denotes a randomly selected spider individual in the current population, $r_1 \neq$ i. The control parameter m for the linear movement mode is a random floating-point number in an interval of [0.4,0.9], and the control parameter β for the spiral movement mode is a random floating-point number in an interval of [−1,1].

Second, the pheromone plays a crucial role in determining the state of individual spiders. During the mating process of male and female spiders, the spider that receives more nutrients exhibits better fecundity, resulting in a higher pheromone value that represents higher fecundity, which means higher fertility. The pheromone value for the ith spider individual in BWOA is calculated as shown in Eq. (7).

$$phermone_i = \frac{fitness_{max} - fitness_i}{fitness_{max} - fitness_{min}} \tag{7}$$

where $fitness_i$ denotes the adaptation value of the ith spider individual, and $fitness_{max}$ and $fitness_{min}$ represent the worst and optimal adaptation values of the current population, respectively. Therefore, the range of pheromone values for spider individuals is

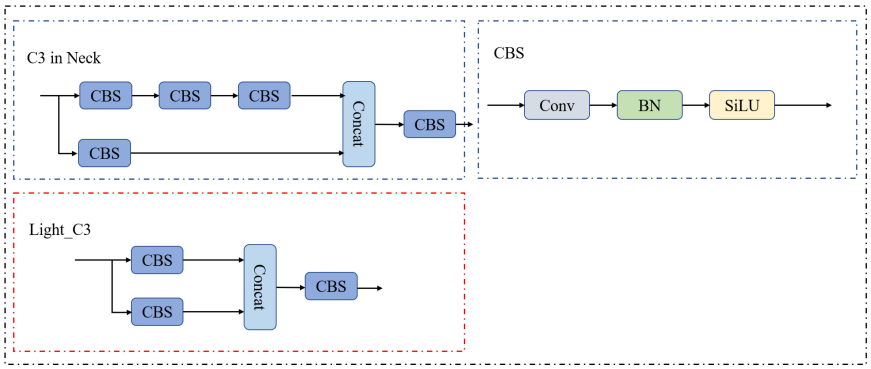

FIGURE 5
C3 module before and after improvement in the neck network.

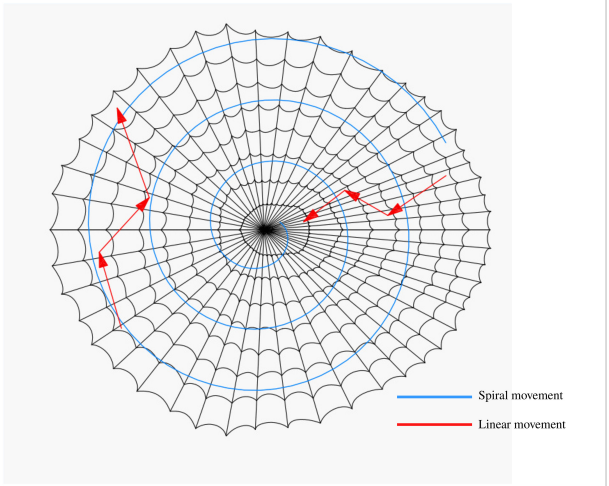

FIGURE 6
Black widow spider movement strategy.

[0,1]. In addition, if the pheromone value of spider individual i is not greater than 0.3, the position will be updated, as shown in Eq. (8).

$$x_i(t) = x_{gbest}(t) + \frac{1}{2}[x_{r_1} - (-1)^{\sigma} \times x_{r_2}(t)] \quad (8)$$

where x_{r1}(t), x_{r2}(t) denote randomly selected spider individuals in the current population, $r_1 \neq r_2 \neq$ i; σ takes values in the set {0,1}.

Figure 7 shows the flowchart of hyperparameter optimization of the detection model based on BWOA, and the computational steps include:

1) Data division: the dataset is collected and divided into training and validation sets.
2) Initialization of parameters and population: the parameters related to the algorithm are set, including the number of populations N, maximum number of iterations T, upper and lower bounds (ub and lb) of the hyperparameters, and the position of the population is initialized. Each individual represents a set of hyperparameters.
3) Calculation of fitness: after checking whether the position of an individual is out of bounds, each individual in the population is brought into the trained model to calculate the fitness value and each pheromone. The historical optimal individual x_{gbest} is updated.
4) Hyperparameter optimization: each searching individual in the population updates the positional information according to the pheromone size using Eqs. (6) and (8), respectively, and updates the number of iterations ($t = t + 1$) and individual pheromones.
5) Algorithm termination: the algorithm terminates when the termination conditions are met, and the optimized hyperparameters x_{gbest} are used to train the model and obtain the final model.

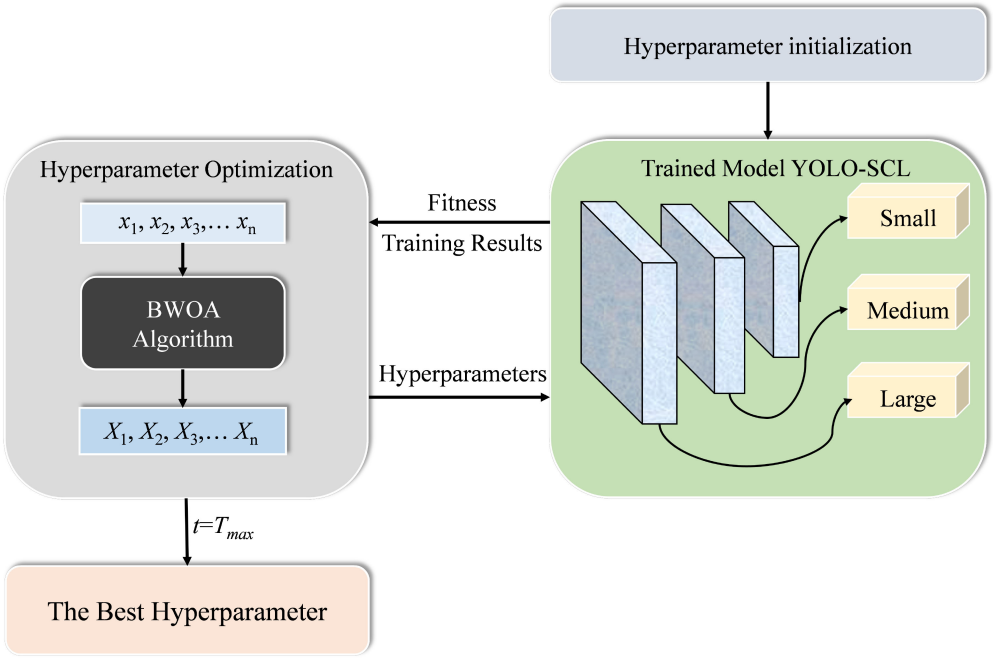

FIGURE 7
Flowchart of hyperparameter optimization of detection model based on BWOA algorithm.

5 Experimental results and analysis

5.1 Experimental environment and model evaluation metrics

The YOLO-SCL model was created based on the deep learning framework pytoch1.12.0, and all model training was performed in Windows 10 with an Intel(R) Core(TM) i7-8700 CPU @ 3.20 GHz 3.19 GHz and a GPU of NVIDIA GeForce RTX 2080 Ti.

During training, each model uses stochastic gradient descent and cosine annealing to reduce the learning rate. To save computational resources, the epoch and batch sizes were set to 300 and 16, respectively, and an early stopping strategy was set to stop the training early if the model performance did not improve after 100 iterations.

In this study, typical evaluation metrics such as size, giga floating-point operations per second (GFlops), precision (P), recall (R), average precision (AP), and the mean average precision (mAP) were used to verify the performance of the target detection model. The calculation formulas are as follows.

$$P = \frac{TP}{TP + FP} \tag{9}$$

$$R = \frac{TP}{TP + FN} \tag{10}$$

$$AP = \int_0^1 P(R)dR \tag{11}$$

$$mAP = \frac{1}{n}\left(\sum_{i=1}^{n} AP_i\right) \tag{12}$$

where true positives(TP) are the number of correctly detected targets, false positives (FP) are the number of samples in which annotation boxes were generated but in the wrong position or incorrectly labeled in the category, false negatives are the number of samples in which no annotation boxes were generated in the target. AP is equal to the area under the accuracy-recall curve, and mAP is the average of the AP in different categories. In this study, citrus psyllid is category 1, and the value of n is 1.

5.2 Benchmark model performance analysis

To achieve efficient and accurate detection of citrus psyllids small targets in complex environments, this study evaluated the performance of different YOLOv5 detection models based on the constructed citrus psyllid dataset. The experimental results are shown in Table 2. Among the different models tested, YOLOv5n had the lowest number of parameters and computations. However, its mAP@0.5 is lower than those of the YOLOv5s, YOLOv5m, YOLOv5l, and YOLOv5x models by 0.73%, 0.72%, 0.94%, and 1.16%, respectively. The mAP@0.5 of the YOLOv5m model is slightly lower than that of the YOLOv5s model, but the number of parameters and computations are approximately 2.97 and 3.03 times that of the YOLOv5s model. The mAP@0.5 of the YOLOv5l and YOLOv5x models are 0.21% and 0.43% higher than that of the YOLOv5s model, respectively. However, the number of parameters and computations amount of the YOLOv5l model is approximately 6.57 and 6.81 times that of the YOLOv5s model, and the number of parameters and computations amount of the YOLOv5x model is approximately 12.28 and 12.83 times more than the YOLOv5s model, respectively. Considering the number of parameters and computations, and mAP@0.5, YOLOv5s was chosen as the baseline model for the citrus psyllid detection task in this study.

TABLE 2 Detection results of different variants of the YOLOv5 model on the citrus psyllid dataset.

Model	Size (M)	GFlops	mAP@0.5 (%)
YOLOv5n	1.9	4.2	95.16
YOLOv5s	7.02	15.9	95.89
YOLOv5m	20.87	48.2	95.88
YOLOv5l	46.1	108.2	96.10
YOLOv5x	86.22	204.6	96.32

5.3 Analysis of the results of the ablation experiment

To achieve efficient and accurate detection of citrus psyllids small targets, ablation experiments were conducted on the constructed citrus psyllid dataset to analyze the importance of each module. The g_nConv, g_nConv ECA, and lightweight C3 (Light C3) modules were added to the model step-by-step to form several improved models, using the YOLOv5s model as the baseline model. The results of the experiments are shown in Table 3.

Table 3 shows that the model detection accuracy is improved by adding g_nConv, g_nConv ECA, and Light C3 modules. This is because the g_nConv module implements global spatial interactions, constructing long-distance dependencies that better represent critical regions' features. The g_nConv ECA module combines global spatial interactions with local channel interactions to further improve the model's ability to extract critical regions for accurate detection. The Light C3 module improves the C3 module by lightweight it, which retains the details of the small targets to a certain extent and achieves the purpose of reducing the number of model parameters, which helps to improve the model's performance and reduce the amount of computation.

The mAP@0.5 and mAP@0.5:.95 of Model 1 (YOLOv5s+ g_nConv model) and Model 2 (YOLOv5s+ g_nConv ECA model) are improved by 0.69%, 0.90% and 1.69%, 2.88%, respectively, compared with the baseline model, which indicates that the global spatial interaction mechanism effectively improves the model's detection of the target and that the g_nConv ECA module incorporates the local channel interaction, which makes the target detection accuracy further enhanced. Model 3 (YOLOv5s+Light C3 model) not only has 1.70M fewer parameters than the baseline model but also has mAP@0.5 and mAP@0.5:.95 is 0.69% and 1.53%

TABLE 3 Results of ablation experiments on the citrus psyllid dataset.

Methods	Baseline	g_nConv	g_nConv ECA	Light C3	Size (M)	GFlops	mAP @0.5 (%)	mAP@0.5:.95 (%)
YOLOv5s	√				7.02	15.9	95.89	50.78
Model 1	√	√			7.09	16.0	96.58	52.47
Model 2	√		√		7.10	16.2	96.79	53.66
Model 3	√			√	6.85	15.2	96.57	52.31
Model 4	√		√	√	6.92	15.5	97.07	53.43

"√" that the component is selected for use into model YOLOv5.

higher than the baseline model, indicating that the lightweight C3 module can effectively reduce the loss of the target feature information and ensure the improved detection accuracy while reducing the number of model parameters. Finally, the mAP@0.5 of model 4 (YOLOv5s+Light C3+ g_nConv ECA model) reaches 97.07%, which is 1.18% higher than the baseline model, and both are higher than the other improved models.

5.4 Comparative analysis with other detection models

In this section, the proposed YOLO-SCL model is compared with mainstream single-stage target detection models, including the YOLOv4-CSP (Wang et al., 2021a), YOLOX (Ge et al., 2021), YOLOR-p6 (Wang et al., 2021b), YOLOv7 (Wang et al., 2022a), YOLOv8 (Reis et al., 2023) models, and transformer-based end-to-end detection model DETR (Carion et al., 2020). Table 4 shows the test results, highlighting the advantage of YOLO-SCL model in terms of the number of parameters, computational load, and mAP compared to other control detection models. The improved architecture combining the g_nConv and lightweight C3 modules effectively improves the feature representation of the model for target regions. This addresses the problem of the model losing semantic information for small targets as the layers deepen. The DETR model benefits from the transformer's self-attention mechanism, and its mAP@0.5 is higher than that of the YOLOX and YOLOR-p6 models by 0.01% and 0.29%, respectively. However, compared with the YOLO-SCL model, the mAP@0.5 and mAP@0.5:.95 of the DETR model is lower than that of the YOLO model by 3.64% and 4.01%. The parameters and computations are 5.31 and 6.54 times higher than those of the YOLO-SCL model. The YOLOv4-CSP model, which is an improved model based on YOLOv4, obtained 94.56% mAP@0.5 and 50.41% mAP@0.5:.95 on the citrus psyllid detection task but was still 2.51% and 3.02% lower than the YOLO-SCL model. The YOLOv7 model mAP@0.5 is higher than other detection models. However, it is 1.23% lower than that of the YOLO-SCL model mAP@0.5 and 3.35% lower than that of the YOLO-SCL model mAP@0.5:.95, and the number of parameters and the amount of computation of the YOLOv7 model is much larger than that of the YOLO-SCL model. The YOLOv8 model mAP@0.5 is 1.86% lower than that of the YOLO-SCL model. However, it is 0.53% higher than the YOLO-SCL model mAP@0.5:.95. In summary, the proposed YOLO-SCL model has a parameter count of 6.92 M, which is easy to deploy on a mobile platform, and the model has the highest mAP@0.5, making it more suitable for the task of citrus psyllids detection in natural environments.

Figure 8 shows the iterative curves of mAP@0.5 and mAP@0.5:.95 during the training process of the YOLO series of detection models. The mAP@0.5 and mAP@0.5:.95 curves of the YOLOv5s, YOLOX, and proposed YOLO-SCL models almost intersect at the 50th epoch. The detection accuracy of the YOLOv5s and YOLOX models rapidly improves at the early stage. In contrast, the YOLO-SCL model steadily improves at the later stage and achieves results superior to those of the YOLOv5s, YOLOX and YOLOv8 models. The mAP@0.5 and mAP@0.5:.95 curves of the YOLOv7, YOLOv4-CSP, and YOLOR-p6 models are considerably inferior to that of the proposed YOLO-SCL model. For these three models, the curves fluctuate more with poor robustness than that of the proposed model.

Figure 9 shows the results of the YOLO series of detection models. The proposed YOLO-SCL model demonstrated effective detection of a higher number of citrus psyllids in complex backgrounds than that of other models, thereby improving

TABLE 4 Comparison of the performance of the latest models on the citrus psyllid dataset.

Methods	Size (M)	GFlops	mAP@0.5 (%)	mAP@0.5:.95 `(%)
YOLOv4-CSP	52.50	119.7	94.56	50.41
YOLOX	8.94	26.76	93.42	48.67
YOLOR-p6	36.8	80.6	93.14	49.46
YOLOv7	37.2	105.1	95.84	50.08
YOLOv8	11.2	28.6	95.21	53.96
DETR	36.74	101.4	93.43	49.42
YOLO-SCL	6.92	15.5	97.07	53.43

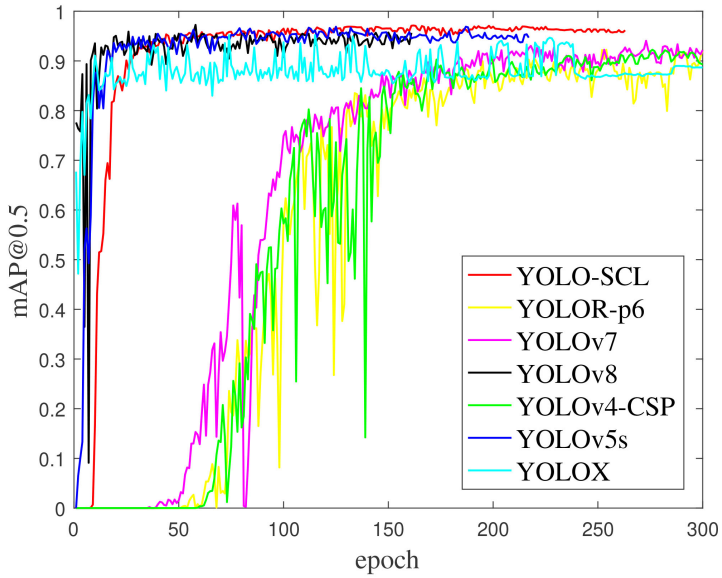

A mAP@0.5.

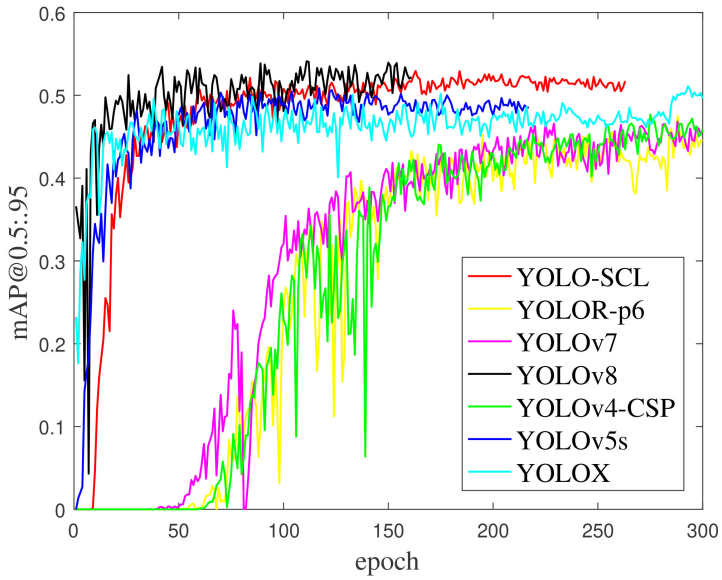

B mAP@0.5:.95.

FIGURE 8
mAP@0.5 and mAP@0.5:.95 iteration curves of training results on different models. **(A)** mAP@0.5. **(B)** mAP@0.5:.95.

detection accuracy. Under the conditions of low light and blurred individual psyllid due to filming problems, the improved model exhibited accurate identification with a low leakage rate, indicating that the g_nConv ECA module enhances the model's ability to express features in critical areas, making it highly efficient in extracting target features in complex backgrounds. Meanwhile, the lightweight C3 module retains the feature information of small targets to a certain extent, contributing to better target localization and identification of the model, thereby reducing the number of missed and false citrus psyllids detections.

5.5 Hyperparameter optimization of the detection model based on BWOA

In this study, 25 hyperparameter combinations of the YOLO-SCL model were used as the optimization objects. Based on the optimization iterative mechanism of swarm intelligence, the characteristics of BWOA, such as few control parameters and fast optimization rate, were used to map the hyperparameters into individual feasible solutions of BWOA and obtain the optimal hyperparameter combinations that are suitable for citrus psyllid

FIGURE 9
Test results of different models on the test images. The test results from top to bottom are YOLOv4-CSP, YOLOR-p6, YOLOv7, YOLOX, YOLOv8, YOLOv5s, and YOLO-SCL. Red boxes indicate missed detections, and blue boxes indicate false detections. **(A)** YOLOv4-CSP. **(B)** YOLOR-p6. **(C)** YOLOv7. **(D)** YOLOX. **(E)** YOLOv8. **(F)** YOLOv5s. **(G)** YOLO-SCL.

detection tasks. The control parameters included 50 epochs, 100 iteration numbers, and 10 iteration numbers. The hyperparameter optimization results are shown in Tables 5 and Table 6 compares the detection results before and after optimization. Table 6 shows that before and after the optimization of hyperparameters, the precision, recall, mAP@0.5, and mAP@0.5:.95 were improved by 1.44%, 1.60%, 0.11%, and 0.75%, respectively, indicating that the optimization of hyperparameters can effectively improve the precision of the detection of citrus psyllids, and further improve the performance of the model.

Figure 10 shows the iterative curves of mAP@0.5 and mAP@0.5:.95 of the YOLO-SCL model training process before and after optimization. The mAP@0.5 and mAP@0.5:.95 curves of the optimized model in the first 10 epochs have large fluctuations, indicating that the optimization of the hyperparameter combination affects the stability of the detection model. However, the iterative curve gradually stabilized as the epoch increased, and better detection accuracy was obtained.

5.6 Lightweight C3 module grad-cam analysis

In this study, lightweight experiments are performed on the C3 modules in layers 17, 20, and 23 of the YOLOv5s model neck network, and the results are shown in Table 7. The YOLOv5s model lightened for the 17th layer C3 module has 0.48% lower mAP@0.5 and 0.50% lower mAP@0.5:.95 than the baseline model YOLOv5s, and this lightning operation affects the performance of the baseline model. The mAP@0.5 of the YOLOv5s model lightened for the 20th and 23rd C3 modules are 0.68% and 0.82% higher than that of the YOLOv5s model, respectively, while the mAP@0.5:.95 of the 20th lightened YOLOv5s model are 1.63% higher than that of the 23rd lightened YOLOv5s model. Therefore, in this study, we chose to improve the 21st layer C3 module of the YOLO-SCL model.

To further verify that the lightweight C3 module can reduce the loss of detailed feature information of small targets by deleting the convolutional layers, this study uses the Grad-CAM method to analyze the attention focused on the target with different improvements in the 20th layer of the C3 module. Figure 11 shows the Grad-CAM thermograms of the several YOLOv5s+Light C3 models trained on the citrus psyllid dataset and the 20th layer of the YOLOv5s model. Figs. b(left), c(left) and d(left) show that the YOLOv5s and YOLOv5s+Light C3(-1×CBS) models lose the feature information of the target to a certain extent, which affects the model's performance of detecting the target, whereas the YOLOv5s+Light C3(-2×CBS) model not only retains the feature information of the target but also improves the attention to the target. Figs. b(right), c (right), and d(right) show that the YOLOv5s and YOLOv5s+Light C3(-1×CBS) models exhibit a more diffuse attention area and are more affected by the complex environment, whereas the YOLOv5s+Light C3(-2×CBS) model focuses more on the target. The comprehensive experimental results show that by lightening the C3 module and deleting the convolutional layer, the feature

TABLE 5 Results before and after hyperparameter optimization.

Hyperparameter	Before Optimization	After Optimization	(lb, ub)
Lr0	0.001	0.04185	(0.00005, 0.1)
Lrf	0.01	0.14641	(0.01, 1.0)
Momentum	0.937	0.70022	(0.6,0. 98)
Weight decay	0.0005	0.00014	(0.0, 0.001)
Warmup epochs	3.0	1.16490	(0.0, 5.0)
Warmup momentum	0.8	0.07027	(0.0, 0.95)
Warmup bias lr	0.1	0.01957	(0.0, 0.2)
Box	0.05	0.02334	(0.02, 0.2)
Cls	0.5	0.63575	(0.2, 4.0)
Cls pw	1.0	0.58352	(0.5, 2.0)
Obj	1.0	1.59100	(0.2, 4.0)
Obj pw	1.0	0.58352	(0.5, 2.0)
Anchor t	4.0	3.64620	(2.0, 8.0)
Hsv h	0.015	0.02919	(0.0, 0.1)
Hsv s	0.7	0.03530	(0.0, 0.9)
Hsv v	0.4	0.01103	(0.0, 0.9)
Degrees	0.0	0.05874	(0.0, 45.0)
Translate	0.1	0.29687	(0.0, 0.9)
Scale	0.5	0.01554	(0.0, 0.9)
Shear	0.0	3.26980	(0.0, 10.0)
Flipud	0.0	0.13026	(0.0, 1.0)
Mosaic	1.0	0.02767	(0.0, 1.0)
Mixup	0.0	0.09442	(0.0, 1.0)
Copy pasts	0.0	0.21605	(0.0, 1.0)
anchors	–	2.40950	(2.0, 10.0)

information of the tiny target is retained to the maximum extent, and the attention is more focused on the target, improving the detection accuracy of the target.

5.7 Detection model porting deployment based on NVIDIA JETSON AGX XAVIER embedded platform

In this study, the YOLO-SCL model porting deployment was performed using NVIDIA Jetson AGX Xavier edge computing platform based on the ARM architecture. The Jetson AGX Xavier edge computing platform is 100 × 87 mm in size, has a GPU of 512 cores, a CPU of 8 cores, and 32 GB of storage. The system of this platform is Ubuntu 18.04.

To facilitate the porting of the YOLO-SCL model, a runtime environment was configured on a Jetson AGX Xavier to debug the hardware performance of the platform, specifically the deep learning gas pedal engine. The model porting and deployment results are shown in Figure 12, demonstrating that the average processing time of a single-frame image is 38.8 ms, and the power consumption is 16.85 W.

TABLE 6 Comparison of detection results before and after hyperparameter optimization.

	P(%)	R(%)	mAP@0.5(%)	mAP@0.5:.95(%)
Before Optimization	93.73	92.35	97.07	53.43
After Optimization	95.17	93.95	97.18	54.18

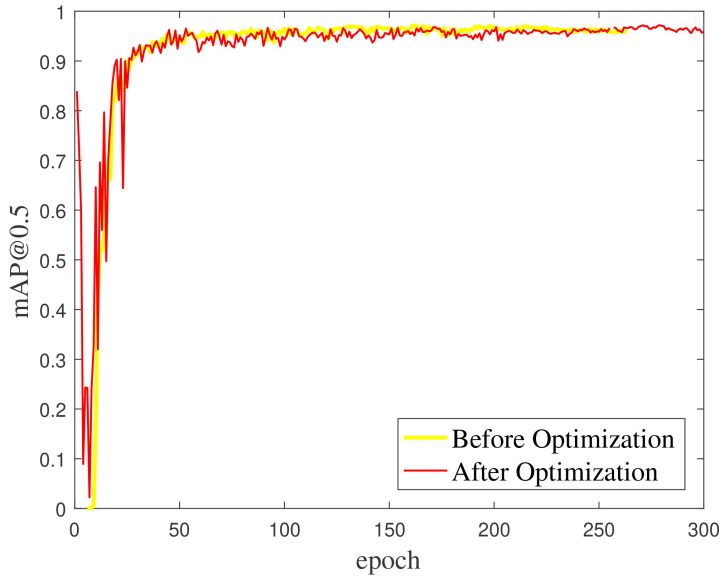

A mAP@0.5.

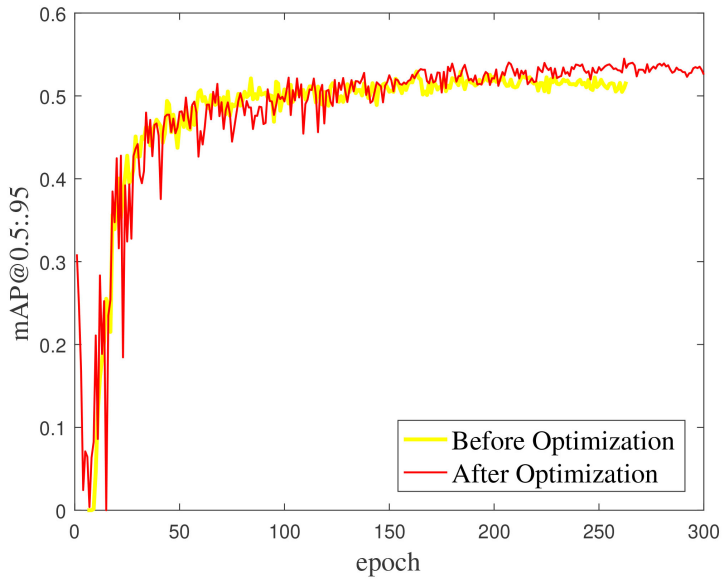

B mAP@0.5:.95.

FIGURE 10
The mAP@0.5 and mAP@0.5.95 curves of the YOLO-SCL model training process before and after hyperparameter optimization. **(A)** mAP@0.5. **(B)** mAP@0.5:.95.

TABLE 7 Experimental results of lightweight C3 modules at layers 17, 20, and 23 in the neck network of the YOLOv5s model.

Methods	mAP@0.5 (%)	mAP@0.5:.95 (%)
YOLOv5s+Light C3(17)	95.41	50.28
YOLOv5s+Light C3(20)	96.57	52.31
YOLOv5s+Light C3(23)	96.71	50.68

6 Conclusions and analyses

6.1 Discussion

The mAP@0.5 results of the YOLO-SCL model on the citrus psyllids detection task were better than those of the other six target detection models, from the prediction result graphs, the YOLO-SCL model effectively solved the missed and false problems that occurred in the other six models. The above results show that the

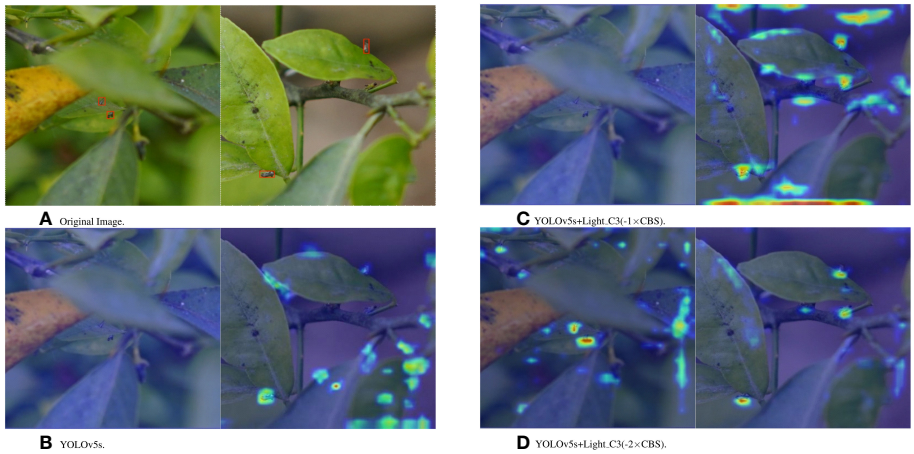

FIGURE 11
Grad-CAM thermograms of the YOLOv5s+Light C3 model trained on the citrus psyllid dataset and YOLOv5s model layer 20. **(A)** Original Picture. **(B)** YOLOv5s. **(C)** YOLOv5s+Light C3(-1×CBS). **(D)** YOLOv5s+Light C3(-2×CBS).

improved architecture combining the g_nConv and lightweight C3 modules effectively improves the feature representation of the model for target regions. In the follow-up work, attempts will be made to apply the improved approach to different target detection models for citrus psyllid detection tasks as well as to apply the YOLO-SCL model to more tasks in other fields.

6.2 Conclusions

In this study, a YOLO-SCL model for detecting citrus psyllids in natural environments was proposed to improve the detection accuracy of citrus psyllids in response to problems such as the difficulty of accurately detecting small targets and complex background interference. First, the g_nConv module based on spatial channel interaction was proposed to improve the model's detection accuracy for small targets; the module is realized through the combination of global spatial and local channel interactions. Second, to maximize the retention of small target feature information, the 21st layer of the C3 module in the YOLO-SCL model was lightened and improved, making the model more target-aware. In addition, optimization of the hyperparameters in the YOLO-SCL model using BWOA. The main conclusions are as follows:

i. The YOLO-SCL model achieved 97.07% mAP@0.5 and 53.43% mAP@0.5:.95 with a model parameter count and computation of 6.92 M and 15.5 GFlops, respectively. The model considerably improved the detection of citrus psyllids and was ported and deployed on the edge computing platform with an average processing time of 38.8 ms and power consumption of 16.85 W for a single-frame image. In addition, optimization of the hyperparameters in the YOLO-SCL model using BWOA

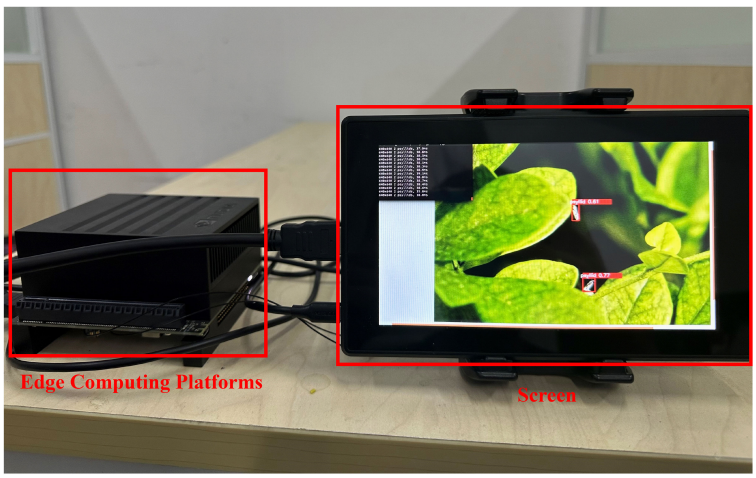

FIGURE 12
Jetson AGX Xavier edge computing platform model porting deployment detection results.

resulted in higher mAP@0.5 and mAP@0.5:.95 of 97.18% and 54.18%, respectively.

ii. Compared with the other six detection models, the YOLO-SCL model achieved the highest mAP@0.5. The YOLO-SCL model is 6.92 M and 15.5 GFlops, which are 14.25% and 2.52% lower than those of the conventional YOLOv5s model, respectively. The above data show that the improved model has achieved better performance in recognition accuracy and efficiency.

iii. This study discusses citrus psyllids detection in natural environments; the above results show that the YOLO-SCL model performs well on the citrus psyllid detection task and provides some values for studying different small target detection tasks.

Data availability statement

The original contributions presented in the study are included in the article/supplementary material, further inquiries can be directed to the corresponding author/s.

Author contributions

SL: Conceptualization, Funding acquisition, Methodology, Supervision, Validation, Writing – original draft. XZ: Writing – original draft, Data curation, Formal Analysis, Methodology, Software, Visualization, Resources. ZL: Conceptualization, Funding acquisition, Supervision, Validation, Writing – review & editing. XL: Data curation, Formal Analysis, Writing – review & editing. YC: Data curation, Formal Analysis, Writing – review & editing. WZ: Data curation, Formal Analysis, Writing – review & editing.

Funding

The author(s) declare financial support was received for the research, authorship, and/or publication of this article. This research was funded by National Natural Science Foundation of China (32271997, 31971797); General Program of Guangdong Natural Science Foundation (2021A1515010923); Special Projects for Key Fields of Colleges and Universities in Guangdong Province (2020ZDZX3061); Key Technologies R&D Program of Guangdong Province (2023B0202100001); and China Agriculture Research System of MOF and MARA (CARS-26).

Conflict of interest

The authors declare that the research was conducted in the absence of any commercial or financial relationships that could be construed as a potential conflict of interest.

Publisher's note

References

Akay, B., Karaboga, D., and Akay, R. (2022). comprehensive survey on optimizing deep learning models by metaheuristics. *Artif. Intell. Rev.* 55, 829–894. doi: 10.1007/s10462-021-09992-0

Bao, M., Zheng, Z., and Sun, X. (2020). Enhancing pcr capacity to detect 'candidatus liberibacter asiaticus' utilizing whole genome sequence information. *Plant Dis.* 104, 527–532. doi: 10.1094/pdis-05-19-0931-re

Carion, N., Massa, F., and Synnaeve, G. (2020). "End-to-end object detection with transformers," in *Computer Vision–ECCV 2020: 16th European Conference, Glasgow, UK, August 23–28, 2020, Proceedings, Part I 16.* (Springer International Publishing), 213–229. arxiv-2005.12872.

Dosovitskiy, A., Beyer, L., and Kolesnikov, A. (2020). An image is worth 16x16 words: Transformers for image recognition at scale. *arXiv preprint.* arxiv-2010.11929.

F.Pena, D., H.Peraza, V., and Almazán, C. (2020). A novel bio-inspired algorithm applied to selective harmonic elimination in a three-phase eleven-level inverter. *Math. Problems Eng* 2020, 1–10. doi: 10.1155/2020/8856040

Gao, X., Mo, M., and Wang, H. (2021). Recent advances in small object detection. *J. Data Acquisition Process.* 36, 391–477. doi: 10.16337/j.10049037.2021.03.001

Ge, Z., Liu, S., and Wang, F. (2021). Yolox: Exceeding yolo series in 2021. *arXiv preprint.* arxiv-2107.08430.

Hu, J., Shen, L., and Sun, G. (2018). Squeeze-and-excitation networks. In. *Proc. IEEE Conf. Comput. Vision Pattern Recognit.*, 7132–7141. doi: 10.1109/CVPR.2018.00745

Jiao, G. (2016). Fruit tree deficiencies and control measures. *Shangcai County Agric. Bureau Secur. Inspection Station* 1, 17. doi: 10.15904/j.cnki.hnny.2016.10.013

Khanramaki, M., Asli-Ardeh, E. A., and Kozegar, E. (2021). Citrus pests classification using an ensemble of deep learning models. *Comput. Electron. Agric.* 186, 106192. doi: 10.1016/j.compag.2021.106192

Lan, Y., Zhu, Z., and Deng, X. (2019). Monitoring and classification of citrus huanglongbing based on uav hyperspectral remote sensing. *Trans. Chin. Soc. Agric. Eng.* 35, 92–100. doi: 10.11975/j.issn.1002-6819.2019.03.012

Li, K., Wang, J., and Jalil, H. (2023). A fast and lightweight detection algorithm for passion fruit pests based on improved yolov5. *Comput. Electron. Agric.* 204, 107534. doi: 10.1016/j.compag.2022.107534

Liang, L., Tian, Z., and Hu, X. (2018). Detection of citrus huanglongbing by conventional pcr. *Plant Prot.* 44, 149–153. doi: 10.16688/j.zwbh.2017071

Liu, H., Zhang, L., and Shen, Y. (2019). Real-time pedestrian detection in orchard based on improved ssd. *Trans. Chin. Soc. Agric.* 50, 29–35. doi: 10.6041/j.issn.1000-1298

Liu, Y., Xiao, H., and Deng, Q. (2016). Nondestructive detection of citrus greening by near infrared spectroscopy. *Trans. Chin. Soc. Agric. Eng.* 32 (14), 202–208. doi: 10.11975/j.issn.1002-6819.2016.14.027

Ma, W., Pang, Z., and Huang, X. (2022). Citrus huanglongbing is a pathogen-triggered immune disease that can be mitigated with antioxidants and gibberellin. *Nat. Commun.* 13, 529. doi: 10.1038/s41467-022-28189-9

Pang, H., Zhang, Y., and Cai, W. (2022). A real-time object detection model for orchard pests based on improved yolov4 algorithm. *Sci. Rep.* 12, 13557. doi: 10.1038/s41598-022-17826-4

Peng, H., He, H., and Gao, Z. (2022). Litchi diseases and insect pests identification method based on improved shufflenetv2. *Trans. Chin. Soc. Agric.* 53, 290–300. doi: 10.6041/j.issn.10001298.2022.12.028

Rao, Y., Zhao, W., and Tang, Y. (2022). Hornet: Efficient high-order spatial interactions with recursive gated convolutions. *Adv. Neural Inf. Process. Syst.* 35, 10353–10366. arxiv-2207.14284.

Reis, D., Kupec, J., and Hong, J. (2023). Real-time flying object detection with yolov8. *arXiv preprint*. arxiv-2305.09972.

Shi, X., Xu, L., and Tang, Z. (2023). Asfl-yolox: An adaptive spatial feature fusion and lightweight detection method for insect pests of the papilionidae family. *Front. Plant Sci.* 14. doi: 10.3389/fpls.2023.1176300

Vaswani, A., Shazeer, N., and Parmar, N. (2017). Attention is all you need. *arXiv preprint. Syst.* 30. arxiv-1706.03762.

Wang, C., Bochkovskiy, A., and Liao, H. (2021a). "Scaled-yolov4: Scaling cross stage partial network," in *Proceedings of the IEEE/cvf conference on computer vision and pattern recognition*, 13029–13038. arxiv-2011.08036.

Wang, C., Bochkovskiy, A., and Liao, H. (2022a). Yolov7: Trainable bag-of-freebies sets new state-of-theart for real-time object detectors. *arXiv preprint*. doi: 10.1109/CVPR52729.2023.00721

Wang, L., Lan, Y., and Liu, Z. (2021c). Development and experiment of the portable real-time detection system for citrus pests. *Trans. Chin. Soc. Agric. Eng.* 37 (9), 282–288. doi: 10.11975/j.issn.1002-6819.2021.09.032

Wang, Z., Niu, Y., and Vashisth, T. (2022b). Nontargeted metabolomics-based multiple machine learning modeling boosts early accurate detection for citrus huanglongbing. *Horticult. Res.* 9. doi: 10.1093/hr/uhac145

Wang, Q., Wu, B., and Zhu, P. (2020). "Eca-net: Efficient channel attention for deep convolutional neural networks," in *Proceedings of the IEEE/CVF conference on computer vision and pattern recognition*. 11534–11542. arxiv-1910.03151.

Wang, C., Yeh, I., and Liao, H. (2021b). You only learn one representation: Unified network for multiple tasks. *arXiv preprint*. arxiv-2105.04206.

Yang, P., Nie, Z., and Yao, M. (2022). Diagnosis of hlb-asymptomatic citrus fruits by element migration and transformation using laser-induced breakdown spectroscopy. *Optics Express* 30, 18108–18118. doi: 10.1364/oe.454646

Yang, D., Wang, F., and Hu, Y. (2021). Citrus huanglongbing detection based on multi-modal feature fusion learning. *Front. Plant Sci.* 12, 809506. doi: 10.3389/fpls.2021.809506

Ye, J., Qiu, W., and Yang, J. (2021). Litchi pest identification method based on deep learning. *Res. Explor. Lab.* 40 (06), 4. doi: 10.19927/j.cnki.syyt.2021.06.007

Yuan, K., Chen, Z., and Yang, T. (2020). Spectral sensitivity and response to light intensity of diaphorina citri kuwayama (hemiptera: Psyllidae). *J. Yunnan Agric. Univ. (Natural Sci.)* 35, 750–755. doi: 10.12101/j.issn.1004-390X(n).201911005

Zhang, Y., Cai, W., and Fan, S. (2022). Object detection based on yolov5 and ghostnet for orchard pests. *Information* 13, 548. doi: 10.3390/info13110548

frontiers | Frontiers in Plant Science

TYPE Original Research
PUBLISHED 27 November 2023
DOI 10.3389/fpls.2023.1280365

OPEN ACCESS

EDITED BY
Andreas Herbst,
Institute for Application Techniques in Plant Protection, Germany

REVIEWED BY
Xiaojuan Zhang,
Sichuan University, China
Wenbin Wu,
Chinese Academy of Agricultural Sciences (CAAS), China

*CORRESPONDENCE
Si Wang
frankly@163.com.cn

RECEIVED 20 August 2023
ACCEPTED 08 November 2023
PUBLISHED 27 November 2023

CITATION
Qiu X, Chen H, Huang P, Zhong D, Guo T, Pu C, Li Z, Liu Y, Chen J and Wang S (2023) Detection of citrus diseases in complex backgrounds based on image–text multimodal fusion and knowledge assistance. *Front. Plant Sci.* 14:1280365. doi: 10.3389/fpls.2023.1280365

Detection of citrus diseases in complex backgrounds based on image–text multimodal fusion and knowledge assistance

Xia Qiu[1,2], Hongwen Chen[1,2], Ping Huang[1], Dan Zhong[1,2], Tao Guo[1,2], Changbin Pu[1,2], Zongnan Li[1,2], Yongling Liu[1], Jin Chen[3] and Si Wang[1,2]*

[1]Institute of Remote Sensing and Digital Agriculture, Sichuan Academy of Agricultural Sciences, Chengdu, China, [2]Science and Technology Center of Intelligent Agriculture, Sichuan Academy of Agricultural Sciences, Chengdu, China, [3]State Key Laboratory of Remote Sensing Science, Institute of Remote Sensing Science and Engineering, Faculty of Geographical Science, Beijing Normal University, Beijing, China

Diseases pose a significant threat to the citrus industry, and the accurate detection of these diseases represent key factors for their early diagnosis and precise control. Existing diagnostic methods primarily rely on image models trained on vast datasets and limited their applicability due to singular backgrounds. To devise a more accurate, robust, and versatile model for citrus disease classification, this study focused on data diversity, knowledge assistance, and modal fusion. Leaves from healthy plants and plants infected with 10 prevalent diseases (citrus greening, citrus canker, anthracnose, scab, greasy spot, melanose, sooty mold, nitrogen deficiency, magnesium deficiency, and iron deficiency) were used as materials. Initially, three datasets with white, natural, and mixed backgrounds were constructed to analyze their effects on the training accuracy, test generalization ability, and classification balance. This diversification of data significantly improved the model's adaptability to natural settings. Subsequently, by leveraging agricultural domain knowledge, a structured citrus disease features glossary was developed to enhance the efficiency of data preparation and the credibility of identification results. To address the underutilization of multimodal data in existing models, this study explored semantic embedding methods for disease images and structured descriptive texts. Convolutional networks with different depths (VGG16, ResNet50, MobileNetV2, and ShuffleNetV2) were used to extract the visual features of leaves. Concurrently, TextCNN and fastText were used to extract textual features and semantic relationships. By integrating the complementary nature of the image and text information, a joint learning model for citrus disease features was achieved. ShuffleNetV2 + TextCNN, the optimal multimodal model, achieved a classification accuracy of 98.33% on the mixed dataset, which represented improvements of 9.78% and 21.11% over the single-image and single-text models, respectively. This model also exhibited faster convergence, superior classification balance, and enhanced generalization capability, compared with the other methods. The image-text multimodal feature fusion network proposed in this study, which integrates text and image features with

domain knowledge, can identify and classify citrus diseases in scenarios with limited samples and multiple background noise. The proposed model provides a more reliable decision-making basis for the precise application of biological and chemical control strategies for citrus production.

KEYWORDS

citrus disease, deep learning, multimodal fusion, background diversity, knowledge assistance

1 Introduction

Citrus crops are among the most important fruit crops worldwide, and they are widely cultivated in more than 140 countries and regions and have significant economic value (Rao et al., 2021). However, citrus pests and diseases pose serious threats to orchard production in terms of quality and yield (Sun et al., 2019) and represent major factors that hinder the sustainable development of the citrus industry. Thus, the development of efficient and applicable methods for detecting citrus pests and diseases is crucial to ensuring the robust expansion of the citrus industry. Previous studies typically identified citrus diseases through field observations (Leong et al., 2022) or pathogen identification (Patané et al., 2019). However, these methods are influenced by subjective factors and require domain knowledge and specialized equipment; further, they often present low accuracy and efficiency. With the advancement of computer vision technology, machine learning methods have gradually been applied to identifying citrus diseases. Initially, researchers explored traditional machine learning algorithms involving commonly used support vector machine (SVM) and random forest (RF) algorithms (Wang et al., 2021c; Dananjayan et al., 2022). Classification and regression trees (CARTs) and multilayer perceptrons (MLPs) have been used to identify storage diseases in citrus (Gómez-Sanchis et al., 2012). However, these methods are not appropriate for complex image features and multicategory classifications; thus, their effectiveness in practical applications is limited. In recent years, significant progress has been made in the use of deep learning technology for citrus disease identification. Convolutional neural networks (CNNs) are representative deep learning methods that have achieved breakthrough results in image classification tasks. Classic and lightweight networks, such as visual geometry group (VGG) (Xing et al., 2019), residual network (ResNet) (Luaibi et al., 2021), and efficient convolutional neural networks for mobile vision (MobileNet) (Barman et al., 2020), have been successively applied to image feature extraction and classification to improve citrus disease classification accuracy through higher-level feature mining. Despite these advances, existing methods face challenges such as insufficient training samples required for higher detection accuracy and poor transferability to complex production environments and diverse disease types. Therefore, improving detection accuracy based on limited sample sizes has become increasingly important.

Deep learning has emerged as a research focal point for the accurate identification of plant diseases. It overcomes the limitations of traditional machine learning, which relies on manually generated features, by enabling the construction of an end-to-end deep network structure. This facilitates an automated process that is advantageous for extracting high-level features (Goodfellow et al., 2016). Previous research on deep learning based methods have achieved promising results in the early detection of plant diseases (Upadhyay and Kumar, 2021), lesion segmentation (Li et al., 2022), disease type classification (Xing et al., 2019), and disease occurrence prediction (Delnevo et al., 2022). Historically, citrus disease identification and classification methods have primarily used single-source data based on image modalities, including images (Barman et al., 2020; Luaibi et al., 2021; Syed-Ab-Rahman et al., 2022), fluorescence spectra (Neves et al., 2023), and Internet of Things (IoT) data (Delnevo et al., 2022). The performance of such methods is highly dependent on large datasets and manual annotation. Expanding datasets to improve disease identification performance can be expensive. Ferentinos (2018) used 87848 images covering 25 plants and 57 diseases and compared the disease identification accuracy of five typical CNN networks; the results showed that the VGG model achieved the highest accuracy of 99.53%. In addition, Chellapandi et al. (2021) and Saleem et al. (2020) used 54306 images of 14 diseases, Abbas et al. (2021) used 16,012 tomato disease images, and Brahimi et al. (2017) used 16012 tomato disease images for training and obtained more than 99% accuracy on networks such as DenseNet, AlexNet, and Xception. However, with smaller datasets, the training accuracy rarely exceeded 95% (Ramcharan et al., 2017; Sibiya and Sumbwanyambe, 2019). In addition, approximately 50% of the data in current plant disease identification research are obtained from public datasets (Ramanjot et al., 2023). Using PlantVillage as an example, images are primarily acquired in laboratories or under unique background conditions. The uniformity of sample backgrounds hinders model feature learning, and uncertainties caused by sample selection biases hinder the adaptation of automated plant disease detection systems production scenarios (Hernandez and Lopez, 2020). Although the aforementioned studies have achieved satisfactory identification results using specific datasets, challenges, there are challenges such as poor model robustness, long model iteration cycles, and difficulty in generating massive datasets. As a result, models cannot easily adapt to complex environments and backgrounds in real-world scenarios.

Given the development of deep learning technologies and the rapid acquisition of multi-source data coupled with complex and varied real-world scenarios involving multiple data types, multimodal fusion technology has been introduced in the field of plant pest and disease detection. The full exploitation of the complementarity and correlations between modalities to achieve multimodal data fusion has emerged as a promising new direction in disease research (Yang et al., 2021). By integrating images with environmental parameters (Zhang et al., 2022), hyperspectral information (Yang et al., 2021), and text information (Wang et al., 2021b), the close relationship between disease occurrence and the environment can be fully exploited. Moreover, the complementarity between modalities facilitates the identification of highly similar symptoms and disease classifications under limited sample conditions. Text data are relatively easy to obtain and can be processed without sophisticated equipment and techniques; thus, they can serve as an excellent source of auxiliary information. Information obtained from text sources can complement that from image sources, thereby alleviating the problem of insufficient image training samples (Wang et al., 2022). In fine-grained image recognition tasks, image and text information are jointly trained through different training forms and feature representations, which effectively addresses the problem wherein the image modality is similarly represented but other modalities are underutilized (Reed et al., 2016; He and Peng, 2020). However, traditional textual information derived from natural language descriptions of observers may be incomplete or erroneous because of subjectivity and limitations in the knowledge background (Wang et al., 2021a). Moreover, the preparation and preprocessing of natural language methods are challenging and time consuming.

Given the needs and weaknesses of existing methods, this study aimed to develop a plant disease detection method based on a deep learning feature fusion network based on a multimodal image-text classification to improve the accuracy and efficiency of citrus disease detection in complex backgrounds. By selecting excellent networks of a single image and text modal information and constructing fusion models, the cross-complementarity of information was fully exploited, which enhanced the comprehensive use of features and improved detection accuracy and robustness. Moreover, we propose the use of agricultural domain knowledge to construct a structured glossary for citrus disease characteristics. This glossary can assist in the preparation of text modal information, increase the efficiency of data production, and improve the credibility of identification results. To evaluate the performance and strengths of the proposed method, we used various sample settings and performed dataset cross-validations.

2 Materials and methods

2.1 Image and text models used in this article

Deep learning architectures are associated with advancements in various domains, including plant disease identification. This section provides a review of the structural features of the models used in this study, as well as their applications and potential advantages in plant disease identification. The basic frameworks of the models are shown in Figure 1. VGG16 has 13 convolutional layers and 3 fully connected layers, and it can use small filters and

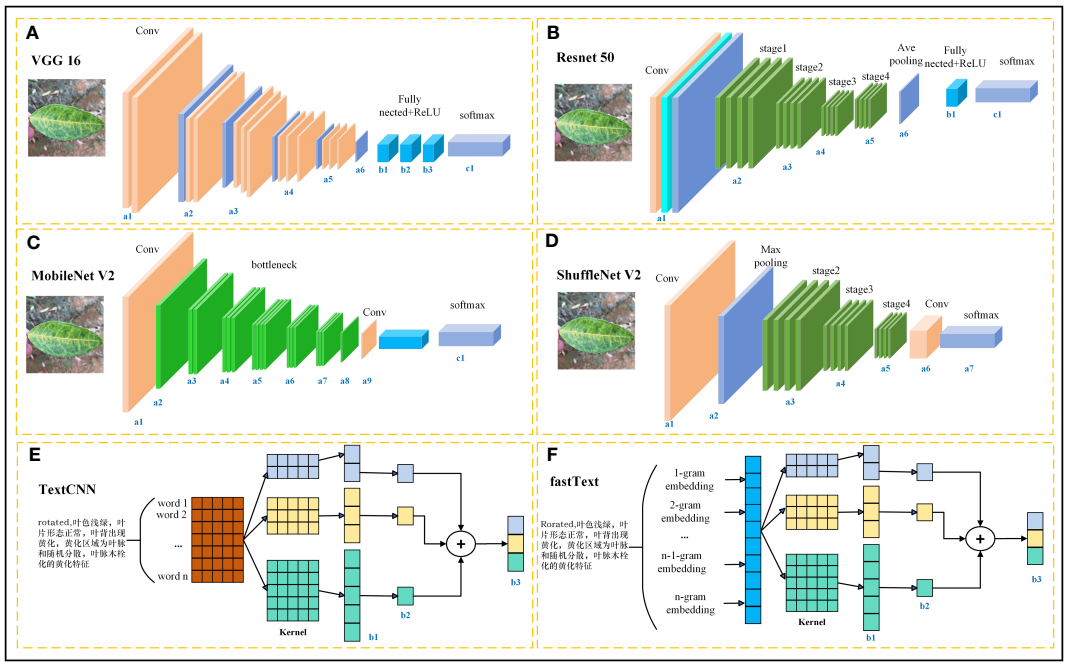

FIGURE 1
Basic framework of the used image and text models. **(A)** VGG16, **(B)** ResNet50, **(C)** MobileNet V2, **(D)** ShuffleNet V2, **(E)** TextCNN, and **(F)** fastText.

deeper layers to extract more complex features from disease images (Simonyan and Zisserman, 2014). In the context of plant disease identification, VGG16 has been used to extract complex patterns and features from disease images of rice (Jiang et al., 2021), millet (Coulibaly et al., 2019), canola (Abdalla et al., 2019), and tomato (Rangarajan et al., 2018). ResNet50 introduced a residual network structure that effectively avoids overfitting problems by increasing the network depth (He et al., 2016); additionally, it has been shown to provide superior performance in scenarios with complex background noise and diverse disease manifestations (Picon et al., 2019). MobileNet V2 and ShuffleNet V2 stand out as lightweight models. MobileNet V2 uses inverted residuals and linear bottlenecks to enhance efficiency (Sandler et al., 2018), while ShuffleNet V2 employs group convolution and channel shuffling (Ma et al., 2018). Thus, they are ideal choices for resource-constrained environments. These lightweight networks with fewer parameters are efficient and accurate in plant disease classification and suitable for deployment on limited-resource devices (Barman et al., 2020; Lu et al., 2023). In terms of the text modality, this study compared the classification performance of TextCNN and fastText. While TextCNN leverages convolutional layers over word embeddings to discern local semantic features in text (Kim, 2014), fastText captures morphological nuances by representing words through character n-grams (Joulin et al., 2016). Textual descriptions accompanying plant images can provide crucial contextual information. Combining visual and textual modalities can enhance the overall accuracy of disease classification and assist in fine-grained disease categorizations (Wang et al., 2021b). With the advancement of technology, the amalgamation and refinement of these models will further increase the precision and applicability of plant disease identification.

2.2 Data preparation

Through field collection, laboratory photography, and web crawling, a total of 2200 citrus image samples were gathered; they comprise healthy leaves, 2 bacterial diseases (citrus greening and citrus canker), 5 fungal diseases (anthracnose, scab, greasy spot, melanose, and sooty mold), and 3 physiological disorders (nitrogen deficiency, magnesium deficiency, iron deficiency). Each sample category contains 100 images with white backgrounds and 100 images with natural backgrounds. Original sample images are shown in Table 1.

In addition to the image data, we used expert knowledge to create a structured citrus disease features glossary (Table S1). This glossary covers 12 categories of citrus disease characteristics, including leaf color, leaf morphology, affected areas, covering features, chlorosis region, chlorosis features, lesion shape, lesion count, lesion size, lesion distribution, lesion color, and lesion features. Such data provide a more accurate and comprehensive description of the original images. To ensure data accuracy, the textual data were generated by three Ph.D. scientists specializing in pomology and checked by a psychologist. Sample origin texts are shown in Table 1.

2.3 Data preprocessing

The original image was uniformly cropped and -adjusted to 224×224 pixels. The image was enhanced by rotation, scaling, flipping, and brightening. Simultaneously, data enhancement methods such as “origin,” “rotated,” “brighter,” “flipped,” and “scaled,” were embedded in the text descriptions to ensure a one-to-one correspondence between the image and text. Symbols from the text were filtered and tokenized using Jieba, and the tokenized results were then mapped to a word index list based on a vocabulary. Words that were not present in the vocabulary were replaced with “<UNK>“. The max_length of the numeric sequence was set to 100, and placeholders were used to supplement any shorter parts. Finally, PyTorch’s tensor conversion was used to transform the numeric sequence into tensors for subsequent calculations. The training, verification, and test sets were divided at a ratio of 7:2:1 for the image–text pairs.

2.4 Single-modality comparative experiments

To identify a network architecture that can effectively extract features from citrus disease images, we compared the classification performance of four deep learning networks: VGG16, ResNet50, MobileNet V2, and ShuffleNet V2. These networks use convolutional operations that target key features in images, such as texture, color, and shape, to produce more abstract feature representations. Throughout the training process, all networks used the Adam optimizer and the learning rate was set to 0.001 to ensure training stability and efficiency. This experiment was conducted to comprehensively evaluate the performance of each network in the citrus disease image classification task and provide a basis for selecting image networks for subsequent multimodal construction.

To select a network structure that can effectively extract features from citrus disease text information, we compared the classification performances of two deep learning networks: TextCNN and fastText. Structured text descriptions were converted into word vectors, and text extraction networks were used to extract features such as contextual relationships. The optimizer and learning rate settings were consistent with the image networks described in Section 4.3.1 to ensure training consistency and fairness for comparison. To avoid overfitting, the dropout was set to 0.5 and the length of the input text vector was set to 20. This experiment was conducted to comprehensively assess the performance of each network on the citrus disease text classification task and provide a basis for selecting the text network in the subsequent multimodal construction.

2.5 Different-dataset comparative experiments

To increase the diversity and practical applications of the data, this study created three types of datasets: white, natural, and mixed

10.3389/fpls.2023.1280365

TABLE 1 Example of the image-text origin database.

Disease category	Origin Image	Origin Text
Healthy leaves (CK)		Deep green in color, normal in morphology, asymptomatic on the front side.
Citrus greening (CGR)		Light green in color, normal in morphology, chlorosis on the back side, chlorosis region is veined and randomly dispersed.
.Citrus canker (CCA)		Deep green in color, normal in morphology, lesions on the front side, lesions shape is subcircular, lesions count is 4–20, lesions size is 3–5 mm, lesions are randomly dispersed, lesion color is brown at the center and yellow at the edges, lesions show a volcano-like feature.
Citrus anthracnose (CAN)		Deep green in color, curled in morphology, lesions on the front side, lesions shape is subcircular, lesions count is less than 3, lesions size is larger than 15 mm, lesions are randomly dispersed, lesions color is light brown, lesions show a withered feature
Citrus scab (CSC)		Light green in color, normal in morphology, lesions on the back side, lesions shape is irregular, lesions count is 4-20, lesions size is 3–5 mm, lesions are randomly dispersed, lesions color is gray-white, lesions show a corked feature.
Citrus greasy spot (CGS)		Light green in color, normal in morphology, lesions on the front side, lesions shape is irregular, lesions count is 4–20, lesions size is 3–5 mm, lesions are randomly dispersed, lesions color is yellow, lesions show a flat and greasy feature.
Citrus melanose (CME)		Deep green in color, normal in morphology, lesions on the front side, lesions shape is irregular, lesions count is more than 20, lesions size is 1–3 mm, lesions are randomly dispersed, lesions color is dark, lesions show a convex and greasy feature.
Citrus sooty mold (CSM)		Deep green in color, normal in morphology, black mold spots or layers covering the front side.
Citrus nitrogen deficiency (CND)		Yellow in color, normal in morphology, chlorosis on the front side, chlorosis region is uniformly dispersed
Citrus magnesium deficiency (CMD)		Light green in color, normal in morphology, chlorosis on the front side, chlorosis region near the leaf margin, inverted V-shaped chlorosis

(Continued)

TABLE 1 Continued

Disease category	Origin Image	Origin Text
Citrus iron deficiency (CID)		Light green in color, normal in morphology, chlorosis on the front side, interveinal netted chlorosis

backgrounds. Specifically, in the white background dataset, each category contains 100 images of single leaves with a white background and multiple leaves with a white background. In the natural background dataset, each category contains 100 images of single leaves with a natural background and multiple leaves with a natural background. The original images in each of the two above datasets were expanded to 5500 images through data augmentation techniques, such as rotation and highlighting. Then 5500 images from these two datasets were randomly obtained in equal proportions to form the mixed background dataset. All three datasets were trained using the selected MobleNet50 and ShuffleNet V2 networks. Testing was always performed using the natural background dataset. The training and testing processes are shown in Figure 2.

2.6 Construction of the image-text multimodal networks

The image-text feature fusion framework proposed in this study consists of two network branches: MobileNet V2/ShuffleNet V2 and TextCNN. The input data consist of a disease image and structured text describing the disease features. These descriptions were corrected by fruit tree experts to ensure the standardization of the feature description. MobileNet V2 and ShuffleNet V2 extract the image feature vectors from the image-text pairs, while TextCNN extracts the text feature vectors from the data pairs. The two types of feature vectors are concatenated to obtain the feature vector for the image-text pair. The model framework is shown in Figure 3.

2.6.1 Image branching in the multimodal framework

The image branch selected two lightweight networks (MobileNet V2 and ShuffleNet V2) that performed well in single-image-modality comparative experiments. MobileNet V2 decomposes traditional convolution operations into depth-wise and point-wise convolution steps, and it also adopts residual connections and dilated convolutions to enhance the expressive capability of models. When training the image modality with MobileNet V2, the input image passes through 2 convolutional layers and 17 bottlenecks to finally obtain the image feature vector. MobileNet V2 introduces an inverted residual module that differs from the traditional bottleneck. It first expands the feature vector dimensionally through an expansion layer and then reduces dimensionally through a pointwise convolution layer, with the expansion factor set to six times. For instance, in the second bottleneck with an input of 112×112×16, it first expands to 112×112×96, and after a depth-wise convolution layer, it decreases to 56×56×96. After the second point-wise convolution layer, it decreases to 56×56×24. As the feature vector passes through the bottleneck, its dimensions increase from 16 to 96 and then reduce to 24. This structure ensures that the depth-wise convolution

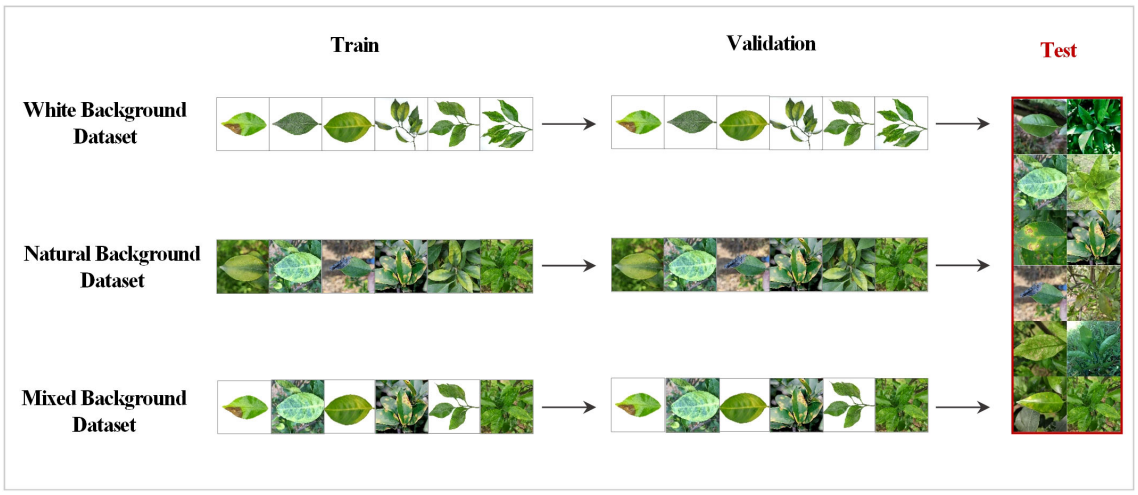

FIGURE 2
Training and testing strategies for the different datasets; 10% of the natural background dataset was randomly extracted as the shared test set.

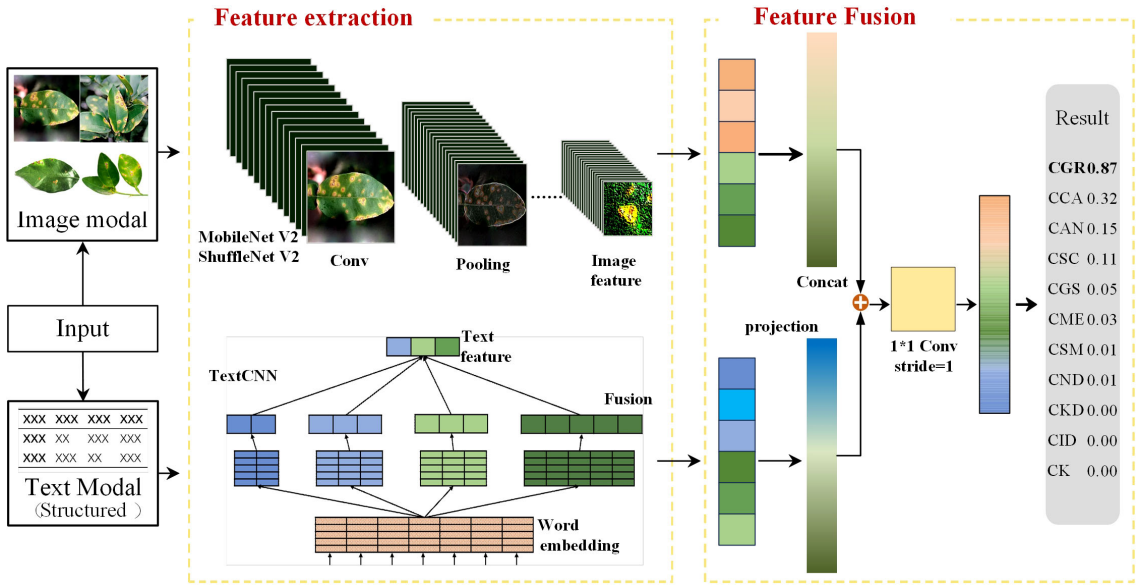

FIGURE 3
Image-text multimodal network framework.

within the bottleneck captures rich feature information while effectively reducing the memory required for model training. To address the feature loss issue when compressing high-dimensional features to low-dimensional features, MobileNet V2 replaces the ReLU6 non-linear activation function in the second pointwise convolution layer with the linear operation Linear while keeping ReLU6 unchanged in other positions, thus ensuring feature information diversity.

Similar to MobileNet V2, ShuffleNet V2 adopts depth-wise separable convolution but also adds channel shuffling and grouped convolution operations. When training the image modality with ShuffleNet V2, the input image first passes through a convolutional layer, a max-pooling layer, three stage modules, and then another convolutional layer to obtain the image feature vector. In Stage 2, Stage 3, and Stage 4, a downsampling operation with Stride = 2 is first performed, followed by different numbers of depth-wise separable convolutions and grouped convolutions. For training, the input vector is divided into two branches, branch1 and branch2. The first inverted residual module performs downsampling on both branches. In subsequent inverted residual modules, only branch2 undergoes depth-wise separable convolution operations. After completing the inverted residual module, the vectors of the two branches are concatenated and channel shuffling is performed to ensure the mutual interaction of information between the two branches.

2.6.2 Text branching in the multimodal framework

The text branch selected TextCNN, which performed well in the single-text modality comparative experiments. It is a convolutional neural network designed for text classification, and its structure is depicted in Figure 1E. The text modality data are derived from the structured citrus disease features glossary, and data enhancement methods are embedded into the textual descriptions at the time of image enhancement to ensure correspondence of the image-text pairs. When training the text with TextCNN, word indices of the input text sequence are first mapped to fixed-dimensional word vectors through an embedding layer. Then, the word vectors pass through a convolutional layer. The width of the convolutional kernel is the same as the dimension of the word vector, and its height corresponds to each value in kernel_sizes. This convolution operation can capture local word sequence features. Then, the ReLU activation function is applied to enhance the network's non-linear capability. Next, a max-pooling operation is applied to each convolution output, and the maximum value from each feature map is selected as the output. This process retains the most significant features extracted by each convolution kernel. Finally, the features extracted by each convolution kernel are concatenated to obtain the text feature vector.

2.6.3 Feature fusion

The features extracted from the different modalities are fused at the feature layer. For the ith object, the features extracted from the image and text are denoted as $f_{img}(x^i_{img})$ and $f_{text}(x^i_{text})$, respectively. The fused feature is represented by $f_{\varnothing}(x^i_{fusion})$. First, the image and text features were projected into low-dimensional space using a projection matrix. The two projected vectors were then concatenated and passed through a convolutional layer for feature learning to obtain the fused feature output. C represents the feature vector learned through the convolutional layer. The convolution uses a 1×1 kernel with a stride of 1. The 1×1 convolution itself does not change the size of the feature map but can reduce the dimension of the vector. During the dimension reduction process, interaction information can be learned between multiple channels. The feature mapping function M is represented in equation (1), and the fused feature is represented in equation (2).

$$M(x) = W_x \cdot x \tag{1}$$

$$f_{\varnothing}(x^i_{fusion}) = C\left(F\left(M\left(f_{img}\left(x^i_{img}\right)\right), M\left(f_{text}\left(x^i_{text}\right)\right)\right)\right) \tag{2}$$

where Fdenotes the feature vector concatenation function and Crepresents the feature vector after convolutional layer processing. $W_x \in \{N \times D_x\}$ is the projection matrix for the features, $D_x$indicates the dimension of the input feature x, and N signifies the dimension after projection.

The loss function employs the Cross-entropy loss function. In this context, x_2 is the predicted result and represented as a vector $x = [x_1, x_2, \ldots, x_n]$. The number of elements in this vector is equivalent to the number of categories. The variable "class" indicates the true label of the sample. For instance, if the sample belongs to the second category, then $class = 2$. Consequently, $x_{[class]}$ refers to x_2. This implies that the second element was extracted from the predicted result vector, which corresponds to the predicted value of the true category, as depicted in equation (3).

$$loss(x, class) = -log\left(\frac{e^{x_{[class]}}}{\sum_j e^{x_j}}\right) = -x_{[class]} + log\left(\sum_j e^{x_j}\right) \tag{3}$$

2.7 Experiment environments

The research and control experiments were conducted in an Ubuntu 20.04 environment (processor: Intel core i9 9820X; RAM: 64G; graphics card: NVIDIA RTX A4000 16G DDR6). The deep learning framework Pytorch was used along with Cuda10.1 for training. In the experimental design and comparison processes, the batch size for the training and validation sets was set to 32. Based on the characteristics and convergence of the modalities data, the number of iterations for the single image modality was set to 200 while the preset number of iterations for the single text modality was set to 50. The multimodal model converged rapidly, and early stopping was applied to prevent overfitting.

2.8 Evaluation indices

This research compared the models from four perspectives: accuracy, precision, recall, and F1. The specific calculation methods are presented in equations (4–7).

$$Accuracy = \frac{TP + TN}{TP + TN + FP + FN} \tag{4}$$

$$Precision = \frac{TP}{TP + FP} \tag{5}$$

$$Recall = \frac{TP}{TP + FN} \tag{6}$$

$$F1 = \frac{TP}{TP + FN} \tag{7}$$

where TP is the number of true positive samples, FP is the number of false positive samples, and FN is the number of false negative samples.

3 Results

3.1 Comparison of image modality models

A comparison of the performance of the deep and lightweight networks in the single-image modality classification tasks showed that the lightweight neural networks exhibited better feature extraction and classification performance on small-sample natural background image datasets (Figure 4). Although deep neural networks such as VGG16 and ResNet50 converged quickly during training, they only achieved classification accuracies of 54.33% and 60.39%, respectively. In contrast, MobileNet V2 and ShuffleNet V2, the two lightweight networks, achieved high classification accuracies of 90.19% and 91.63% respectively, despite converging at a slower rate. This might be because VGG16 and ResNet50 have

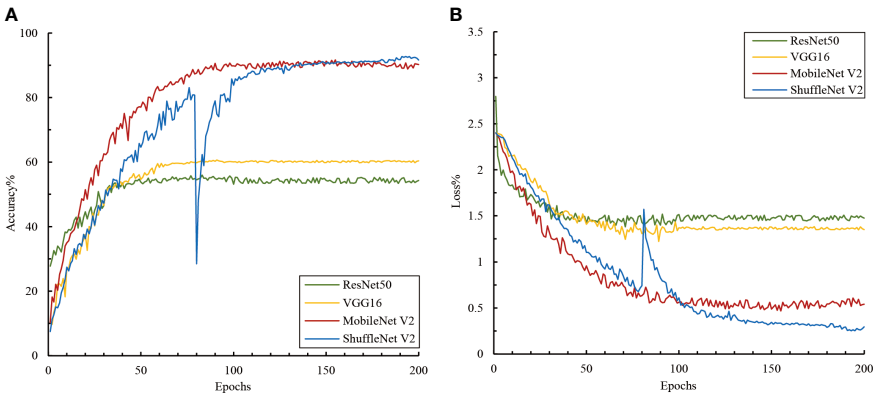

FIGURE 4
Accuracy and loss variations among the image models. **(A)** Accuracy and **(B)** loss.

complex structures that allow them to rapidly capture features in the data. However, this depth might also render them more susceptible to limitations imposed by data volume, impacting accuracy. The results suggest that lightweight networks are more suitable for small sample data. Their simplified structures and various strategies, such as depth-wise separable convolutions and channel shuffling, enhance their adaptability to complex background data.

Additionally, we observed noticeable fluctuations in ShuffleNet V2 during training. A local minimum or plateau area was encountered around the 80th epoch, and it was subsequently adjusted using the algorithm to escape this state and achieve better convergence. Although ShuffleNet V2 exhibited fluctuations around the 80th epoch, it could converge normally and reach a high accuracy afterward. This demonstrated the robustness and self-recovery capabilities of the proposed model.

We further analyzed the ability to recognize different disease categories based on a single-image modality at a finer granularity. The average precision, recall, and F1 values for all image networks presented ranges of 58.12–84.89%, 57.21–85.72%, and 56.82–85.62%, respectively (Table 2). The lightweight network ShuffleNet V2, which boasts high generalization capability and computational efficiency, performed the best, and its confusion matrix of validation and training results is presented in Figure 4. An analysis of the convolutional neural network feature extraction and classification results for the 11 citrus leaf sample images revealed significant differences between different category samples. The four models perform well in extracting features for citrus scab (CSC), citrus greening (CGR), citrus canker (CCA), healthy leaves (CK), and citrus sooty mold (CSM). However, their classification results for citrus greasy spot (CGS), citrus magnesium deficiency (CMD), and citrus anthracnose (CAN) were less satisfactory, with F1 average values of <70%. Further examination of the image dataset revealed that several disease categories with higher error rates contained background noise, including non-disease features, such as fingers and fruits, which may confuse the model's classification of these samples. Additionally, the disease categories CGS and CAN included some early stage symptoms, which increased the difficulty of distinguishing between the more challenging diseases and subsequently affected the classification performance.

3.2 Comparison of the text modality models

The accuracy and loss curves during the training of the text branch training set are shown in Figure 5. An analysis of the performance of the different text models in the citrus disease classification task showed that the two models in the text branch displayed approximately the same performance (Figure 5) and converged quickly around the 10th epoch. The final training accuracies of TextCNN and fastText were 77.22% and 74.42% respectively, with both showing reduced loss values of approximately 0.6. A comparison with the image modality model showed that the text modality model converged faster, with its accuracy lying between that of the lightweight and deep convolutional image networks. This might be attributed to the fact that text data are more structured than are image data; thus, the features can be more quickly learned by the model. However, the relatively lower accuracy might indicate that the information contained in the text data is not as rich as that in the image data for the task of citrus disease classification.

The precision, recall, and F1 values of the two text networks were between 78.36% and 82.83% (Table 3). TextCNN, which benefits from the features of both convolutional and recurrent neural networks, exhibited superior performance relative to fastText.

TABLE 2 Eleven classification results of the image modal networks.

Disease category	VGG16			ResNet50			MobileNet V2			ShuffleNet V2		
	Precision (%)	Recall (%)	F1 (%)	Precision (%)	Recall (%)	F1 (%)	Precision (%)	Recall (%)	F1 (%)	Precision (%)	Recall (%)	F1 (%)
CK	72.55	67.27	69.81	57.89	60.00	58.93	92.00	83.64	87.62	88.68	85.45	87.04
CGR	59.26	65.31	62.14	68.18	61.22	64.52	90.20	93.88	92.00	97.87	93.88	95.83
CCA	56.94	73.21	64.06	73.91	60.71	66.67	92.00	82.14	86.79	85.96	87.50	86.73
CAN	60.78	56.36	58.49	57.89	40.00	47.31	74.24	89.09	80.99	79.41	98.18	87.80
CSC	77.78	77.78	77.78	75.00	73.33	74.16	87.80	80.00	83.72	97.56	88.89	93.02
CGS	40.63	26.00	31.71	46.15	36.00	40.45	75.47	80.00	77.67	96.55	56.00	70.89
CME	60.53	80.70	69.17	43.88	75.44	55.48	75.41	80.70	77.97	84.75	87.72	86.21
CSM	68.42	56.52	61.90	60.00	65.22	62.50	81.48	95.65	88.00	82.69	93.48	87.76
CND	57.58	76.00	65.52	51.72	60.00	55.56	97.67	84.00	90.32	80.00	80.00	80.00
CMD	58.70	45.76	51.43	48.78	33.90	40.00	82.35	71.19	76.36	83.58	94.92	88.89
CID	72.09	59.62	65.26	55.93	63.46	59.46	85.19	88.46	86.79	78.43	76.92	77.67
Avg.	62.30	62.23	61.57	58.12	57.21	56.82	84.89	84.43	84.39	86.86	85.72	85.62

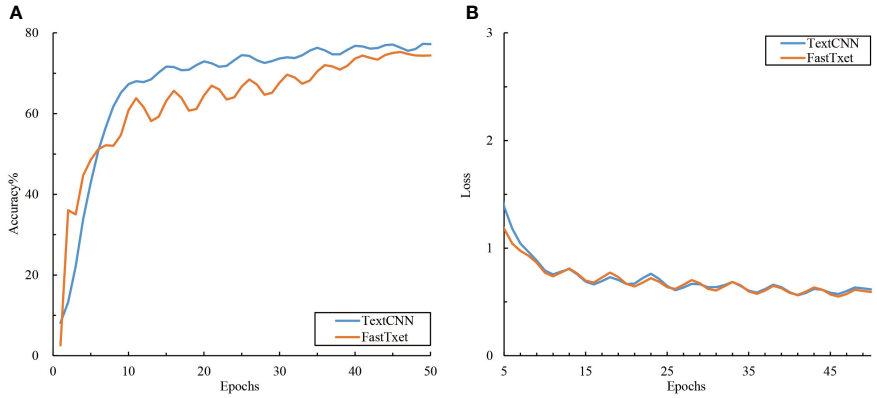

FIGURE 5
Accuracy and loss variations among the text models. **(A)** Accuracy and **(B)** loss.

When extracting text features and classifying the 11 categories of citrus leaf samples, the performance between the different sample categories varied significantly. Specifically, for categories such as CK, CSM, CMD, and Citrus iron deficiency (CID), the text models effectively extracted features with F1 scores >95%. However, for the CGS and CCA categories, the classification results of the text models were suboptimal, with F1 scores<50%. The analysis of the disease text dataset showed that certain descriptors of disease spots, such as "yellow," "smooth," and "randomly distributed," frequently occurred in the descriptions of several disease categories. Conversely, highly distinctive descriptive phrases such as "asymptomatic" for healthy leaves and "volcano-like spots" for ulcers were missing from these two disease categories. Such descriptors have a stronger discriminatory power for text classification. In summary, although text modality performs relatively well in classifying citrus diseases, it faces challenges such as variations in sample categories and disparities in descriptive phrases.

A confusion matrix is a tool for visualizing and quantifying the relationship between predicted results and actual labels. The confusion matrices of the best models for the image and text modalities are shown in Figure 6. In the confusion matrix for MobileNet V2, misclassifications were scattered in almost every category, suggesting that the image model has greater complexity and learning capacity and may have more flexibility when processing samples compared with the other models, thus enabling it to learn features more evenly across different categories. Compared with the image modality, misclassifications in the TextCNN confusion matrix were relatively concentrated but showed a higher error rate for individual points. This may be related to the limitations in text information when describing citrus leaf diseases as well as the lack of semantic richness, which increases the difficulty of accurately expressing and distinguishing all the features of different diseases. Consequently, the ability of TextCNN to extract features from certain citrus disease categories was

TABLE 3 Eleven classification results of the text modal networks.

Disease category	FastText			TextCNN		
	Precision (%)	Recall (%)	F1 (%)	Precision (%)	Recall (%)	F1 (%)
CK	100.00	100.00	100.00	100.00	100.00	100.00
CGR	78.79	98.11	87.39	78.79	98.11	87.39
CCA	43.14	44.90	44.00	43.14	44.90	44.00
CAN	84.78	88.64	86.67	84.44	86.36	85.39
CSC	70.69	78.85	74.55	70.69	78.85	74.55
CGS	61.11	18.97	28.95	57.89	18.97	28.57
CME	48.65	81.82	61.02	48.65	81.82	61.02
CSM	100.00	100.00	100.00	100.00	100.00	100.00
CND	96.97	71.11	82.05	96.97	71.11	82.05
CMD	100.00	98.08	99.03	100.00	98.08	99.03
CID	100.00	100.00	100.00	100.00	100.00	100.00
Avg.	80.38	80.04	78.51	80.05	79.84	78.36

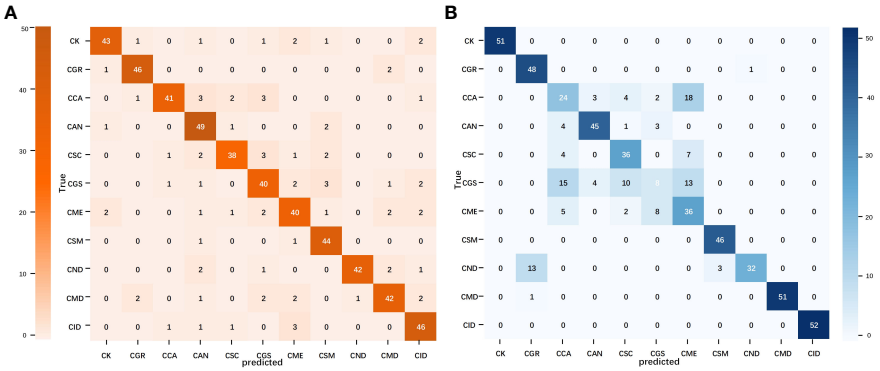

FIGURE 6
Confusion matrix of the image and text modality optimal models. **(A)** MobileNet V2 confusion matrix and **(B)** TextCNN confusion matrix.

comparatively weaker than that of MobileNet V2. In summary, the image and text modalities exhibited different strengths and limitations in classifying citrus leaves. A comparative analysis of single-modality models provided crucial insights and directions for subsequent modal fusion.

3.3 Effect of different datasets on classification performance

The accuracy and loss curves for model training using different datasets are shown in Figure 7. An analysis of the performance of different datasets in the citrus disease classification task revealed that the citrus disease samples from the white background dataset achieved the highest classification accuracy of 89.61% and 94.76%, respectively, with the loss function stabilizing at<0.5. As the complexity of the sample background increased, the classification accuracy showed a decreasing trend, with the accuracy for the natural and mixed background data falling between 83.45% and 91.63%. This suggests that a simplified background can assist the model in more easily identifying the target, thereby improving accuracy. However, in natural and mixed-background datasets, a complex background might introduce considerable irrelevant information and noise, such as shadows and light variations. These factors could interfere with the model's ability to extract key features. Nevertheless, the model still demonstrated a relatively high accuracy under these complex backgrounds, indicating that the selected models are robust and adaptable.

In the unified natural background test set, the models trained on different datasets showed significant differences (Table 4). The test accuracy of the model trained on the white background dataset was<21%, which is significantly lower than its training accuracy.

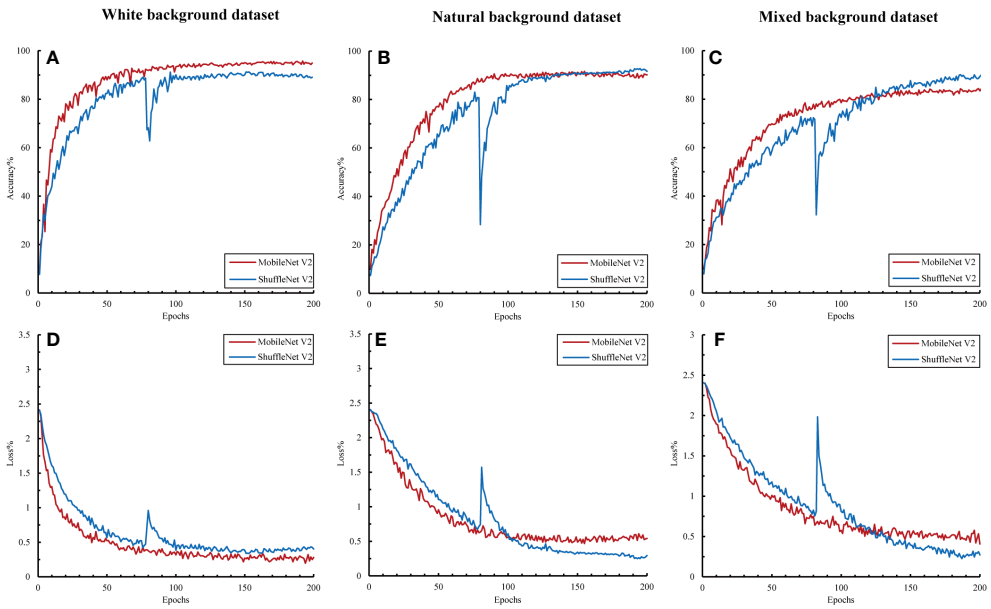

FIGURE 7
Accuracy and loss variations among the different datasets. **(A, D)** Accuracy and loss in the white background dataset; **(B, E)** accuracy and loss in the natural background dataset; and **(C, F)** accuracy and loss in the mixed background dataset.

This indicates that the model overfilled on a simplified and non-disturbed background and failed to fully learn the clutter features, resulting in a poor generalization ability. Conversely, the models trained on the natural and mixed-background datasets presented similar accuracy as their training accuracy. The test accuracy of ShuffleNet V2 reached 92.31%, surpassing its performance in the training and validation sets. This suggests that sample diversity helps the model learn to distinguish target objects from key features during training and resist background interference, thereby significantly improving the robustness and generalization of the model.

The ability of the models to recognize different disease categories under different training datasets was analyzed at a finer granularity. Box plots for the precision, recall, and F1 values of each disease category showed that the models exhibited greater balance when trained with mixed background datasets (Figure 8). Although the test accuracy of the mixed dataset was slightly lower than that of the complex background, its performance in recognizing different disease categories was more balanced, with no particular category showing significantly lower recall or F1 values. This finding may be related to the ability of the mixed dataset to promote learning of target features related only to the disease and the capture of auxiliary information highly correlated with the background. Although a slight decrease in accuracy may have occurred, the adaptability to complex backgrounds and disturbances was stronger.

In conclusion, different dataset backgrounds, model structures, and training strategies can influence the model's classification performance in real-world applications. The single-image modality analysis showed that the use of a mixed dataset combined with a lightweight neural network can yield a superior classification accuracy, generalization capability, and category balance.

3.4 Comparison of the multimodal models

To further explore the complementarity between the image and text modalities, we investigated the potential of feature fusion strategies to address the classification problem of citrus diseases with complex backgrounds. The accuracy and loss curves of the fusion model during the training process for the training set are

TABLE 4 Test set results in the image modal networks.

Dataset class	MobileNet V2			ShuffleNet V2		
	Precision (%)	Recall (%)	F1 (%)	Precision (%)	Recall (%)	F1 (%)
White	21.00	17.17	17.36	19.20	15.12	16.03
Natural	84.89	84.43	84.39	86.86	85.72	85.62
Mixed	85.11	84.18	84.37	92.31	91.72	91.81

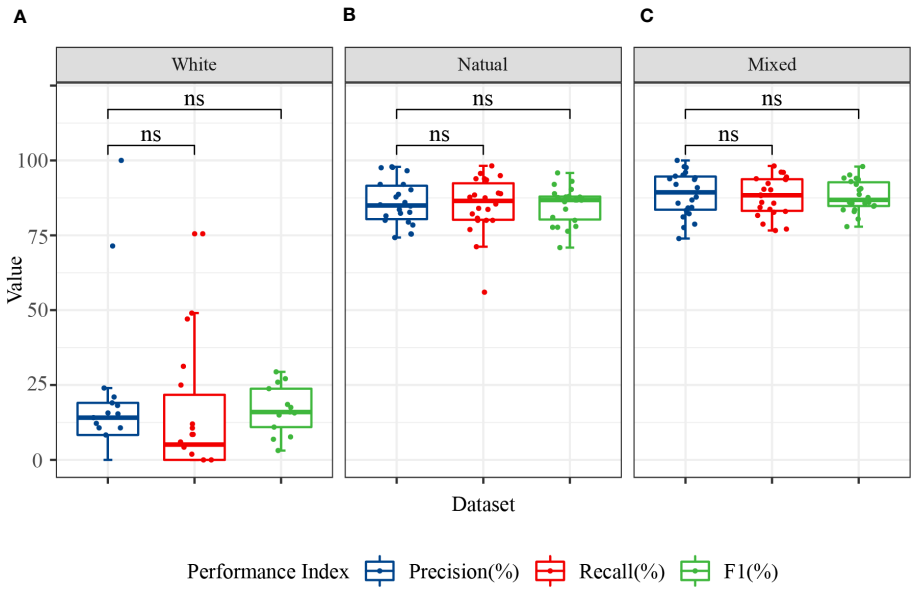

FIGURE 8
Classification performance of the image modality models for 11 categories. The data in the figure represent the precision, recall, and F1 of the 11 citrus samples classified using MobileNet V2 and ShuffleNet V2 models. **(A)** Precision, recall, and F1 in the white background dataset; **(B)** precision, recall, and F1 in the natural background dataset; and **(C)** precision, recall, and F1 in the mixed background dataset. ns, no significance.

shown in Figure 9. Compared with the previous unimodal results, the results of the multimodal network exhibited significant improvements. The fused networks MobileNet50 + TextCNN and ShuffleNet V2 + TextCNN both achieved training accuracies of over 95% on the two datasets and reduced the loss to below 0.2. Among them, ShuffleNet V2 + TextCNN yielded the best training results on the mixed-background dataset, with an accuracy of 98.34%. Moreover, the multimodal network converged within 10 epochs. To prevent overfitting, we applied early stopping. The results show that all models stopped within 22 epochs, indicating marked acceleration in training. No further fluctuations were observed, indicating that the multimodal network fully uses the complementarity between the image and text modalities. The cross-transfer of information and comprehensive use of features enhanced the network's ability to extract and recognize different characteristics of citrus diseases.

The precision, recall, and F1 of the two fusion networks ranged from 97% to 99%, thus showing excellent performance (Table 5). Notably, the multimodal model achieved satisfactory results in classifying each type of citrus sample. In the two datasets, the F1 score for each sample type exceeded 90%. This performance enhancement may be attributable to the fact that after fusing unimodal information, the model can fully use the complementarity between this information and the cross-validation effect, helping the model to capture each category's features more accurately and reducing the likelihood of misclassification.

The confusion matrix of the optimal multimodal model–ShuffleNet V2 + TextCNN–further confirms the superiority of the multimodal strategy (Figure 10). Compared with the unimodal model, this model reduced the number of misclassifications and avoided the concentration of misclassifications in specific categories, demonstrating better balance and generalization. Only a few groups had errors, which did not exceed 2. Overall, when handling the citrus disease classification task in complex backgrounds, the multimodal strategy displayed higher robustness and stability than the unimodal strategy.

4 Discussion

Multimodal feature fusion has become a popular research direction in the field of plant disease classification. From the perspective of information complementarity, a single modality, such as image or text, has inherent limitations. While the image modality can capture rich visual features, it may be affected by factors such as lighting, shadows, and background noise (Huang et al., 2022). Moreover, although the text modality can provide semantic and contextual information about the disease (He and Peng, 2020), it

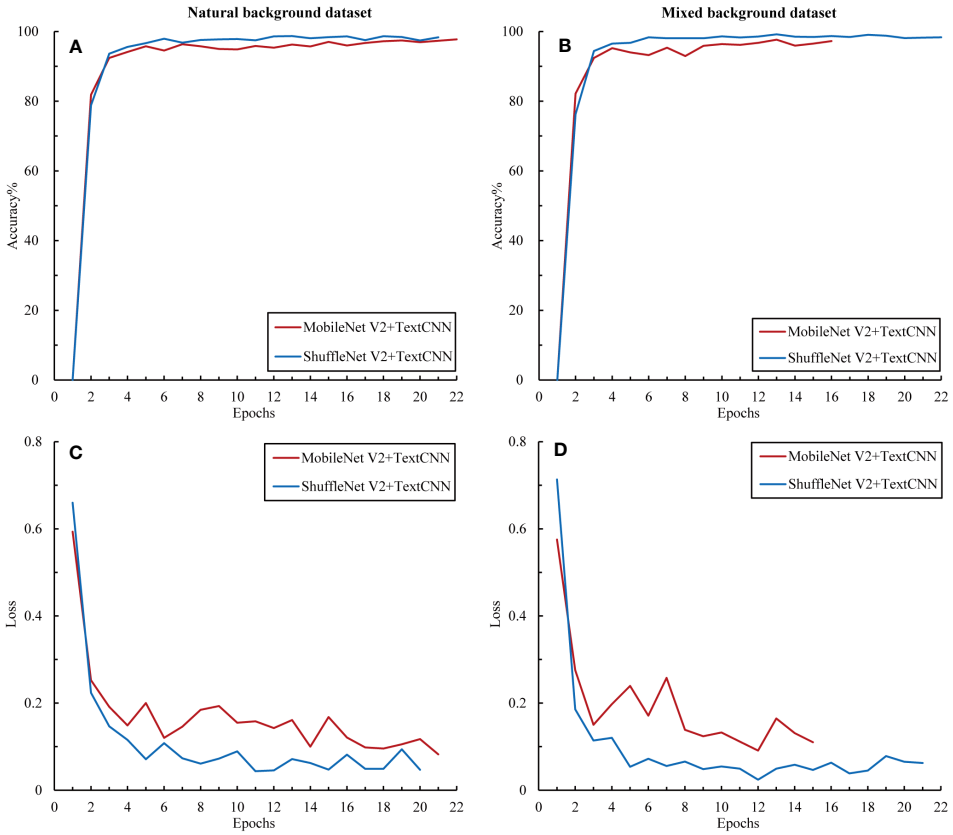

FIGURE 9
Accuracy and loss variations among the multimodal models. **(A)** Accuracy in the natural background dataset, **(B)** loss in the natural background dataset, **(C)** accuracy in the mixed background dataset, and **(D)** loss in the mixed background dataset.

10.3389/fpls.2023.1280365

TABLE 5 Eleven classification results of Multimodal networks.

Disease category	Natural Background Dataset						Mixed Background Dataset					
	MobileNet V2+TextCNN			ShuffleNet V2+TextCNN			MobileNet V2+TextCNN			ShuffleNet V2+TextCNN		
	Precision (%)	Recall (%)	F1 (%)	Precision (%)	Recall (%)	F1 (%)	Precision (%)	Recall (%)	F1 (%)	Precision (%)	Recall (%)	F1 (%)
CK	1.00	1.00	1.00	1.00	1.00	1.00	1.00	1.00	1.00	1.00	1.00	1.00
CGR	0.96	0.96	0.96	1.00	0.96	0.98	0.98	0.92	0.95	1.00	0.96	0.98
CCA	1.00	1.00	1.00	0.98	0.96	0.97	0.90	0.92	0.91	0.94	0.96	0.95
CAN	0.98	0.98	0.98	1.00	1.00	1.00	0.98	0.85	0.91	0.98	0.94	0.96
CSC	1.00	0.96	0.98	1.00	1.00	1.00	1.00	0.98	0.99	0.98	0.98	0.98
CGS	0.94	0.98	0.96	0.96	0.98	0.97	0.85	0.96	0.90	0.88	0.96	0.92
CME	0.96	0.96	0.96	1.00	1.00	1.00	1.00	1.00	1.00	1.00	0.94	0.97
CSM	1.00	1.00	1.00	1.00	0.98	0.99	1.00	1.00	1.00	1.00	1.00	1.00
CND	1.00	0.94	0.97	0.96	1.00	0.98	0.93	0.98	0.95	0.96	1.00	0.98
CMD	0.94	1.00	0.97	0.98	1.00	0.99	1.00	1.00	1.00	1.00	1.00	1.00
CID	1.00	1.00	1.00	1.00	1.00	1.00	1.00	1.00	1.00	1.00	1.00	1.00
Avg.	0.98	0.98	0.98	0.99	0.99	0.99	0.97	0.96	0.96	0.98	0.98	0.98

might lack sufficient details to describe certain subtle visual features. These limitations can lead to classification inaccuracies. Combining multi-source data, such as image and text (Feng et al., 2022), image and hyperspectral data (Yang et al., 2021), or image and sensor information (Zhao et al., 2020), leverages the strengths of each modality and is beneficial in improving classification accuracy and model robustness. In our experiments, we observed a clear advantage of multimodal joint analysis. The accuracy of ShuffleNet V2 +TextCNN using the mixed dataset reached 98.33%, representing an improvement of 9.78% and 21.11%, compared with those of single image and single text modalities, respectively. This is consistent with previous results showing that the complementary information from multimodal data could enhance object detection capabilities, thus demonstrating the significant advantage of multimodal strategies in handling complex backgrounds and noisy data (Liu et al., 2020). Second, from the perspective of data fusion, feature fusion helps to

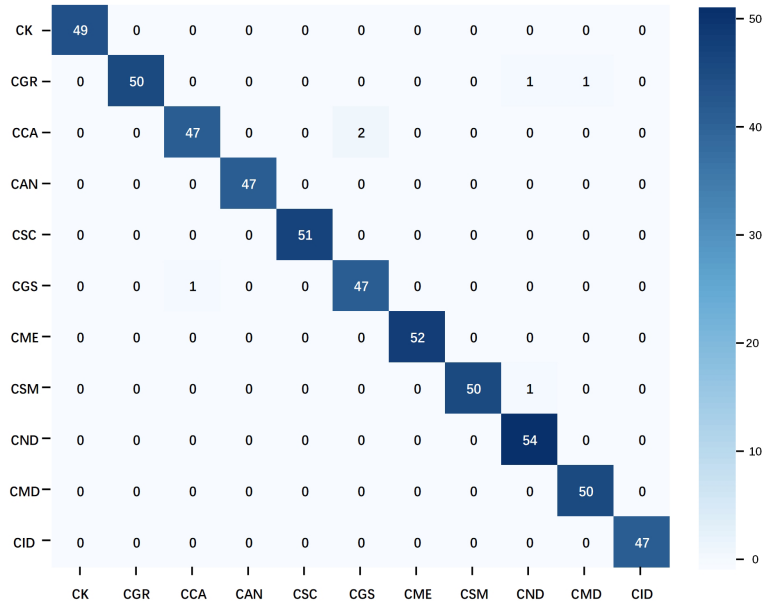

FIGURE 10
Confusion matrix of the multimodal optimal model. The data used in the matrix are the test results of ShuffleNet V2 on natural background images after training on the mixed dataset.

enhance multimodal interaction and generalization performance, compared with decision fusion. Combining multi-source data at an early stage allows the model to better understand and distinguish complex backgrounds and noise, thereby improving classification accuracy (Yang et al., 2021). In contrast, decision fusion is typically performed at the later stages of the model and might not fully capture the fine-grained feature interactions between modalities. Moreover, classifying diseases using decision fusion might require a high classification confidence level from one modality (Wang et al., 2021a). Therefore, multimodal feature fusion has a more pronounced advantage in tasks with complex and varied backgrounds, especially in scenarios requiring cross-modal collaboration, and showed promising results in our experiments.

Sample diversity has always been regarded as a key factor in the field of deep learning. However, due to the challenges of dataset preparation, its importance is often underestimated. Previous studies on citrus disease identification and classification preferred to use datasets with a single background (Barman et al., 2020; Yang et al., 2021; Dananjayan et al., 2022), with few utilizing natural background datasets (Xing et al., 2019). In addition, the disease categories and scenarios were relatively limited. The text involves 4 scenarios and 11 types of samples, rendering this citrus disease classification task with small samples, multiple scenarios, and multiple categories a higher challenge for model recognition performance. To address this, we designed a dataset with diverse backgrounds, including white, natural, and mixed backgrounds. This design has shown significant advantages in enhancing the model's generalization capabilities and preventing data leakage issues. A diversified training set provides the model with a broader data distribution, enabling it to better handle unknown data. Studies have shown that training with diverse data helps the model to capture the underlying structures and patterns of the data, resulting in better performance in real-world applications (Hernandez and Lopez, 2020). In this study, training with natural and mixed backgrounds significantly improved the model's test accuracy and led to better classification balance, thereby demonstrating the importance of sample diversity in enhancing the model's generalization capabilities in real complex backgrounds. Moreover, data in the same dataset often come from the same location, the same environment, or even the same plant. This sample autocorrelation might pose a risk of data leakage (Stock et al., 2023). In this study, cross-validation of the dataset effectively reduced the potential for data leakage and overfitting, ensuring the fairness and authenticity of model evaluation and effectively ensuring the model's generalization capabilities on natural background data.

The effective application of knowledge has demonstrated undeniable value in enhancing model accuracy and credibility. To improve the comprehensiveness, objectivity, and efficiency of text description, expert knowledge was fully utilized and a glossary of citrus disease characteristics was innovatively constructed to provide a new approach to text description. The construction of the feature word list allows describers to choose from 12 categories of feature words, comprehensively covering information such as leaf color, leaf morphology, affected parts, covering features, yellowing characteristics, and lesion features, effectively avoiding omissions or errors. Notably, in subsequent practical applications, users without a professional knowledge background can easily select highly specialized and specific phrases such as "netted chlorosis," "leaf vein corking," and "volcano-like lesions," further enhancing the professionalism and reliability of the text modality. Zhou's research also indicates that the application of domain knowledge is beneficial for improving classification accuracy and the interpretability of the model's inference process (Zhou et al., 2021).

This study achieved satisfactory results in the citrus disease classification task with complex backgrounds by leveraging the complementary information of image-text multimodal and the advantages of sample diversity. However, there are still some shortcomings. First, although this experiment explored the feature fusion of image-text multimodal, the fusion strategy is relatively simple and may not fully mine the potential association information between image and text modalities. Further research on more advanced fusion strategies, such as attention mechanisms and multi-task learning, can better utilize the complementary information between images and text. Second, the interpretability and explainability of the model in this experiment require improvement. To enhance the credibility and application value of the model, further research on model interpretability methods is needed. This will help researchers and agricultural practitioners to better understand how the model works, which is of great significance for improving productivity and reducing economic losses in the citrus industry.

5 Conclusion

The image-text multimodal deep learning method proposed in this study combined text and image features with domain knowledge to fully characterize the features of various diseases and accurately identify and infer the main types of citrus diseases. Even when dealing with small-sample and multi-background noise datasets, this method achieved a high classification accuracy and generalization performance. Moreover, by constructing a structured feature word table as prior knowledge for text information preparation, this study significantly reduced the volume and preprocessing difficulty of the text modality. The inclusion of domain knowledge also provided prediction results with higher credibility. Taken together, the multimodal deep learning method proposed in this study can effectively extract and integrate features from multiple data sources and domain knowledge, thereby achieving precise identification of citrus diseases in complex backgrounds. This provides a more reliable basis for making decisions regarding the precise application of biological and biochemical control strategies in production.

Data availability statement

The original contributions presented in the study are included in the article/Supplementary Material. Further inquiries can be directed to the corresponding author.

Author contributions

XQ: Conceptualization, Investigation, Writing – original draft. HC: Methodology, Software, Writing – original draft. PH: Formal Analysis, Writing – review & editing. DZ: Data curation, Software, Writing – original draft. TG: Writing – original draft, Data curation, Software. CP: Investigation, Writing – original draft. ZL: Writing – review & editing, Formal Analysis. YL: Writing – review & editing, Investigation. JC: Methodology, Writing – review & editing. SW: Conceptualization, Writing – review & editing.

Funding

The author(s) declare financial support was received for the research, authorship, and/or publication of this article. This research was supported by the National Key Research and Development Program of China, grant number 2021YFD1600800; Sichuan Science and Technology Program, grant number 2021YFG0028; and the Science and Technology Program of Sichuan Academy of Agricultural Sciences grant numbers 1 + 9KJGG008/022ZZCX032.

Acknowledgments

Special thanks to Prof. Zhihui Wang, Dr. Tie Wang, and Dr. Hang Li of the Fruit Cultivation and Physiology Research Team of Sichuan Agricultural University for their guidance during the image-text data pairing process.

Conflict of interest

The authors declare that the research was conducted in the absence of any commercial or financial relationships that could be construed as a potential conflict of interest.

Publisher's note

Supplementary material

The Supplementary Material for this article can be found online at: https://www.frontiersin.org/articles/10.3389/fpls.2023.1280365/full#supplementary-material

References

Abbas, A., Jain, S., Gour, M., and Vankudothu, S. (2021). Tomato plant disease detection using transfer learning with C-GAN synthetic images. *Comput. Electron. Agric.* 187, 106279. doi: 10.1016/j.compag.2021.106279

Abdalla, A., Cen, H., Wan, L., Rashid, R., Weng, H., Zhou, W., et al. (2019). Fine-tuning convolutional neural network with transfer learning for semantic segmentation of ground-level oilseed rape images in a field with high weed pressure. *Comput. Electron. Agric.* 167, 105091. doi: 10.1016/j.compag.2019.105091

Barman, U., Choudhury, R. D., Sahu, D., and Barman, G. G. (2020). Comparison of convolution neural networks for smartphone image based real time classification of citrus leaf disease. *Comput. Electron. Agric.* 177, 105661. doi: 10.1016/j.compag.2020.105661

Brahimi, M., Boukhalfa, K., and Moussaoui, A. (2017). Deep learning for tomato diseases: classification and symptoms visualization. *Appl. Artif. Intell.* 31, 299–315. doi: 10.1080/08839514.2017.1315516

Chellapandi, B., Vijayalakshmi, M., and Chopra, S. (2021). *2021 International Conference on Computing, Communication, and Intelligent Systems (ICCCIS)* (India: Greater Noida), 383–387. doi: 10.1109/ICCCIS51004.2021.9397098

Coulibaly, S., Kamsu-Foguem, B., Kamissoko, D., and Traore, D. (2019). Deep neural networks with transfer learning in millet crop images. *Comput. Ind.* 108, 115–120. doi: 10.1016/j.compind.2019.02.003

Dananjayan, S., Tang, Y., Zhuang, J., Hou, C., and Luo, S. (2022). Assessment of state-of-the-art deep learning based citrus disease detection techniques using annotated optical leaf images. *Comput. Electron. Agric.* 193, 106658. doi: 10.1016/j.compag.2021.106658

Delnevo, G., Girau, R., Ceccarini, C., and Prandi, C. (2022). A Deep learning and social ioT approach for plants disease prediction toward a sustainable agriculture. *IEEE Internet Things.* 9, 7243–7250. doi: 10.1109/JIOT.2021.3097379

Feng, X. G., Zhao, C. J., Wang, C. S., Wu, H. R., Miao, Y. S., and Zhang, J. J. (2022). A vegetable leaf disease identification model based on image-text cross-modal feature fusion. *Front. Plant Sci.* 13. doi: 10.3389/fpls.2022.918940

Ferentinos, K. P. (2018). Deep learning models for plant disease detection and diagnosis. *Comput. Electron. Agric.* 145, 311–318. doi: 10.1016/j.compag.2018.01.009

Gómez-Sanchis, J., Martín-Guerrero, J. D., Soria-Olivas, E., Martínez-Sober, M., Magdalena-Benedito, R., and Blasco, J. (2012). Detecting rottenness caused by Penicillium genus fungi in citrus fruits using machine learning techniques. *Expert Syst. Appl.* 39, 780–785. doi: 10.1016/j.eswa.2011.07.073

Goodfellow, I., Bengio, Y., and Courville, A. (2016). *Deep learning* (Cambridge, MA, USA: MIT press), 1–438.

He, X. T., and Peng, Y. X. (2020). Fine-grained visual-textual representation learning. *IEEE Trans. Circuits. Syst. Video. Technol.* 30, 520–531. doi: 10.1109/tcsvt.2019.2892802

He, K., Zhang, X., Ren, S., and Sun, J. (2016). *2016 IEEE Conference on Computer Vision and Pattern Recognition (CVPR)* (Las Vegas, NV, USA), 770–778. doi: 10.1109/CVPR.2016.90

Hernandez, S., and Lopez, J. L. (2020). Uncertainty quantification for plant disease detection using Bayesian deep learning. *Appl. Soft. Comput.* 96, 1568. doi: 10.1016/j.asoc.2020.106597

Huang, L., Chen, C., Yun, J., Sun, Y., Tian, J., Hao, Z., et al. (2022). Multi-scale feature fusion convolutional neural network for indoor small target detection. *Front. Neurorobotics.* 16. doi: 10.3389/fnbot.2022.881021

Jiang, Z. C., Dong, Z. X., Jiang, W. P., and Yang, Y. Z. (2021). Recognition of rice leaf diseases and wheat leaf diseases based on multi-task deep transfer learning. *Comput. Electron. Agric.* 186, 106184. doi: 10.1016/j.compag.2021.106184

Joulin, A., Grave, E., Bojanowski, P., Douze, M., Jégou, H., and Mikolov, T. (2016). Fasttext. zip: Compressing text classification models. *arXiv. preprint.: 1612.03651.* doi: 10.48550/arXiv.1612.03651

Kim, Y. (2014). Convolutional neural networks for sentence classification. *arXiv. preprint.: 1408.5882.* doi: 10.48550/arXiv.1408.5882

Leong, S., Leong, S., and Beattie, G. (2022). Diaphorina citriIntegrated pest management strategies for asian citrus psyllid kuwayama (Hemiptera: psyllidae) and huanglongbing in citrus for sarawak, east Malaysia, borneo. *Insects* 13, 960. doi: 10.3390/insects13100960

Li, X. D., Zhou, Y. H., Liu, J. Y., Wang, L. B., Zhang, J., and Fan, X. F. (2022). The detection method of potato foliage diseases in complex background based on instance

segmentation and semantic segmentation. *Front. Plant Sci.* 13. doi: 10.3389/fpls.2022.899754

Liu, S., Liu, H., John, V., Liu, Z., and Blasch, E. (2020). Enhanced situation awareness through CNN-based deep multimodal image fusion. *Optical. Eng.* 59, 1. doi: 10.1117/1.oe.59.5.053103

Lu, J., Shi, R., Tong, J., Cheng, W., Ma, X., and Liu, X. (2023). Lightweight method for plant disease identification using deep learning. *Intelligent. Automation. Soft. Computing.* 37, 525–544. doi: 10.32604/iasc.2023.038287

Luaibi, A. R., Salman, T. M., and Miry, A. H. (2021). Detection of citrus leaf diseases using a deep learning technique. *Int. J. Electrical. Comput. Eng. (IJECE).* 11, 1719. doi: 10.11591/ijece.v11i2.pp1719-1727

Ma, N. N., Zhang, X. Y., Zheng, H. T., and Sun, J. (2018). *15th european conference on computer vision (ECCV)* (Munich, GERMANY), 122–138. doi: 10.1007/978-3-030-01264-9_8

Neves, R. F. O., Wetterich, C. B., Sousa, E. P. M., and Marcassa, L. G. (2023). Multiclass classifier based on deep learning for detection of citrus disease using fluorescence imaging spectroscopy. *Laser. Phys.* 33, 055602. doi: 10.1088/1555-6611/acc6bd

Patané, J. S. L., Martins, J.Jr., Rangel, L. T., Belasque, J., Digiampietri, L. A., Facincani, A. P., et al. (2019). Origin and diversification of Xanthomonas citri subsp. citri pathotypes revealed by inclusive phylogenomic, dating, and biogeographic analyses. *BMC Genomics* 20, 700. doi: 10.1186/s12864-019-6007-4

Picon, A., Alvarez-Gila, A., Seitz, M., Ortiz-Barredo, A., Echazarra, J., and Johannes, A. (2019). Deep convolutional neural networks for mobile capture device-based crop disease classification in the wild. *Comput. Electron. Agric.* 161, 280–290. doi: 10.1016/j.compag.2018.04.002

Ramanjot, M. U., Wadhawan, A., Singla, J., Jhanjhi, N. Z., Ghoniem, R. M., Ray, S. K., et al. (2023). Plant disease detection and classification: A systematic literature review. *Sensors. (Basel).* 23, 4769. doi: 10.3390/s23104769

Ramcharan, A., Baranowski, K., Mccloskey, P., Ahmed, B., Legg, J., and Hughes, D. P. (2017). Deep learning for image-based cassava disease detection. *Front. Plant Sci.* 8. doi: 10.3389/fpls.2017.01852

Rangarajan, A. K., Purushothaman, R., and Ramesh, A. (2018). Tomato crop disease classification using pre-trained deep learning algorithm. *Proc. Comput. Sci.* 133, 1040–1047. doi: 10.1016/j.procs.2018.07.070

Rao, M., Zuo, H., and Xu, Q. (2021). Genomic insights into citrus domestication and its important agronomic traits. *Plant Commun.* 2, 100138. doi: 10.1016/j.xplc.2020.100138

Reed, S., Akata, Z., Lee, H., Schiele, B.Ieee (2016). *2016 IEEE conference on Computer Vision and Pattern Recognition (CVPR)* (Seattle, WA), 49–58. doi: 10.1109/cvpr.2016.13

Saleem, M., Potgieter, J., and Arif, K. (2020). Plant disease classification: a comparative evaluation of convolutional neural networks and deep learning optimizers. *Plants* 9, 1319. doi: 10.3390/plants9101319

Sandler, M., Howard, A., Zhu, M., Zhmoginov, A., and Chen, L.-C. (2018). *2018 IEEE/CVF Conference on Computer Vision and Pattern Recognition* (Salt Lake City, UT, USA), 4510–4520. doi: 10.1109/CVPR.2018.00474

Sibiya, M., and Sumbwanyambe, M. (2019). A computational procedure for the recognition and classification of maize leaf diseases out of healthy leaves using convolutional neural networks. *AgriEngineering* 1, 119–131. doi: 10.3390/agriengineering1010009

Simonyan, K., and Zisserman, A. (2014). Very deep convolutional networks for large-scale image recognition. *arXiv. preprint.: 1409.1556*. doi: 10.48550/arXiv.1409.1556

Stock, A., Gregr, E. J., and Chan, K. M. A. (2023). Data leakage jeopardizes ecological applications of machine learning. *Nat. Ecol. Evol.* 8, 1743–1745.. doi: 10.1038/s41559-023-02162-1

Sun, L., Ke, F., Nie, Z., Wang, P., and Xu, J. (2019). Citrus genetic engineering for disease resistance: past, present and future. *Int. J. Mol. Sci.* 20, 5256. doi: 10.3390/ijms20215256

Syed-Ab-Rahman, S. F., Hesamian, M. H., and Prasad, M. (2022). Citrus disease detection and classification using end-to-end anchor-based deep learning model. *Appl. Intell.* 52, 927–938. doi: 10.1007/s10489-021-02452-w

Upadhyay, S. K., and Kumar, A. (2021). Early-stage brown spot disease recognition in paddy using image processing and deep learning techniques. *Trait. Signal* 38, 1755–1766. doi: 10.18280/ts.380619

Wang, C., Zhao, C., Wu, H., Li, J., and Zhu, H. (2021a). Recognizing crop diseases using bimodal joint representation learning. *Trans. Chin. Soc. Agric. Eng.* 37, 180–188. doi: 10.11975/j.issn.1002-6819.2021.11.020

Wang, C. S., Zhou, J., Zhang, Y., Wu, H. R., Zhao, C. J., Teng, G. F., et al. (2022). A plant disease recognition method based on fusion of images and graph structure text. *Front. Plant Sci.* 12. doi: 10.3389/fpls.2021.731688

Wang, C., Zhou, J., Zhao, C., Li, J., Teng, G., and Wu, H. (2021b). Few-shot vegetable disease recognition model based on image text collaborative representation learning. *Comput. Electron. Agric.* 184, 106098. doi: 10.1016/j.compag.2021.106098

Wang, Y., Zhou, M., Zou, Q., and Xu, L. (2021c). Machine learning for phytopathology: from the molecular scale towards the network scale. *Briefings Bioinf.* 22, bbab037. doi: 10.1093/bib/bbab037

Xing, S., Lee, M., and Lee, K. K. (2019). Citrus pests and diseases recognition model using weakly dense connected convolution network. *Sensors. (Basel).* 19, 3195. doi: 10.3390/s19143195

Yang, D., Wang, F., Hu, Y., Lan, Y., and Deng, X. (2021). √Citrus huanglongbing detection based on multi-modal feature fusion learning. *Front. Plant Sci.* 12. doi: 10.3389/fpls.2021.809506

Zhang, N., Wu, H., Zhu, H., Deng, Y., and Han, X. (2022). Tomato disease classification and identification method based on multimodal fusion deep learning. *Agriculture* 12, 1–13. doi: 10.3390/agriculture12122014

Zhao, Y., Liu, L., Xie, C., Wang, R., Wang, F., Bu, Y., et al. (2020). An effective automatic system deployed in agricultural Internet of Things using Multi-Context Fusion Network towards crop disease recognition in the wild. *Appl. Soft. Computing.* 89, 106128. doi: 10.1016/j.asoc.2020.106128

Zhou, J., Li, J., Wang, C., Wu, H., Zhao, C., and Teng, G. (2021). Crop disease identification and interpretation method based on multimodal deep learning. *Comput. Electron. Agric.* 189, 106408. doi: 10.1016/j.compag.2021.106408

frontiers | Frontiers in Plant Science

TYPE Original Research
PUBLISHED 29 November 2023
DOI 10.3389/fpls.2023.1303669

OPEN ACCESS

EDITED BY
Xiaolan Lv,
Jiangsu Academy of Agricultural Sciences (JAAS), China

REVIEWED BY
Shilin Wang,
Jiangsu Academy of Agricultural Sciences (JAAS), China
Qin Weicai,
Suzhou Polytechnic Institute of Agriculture, China

*CORRESPONDENCE
Cancan Song
songcc@sdut.edu.cn
Yubin Lan
ylan@sdut.edu.cn

RECEIVED 28 September 2023
ACCEPTED 13 November 2023
PUBLISHED 29 November 2023

CITATION
Yan Y, Lan Y, Wang G, Hussain M, Wang H, Yu X, Shan C, Wang B and Song C (2023) Evaluation of the deposition and distribution of spray droplets in citrus orchards by plant protection drones. *Front. Plant Sci.* 14:1303669. doi: 10.3389/fpls.2023.1303669

Evaluation of the deposition and distribution of spray droplets in citrus orchards by plant protection drones

Yu Yan[1,2], Yubin Lan[1,2]*, Guobin Wang[1,2], Mujahid Hussain[1,2], Huizheng Wang[1,2], Xiaoqing Yu[3], Changfeng Shan[1,2], Baoju Wang[1,2] and Cancan Song[1,2]*

[1]College of Agricultural Engineering and Food Science, Shandong University of Technology, Zibo, China, [2]Shandong University of Technology Sub-center, National Center for International Collaboration Research on Precision Agricultural Aviation, Zibo, China, [3]Plant Protection Station of Shandong Province, Jinan, China

Plant protection drone spraying technology is widely used to prevent and control crop diseases and pests due to its advantages of being unaffected by crop growth patterns and terrain restrictions, high operational efficiency, and low labor requirements. The operational parameters of plant protection drones significantly impact the distribution of spray droplets, thereby affecting pesticide utilization. In this study, a field experiment was conducted to determine the working modes of two representative plant protection drones and an electric backpack sprayer as a control to explore the characteristics of droplet deposition with different spray volumes in the citrus canopy. The results showed that the spraying volume significantly affected the number of droplets and the spray coverage. The number of droplets and the spray coverage area on the leaf surface were significantly increased by increasing the spray volume from 60 L/ha to 120 L/ha in plant protection drones. Particularly for the DJI T30, the mid-lower canopy showed a spray coverage increase of 52.5%. The droplet density demonstrated the most significant variations in the lower inner canopy, ranging from 18.7 droplets/cm^2 to 41.7 droplets/cm^2 by XAG V40. From the deposition distribution on fruit trees, the plant protection drones exhibit good penetration ability, as the droplets can achieve a relatively even distribution in different canopy layers of citrus trees. The droplet distribution uniformity inside the canopy is similar for XAG V40 and DJI T30, with a variation coefficient of approximately 50%-100%. Compared to the plant protection drones, the knapsack electric sprayer is suitable for pest and disease control in the mid-lower canopy, but they face challenges of insufficient deposition capability in the upper canopy and overall poor spray uniformity. The distribution of deposition determined in this study provides data support for the selection of spraying agents for fruit trees by plant protection drones and for the control of different pests and diseases.

KEYWORDS

plant protection drones, citrus, application volume, number of droplets, spray coverage

1 Introduction

Citrus is one of the top fruit tree species in the world, is incredibly vitamin-rich, has significant economic and therapeutic significance, and has overtaken apples as the most popular fruit in China. Citrus plants in China accounted for about a fifth of all garden fruit plantings in 2022, according to the list of China's beneficial agricultural products (Kui and Qi, 2022). In the production activities of citrus cultivation, the reduction of citrus yield caused by infection with citrus pests and diseases is the main factor limiting the safe production of citrus (Glienke et al., 2011; Brentu et al., 2012; Sun, 2022). Regular pest and disease control is required to ensure crop yield and quality. As citrus planting areas are mostly on mountainous slopes with complicated road conditions, it is not convenient for ground mechanical spraying, which leads to a knapsack electric sprayer, which is still the main way of pesticide spraying. However, this spraying method not only requires a lot of human and material resources but also has a low efficiency, which causes an increase in planting costs and is not conducive to the development of the citrus industry. Therefore, growers need to use modern and efficient plant protection machinery to replace traditional spraying equipment (Yamane and Miyazaki, 2017).

In recent years, the rapid development of aerial spraying by plant protection drones has attracted attention and has been widely promoted and applied (Lan et al., 2017; Yang et al., 2018; Wang et al., 2019). Plant protection drones get rid of the ground operation mode, break through the restrictions of crop types (low and high crops, etc.), and have the advantages of high operational efficiency, low cost, good application effect, and strong ability to deal with sudden disasters (Xue et al., 2014). With the development and application of plant protection drones, plant protection drone flight operations have begun to extend from field crops to fruit trees, and relevant researchers are exploring the effects of different operating parameters of plant protection drones on the distribution of the number of droplets. Citrus canopy is relatively simple and mostly planted in patches and scales, which is more suitable for plant protection drones to operate. In 2016, Zhang et al. (2016) explored the spraying effect of a small electric quadrotor plant protection drones on the canopy of citrus trees at different flight heights and found that the plant protection drones deposited best when working on open-centered shaped plants at 1.0 m for height. Tang et al. (2018) studied the effects of operating height and tree shape on sap droplet deposition in citrus trees using plant protection drones. When the operation height was 1.2 m and the flight speed was 3.5 m/s, the number of droplets and the spray coverage in the canopy reached the maximum. Guo et al. (2022) evaluated four types of nozzles (SX110015, XR80015, IDK90015, and TR80015) based on a point spray pattern in a southern pear orchard experiment and showed that the IDK90015 nozzle showed significantly higher deposition and penetration. Several studies on fruit trees have compared plant protection drone applications with conventional application equipment. Martinez-Guanter et al. (2020) found that conventional shower applications cause excessive waste and that treatments using plant protection drones are more uniform while significantly reducing drift. There are still many barriers to using plant protection drones in citrus orchards, and in terms of plant protection drone technology, a combination of electrostatic nozzles and spray aids can improve droplet deposition. In addition, field testing requires attention to suitable weather conditions, especially wind speed. Zhang et al (Pan et al., 2017). 2017 verified that plant protection drones are twice as efficient as manual applications using field trials. Junior et al. (2016) studied water use and application rates for the control of citrus black spot and found that a change in spray volume from 125 mL/m3 to 75 mL/m3 resulted in a 40% reduction in CBS spray cost and water use and an increase in profit of up to 35%. Li et al. (2021) used an electric hexacopter plant protection drone to compare the overall residue levels of chlorothalonil insecticide at application rates of 46.8 L/ha and 93.5 L/ha in an almond crop protection application study.

In recent years, there has been rapid development of plant protection drones in China. Research related to plant protection drones in field crops has become relatively developed, while their application in fruit trees is still in its early stages. For example, research on parameters such as optimal operating height, optimal flight speed, and optimal spraying flow rate has been carried out on crops with small canopies, such as wheat, rice, and corn (Zheng et al., 2017; Kharim et al., 2019; Chen et al., 2020). In contrast, less research has been conducted on crops with large canopies such as fruit trees. Regarding whether the spray droplets from plant protection drones can penetrate the canopy of fruit trees? How can the optimal spraying volume be set to ensure better droplet deposition and suitable operational efficiency? What is the difference between plant protection drone spraying and backpack spraying deposition? These are the questions that bother everyone. Therefore, we conducted this study to address these questions. The flight control technology in orchard environments is challenging, and there is a high demand for it. In response to complex terrains such as hilly areas and basins, several drone companies in China have developed various product categories to ensure more uniform pesticide application using plant protection drones (Lan et al., 2022).To make plant protection drones meet the requirements of precision application operations, further research is needed on the effects of the number of droplets, spray coverage, and spray uniformity of representative plant protection drones. On the other hand, the Application Volume is an essential parameter for evaluating the effectiveness of plant protection drones. Due to the limited tank capacity and flight speed of plant protection drone sprayers, plant protection drones only use low-volume spraying during spraying (Lan and Chen, 2018). It is crucial to investigate whether plant protection drones' low-volume spraying can achieve good droplet deposition and determine the optimal spray volume for plant protection drones' spraying. Therefore, this paper conducted field experiments on mist droplet deposition distribution in citrus canopies at two spray volumes (60 L/ha and 120 L/ha) using two representative plant protection drones, XAG V40 and DJI T30, compared the results to mist droplet deposition with a knapsack electric sprayer (Knapsack Electric Sprayer, KES) at a spray volume of 2400 L/ha to investigate the spraying effect of plant protection drones in citrus orchards. The goal was to provide theoretical guidance and data support for the optimization of

application parameters of plant protection drone orchard operation and pesticide application reduction and efficiency increase.

2 Materials and methods

2.1 Field plots

The experiments were conducted in experimental fields located at the Tong Gong Township, Zhejiang Province (118°45'68″E, 28°58'52″ N), China, in June 2021. The experiment material was citrus in the fruit-expanding stage. (2.6 ± 0.3) m high with a canopy diameter of (2.9 ± 0.3) m, planted at a density of 1523 trees/ha with a between-row spacing of (3.5 ± 0.5) m and a between-tree spacing of (2 ± 0.5) m (Figure 1). During the spray operation, the temperature was between 30.7°C and 32.6°C, relative humidity between 56.4% and 60.3%, and wind speeds between 0.0 and 1.3m/s. All meteorological parameters during the test period complied with the comparative measurement conditions of the ISO 22522 standard (International Organization for Standardization, 2007).

2.2 Plant protection drones and reference equipment selection

The spraying equipment was XAG V40 (XAG Co., Ltd., China) and DJI T30 (SZ DJI Technology Co., Ltd., China) (Figure 2). XAG V40 adopts a tilting dual-rotor structure, with rotor rotors on top of the two folding arms and a nozzle at the bottom, equipped with a 16 L tank, centrifugal nozzle, peristaltic pump, etc. It is equipped with a standard front dynamic radar, upward-looking radar, and ground-like radar, bringing a more comprehensive and delicate perception and obstacle avoidance capability. DJI T30 spray system is equipped with a horizontally opposed six-cylinder dual plunger pump design, a dual-channel electromagnetic flow meter error of ±2%, eight nozzles distributed downward on both sides of the fuselage, equipped with a spherical radar system, omnidirectional perception of the surrounding environment, to achieve intelligent around the obstacles and ground-like flight. The two representative plant protection drones, the XAG V40 and DJI T30 are officially given as having a maximum operating efficiency of up to 16 ha/h. The battery capacity of DJI T30 is 30Ah, and the battery capacity of XAG V40 is 20 Ah. One full charge allows for approximately 15 minutes of flight. The XAG V40 utilizes the XAG agricultural services software to plan flights and automatically carry out operations based on the preset routes. On the other hand, the DJI T30 uses the DJI agricultural software to plan flights and also performs operations automatically according to the preset routes. The detailed parameters of the equipment are shown in Table 1. Other test spraying equipment included a knapsack electric sprayer (3WBD-20-1, Taizhou Luqiao Huyue Sprayer Factory, China). The knapsack electric sprayer is equipped with an electric pump and atomizing nozzle, with a maximum spray width of 9 m, and a spray volume of 2400 L/ha was used for operation in this test. Other test materials included a scanner, a meteorological instrument, Kromekote cards, etc.

2.3 Experimental design

The pesticide used in this experiment was Mancozeb 430 g/L SC. Before application, the Allura Red solution (80% purity, purchased from Beijing Oriental Care Trading Ltd., China) at a concentration of 5 g/L was added to the tank as a tracer. Before the experiment, set the experimental parameters such as flight height, flight speed, spraying width, droplet size, and application liquid volume according to the orchard situation. The spraying system automatically calculates the pump's flow rate according to the parameters of flight speed, spraying width, and application liquid volume to ensure the accuracy of the application liquid volume. Two representative plant protection drones (XAG V40 and DJI T30) were tested for spray droplet deposition distribution in the citrus canopy, with a knapsack electric sprayer as a control. The application volume (APV) of the plant protection drones was set at 60 L/ha and 120 L/ha (Table 2). Other operating parameters of the plant protection drone application were set at flight height: 3 m,

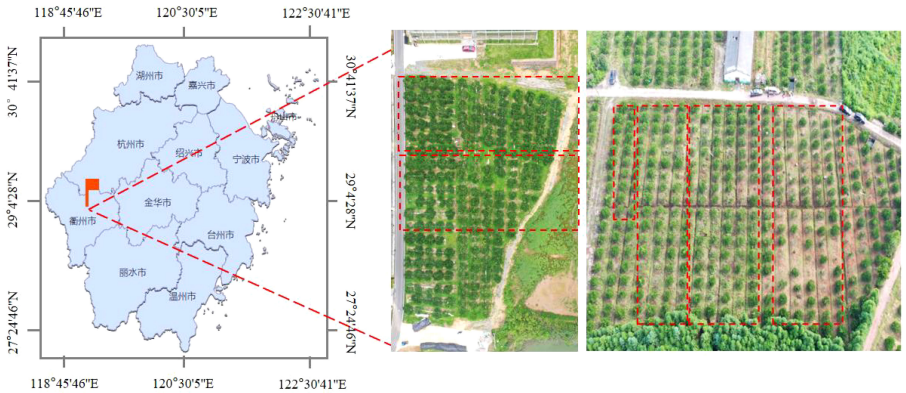

FIGURE 1
Experiment location.

10.3389/fpls.2023.1303669

TABLE 1 Technical parameters for the plant protection drone sprayer.

Classification	XAG V40	DJI T30	KES
Dimensions/mm	2110mm×2127mm×555mm	2858mm×2685 mm×790mm	390mm×210mmx495mm
Rotor numbers	2	6	—
Nozzle number	2	16	1
Nozzle type	Centrifugal nozzle	Hydraulic nozzle	Hydraulic nozzle
Droplet size	130μm(10000 rpm)	105 μm(0.3 MPa)	175 μm(0.3 MPa)
Tank capacity/L	16 L	30 L	20 L
Spraying width/m	4m	4m	3m

flight speed: 3 m/s, route spacing: 3.5 m, and Flow Rate:3.78L/min. During the trial, the plant protection drones flew along the tree rows and above the rows of citrus trees. The application volume of the knapsack electric sprayer was set at 2400 L/ha based on pesticide to water. The test personnel wear appropriate protective clothing, gloves, masks, and other personal protective equipment to ensure safety. Adjust the spray angle and pressure of the knapsack electric sprayer before the test. Carry the knapsack electric sprayer on the back to maintain the correct spraying distance and even moving speed. Spray different parts of the fruit tree, including the crown, branches, and leaves.

In the sampling survey, each treatment group was divided into 5 plots in equal amounts according to the length of the treatment area, and 5 fruit trees of the same growth and shape were selected for each treatment group as multiple replications of the same treatment. For comparison with the reduced application by plant protection drones, one conventional control treatment area with the manual application by a knapsack electric sprayer was set up, and a blank control treatment area without pesticide application was designed. To avoid the effect of droplet drift between adjacent treatment zones, each treatment zone was used as a buffer zone within 10 m from the edge, and no droplet deposition data were collected within the buffer zone. Twenty-five sampling points were selected for each tree, and paper cards were fixed to the leaves with paper clips at each sampling point. The canopy of each citrus tree was divided into three layers, i.e., upper, middle, and lower, which included the upper layer (5 points), middle layer (inner canopy: 5 points; outer canopy: 5 points) and lower layer (inner canopy: 5 points; outer canopy: 5 points), and the deposition of droplets in different parts of the fruit tree canopy was collected (Figures 3, 4).

TABLE 2 Treatments designed for the field experiments.

Treatment	Sprayer	Application Volume(L/ha)
T1	XAG V40	60
T2	XAG V40	120
T3	DJI T30	60
T4	DJI T30	120
T5	KES	2400

During the experiment, the pesticide droplets were not completely deposited in the canopy, and some droplets would pass through the canopy and deposit on the ground, causing soil contamination; therefore, 10 sampling points were arranged on the ground under each target citrus tree to collect the pesticides lost on the ground.

2.4 Sample and data analyses

After 30 minutes of each spraying test, dried WSPs were retrieved in sequence using disposable gloves. Put the WSPs into sealed bags marked according to the different treatments and add desiccant to prevent moisture from affecting the test results. Store the bags in a cool place and bring them back to the laboratory for analysis. All collected paper cards were scanned using a scanner, and the results were analyzed using the image processing software Deposit Scan (U.S. Department of Agriculture, Wooster, Ohio). Experimental results were processed using Excel 2019, and statistical analysis using SPSS 21.0. Duncan's multiple comparisons test was used to analyze the significance of differences among various treatments.

Spray uniformity refers to the uniformity of spray droplet distribution on the target, and the uniformity of droplet distribution in the field has an important impact on pest control. To describe the uniformity of droplet distribution in the field, the Coefficient of Variation (CV) of the number of droplets in each sampling area was used to indicate the uniformity of droplet distribution for a set of data. The smaller the coefficient of variation, the smaller the variation in the data, i.e., the more uniform the distribution of droplet deposition, and the coefficient of variation was calculated as follows:

$$\mathbf{CV} = \frac{\mathbf{S}}{\bar{\mathbf{X}}} \times 100\,\% \tag{1}$$

$$\mathbf{S} = \sqrt{\sum_{\mathbf{i}=1}^{\mathbf{n}} (\mathbf{X_i} - \bar{\mathbf{X}})^{\,2} / (\mathbf{n} - 1)} \tag{2}$$

where S is the standard deviation of samples from the same test group; X_i is the number of droplets or spray coverage at each sampling point; $\bar{X}$ is the mean value of samples from the same test group; and n is the number of sampling points in each test group.

FIGURE 2
Spraying operations of the plant protection drones sprayer and KES in the citrus orchard: **(A)** XAG V40 two-rotor electric unmanned aerial vehicle. **(B)** DJI T30 six-rotor electric unmanned aerial vehicle. **(C)** Knapsack Electric Sprayer.

3 Results

3.1 Analysis of the number of droplets and spray coverage

Figure 5 presents the test results of the XAG V40 fruit tree application. From the perspective of the number of droplets, the results show that the number of droplets within the canopy of XAG V40 ranged from 18.7 droplets/cm^2 to 35.5 droplets/cm^2 at a spray volume of 60 L/ha. At a spray volume of 120 L/ha, the droplet density within the canopy ranged from 27.9 droplets/cm^2 to 41.7 droplets/cm^2. The percentage increase of the number of droplets in different parts of the canopy was 12.4% to 123.2% with an average increase of 34.5% compared to 60 L/ha. At a spray volume of 120 L/ha, the spray coverage in the canopy of XAG V40 ranged from 6.6% to 20.5%, while at 60 L/ha, it ranged from 3.2% to 11.0%. The increase in spray coverage in different parts of the canopy at a spray volume of 120 L/ha ranged from 65.7% to 127.6%, with an average increase of 87.8% compared to 60 L/ha.

Significant differences existed in the number of droplets and spray coverage of XAG V40 at different canopy sampling points of citrus trees. The results of spray coverage showed significant differences in spray coverage in the upper, middle, and lower layers of citrus trees. At a spray volume of 60 L/ha, the spray coverage at different canopy locations was in the following order: upper canopy > middle outer canopy > middle inner canopy > lower outer canopy > lower inner canopy. When the spray volume increased from 60 to 120 L/ha, the number of droplets showed the most significant change in the lower inner canopy, from 18.7 droplets/cm^2 to 41.7 droplets/cm^2, an increase of 123.2%. Additionally, the spray coverage in the lower canopy of the fruit trees was higher than that in the middle.

Figure 6 shows the test results of the DJI T30 fruit tree application. It can be seen from the perspective of the number of droplets that at a spray volume of 60L/ha, the number of droplets within the canopy was 151.7 droplets/cm^2 - 194.2 droplets/cm^2, and at a spray volume of 120 L/ha, the number of droplets within the canopy was 146.0 droplets/cm^2 - 205.3 droplets/cm^2. However, there was no significant increase in the number of droplets at a spray volume of 120 L/ha, and the percentage variation in different parts of the canopy was -24.8% to 24.8%, with a spray coverage variation of -2.3%. From the perspective of spray coverage, this demonstrates that the DJI T30 had 8.6% - 24.2% spray coverage at a spray volume of 60 L/ha and 12.1% - 22.0% spray coverage at a spray volume of 120 L/ha. Compared with 60 L/ha, the spray coverage increased at a spray volume of 120 L/ha, especially in the lower and middle canopy, with a spray coverage increase of 52.5%.

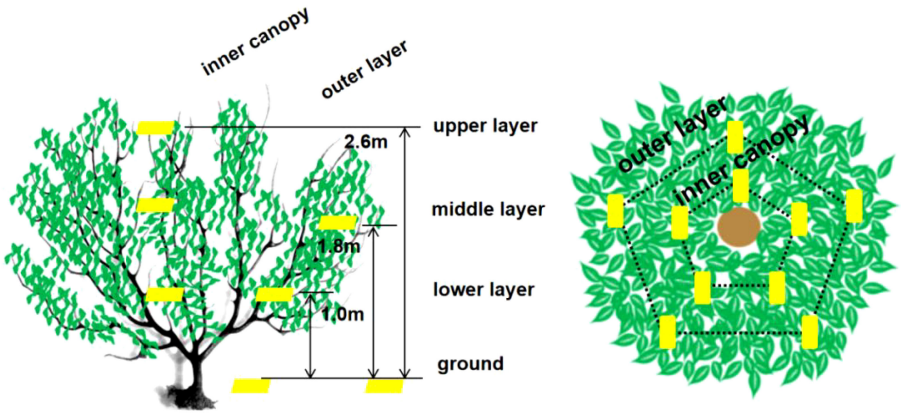

FIGURE 3
Sampler locations for assessing spray deposition in the target apple tree canopy and ground loss.

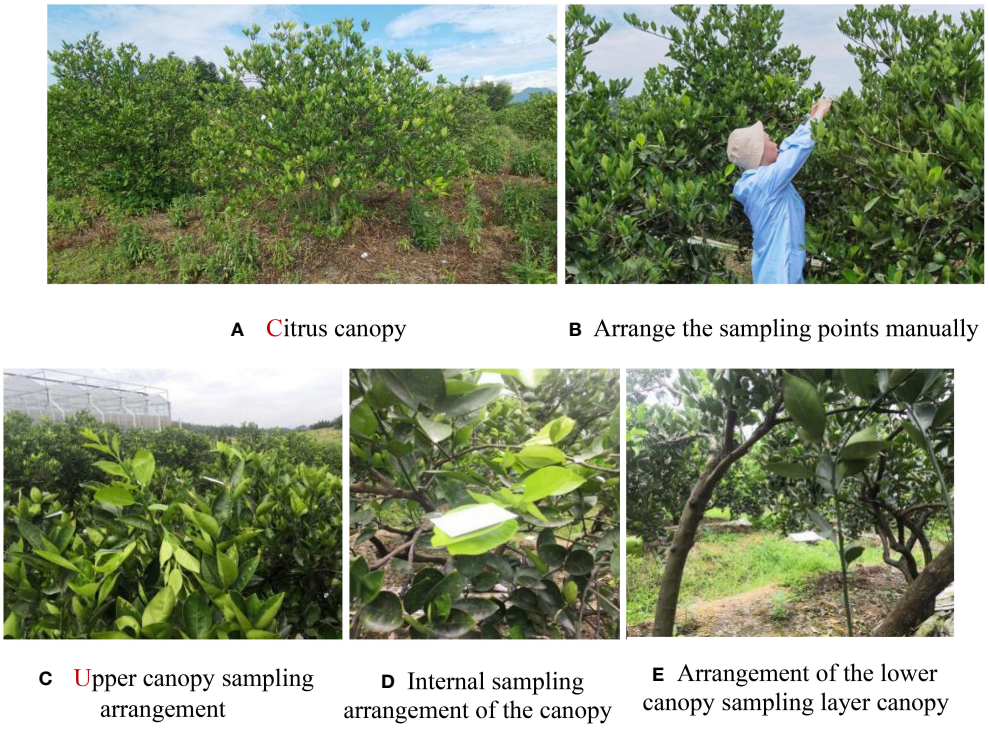

FIGURE 4
Materials of the field test. **(A)** Citrus canopy, **(B)** Arrange the sampling points manually, **(C)** Upper canopy sampling arrangement, **(D)** Internal sampling arrangement of the canopy, **(E)** Arrangement of the lower canopy sampling layer canopy.

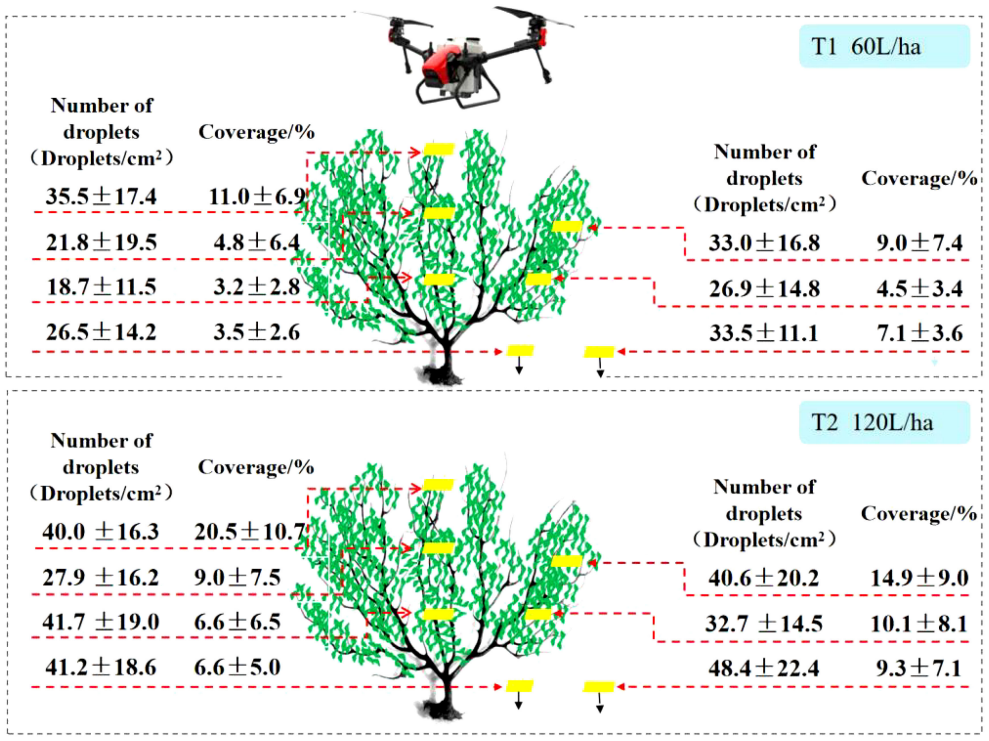

FIGURE 5
Different APV on the Number of droplets and spray coverage of XAG V40.

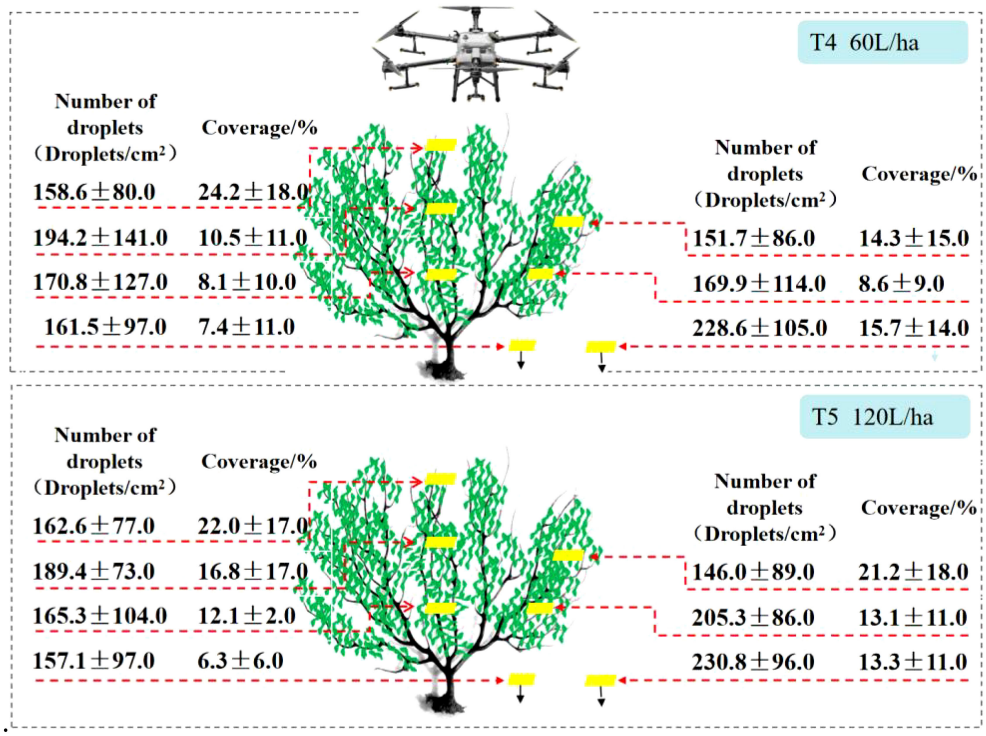

FIGURE 6
Different APV on the Number of droplets and spray coverage of DJI T30.

In the DJI T30 fruit tree application test, there was no significant increase in the number of droplets in different canopies of citrus trees when the APV was increased from 60 to 120 L/ha. The change in spray coverage was more significant in the middle canopy, with an increase of 48.5% from 14.3% to 21.2% in the middle outer canopy and 60.1% from 10.5% to 16.8% in the middle inner canopy. Significant differences in the number of droplets were observed in different canopies of citrus trees. The spray coverage at different canopy locations at spraying rates of 60 L/ha and 120 L/ha followed this order: upper canopy > middle outer canopy > middle inner canopy > lower outer canopy > lower inner canopy.

The results showed that the spray volume of the plant protection drones affected the distribution of the number of droplets during the spraying operation, and the number of droplets and spray coverage varied at different spray volumes. When the APV increased from 60 to 120 L/ha, the number of droplets and spray coverage increased significantly, but this increase was not linearly proportional to the increase in APV.

Figure 7 displays the experimental results of the knapsack electric sprayer fruit tree application. From the perspective of droplet deposition density, it can be seen that with a knapsack electric sprayer in 2400 L/ha spray liquid volume, droplet density within the canopy is 39.1 droplets/cm^2-149.0 droplets/cm^2; coverage within the canopy is 40.3% - 42.4%. The coverage within the canopy was 40.3% - 42.4%. The difference between the maximum and minimum values of Figure 7 displays the experimental results of the knapsack electric sprayer fruit tree application. fruit tree applied droplet density was 109.9 droplets/cm^2. The deposition in the lower canopy was much larger than in the upper canopy. The knapsack electric sprayer at 2400 L/ha of spray liquid volume had 48.3% higher upper canopy coverage than the XAG V40 at 120 L/ha and 51.9% higher upper canopy coverage than the DJI T30 at 120 L/ha. The knapsack electric sprayer had lower droplet density in the upper canopy than the two typical plant protection drones.

3.2 Analysis of droplet distribution uniformity

Figure 8A shows the analysis results of the coefficient of variation of the number of droplets and the coefficient of variation of spray coverage for XAG V40. As can be seen from the figure, the coefficient of variation of the number of droplets decreased to 2.6% - 39.3% when the spray volume increased from 60 to 120 L/ha. The mean coefficient of variation of the number of droplets within the canopy decreased by 22.0%. The mean coefficient of variation of intra-canopy spray coverage decreased by 14.9% when the spray volume was increased from 60 to 120 L/ha.

Figure 8B shows the results of the analysis of the coefficient of variation of the number of droplets and the coefficient of variation of spray coverage of DJI T30, and the results indicate that the increase of spraying volume helps to improve the uniformity of the number of droplets. When the spray volume increased to 120 L/ha, the coefficient of variation of the number of droplets decreased in all

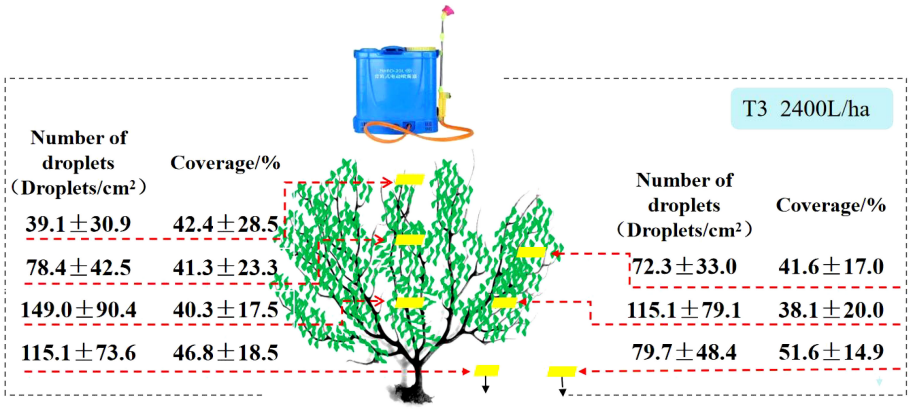

FIGURE 7
The Number of droplets and spray coverage of Knapsack Electric Sprayer.

canopies, the mean coefficient of variation of the number of droplets decreased by 26.8% and the mean coefficient of variation of spray coverage decreased by 11.5%. The results showed that the uniformity of the number of droplets in the upper part of the canopy was better than that in the middle and lower parts of the canopy, whether it was 60 L/ha or increased to 120 L/ha. The deposition of droplets in the upper canopy of fruit trees is better than in the lower canopy, primarily because of the higher spraying position and smaller droplets used by plant protection drones, making it difficult for the droplets to penetrate the dense foliage. Although increasing the downdraft can enhance the deposition of droplets in some lower positions of the canopy, it can also cause the canopy to collapse, resulting in poorer uniformity of droplet distribution in the lower canopy. As shown in Figure 8, the change in the middle and lower canopy is most noticeable after increasing the application volume. This indicates that increasing the application volume enhances droplet deposition in different canopy layers and improves penetration, thereby influencing the uniformity of droplet deposition in the middle and lower layers. Suitable working parameters can be selected for different spraying requirements and machine types.

From the above analysis, it is clear that an increase in spray volume also improves spray uniformity. Within the canopy, the coefficient of variation of the number of droplets in the central inner part showed the greatest variation, decreasing by 34.9%. This indicates that increasing the spray volume increased droplet penetration and made it easier to penetrate the canopy. The humidity inside the crop canopy is generally higher, and some diseases occur from inside the canopy. Therefore, less distribution of droplets inside the canopy will reduce the spraying effect. Therefore, the use of plant protection drones for the application of chemicals, for the control of pests and diseases mainly in the inner

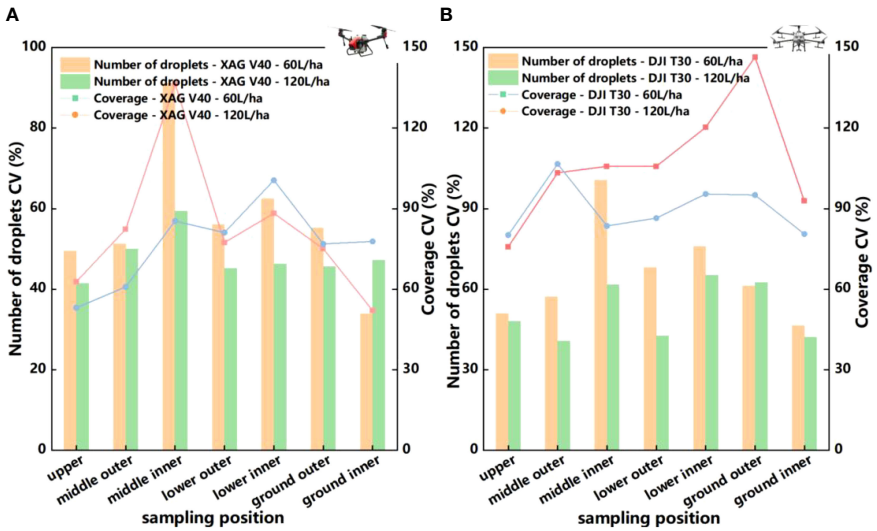

FIGURE 8
(A) Deposition distribution uniformity of XAG V40 two-rotor electric unmanned aerial vehicle in blade surface under 60 L/ha and 120 L/ha application volume. **(B)** Deposition distribution uniformity of DJI T30 six-rotor electric unmanned aerial vehicle in blade surface under 60L/ha and 120 L/ha application volume.

canopy of citrus, increasing the amount of spray liquid can improve the coverage and deposition uniformity to achieve better prevention effect, but the specific impact also needs to take into account the effect of canopy size, resistance and wind and other factors. The effect of other factors such as droplet size and leaf density on spraying effectiveness should also be noted.

3.3 Comparative analysis of deposition on the citrus

A visualization of the droplet deposition distribution for the XAG V40, DJI T30, and knapsack electric sprayer segments (Figure 9) shows that the droplet particle size of the plant protection drones is on average smaller than that of the knapsack electric sprayer and is better droplet uniformity. The knapsack electric sprayer spray may have droplets that will converge into larger droplets.

In the liquid spray volume application test between two plant protection drones, XAG V40, and DJI T30, the DJI T30 had finer droplet particle size, 4.9 - 8.1 times higher number of droplets, and 1.1-2.5 times higher coverage compared with XAG V40. It indicates that under the wind field and operating parameters conditions of this test plant protection drone, the fruit tree nozzle used by DJI T30 is beneficial to deliver the liquid to each canopy layer. The changes in the number of droplets and coverage of XAG V40 were more significant when the spray volume was increased from 60 L/ha to 120 L/ha, indicating that the spray volume could be increased to increase the droplet deposition distribution as well as the droplet penetration.

The rotor wind field of plant protection drones facilitates the penetration of droplets into the canopy, but it also tends to cause uneven droplet distribution. As shown in the Table 3, the uniformity of droplet distribution within the canopy is similar between XAG V40 and DJI T30, and the coefficient of variation of the number of droplets is between 50% and 100%. The increase in APV from 60 to 120 L/ha and the increase in the coefficient of variation of the number of droplets between XAG V40 and DJI T30 indicates that the increase in spray volume helps to improve the uniformity of spraying. At the same time, the statistics show that XAG V40 has relatively high uniformity despite its lower number of droplets. This indicates that the wind field under the rotor of the plant protection drones is the main factor affecting the distribution pattern of droplet deposition (Figure 10). A weak or disturbed wind field is very likely to make it unable to penetrate the crop canopy, and the droplets cannot reach the lower and inner layers of the canopy, resulting in uneven distribution among the canopies and affecting the control effect. The wind field generated by different types of plant protection drones differs due to different aerodynamic principles and significant structural differences. The wind field generated by multi-rotor plant protection drones during operation is the result of the interaction of airflow generated by multiple rotors (Chen et al., 2017), which differs greatly from the wind field and downforce airflow generated by dual-rotor plant protection drones, resulting in significant differences in the deposition distribution of droplets in the crop canopy between different types of plant protection drones.

Compared to the plant protection drones, the knapsack electric sprayer applied 20 times more liquid. It increased the number of droplets by 100.7% - 241.9% at different locations in the middle and

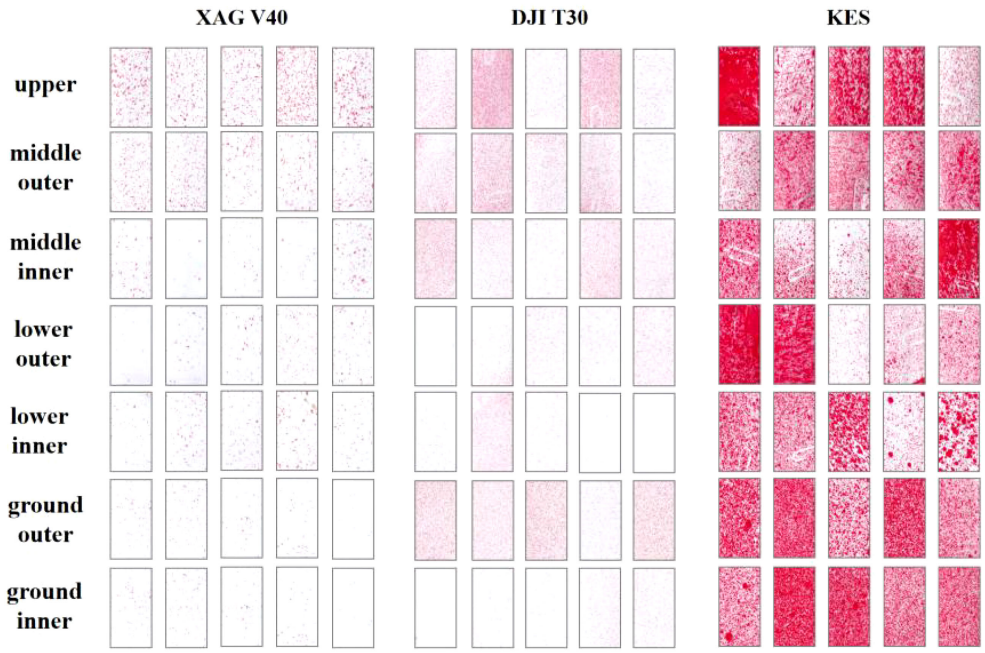

FIGURE 9
Visual diagram of the deposition of spray droplets in citrus orchards by different plant protection machinery.

TABLE 3 Number of droplets coefficient variation and spray coverage coefficient variation of XAG V40 and DJI T30.

The type of drone of application volume		Coefficient of variation of number of droplets (%)	Coefficient of variation of spray coverage(%)
XAG V40	60L/ha	62.1	89.5
	120L/ha	48.5	76.2
Ratio		-22.0	-14.9
DJI T30	60L/ha	70.6	102.2
	120L/ha	51.7	90.5
Ratio		-26.8	-11.5

lower part of the crop canopy, with the highest growth rate of 241.9% in the lower outer layer (Figure 11). Due to the high spray volume of the knapsack electric sprayer, the inner canopy leaf droplet density was higher compared to the plant protection drones, but the upper canopy was lower than the plant protection drones. The deposition of the knapsack electric sprayer treatment group was concentrated on the outer part of the middle and lower canopy, indicating that under the present test conditions, the pesticide droplets from the knapsack electric sprayer still cannot penetrate the upper canopy, while the droplets produced by the plant protection drones are conducive to deposition in the upper canopy, which can improve the pest and disease control effect in the upper canopy. The knapsack electric sprayer showed a decreasing trend from bottom to top, while the plant protection drones were relatively more uniform in the upper, middle, and lower canopy layers of the fruit tree canopy. This is because the low-volume spraying of plant protection drones can ensure the maximum increase of droplet deposition distribution with small droplet particle size, whereas the traditional manual spraying results in larger droplet particle size and poor penetration. In addition, the limitation of the number of droplets and the spray coverage in the citrus canopy and weed inter-distribution further affects the spraying efficiency.

3.4 Analysis of loss in ground

In actual operation, due to the complex distribution of the overall leaf inclination angle of citrus tree leaves, the large droplets generated by plant protection equipment spraying are prone to run off from the leaves and cause pesticide loss. The results of the droplet deposition on the ground sampling area of XAG V40, DJI T30, and the knapsack electric sprayer are shown in Figure 12.

In the XAG V40 application test, the number of droplets was higher at locations where the ground was unobstructed by branches and leaves. When the spray volume was increased, the droplet density increased at all ground sampling points. When the APV increased from 60 L/ha to 120 L/ha, there was a 58.6% increase in droplet density at ground locations with branch and leaf shading. The number of droplets increased by 44.3% at the ground level without branch and leaf shading. In the DJI T30 application test, the ground loss was insignificant when the spray volume was increased. Increasing the APV from 60 L/ha to 120 L/ha reduced the number of droplets by 2.7% at the ground level with branch and leaf shading and increased it by 0.9% at the ground level without shading.

Compared to the plant protection drones, the number of droplets from the knapsack electric sprayer on the ground in both shaded and unshaded positions was higher than that of XAG V40 but lower than that of DJI T30. The number of droplets in the unshaded position on the ground of the knapsack electric sprayer was lower than that of the shaded position on the ground. Even though the number of droplets in the shaded position on the ground was higher than that inside the lower canopy, the reason is that the knapsack electric sprayer nozzle has a high flow rate, and the atomization effect is poor, causing droplets to form large droplets or even spray directly to the ground, resulting in poor spraying effectiveness. Moreover, due to the presence of branches inside the canopy, the absorption of the droplets is weaker than that of the leaves, and droplets fall to the ground above the inter-plant gap area.

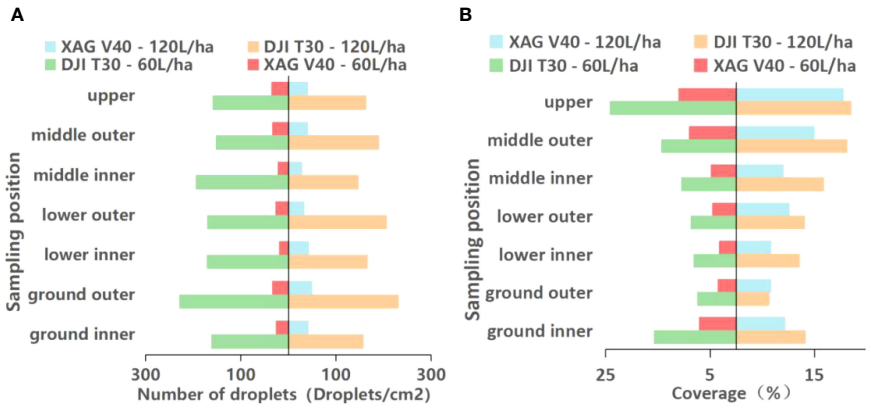

FIGURE 10
(A) Number of droplets of XAG V40 and DJI T30 on blade surface. **(B)** Coverage rate of XAG V40 and DJI T30 in the blade surface.

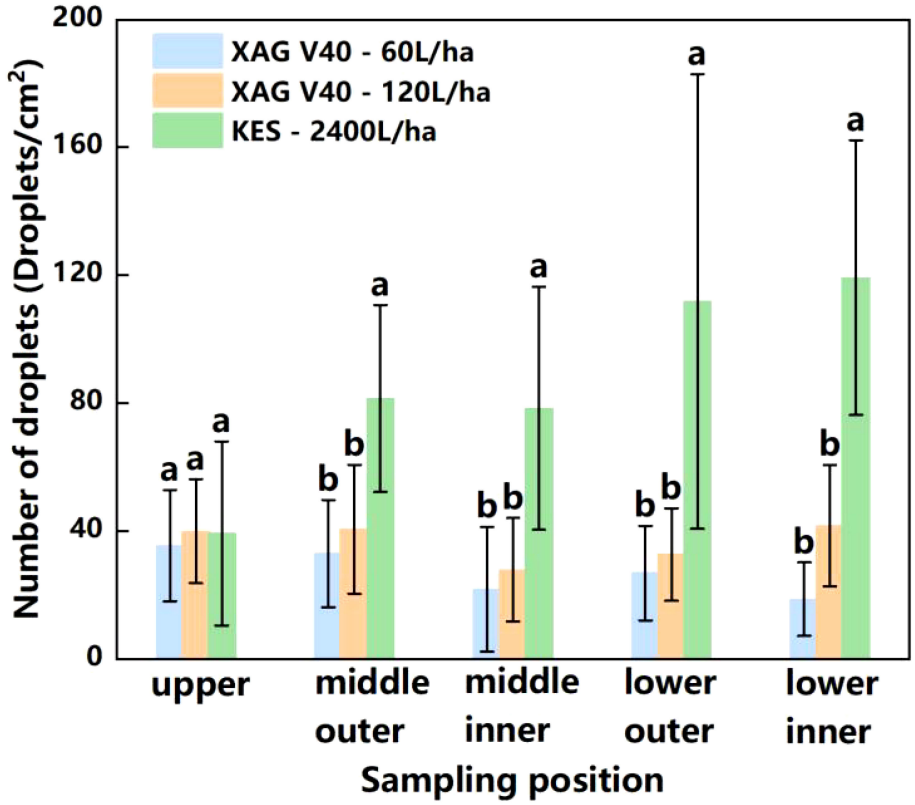

FIGURE 11
Number of droplets of XAG V40 and Knapsack Electric Sprayer. (a, b express that there are significant differences between different spray methods and spray volume. P<0.05).

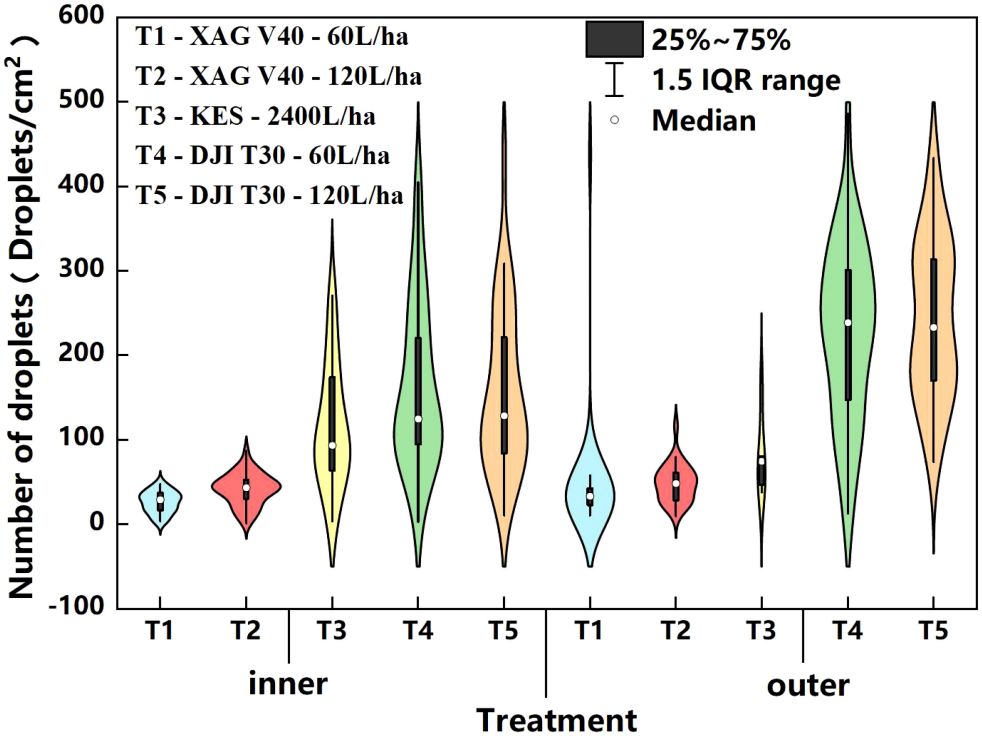

FIGURE 12
Ground loss for the five treatment groups.

4 Discussion

Pesticide application technology plays a vital role in orchard production and is essential for improving citrus quality. Plant protection drones enable independent spraying operations without being subject to crop growth patterns and terrain restrictions, which significantly improves application efficiency and precision. However, the main concern with using plant protection drones is whether low-volume application leads to insufficient deposition and affects the effectiveness of control. Furthermore, not all sprayed solute ions are deposited on the target, and the off-target portion can be lost to the environment, causing contamination. These benefits can only be realized if a full assessment of spray droplet deposition effects is conducted. This study examined two typical plant protection drones, XAG V40, and DJI T30, for their reduced application in citrus orchards. The results showed that the plant protection drones deposited droplets with a density of approximately greater than 25 droplets/cm^2 in each longitudinal and lateral layer of fruit trees, meeting the plant protection requirements of orchards (Administration of Quality Supervision, Inspection and Quarantine of the People's Republic of China, 2008). The use of different spray volumes by plant protection drones significantly affected leaf coverage, droplet density, and spray uniformity (Wandkar et al., 2018; Gil et al., 2021). The DJI T30 achieves better deposition effects compared to a manually operated knapsack electric sprayer with a spray volume of 2400 L/ha by using a spray volume of 60 L/ha. Citrus crops require a lower droplet density when lightly infected or when applying systemic agents. This allows the use of plant protection drones with a lower application volume, which can achieve a droplet density of approximately 25 droplets/cm^2, meeting the requirements for pest control. This study found that increasing the spray volume of the XAG V40 from 60 L/ha to 120 L/ha resulted in an average increase of 34.5% in droplet density in different canopy parts. Therefore, in the case of severe disease infection in citrus crops, increasing the application volume can improve droplet deposition effects and meet the requirements for pest control.

The use of different spray volumes by plant protection drones has a significant impact on leaf coverage and droplet density. Previous studies have shown that droplet density increases with increasing spray volume, which is consistent with our findings that both droplet density and coverage increased when the spray volume of the plant protection drone was increased from 60 L/ha to 120 L/ha in the trial. However, in a controlled trial with manual application from a knapsack electric sprayer, it was found that the knapsack electric sprayer using 20 times higher spray liquid volume than that of the plant protection drone increased droplet density at different locations in the lower and middle parts of the crop canopy by only 100.7% - 241.9%. The upper spray liquid effect of the knapsack electric sprayer was significantly lower than that of the plant protection drone. This is due to the lack of droplet-assisted diffusion device in the knapsack electric sprayer, and it takes some time for the liquid to reach the surface of the crop leaves from the nozzle, resulting in part of the liquid evaporating and drifting away, and reducing the surface coverage of the leaves (Hussain et al., 2022a; Hussain et al., 2022b). At the same time, the spraying height of the knapsack electric sprayer in the actual application process depends on the operator, and the deposition effect is also closely related to the operator's spraying method.

Increasing the amount of liquid spray can improve the uniformity and penetration of spray droplets applied by plant protection drones. Theoretically, the number of droplets generated by plant protection drone operations in the citrus canopy should gradually decrease from the upper to the lower layers. However, the results of this experiment did not show a gradual weakening trend from top to bottom, and the number of droplets in the lower or middle layer of the fruit tree canopy was slightly higher than that in the upper layer. This may be mainly because, in practice, plant protection drones can penetrate droplets better into the canopy. Guo et al. (2020) verified through experiments that the downward spiral of plant protection drones downwash airflow can blow open the fruit tree canopy and improve the penetration of droplets. The downward airflow generated by the rotor also helps increase the adhesion and penetration of droplets on the crop, making the plant protection drones relatively more uniform in the different canopy layers of fruit trees at the top, middle, and bottom. The Miranda-Fuentes (Praat et al., 2000) trial showed that an increase in application rate increased average deposition and coverage but decreased application efficiency, spray penetration, and deposition uniformity. However, in this trial, comparing the deposition uniformity of the XAG V40 plant protection drone and the DJI T30 plant protection drone, the results showed that the uniformity of droplet distribution within the canopy was essentially similar between the XAG V40 plant protection drone and the DJI T30 plant protection drone, with coefficients of variation for droplet deposition in the range of 50% - 100%. the APV increased from 60 L/ha to 120 L/ha, the coefficient of variation of fog droplet density increased for the XAG V40 plant protection drone and DJI T30 plant protection drone, suggesting that the increase in spray volume also contributed to improved spray uniformity. The uniformity of fog droplet deposition on each layer of the fruit tree canopy was poor in this experiment. The reason for this phenomenon may be that the wind field below the rotor of the plant protection UAV is too strong, causing the upper branches of the fruit tree plants to tilt in all directions. Most of the droplets reach the middle and lower parts of the fruit tree plants with the wind field, and fewer droplets are deposited around the upper layers of the canopy, and the tilted branches affect the deposition of droplets on the leaves of the fruit trees so that the amount of droplet deposition on the leaves in the direction of the inverted direction is less.

Spray volume and sprayer type affect spray distribution and off-target losses in the canopy. Both liquid spray volume and sprayer type affect spray distribution and off-target losses in the canopy. The results of this experiment showed that when the liquid spray volume was increased from 60 L/ha to 120 L/ha, the droplet density at the ground sampling point increased with the elevated liquid spray volume. Compared with XAG V40 and DJI T30 plant protection UAVs, the loss of knapsack electric sprayer on the ground was higher than the XAG V40 plant protection UAV and lower than the DJI T30 plant protection UAV. Wise et al (Zhang et al., 2016).

sprayed with different liquid spray volumes, and the loss of liquid solution was the most significant at the highest liquid spray volume. However, the effect of this liquid loss also depended on the canopy size, with a gradual decrease in fog droplet coverage from top to bottom for the different canopies tested by plant protection drones, which was mainly related to the structural state of the fruit tree form (Ferguson et al., 2015). Zhang Pan et al (Miranda-Fuentes et al., 2015). found that during production management, open citrus trees were suitable for plant protection drone spraying, but fluctuations and large dispersions showed poor uniformity, and these consequences may be related to the pruning of the tree structure. Maintaining a high standard and uniformity of the open canopy is difficult, and this still needs improvement. Combined with the plant protection UAV spraying test in this study, increasing the amount of liquid spray has a significant effect on improving uniformity, and how to obtain the optimal parameters for plant protection UAV spraying and reducing the loss of liquid solution will be a key issue that will continue to be of concern for the future application of plant protection UAVs.

Many other factors affect the effect of fog droplet deposition by plant protection drones, and more comprehensive field trial studies are needed. Including nozzle type, nozzle installation position, and angle, the interface of spray width between multiple nozzles, the use of parameters (such as spray pressure, flight speed, etc.), and the natural environmental conditions during spraying. In addition, the rotor wind and side wind in aerial applications can also easily cause uneven droplet distribution. Researchers have conducted comprehensive indoor performance tests on nozzles. Ferguson et al (Wise et al., 2010). compared the droplet size distribution of 21 spray drift reduction nozzles in a wind tunnel for three liquids with different dynamic surface tensions. The nozzle types classified as homogeneous in the study were XR, ABJ 11002, AITTJ60, and AIXR 110015, among others. The average CV for each nozzle type was equal to or less than 4%, and most of the tested nozzles were homogeneous in the nozzle cell. However, the uniformity of droplet distribution at different operating parameters needs to be analyzed for specific aerial application equipment.

Improving deposition also requires the right amount of spray liquid in conjunction with other operating parameters and minimizing drift. Experts suggest that additives can improve deposition. Gimenes et al. (2013)found that the use of spraying aids has great potential to improve the uniformity of pesticide spraying, increase spray coverage, and reduce the amount of pesticide applied. Guo Shuang et al (Guo et al., 2022). found that the use of additives significantly increased the particle size of droplets and reduced the proportion of small droplets in the experiment of evaluating additives in the South Fruit Pear Garden, which can effectively reduce the risk of droplet drift and help to improve the pesticide utilization rate. In addition, studies have shown that flight mode, flight altitude, and side wind speed all affect plant protection UAV spray droplets (Qin et al., 2016; Wang et al., 2016), because the downward rotating airflow wind field affects the droplet motion during plant protection UAV operations, and changes in altitude alter the uniformity of droplet distribution (Wang et al., 2022). Therefore, it is necessary to fully study the effects of the body structure and flight parameters of plant protection UAVs on droplet deposition, explore reasonable use techniques in the field, and provide data support for future use, to minimize the adverse effects of plant protection UAV operations and better utilize the advantages of plant protection UAVs in orchard control.

5 Conclusion

Plant protection drones are a powerful tool for improving fruit tree spraying operations and enhancing the quality of droplet deposition. Due to factors such as the rotor wind field of the plant protection drones, the unique tree structure of different fruit trees, the terrain environment, and other influencing factors, it is necessary to optimize the operating parameters of the plant protection drones to ensure the effective distribution of droplets during aerial spraying operations in the fruit tree canopy. In this paper, the effects of XAG V40 and DJI T30 on droplet deposition distribution on citrus trees at 60 L/ha and 120 L/ha spray volume were compared experimentally, and the droplet deposition distribution characteristics of the knapsack electric sprayer on citrus trees were also analyzed, along with ground loss for each experiment. Extensive field experimental results showed that the pesticide droplets still cannot penetrate the upper canopy when applied by a knapsack electric sprayer, while the droplets produced by plant protection drones are conducive to deposition in the upper part of the canopy. Increasing the amount of applied liquid is more significant for the deposition of droplets in the upper part of the citrus canopy, which helps the utilization of pesticides. Therefore, using plant protection drones to control pests and diseases in the middle and upper part of the citrus canopy and increasing the amount of liquid applied will achieve better control effectiveness. Further research should seek to assess the impact of additional fungicides and insecticides to ascertain the relevance of the conclusions since the data are only based on a small spectrum of active ingredients. It is worth noting that the wind field under the plant protection drone rotor can increase the penetration of droplets among crop plants, and the strength of the rotor wind field varies among different types of plant protection drones. Thus, further research on the rotor wind field of plant protection drones is needed to improve the spraying performance of plant protection drones. Additionally, some pests and diseases attached to the abaxial surface of leaves should be considered in future studies to further investigate the deposition effect on the abaxial surface of leaves to better understand the performance of fog droplet deposition.

Data availability statement

The original contributions presented in the study are included in the article/supplementary material. Further inquiries can be directed to the corresponding authors.

Author contributions

YL: Methodology, Resources, Writing – review & editing. YY: writing – Original draft, Validation. GW: Formal analysis, Validation, Writing – original draft. MH: Investigation, Writing – review & editing. HW: Investigation, Writing – review & editing. XY: Investigation, Writing – review & editing. CFS: Data curation, Writing – review & editing. BW: Data curation, Writing – review & editing. CCS: Formal analysis, Validation, Writing – review & editing.

Funding

The author(s) declare financial support was received for the research, authorship, and/or publication of this article. This research was funded by the Top Talents Program for One Case One Discussion of Shandong Province and Shandong Province Natural Science Foundation (ZR2021QC154).

Acknowledgments

We acknowledge the support provided by the members of the Shandong University of Technology Smart Agriculture team. The authors would like to thank Ms. Haihong Wang for giving references in the data collection and data analysis of the paper, and for giving useful research discussions and writing guidance.

Conflict of interest

The authors declare that the research was conducted in the absence of any commercial or financial relationships that could be construed as a potential conflict of interest.

Publisher's note

References

Administration of Quality Supervision, Inspection and Quarantine of the People's Republic of China. (2008). GB/T 17997-2008, Evaluating regulations for the operation and spraying quality of sprayers in the field. Beijing: Standards Press of China.

Brentu, F. C., Oduro, K. A., Offei, S. K., Odamtten, G. T., Antonio, V., Peres, N. A., et al. (2012). Crop loss, etiology, and epidemiology of citrus black spot in Ghana. *Eur. J. Plant Pathol.* 133, 657–670. doi: 10.1007/s10658-012-9944-1

Chen, S. D., Lan, Y. B., Bradley, K. F., Li, J. Y., Liu, A. M., and Mao, Y. D. (2017). Effect of wind field below rotor on distribution of aerial spraying droplet deposition by using multi-rotor UAV. *Trans. Chin. Soc. Agric. Machine.* 48, 105–113. doi: 10.6041/j.issn.1000-1298.2017.08.011

Chen, S., Lan, Y., and Zhou, Z. (2020). Effect of droplet size parameters on droplet deposition and drift of aerial spraying by using plant protection UAV. *Agronomy* 10, 195. doi: 10.3390/agronomy10020195

Ferguson, J. C., O'Donnell, C. C., Chauhan, B. S., Adkins, S. W., Kruger, G. R., Wang, R. B., et al. (2015). Determining the uniformity and consistency of droplet size across spray drift reducing nozzles in a wind tunnel. *Crop Protect.* 76, 1–6. doi: 10.1016/j.cropro.2015.06.008

Gil, E., Salcedo, R., Soler, A., Ortega, P., Llop, J., Campos, J., et al. (2021). Relative efficiencies of experimental and conventional foliar sprayers and assessment of optimal LWA spray volumes in trellised wine grapes. *Pest Manage. sci.* 77, 2462–2476. doi: 10.1002/ps.6276

Gimenes, M., Zhu, H., Raetano, C. G., and Oliveira, R. (2013). Dispersion and evaporation of droplets amended with adjuvants on soybeans. *Crop Prot.* 44, 84–90. doi: 10.1016/j.cropro.2012.10.022

Glienke, C., Pereira, O. L., Stringari, D., Fabris, J., Kava-Cordeiro, V., Galli-Terasawa, L., et al. (2011). Endophytic and pathogenic Phyllosticta species. *Persoonia-Molecular Phylogen. Evol. Fungi* 26, 47–56. doi: 10.3767/003158511X569169

Guo, S., Yao, W. X., Xu, T. Y., Ma, H., Sun, M. J., and Xhen, C. L. (2022). Assessing the application of spot spray in Nanguo pear orchards: Effect of nozzle type, spray volume rate, and adjuvant. *Pest Manage. Science.* 78, 3564–3575. doi: 10.1002/ps.6999

Guo, Q., Zhu, Y., Tang, Y., Hou, C. J., He, Y., Zhuang, J. J., et al. (2020). CFD simulation and experimental verification of the spatial and temporal distributions of the downwash airflow of a quad-rotor agricultural UAV in hover. *Comput. Electron. Agricult.* 172, 105343. doi: 10.1016/j.compag.2020.105343

Hussain, M., Wang, Z., Huang, G., Mo, Y., Guo, Y., Kaousar, R., et al. (2022a). Evaluation of droplet deposition and efficiency of 28-homobrassinolide sprayed with unmanned aerial spraying system and electric air-pressure knapsack sprayer over wheat field. *Comput. Electron. Agricult.* 202, 107353. doi: 10.1016/j.compag.2022.107353

Hussain, M., Wang, Z., Huang, G., Mo, Y., Kaousar, R., Duan, L., et al. (2022b). Comparison of droplet deposition, 28-homobrassinolide dosage efficacy and working efficiency of the unmanned aerial vehicle and knapsack manual sprayer in the maize field. *Agronomy* 12 (2), 385. doi: 10.3390/agronomy12020385

International Organization for Standardization. (2007). ISO, 22522, crop protection equipment-field measurement of spray distribution in tree and bush crops (ISO Int Stand).

Junior, G. J. S., Scapin, M. D. S., Silva, F. P., Silva, A. R. P., Behlau, F., and Ramos, H. H. (2016). Spray volume and fungicide rates for citrus black spot control based on tree canopy volume. *Crop Protect.* 85, 38–45. doi: 10.1016/j.cropro.2016.03.014

Kharim, M. N. A., Wayayok, A., and Shariff, A. R. M. (2019). Droplet deposition density of organic liquid fertilizer at low altitude UAV aerial spraying in rice cultivation. *Comput. Electron. Agric.* 167, 105045. doi: 10.1016/j.compag.2019.105045

Kui, G. X., and Qi, C. J. (2022). Study on the evolution of world citrus trade pattern based on social network analysis. *World Agric.* 6, 18–30.

Lan, Y. B., and Chen, S. D. (2018). Current status and trends of plant protection UAV and its spraying technology in China. *Int. J. Precis Agric. Aviat.* 1, 1–9. doi: 10.33440/j.ijpaa.20180101.0002

Lan, Y. B., Chen, S. D., and Fritz, B. K. (2017). Current status and future trends of precision agricultural aviation technologies. *Int. J. Agric. Biol. Eng.* 10, 1–17. doi: 10.3965/j.ijabe.20171003.3088

Lan, Y. B., Yan, Y., Wang, B. J., Song, C. C., and Wang, G. B. (2022). Current status and future development of the key technologies for intelligent pesticide spraying robots. *Trans. Chin. Soc. Agric. Engine.* 38, 30–40. doi: 10.11975/j.issn.1002-6819.2022.20.004

Li, X., Giles, D. K., Niederholzer, F. J., Aloro, J. T., Lang, E. B., and Watson, L. J. (2021). Evaluation of an unmanned aerial vehicle as a new method of pesticide application for almond crop protection. *Pest Manage. Science.* 77, 527–537. doi: 10.1002/ps.6052

Martinez-Guanter, J., Agüera, P., Agüera, J., and Pérez-Ruiz, M. (2020). Spray and economic assessment of a UAV-based ultra-low-volume application in olive and citrus orchards. *Precis. Agricult.* 21, 226–243. doi: 10.1007/s11119-019-09665-7

Miranda-Fuentes, A., Rodríguez-Lizana, A., Gil, E., Agüera-Vega, J., and Gil-Ribes, J. A. (2015). Influence of liquid-volume and airflow rates on spray application quality and homogeneity in super-intensive olive tree canopies. *Sci. Total Environ.* 537, 250–259. doi: 10.1016/j.scitotenv.2015.08.012

Pan, Z., Wang, K. J., Qiang, L. Y., and He, S. L. (2017). Droplet distribution and control against citrus leafminer with UAV spraying. *Int. J. Robot. Automation.* 32, 299–307. doi: 10.2316/Journal.206.2017.3.206-4980

Praat, J. P., Mabe, J., and Manktelow, D. (2000). The effect of canopy development and sprayer position on spray drift from a pip fruit orchard. *New Z. Plant Protect.* 53, 241–247. doi: 10.30843/nzpp.2000.53.3696

Qin, W. C., Qiu, B. J., Xue, X. Y., Chen, C., Xu, Z. F., and Zhou, Q. Q. (2016). Droplet deposition and control effect of insecticides sprayed with an unmanned aerial vehicle against plant hoppers. *Crop Prot.* 85, 79–88. doi: 10.1016/j.cropro.2016.03.018

Sun, Y. Q. (2022). Research on intelligent identification of citrus fine-grained diseases based on convolutional neural network.Electronic science. *Technology*.

Tang, Y., Hou, C. J., Luo, S. M., Lin, J. T., Yang, Z., and Huang, W. F. (2018). Effects of operation height and tree shape on droplet deposition in citrus trees using an unmanned aerial vehicle. *Comput. Electron. Agricult.* 148, 1–7. doi: 10.1016/j.compag.2018.02.026

Wandkar, S. V., Bhatt, Y. C., Jain, H. K., Nalawade, S. M., and Pawar, S. G. (2018). Real-time variable rate spraying in orchards and vineyards: A review. *J. Instit. Engine. (India): Ser. A.* 99, 385–390. doi: 10.1007/s40030-018-0289-4

Wang, C., He, X., Wang, X., Wang, Z., Pan, H., and He, Z. (2016). Testing method of spatial pesticide spraying deposition quality balance for unmanned aerial vehicle. *Transac. Chin. Soc Agric. Eng.* 32, 54–61. doi: 10.11975/j.issn.1002-6819.2016.11.008

Wang, Z., Hussain, M., Huang, G., Yin, J., Guo, Y., and Mo, Y. (2022). Better droplet deposition and internode shortening effects of plant growth regulator EDAH on maize applied by small unmanned aerial vehicle than electric knapsack sprayer. *Agriculture* 12, 404. doi: 10.3390/agriculture12030404

Wang, L. L., Lan, Y. B., Zhang, Y. L., Zhang, H. H., Muhammad, N. T., Ou, S. C., et al. (2019). Applications and prospects of agricultural unmanned aerial vehicle obstacle avoidance technology in China. *Sensors* 19, 642. doi: 10.3390/s19030642

Wise, J. C., Jenkins, P. E., Schilder, A. M. C., Vandervoort, C., and Isaacs, R. (2010). Sprayer type and water volume influence pesticide deposition and control of insect pests and diseases in juice grapes. *Crop Protect.* 29, 378–385. doi: 10.1016/j.cropro.2009.11.014

Xue, X. Y., Tu, K., Qin, W. C., Lan, Y. B., and Zhang, H. H. (2014). Drift and deposition of ultra-low altitude and low volume application in paddy field. *Int. J. Agric. Biol. Eng.* 7, 23–28. doi: 10.3965/j.ijabe.20140704.003

Yamane, S., and Miyazaki, M. (2017). Study on electrostatic pesticide spraying system for low-concentration, high-volume applications. *Japan Agric. Res. Quarterly: JARQ.* 51, 11–16. doi: 10.6090/jarq.51.11

Yang, S. L., Yang, X. B., and Mo, J. Y. (2018). The application of unmanned aircraft systems to plant protection in China. *Precis. Agricult.* 19, 278–292. doi: 10.1007/s11119-017-9516-7

Zhang, P., Deng, L., Lyu, Q., He, S. L., Yi, S. L., Liu, Y. D., et al. (2016). Effects of citrus tree-shape and spraying height of small unmanned aerial vehicle on droplet distribution. *Int. J. Agric. Biol. Engine.* 9, 45–52. doi:10.3965/j.ijabe.20160904.2178

Zheng, Y. J., Yang, S. H., and Zhao, C. J. (2017). Modelling operation parameters of UAV on spray effects at different growth stages of corns. *Int. J. Agric. Biol. Eng.* 10, 57–66. doi: 10.3965/j.ijabe.20171003.2578

frontiers | Frontiers in Plant Science

TYPE Original Research
PUBLISHED 21 December 2023
DOI 10.3389/fpls.2023.1297879

OPEN ACCESS

EDITED BY
Xiaolan Lv,
Jiangsu Academy of Agricultural Science (JAAS), China

REVIEWED BY
Jean-paul Douzals,
Institut National de recherche pour l'agriculture, l'alimentation et l'environnement (INRAE), France
Tao Wen,
Central South University Forestry and Technology, China

*CORRESPONDENCE
Zhen Li
lizhen@scau.edu.cn

RECEIVED 20 September 2023
ACCEPTED 08 December 2023
PUBLISHED 21 December 2023

CITATION
Xue X, Luo Q, Ji Y, Ma Z, Zhu J, Li Z, Lyu S, Sun D and Song S (2023) Design and test of Kinect-based variable spraying control system for orchards.
Front. Plant Sci. 14:1297879.
doi: 10.3389/fpls.2023.1297879

Design and test of Kinect-based variable spraying control system for orchards

Xiuyun Xue[1,2,3,4], Qin Luo[1], Yihang Ji[1], Zhaoyong Ma[1], Jiani Zhu[1], Zhen Li[1,2,3,4]*, Shilei Lyu[1,2,3], Daozong Sun[1,2,3] and Shuran Song[1,2,3]

[1]College of Electronic Engineering (College of Artificial Intelligence), South China Agricultural University, Guangzhou, China, [2]National Citrus Industry Technical System Machinery Research Office, Guangzhou, China, [3]Guangdong Provincial Agricultural Information Monitoring Engineering Technology Research Center, Guangzhou, China, [4]Meizhou SCAU-Zhensheng Research Institute for Modern Agricultural Equipment, Meizhou, China

Target detection technology and variable-rate spraying technology are key technologies for achieving precise and efficient pesticide application. To address the issues of low efficiency and high working environment requirements in detecting tree information during variable spraying in orchards, this study has designed a variable spraying control system. The system employed a Kinect sensor to real-time detect the canopy volume of citrus trees and adjusted the duty cycle of solenoid valves by pulse width modulation to control the pesticide application. A canopy volume calculation method was proposed, and precision tests for volume detection were conducted, with a maximum relative error of 10.54% compared to manual measurements. A nozzle flow model was designed to determine the spray decision coefficient. When the duty cycle ranged from 30% to 90%, the correlation coefficient of the flow model exceeded 0.95, and the actual flow rate of the system was similar to the theoretical flow rate. Field experiments were conducted to evaluate the spraying effectiveness of the variable spraying control system based on the Kinect sensor. The experimental results indicated that the variable spraying control system demonstrated good consistency between the theoretical spray volume and the actual spray volume. In deposition tests, compared to constant-rate spraying, the droplets under the variable-rate mode based on canopy volume exhibited higher deposition density. Although the amount of droplet deposit and coverage slightly decreased, they still met the requirements for spraying operation quality. Additionally, the variable-rate spray mode achieved the goal of reducing pesticide use, with a maximum pesticide saving rate of 57.14%. This study demonstrates the feasibility of the Kinect sensor in guiding spraying operations and provides a reference for their application in plant protection operations.

KEYWORDS

Kinect sensor, target detection, canopy volume, pulse width modulation, variablerate spraying

1 Introduction

Fruit trees are often attacked by pests and diseases during their growth, which not only affects the yield and quality of fruits but also threatens the production efficiency and economic benefits of fruit farmers (Popusoi, 2018). Among many orchard management operations, orchard pest control is the most time-consuming and laborious operation. According to statistics, fruit trees need to be sprayed at least 8 to 15 times per year during the growth period, accounting for about 30% of the total orchard operations (Jiang et al., 2016a). Chemical control is usually carried out through spraying, where spray test is used to disperse the liquid into droplets. These droplets are then applied to the fruit branches and leaves, allowing for chemical control to be achieved (He, 2020). Currently, pesticide application in citrus orchards in China mainly relies on the use of small and medium-sized spray equipment or manual spray poles and spray guns for continuous pesticide application. During pesticide application, the goal is to achieve a rinse-type application mode that thoroughly covers the fruit trees and completely wets the leaves. During the pesticide spraying process, although continuous spraying can achieve high coverage, it overlooks the canopy characteristics of different fruit trees and the variations among them, which often leads to over-spraying, under-spraying and run-off of fruit trees under continuous spraying conditions (Chen et al., 2019; He, 2020; Salcedo et al., 2020).

Variable-rate spraying technology is an intelligent operational method that adjusts the amount of pesticide application based on the characteristics of the target area. As an advanced and efficient orchard pesticide application technology, it can reduce pesticide use by more than 25% compared to continuous spraying (Kang et al., 2011; Stajnko et al., 2012). Variable-rate spraying technology primarily consists of two research directions: (1) Sensor-based detection of fruit tree canopy information, utilizing sensors to detect specific characteristic parameters, such as target fruit tree presence, leaf wall area (LWA), canopy volume (CV), leaf area density, and leaf area index as decision factors for variable-rate spraying (Nørremark et al., 2008). (2) Variable-rate spraying execution system based on different application rate models and flow models, which calculates the amount of application for target fruit trees based on different decision factors, then controls system status including the rotation speed of pumps and the opening and closing of solenoid valves to adjust parameters such as spray pressure, number of nozzles, and liquid flow rate. It ultimately achieves the purpose of on-demand pesticide application (Qiu et al., 2015; Xia, 2016).

The core of variable-rate spraying technology is to accurately obtain target feature information (Zhai et al., 2018). Currently, target feature information detection is primarily achieved through technologies such as laser sensors, infrared sensors, ultrasonic sensors, and machine vision (Balsari et al., 2009; Palleja and Landers, 2015; Berk et al., 2016; Zhang et al., 2018; Comba et al., 2019). The laser sensor detects target canopy structure by measuring the distance from the laser point cloud to the sensor, offering high accuracy and a long detection range. However, the laser sensor system is complex, expensive, and not suitable for environments with high dust, fog, or humidity. As a result, it is challenging to use in practical production. The infrared sensor determines the actual condition of the target by receiving the infrared radiation reflected by the target. It has a short response time, but its detection range is limited and it is highly influenced by lighting conditions (Li et al., 2012). The ultrasonic sensor measures the distance to the target by calculating the time difference between emitting the ultrasonic wave and receiving the echo. It has a farther detection range compared to the infrared sensor. However, its response time is longer, making it unsuitable for real-time detection (Solanelles et al., 2006). The ultrasonic sensor measures the distance to the target by calculating the time difference between emitting the ultrasonic wave and receiving the echo. Although it has a farther detection range compared to the infrared sensor, its response time is longer, making it unsuitable for real-time detection (Solanelles et al., 2006). Machine vision technology can detect the shape of fruit trees and determine the spraying range through image processing techniques. However, monocular vision technology faces challenges in fully eliminating the background, resulting in poor stability. On the other hand, stereo vision technology requires processing a large amount of data, which affects the response speed (Ge et al., 2005; Wang et al., 2019). The Microsoft device Kinect is equipped with both an infrared camera and an RGB camera, enabling it to capture real-time color and depth information within a scene. This combination of machine vision and infrared technology allows the device to leverage the advantages of both.

In the variable-rate spraying execution system, control is achieved through the use of application rate models and nozzle flow models. Researchers have proposed using the decision coefficient to characterize the combined effect of leaf density and leaf wall area on variable-rate spraying, and developing a multi-nozzle flow rate function, which achieves a maximum pesticide savings rate of 68.34% during operations (Xue et al., 2020a). Pulse width modulation (PWM) technology is commonly used to control the spray flow rate when implementing variable spraying (Zhu et al., 2010). When the PWM signal frequency is fixed, there is a good linear relationship between the nozzle flow rate and the PWM signal duty cycle (Fan et al., 2021). At lower PWM signal frequencies (1 ~ 5 Hz), the spray flow rate is less affected by the PWM signal frequency and more influenced by the spray pressure. It also exhibits an approximate proportional relationship with the duty cycle of the PWM signal (Wei et al., 2013). At higher PWM signal frequencies (10 ~ 40 Hz), the impact of different frequencies on the flow rate is also minimal. Although higher frequencies can effectively increase the flow rate adjustment range, they reduce the size of the linear range between flow rate and duty cycle (Li et al., 2016). Under both unregulated and constant pressure spraying conditions, fitting the relationship between the control signal duty cycle and nozzle spray flow rate results in regression equations with determination coefficients greater than 98% (Silva et al., 2018). This indicates that the spray flow models obtained under both spraying conditions have high accuracy and can be used for flow control in the variable-rate spraying execution process.

To systematically investigate the detection methods for canopy volume and spray characteristics of the spraying unit, this study focused on researching target information acquisition and

extraction methods using the Kinect sensor based on target detection technology and variable-rate spraying theory, providing theoretical and technical support for real-time detection of canopy parameters. By conducting experimental research and analyzing the application rate decision model for corresponding canopy parameters and the flow model of the corresponding spraying unit, the deposition effects were compared between the constant-rate spraying mode and the CV-based variable-rate spraying mode, to provide theoretical basis and technical support for precise variable-rate pesticide application.

2 Materials and methods

2.1 Variable-rate spray system

The main components of the variable-rate spray system in this research are shown in Figure 1A. The system can be divided into target detection unit and variable-spray unit. The target detection unit used a Kinect V2 sensor to collect color information and depth information of the fruit tree canopy in real time and saved it on the laptop. One personal computer was used as an upper computer, responsible for processing the fruit tree information data in real time, determining the spraying scheme based on the application rate decision model, and generating variable spray control instructions, which were then fed back to the spray control module; in the spraying control system, a STM32F103 microcontroller (Minimum system board, STMicroelectronics N.V., Geneva, Switzerland) served as a lower computer and was used to receive and process control command information sent by the upper computer in real time. The spraying equipment was equipped with a standard full cone nozzle JJXP-010-PVDF (H.Ikeuchi&Co, Ltd., Nishi-ku, Japan) and an solenoid valve with a working pressure up to 1 MPa (Delixi Group Co., Ltd., Zhejiang, China). The spraying equipment was mounted at a height of 1.2 meters above the ground, and there were four sets of spray units, each spaced 55 cm apart, as illustrated in Figure 2. The chemical liquid was supplied by the diaphragm pump, then it was transported through the pipeline to each solenoid valve, and finally reached each nozzle by the solenoid valve. The overall control process of the variable spray system is to collect the color and depth images of the fruit tree canopy in real time by the Kinect V2 sensor, then transfer the image information to the PC for processing and calculating the leaf wall area and canopy volume, and use the pesticide dosage decision model to calculate the pesticide dosage for the corresponding area, then convert the

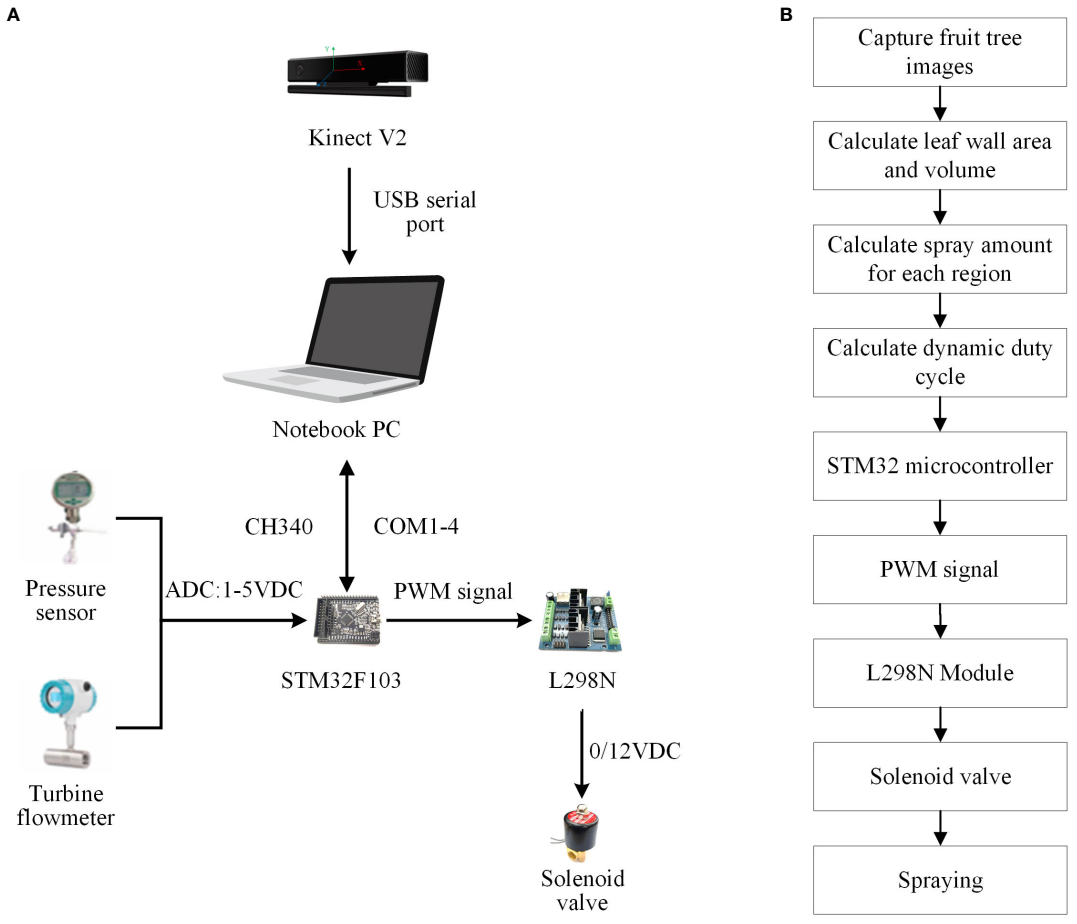

FIGURE 1
The variable-rate spray system. **(A)** Basic components. **(B)** Control flowchart.

FIGURE 2
The overall structure of the variable-rate spray system. 1. Kinect sensor, 2. Tractor, 3. Spray unit, 4. Personal computer, 5. Liquid turbine flowmeter, 6. Diaphragam pump, 7. Sprayer tank, 8. DC12V battery, 9. Digital pressure gauge.

pesticide dosage into the dynamic duty cycle information for the corresponding area spraying, and finally transfer it to the STM32 microcontroller through serial communication, and output the corresponding PWM duty cycle control command to the four-way drive module L298N, which controls the opening and closing of the corresponding solenoid valve, and then sprays the pesticide through the nozzle. The control flow chart of the variable spray system is shown in Figure 1B.

2.2 Canopy volume calculation model

In the citrus orchard where field experiments were conducted, the tree row spacing was 4.5 meters, and the tree spacing was 2.5 meters. Based on the imaging principles of the camera and the actual conditions of the citrus orchard, the distance of the Kinect sensor from the center axis of the sprayer, e, was determined to be 0.35 meters, and the installation height from the ground was 1.5 meters (the central position in the direction of the canopy height). For citrus orchards with different planting row spacing and canopy growth conditions, it is available to input the row spacing and adjust the camera installation position so that the sensor's imaging field of view can adapt to the actual canopy height of the citrus orchard while retaining detection accuracy to the maximum extent. This article only takes the actual situation of the experimental citrus orchard as an example to explain the canopy volume calculation method. The measurement principle of canopy volume is as follows: the sensor uses the canopy's RGB data and depth data detected within the current field of view as the raw data for calculation. Within the range of the depth matrix currently output by the sensor, the actual height and width of the detection area in the field of view can be calculated in accordance with imaging principles (Yan et al., 2021), as shown in Equation 1.

$$\frac{f}{R/2-e}=\frac{H_p}{H_t}=\frac{W_p}{W_t} \tag{1}$$

Where: f is the focal length of the sensor, and in this paper, $f = 3.3mm$; H_p is the pixel height of the detection area in mm; H_t is the actual height of the detection area in mm; W_p is the pixel width of the detection area in mm; W_t is the actual width of the detection area in mm.

Considering the spray unit's spray width and sensor detection accuracy, the 171×424 (width × height) pixel area within the sensor's central field of view was selected as the spray target area, and the depth values of the 171×424 (width × height) pixel area in the central field of view were selected as the region for target canopy volume. Considering the number of spray units in the actual research, the continuous citrus fruit tree canopy within the sensor's field of view was discretized into four rectangular volumes: upper, upper-middle, lower-middle and lower. As shown in Figure 3, the canopy volume calculation of each unit spray target area was as described in Equations 2-4.

$$C_V = S_{LWA} \cdot C_W \tag{2}$$

$$S_{LWA}=\frac{H_t \cdot W_t \cdot N_{LWA}}{N_{all}} \tag{3}$$

$$C_W=\frac{R}{2}-e-d \tag{4}$$

Where: C_V is the volume of unit spray target canopy in m^3; S_{LWA} is the leaf wall area of unit spray target area in m^2; C_W is the average canopy thickness of unit spray target area in m; N_{LWA} is the number of pixels in unit spray target canopy; N_{all} is the number of pixels in unit spray target area; d is the depth of unit spray target canopy detected by the sensor in m.

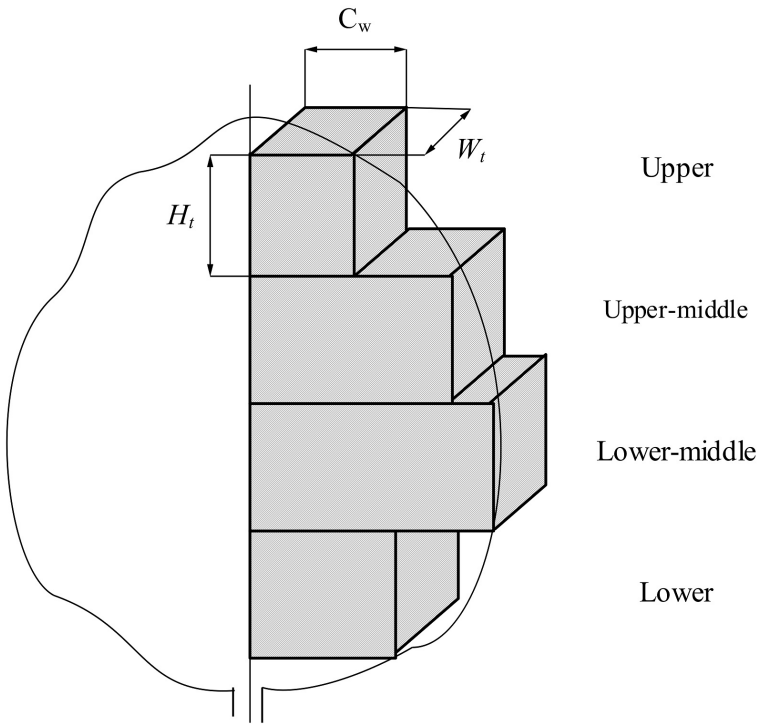

FIGURE 3
Discretized canopy volume segmentation model.

Because the outdoor lighting environment can significantly impact the sensor's detection accuracy, and based on actual tests, variations in canopy depth detection errors were observed with the binocular camera at different depth detection ranges. By considering the actual depth of the citrus fruit tree canopy and the sensor's installation position, the canopy detection depth in this study falls within the range of 700 mm to 1900 mm.

To verify the accuracy of the Kinect sensor detection system, five citrus trees at different growth stages were selected for the exploratory test. The test was conducted at a travel speed of 1 m·s^{-1}, and each experiment was repeated three times. Additionally, to compare the results obtained from the Kinect sensor detection, the LWA and canopy volume of each citrus tree were manually measured. Referring to the methods employed by other scholars (Rosell Polo et al., 2009; Yan et al., 2021) for manually measuring the area and volume of canopy leaf wall, the canopy was divided from bottom to top into measurement units with a height of 25.5 cm and a width of 17.0 cm in both vertical and horizontal directions. If the height or width at the edges was insufficient, the actual height and width were measured. Then, the LWA of each fruit tree was calculated by summing the area of each unit. When manually measuring the volume, the thickness of each canopy measurement unit was measured three times, and the average value was multiplied by the corresponding unit area to calculate the canopy volume of each measurement unit. Finally, the sum of all unit volumes yielded the canopy volume of the fruit tree. The actual manual measurements are shown in Figure 4.

2.3 Construction of application rate model

Implementing variable-rate spraying operations with a Kinect sensor primarily involved two components: a decision-making process and an execution process. The application rate model played a role in the decision-making process of variable-rate spraying. It utilized the LWA and canopy volume detected by the Kinect to determine the pesticide application volume in corresponding area. Meanwhile, the nozzle flow model operated during the execution process of variable-rate spraying. With the nozzle flow model, the pesticide application volume was converted into dynamic duty cycle information for the corresponding application area. This information was then transmitted to the STM32 microcontroller through serial communication, and subsequently, relevant PWM duty cycle control instructions were generated to manage the opening and closing of the solenoid valve. This enabled the execution of pesticide application work in the designated area through the nozzle.

The application rate model, designed to make better real-time decisions on the amount of pesticides to be sprayed in the spray area, is shown in Equation 5.

$$q_{flow} = \rho v(a + b \cdot K) \tag{5}$$

Where: q_{flow} is the real-time spray flow in L·min^{-1}; v is the travel speed in m·s^{-1}; K is the decision coefficient of the application rate model, $K \in [0, 1]$; a and b are constant coefficients of the model, which can be calibrated by the flow model of the nozzle; ρ is the

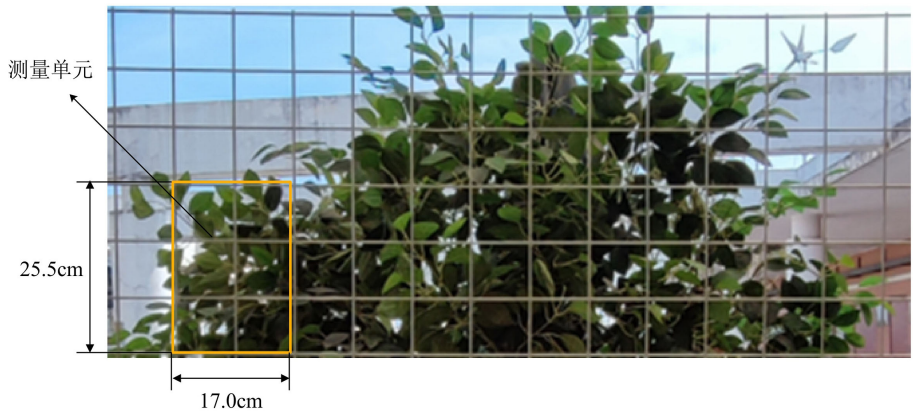

FIGURE 4
Manual measurement schematic of canopy volume.

coefficient for the spray volume adjustment, taking into account the actual pest control needs in citrus orchards and referencing other scholars' research (Li et al., 2017; Jiang et al., 2019b), ρ=1 was determined.

Fruit trees vary in canopy volumes, which in turn affect the required pesticide quantities for their control. The larger canopy volume of the fruit tree, the corresponding application of pesticide should also increase. The canopy volume of fruit trees is a three-dimensional characteristic that combines canopy area and thickness. To better represent its three-dimensional nature, the decision coefficient for the pesticide application rate model based on parameter canopy volume is denoted as K_{CV}, and its calculation model is presented in Equation 6.

$$K_{CV} = 0.5 \times \frac{N_{LWA}}{N_{allI}} + 0.5 \times \frac{C_w}{C_{max}} \quad (6)$$

Where: C_{max} is the maximum thickness of unit spray target area in m.

The ratio of the average thickness of different volume elements to the maximum thickness of each pixel within that volume element reflects the relative size of the true thickness of the volume element. The decision coefficient K_{CV} of the CV-based application rate model incorporated information about the LWA and depth within the spray target area, with a 50% weight allocation. This approach better captures the genuine spatial characteristics of fruit tree canopies compared to relying solely on canopy volume for pesticide application (Chen, 2018). It is more flexible and efficient than the use of the original canopy volume values and serves as a guiding factor in rationalizing precise variable-rate pesticide application.

The nozzle flow model operated in the variable-rate spraying execution process and was used for the actual control of spray flow. After obtaining the dynamic spray amount through the application rate model, it was input into the nozzle flow model to derive the relationship between the decision coefficient K and the PWM duty cycle. To clarify the flow model of the pesticide application unit and establish the specific relationship between nozzle flow rate and PWM control signal duty cycle, spray flow tests were conducted at spray pressures of 0.3, 0.4, and 0.5 MPa, with measurements taken of the flow conditions at different spray pressures. Taking into account the impact of the PWM signal frequency on nozzle flow rate and the operational frequency of the 2W-025-08 solenoid valve, a control signal frequency of 10 Hz was chosen for flow rate testing. The flowmeter was used to measure the total flow values of four nozzles at different PWM duty cycles. From preliminary tests, it was discovered that when the control signal duty cycle fell below 30%, the solenoid valve coil struggled to maintain stable operation due to difficulties in charging for a short period and discharging for an extended period. In such cases, the nozzle's spray flow became excessively low, leading to irregular spray operation. Similarly, when the PWM duty cycle exceeded 90%, the electromagnetic force in the valve coil was unable to release quickly, making it challenging to maintain a short-closed and long-open state. In this situation, the nozzle flow was essentially unaffected by changes in the duty cycle. Hence, during the flow rate testing experiments, it was only necessary to measure the flow conditions of the nozzles with duty cycles between 30% and 90%, incrementing by 10%. Due to the high-frequency switching operation of the solenoid valve, there may be fluctuations in the instantaneous flow results from the flowmeter. Therefore, it was essential to measure the total pesticide application quantity over a specific time period and then divide it by the time to obtain the average flow rate during the actual spraying process. In the flow rate measurement experiments of this study, the total spray quantity of four nozzles within a 10-second period was measured using the flowmeter. Each measurement was repeated five times, and the average value was taken as the final measurement result.

2.4 Analysis of system response time

Real-time and accurate calculation of dynamic delay time is the guarantee for achieving accurate variable spray. Since there is a horizontal distance between the Kinect sensor and the spray unit, it is necessary to compensate for the delay in the spray command, which ensures that the spray command aligns with the actual spray

target area. The time required for delay compensation can be calculated by Equation 7.

$$t_{com} = \frac{L}{v} - t_{sys} \quad (7)$$

Where: t_{com} is the time required for delay compensation in the spray system in s; L is the horizontal distance between the Kinect sensor and the spray unit in m; v is the travel speed of the spraying system in m·s^{-1}; t_{sys} is the total response time of the entire variable-rate spray system in s.

According to Equation 7, when $\frac{L}{v} > t_{sys}$, the system can achieve correspondence between the spray command and the spray area through delay compensation in the software. When $\frac{L}{v} < t_{sys}$, the correspondence of the target area can only be achieved by adjusting the installation distance between the sensor and the spray unit.

The response time of the variable spray system is mainly composed of four parts, including:

(1) Front-end time t_1: it takes t_1 for Kinect sensors to collect tree canopy information from start to finish;

(2) Data processing time t_2: the time taken after the Kinect sensor has collected data, for the calculation model to compute specific canopy parameters and then the pesticide application decisions to obtain PWM duty cycle information. By setting "start = clock()" in the software program as the time when the canopy information calculation begins, and setting "end = clock()" as the end time when the canopy information is fully converted into duty cycle information, the difference between the two can be calculated as the data processing time t_2.

(3) Communication time between the upper computer and the lower computer, t_3, can be calculated using Equation 8.

$$t_3 = \frac{8 \times n}{B} \quad (8)$$

Where: n is the number of bytes in serial communication; B is the baud rate in serial communication and, and B is set to 115200; the calculated communication time between the PC and STM32 microcontroller is represented by t_3.

(4) Spray response time t_4: duration starts from when the lower computer receives the duty cycle information until the solenoid valve responds to the nozzle and initiates the spraying process.

The spray response time can be calculated by capturing the spray response process using a high-speed camera. In the control program, the LED light was adjusted to reflect the status of serial communication and communication completion. During the high-speed camera capture, set the exposure time to 0.916363 ms and the frame rate to 1056.250 fps. Recorded the timing of the nozzle spray before and after communication with the lower computer, as depicted in Figure 5. Then calculated the spray response time t_4.

After calculation, the total system response time t_{sys} was 203 ms, less than 300 ms. When the travel speed of the spraying system was 1 m·s^{-1}, a horizontal distance greater than 500 mm between the spray unit and the Kinect sensor ensured that the system can achieve the matching between the characteristics of the corresponding spray target area and the spray instructions through delay compensation.

2.5 System performance verification tests

Due to the hardware response and control capabilities of the variable-rate spray system, which may result in variations between the actual flow rate of the nozzle and the theoretical flow rate, a consistency test between the actual spray flow rate and the target flow rate was conducted under static conditions before proceeding with the spray deposition test, referring to the test methods used by other scholars (Sun et al., 2022). During the test, clean water was used as the medium instead of pesticides, the differences between the nozzles were ignored, and a single nozzle was selected for the flow test. First of the test, the simulated LWA ratio and thickness ratio of the corresponding partition were uniformly set to 0.1, 0.2, 0.3, 0.4, 0.5, 0.6, 0.7, 0.8, 0.9, and 1.0 in the PC upper computer program. The corresponding decision coefficient K values were 0.1, 0.2, 0.3, 0.4, 0.5, 0.6, 0.7, 0.8, 0.9, and 1.0. These values were then sent to the STM32 lower computer for the variable spraying test. In

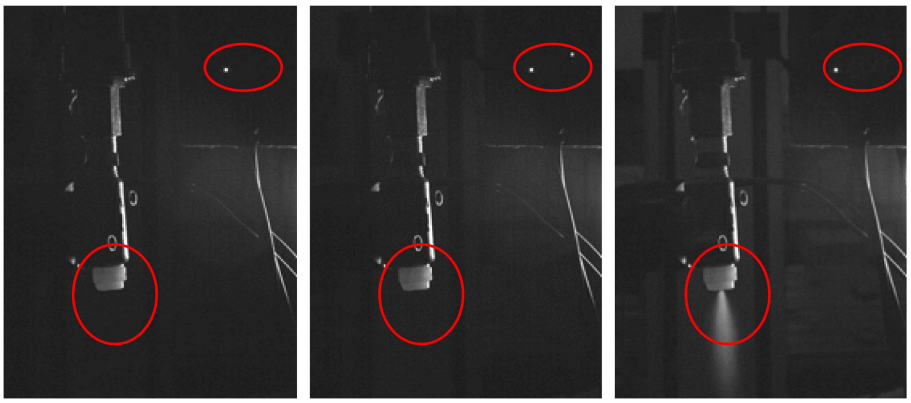

FIGURE 5
Spraying process captured by high-speed camera.

each test, the total spray volume of the nozzle within a 10-second timeframe was measured. The measurement was repeated 5 times, and the average value was calculated. Subsequently, the actual flow rate of the nozzle was determined through conversion based on these measurements.

2.6 Field test

Deposition effect is the main indicator to evaluate the performance of a spray system. In order to validate the spray effectiveness of the Kinect sensor-based variable-rate spray system, experiments on constant spray and CV-based variable spray were conducted both indoors and in the field using full cone nozzles and fan-shaped nozzles to analyze the deposition effects.

The main evaluation parameters of deposition effect include droplet deposition density, droplet deposition amount and droplet coverage, calculated by Equations 9–11 respectively. Droplet deposition density refers to the number of droplets per unit area in the target area, measured in droplets·cm^{-2}. In plant protection spraying, it has been observed that higher deposition density results in higher efficiency of pesticide, which contributes to effectively reducing pesticide waste (Ahmad et al., 2021). Droplet deposition amount refers to the volume or mass of the chemical liquid per unit area in the target area, typically measured in μL·cm^{-2} or μg·cm^{-2}. It directly reflects the quantity of active ingredients of the chemical solution acting on the target and can be used to calculate the pesticide utilization rate. Droplet coverage refers to the ratio between the area covered by droplets on the target surface and the total area of the target. It can be used to measure the coverage of droplets during the spraying process. The larger the coverage rate, the greater the area of droplets attached to the target surface. At the same time, a smaller coefficient of variation for the droplet coverage indicates better penetration of the droplets (Chen et al., 2020).

$$\varepsilon = \frac{A_1}{A_2} \times 100\,\% \tag{9}$$

$$\lambda = \frac{n}{A_2} \tag{10}$$

Where: ε represents the droplet coverage in %; A_1 represents the area covered by droplets in the water-sensitive paper region in cm^2; A_2 represents the total area of the water-sensitive paper region in cm^2; λ represents the droplet deposition density in droplets/cm^2; n represents the total number of droplets in the water-sensitive paper region.

$$\gamma = \frac{Ce_1 \cdot V}{Ce_2 \cdot S} \tag{11}$$

Where: γ represents the deposition volume of droplets per unit area in μL/cm^2; Ce_1 represents the concentration of methyl orange in the elution solution in mg/L; V represents the volume of distilled water added before elution in μL; Ce_2 represents the concentration of the methyl orange solution used during spraying in μL/cm^2; S represents the area of the filter paper in cm^2.

When the droplet coverage exceeds 17%, the overlapping of droplets will cause significant errors in the measurement of droplet size (Wang et al., 2021), thereby affecting the calculation of droplet deposition amount. Hence, this study employed water-sensitive paper and filter paper to measure the droplet deposition density, droplet coverage, and droplet deposition amount, respectively. Water-sensitive papers with dimensions of 110 mm (length) × 35 mm (width), produced by Chongqing Liu Liu Shan Xia Plant Protection Technology Co., Ltd., were chosen for measuring the droplet deposition density and droplet coverage. Circular filter papers with a pore size of 0.22 μm and a diameter of 50 mm, produced by Shanghai Bandaoshiye Co., Ltd., were selected for collecting droplet deposition amount.

To evaluate the effectiveness of the variable-rate spraying system based on CV and the pesticide saving rate, a spray test was conducted on citrus fruit trees. In the conducted test, methyl orange and distilled water were combined in order to create a solution with a concentration of 0.5 g·L^{-1} of methyl orange, which served as the medium to be used instead of pesticide. The field test was conducted in a citrus orchard at Daju Fruit Industry in Pingtan Town, Huiyang District, Huizhou City, Guangdong Province. The spacing between rows of fruit trees was 4.5 meters, and the spacing between individual trees was 2.5 meters. During the test, the ambient temperature ranged from 21 to 26 °C, the ambient humidity ranged from 46% to 55%, and the ambient wind speed was at level 0 (also known as calm wind, with a speed below 0.2 m·s^{-1}). Due to the symmetry of the sensor detection angle, the spray deposition experiment was conducted on a single side of the citrus tree canopy. According to the national industry standard JB/T 9782—2014, the sampling points in the canopy of the fruit tree were arranged as shown in Figure 6A. The target tree was divided into four layers vertically: upper, upper- middle, lower- middle, and lower, each of which had three sampling points, numbered from 1 to 12 from left to right and top to bottom. At each sampling point, one water-sensitive paper and one filter paper were placed, as illustrated in Figure 6B. To minimize the randomness of the experimental results, each group of the test was repeated three times.

Based on previous tests, the spray test was performed at a spray pressure of 0.4 MPa and a travel speed of 1 m·s^{-1}, during which a distance of 30 m was covered each time. The total flow rate values from the flowmeter were recorded before and after the test to calculate the amount of pesticide application. After the test, once the water-sensitive papers had dried, they were sequentially removed along with the filter papers using disposable gloves. The water-sensitive papers and filter papers were then stored separately in sealed bags to prevent moisture damage. Upon returning to the laboratory, the collected water-sensitive papers were scanned at a resolution of 600 dpi using a scanner and saved for further analysis.

Following the completion of the test, samples of water-sensitive paper and filter paper were obtained, as shown in Figure 7. To process the water-sensitive papers, the scanned images were imported into the image processing software Deposit Scan. After configuring the scale, the color images of the water-sensitive paper were converted to 8-bit grayscale. Then, suitable regions and thresholds were selected to process the images, and the parameters of droplet coverage and droplet deposition density were calculated separately using Equations 9 and 10:

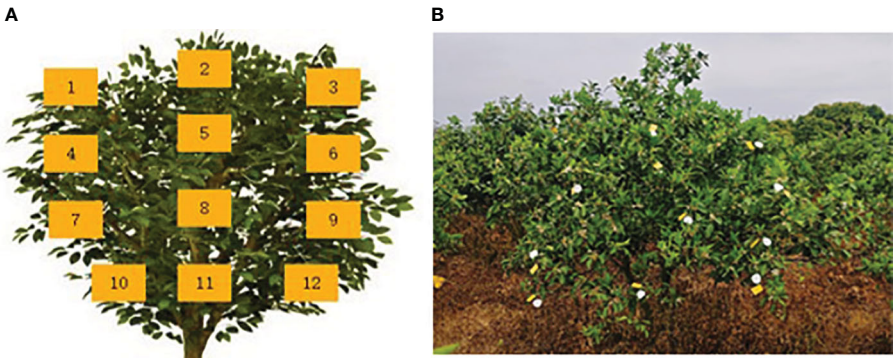

FIGURE 6
Arrangement of sampling points for deposition test. **(A)** Distribution of sampling points in the fruit tree canopy. **(B)** Distribution of water-sensitive paper and filter paper.

To determine the droplet deposition on the filter paper, a UV/Visible spectrophotometer (UV-752, Shanghai Tianpu Analytical Instrument Co., Ltd) was first used to calibrate the concentration-absorbance of the methyl orange solution. Through preliminary calibration tests, a linear regression equation (R^2=0.998) was obtained by fitting the concentration-absorbance calibration results, shown as Equation 12.

$$\boldsymbol{Abs = 0.03461Ce - 0.0005} \quad (12)$$

Where: *Abs* is the absorbance value of the measured solution; *Ce* is the concentration of the measured methyl orange solution in $mg{\cdot}L^{-1}$.

Subsequently, 10 mL of distilled water was added to each filter paper stored in sealed bags. They were then subjected to shaking on an oscillator and elution for 30 minutes. Afterward, 3 mL of eluate was separately measured for absorbance using a spectrophotometer at a wavelength of 465 nm. Finally, the deposition volume of droplets per unit area, which was the droplet deposition amount, was calculated based on Equation 11 (Xue et al., 2022b).

FIGURE 7
The water-sensitive paper and filter paper after the spray test.

To investigate the uniformity and penetration of droplet deposition in the deposition test, it is common to calculate the coefficient of variation for each parameter. In the deposition test, a smaller coefficient of variation for the distribution of droplet deposition indicates a more uniform deposition, indicating better droplet penetration. The specific calculation of the coefficient of variation is shown in Equations 13-15.

$$CV = \frac{S}{\overline{X}} \times 100\,\% \tag{13}$$

Where:

$$\overline{X} = \frac{\sum_{i=1}^{n} X_i}{n} \tag{14}$$

$$S = \sqrt{\frac{\sum_{i=1}^{n} (X_i - \overline{X})^2}{n-1}} \tag{15}$$

Where: CV is the coefficient of variation for the sample; S is the standard deviation of the sample; $\overline{X}$ is the mean of the sample; X_i is the observed values of the sample; n is the number of samples in the dataset.

3 Results and discussion

3.1 Results and analysis of canopy volume measurement

The detection results and relative errors of canopy volume for citrus trees at different growth stages are shown in Figure 8, with a travel speed of 1 m·s^{-1}. The measurements based on the Kinect sensor exhibit ted small deviations, indicating that the detection system had low variability in measuring canopy volume and produced stable results. The calculation model for canopy volume demonstrated its universality. Comparing the sensor measurements to manual measurements, the relative errors were relatively small, ranging from a minimum of 5.98% to a maximum of 10.54%. The Kinect-based citrus tree information detection system and canopy volume calculation model met the accuracy requirements for measuring canopy volume.

3.2 The results and analysis of the construction of application rate model

According to the test design, the average values of multiple sets of test data were calculated, then divided by the spraying time and the number of nozzles to obtain the relationship between the PWM duty cycle and the nozzle flow rate for full cone nozzles and fan-shaped nozzles at spraying pressures of 0.3, 0.4, and 0.5 MPa. During the test, when the PWM control signal duty cycle was less than or equal to 30%, the nozzle spraying was unstable, and the flow rate was too low. But when the duty cycle exceeded 90%, the nozzle flow rate was not significantly affected by the duty cycle. The flow rate data was imported into Origin 2018 software for linear regression analysis. The fitting results of the PWM signal duty cycle and nozzle flow rate at different spraying pressures are shown in Figure 9. For spraying pressures of 0.4 and 0.5 MPa, the relationship between the flow rate of the full cone nozzle and the

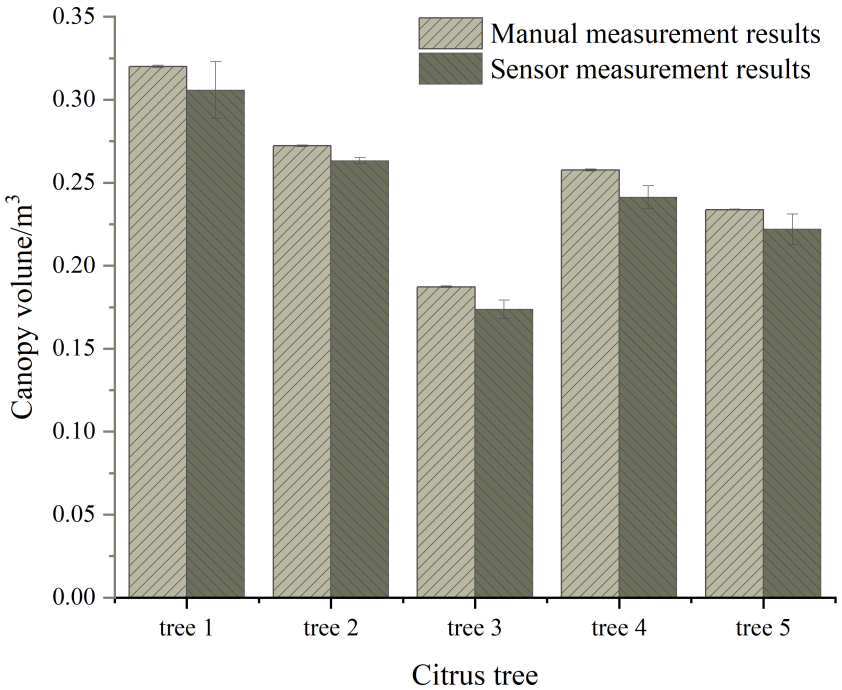

FIGURE 8
The detection results and relative errors of canopy volume.

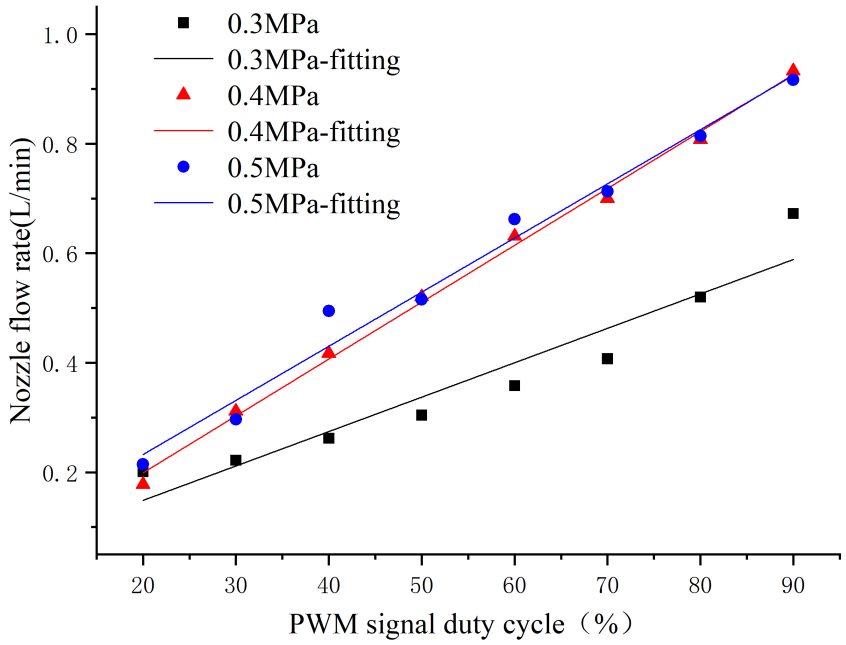

FIGURE 9
The fitting results of the full cone nozzle flow rate and the PWM signal duty cycle at different spraying pressures.

control signal duty cycle was relatively close. However, when the spraying pressure was set to 0.3 MPa, the overall flow rate was smaller due to insufficient pressure.

The fitting results of the spray flow model at three different spraying pressures all had R^2 values greater than 0.9. Specifically, the R^2 value obtained from the fitting at 0.4 MPa was 0.997, indicating that the PWM signal duty cycle can explain 99.7% of the variation in nozzle flow rate. Therefore, the spray flow model obtained at this spraying pressure was considered highly reliable. The nozzle flow model for the full cone nozzle at a spraying pressure of 0.4 MPa is shown in Equation 16, where 0.01039 corresponds to the slope of the fitted line at a spray pressure of 0.4 MPa with units of L/(min×%), and 0.00880 corresponds to the intercept of the fitted line with units of L/min.

$$q_{con} = 0.01039\alpha - 0.00880 \tag{16}$$

Where: q_{cone} is the flow rate of the full cone nozzle in L·min^{-1}; α is the PWM control signal duty cycle in %.

Considering the practical situation of nozzle spraying, when the α calculated from the flow model was less than or equal to 30, the response of the solenoid valve became unstable. In this case, the duty cycle of PWM signal α_Duty controlling the solenoid valve was set to 30. If the α calculated was greater than or equal to 90, it indicated that the nozzle flow rate was less affected by the PWM signal duty cycle. Therefore, a duty cycle of 90 was chosen in this scenario. For other situations, a duty cycle of α was used. Hence, the specific expression of α_Duty for the full cone nozzle flow control was given by Equation 17, and the expression of α_Duty for the fan-shaped nozzle flow rate control was given by Equation 18.

$$\begin{cases} \alpha\_Duty = 30, & \alpha \le 30 \\ \alpha\_Duty = \frac{q_{flow}+0.0080}{0.01039}, & 30 \le \alpha \le 90 \\ \alpha\_Duty = 90, & \alpha \ge 90 \end{cases} \tag{17}$$

$$\begin{cases} \alpha\_Duty = 30, & \alpha \le 30 \\ \alpha\_Duty = \frac{q_{flow}-0.12131}{0.00906}, & 30 \le \alpha \le 90 \\ \alpha\_Duty = 90, & \alpha \ge 90 \end{cases} \tag{18}$$

By substituting the effective duty cycle range of 30 to 90 into the corresponding flow rate models for the nozzles at 0.4 MPa, the maximum and minimum flow rates for each nozzle at this spraying pressure can be obtained. The results indicated that the flow rate range of the full cone nozzle was slightly greater than that of the fan nozzle, as shown in Table 1.

To calibrate the coefficients a and b in Equation 19 while ensuring that the PWM control signal duty cycle ranged from 30% to 90%, the minimum flow rate was taken as the flow rate value

TABLE 1 The extreme values of the flow rates for the full cone nozzle and the fan-shaped nozzle at 0.4 MPa.

Nozzle	Full cone nozzle	Fan-shaped nozzle
Minimum flow rate/ L·min^{-1}	0.3029	0.3931
Maximum flow rate/ L·min^{-1}	0.9263	0.9367

when the PWM signal duty cycle was 30%. The corresponding decision coefficient K was set to a non-zero extremely small value. Similarly, the maximum flow rate was taken when the PWM signal duty cycle was 90%, and K was set to 1. In this case, application rate model for the full cone nozzle is shown in Equation 19.

$$q_{flow\_cone} = \rho v(0.3029 + 0.6234 \cdot K_{CV}) \times 60 \quad (19)$$

3.3 Results and analysis of performance validation test

During the flow rate validation test, the calculated flow rate of the nozzle, obtained by dividing by the spraying time, is shown in Figure 10. From the graph, it can be observed that in most cases, the actual flow rate of the nozzle was slightly higher than the theoretical flow rate. However, compared to the theoretical flow rate, the fluctuation range was small. Although it may result in excessive spraying in some canopy areas, it effectively prevented the occurrence of under-spraying or missed spraying in sparse canopy regions.

Furthermore, the graph demonstrates a close proximity between the actual and theoretical flow rates of the nozzle during the spray test. The R^2 for the decision coefficient of the linear fit exceeded 0.99, indicating strong stability of the control program in the variable-rate spray system, as well as the responsiveness and capability of the hardware equipment to execute the spraying accurately. Moreover, it demonstrates good consistency between the theoretical and actual flow rates for different canopy layers of fruit trees during variable spraying.

3.4 Results and analysis field test

In the field test, the average parameter values of droplet deposition under different spraying modes obtained through water-sensitive paper and filter paper treatments are shown in Table 2. According to the agricultural standard NYT 650-2013, a spray operation requires a droplet coverage greater than 33% and a droplet deposition density greater than 25 droplets cm^{-2}. Table 1 indicates that the variable-rate spraying based on CV slightly reduced the droplet deposition amount and droplet coverage compared to the constant-rate spraying. However, overall, it still met the quality requirements of spray operations and the droplet deposition density showed an increase. The potential reason for this could be that the constant-rate spraying mode utilized a higher application of the pesticide, causing the atomized droplets to recondense on the foliage of the fruit trees. As a result, the number of droplets decreased. On the other hand, the variable-rate spraying based on CV controlled the spray flow rate. The frequent opening and closing of the solenoid valve created a water hammer effect, resulting in smaller droplet sizes being sprayed. Consequently, more small droplets settles in the canopy of the fruit trees, leading to a higher deposition density.

3.4.1 Analysis of droplet deposition distribution

The deposition effect of droplets in field test is shown in Figure 11, where the deposition density under the variable-rate spraying was significantly higher than that under the constant-rate spraying. This is because during the variable-rate spraying process, the solenoid valve switched its working state frequently, leading to an increase in local pressure at the nozzle of the spray head. As a

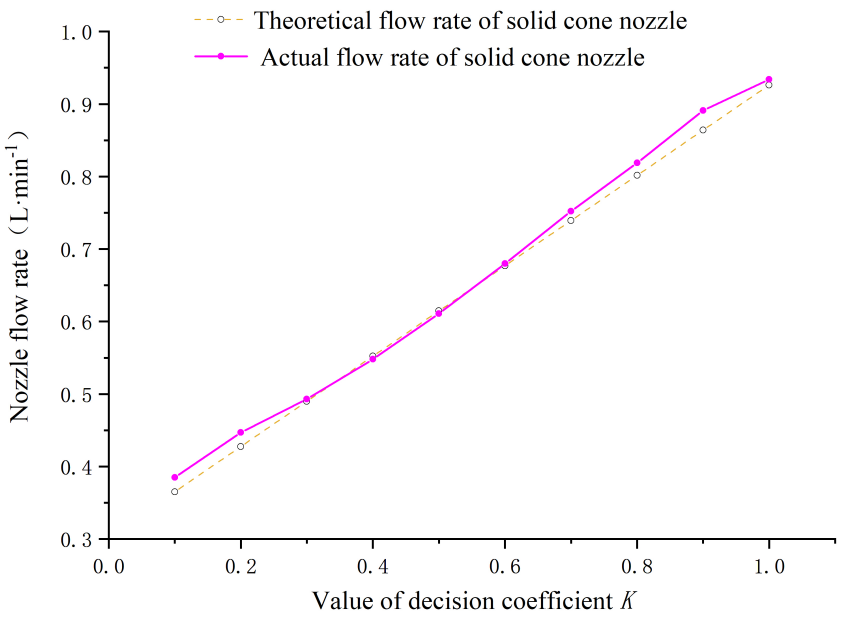

FIGURE 10
Test results of flow rate consistency for full cone nozzles and fan nozzles.

TABLE 2 Deposition parameters under different spraying modes.

Spraying mode	Full cone nozzle		
	Deposition density/ droplets·cm-2	Deposition amount/ μL·cm^{-2}	Coverage/ %
Constant-rate	42	1.33	43.03
CV-based variate-rate	57	1.12	34.16

result, smaller droplets were produced, resulting in a higher deposition density under this mode. Specifically, when conducting CV-based variable-rate spraying, the maximum of droplet deposition density was 79 droplets·cm^{-2}, which was a 23.44% increase compared to the constant-rate mode.

The deposition results of droplets under different spraying modes are shown in Figure 12. From the figure, it can be observed that both spraying modes exhibited relatively high levels of droplet deposition. Under the variable-rate mode, the droplet deposition density was higher, but the overall deposition quantity appeared to be slightly lower. This is due to the fact that the droplets produced under the variable-rate mode had smaller diameters, resulting in a smaller volume despite the same number of droplets being present.

3.4.2 Analysis of droplet coverage

The droplet coverage results under different spraying modes in the field test are shown in Figure 13. The results indicate that in most areas, the droplet coverage under both spraying modes met the quality requirements of the spraying operation. Additionally, the constant-rate spraying exhibited higher droplet coverage compared to the CV-based variable-rate spraying. The droplet coverage under CV-based variable spray was lower, with a decrease of 18.25 percentage points compared to the constant-rate mode.

The smaller the variation coefficient, the stronger the penetrability of the droplets. In this study, the variation coefficient for the constant spray mode was 22.45, while the variation coefficient for the CV-based variable-rate mode was 17.89. From the results, it can be observed that the variation coefficient for droplets under the variable-rate mode was significantly smaller than that of the constant-rate mode. The variation coefficient for the CV-based variable-rate mode was reduced by 20.31 percent compared to the constant-rate mode. Under the variable-rate mode, due to the water hammer effect, droplets exhibited better uniformity and stronger penetrability during the variable-rate spraying process.

3.4.3 Analysis of spray efficiency

In the field deposition test, the application amount for constant-rate spraying was 1.778 L, while the application amount for CV-based variable-rate mode was 0.762 L. Compared to constant-rate mode, the variable-rate mode required a lower application. The CV-based variable-rate mode, using the CV model, achieved a 57.14% reduction in pesticide use. This indicates that, while ensuring spray quality, the CV-based variable-rate mode exhibited a higher spray efficiency in terms of saving pesticide.

4 Conclusions

Based on Kinect sensor detection technology and variable spraying techniques, this study constructed a test platform to investigate the canopy volume calculation model for fruit tree canopies, application rate models, spray characteristics of nozzles, and nozzle flow models. The main results and conclusions are as follows:

(1) The study investigated a canopy volume detection model for fruit trees based on the Kinect sensor. By comparing the manually measured canopy parameter values with the results obtained from sensor detection, the canopy volume detection results showed low dispersion and small relative errors. The relative error ranged from 5.98% to 10.54%, verifying the accuracy of the calculation model in the detection system.

(2) The study involved studying and analyzing the use of the decision coefficient K to characterize the canopy

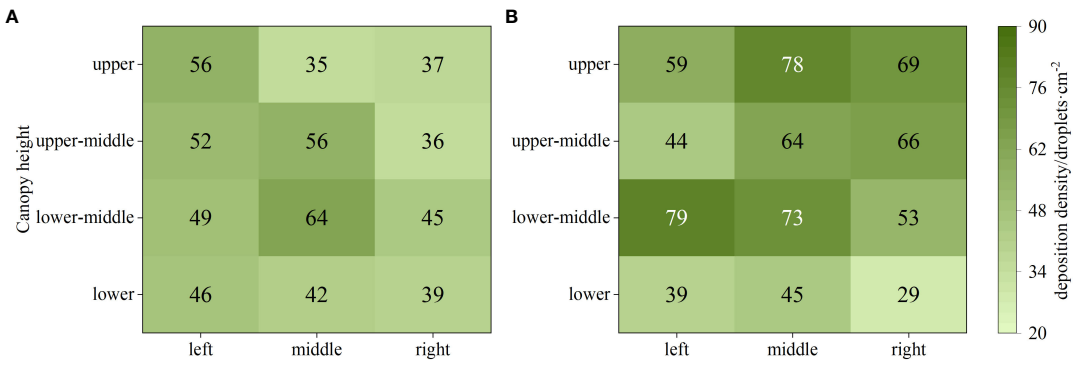

FIGURE 11
Droplet deposition density under different spraying modes. **(A)** Constant-rate spraying. **(B)** CV-based variable-rate spraying.

10.3389/fpls.2023.1297879

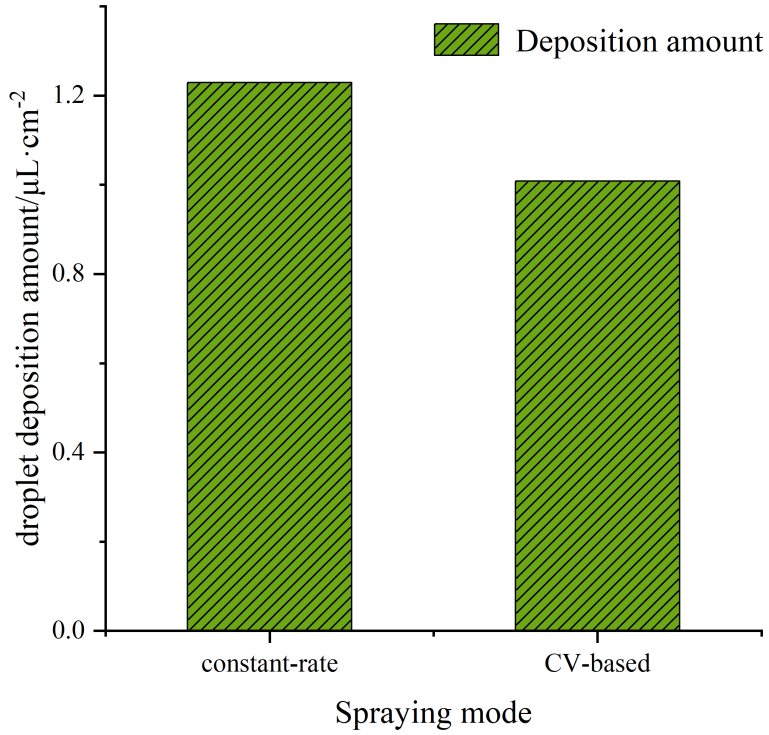

FIGURE 12
Droplet deposition amount under different spraying mode.

characteristics of fruit trees. A corresponding decision-making model for pesticide application rates was established, and the spray characteristics of nozzles and flow models were investigated. Test results demonstrated that under a spray pressure of 0.4 MPa, there was a good linear correlation between nozzle flow rate and PWM control signal duty cycle, with R^2 greater than 0.95. Based on the fitted nozzle flow model, the flow rate regulation ranges for each nozzle were determined. The constant coefficients in the pesticide application rate model were calibrated, and an expression relating PWM duty cycle to the decision coefficient K was obtained. This expression was used to guide the decision-making and execution stages of variable-rate spraying.

(3) The spray effectiveness of the variable-rate spray system based on the Kinect sensor was tested. The measured theoretical spray volume and actual spray volume showed a high degree of fit, with a decision coefficient R^2 greater than 0.99, indicating good consistency of the variable-rate spray system. Field test was conducted comparing constant-rate spraying and CV-based variable-rate spraying in terms of droplet deposition density, droplet deposition amount, and droplet coverage. The test results demonstrated that the variable-rate spraying based on Kinect achieved higher droplet deposition density compared to constant-rate spraying. The maximum increase in droplet deposition density reached 28.13%. However, due to the reduction of pesticide dosage, the droplets reaching the target area

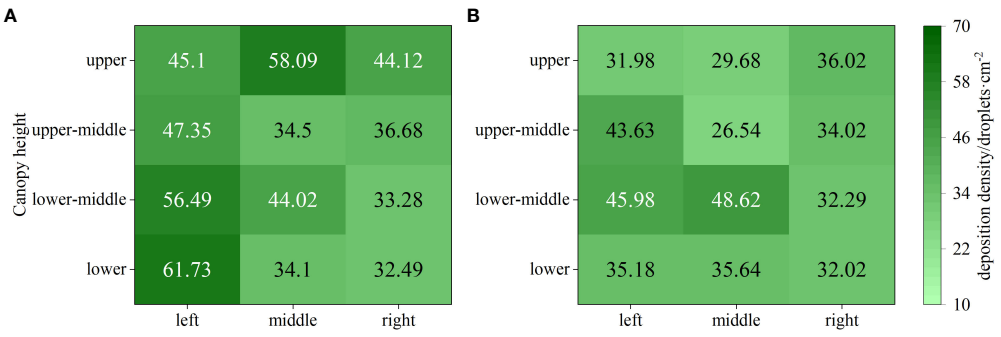

FIGURE 13
Droplet coverage under different spraying modes. **(A)** Constant-rate spraying. **(B)** CV-based variable-rate spraying.

decreased, and the water hammer effect produced droplets with smaller inertia and more prone to drift, which eventually resulted in the decrease of droplet deposition and coverage, but they all met the quality requirements of spraying operation. Compared to the dosage under constant spraying methods, the drug-saving rate of variable spraying based on CV reached up to 57.14%. In conclusion, the experimental results show that the variable spraying based on CV has a better deposition effect, which can adjust the spray flow rate according to the characteristics of the fruit trees, thereby saving pesticide, improving the efficiency and quality of spraying, and reducing the pollution to the environment and human body. However, our experiment also has some limitations, such as we only consider the leaf wall area and canopy volume of the fruit trees, and do not consider other factors of the fruit trees, such as fruit, flower, etc., which may also affect the deposition and coverage of spraying. In the future, we will further optimize our application rate decision model, consider more factors of the fruit trees, as well as the uniformity and effectiveness of spraying, to find the more suitable parameters for variable spraying.

Data availability statement

The raw data supporting the conclusions of this article will be made available by the authors, without undue reservation.

Author contributions

XX: Funding acquisition, Investigation, Methodology, Resources, Supervision, Writing – review & editing. QL: Data curation, Formal analysis, Methodology, Validation, Writing – original draft. YJ: Methodology, Visualization, Writing – original draft. ZM: Validation, Writing – review & editing. JZ: Data curation, Validation, Writing – review & editing. ZL: Conceptualization, Funding acquisition, Resources, Writing – review & editing. SL: Project administration, Writing – review & editing. DS: Supervision, Writing – review & editing. SS: Resources, Writing – review & editing.

Funding

The author(s) declare financial support was received for the research, authorship, and/or publication of this article. This research was supported by Key-Area Research and Development Program of Guangdong Province (2023B0202090001), National Natural Science Foundation of China (Grant No. 31971797), National Natural Science Foundation of China (Grant No. 32271997), China Agriculture Research System of MOF and MARA (CARS-26), General Program of Guang-dong Natural Science Foundation (2021A1515010923), Guangdong Provincial Special Fund For Modern Agriculture Industry Technology Innovation Teams (Grant No. 2023KJ108), National College Students' Innovation and Entrepreneurship Training Program (202210564010).

Acknowledgments

The authors would like to thank the reviewers for their critical comments and suggestions for improving the manuscript.

Conflict of interest

The authors declare that the research was conducted in the absence of any commercial or financial relationships that could be construed as a potential conflict of interest.

Publisher's note

References

Ahmad, F., Qiu, B. J., Dong, X. Y., Ma, J., Huang, X., Ahmed, S., et al. (2021). Effect of operational parameters of UAV sprayer on spray deposition patternin target and off-target zones during outer field weed control application. *Comput. Electron. Agric.* 42, 74–82. doi: 10.13733/j.jcam.issn.2095-5553.2021.08.11

Balsari, P., Marucco, P., and Tamagnone, M. (2009). A crop identification system (CIS) to optimise pesticide applications in orchards. *J. Hortic. Sci. Biotechnol.* 84, 113–116. doi: 10.1080/14620316.2009.11512606

Berk, P., Hocevar, M., Stajnko, D., and Belsak, A. (2016). Development of alternative plant protection product application techniques in orchards, based on measurement sensing systems: A review. *Comput. Electron. Agric.* 124, 273–288. doi: 10.1016/j.compag.2016.04.018

Chen, B. T., Zheng, Y. J., Jiang, S. J., Yang, S. H., Lü, H. T., and Kang, F. (2020). Resource consumption evaluation model of orchard spray machinery. *Trans. Chin. Soc Agric. Mach.* 51, 289–297. doi: 10.6041/j.issn.1000-1298.2020.S2.034

Chen, J. Z. (2018). *Study on detection of characteristic parameters of canopy and variable spray characteristics based on LiDAR* (Guangdong (GZ: South China Agricultural University).

Chen, L. M., Wallhead, M., Zhu, H. P., and Fulcher, A. (2019). Control of insects and diseases with intelligent variable-rate sprayers in ornamental nurseries. *J. Environ. Hortic.* 37, 90–100. doi: 10.24266/0738-2898-37.3.90

Comba, L., Biglia, A., Aimonino, D. R., Barge, P., Tortia, C., and Gay, P. (2019). "2D and 3D data fusion for crop monitoring in precision agriculture," in *2019 IEEE International Workshop on Metrology for Agriculture and Forestry*. Portici, Italy: MetroAgriFor, 62–67. doi: 10.1109/MetroAgriFor.2019.8909219

Fan, D. Q., Zhang, M. N., Pan, J., and Lyu, X. L. (2021). Development and performance test of variable spray control system based on target leaf area density parameter. *Smart Agric.* 3, 60–69. doi: 10.12133/j.smartag.2021.3.3.202107-SA007

Ge, Y. F., Zhou, H. P., Zheng, J. Q., and Zhang, H. C. (2005). Indoor pesticide smart spraying system based on machine vision. *Trans. Chin. Soc Agric. Mach.* 36, 86–89. doi: 10.3969/j.issn.1000-1298.2005.03.025

He, X. K. (2020). Research progress and developmental recommendations on precision spraying technology and equipment in China. *Smart Agric.* 2, 133–146. doi: 10.12133/j.smartag.2020.2.1.201907-SA002

Jiang, H. H., Bai, P., Liu, L. M., Deng, X. F., Song, J. L., and Zhang, X. H. (2016a). Caterpillar self-propelled and air-assisted orchard sprayer with automatic target spray system. *Trans. Chin. Soc Agric. Mach.* 47, 189–195. doi: 10.6041/j.issn.1000-1298.2016.S0.029

Jiang, H. H., Liu, L. L., Liu, P. Z., Wang, J. Y., Zhang, X. H., and Gao, D. S. (2019b). Online calculation method of fruit trees canopy volume for precision spray. *Trans. Chin. Soc Agric. Mach.* 50, 120–129. doi: 10.6041/j.issn.1000-1298.2019.07.012

Kang, F., Pierce, F. J., Walsh, D. B., Zhang, Q., and Wang, S. (2011). An automated trailer sprayer system for targeted control of cutworm in vineyards. *Trans. Asabe.* 54, 1511–1519. doi: 10.13031/2013.39014

Li, L. L., He, X. K., Song, L. J., Wang, X. N., Jia, X. M., and Liu, C. H. (2017). Design and experiment of automatic profiling orchard sprayer based on variable air volume and flow rate. *Trans. Chin. Soc Agric. Eng.* 33, 70–76. doi: 10.11975/j.issn.1002-6819.2017.01.009

Li, L. L., He, X. K., Song, L. J., and Zhong, C. S. (2016). Spray characteristics on pulse-width modulation variable application based on high frequency electromagnetic valve. *Trans. Chin. Soc Agric. Eng.* 32, 97–103. doi: 10.11975/j.issn.1002-6819.2016.01.013

Li, L., Li, H., He, X. K., and Andreas, H. (2012). Development and experiment of automatic detection device for infrared target. *Trans. Chin. Soc Agric. Eng.* 28, 159–163. doi: 10.3969/j.issn.1002-6819.2012.12.026

Nørremark, M., Griepentrog, H. W., Nielsen, J., and Søgaard, H. T. (2008). The development and assessment of the accuracy of an autonomous GPS-based system for intra-row mechanical weed control in row crops. *Biosyst. Eng.* 101, 396–410. doi: 10.1016/j.biosystemseng.2008.09.007

Palleja, T., and Landers, A. J. (2015). Real time canopy density estimation using ultrasonic envelope signals in the orchard and vineyard. *Comput. Electron. Agric.* 115, 108–117. doi: 10.1016/j.compag.2015.05.014

Popusoi, D. (2018). *China's policy on agroecology-how Chinese farmers interact with policies and regulations* (Wuhan (HB: Central China Normal University).

Qiu, B. J., Yan, R., Ma, J., Guan, X. P., and Ou, M. X. (2015). Research progress analysis of variable rate sprayer technology. *Trans. Chin. Soc Agric. Mach.* 46, 59–72. doi: 10.6041/j.issn.1000-1298.2015.03.009

Rosell Polo, J. R., Sanz, R., Llorens, J., Arnó, J., Escolà, A., Ribes-Dasi, M., et al. (2009). A tractor-mounted scanning lidar for the non-destructive measurement of vegetative volume and surface area of tree-row plantations: a comparison with conventional destructive measurements. *Biosyst. Eng.* 102, 128–134. doi: 10.1016/j.biosystemseng.2008.10.009

Salcedo, R., Zhu, H. P., Zhang, Z. H., Wei, Z. M., Chen, L. M., Ozkan, E., et al. (2020). Foliar deposition and coverage on young apple trees with PWM-controlled spray systems. *Comput. Electron. Agric.* 178, 105794. doi: 10.1016/j.compag.2020.105794

Silva, J. E., Zhu, H. P., and Cunha, J. P. A. R. (2018). Spray outputs from a variable-rate sprayer manipulated with PWM solenoid valves. *Appl. Eng. Agric.* 34, 527–534. doi: 10.13031/aea.12556

Solanelles, F., Escolà, A., Planas, S., Rosell, J. R., Camp, F., and Gràcia, F. (2006). An electronic control system for pesticide application proportional to the canopy width of tree crops. *Biosyst. Eng.* 95, 473–481. doi: 10.1016/j.biosystemseng.2006.08.004

Stajnko, D., Berk, P., Lešnik, M., Jejčič, V., Lakota, M., Štrancar, A., et al. (2012). Programmable ultrasonic sensing system for targeted spraying in orchards. *Sensors* 12, 15500–15519. doi: 10.3390/s121115500

Sun, D. Z., Liu, W. K., Luo, R. M., Zhan, X. R., Chen, Z. H., Wie, T., et al. (2022). Monocular vision for variable spray control system. *Int. J. Agric. Biol. Eng.* 15 (6), 206–215. doi: 10.25165/j.ijabe.20221506.7646

Wang, G. B., Li, X., Andaloro, J., Chen, S., Han, X. Q., Wang, J., et al. (2021). Current status and prospects of precise sampling of pesticide droplets. *Trans. Chin. Soc Agric. Eng.* 37, 1–12. doi: 10.11975/j.issn.1002-6819.2021.16.005

Wang, H. Y., Yan, R. Q., Zhou, X. L., Ma, S. H., Hu, H. X., and Xu, H. L. (2019). Apple shape index estimation method based on local point cloud. *Trans. Chin. Soc Agric. Mach.* 50, 205–213. doi: 10.6041/j.issn.1000-1298.2019.05.024

Wei, X. H., Yu, D. Z., Bai, J., and Jiang, S. (2013). Static spray deposition distribution characteristics of PWM-based intermittently spraying system. *Trans. Chin. Soc Agric. Eng.* 29, 19–24. doi: 10.3969/j.issn.1002-6819.2013.05.003

Xia, W. (2016). *Development and research of 3D target detection system based on laser scanning sensor* (Zhejiang(JS: Jiangsu University).

Xue, X. Y., Xu, X. F., Li, Z., Hong, T. S., Xie, J. X., Chen, J. Z., et al. (2020a). Design and test of variable spray model based on leaf wall area in orchards. *Trans. Chin. Soc Agric. Eng.* 36, 16–22. doi: 10.11975/j.issn.1002-6819.2020.02.003

Xue, X. Y., Yang, Z. Y., Liang, X. Q., Luo, Q., Lyu, S. L., and Li, Z. (2022b). Application and experiments of the atomization mesh used on the plant protection spraying in orchards. *Trans. Chin. Soc Agric. Eng.* 38, 1–10. doi: 10.11975/j.issn.1002-6819.2022.18.001

Yan, C. G., Xu, L. M., Yuan, Q. C., Ma, S., Niu, C., and Zhao, S. J. (2021). Design and experiments of vineyard variable spraying control system based on binocular vision. *Trans. Chin. Soc Agric. Eng.* 37, 13–22. doi: 10.11975/j.issn.1002-6819.2021.11.002

Zhai, C. Y., Zhao, C. J., Ning, W., John, L., Wang, X., Paul, W., et al. (2018). Research progress on precision control methods of air-assisted spraying in orchards. *Trans. Chin. Soc Agric. Eng.* 34, 1–15. doi: 10.11975/j.issn.1002-6819.2018.10.001

Zhang, Z. H., Wang, X. Y., Lai, Q. H., and Zhang, Z. G. (2018). "Review of variable-rate sprayer applications based on real-time sensor technologies," in *Automation in Agriculture - Securing Food Supplies for Future Generations*. Ed. S. Hussmann (Croatia, Rijeka: InTech Press), 53–79.

Zhu, H., Lan, Y. B., Wu, W. F., Hoffmann, W. C., Huang, Y. B., Xue, X. Y., et al. (2010). Development of a PWM precision spraying controller for unmanned aerial vehicles. *J. Bionic Eng.* 7, 276–283. doi: 10.1016/S1672-6529(10)60251-X

frontiers | Frontiers in Plant Science

TYPE Methods
PUBLISHED 29 January 2024
DOI 10.3389/fpls.2024.1276799

OPEN ACCESS

EDITED BY
Xiaolan Lv,
Jiangsu Academy of Agricultural Sciences (JAAS), China

REVIEWED BY
Bingbo Cui,
Jiangsu University, China
Ping Xu,
Hangzhou Dianzi University, China

*CORRESPONDENCE
Minli Yang
qyang@cau.edu.cn
Liping Chen
chenlp@nercita.org.cn

†These authors have contributed equally to this work

RECEIVED 13 August 2023
ACCEPTED 03 January 2024
PUBLISHED 29 January 2024

CITATION
Tan H, Zhao X, Zhai C, Fu H, Chen L and Yang M (2024) Design and experiments with a SLAM system for low-density canopy environments in greenhouses based on an improved Cartographer framework. *Front. Plant Sci.* 15:1276799. doi: 10.3389/fpls.2024.1276799

Design and experiments with a SLAM system for low-density canopy environments in greenhouses based on an improved Cartographer framework

Haoran Tan[1,2†], Xueguan Zhao[2,3,4†], Changyuan Zhai[2,3], Hao Fu[2], Liping Chen[2,3*] and Minli Yang[1*]

[1]College of Engineering, China Agricultural University, Beijing, China, [2]Intelligent Equipment Research Center, Beijing Academy of Agriculture and Forestry Sciences, Beijing, China, [3]National Engineering Research Center for Information Technology in Agriculture, Beijing, China, [4]Beijing PAIDE Science and Technology Development Co., Ltd, Beijing, China

To address the problem that the low-density canopy of greenhouse crops affects the robustness and accuracy of simultaneous localization and mapping (SLAM) algorithms, a greenhouse map construction method for agricultural robots based on multiline LiDAR was investigated. Based on the Cartographer framework, this paper proposes a map construction and localization method based on spatial downsampling. Taking suspended tomato plants planted in greenhouses as the research object, an adaptive filtering point cloud projection (AF-PCP) SLAM algorithm was designed. Using a wheel odometer, 16-line LiDAR point cloud data based on adaptive vertical projections were linearly interpolated to construct a map and perform high-precision pose estimation in a greenhouse with a low-density canopy environment. Experiments were carried out in canopy environments with leaf area densities (LADs) of 2.945–5.301 m^2/m^3. The results showed that the AF-PCP SLAM algorithm increased the average mapping area of the crop rows by 155.7% compared with that of the Cartographer algorithm. The mean error and coefficient of variation of the crop row length were 0.019 m and 0.217%, respectively, which were 77.9% and 87.5% lower than those of the Cartographer algorithm. The average maximum void length was 0.124 m, which was 72.8% lower than that of the Cartographer algorithm. The localization experiments were carried out at speeds of 0.2 m/s, 0.4 m/s, and 0.6 m/s. The average relative localization errors at these speeds were respectively 0.026 m, 0.029 m, and 0.046 m, and the standard deviation was less than 0.06 m. Compared with that of the track deduction algorithm, the average localization error was reduced by 79.9% with the proposed algorithm. The results show that our proposed framework can map and localize robots with precision even in low-density canopy environments in greenhouses, demonstrating the satisfactory capability of the proposed approach and highlighting its promising applications in the autonomous navigation of agricultural robots.

KEYWORDS

mobile robot, lidar, simultaneous localization and mapping (SLAM), greenhouse, perception

1 Introduction

The development of agricultural facilities ensures the stable and safe supply of important agricultural products while reducing the occupation of arable land. These facilities are important for promoting the modernization of agriculture in rural areas (Bai et al., 2023). The development of intelligent equipment suitable for greenhouses is needed to ensure stable and efficient production in agricultural facilities (Jin et al., 2021; Zhai et al., 2022). Due to the narrow working environment of greenhouses, the applicability of conventional field operation equipment in greenhouses is limited. The traditional manual greenhouse management method has high labor intensity, and the application of pesticides in a closed environment may cause serious harm to the human body (Fu et al., 2022; Li et al., 2022). Therefore, it is necessary to study intelligent navigation robots that are suitable for application in greenhouse environments (Huang and Sugiyama, 2022; Qiao et al., 2022).

Environmental perception and real-time localization are the basis of greenhouse robot navigation studies and are prerequisites for autonomous navigation (Shamshiri et al., 2018; Chen et al., 2020). However, the closed nature of the greenhouse environment severely blocks satellite signals. Therefore, it is highly important to study perception and localization methods that do not depend on satellite navigation to develop navigation technology for greenhouse environments (Mendes et al., 2019; Choi et al., 2022). High-precision mapping and localization of agricultural robots are critical for the automation of greenhouse operations (Dong et al., 2020; Westling et al., 2021; Zhou et al., 2021). Using the prior map, the robot can obtain prior information about the environment and realize global path planning to achieve safe and accurate autonomous navigation. To this end, researchers have carried out many studies in the fields of sensor environment perception and simultaneous localization and mapping (SLAM) (Matsuzaki et al., 2018; Shi et al., 2020; Ouyang et al., 2022; Jiang and Ahamed, 2023; Su et al., 2023).

In recent years, with the development of computer technology and edge computing equipment, the sensors used for greenhouse operating environment perception and localization have included ultrasonic technology (Palleja and Landers, 2017; Chen et al., 2018; Lao et al., 2021), ultra-wideband (UWB) technology (Hou et al., 2020; Yao et al., 2021), LiDAR technology (Chen et al., 2019; Zhang et al., 2020; Saha et al., 2022; Sun et al., 2022), and machine vision technology (Nissimov et al., 2015; Wang et al., 2022a; Wang et al., 2022b). Huang et al. (2021) designed a robot localization system based on spread spectrum sounds for a greenhouse containing a strawberry ridge and achieved centimeter-level localization accuracy in a small greenhouse. However, the coverage of sound localization technology is limited, which significantly increases the cost in large-scale scenarios. Aiming to address the problem of insufficient features in greenhouse environments, Zhang et al. (2022) proposed a visual localization method based on benchmark markers and factor graphs. This method considers the constraint relationship between robot motion characteristics and variables, and the standard deviation of the localization error is less than 0.05 m. This method solves the problem of unstructured and insufficient features in greenhouses by adding benchmark markers to the SLAM front-end module. Although this method can achieve stable localization of the robot, it depends on the number of tags detected. In the case in which the plant is occluded or the number of tags is insufficient, inaccurate localization or even failure may occur. Yan et al. (2022) designed a loosely coupled real-time localization and mapping system based on an extended Kalman filter and visual-inertial odometry (VIO) using multisensor fusion and the visual-IMU-wheel odometry method to achieve accurate pose estimation and dense three-dimensional (3D) point cloud mapping in greenhouses. However, while the localization method based on visual SLAM performs well under good light conditions, the high light intensity in the environment interferes with the extraction of visual features, which may cause issues with map construction in the greenhouse environment and errors in robot pose calculation results.

To address the effects of greenhouse environment lighting on robot perception, LiDAR, which has advantages such as high stability and robustness, is a competitive perception and localization technology for all-weather greenhouse operations. The AgriEco Robot, designed by Abanay et al. (2022), is based on a two-dimensional (2D) LiDAR sensor and performs autonomous navigation. This robot can accurately navigate between rows of strawberry greenhouse crops, detect the end of a row, and switch to the next row. To solve the problem of inaccurate localization caused by the lack of structure in grape greenhouse scenes, Aguiar et al. (2022) designed a VineSLAM algorithm. The algorithm is based on 3D LiDAR point cloud extraction and uses half-plane features to construct an environmental map. The robot can achieve accurate localization in symmetrical long vineyard corridors. However, with seasonal changes, a decrease in grape canopy density affects map construction results and localization effects. Long et al. (2022) proposed a method to reduce the cumulative errors of odometers in long-distance greenhouse operations and the problem of mapping and localization accuracy. Their method is based on the UWB/IMU/ODOM/LiDAR-integrated localization system and integrates LiDAR with the two-dimensional map established through the adaptive Monte Carlo localization (AMCL) algorithm for global localization of the robot. The method is suitable for relatively open greenhouse environments where shorter crops are planted. However, in greenhouse environments with taller crops, due to the physical characteristics of UWB technology, the occlusion of plants affects the stability of the SLAM system. However, due to the large number of unstructured crops and irregular planting gaps in greenhouses, it is difficult for LiDAR-based methods to obtain clear map boundaries. Hou et al. (2020) developed a greenhouse robot navigation system based on a Cartographer with dual LiDAR. This system improved the efficiency of map building and enabled robotic mapping and autonomous navigation in a strawberry greenhouse environment. However, as the environmental map construction of strawberry plants is based on strawberry ridges, the results cannot be generalized to typical unridged greenhouse environments. At present, there are no researchers dedicated to solving the laser SLAM problem in greenhouse sparse feature environments. In the industrial field, Xie et al. (2021) proposed a visual-inertial fusion SLAM method for sparse lunar feature environments that integrates

visual measurements and inertial sensor information via pose optimization methods to achieve high-precision joint positioning and improve the accuracy of relative pose estimation between key frames.

Although the above studies proposed improved methods to address problems such as greenhouse terrains, cumulative odometer errors, and irregular greenhouse structures, the impact of the sparse canopy characteristics of greenhouse crops on laser SLAM-based methods has not been considered. For crop environments such as low-density canopies in greenhouses, traditional laser SLAM methods have difficulty constructing accurate and complete environmental maps due to the loss of contour information caused by map degradation; thus, these methods cannot meet the localization accuracy needs for agricultural robot operation. In addition, SLAM methods based on 2D LiDAR can obtain environmental information only at the installation height level, while SLAM methods based on 3D LiDAR have higher computational costs and higher requirements for achieving good industrial computing performance (Jiang et al., 2022). The purpose of this study was to explore a low-cost spatial downsampling-based map construction and localization method based on the Cartographer framework to optimize the map construction effect and localization accuracy in suspended crop environments in greenhouses to construct maps and realize high-precision pose estimates in low-density canopy environments in greenhouses.

2 Materials and methods

2.1 Test platform

The map construction and localization hardware system built in this paper is primarily composed of a perception module, control module, power module, and drive module, as shown in Figure 1. The Autolabor Pro1 platform produced by Qingke Intelligent Company (Shanghai, China) was selected as the robot chassis. The maximum movement speed of the robot is 1 m/s, and the robot can carry a maximum load of 50 kg. The four-wheel differential control of the robot can achieve stationary turning, allowing for turning in narrow spaces. The size was 726 × 617 × 273 mm, and the system was equipped with an RS-LiDAR-16 three-dimensional LiDAR system from Suteng Juchuang Company (Shenzhen, China). The LiDAR system can collect 300,000 data points per second, the acquisition frequency ranges from 5 to 20 Hz, the horizontal viewing angle range is 360°, and the resolution ranges from 0.1° to 0.4°. The vertical viewing angle is 30°, and the resolution is 2°. The measurement range is 0.2–100 m. The industrial computer that the robot is equipped with the Ubuntu 18.04 operating system, and the algorithm for the overall software system of the greenhouse mobile robot is designed based on the ROS Melodic. The specific model of the sensor is shown in Table 1.

The STM32 microcontroller can control the linear speed and angular velocity of the mobile robot, provide real-time feedback based on the motion state information of the robot, and interact with the industrial computer through RS232 serial communication. The industrial computer collects, fuses, and processes the robot sensor information; constructs the map; plans the path; and performs autonomous localization and navigation according to the control instructions. The ROS system installed on the industrial computer has a distributed architecture, which allows each functional module in the framework to be designed and compiled separately during runtime, with loose coupling between the modules.

2.2 Research method

2.2.1 Improved Cartographer algorithm design

The Cartographer algorithm (Hess et al., 2016) is an open-source laser SLAM framework proposed by Google that is widely

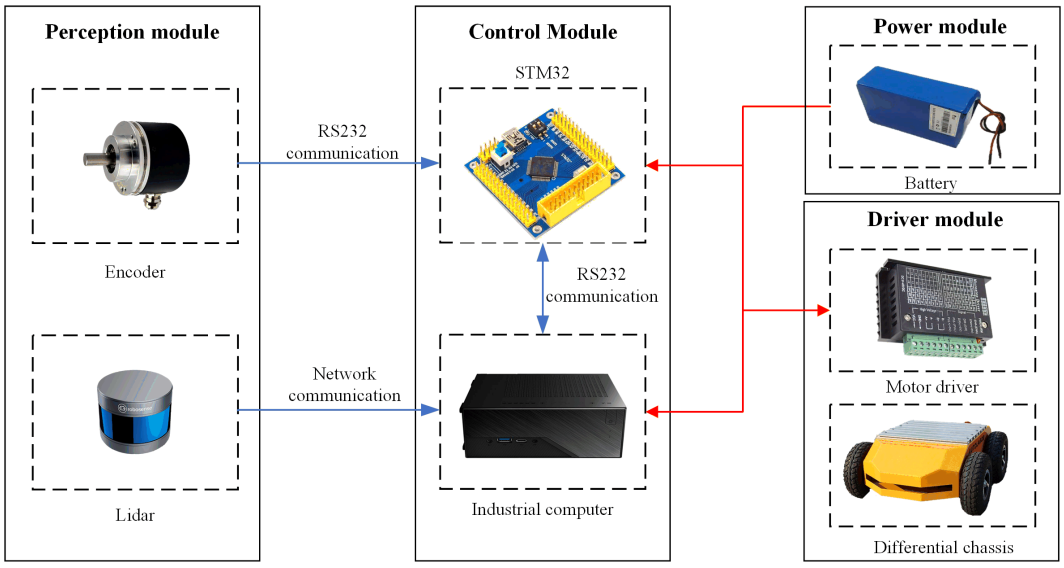

FIGURE 1
Map construction and localization hardware system of the greenhouse mobile robot.

TABLE 1 Greenhouse map construction and localization system equipment model.

No.	Equipment	Specification
1	Encoder	HTS-5008 encoder
2	LiDAR	RS-LiDAR-16LiDAR
3	Battery	24 V 40AH lithium iron phosphate battery
4	Motor drive	BLDH-750 brushless motor drive
5	Controller	STM32F103zet6 computer on a chip
6	Industrial computer	AMD Ryzen3 3200G
7	Chassis	Autolabor Pro1

used in the fields of robotics and autonomous systems. The Cartographer algorithm mainly establishes a series of submaps based on LiDAR data, inserts point cloud data into the submap through scan matching, and forms a complete map through loop closure detection and optimization, eliminating the cumulative error between submaps. The software framework of the adaptive filtering point cloud projection (AF-PCP) SLAM system based on the Cartographer algorithm is shown in Figure 2.

The LiDAR driver releases 3D point cloud data/rsldiar_points and performs z-axis threshold filtering based on the point cloud by setting the LiDAR perception region of interest (ROI). The key parameters of the algorithm are as follows: *min_height* represents the minimum height of the z-axis involved in point cloud compression, and the unit is m; *max_height* represents the maximum height involved in point cloud compression, and the unit is m; *range_min* and *range_min* represent the minimum and maximum measurement ranges of the output point cloud, respectively, and the units are both m; and *scan_time* represents the scanning time, and the unit is s. The data format of the input point cloud is sensor_msgs/PointCloud2, and the message format of the processed point cloud is sensor_msgs/LaserScan. The pose of the robot is estimated by a two-wheel differential kinematics model, and the odometer data are published in the message format of nav_msgs/Odometry.

The greenhouse tomato plant is taken as an example, and the height of the tomato plant is 1.5–2 m. First, the ROI of the greenhouse robot is set, and the ROI is selected based on the LiDAR coordinate system to delineate a three-dimensional ROI. The motion speed of the greenhouse robot, the braking distance, and the reserved space between the body and the crops are considered in determining the area. The specific parameters are set as follows: *min_height* is set to 0.5 m, *max_height* is set to 1.5 m, *scan_time* is set to 0.1 s, *range_min* is set to 0.2 m, and *range_max* is set to 15 m. Based on the above parameter settings, the adaptive projection process for the greenhouse crop point clouds is designed, as shown in Figure 3.

After receiving a frame of complete multiline LiDAR data, the greenhouse map construction system filters the point cloud data outside the perceived ROI area. The filtered point cloud data $p = \{p_1, p_2, p_3 \ldots p_n\}$ are stored in the array *points_range*. For the adaptive vertical projection of the point cloud, the specific processing steps are as follows: First, the kth scanning frame of the LiDAR p_k is selected, each point in the frame is represented $p_k(x, y, z, i)$, and an iterator is used to record the starting position of the point. The x coordinate information of the point cloud is obtained; the y and z information and intensity value i corresponding to the point are obtained using the offset pointers *offset_y*, *offset_z*, and *offset_i*; the point $p_k(x_k, y_k, z_k, i_k)$ is represented in the LiDAR Cartesian coordinate system. The points are converted to the polar coordinate representation of the x–y plane by vertical projection. The Euclidean distance ρ_k, angle θ_k, and index $index_k$ of the point in the polar coordinate system are calculated, and the calculation formulas are shown in Formulas 1–4.

$$p_k = \{p_k, \theta_k, i_k\} \tag{1}$$

$$\rho_k = \sqrt{x_k^2 + y_k^2} \tag{2}$$

$$\theta_k = \arctan\frac{y_k}{x_k} \tag{3}$$

$$index_k = \frac{\arctan\frac{y_k}{x_k} + \pi}{r} \tag{4}$$

where ρ_k θ_k are the distance and angle of the laser point in the polar coordinate system, i_k is the corresponding intensity value, x_k and y_k are the corresponding coordinate values, and r is the angular

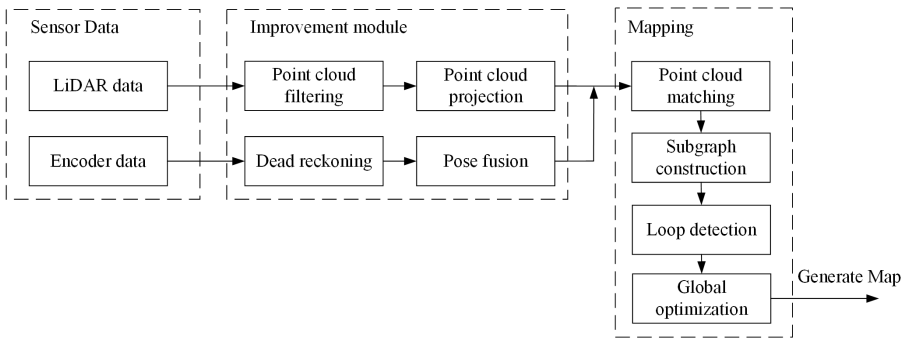

FIGURE 2
AF-PCP SLAM algorithm framework. AF-PCP, adaptive filtering point cloud projection.

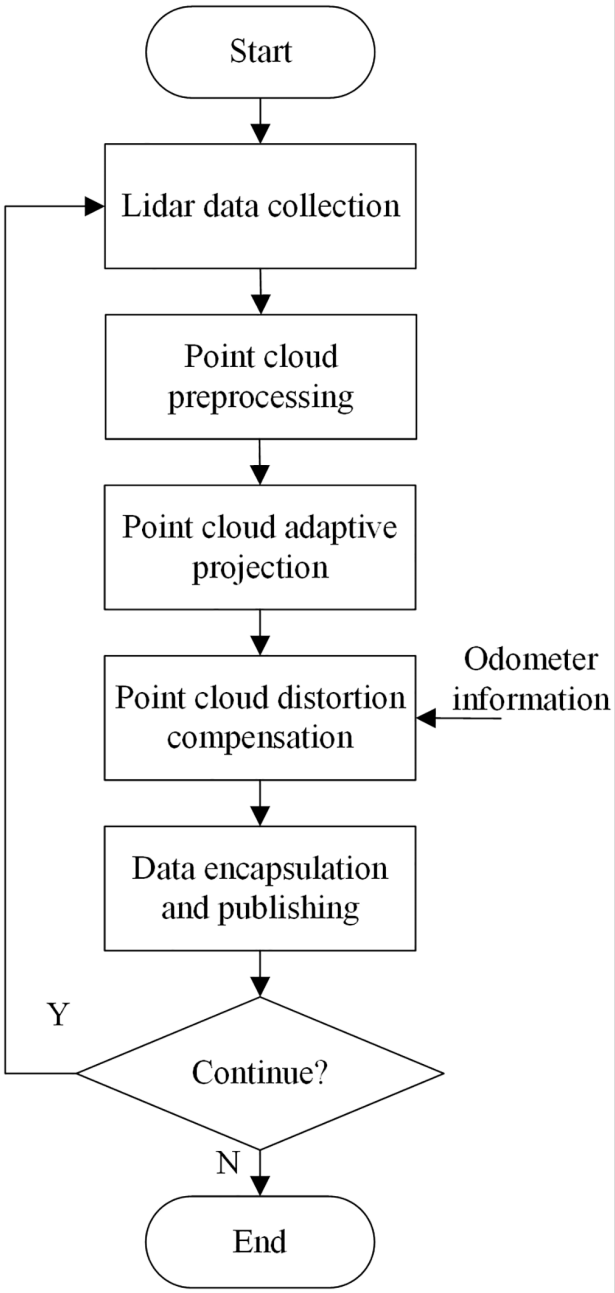

FIGURE 3
Flowchart of the greenhouse crop point cloud adaptive projection algorithm.

resolution of the LiDAR system. The selected LiDAR angle beam contains 1,800 lines, and the angular resolution calculation formula is $r = \frac{2\pi}{1800} \approx 0.00349$.

Similarly, the point distances at this angle for the remaining 15-beam LiDAR data are calculated. The minimum distance obtained by the sorting algorithm is stored in the *scan_ranges* container as the distance value of the point.

Since the acquisition of laser point cloud data is not instantaneous, the robot distorts the motion of the point cloud data in the motion state. To eliminate this motion distortion, in this paper, the wheel odometer data calculated by the encoder are used to increase the pose update frequency, reflecting the pose change of the greenhouse robot during the laser data acquisition process. By calculating the odometer pose in the coordinate system corresponding to each point cloud in the current frame of the point cloud data, the coordinates of each point cloud are transformed into the same coordinate system, with the point of the first laser serving as the origin according to the obtained pose.

It is assumed that the robot accelerates uniformly in the process of collecting a frame of point cloud data. To ensure the accuracy of the data, a double-ended queue is used to save the point cloud data and ensure that there are at least two data points in the queue to prevent the data time of the wheel odometer from being less than the time of receiving the point cloud data. The start time and end time for a frame of point cloud data are t_{start} and t_{end}, respectively, and the corresponding starting position and end position of the origin of the LiDAR coordinate system in the odometer coordinate system are expressed as p_{start} and p_{end}, respectively. A total of n pose information data points $\{P_{start}, \quad P_{start+1}, P_{start2,}, \ldots, P_{start+n-1}, P_{end}\}$ are obtained. Linear interpolation is performed based on the LiDAR pose information to obtain the approximate odometer pose corresponding to the timestamp for the point cloud data. By transforming the point cloud data into the odometer coordinate system, LiDAR point cloud data based on the robot coordinate system can be obtained in cases with distortion. The method for calculating the coordinates of point o_x, o_y in the odometer coordinate system is shown in Formula 5:

$$\begin{bmatrix} o_x \\ o_y \end{bmatrix} = R \begin{bmatrix} x_1 \\ y_1 \end{bmatrix} + l \tag{5}$$

$$R = \begin{bmatrix} \cos\theta & -\sin\theta \\ \sin\theta & \cos\theta \end{bmatrix} \tag{6a}$$

$$l = \begin{bmatrix} x_t \\ y_t \end{bmatrix} \tag{7a}$$

where (o_x, o_y) are the coordinates of the odometer coordinate system after conversion, (x_1, y_1) are the point cloud data points before the transformation, and R (Formula 6a) is a rotation matrix that describes two coordinate systems. l (Formula 7a) is a translation vector that describes two coordinate systems, θ is the polar coordinate system angle corresponding to the point cloud, and (x_t, y_t) is the translation amount from the odometer coordinate system to the LiDAR coordinate system.

The laser point cloud data are transformed from the odometer coordinate system to the reference coordinate system of the data frame, and the starting point in the coordinate system of the current frame of the point cloud data is the reference coordinate system of the data frame. The method for calculating the coordinate of the transformed point $(o_x^{'}, o_y^{'})$ in the reference coordinate system is shown in Formula 6b:

$$\begin{bmatrix} o_x^{'} \\ o_y^{'} \end{bmatrix} = R^{-1} \begin{bmatrix} o_x \\ o_y \end{bmatrix} - R^{-1} \begin{bmatrix} x_0 \\ y_0 \end{bmatrix} \tag{6b}$$

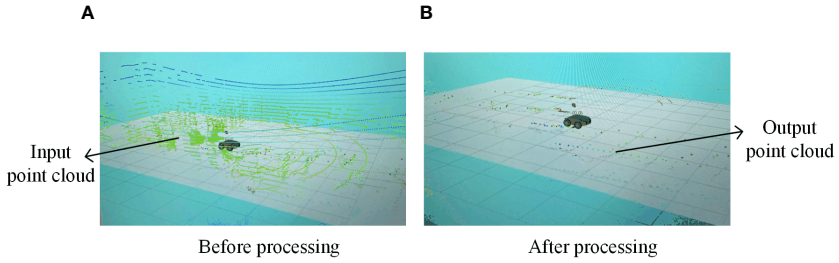

FIGURE 4
Point cloud processing results. **(A)** Before processing point cloud. **(B)** After processing point cloud.

where (x_0, y_0) are the coordinates of the origin of the reference coordinate system in the odometer coordinate system and R^{-1} is the inverse matrix that describes the rotation matrix of two coordinate systems.

Finally, the frame head timestamp, intensity value, and other information for each frame of the LiDAR point cloud data are supplemented, and the LiDAR data after the adaptive vertical projection process are output in the sensor_msgs/LaserScan format with a release frequency of 10 Hz. The effect of the point cloud processing is shown in Figure 4.

The scan-to-map matching method was used to construct the map, as shown in Figure 5. First, we used a submap to organize the whole map. Each submap consists of several LiDAR scanning frames {Scan(n)}, and the complete global map is composed of all the submaps. Assuming that the initial pose of the robot is $\xi_1 = (0, 0, 0)$, the LiDAR scanning frame is denoted as Scan_1 (1). At this pose, the first submap (1) is initialized by Scan_1 (1). The robot pose ξ_2 corresponding to Scan_1 (2) is calculated by the scan-to-map matching method, and Scan_1 (2) is added to Submap (1) based on pose ξ_2. The scan-to-map matching method is continuously

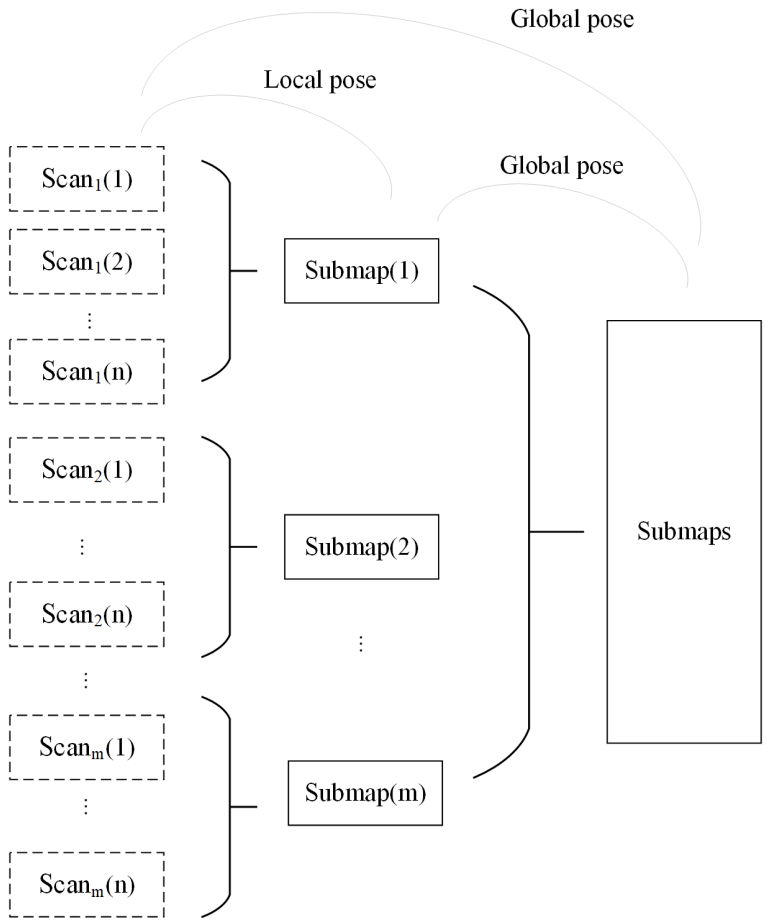

FIGURE 5
Schematic diagram of the map construction process.

executed, and the newly obtained LiDAR frames are added until the new LiDAR frame is completely included in Submap (1); that is, when the new LiDAR frame does not contain new information other than that included in Submap (1), the creation of Submap (1) is completed. The above process is performed to create all the submaps (m). Finally, all the local subgraphs {Submap(m)} are used to form the complete global map.

2.2.2 Layout of the test site

In this paper, a simulated greenhouse scene was built, which included 30 mm * 30 mm aluminum profiles, fixed bases, and simulated plants. The simulated crop has three rows; each row is 4 m long, the row height is 1.3 m, and the row spacing is 1.2 m. The test scene is shown in Figure 6. In the crop row, aluminum profiles were used as support rods every other distance, a set of simulated crops was arranged every 0.2 m, and the number of leaves per crop was counted.

2.3 Test scheme

2.3.1 Different sparse degree mapping tests

To verify the mapping effect of the algorithm for different sparse canopy crops in the greenhouse, based on the robot platform built in Section 2.1 and the simulated greenhouse scene constructed in Section 2.2.2, the crops were randomly pruned five times, and 10% of the leaves were pruned each time. A total of six simulated environments with different degrees of sparseness were generated. The experiment was carried out at the National Agricultural Information Demonstration Test Base in Xiaotangshan town, Beijing, in May 2023. In this experiment, the AF-PCP SLAM algorithm was used for SLAM mapping, and the Cartographer algorithm was used for the control group. The remote control robot moves between the crop rows to construct a map of the entire environment. The specific mapping operation was performed as follows:

1 The ROS core node, chassis control node, and LiDAR mapping node are started.

2 The robot movement speed is set to 0.2 m/s, and the remote control operation is performed according to the running track for the interrow operation.

3 The visualization tool Rviz is used to monitor the robot mapping results in real time, and the map is saved after map construction is completed.

The canopy biomass, leaf area (LA), leaf area index (LAI), and leaf area density (LAD) are the main indicators of canopy density. The distribution of leaf density in the canopy is random and unpredictable in three-dimensional space, which complicates the quantitative analysis process (Gu et al., 2021). In this paper, the LAD was used as a measure of canopy density to divide the six experiments. A YMJ-G leaf area meter (Shandong Fangke Instrument Co., Ltd., Shandong, China) was used to measure the leaf density 10 times. The average leaf area was 21.203 cm^2, and environments with six LAD values were constructed. The number of crop row pixels, the crop row length, and the maximum gap length for each LAD were used as evaluation indicators. The actual length of the crop row was 3.985 m, and the actual value of the crop row spacing gap was 0.08 m. The method for counting the number of pixels involved counting the number of pixels in the middle crop row in the PGM image via the two algorithms. The crop row length and maximum gap length were calculated by importing the Pbstream file calculated by the two algorithms into the cost map tool under the ROS open source function package Movebase; the scale measurement tool in Rviz was used to measure the crop row length in the middle row, and the maximum gap length was determined.

2.3.2 Localization system performance test

To verify the localization accuracy of the proposed method at different speeds, the robot was controlled to move along the crop row by setting different robot motion speeds, namely, a low speed of 0.2 m/s, a medium speed of 0.4 m/s, and a high speed of 0.6 m/s. The ROSBag tool was used to record the real-time data of the sensor and the localization algorithm output results. The starting position in each test was aligned with a laser pen to ensure that the initial pose in each test was the same, as shown in Figure 7A.

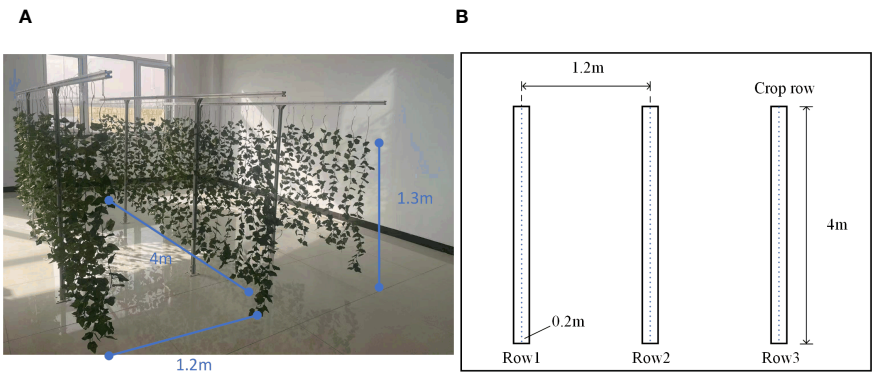

FIGURE 6
Simulated greenhouse test scene. **(A)** Physical display of simulated test scenarios. **(B)** Schematic diagram of simulation test scenario.

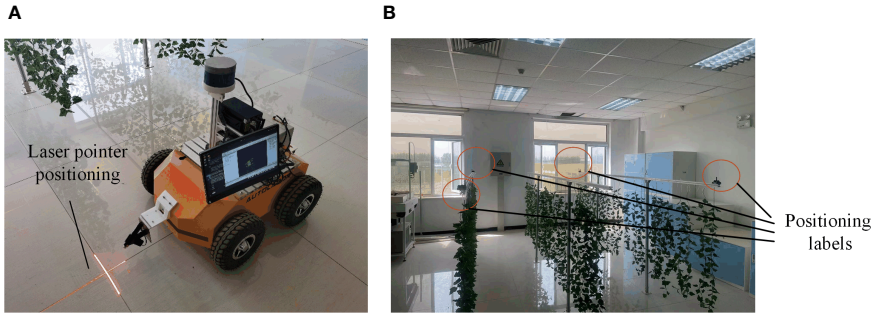

FIGURE 7
Pose alignment and test environment localization equipment construction. **(A)** Using a laser pointer for pose alignment. **(B)** test environment localization equipment construction.

In this paper, according to the localization evaluation equipment selected in Reference (Zhang et al., 2022), the Starter Set Super-MP-3D ultrasonic localization device from the Marvelmind Company was selected to determine the true value to evaluate the localization accuracy of the robot. The device consists of four fixed labels, a mobile vehicle label, and a localization route. The device can theoretically obtain an accuracy of up to ±2 cm. In addition, in this paper, the dead reckoning localization method was used as a comparison method to evaluate the performance of the AF-PCP SLAM algorithm comprehensively. Four localization labels were strategically placed in the greenhouse, and four vertices in the test area were selected for placement. To reduce the interference of crop occlusion on ultrasonic signals and ensure maximum signal coverage, four positioning labels were placed at the vertices of two outer crop rows. Fixing labels at the same height can improve positioning accuracy. Each label was fixed on a beam 1.4 m above the ground, as shown in Figure 7B.

To prove the effectiveness of the AF-PCP SLAM algorithm, the localization accuracy was evaluated using EVO (https://github.com/MichaelGrupp/evo, accessed on June 28, 2022). To verify the results, the ultrasonic localization data were used as the ground truth to analyze the localization effect. The relative pose error (RPE) describes the accuracy of the two-frame pose difference between the estimated pose and the real pose at a fixed time difference t, which is equivalent to the error of directly measuring the pose results. The RPE for frame i is shown in Formula 7b:

$$E_{\mathrm{i}} = (Q_i^{-1} Q_{i+\Delta t})^{-1} (P_i^{-1} P_{i+\Delta t}) \tag{7b}$$

where E_{i} represents the RPE of the ith frame, Q_i represents the true ultrasonic pose value, P_i represents the estimated pose value, and Δt represents a fixed interval time coefficient.

Assuming that there are n pose frames, the $n - \Delta t$RPE values can be calculated, and the total value is obtained using the root mean square error (RMSE) statistics, as shown in Formula 8:

$$RMSE(E_{1:n}, \Delta t) = \left(\frac{1}{m}\sum_{i=1}^{m} \| trans(E_i) \|^2\right)^{\frac{1}{2}} \tag{8}$$

Here, $m = n - \Delta t$ and $trans(E_i)$ represent the translation of the RPE. To comprehensively evaluate the performance of the algorithm, the average RMSE is calculated, as shown in Formula 9:

$$RMSE(E_{1:n}) = \frac{1}{n}\sum_{\Delta t=1}^{n} RMSE(E_{1:n}, \Delta t) \tag{9}$$

3 Results

3.1 Mapping performance

To verify the wide applicability of the AF-PCP SLAM algorithm for different crop densities, six tests were carried out in the same environment. The localization trajectory and surrounding environment information of the different methods are displayed in real time in Rviz, as shown in Figure 8.

Figure 8 shows that the Cartographer algorithm accurately constructs structured walls and glass into grayscale grid maps. However, these maps are still not perfect. Unstructured suspended crops occupy most of the space in the greenhouse environment. However, based on the mapping results, the Cartographer algorithm results in a large loss of crop row mapping, whereas the AF-PCP SLAM algorithm yields more accurate mapping results. To better show the effect of the AF-PCP SLAM algorithm on crop row mapping under different degrees of sparseness, Figure 9 shows the map construction results of the two methods for six degrees of sparseness.

Figure 9 shows the crop mapping results of the Cartographer algorithm and AF-PCP SLAM algorithm for six degrees of sparseness. According to the LAD calculation method presented in Section 2.3.1, the LADs corresponding to the six sparsities are 5.301 m^2/m^3, 4.830 m^2/m^3, 4.358 m^2/m^3, 3.887 m^2/m^3, 3.416 m^2/m^3, and 2.945 m^2/m^3. The quantitative statistical results, including the number of pixels, the crop row lengths, and the maximum gap lengths, for the six LADs were calculated, as shown in Figure 10.

According to the results shown in Figure 10, as the LAD increased, the number of pixels in the crop row generally increased. The AF-PCP SLAM algorithm outperforms the Cartographer algorithm in terms of the number of pixels. The number of pixels in the crop row reflects the effective area of the grid map, and the results indicate that the AF-PCP SLAM algorithm is better at constructing the map of the crop row. Specifically, the number of pixels in the AF-PCP SLAM algorithm

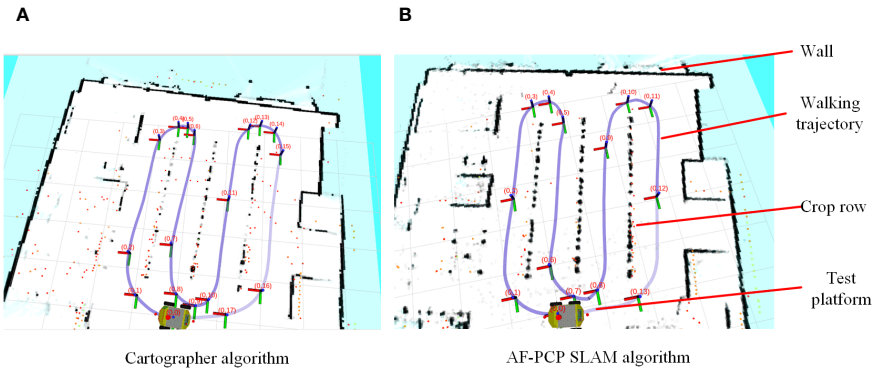

FIGURE 8
Visualization of the results of the Rviz map construction and localization trajectories. **(A)** The map construction results of the Cartographer algorithm. **(B)** The map construction results of the AF-PCP SLAM algorithm.

increased by 63.3%, 144.4%, 160%, 100%, 350%, and 116.7%, with an average increase of 155.7%.

In addition, as the LAD increased, the length of the crop rows constructed by the AF-PCP SLAM algorithm was close to the real length of the crop rows. When the LAD was greater than 3.877 m^2/m^3, the length of the crop row constructed by the Cartographer algorithm was close to the real length of the crop row. However, when the LAD was less than 3.877 m^2/m^3, the error between the crop row length constructed by the Cartographer algorithm and the real length was large. The average error in the crop row length calculated by the Cartographer algorithm was 0.086 m, and the coefficient of variation was 1.741%. The mean error of the crop row length constructed by the AF-PCP SLAM algorithm was 0.019 m, and the coefficient of variation was 0.217%. Thus, the mean error and coefficient of variation of the crop row length were reduced by 77.9% and 87.5%, respectively, with the AF-PCP SLAM algorithm.

Moreover, as the LAD increases, the maximum gap length decreases for both algorithms. When the LAD was 5.301 m^2/m^3, the maximum gap lengths obtained by the two methods were consistent with the true value of the set crop row spacing gap. When the LAD was between 3.887 m^2/m^3 and 4.83 m^2/m^3, the maximum gap length obtained by the Cartographer algorithm changed more slowly. However, when the LAD was between 2.945 m^2/m^3 and 3.416 m^2/m^3, the maximum gap lengths obtained by the Cartographer algorithm were 0.458 m and 1.2 m, respectively. The maximum gap lengths obtained by the AF-PCP SLAM algorithm were 0.125 m and 0.223 m, which were better than those obtained by the Cartographer algorithm. The maximum gap length obtained by the Cartographer algorithm was 1.2 m, and the mean value was 0.456 m. The maximum gap length obtained by the AF-PCP SLAM algorithm was 0.223 m, and the mean value was 0.124 m, which is 72.8% lower than that of the Cartographer algorithm.

The crop row length in the mapping results reflects the quality of the crop row end map construction to a certain extent, and the lack of a constructed row end map and the increase in the maximum gap length increase the error rate of the path planning algorithm. When the maximum gap length exceeds the width of the robot body, the path planning algorithm chooses a closer route, resulting in errors in the global path planning of the robot. When the LAD is reduced to 3.877 m^2/m^3, the mapping results of the Cartographer algorithm no longer represent most of the crop information in the environment, while the AF-PCP SLAM algorithm can still achieve accurate mapping of crop rows; thus, the AF-PCP SLAM algorithm has higher mapping robustness.

3.2 Localization performance

According to the localization accuracy evaluation criteria presented in Section 2.3.2, the localization errors of the AF-PCP SLAM algorithm and track deduction algorithm were calculated at different speeds. Figure 11 shows the trajectories of robots operating at speeds of 0.2 m/s, 0.4 m/s, and 0.6 m/s and the error curves in the *x*, *y*, and *z* directions. The RPE was used to analyze these results, and for each timestamp, the absolute difference between the true pose and the estimated pose was calculated. To highlight the RPE during the robot's movement, Figure 12 shows the error between the AF-PCP SLAM algorithm, the track deduction algorithm, and the real trajectory and maps the error to the trajectory through color coding. Figure 13 shows the curves of the RPE, mean, median, root mean square error, and standard deviation over time. The quantitative results of the error calculation are shown in Table 2.

Figure 11A shows different trajectories: location_pos_remap represents the localization trajectory of the true ultrasonic value, tracked_pose represents the pose trajectory calculated by the AF-PCP SLAM algorithm, and Odom represents the pose trajectory calculated by the track inference algorithm. Figure 11B shows the time-varying pose values in the *x*, *y*, and *z* directions. Since the robot moves in a two-dimensional plane, the value in the *z* direction is always 0. In each experiment, three extreme values are generated, which represent the moment when the robot turns at the end of a row. The results of the three experiments show that the pose trajectory calculated by the AF-PCP SLAM algorithm is closer to the real value than that calculated by the track deduction algorithm. The red circle in Figure 11 marks the position where the robot turns at the end of the last row, which corresponds to the maximum localization error.

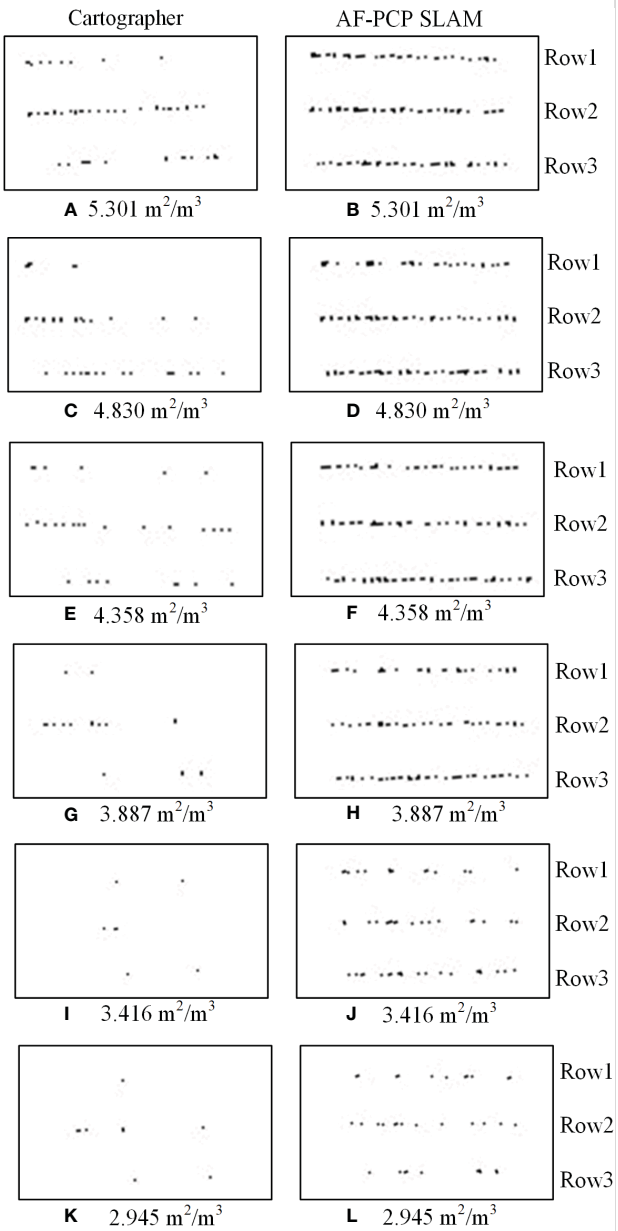

FIGURE 9
Results of the mapping of the two algorithms. The map construction results of the Cartographer algorithm under sparsities of **(A)** 100%, **(C)** 90%, **(E)** 80%, **(G)** 70%, **(I)** 60%, and **(K)** 50%. The map construction results of the AF-PCP SLAM algorithm under sparsities of **(B)** 100%, **(D)** 90%, **(F)** 80%, **(H)** 70%, **(J)** 60%, and **(L)** 50%. AF-PCP, adaptive filtering point cloud projection.

According to the test results shown in Figures 12, 13, the average localization error is 0.026 m, and the maximum localization error is 0.127 m when the robot moves at 0.2 m/s. When the robot moves at 0.4 m/s and 0.6 m/s, the initial fluctuation in the ultrasonic signal affects the maximum localization error; the average localization errors are 0.029 m and 0.046 m, respectively, which indicates that the localization accuracy is relatively stable. In contrast, the track deduction algorithm has a serious error accumulation problem. The average localization error of the track deduction algorithm is generally greater than 0.12 m, and the average localization error reaches as high as 0.233 m at a speed of 0.6 m/s. The AF-PCP SLAM algorithm is based on the localization of laser matching, which is not sensitive to error accumulation or the environment, so it has higher localization accuracy. The experimental results in Table 2 show that the AF-PCP SLAM algorithm proposed in this paper can achieve high-precision localization of robots at movement speeds of 0.2 m/s, 0.4 m/s, and 0.6 m/s. The average localization error of the AF-PCP SLAM algorithm is reduced by 79.8%, 78.9%, and 80.3% at these three speeds compared with the error of the track deduction algorithm, and the average localization error is reduced by 79.9%.

3.3 The actual greenhouse environment performance

To verify the ability of the AF-PCP SLAM algorithm to construct maps in actual greenhouse scenes, a greenhouse experiment was carried out at the “Doctor” farm base in Pinggu District, Beijing. The cucumber cultivar Yutian 156 was planted in this field, with a row width of 1.2 m. In the experiment, the Cartographer algorithm and AF-PCP SLAM algorithm were used to construct the map of the greenhouse. The robot walked along the crop rows at a speed of 0.2 m/s, and a map of the three rows of crops was constructed. The experimental environment and the map construction results of the two algorithms are shown in Figure 14.

Figure 14A shows the greenhouse test scenario, and Figures 14B, C are the map construction results of the Cartographer algorithm and AF-PCP SLAM algorithm, respectively. Figure 14A shows that due to the larger leaves of the actual greenhouse crops, the difference between the two algorithms in the actual greenhouse scene is more obvious. Figures 14B, C show that, compared with the Cartographer algorithm, the AF-PCP SLAM algorithm has a larger mapping area for crop rows. Accurate mapping of crop row contours can effectively control the moving trajectory and range of motion during robot navigation and effectively avoid damaging crops during robot operation. Moreover, row2 and row3 in Figure 14B exhibit obvious drifts because uneven ground reduces the mapping accuracy of crop rows and leads to map drift compared with that in the laboratory scene. The corresponding row2 and row3 drifts in Figure 14C are small, which also reflects, to some extent, that the AF-PCP SLAM algorithm has higher mapping robustness in actual greenhouse scenes.

4 Discussion

4.1 Discussion of the mapping results

Suspended plant patterns are widely used in greenhouses and agricultural environments. In this experiment, mobile robots walked along crop rows in greenhouses. However, the robot is in a repeated scene when walking between crop rows. Because crop rows usually have highly repetitive structures, with long, narrow, and tall rows, this poses a challenge in map construction. When

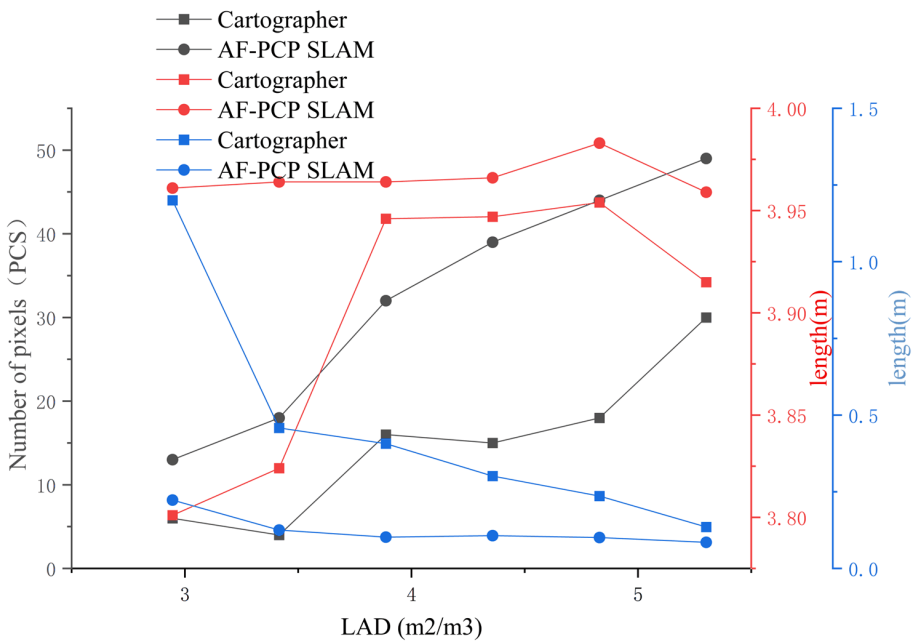

FIGURE 10
Map quantitative indicators under different LADs. The black, red, and blue symbols represent the number of pixels in the crop row, the length of the crop row, and the maximum gap length, respectively. LADs, leaf area densities.

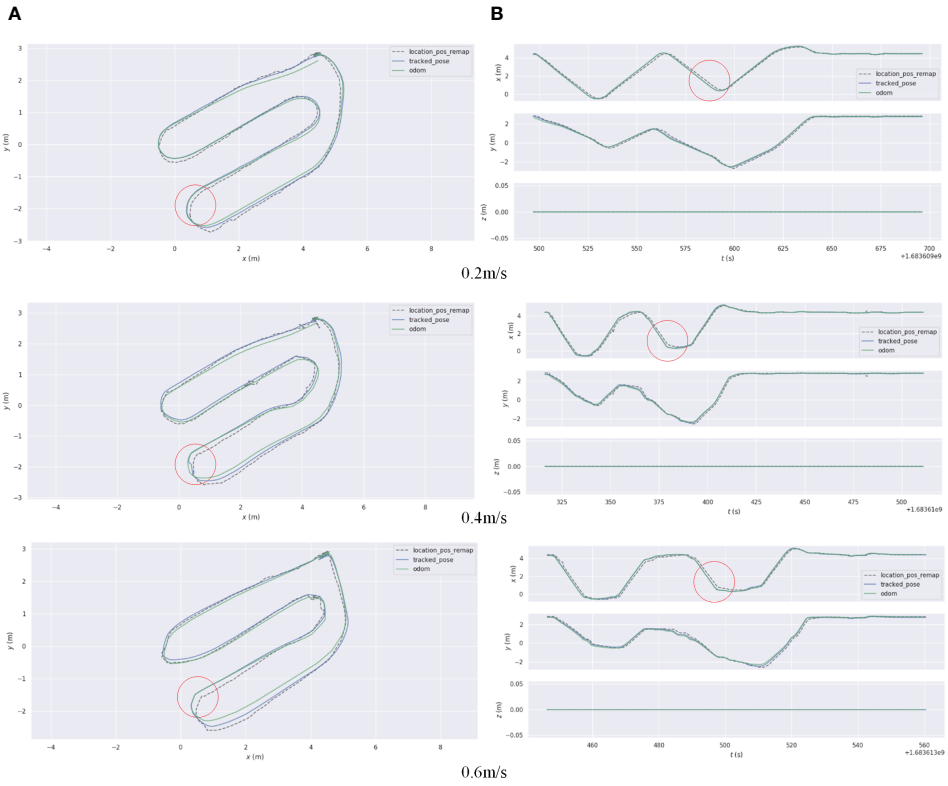

FIGURE 11
(A) A comparison of the absolute localization errors between the AF-PCP SLAM algorithm and Odom and the real trajectory. **(B)** A comparison of the error curves in the *x* and *y* directions over time. AF-PCP, adaptive filtering point cloud projection.

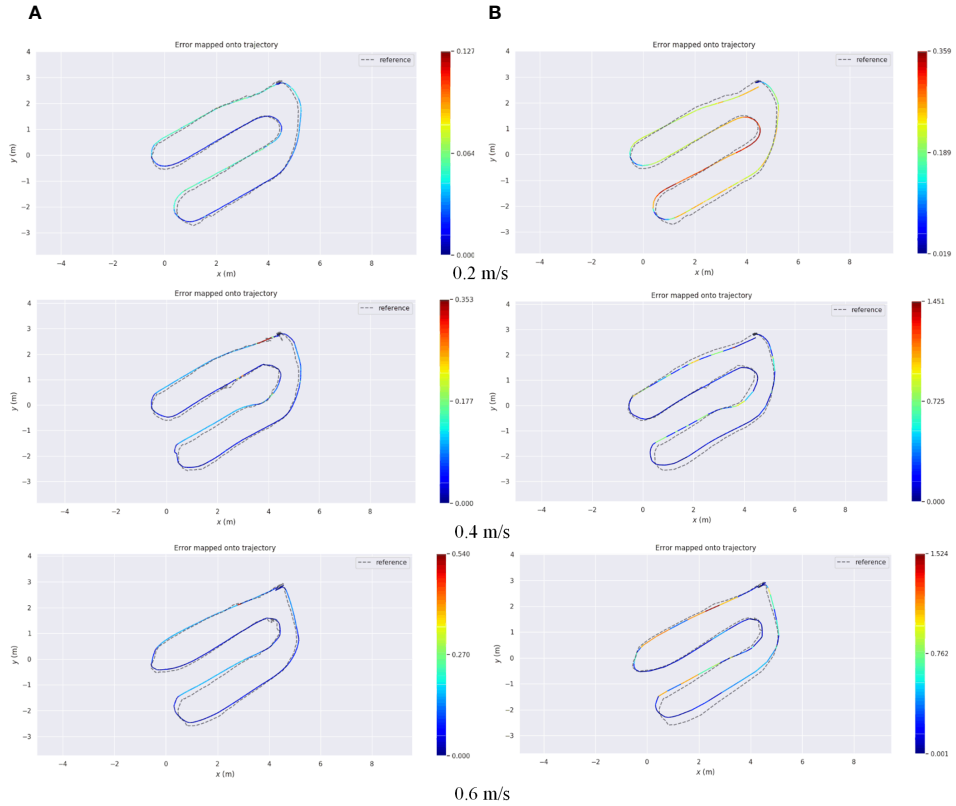

FIGURE 12
AF-PCP SLAM algorithm and Odom localization error. **(A)** The error in the trajectory of the AF-PCP SLAM algorithm. **(B)** The error in Odom. AF-PCP, adaptive filtering point cloud projection.

constructing a map in a low-density canopy environment, crop rows may have missing content, such as voids and gaps. There are two reasons for this. First, when the laser beam passes through a gap in the leaves, another row of crops may be detected, or the wall may be directly detected, resulting in inconsistent observation results. This reduces the probability of obstacles in the occupied grid map corresponding to this position, which leads to the degradation of the map. Second, the irregular structure of the blade may cause the laser detection results of blades at the same position to be inconsistent under different robot poses. As the canopy leaf area density decreases, this situation is aggravated, resulting in the absence of crop rows on the map. To address these problems, in this paper, the innovative AF-PCP SLAM algorithm is designed, which fully considers the spatial characteristics of suspended crops in greenhouses, extracts and compresses the map contour based on 16-line LiDAR data, and maps the data to a 2D plane to establish the environment map and localize the robot. This innovative approach addresses the abovementioned map degradation problem, thereby improving the accuracy and robustness of the mapping results.

4.2 Discussion of the localization results

Due to the equidistant distribution of greenhouse crop rows, greenhouse environments have a high degree of symmetry, forming a "corridor scene". The corridor problem is one of the key problems faced by the SLAM method. Because the LiDAR detection results are similar, they cannot reflect the actual displacement in the forward direction, which may introduce localization inaccuracies in the forward direction with the SLAM method. According to Figure 11A, in this experiment, the results estimated by the Odom localization method are accurate in the initial row. However, when the robot moves to the end of the crop row and turns into the next row, the localization error of the Odom algorithm in the *y* direction increases with increasing distance. When the robot returns to the starting point, the pose estimation error of the Odom algorithm is approximately 0.2 m. According to Figure 11B, the position of the extreme point corresponds to the trajectory in Figure 11A. The trajectory position of the red circle in Figure 11A corresponds to the error at the position of the red circle labeled in Figure 11B. The three tests show that the error in the *x* direction is the largest at this time. We believe that this phenomenon occurs because when the agricultural robot turns, the deviation in the *y* direction increases due to errors in the robot's coordinate system. This is due to the limitations of the two-wheel differential model. Even after the odometer calibration, the deviation in the *y* direction increases rapidly as the distance increases. The *x*-direction error in Figure 11B is mainly caused by the *y*-direction error component in the robot coordinate system, so the maximum error is generated after the robot turns down the last row. At this moment, the localization error of the AF-PCP SLAM algorithm proposed in

10.3389/fpls.2024.1276799

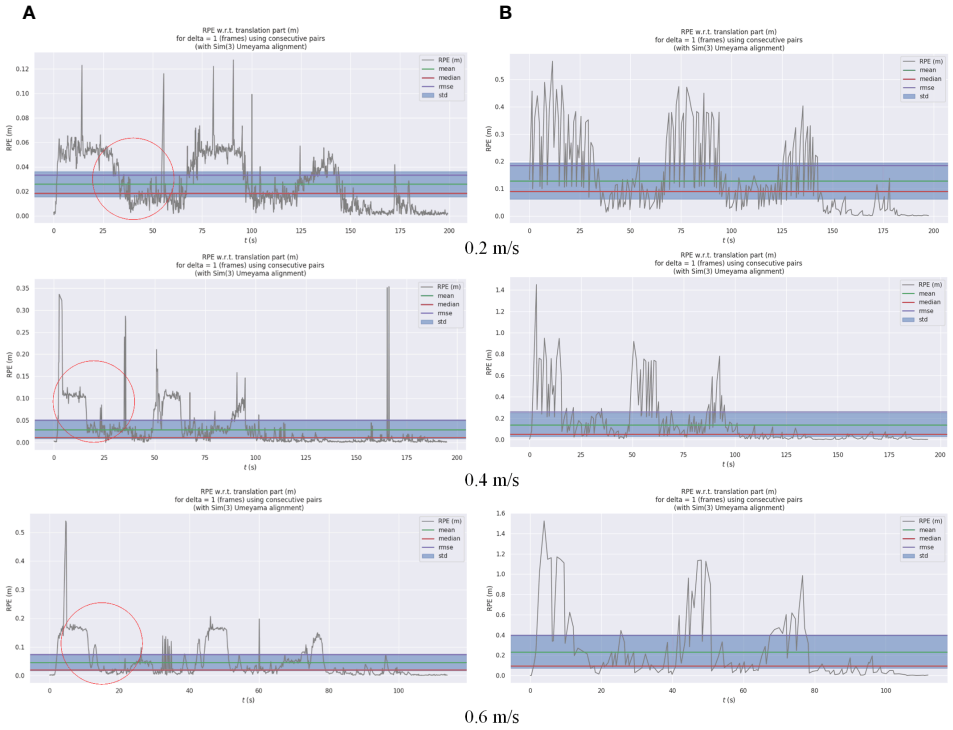

FIGURE 13
Odom and AF-PCP SLAM algorithm localization errors. **(A)** The curve of the relative pose error (RPE) of the AF-PCP SLAM algorithm with time. **(B)** The curve of the RPE of Odom with time. AF-PCP, adaptive filtering point cloud projection.

this paper is much smaller than that of the track deduction algorithm, which allows the robot to accurately navigate to the next crop row according to the path planning algorithm, thus reducing the risk of row-end collisions during robot navigation. The results shown in Table 2 intuitively reflect the influence of the three moving speeds on the localization accuracy. With increasing moving speed, the mean, maximum, and standard deviation of the localization error increase. The reason is that the increase in the mechanical vibration of the robot causes additional input noise, which affects the collection of the point cloud data and the matching effect of the point cloud. Moreover, as the processing efficiency of the algorithm remains unchanged, an increase in the rate of change in the robot pose leads to a decrease in the localization accuracy.

In Figure 12, there is a certain regularity between the fluctuations in the RPE value and the extreme point position of the error curve in the x direction in Figure 10B. For example, the RPE value at the position indicated by the red circle in Figure 12A decreases in all three speed tests. The position of the decrease corresponds to the extreme point in the error curve, that is, the moment when the robot moves to the end of the row. Although the increase in the error is small (only 2 cm), there is a certain regularity in the results. This phenomenon may be related to robot system errors and may also be related to ultrasonic localization labeling errors. Through repeated comparisons, we believe that this phenomenon is related to the physical characteristics of the ultrasonic localization labeling method. When the robot moves between rows, the localization accuracy of the ultrasonic label is reduced due to the occlusion of the canopy crop. When the robot moves to the end of the crop row, the occlusion effect of the crop row is reduced. At this time, the vehicle label carried by the robot is

TABLE 2 RPE values of the AF-PCP SLAM algorithm, Cartographer algorithm, and Odom.

Test ID	Methods	Max	Mean	Median	RMSE	Std
0.2	AF-PCP SLAM	0.127	0.026	0.018	0.033	0.021
	Cartographer	0.371	0.038	0.039	0.063	0.022
	Odom	0.567	0.129	0.090	0.185	0.133
0.4	AF-PCP SLAM	0.353	0.029	0.012	0.051	0.042
	Cartographer	0.109	0.047	0.044	0.085	0.028
	Odom	1.451	0.138	0.050	0.259	0.220
0.6	AF-PCP SLAM	0.540	0.046	0.020	0.074	0.058
	Cartographer	0.842	0.035	0.031	0.087	0.020
	Odom	1.524	0.233	0.095	0.397	0.322

RPE, relative pose error; AF-PCP, adaptive filtering point cloud projection; RMSE, root mean square error.

FIGURE 14
The actual greenhouse scenario test **(A)** The greenhouse test scenario. **(B)** The map construction results of the Cartographer algorithm. **(C)** Tthe map construction results of the AF-PCP SLAM algorithm.

closer to the localization label arranged in the environment, thereby improving the localization accuracy. This study did not deploy ultrasound tags in greenhouse scenarios. In future work, we will deploy this module in actual greenhouse scenarios as an input to the system for large-scale scene localization. Based on the error characteristics of ultrasound tags, trajectory inference algorithms, and SLAM positioning algorithms, the fusion of the three can achieve robust localization in complex environments. This is also another research work we are currently conducting.

For agricultural robots, real-time localization of crop rows and turns in large-scale greenhouse environments must be achieved. The proposed AF-PCP SLAM algorithm can accurately estimate the trajectory, as shown in Figure 12A. The maximum average RPE is 0.046 m. The proposed method was shown to have high robustness and accuracy in challenging agricultural environments, outperforming the current state-of-the-art approaches.

5 Conclusion

Aiming to address the problem that low-density canopy environments in greenhouses affect the robustness and localization accuracy of SLAM methods, in this paper, a spatial downsampling map construction and localization method based on the Cartographer framework is proposed, an adaptive filtering spatial point cloud projection algorithm is designed, and a

greenhouse map construction and high-precision pose estimation system are developed. For greenhouse crop leaf area densities ranging from 2.945 m^2/m^3 to 5.301 m^2/m^3, the method proposed in this paper can accurately model the contours of sparse crop rows. Compared with that of the Cartographer algorithm, the map area of the AF-PCP SLAM algorithm for the crop row increased by 155.7%. The mean error and coefficient of variation for the crop row length were 0.019 m and 0.217%, respectively, which were respectively 77.9% and 87.5% less than those of the Cartographer algorithm. The average maximum void length was 0.124 m, which was 72.8% less than that of the Cartographer algorithm. Localization tests were carried out at speeds of 0.2 m/s, 0.4 m/s, and 0.6 m/s. The average relative localization errors of the actual motion trajectory and the real path were 0.026 m, 0.029 m, and 0.046 m, respectively, and the standard deviations were less than 0.06 m. Compared with those of the track deduction algorithm, the average localization error was reduced by 79.9%. These results show that the method can meet the requirements of map construction and localization in greenhouse environments. Thus, the proposed method is an effective approach for the autonomous operation of agricultural robots, providing a basis for localization and perception for efficient decision-making and safe operation of intelligent agricultural machinery and equipment in greenhouses.

Data availability statement

The raw data supporting the conclusions of this article will be made available by the authors, without undue reservation.

Author contributions

HT: Conceptualization, Data curation, Funding acquisition, Investigation, Methodology, Resources, Supervision, Validation, Visualization, Writing – original draft, Writing – review & editing. XZ: Conceptualization, Data curation, Investigation, Methodology, Software, Validation, Writing – review & editing. CZ: Conceptualization, Funding acquisition, Investigation, Methodology, Project administration, Resources, Supervision, Validation, Writing – original draft, Writing – review & editing. HF: Software, Visualization, Writing – review & editing. LC: Formal Analysis, Funding acquisition, Writing – review & editing. MY: Formal Analysis, Funding acquisition, Writing – review & editing.

Funding

The author(s) declare financial support was received for the research, authorship, and/or publication of this article. This work was financially supported by the Jiangsu Province Agricultural Science and Technology Independent Innovation Fund Project (Grant number: CX (21) 2006), the Jiangsu Province Key Research and Development Plan Project (BE2021302), the Youth Research Fund of the Beijing Academy of Agriculture and Forestry Sciences (Grant number: QNJJ202013), the Beijing Academy of Agricultural and Forestry Sciences Science and Technology Innovation Capacity Construction Project (KJCX20210402).

Conflict of interest

Author XZ was employed by company Beijing PAIDE Science and Technology Development Co., Ltd.

The remaining authors declare that the research was conducted in the absence of any commercial or financial relationships that could be construed as a potential conflict of interest.

Publisher's note

References

Abanay, A., Masmoudi, L., El Ansari, M., Gonzalez-Jimenez, J., and Moreno, F.-A. (2022). LIDAR-based autonomous navigation method for an agricultural mobile robot in strawberry greenhouse: agriEco robot. *AIMS Electron. Electr. Eng.* 6, 317–328. doi: 10.3934/electreng.2022019

Aguiar, A. S., dos Santos, F. N., Sobreira, H., Boaventura-Cunha, J., and Sousa, A. J. (2022). Localization and mapping on agriculture based on point-feature extraction and semiplanes segmentation from 3D LiDAR data. *Front. Robot. AI* 9. doi: 10.3389/frobt.2022.832165

Bai, Y., Zhang, B., Xu, N., Zhou, J., Shi, J., and Diao, Z. (2023). Vision-based navigation and guidance for agricultural autonomous vehicles and robots: a review. *Comput. Electron. Agric.* 205, 107584. doi: 10.1016/j.compag.2022.107584

Chen, X., Milioto, A., Palazzolo, E., Giguere, P., Behley, J., and Stachniss, C. (2019). "Suma++: efficient lidar-based semantic slam," in *2019 IEEE/RSJ International Conference on Intelligent Robots and Systems (IROS)*, Macau, China. 4530–4537 (IEEE).

Chen, S. W., Nardari, G. V., Lee, E. S., Qu, C., Liu, X., Romero, R. A. F., et al. (2020). Sloam: semantic lidar odometry and mapping for forest inventory. *IEEE Robot. Autom. Lett.* 5 (2), 612–619. doi: 10.1109/LRA.2019.2963823

Chen, X., Wang, S. A., Zhang, B., and Luo, L. (2018). Multi-feature fusion tree trunk detection and orchard mobile robot localization using camera/ultrasonic sensors. *Comput. Electron. Agric.* 147, 91–108. doi: 10.1016/j.compag.2018.02.009

Choi, T., Park, J., Kim, J.-J., Shin, Y.-S., and Seo, H. (2022). Work efficiency analysis of multiple heterogeneous robots for harvesting crops in smart greenhouses. *Agronomy* 12 (11), 2844. doi: 10.3390/agronomy12112844

Dong, W., Roy, P., and Isler, V. (2020). Semantic mapping for orchard environments by merging two-sides reconstructions of tree rows. *J. Field Robot.* 37 (1), 97–121. doi: 10.1002/rob.21876

Fu, H., Zhao, X., Wu, H., Zheng, S., Zheng, K., and Zhai, C. (2022). Design and experimental verification of the YOLOV5 model implanted with a transformer module for target-oriented spraying in cabbage farming. *Agronomy* 12 (10), 2551. doi: 10.3390/agronomy12102551

Gu, C., Zhai, C., Chen, L., Li, Q., Hu, L. N., and Yang, F. (2021). Detection model of tree canopy leaf area based on LiDAR technology. *Trans. Chin. Soc Agric. Mach.* 52 (11), 278–286. doi: 10.6041/j.issn.1000-1298.2021.11.030

Hess, W., Kohler, D., Rapp, H., and Andor, D. (2016). "Real-time loop closure in 2D LIDAR SLAM," in *2016 IEEE International Conference on Robotics and Automation (ICRA)*, Stockholm, Sweden. 1271–1278 (IEEE).

Hou, J., Pu, W., Li, T., Ding, X., and Zhang, G. (2020). Design and implementation of mobile greenhouse environmental monitoring system based on UWB and internet of things. *Trans. Chin. Soc Agric. Eng. (Trans. CSAE)* 36 (23), 229. doi: 10.11975/j.issn.1002-6819.2020.23.027

Huang, Z., Shiigi, T., Tsay, L. W. J., Nakanishi, H., Suzuki, T., Ogawa, Y., et al. (2021). A sound-based positioning system with centimeter accuracy for mobile robots in a greenhouse using frequency shift compensation. *Comput. Electron. Agric.* 187, 106235. doi: 10.1016/j.compag.2021.106235

Huang, Z., and Sugiyama, S. (2022). Research progress and enlightenment of Japanese harvesting robot in facility agriculture. *Smart Agric.* 4 (2), 135–149. doi: 10.12133/j.smartag.SA202202008

Jiang, A., and Ahamed, T. (2023). Navigation of an autonomous spraying robot for orchard operations using LiDAR for tree trunk detection. *Sensors* 23 (10), 4808. doi: 10.3390/s23104808

Jiang, S., Wang, S., Yi, Z., Zhang, M., and Lv, X. (2022). Autonomous navigation system of greenhouse mobile robot based on 3D lidar and 2D lidar SLAM. *Front. Plant Sci.* 13. doi: 10.3389/fpls.2022.815218

Jin, Y., Liu, J., Xu, Z., Yuan, S., Li, P., and Wang, J. (2021). Development status and trend of agricultural robot technology. *Int. J. Agric. Biol. Eng.* 14 (4), 1–19. doi: 10.25165/j.ijabe.20211404.6821

Lao, C., Li, P., and Feng, Y. (2021). Path planning of greenhouse robot based on fusion of improved A* algorithm and dynamic window approach. *Nongye Jixie Xuebao/Trans. Chin. Soc Agric. Mach.* 52 (1), 14–22. doi: 10.6041/j.issn.1000-1298.2021.01.002

Li, C., Li, Y., Tan, H., Wang, X., and Zhai, C. (2022). Grading detection method of grape downy mildew based on K-means clustering and random forest algorithm. *J. Agric. Mach.* 53 (05), 225–236. doi: 10.6041/j.issn.1000-1298.2022.05.023

Long, Z., Xiang, Y., Lei, X., Li, Y., Hu, Z., and Dai, X. (2022). Integrated indoor positioning system of greenhouse robot based on UWB/IMU/ODOM/LIDAR. *Sensors* 22 (13), 4819. doi: 10.3390/s22134819

Matsuzaki, S., Masuzawa, H., Miura, J., and Oishi, S. (2018). "3D semantic mapping in greenhouses for agricultural mobile robots with robust object recognition using robots' trajectory," in *2018 IEEE International Conference on Systems, Man, and Cybernetics (SMC)*, Miyazaki, Japan. 357–362 (IEEE).

Mendes, J. M., dos Santos, F. N., Ferraz, N. A., do Couto, P. M., and dos Santos, R. M. (2019). Localization based on natural features detector for steep slope vineyards. *J. Intell. Robot. Syst.* 93 (3), 433–446. doi: 10.1007/s10846-017-0770-8

Nissimov, S., Goldberger, J., and Alchanatis, V. (2015). Obstacle detection in a greenhouse environment using the kinect sensor. *Comput. Electron. Agric.* 113, 104–115. doi: 10.1016/j.compag.2015.02.001

Ouyang, C., Hatsugai, E., and Shimizu, I. (2022). Tomato disease monitoring system using modular extendable mobile robot for greenhouses: automatically reporting locations of diseased tomatoes. *Agronomy* 12 (12), 3160. doi: 10.3390/agronomy12123160

Palleja, T., and Landers, A. J. (2017). Real time canopy density validation using ultrasonic envelope signals and point quadrat analysis. *Comput. Electron. Agric.* 134, 43–50. doi: 10.1016/j.compag.2017.01.012

Qiao, Y., Valente, J., Su, D., Zhang, Z., and He, D. (2022). Editorial: AI, sensors and robotics in plant phenotyping and precision agriculture. *Front. Plant Sci.* 13. doi: 10.3389/fpls.2022.1064219

Saha, K. K., Tsoulias, N., Weltzien, C., and Zude-Sasse, M. (2022). Estimation of vegetative growth in strawberry plants using mobile LiDAR laser scanner. *Horticulturae* 8 (2), 90. doi: 10.3390/horticulturae8020090

Shamshiri, R. R., Weltzien, C., Hameed, I. A., Yule, I. J., Grift, T. E., Balasundram, S. K., et al. (2018). Research and development in agricultural robotics: a perspective of digital farming. *Int. J. Agric. Biol. Eng.* 11 (4), 1–14. doi: 10.25165/j.ijabe.20181104.4278

Shi, Y., Wang, H., Yang, T., Liu, L., and Cui, Y. (2020). Integrated navigation by a greenhouse robot based on an odometer/lidar. *Instrum. Mes. Métrol.* 19 (2), 91–101. doi: 10.18280/i2m.190203

Su, L., Liu, R., Liu, K., Li, K., Liu, L., and Shi, Y. (2023). Greenhouse tomato picking robot chassis. *Agriculture* 13 (3), 532. doi: 10.3390/agriculture13030532

Sun, N., Qiu, Q., Fan, Z., Li, T., Ji, C., Feng, Q., et al. (2022). Intrinsic calibration of multi-beam LiDARs for agricultural robots. *Remote Sens.* 14 (19), 4846. doi: 10.3390/rs14194846

Wang, T., Chen, B., Zhang, Z., Li, H., and Zhang, M. (2022a). Applications of machine vision in agricultural robot navigation: a review. *Comput. Electron. Agric.* 198, 107085. doi: 10.1016/j.compag.2022.107085

Wang, Y., Yan, G., Meng, Q., Yao, T., Han, J., and Zhang, B. (2022b). DSE-YOLO: detail semantics enhancement YOLO for multi-stage strawberry detection. *Comput. Electron. Agric.* 198, 107057. doi: 10.1016/j.compag.2022.107057

Westling, F., Underwood, J., and Bryson, M. (2021). A procedure for automated tree pruning suggestion using LiDAR scans of fruit trees. *Comput. Electron. Agric.* 187, 106274. doi: 10.1016/j.compag.2021.106274

Xie, H., Chen, W., and Fan, Y. (2021). Visual-inertial SLAM in featureless environments on lunar surface. *Acta Aeronautica Astronautica Sinica.* 42 (1), 524169. doi: 10.7527/S1000-6893

Yan, Y., Zhang, B., Zhou, J., Zhang, Y., and Liu, X. A. (2022). Real-time localization and mapping utilizing multi-sensor fusion and visual–IMU–wheel odometry for agricultural robots in unstructured, dynamic and GPS-denied greenhouse environments. *Agronomy* 12 (8), 1740. doi: 10.3390/agronomy12081740

Yao, L., Hu, D., Zhao, C., Yang, Z., and Zhang, Z. (2021). Wireless positioning and path tracking for a mobile platform in greenhouse. *Int. J. Agric. Biol. Eng.* 14 (1), 216–223. doi: 10.25165/j.ijabe.20211401.5627

Zhai, C., Yang, S., Wang, X., Zhang, C., and Song, J. (2022). Status and prospect of intelligent measurement and control technology for agricultural equipment. *Trans. Chin. Soc Agric. Mach.* 53 (4), 1–20. doi: 10.6041/j.issn.1000-1298.2022.04.001

Zhang, W., Gong, L., Huang, S., Wu, S., and Liu, C. (2022). Factor graph-based high-precision visual positioning for agricultural robots with fiducial markers. *Comput. Electron. Agric.* 201, 107295. doi: 10.1016/j.compag.2022.107295

Zhang, S., Guo, C., Gao, Z., Sugirbay, A., Chen, J., and Chen, Y. (2020). Research on 2D laser automatic navigation control for standardized orchard. *Appl. Sci.* 10 (8), 2763. doi: 10.3390/app10082763

Zhou, H., Zhang, J., Ge, L., Yu, X., Wang, Y., and Zhang, C. (2021). Research on volume prediction of single tree canopy based on three-dimensional (3D) LiDAR and clustering segmentation. *Int. J. Remote Sens.* 42 (2), 738–755. doi: 10.1080/01431161.2020.1811917

frontiers | Frontiers in Plant Science

TYPE Original Research
PUBLISHED 05 March 2024
DOI 10.3389/fpls.2024.1297182

OPEN ACCESS

EDITED BY
Jianli Song,
China Agricultural University, China

REVIEWED BY
Yunling Liu,
China Agricultural University, China
Longlong Li,
Beijing Academy of Agricultural and Forestry Sciences, China
Muhammad Shoaib,
Bahauddin Zakariya University, Pakistan
Pengchao Chen,
South China Agricultural University, China
Qiang Lyu,
Southwest University, China

*CORRESPONDENCE
Xiao-Ya Dong
dongxiaoya@ujs.edu.cn
Bai-Jing Qiu
qbj@ujs.edu.cn

RECEIVED 19 September 2023
ACCEPTED 15 February 2024
PUBLISHED 05 March 2024

CITATION
Dong X-Y, Tong X, Ma J and Qiu B-J (2024) Design and evaluate the performance of a mechanical system for the release of *Harmonia axyridis* adults. *Front. Plant Sci.* 15:1297182. doi: 10.3389/fpls.2024.1297182

Design and evaluate the performance of a mechanical system for the release of *Harmonia axyridis* adults

Xiao-Ya Dong[1,2*], Xiang Tong[1], Jing Ma[1] and Bai-Jing Qiu[1,2*]

[1]Key Laboratory of Modern Agricultural Equipment and Technology, Ministry of Education, Jiangsu University, Zhenjiang, Jiangsu, China, [2]Key Laboratory of Plant Protection Engineering, Ministry of Agriculture and Rural Affairs, Jiangsu University, Zhenjiang, Jiangsu, China

Harmonia axyridis (*H. axyridis*) is the natural enemy of many aphid species. Traditional manual release of *H. axyridis* adults requires substantial manpower, and release efficiency is low. Automatic mechanical devices can improve the efficiency of delivery. Based on *H. axyridis* adults' morphological size, a prototype release system for *H. axyridis* was designed, which considered the adhesion characteristics of *H. axyridis* adults. According to the measured physical characteristics of *H. axyridis* adults, the structural parameters of the mechanical system for the release of the *H. axyridis* adults were determined. The relationship of the quantity of release, the impeller rotating speed, and the time for the release of *H. axyridis* adults were constructed. The mechanism can quantitatively adjust the number of *H. axyridis* adults to meet a certain *H. axyridis*–aphids ratio. Combining the image processing technology with the camera function of a mobile phone, the maximum cross-sectional area method was used to count the *H. axyridis* adults in the designated area. Results showed that the impeller rotating speed had a significant effect on the survival rate of the *H. axyridis* adults. When the airflow velocities were 29.5 m/s and 38.3 m/s, the survival rates of the *H. axyridis* adults were 93.8% and 94.5% at 4.2 rpm. The adhesion rate of the *H. axyridis* adults was 2.5%–4.6%. This work will provide technical support for the research of biological control.

KEYWORDS

biological control, mechanical release, *Harmonia axyridis*, natural enemies, mechanical distribution

1 Introduction

The primary method for protecting crops from pests is currently chemical control. However, the long-term use of chemical insecticides can lead to pest resistance and compromise the effectiveness of pest control (Alyokhin et al., 2007; Andrei et al., 2008; Yu and Powles, 2014). Biological control is a sustainable and environmentally friendly approach

(Pilkington et al., 2010). This approach usually uses natural enemies to manage pests such as insects, mites, weeds, and plant diseases (Lanzoni et al., 2017). Compared to chemical control, biological control has been widely recognized as a promising solution to address environmental pollution and pesticide residues (Gan-Mor and Matthews, 2003). Therefore, biological control has attracted considerable interest in the field of crop protection. However, the manual release of natural enemies for crop protection necessitates a large labor force. The workers who released natural enemies were required to endure a prolonged period in a humid and hot environment, experiencing fatigue and discomfort. To solve this issue, considerable efforts have been dedicated to creating mechanical systems for the distribution of natural predators.

Since the advent of mechanical systems for the release of natural enemies (Pickett et al., 1987), numerous strategies have been developed to cater to varying release requirements. Based on the type of external force employed, these mechanical systems for releasing natural enemies can be categorized into three classes. The first class is the centrifugal release system, which utilizes centrifugal force generated by the rotation of a disc or sliding plate to eject predators (Giles et al., 1995; Casey and Parrella, 2005; Blandini et al., 2008; Emma et al., 2010; Zappala et al., 2012). In a typical centrifugal release system, predators are enclosed in a hopper with carrier materials, and the release process is powered by two electric motors. The second class is the pneumatic release system. The natural predators were released into a diffuser by force of gravity (Papa et al., 2018). The diffuser relies on a centrifugal fan to generate high-speed airflow to transport the natural predators. Pezzi and his coworkers (Pezzi et al., 2015) designed a novel air-assisted release prototype, wherein a commercial bottle filled with beneficial organisms and substrate can be inverted on the extraction system. The extraction system is constituted of a push rod with a metal spike with reciprocating movement generated by an electromagnet powered by a handheld battery. Last, the beneficial arthropods were transported via airflow. The last class is the vibration release system. The vibration release system combines vibration force with gravity. The predator-releasing device is fixed to the tractor using a three-point suspension in this system. As the tractor moves, Perillus binoculars are transported to the designated location. Using this release system, Khelifi and his work team (Khelifi et al., 2011) deployed two spotted stink bugs to manage the Colorado potato beetle. The aforementioned mechanical systems for the release of natural enemies predominantly release predators with a volume at the micron level. These systems disseminate mixtures of mites and carrier materials (Giles et al., 1995; Opit et al., 2005).

Harmonia axyridis (*H. axyridis*) has been extensively introduced for the biological control of agricultural pests (Haelewaters et al., 2017). These agricultural pests include aphids, bugs, psyllids, moths, and others. Instar larvae often exhibit cannibalism behavior (Osawa, 1992), and adult *H. axyridis* are more proficient at preying on pests. Consequently, *H. axyridis* adults are frequently released in fields or greenhouses for biological control purposes. To date, the mechanicalization of *H. axyridis* adult release has not been significantly advanced. Based on previous research, combining the first type of centrifugal release system and the second type of pneumatic release system, we design a release device that combines the centrifugal and the centrifugal. Based on the morphological size, area-restricted searching behavior, and adhesion properties of *H. axyridis* adults, we have developed a prototype for the release of *H. axyridis* adults. The prototype can be carried over the shoulder. The prototype can perform the following functions: (i) continuous or cycle-interrupted release and (ii) adjustment of working parameters: distribution distance and the number of *H. axyridis* adults. To assess the distribution performance of the prototype, the survival rate, distribution uniformity, and adhesion rate of *H. axyridis* adults have been characterized.

2 Materials and methods

2.1 Morphological size of *H. axyridis* adults

The morphological size of adult *H. axyridis* individuals is a crucial parameter in the design process of mechanical systems for the release. Therefore, *H. axyridis* adults purchased from a commercial insectary (J.D. Crop Protection Market, China) were used in this study. To overcome the challenges posed by the active movements of *H. axyridis* adults, 50 samples were placed in airtight tubes for 30 min to lose activity. As shown in Figure 1, the *H. axyridis* adult was approximated as a semi-ellipse. The length (L) of an *H. axyridis* adult was determined by measuring the distance from its head to its tail. The width (W) was defined as the distance perpendicular to the length in the horizontal plane. The H shown in Figure 1 is the height (H) of the *H. axyridis* adult. The L, W, and H of *H. axyridis* adults were measured using a digital display vernier caliper (German Knight MNT-150). The weight (m) of *H. axyridis* adults was determined using the electronic balance (Sartorius BT-125D).

To design an *H. axyridis* adult population adjustment mechanism, it was necessary to measure the angle of repose (φ) of *H. axyridis* adults. The φ has reference significance for the design of the tilting angle of the wall of the *H. axyridis* adults container

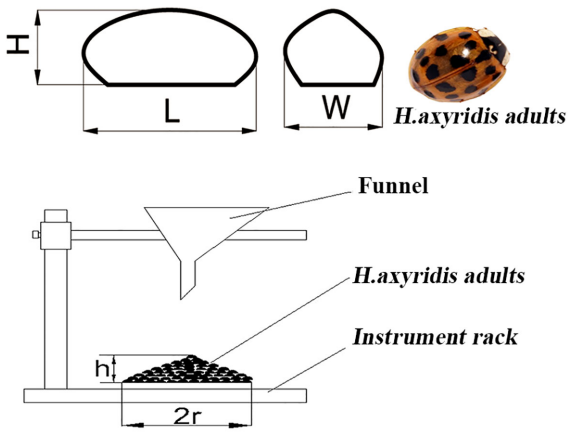

FIGURE 1
Measurement schematic of *H. axyridis* adults morphological size. L, W, and H are the length, width, and height of *H. axyridis* adults. h and 2r are the height and bottom surface length of the cone.

(Amidon et al., 2017). Theoretically, the tilting angle of the wall of the *H. axyridis* adults container should be smaller than φ of the *H. axyridis* adults, which is conducive to the flow of *H. axyridis* adults. A sample of 50 g of *H. axyridis* adults was packed into a funnel and freely dropped onto an instrument rack. H. Axridis adults form a cone pile on the instrument rack. The accumulation height h and the maximum section length of the bottom surface 2r were measured, and the angle of repose was calculated using the equation: φ = arctg h/r. The angle of repose was repeated five times. The morphological parameters of *H. axyridis* adult individuals are listed in Table 1.

2.2 Description of the mechanical system for the release of *H. axyridis* adults

The prototype of mechanical for release *H. axyridis* adults was designed to meet the following: (i) the *H. axyridis* adults are unharmed when they are released smoothly and (ii) can be carried on the shoulder of the operator.

To meet the requirement of mechanical release, we designed a release system for the distribution of *H. axyridis* adults. The structure of the release system is depicted in Figure 2. The release system mainly consisted of two parts. One was a mechanical section, and the other was a control section. The mechanical section included a centrifugal fan, rotating plate, impeller, and spray duct. The control section included a programmable logic controller (PLC) module, relay, and DC motor. The main characteristics of the prototype are detailed in Table 2.

The working principle is as follows: the gasoline engine drives the rotation of the centrifugal fan. The airflow velocity in the air channel is regulated by adjusting the speed of the centrifugal fan. The lithium battery supplies power to the PLC module and the DC motor. A timer in the PLC module regulates relay timings and determines how long the DC motor stays powered. During operation, the DC motor drives an adjustment mechanism to release *H. axyridis* adults, enabling them to enter the air channel. At high-speed airflow, *H. axyridis* adults are propelled through an air channel for their release. A 70° incline of the rotating plate relative to the horizontal plane is set for *H. axyridis* adults to effectively enter the air channel. If there is any malfunction in circuit control components, a drawbar is employed to rotate and align with the horizontal plane angle position. By manipulating the drawbar, the *H. axyridis* adults can be prevented from entering the air channel, effectively preventing further release. The mechanical system for the release of *H. axyridis* adults can be carried on the back via two shoulder straps.

TABLE 1 The morphological parameters of *H. axyridis* adult individuals.

Characteristics	Unit	Value
Length (L)	mm	5.89 ± 1.21
Width (W)	mm	4.29 ± 1.46
Height (H)	mm	1.95 ± 0.87
Angle of repose (φ)	°	36.32 ± 5.17
weight (m)	mg	21.36 ± 4.24

2.3 Adjustment mechanism for the release of *H. axyridis* adults

The crucial component of the mechanical system facilitating the release of *H. axyridis* adults was the adjustment mechanism. It included a coupling, a DC motor, an impeller, and a container. The *H. axyridis*–transport mechanism is illustrated in Figure 3. Because of gravity, the *H. axyridis* adults moved toward the space between the vanes. Upon rotation of the DC motor driving the impeller, *H. axyridis* adults were funneled toward the BC exit and cascaded into

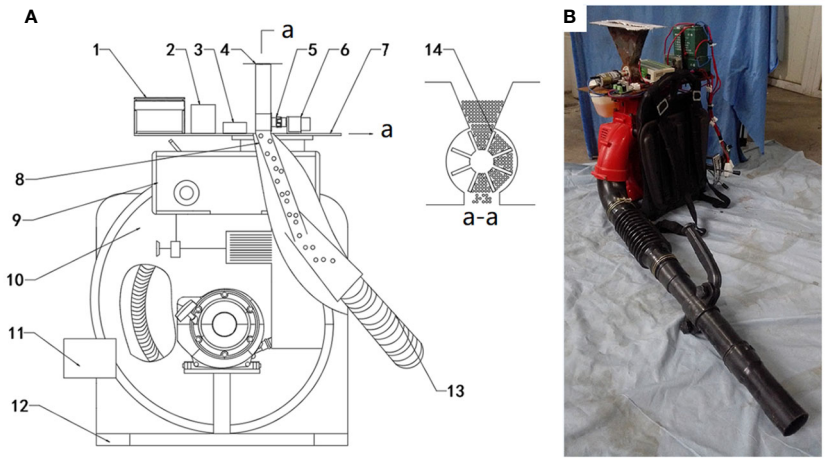

FIGURE 2
(A) Structure diagram of release system for *H. axyridis* adults: 1, lithium battery; 2, relay; 3, PLC module; 4, container; 5, coupling; 6, DC motor; 7, joint plate; 8, rotating plate; 9, petrol tank; 10, centrifugal fan; 11, control board; 12, frame; 13, air channel; 14, impeller. **(B)** Release system for the release of *Harmonia axyridis* adults.

TABLE 2 Main characteristics of the release system.

Characteristics	Unit	Value
Length	mm	590
Width	mm	320
Height	mm	600
Weight	kg	11.5
Capacity *H. axyridis* container	L	0.8
Matching power	kw	1.95
Air channel diameter	mm	75
Airflow velocity	m s^{-1}	29.5–38.3
Maximum horizontal distribution distance	m	5
H. axyridis number adjustment range		60–300

the air channel. The release of *H. axyridis* adults was completed with the addition of high-speed airflow. To ensure a uniform and steady release of *H. axyridis* adults, eight vanes were designed at equal intervals along the periphery of the impeller. The angle between two adjacent vanes was labeled as α, and the angle of repose was denoted as should correspond. Based on the value of the angle of repose measured in Table 1, we determined that the value of α is 45°.

For normal operation of the impeller, a gap between the impeller and the container's shell was necessary. Otherwise, a malfunction may occur during the coordinated movement between the shell and the impeller. The radial gap between the impeller and the shell should satisfy the following conditions:

$$0 < \frac{D_0 - D}{2} < \{L, W, H\} \tag{1}$$

Here, D_0 represents the diameter of the container's shell, D denotes the external diameter of the impeller, and L, W, and H correspond to the length, width, and height of *H. axyridis* adults, as visualized in Figure 2.

To ensure the proper distribution of *H. axyridis* adults between the vanes and a smooth drop from the BC exit, the length of line segment BC should slightly exceed the maximum distance between two adjacent vanes.

$$BC > D \cdot \sin\left(\frac{\alpha}{2}\right) \tag{2}$$

Assuming that *H. axyridis* adults have a semi-ellipsoid shape, we calculated the average volume of each individual adult:

$$V_1 = \frac{1}{2} \times \frac{4}{3}\pi \cdot (L \cdot W \cdot H) \tag{3}$$

The total volume of the space between the vanes that can accommodate *H. axyridis* adult is

$$V = [\pi \cdot \frac{(D^2 - d^2)}{4} - n \cdot \delta \cdot \frac{D - d}{2}] \cdot L_1 \tag{4}$$

Here, d represents the impeller's inner diameter, δ represents the thickness of a vane, L_1 represents the length of the impeller. From Equations 2, 3, it can be deduced that a single space can house a certain number of *H. axyridis* adults.

$$N = \frac{V}{n \cdot V_1} \tag{5}$$

Linking Points A and C, Points B and E in line, both line AC and line BE pass through the center of the circle. The initial position is shown in Figure 3. The time it takes for *H. axyridis* adults to fall into an air channel from the container is

$$T = \frac{37.5}{n_1} + \left[\frac{S}{N}\right] \cdot \frac{7.5}{n_1} \tag{6}$$

where n_1 represents the impeller rotating speed, S represents the total number of *H. axyridis* adults in the container, and [] is the round symbol.

2.4 Test of *H. axyridis*–transport mechanism

To test the validity of Equation 6, an experiment was carried out. Initially, a specific quantity(S)of an *H. axyridis* adult was poured into a container. The value of S was predetermined as 60, 120, 180, 240, or 300. A reflective paper was attached to the coupling, and the tachometer tracked the coupling's real-time speed. Then, subsequently, the impeller rotating speed was adjusted. Since the coupling is connected to the impeller, the rotation speed of the coupling is equal to that of the impeller. The tachometer recorded impeller rotating speeds (n1). The release time (t) of *H. axyridis* adults was recorded. The experiment was replicated twice.

2.5 Statistical analysis

2.5.1 Camera calibration and counting of *H. axyridis* adults

To investigate the distribution, it was necessary to count the number of *H. axyridis* adults in designated areas. Traditional counting methods include weighing and manual counting (Opit et al., 2005; Pezzi et al., 2015). However, these approaches are time

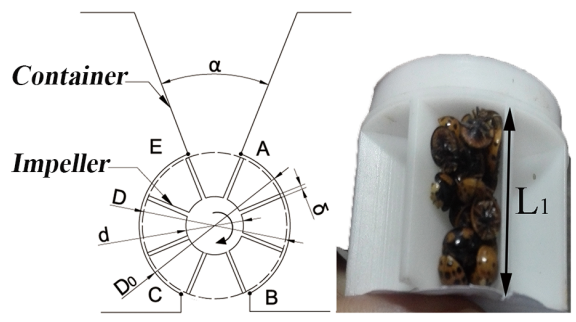

FIGURE 3
H. axyridis–transport mechanism.

consuming and challenging due to the mobility of *H. axyridis* adults.

For improved counting efficiency, an image processing method based on MATLAB (2012a) software was developed (refer to the Supporting Information for further details on the procedure code). When counting *H. axyridis* adults in a particular region, there is often a problem with *H. axyridis* adult adhesion. If we do not segment the attached *H. axyridis* adults, the accuracy of the final count will be affected. We used the watershed algorithm, the corrosion algorithm, and the maximum cross-sectional area method at the beginning of the experiment. We then found that the maximum cross-sectional area method was the most accurate for counting adult *H. axyridis* adults. Therefore, the method was chosen to count *H. axyridis* adults in the following experiment. When reading the image using MATLAB, each pixel represents the area of an *H. axyridis* adult in the picture. Considering ease of use, a phone's built-in camera (H60-L01, Huawei, Resolution: 1920×1080 pixels) was selected as the hardware for capturing images. However, factors such as camera angle and distortion can impact image accuracy. Consequently, a camera calibration experiment was conducted, as illustrated in Figure 4.

A white paper box (25 cm × 25 cm × 5 cm) was placed horizontally. A retort stand and clamp were used to keep the mobile phone parallel to the white paper box (Figure 4). The vertical distance from the lens to the center of the white box is 45 cm. This distance ensures that the phone's built-in camera fully captures the white paper box. A cross-calibration line on white paper (8 cm × 8 cm) was employed to calibrate the true value of the pixel. Each cross-calibration line was divided into eight 1-cm segments. The least squares method had been utilized to fit the pixels to the actual distance. The fitting graph is shown in Figure 5. Figure 5A is the fitting graph of the actual distance to the number of pixels in the horizontal direction, and Figure 5B is that of the vertical direction.

2.5.2 Performance experiment of the mechanical distribution prototype

To evaluate the survival, uniformity of distribution, and adhesion rate of *H. axyridis* adults after release, the experimental design is shown in Figure 6. A 4.0 m × 2.5 m rectangle was established using interconnected white paper boxes. To prevent the white paper boxes from being blown away by the wind, use thumbtacks to secure them to the ground. After carefully pouring a specific quantity of *H. axyridis* adults into the container, the operator stood motionless at the release point o with the release device fastened to his back (as shown in Figure 6). To ensure that the *H. axyridis* adults fell into the rectangle, the release point was positioned 1.2 m away from the rectangle formed by the connected white paper boxes. This distance was established through a preliminary experiment. The air channel tube was positioned parallel to the ground at an outlet height of 1.3 m. Next, the power supply was initiated, and the operator sets the impeller rotation speed and airflow velocity. The *H. axyridis* adults were then released by activating the switch. After the release of the *H. axyridis* adults, the machine was turned off. The operator remained stationary throughout the process. The natural wind velocity during the experiment ranged from 0.2 to 0.4 m/s, and the ambient temperature was 23.4°C. The effects of different impeller rotating speeds (4.2 rpm, 9.8 rpm, and 16.8 rpm) and airflow velocities (29.5 m/s and 38.3 m/s) on the distribution, survival, and adhesion of *H. axyridis* adults were investigated.

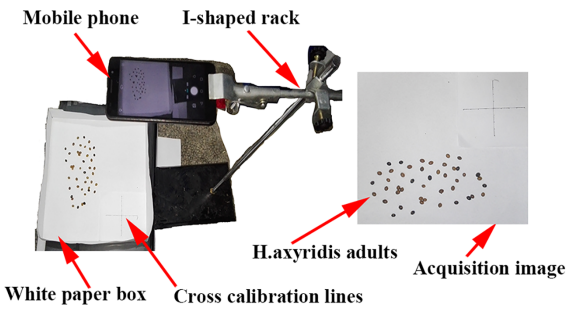

FIGURE 4
Camera calibration device and acquisition image.

Taking point O as the origin in Figure 6, a coordinate system was established. The horizontal direction was perpendicular to the air channel, and the vertical direction was parallel to the air channel. The number of *H. axyridis* adults in the paper boxes was counted using an image processing method based on MATLAB (2012a, MathWorks Inc.) software (see Supporting Information for further details of the procedure code). The distribution of the *H. axyridis* adults was calculated. The number of dead *H. axyridis* adults in every box and the number of *H. axyridis* adults attached to the walls of the container were recorded.

The coefficient of variation (CV) of horizontal or vertical distribution was defined as Equation 7:

$$CV = \frac{SD}{Mean} \times 100 \tag{7}$$

Where SD is the standard deviation of the number of *H. axyridis* adults in the white paper boxes of each row or column, Mean represents the average *H. axyridis* adults number of in each row or column of the white paper boxes.

In the process of distribution, some *H. axyridis* adults adhered to the container wall, resulting in incomplete release. The adhesive force of *H. axyridis* adults amounts to approximately five times their body weight (Ishii, 1987). Adhesion rate (AR) was calculated according to Equation 8.

$$AR = \frac{N_1}{T + N_1} \times 100\,\% \tag{8}$$

Where N_1 represents the number of *H. axyridis* adults adhering to the container wall and T represents the total number of *H. axyridis* adults in the white paper boxes.

During the release, *H. axyridis* adults came into contact with the impeller and were distributed by the airflow in the air channel. After distribution, the survival rate (SV) was evaluated using Equation 9.

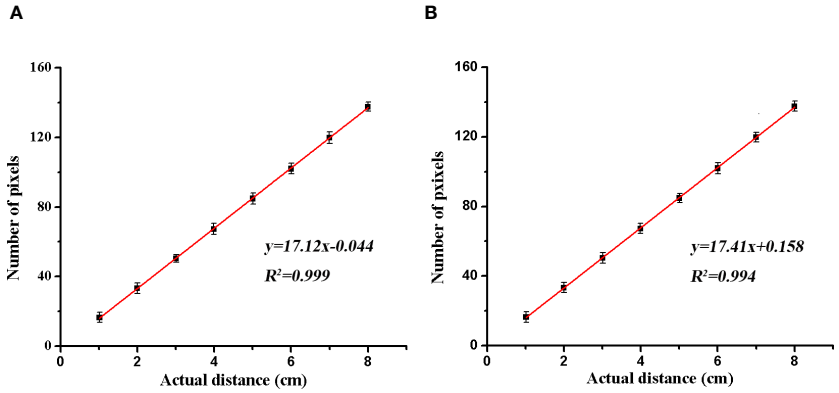

FIGURE 5
The fitting graph of the pixels to the actual distance. **(A)** The horizontal direction; **(B)** the vertical direction.

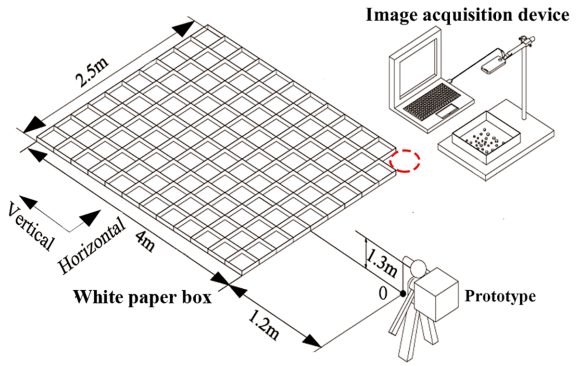

FIGURE 6
Schematic diagram of the release experiment.

$$SV = (1 - \frac{N_2}{T}) \times 100\,\% \quad (9)$$

Where N_2 represents the number of deceased *H. axyridis* adults.

3 Results and discussion

3.1 Quantitative adjustment model

The number of *H. axyridis* adults accommodated by the space between the vanes is an important factor in determining the parameter of impeller rotating speed. If the release amount of *H. axyridis* adults is certain, the space between the vanes contains more *H. axyridis* adults, and then the impeller rotating speed can be relatively reduced. According to the morphological size of the *H. axyridis* adults as shown in Table 1 and the Equations 1–5, the other parameters of the impeller (Figure 3) were determined as follows: D = 40 mm, d = 15 mm, δ = 2 mm, L_1 = 30 mm, D_0 = 43 mm, BC = 18 mm. Due to manufacturing errors, actual values are D = 40.72 mm, d = 14.84 mm, δ = 1.77 mm, L_1 = 30.57 mm, D_0 = 43.08 mm, BC = 18.63 mm. The materials for the impeller are ABS plastic and the container is no. 45 steel. Considering the complex factors such as the impeller rotating speed (0–24 rpm) and the ratio of *H. axyridis* adults to aphids, the quantity of *H. axyridis* accommodated in the space between the vanes (N) was established as 35.

To determine if the actual number of *H. axyridis* adults found in the space between the vanes was consistent with the theoretical value, a certain amount of *H. axyridis* adults were introduced into the space and the experiment was repeated ten times. The resulting number of *H. axyridis* adults was recorded and analyzed. The results showed that there were 33 ± 3.06 *H. axyridis* adults identified, with an error rate of 5.7% compared to the predetermined value. The errors were mainly caused by three factors: (i) the morphology of *H. axyridis* adults was similar to that of a semi-ellipsoid, but not a normal semi-ellipsoid. When the *H. axyridis* adults were in contact with the impeller vanes, there was a seam between the *H. axyridis* adults and the container wall, (ii) errors in processing techniques, and (iii) individual differences in the size of *H. axyridis* adults.

To evaluate the quantitative release performance of the mechanical system for *H. axyridis* adults, we can not only control the number of *H. axyridis* adults to test the release time but also control the number of *H. axyridis* adults to test the release time. Considering the convenience of the experiment operation, this experiment adopts the number of *H. axyridis* adults controlled to test the release time. To determine the relationship between theoretical and actual values of release time, a serials of experiments was implemented. The release time is shown in Table 3. Setting the needing time t as the dependent variable, the total number of *H. axyridis* adults S and the impeller rotating speed n_1 as an independent variable. Linear regression was performed using the SPSS 17.0. The fitting equation was established as Equation 10:

$$t = 0.808 + 27.897 \times \frac{1}{n_1} + 0.277 \times \frac{S}{n_1} \quad (10)$$

The correlation coefficient of R^2 is 0.943, which means the fitting is well.

To evaluate the precision of the release mechanism, different quantities of *H. axyridis* adults were released via the release system. The obtained results were compared to the theoretical results, as shown in Figure 7. The dotted line is the theoretical value of the

10.3389/fpls.2024.1297182

TABLE 3 Experimental data of *H. axyridis* adults release time.

Impeller rotating speed (rpm)	Number of *H. axyridis* adults				
	60	120	180	240	300
4.2	11.95 ± 0.51	14.71 ± 0.03	19.00 ± 0.68	22.84 ± 0.57	28.45 ± 0.83
7.4	7.24 ± 0.29	9.21 ± 0.03	11.33 ± 0.02	13.48 ± 0.09	15.90 ± 0.32
9.8	5.10 ± 0.35	7.36 ± 0.81	8.38 ± 0.05	9.78 ± 0.19	11.54 ± 0.13
14.3	4.13 ± 0.21	5.44 ± 0.02	6.38 ± 0.06	7.42 ± 0.01	8.85 ± 0.16
16.8	3.87 ± 0.08	4.72 ± 0.01	5.32 ± 0.15	5.66 ± 0.33	7.18 ± 0.23
21.2	3.18 ± 0.08	4.09 ± 0.06	4.93 ± 0.13	4.95 ± 0.59	5.94 ± 0.10
24	2.77 ± 0.13	3.41 ± 0.35	4.32 ± 0.15	4.04 ± 0.13	5.26 ± 0.30

release time under different impeller rotating speeds. The solid line is the value measured by the experiment. As shown in Figure 6, there is a consistent correlation between the theoretical and actual values, indicating a good agreement between the two. The result shows that controlled release can be achieved by adjusting the impeller rotating speed.

3.2 Counting based on image processing

The morphological characteristics of *H. axyridis* adults in the white paper box were photographed after the release. Subsequently, the images were processed and the number of *H. axyridis* adults was counted according to the procedure code in the Supporting Information. One of the boxes was selected and photographed. Figure 8 illustrates the processing of the selected image. Using the maximum cross-linked area method, we performed a statistical analysis on the gathering behavior and obtained the cross-linked area of *H. axyridis* adult in the box. The results are presented in Figure 9.

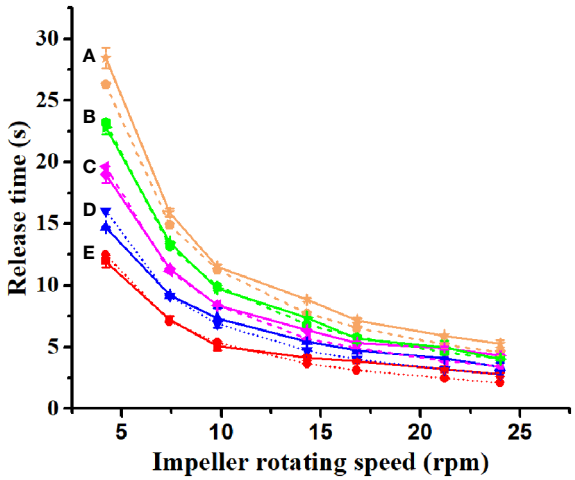

FIGURE 7
The theoretical (dotted line) and experimental values (solid line) of the time for the release of *H. axyridis* adults at different impeller rotating speeds. The number of *H. axyridis* adults was 300, 240, 180, 120, and 60 (A–E).

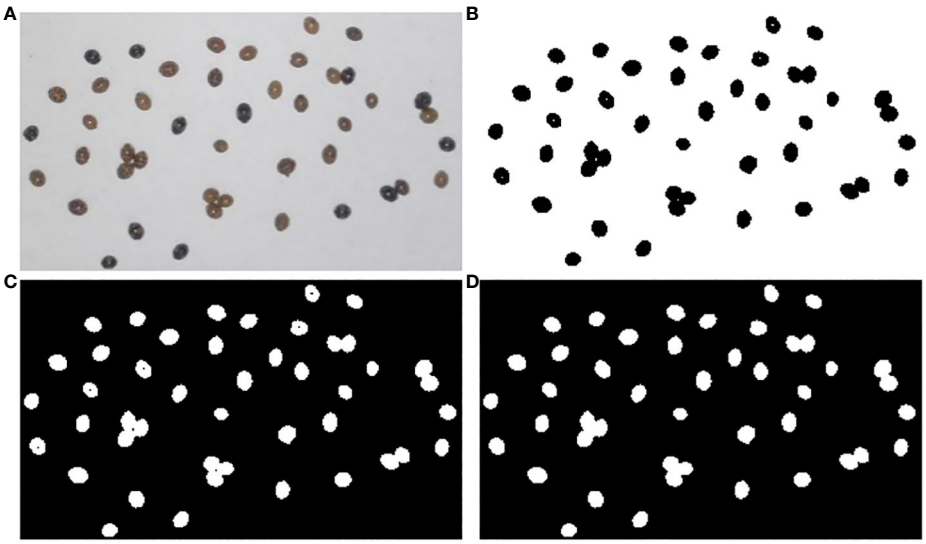

FIGURE 8
Image processing: **(A)** original image; **(B)** thresholding method; **(C)** thresholding inversion; **(D)** background fill.

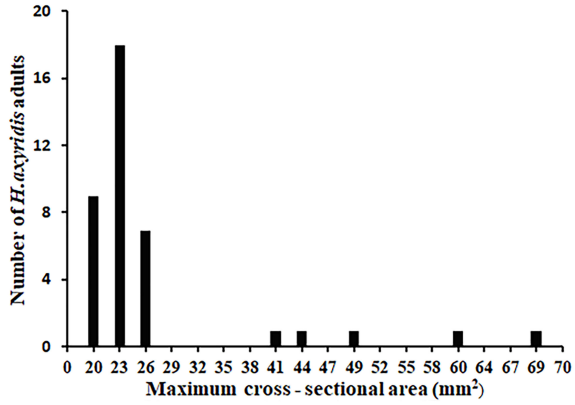

FIGURE 9
Maximum cross-sectional area statistics of *H. axyridis* adults.

The cross-sectional area of an individual *H. axyridis* adult ranged from 20 mm^2 to 26 mm^2, with a total of 34 *H. axyridis* adults. The total number of two connected *H. axyridis* adults was 3, with a combined cross-sectional area ranging from 41 mm^2 to 49 mm^2. Similarly, the total for three connected *H. axyridis* adults was 2, and the cross-sectional area ranges from 60 mm^2 to 69 mm^2. Based on the criterion of the range of cross-sectional area, it is possible to calculate the number of present *H. axyridis* adults.

During the release process, there were several *H. axyridis* adults in the white paper box. Even if there are severely connected *H. axyridis* adults in the white paper box, we can separate the severely attached *H. axyridis* adults by shaking the white paper box. Afterward, we can determine the number of them. To validate the maximum cross-sectional area method, we counted the number of *H. axyridis* adults in 100 white paper boxes, achieving an accuracy rate of 100%.

3.3 Performance of prototype

To assess the distribution law of the prototype, we released the *H. axyridis* adults under the air velocity of 29.5 m/s and 38.3 m/s, with impeller rotating speeds of 4.2 rpm, 9.8 rpm, and 16.8 rpm. A schematic diagram of the release experiment can be seen in Figure 6. The distribution of *H. axyridis* adults is shown in Figure 10. As the impeller rotating speed increased, the distribution of *H. axyridis* adults in the horizontal direction became more uniform. However, the impeller speed had no significant effect on the distribution of *H. axyridis* adults in the vertical direction. This result may be

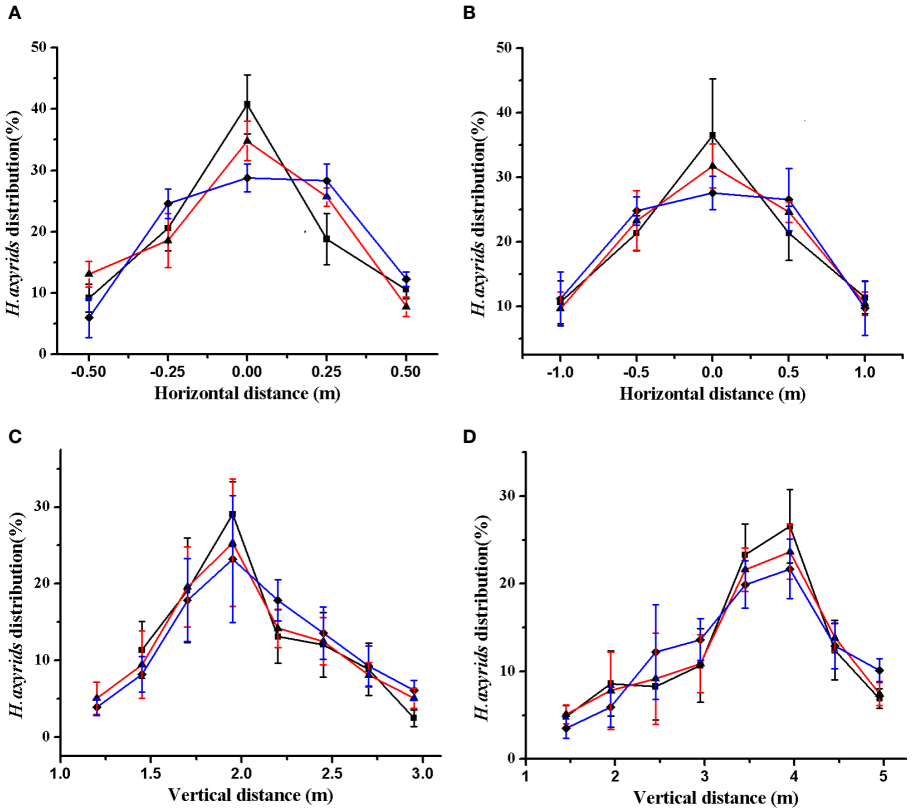

FIGURE 10
Distribution law. **(A)** horizontal distribution(29.5 m s^{-1}); **(B)** horizontal distribution (38.3m s^{-1}); **(C)** vertical distribution (29.5 m s^{-1}); **(D)** horizontal distribution (38.3 m s^{-1}). The black, red, and blue lines show the distribution of *H. axyridis* adults at the impeller rotating speeds of 4.2 rpm, 9.8 rpm, and 16.8 rpm, respectively.

attributed to the reduced time taken for the vanes to pass through the EA section as the impeller speed increases (see Figure 3). Before the space between the vanes can fill with *H. axyridis* adults, it's already rotated to exit BC. The *H. axyridis* adults are then transported out by the airflow. The *H. axyridis* adults are then transported out by the airflow. At higher impeller rotating speeds, less space between the vanes can be filled. A higher number of releases is needed when the same number of *H. axyridis* adults. So Horizontal dispersion of *H. axyridis* adults becomes more even when they are released more frequently.

As for horizontal distribution, at an airflow velocity of 29.5m/s, at least 70% of the *H. axyridis* adults were distributed between −0.25 m and 0.25 m. At an airflow velocity of 38.3 m/s, the distribution of *H. axyridis* adults is between −0.5 m and 0.50 m. For vertical distribution at an airflow velocity of 29.5 m/s, at least 70% of *H. axyridis* adults are found between 1.75 m and 2.25 m. Similarly, at an airflow velocity of 38.3 m/s, at least 70% of *H. axyridis* adults can be found between 3.00 m and 4.5 m. The distribution of *H. axyridis* adults is influenced by variations in airflow velocity. Pezzi and coworkers (Pezzi et al., 2015) summarized the airflow distribution at the outlet speed of the 30m/s and 45m/s using a fan anemometer positioned at regular intervals. They found that with the 45 m/s setting the airflow was detectable at a distance of 6 m from the blower and had a width of 1.8 m, whereas with the 30 m/s setting this was reduced to 4.5 m with a width of 1.25 m. The results of this study show that the distribution area is larger at high airflow velocity compared to low airflow velocity, which is according to Pezzi's Law.

Distribution uniformity, survival, and adhesion are the crucial parameters for evaluating the performance of the mechanical system. As shown in Table 4, the CV of horizontal and vertical distribution decreased with the increase of impeller rotating speed at certain airflow of the air channel. The CV of the horizontal direction was larger than that of the vertical direction, which indicated that the uniformity of the horizontal distribution was inferior to that of the vertical distribution. When the airflow velocities were 29.5 m/s and 38.3 m/s, the survival rates of the *H. axyridis* adults were 93.8% and 94.5% at 4.2 rpm, while the survival rates of *H. axyridis* adults were 78.6% and 78.7% at 16.8rpm. The low survival rate of *H. axyridis* adults at high-impeller rotating speed could be attributed to their injury upon contact with the mechanical wall. Martelli (Martelli et al., 2020) found that 88% of Orius laevigatus nymphs survived after release. In this study, the survival rate of *H. axyridis* adults was up to 94.5%. The difference in survival rate between the two studies may be due to the fact that Martelli released Orius laevigatus nymphs, while *H. axyridis* adults were released in this study. The streamlined shape of *H. axyridis* adults results in less damage when in contact with the machine wall.

Based on the information presented in Table 4, a two-factor analysis of variance was conducted with survival rate as the dependent variable and impeller rotating speed and airflow velocity as the independent variables. The results indicate that airflow velocity did not have a significant impact on the survival rate of *H. axyridis* adults ($P > 0.05$). In contrast, impeller rotating speed had a significant effect on the survival rate of *H. axyridis* adults ($P< 0.001$). The survival rate of the *H. axyridis* adults decreased with the increase of impeller rotating speed. Considering the release survival rate and the area search ability of *H. axyridis* adults, a lower impeller rotating speed should be selected when releasing *H. axyridis* adults.

4 Conclusion

A mechanical system was developed for the release of *H. axyridis* adults, which combined centrifugal and pneumatic strategies. The impeller for transporting *H. axyridis* adults was designed based on the physical characteristics of the *H. axyridis* adults. A mobile phone and image processing method were employed to develop a technique for enumerating *H. axyridis* adults. The effects of different airflow velocities and impeller rotating speeds on the distribution and survival rate of *H. axyridis* adults were studied. The results showed that the impeller rotating speed had little effect on the vertical distribution of *H. axyridis* adults. At an airflow velocity of 29.5m/s, the distribution range of *H. axyridis* adults was 0.5 m × 0.5 m. At an airflow velocity of 38.3m/s, the distribution range of *H. axyridis* adults was 1.0 m × 1.5 m. The impeller rotating speed had a significant effect on the survival rate of *H. axyridis* adults. At low impeller rotating speed, the survival rate of the *H. axyridis* adults could reach 94.5%. This work presented equipment for the release of natural enemies, which will significantly increase the potential for the use of natural enemies to control pests and diseases in the field.

TABLE 4 Coefficient of variation, survival, and adhesion of *H. axyridis* adults under different operating parameters.

Airflow speed ($m\ s^{-1}$)	Impeller rotating speed(rpm)	Horizontal CV (%)	Vertical CV (%)	Survival (%)	Adhesion (%)
29.5	4.2	35.60 ± 3.39	24.03 ± 4.20	93.82 ± 2.79	4.63 ± 0.75
	9.8	33.37 ± 4.12	22.89 ± 3.48	89.06 ± 3.65	2.50 ± 1.49
	16.8	29.71 ± 2.56	18.84 ± 3.13	78.64 ± 4.04	2.87 ± 1.78
38.3	4.2	31.14 ± 2.49	23.27 ± 1.77	94.48 ± 3.09	4.13 ± 0.57
	9.8	28.31 ± 5.13	20.17 ± 2.11	88.19 ± 5.54	2.77 ± 1.15
	16.8	21.03 ± 3.62	14.78 ± 1.42	78.74 ± 3.41	3.50 ± 1.91

Data availability statement

The original contributions presented in the study are included in the article/Supplementary Material. Further inquiries can be directed to the corresponding authors.

Ethics statement

The manuscript presents research on animals that do not require ethical approval for their study.

Author contributions

X-YD: Writing – original draft, Writing – review & editing. XT: Writing – original draft. JM: Writing – original draft. B-JQ: Writing – review & editing.

Funding

The author(s) declare that financial support was received for the research, authorship, and/or publication of this article. The present study was supported by grants from the National Science Foundation of China (No. 31971790), Primary Research & Development Plan of Jiangsu Province (No. BE2020328), Priority Academic Program Development of Jiangsu Higher Education Institutions (No. PAPD-2018-87).

Conflict of interest

The authors declare that the research was conducted in the absence of any commercial or financial relationships that could be construed as a potential conflict of interest.

Publisher's note

Supplementary material

The Supplementary Material for this article can be found online at: https://www.frontiersin.org/articles/10.3389/fpls.2024.1297182/full#supplementary-material

References

Alyokhin, A., Dively, G., Patterson, M., Castaldo, C., Rogers, D., Mahoney, M., et al. (2007). Resistance and cross-resistance to imidacloprid and thiamethoxam in the Colorado potato beetle Leptinotarsa decemlineata. *Pest Manage. Sci.* 63, 32–41. doi: 10.1002/ps.1305

Amidon, G. E., Meyer, P. J., and Mudie, D. M. (2017). Developing solid oral dosage forms. *Pharm. Theory Pract. Elsevier Inc. Chapt.* 10, 271–293. doi: 10.1016/B978-0-12-802447-8.00010-8

Andrei, A., Mitchell, B., David, M. S., Galen, D., and Edward, G. (2008). Colorado potato beetle resistance to insecticides. *Am. J. Potato Res.* 85, 395–413. doi: 10.1007/s12230-008-9052-0

Blandini, G., Emma, G., Failla, S., and Manetto, G. (2008). A prototype for mechanical distribution of beneficials. *ActaHortic.* 801, 1515–1522. doi: 10.17660/ActaHortic.2008.801.187

Casey, C. A., and Parrella, M. P. (2005). Evaluation of a mechanical dispenser and interplant bridges on the dispersal and efficacy of the predator, Phytoseiulus persimilis (Acari : Phytoseiidae) in greenhouse cut roses. *Biol. Control* 32, 130–136. doi: 10.1016/j.biocontrol.2004.09.002

Emma, G., Failla, S., Manetto, G., and Restuccia, A. (2010). "Mechanical distribution of natural enemies in the open field." in *International Conference Ragusa SHWA2010, Ragusa Ibla Campus, Italy*, September 16–18, 2010. (Work Safety and Risk Prevention in Agro-food and Forest Systems). 479–486.

Gan-Mor, S., and Matthews, G. A. (2003). Recent developments in sprayers for application of biopesticides - an overview. *Biosyst. Eng.* 84, 119–125. doi: 10.1016/S1537-5110(02)00277-5

Giles, D. K., Gardner, J., and Studer, H. E. (1995). Mechanical release of predacious mites for biological pest control in strawberries. *Trans. Asae* 38, 1289–1296. doi: 10.13031/2013.27950

Haelewaters, D., Zhao, S. Y., Clusella-Trullas, S., Cottrell, T. E., De Kesel, A., Fiedler, L., et al. (2017). Parasites of *Harmonia axyridis*: current research and perspectives. *Biocontrol* 62, 355–371. doi: 10.1007/s10526-016-9766-8

Ishii, S. (1987). Adhesion of a leaf feeding ladybird epilachna vigintioctomaculta (Coleoptera: coccinellidae) on a virtically smooth surface. *Appl. Ent. Zool.* 22, 222–228. doi: 10.1303/aez.22.222

Khelifi, M., Paré, F., and Aider, M. (2011). Test bench for the mechanical distribution of predators to control insect pests. *J. Environ. Sci. Eng.* 5, 1445–1453.

Lanzoni, A., Martelli, R., and Pezzi, F. (2017). Mechanical release of Phytoseiulus persimilis and Amblyseius swirskii on protected crops. *Bull. Insectol.* 70 (2), 245–250.

Martelli, R., Lanzoni, A., Maini, S., and Pezzi, F. (2020). Mechanical application of orius laevigatus nymphs for the control of Frankliniella occidentalis in greenhouse crops. *Bull. Insectol.* 73 (1), 59–69.

Opit, G. P., Nechols, J. R., Margolies, D. C., and Williams, K. A. (2005). Survival, horizontal distribution, and economics of releasing predatory mites (Acari: Phytoseiidae) using mechanical blowers. *Biol. Control* 33, 344–351. doi: 10.1016/j.biocontrol.2005.03.010

Osawa, N. (1992). Sibling cannibalism in the ladybird beetle *Harmonia axyridis*: Fitness consequences for mother and offspring. *Popul. Ecol.* 34, 45–55. doi: 10.1007/bf02513521

Papa, R., Manetto, G., Cerruto, E., and Failla, S. (2018). Mechanical distribution of beneficial arthropods in greenhouse and open field: A review. *J. Agric. Eng.* 49, 81–91. doi: 10.4081/JAE.2018.785

Pezzi, F., Martelli, R., Lanzoni, A., and Maini, S. (2015). Effects of mechanical distribution on survival and reproduction of Phytoseiulus persimilis and Amblyseius swirskii. *Biosyst. Eng.* 129, 11–19. doi: 10.1016/j.biosystemseng.2014.09.004

Pickett, C. H., Gilstrap, F. E., Morrison, R. K., and Bouse, L. F. (1987). Release of predatory mites (Acari: phytoseiidae) by aircraft for the biological control of spider mites (Acari: tetranychidae) infesting corn. *J. Econ. Entomol.* 80, 906–910. doi: 10.1093/jee/80.4.906

Pilkington, L. J., Messelink, G., Van Lenteren, J. C., and Le Mottee, K. (2010). Protected Biological Control - Biological pest management in the greenhouse industry. *Biol. Control* 52, 216–220. doi: 10.1016/j.biocontrol.2009.05.022

Yu, Q., and Powles, S. (2014). Metabolism-based herbicide resistance and cross-resistance in crop weeds: A threat to herbicide sustainability and global crop production. *Plant Physiol.* 166, 1106–1118. doi: 10.1104/pp.114.242750

Zappala, L., Manetto, G., Garzia, G. T., Emma, G., and Failla, S. (2012). Mechanical distribution of phytoseiulus persimilis on chrysanthemum. *Acta Hortic.* 952, 793–800. doi: 10.17660/ActaHortic.2012.952.100

frontiers | Frontiers in Plant Science

TYPE Original Research
PUBLISHED 28 March 2024
DOI 10.3389/fpls.2024.1309088

OPEN ACCESS

EDITED BY
Andreas Herbst,
Julius Kühn Institute (JKI), Germany

REVIEWED BY
Andżelika Krupińska,
Poznań University of Technology, Poland
João Paulo Arantes Rodrigues Da Cunha,
Federal University of Uberlandia, Brazil

*CORRESPONDENCE
Weidong Jia
jiaweidong@ujs.edu.cn

RECEIVED 07 October 2023
ACCEPTED 11 March 2024
PUBLISHED 28 March 2024

CITATION
Zhou H, Ou M, Dong X, Zhou W, Dai S and Jia W (2024) Spraying performance and deposition characteristics of an improved air-assisted nozzle with induction charging. *Front. Plant Sci.* 15:1309088. doi: 10.3389/fpls.2024.1309088

Spraying performance and deposition characteristics of an improved air-assisted nozzle with induction charging

Huitao Zhou[1,2], Mingxiong Ou[1,2], Xiang Dong[1,2], Wang Zhou[1], Shiqun Dai[1,2] and Weidong Jia[1,2]*

[1]School of Agricultural Engineering, Jiangsu University, Zhenjiang, China, [2]Key Laboratory of Plant Protection Engineering of Ministry of Agriculture and Rural Affairs, Jiangsu University, Zhenjiang, China

Electrostatic spraying technology can improve the efficiency of pesticide deposition on the surface of leaves and reduce the environmental pollution caused by pesticide drift, which has an important prospect in agricultural pesticide application. To improve the deposition and penetration of droplets in the crop canopy, we designed and optimized an air-assisted electrostatic nozzle and conducted the spraying performance experiment. Parameters, such as charge-to-mass ratio (CMR) and particle size, were tested and analyzed to obtain the suitable operating parameters of nozzle. The results proved that the improved air-assisted electrostatic nozzle has good atomization and chargeability. There is a good charging effect with a charging voltage of 3,000–5,000 V, the CMR increased 127.8% from 0.86 to 1.97 mC/kg as the charge voltage increases from 1,000 to 4,000 V, at an air pressure of 1.0 bar and liquid flow rate of 200 ml/min. Furthermore, we designed a multi-factor orthogonal experiment, which was conducted using a four-factor, three-level design to investigate the effects of operational parameters and canopy characteristics on droplet deposition and penetration. Analysis of variance (ANOVA) and F-test were performed on the experiment results. The results showed that the factor effect on droplet penetration, in descending order, was as follows: spray distance, leaf area index, air pressure, and air pressure × spray distance. The factor effect on abaxial leaf deposition, in descending order, was as follows: air pressure, spray distance, air pressure × charge voltage, spray distance × charge voltage, and charge voltage. For optimal droplet penetration and abaxial leaf deposition, option $A_3B_1D_2$ (air pressure 1.5 bar, spray distance 0.2 m, charge voltage 2,500 V) is recommend. The spray nozzle atomization performance and deposition regulation were studied by experimental methods to determine the optimal values of operating parameters to provide a reference for electrostatic spray system development.

KEYWORDS

electrostatic spraying, air-assisted electrostatic nozzle, charge-to-mass ratio, droplet deposition and penetration, multi-factor orthogonal experiment method

1 Introduction

Pesticide spraying is an important activity of crop production in modern agriculture (Appah et al., 2019a). It ensures the deposition of pesticide spray droplets on target surfaces to control pests and diseases, and contributes to productivity as well as the quality of the yield (Chambers et al., 2014; Ahmad et al., 2020). Conventional hydraulic spraying for pesticide application using coarse droplet and large flow rate has been recognized as inefficient and cannot adhere well to the surface of the target, which causes off-target losses of pesticide droplets and gives rise to high residues in crop products and soil (Zhou et al., 2021; Wang et al., 2022). The electrostatic spray is used for agricultural application as an innovative plant protection strategy to overcome the above shortfalls during the 20th century (Hoffmann et al., 2007; Esehaghbeygi et al., 2010; Martini et al., 2016). The droplets are charged by the electric field of the electrode, which are rapidly deposited on the plant surface by static electricity, airflow traction, and gravity. It has been confirmed that the electrostatic method of pesticide application can provide greater control of droplet transport, improve overall deposition (especially the abaxial surface of leaves) and uniform distribution due to "wrap-around" effect, hence, reduce the off-target drift of pesticide droplets and the quantities of applied chemical pesticides (Zhu et al., 1989; Patel, 2016; Zhou et al., 2018). However, electrostatic spray also has some problems in agricultural pesticide application. Short charge retention time, easy leakage of charge, and easy adsorption of charged droplets near the electrode (Patel et al., 2017; Zhou et al., 2018) may cause the electrostatic spray to be not effective.

The scientific and engineering contributions of numerous researchers throughout the 20th century have established both the fundamental basis and the technical implementation of reliable and spray-charging methods (Law, 2001). Bowen et al. elucidated that a charged droplet population generates electric fields in space to facilitate pesticide droplet deposition from both theoretical and experimental aspects, which enriched the basic theory of electrostatic spraying (Bowen et al., 1964). Law et al. used inductive charging for electrostatic spraying of pesticides and proposed that the combination of electrostatic and air-assisted spraying would contribute to the deposition and penetration of droplets (Law and Bowen, 1966; Law, 1983). Since the 21st century, further research on the application of electrostatic spraying in orchards, greenhouses, and agricultural aviation were carried out. Pascuzzi and Cerruto (2015) conducted a study on spray deposition in "tendone" vineyards using an ESS "150RB14" air-assisted electrostatic spray system. The results showed that electrostatic spraying effectively improved the density and uniformity of droplet deposition on the lower layer of the canopy, but reduced the penetration of droplets compared with non-electrostatic spraying. Gan-Mor et al. (2014) investigated the charging of a conventional hydraulic nozzle. The results showed that electrostatic charging with an air-assisted electrostatic spray system improved the deposition of droplets by 200% and 500% on the leaf undersides and the rear of grape clusters, respectively. These demonstrate the effectiveness of the electrostatic application method in improving droplet deposition on leaf surface (especially abaxial side) and droplet penetration in crop canopy with the air-assisted electrostatic spray system (Ferguson et al., 2016).

Many relevant studies on the performance and deposition characteristics of the electrostatic spray had been conducted by researchers. Most of these researches focus on the effects of charging parameters (such as charging method, electrode material and mounting position, charging voltage, and electrode polarity). Law and Thompson (1996) concluded that the most widely used method for charging agricultural sprays is induction charging. The closer the electrode is to the liquid sheet, the better the charging effect, but the droplets are easily adsorbed on the electrode by Coulomb forces. Therefore, it is necessary to find the optimal electrode-mounting distance. Patel et al. (2013, 2015) researched the effect of electrode shape and position on the charging effect. The results showed that the square electrode with an inner circular section has the best effect, and the suitable distance range from the electrode to the cross-section of the nozzle outlet is 2–3 mm. Maski and Durairaj (2010) studied the effect of charging voltage on droplet deposition and concluded that moderate application speed and high charging voltage contribute to droplet deposition. Yule et al. (1995) investigated the relationship between charging voltage and spray angle. The results showed that the spray angle was positively correlated with the charging voltage. Zhou et al. (2015) and Li et al. (2007) found that the charging voltage was the most important factor affecting the deposition of droplets on the abaxial surface of leaves. Lan et al. (2018) and Patel et al. (2013) studied the effect of different electrode materials on the charging ability. The results showed that the electrode with purple copper as the material had the best charging effect. So, with the application of induction charging method, suitable material and structure used in electrode design and its insulation, spray atomization methods, combined with external air assistance, the charging performance of electrostatic nozzles and the efficiency of pesticide deposition on leaves could be improved to reduce the environmental pollution by pesticide off-target loss (Shrimpton and Laoonual, 2006; Patel, 2016). Despite our abovementioned efforts to improve the performance of electrostatic spray, we get the fine charged droplets with adhesion ability that we need. What still needs our attention is that the electrostatic spray system may not be effective as it is affected by the complex operating environment of agriculture. Pascuzzi and Cerruto (2015) used the ESS electrostatic-induction nozzle in "tendone" vineyards. The activation of the electrostatic system produced a significant increase in the mean foliar deposit only on the lower layer, while it had no effect on the upper layer. Zhou et al. (2015) found that in the application of an air electrostatic nozzle, the adhesion ability of the charged droplets is weakened due to the charge decay, when the spraying distance is far. At the same time, the fine droplets are more prone to drift due to ambient winds when transported over long distances. Therefore, in addition to studying how to improve the performance of electrostatic spraying devices, we also need to study what working conditions to better utilize the effect of electrostatic spraying.

Additionally, some researchers (Shang et al., 2004; Wu et al., 2009; Zhou et al., 2019) conducted studies on operational parameters such as spray pressure, external airflow supply, application speed, and spray

distance. Appah et al. (2019b) conducted studies that showed that the combined parameters of applied voltage, liquid flow pressure, and spraying height produced maximum charged spray swath and fine droplets. Patel et al. (2016a) found that external airflow had a significant effect on spray atomization and the distribution of external airflow field could affect the spray coverage. Maski and Durairaj (2010) concluded that both spray distance and application speed have an effect on droplet deposition efficiency. It was concluded that the optimization of the operating parameters can effectively improve the spray performance and deposition effect of the electrostatic nozzle (Patel et al., 2017).

From the above literature studies, it is clear that air-assisted electrostatic spraying can effectively improve the deposition of pesticide droplets in the crop canopy helping to improve the utilization rate of pesticides and pest control effects. However, further optimization and design are needed to the internal flow channel structure and electrode parameters of the nozzle to meet the actual requirements of pesticide application. Furthermore, the analysis of charge droplet deposition mechanism and its influencing factors is a hot research topic at present, but the main research focused on the influence of charge parameters on deposition with CMR as an indicator. The canopy characteristic parameters and spraying operation parameters have not been sufficiently studied, and the interaction effects between each parameter are still unclear. To solve the above situation, an improved air-assisted electrostatic nozzle with induction charging will be designed and optimized in this article. Spraying performance experiments will be conducted to obtain the appropriate operating parameters with good atomization and chargeability. The multi-factor orthogonal experiment will be designed and analyzed to ensure the influence of each factor on the droplet penetration and deposition, which could provide a technical reference for the optimization of operating parameters of electrostatic spraying. With these improvements and research, farmers could be guided to spray pesticides better, reduce pesticide usage, and increase pesticide utilization efficiency.

2 Materials and methods

2.1 Air-assisted electrostatic spraying system

An air-assisted electrostatic spraying system has been designed and developed as shown in the schematic diagram of Figure 1. It mainly consists of air-assisted induction electrostatic nozzle, high-voltage charging device, flow rate adjustment device, liquid supply device, and air supply device. The high-voltage charging device (GF-2A, Wuxi, China) is required to provide high voltage (Ultra Volt +20 kV, 1 mA, 20 W, for laboratory experiments only) for the charging of the conductive liquid, which was connected to the ring electrode inside the nozzle by an insulated wire. The charging of conductive liquid is based on the induction principle, which is the most reliable, safe, and experimentally proven method for efficient charging (Patel et al., 2017). A pulse width modulation (PWM) (Mingwei, Shenzhen, China) controller was used to control the flow rate of liquid from a tank. Liquid flows from a pump (Xishan DP-150, Shanghai, China) into a nozzle and is atomized by high-speed airflow. An air compressor (Model JB-750×3, Zhejiang, China) and a pressure regulator were used to obtain the required high-speed steady airflow. A high-voltage meter (Model 900B, Chroma Electronics (Shenzhen) Co. Ltd, China) is responsible for real-time monitoring and showing voltage variations. Both the high-voltage electrostatic device and the high-volt meter need to be well grounded.

The electrostatic nozzle is a key component to achieve the atomization of pesticide liquid and charge of droplets in an electrostatic spraying system. The structure of the air-assisted electrostatic nozzle is shown in Figure 2. The internal structure and charging electrode parameters need to be considered in the design of the electrostatic nozzle, since they are critical to atomization performance and charge performance of the nozzle. The traditional hydraulic electrostatic nozzle has a problem of

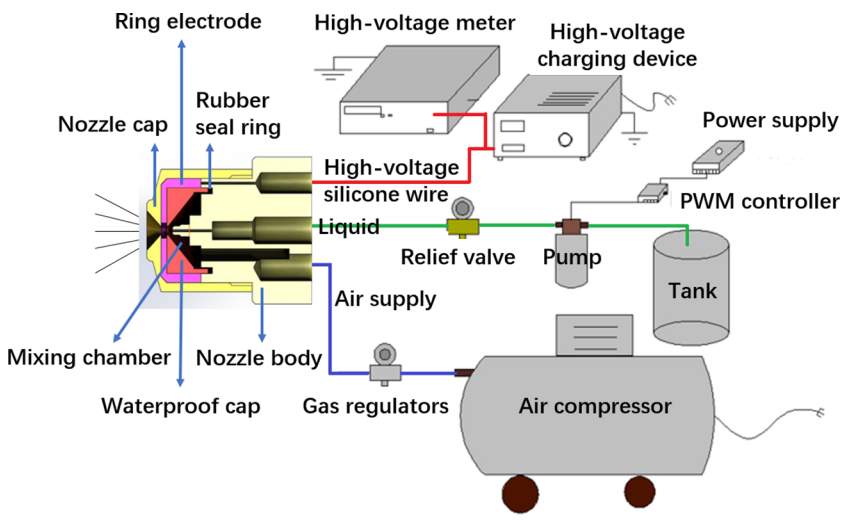

FIGURE 1
Schematic diagram of an air-assisted electrostatic spraying system.

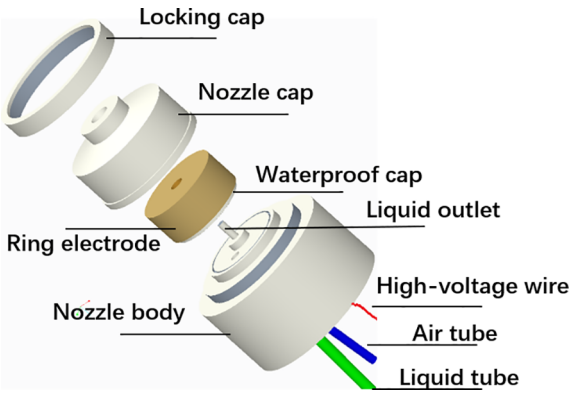

FIGURE 2
Structural diagram of an air-assisted electrostatic nozzle.

short spray distance, leakage, and reverse ionization causing short droplet transport distance and poor charging and deposition effect. To improve the above problems, we designed and optimized the nozzle structure and electrode parameters using a coaxial gas–liquid twin fluid, internal mixing, air-assisted atomization method. The charging of conductive liquid based on the induction principle was used, which is the most reliable and field-proven method for imparting charge efficiently (Patel et al., 2017).

In addition, we have improved the air-assisted electrostatic nozzle in terms of runner structure, electrode parameters, insulation, and waterproof measures. First, the diameter of the liquid outlet is one of the factors that determine the droplet size and atomization effect; the smaller the diameter, the finer the droplet. Considering the limitations of machine processing, we set the diameter of liquid outlet to 1 mm. Concurrently, we increased the size of the internal gas–liquid mixing chamber and ensured sufficient airflow at the nozzle outlet, which would be more beneficial to liquid atomization. The throat size is set to 3 mm. With a tapered shrinkage structure, the airflow creates a choking effect at the throat, which leads to a sharp increase in air velocity. In this way, the charged droplets were able to be carried away by the airflow quickly and did not adhere to the inner circle surface of the electrode improving charge capacity (Patel et al., 2016b, Patel et al., 2017). Second, a ring copper electrode with an inner circular section was used, and the distance from the nozzle exit to the electrode is 3 mm, close to the atomization zone, which were proven by Patel to be the suitable electrode parameters for charging (Patel et al., 2013, Patel et al., 2015). To avoid liquid droplets hitting the inner circle cross of the copper electrode, the diameter of the inner circular section is set at 5 mm. Third, we used an insulated waterproof cap and a rubber seal ring to form a grooved sealing structure to isolate the ring electrode from the gas–liquid mixing chamber avoiding leakage and reverse ionization caused by direct contact of the electrode with the conductive liquid. To improve the insulation and prevent electrical breakdown, the waterproof cap and nozzle cap are made of Teflon material.

2.2 Spraying performance experiment

The spraying performance of the electrostatic nozzle is essential to the quality of spraying operations. Good atomization and chargeability are required to ensure that the pesticide liquid is fully atomized, the droplets are fine and uniform with sufficient charge to adhere to the surface of leaves. In this study, we measured the CMR, droplet size, and distribution to evaluate the charge ability and atomization performance of the electrostatic nozzle. All the experiments were conducted at the Key Laboratory of Plant Protection Engineering in Jiangsu University, a closed laboratory with static air inside to prevent droplet spraying out of the test areas, with humidity of 68% and temperature of 25°C to provide ideal droplet evaporation simulating field conditions.

2.2.1 Charging performance

In electrostatic spraying, the foremost aim is to provide a significant charge to spray droplets to deliver them effectively and efficiently to the intended target. The more electrostatic charge carried by the droplets, the better will be the performance in terms of increased uniformity, deposition efficiency, wraparound effect, and reduced off-target losses (Patel et al., 2022). The chargeability of the droplets, i.e., their capability to acquire charge, is evaluated based on the amount of electrostatic charge per unit mass of the droplet, called the CMR (Maski and Durairaj, 2010; Pascuzzi and Cerruto, 2015). The CMR is the most important parameter that defines the charge performance of the electrostatic nozzle. According to the above definition, the CMR could be calculated from the following relation [Equation 1]:

$$CMR = \frac{q}{m} = \frac{it}{m} = \frac{i}{Q_m} \quad (1)$$

where i is the measured spray current (A), Q_m is the mass flow rate of liquid (kg s^{-1}), m is the mass of liquid collected in the beaker at a specific time, and q is the droplet charge (C).

The Faraday cage method was used in the CMR measurement; a specially designed Faraday cage was connected to the digital multimeter (Model No. 6485, Keithley A Tektronix Inc. Company, Ohio) via a conducting wire as show in Figure 3. The digital multimeter must be reliably grounded. The charge droplets contact the wire mesh of the Faraday cage and transfer the charge to the ground causing an electrical current, which was detected and measured by the digital multimeter in real-time. The current data was logged into ExceLINX (ELNX-852C04) software in a computer through a USB cable during the operation for data storage and analysis (Appah et al., 2019b). The charged liquid spray was collected at a specific time in a beaker and weighed by precision electronic balance.

The experiment was designed to be divided into two groups to measure the variation of CMR with charge voltage at different distances (0.1, 0.4, 0.7, and 1.0 m) and air pressure (0.5, 1.0, and 1.5 bar) conditions. The flow rate of the nozzle was 200 ml/min, and continuous spray and current measurement for 1 min (60 s). The charged voltage ranges from 0 to 10 kV, adjustable every 1 kV.

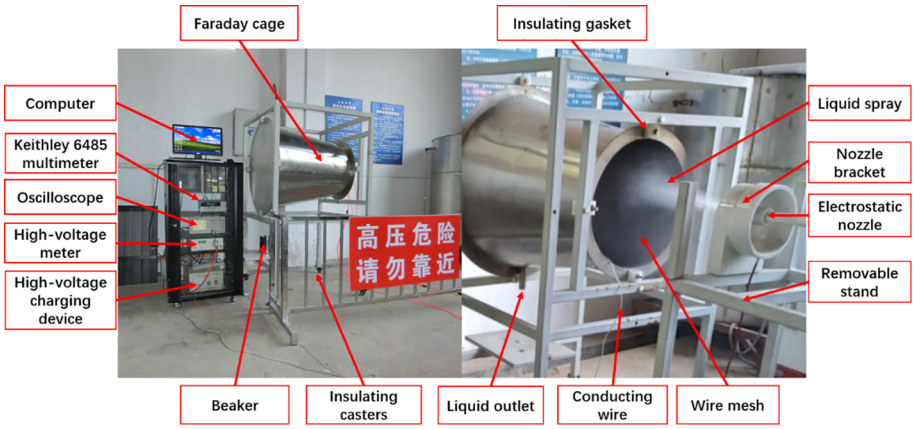

FIGURE 3
Charge-to-mass ratio measurement system.

2.2.2 Droplet size and distribution

Droplet size is one of the main factors affecting the deposition and distribution uniformity of pesticides on the target. Droplet size and distribution uniformity are identified as essential factors to evaluate the spray performance and deposition efficiency in agricultural spray application (Liao et al., 2020). Only with a suitable droplet size can more droplets be captured on the target surface and the better control effect of pests and diseases.

The volume median diameter (VMD) and the relative span (RS) were used to characterize the mean droplet size and the uniformity of droplet distribution in this research. The droplet size parameters (such as $D_{V0.1}$, $D_{V0.5}$, and $D_{V0.9}$) were able to be measured and recorded by the Laser Particle Size Analyzer (LPSA) (model Winner 318, Shandong, China). The $D_{V0.5}$ indicates that half of the volume of spray is in droplets smaller than this value ($D_{V0.5}$ = VMD). With $D_{V0.1}$, $D_{V0.5}$, and $D_{V0.9}$, the RS of the droplet spectrum can be calculated from Equation 2. RS was used to characterize the uniformity of droplet distribution; the smaller the RS values, the less variation there is between the size of the droplets in spray spectrum, and the more uniform the droplet distribution is (Ru et al., 2020).

$$RS = \frac{[D_{V0.9} - D_{V0.1}]}{D_{V0.5}} \quad (2)$$

The air-assisted electrostatic nozzle was fixed on the test bench, turning on the spray system, and adjusting the position of the LPSA so that the emitted laser passed through the center of the droplet cluster and reflected back to the receiver side. Tests need to be conducted in weak light environment to reduce the interference of ambient light. The height of the nozzle from the laser beam is kept at 0.5 m. The air pressure was set at 0.5 bar, 1.0 bar, and 1.5 bar, and the charged voltage was adjusted from 0 V to 10 kV. The experimental set-up is shown in Figure 4.

2.3 Experiment to study the deposition characteristic of charged droplet

The experiment was carried out inside the Key Laboratory of Plant Protection Engineering in Jiangsu University with a

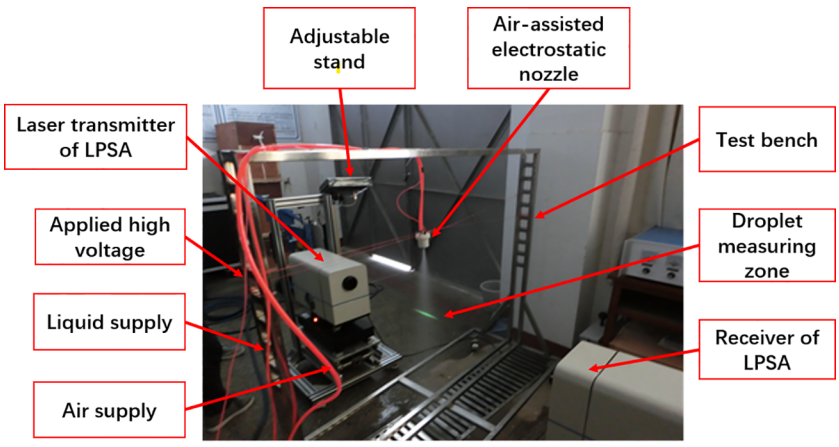

FIGURE 4
Experimental set-up to measure the droplet size.

temperature of 25.1°C and relative humidity of 42%. In this experiment, the improved air-assisted electrostatic nozzle was used to conduct experimental research on spray penetration and deposition characteristics with the canopy of grapevine. The nozzle was fixed to the slide and moves with the slide at a speed of 1 m/s when spraying. Simulated leaves similar to the size of grape leaves were selected for canopy construction according to the characteristics of the grapevine. The leaf area index (LAI) were measured to characterize the canopy, which is referred to as the total one-sided area of leaf tissue per unit ground surface area. The area for each leaf was evaluated in the laboratory using a scanner (Lenovo M7605D) and a measuring software (Image Pro Plus, Media Cybernetics). The canopy size of the grapevine is 0.6 m (thickness) × 0.8 m (width) × 0.8 m (height). The leaf area index was set at three levels of 1, 1.5, and 2 by changing the arrangement and number of leaves. Three sampling points were selected inside the canopy at a distance of 0.3 m from the front of the canopy. Water-sensitive papers (WSPs) were arranged at each sample point to collect droplets during spraying. The WSPs were fixed by a double-ended clip with one end clamped to the branch of the grape canopy and the other end clamped to WSPs ensuring a fixed position of WSPs for each group of experiments. The experiment set-up is shown in Figure 5.

The WSPs needed to dry before collecting into labeled ziplock bags after each spraying test and were then numbered and scanned. It is essential to wear rubber gloves during the WSP collection process. A high definition scanner was used to obtain the 600-dpi image of scanned WSPs. The "DepositScan" software, which was developed by the USDA-ARS Application Technology Research Center, was applied to evaluate droplet size, droplet distribution, total droplet number, droplet density, amount of spray deposits, and percentage of spray coverage (Zhu et al., 2011). The scanned images were imported into the DepositScan for analysis, and the amount of droplet deposition per unit area of each WSP was derived. In the penetration experiment, the penetration was reflected by the average of the adaxial deposition captured by the WSP at three sampling points; in the abaxial deposition experiment, the WSP was arranged in the reverse direction at the original three sampling points. The abaxial droplet deposition was reflected by the average value of the abaxial droplet deposition.

The Equation 3 was used to convert the spot area to the actual droplet diameter (d, μm) in the DepositScan software is as follows (Zhu et al., 2011):

$$d = 0.95 d_s^{0.910} \tag{3}$$

where, d_s can be calculated from the following Equation 4

$$d_s = \sqrt{\frac{4A}{\pi}} \tag{4}$$

and A is the spot area (μm^2) acquired from ImageJ. The spot area was calculated from the number of spot image pixels divided by the scanning resolution. In this program, the scanning resolution was chosen up to 2,400 dots per inch (dpi), or 10.58 μm per pixel length, which would allow detection of a droplet that has a minimum diameter of 17 μm (Zhu et al., 2011; Ahmad et al., 2020). However, the image software cannot consider the impact of spread factor (Hoffmann and Hewitt, 2005). The final actual droplet diameter D can be calculated from the Equation 5 (Zhu et al., 2011),

$$D = 1.06 A^{0.455} \tag{5}$$

To clarify the main factors influencing the experiment results and obtain the optimal combination of different factors at different levels with fewer experiments, a four-factor, three-level orthogonal experiment was designed. Considering the air pressure, charge voltage, spray distance, and leaf area index as the factors of the orthogonal experiment, orthogonal experiment factor levels are shown in Table 1. Analysis of variance (ANOVA), performed using the SPSS Statistical Software Package (version 22.0, IBM, New York, USA), was used to determine the effect of each single factor and the interaction term on penetration and adhesion, and select the optimal operating parameters accordingly. The least significant difference (LSD0.05) test was applied to separate treatment means after F-test indicated the statistical significance at a probability level of 0.05.

Through the pre-test, it was found that in the droplet penetration experiment, there was a significant difference in droplet deposition volume of leaf adaxial when the leaf area index was increased from 1 to 2 at different spraying distances; similarly,

FIGURE 5
Experimental set-up to study spray deposition characteristics and canopy penetration.

10.3389/fpls.2024.1309088

TABLE 1 Orthogonal experiment factor levels.

Number	A (air pressure/bar)	B (spray distance/m)	C (leaf area index)	D (charge voltage/V)
1	0.5	0.2	1.0	0
2	1.0	0.6	1.5	2,500
3	1.5	1.0	2.0	5,000

there was a significant difference also when the air pressure was increased from 0.5 to 1.5 bar. Thus, the interaction term air pressure × distance and the interaction term distance × leaf area index were both included in the experimental design. The droplet penetration experiment was performed using an $L_{27}(3^{13})$ orthogonal design. The orthogonal test head is shown in Table 2.

The results of the pre-test showed that the effect of charge voltage on droplet deposition of leaf abaxial was not absolute. There was a significant difference in the incremental amount of droplet deposition of leaf abaxial induced by an increase in charge voltage, with different air pressure and spray distance conditions, which proved that there were significant interactions between air pressure and charge voltage, and spray distance and charge voltage in the droplet deposition of the abaxial leaf experiment. Thus, both the interaction term air pressure × charge voltage and the interaction term spray distance × charge voltage were incorporated into the experimental design to investigate the factors affecting the abaxial leaf adhesion. The experiment was performed using an $L_{27}(3^{13})$ orthogonal design. The orthogonal test head is shown in Table 3.

3 Results and discussion

3.1 Effect of air pressure, charge voltage, and spray distance on the CMR

Figure 6A reflects the results of CMR with variation of air pressure and spray distance, at an air pressure of 1.0 bar and a flow rate of 200 ml/min. The results show that the CMR increased by 127.8% from 0.86 to 1.97 mC/kg as the charge voltage increases from 1,000 to 4,000 V at a spray distance of 0.1 m. The CMR is on a downward tendency as the charge voltage increases from 5,000 to 10,000 V. The CMR ranges from 0.44 to 0.74 mC/kg at a spray distance of 1 m. When the spray distance is 1 m, the maximum CMR is only 0.34 mC/kg. It is clear that the CMR has a significant attenuation with the increase in spray distance.

Figure 6B describes the variation of CMR with charge voltage under different air pressure conditions at a spray distance of 0.4 m and a flow rate of 200 ml/min. The result shows that the CMR reaches a maximum of 1.5 mC/kg at a charge voltage of 3,000 V, when the air pressure is 1.5 bar. The CMR reaches its maximum at a voltage of 4,000 V, but decreases as the charge voltage increases after exceeding 4,000 V. When the air pressure is at 0.5 bar, the CMR is small, ranging from 0.2 to 0.4 mC/kg.

With the analysis of the above results, it is clear that the CMR has a critical peak when the charge voltage is between 3,000 and 4,000 V. The CMR conversely decreases as the charge voltage continues to increase. Therefore, for the electrostatic nozzle, "the higher the charging voltage, the better the charging effect" does not apply. It is impractical to increase the CMR by increasing the charge voltage alone. It will increase the electrical power consumption and costs, which are not beneficial to agricultural pesticide application. Applied air pressure also has a significant effect on the CMR, especially when the CMR increases significantly when the air pressure increases and reaches a peak at a relatively small charge voltage. It is due to the increase in air pressure, which improves the atomization effect of the nozzle, which leads to the formation of more small droplets. The same amount of liquid with smaller-sized droplets will have more charge in comparison to bigger-sized droplets (Patel et al., 2016b, Patel et al., 2017). In addition, the appropriate spray distance needs to be selected because the charge would decay with time and distance in the transport of charged droplets in the air. Therefore, optimization of design and performance parameters is important for optimum performance.

3.2 Effect of air pressure and charge voltage on droplet size and distribution

Figure 7 shows the results of VMD and RS of the droplets with variation in the charge voltage and air pressure. In Figure 7, the VMD showed a significant change with the variation in charge voltage when the air pressure is 0.5 bar. The VMD achieves a minimum value of 67.025 μm at a voltage of 5,000 V, which is a 48.9% reduction from 131.153 μm without electrostatic charge. When the air pressure is 1.5 bar, the VMD ranges from 35.102 to 40.232 μm. The charge voltage has a relatively smaller effect on VMD at this time.

From the results, it can be seen that under the same charging conditions, the VMD decreases with the increase in air pressure. From the red line, the droplet size is most obviously affected by the charge voltage, and the maximum decrease is 48.9%, when the air

TABLE 2 The orthogonal experiment head of penetration experiment.

Number	1	2	3	4	5	6	7	8	9	10	11	12	13
Factor	A	B	(A × B)1	(A × B)2	C			(B × C)1		D	(B × C)2		

10.3389/fpls.2024.1309088

TABLE 3 The orthogonal experiment head of deposition on abaxial leaf.

Number	1	2	3	4	5	6	7	8	9	10	11	12	13
Factor	B	D	(B × D)1	(B × D)2	A			(A × D)1		C	(A × D)2		

pressure is 0.5 bar. It was concluded that the charge effect would affect the atomization effect of the droplets. The electrostatic charging could affect the secondary atomization of the liquid droplets, especially for large droplets over 100 µm, which creates more small droplets and leads to a significant reduction in VMD. However, when the air pressure increases, the atomization of liquid droplets is intensified by the impact force and shearing effect of the airflow. The liquid droplets are fully atomized and evenly broken into smaller droplets at this time. The VMD ranges smoothly from 25 to 50 µm. The atomization and break-up of these fine droplets by electrostatic forces become limited.

The relative span (RS) was used to characterize the uniformity of droplet distribution in this research. The smaller the RS, the less variation there is between the size of the droplets in spray spectrum. In Figure 7, the RS shows an increasing trend as the charge voltage increase at an air pressure of 0.5 bar. Liquid droplets break up into small droplets under electrostatic action, which reduces the VMD but increases the particle size spectrum. This results in an RS much higher than 1. When the air pressure is 1.0 bar, the RS tends to be close to 1 under the action of electrostatic forces. The closer the RS is to 1, the closer the droplet size distribution is to the normal distribution, that is, the more uniform the droplet distribution is (Ru et al., 2020). Additionally, in terms of the results of VMD and RS, electrostatic atomization works with particle sizes approximately 50–75 µm under the above experimental conditions. Air atomization or hydraulic atomization plays a leading role in some situations.

For most crops, the optimum particle size suitable for deposition ranges from 20 to 50 µm. In electrostatic spray, the fine droplets have better charge ability and were able to overcome the drift due to their light mass with the help of electrostatic force and air (Patel et al., 2017). The higher the air pressure, the smaller the VMD and RS, and the smaller the particle size, which indicate that the nozzle has good atomization effect and the droplet size distribution is uniform. However, pesticide droplets with too small particle size are volatile and more prone to drift from the actual target, which are not suitable for agricultural spraying operation requirements (Patel et al., 2022). Furthermore, the higher air pressure can also lead to increasing gas power consumption, which can increase agricultural costs and discourage the design and development of spraying equipment.

3.3 Experiment to study the deposition characteristic of charged droplet

For electrostatic spraying, interactions between the various factors affecting spray deposition may exist. Considering the interactions provides a more description of the relationship between spraying parameters and spraying effect, making it easier to obtain the optimal combination parameters for spraying operations.

3.3.1 Effect of spraying parameters and canopy characteristics on droplet penetration

The results of the penetration orthogonal experiment are shown in Table 4 based on the orthogonal experiment table.

ANOVA was performed on the experiment results in Table 4. The results of the ANOVA are shown in Table 5.

Referring to the table of F-distribution, $F_{0.05}$ (2,10) = 4.10 and $F_{0.05}$ (4,10) = 3.48; the value of F_A, F_B, F_C, F_{A*B} exceed the threshold values, which shows that air pressure, spray distance, canopy leaf area index, and the interaction term air pressure × spray distance all had a significant effect on drop penetration, with the factor of spray distance having a determining effect on the results, followed by leaf area index, air pressure, and air pressure × spray distance. The results of the experiment are as follows: $T_{A3} > T_{A2} > T_{A1}$, $T_{B3} < T_{B2} <$

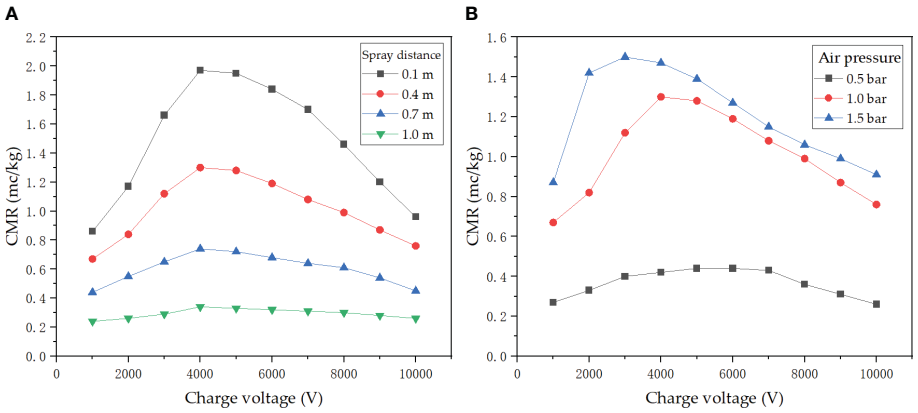

FIGURE 6
(A) Effect of spray distance and charge voltage on CMR. **(B)** Effect of air pressure and charge voltage on CMR.

10.3389/fpls.2024.1309088

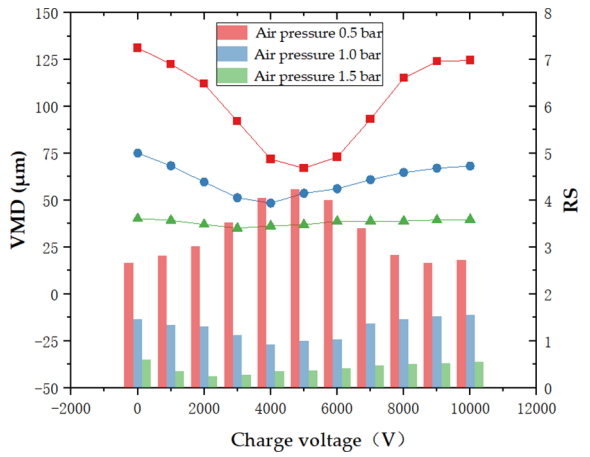

FIGURE 7
Effect of air pressure and charge voltage on VMD and RS.

T_{B1}, T_{C3}< T_{C2}< T_{C1}. Overall, droplet penetration increased with increasing air pressure and decreased with increasing spray distance and leaf area index. Analyzing the above results, we found the following.

The effect of air pressure on droplet penetration is affected by changes in spray distance. When the distance is closer, the effect of air pressure on droplet penetration is significant; when the distance increases, the effect of air pressure on penetration is weakened. This is due to the wind speed generated at different air pressure decay at different rates with the increase in spray distance. This is shown by the fact that the higher the air pressure, the faster the wind speed decay.

The effect of charge voltage on droplet penetration was not significant. Voltage affects the charging effect of droplets. Charged droplets are more likely to be adsorbed on the leaves, which improves droplet attachment on the leaf surface. However, the effect on the deposition inside the canopy was not significant. It suggests that the "surround adsorption effect" of charged droplets

TABLE 4 Results of orthogonal experiments for droplet penetration.

Numbers	Factors								Droplet deposition (μl/cm^2)
	A	B	(A × B)1	(A × B)2	C	(B × C)1	D	(B × C)2	
1	1	1	1	1	1	1	1	1	0.998
2	1	1	1	1	2	2	2	2	0.710
3	1	1	1	1	3	3	3	3	0.480
4	1	2	2	2	1	2	2	3	0.691
5	1	2	2	2	2	3	3	1	0.422
6	1	2	2	2	3	1	1	2	0.288
7	1	3	3	3	1	3	3	2	0.346
8	1	3	3	3	2	1	1	3	0.154
9	1	3	3	3	3	2	2	1	0.115
10	2	1	1	3	1	1	2	1	1.267
11	2	1	2	3	2	2	3	2	1.018
12	2	1	3	3	3	3	1	3	0.826
13	2	2	1	1	1	2	3	3	0.960
14	2	2	2	1	2	3	1	1	0.672
15	2	2	3	1	3	1	2	2	0.442
16	2	3	1	2	1	3	1	2	0.499
17	2	3	2	2	2	1	2	3	0.269
18	2	3	3	2	3	2	3	1	0.134
19	3	1	3	2	1	1	3	1	1.325
20	3	1	3	2	2	2	1	2	1.133
21	3	1	3	2	3	3	2	3	0.941
22	3	2	1	3	1	2	1	3	1.075
23	3	2	1	3	2	3	2	1	0.806

(Continued)

10.3389/fpls.2024.1309088

TABLE 4 Continued

Numbers	Factors								Droplet deposition (μl/cm^2)
	A	B	(A × B)1	(A × B)2	C	(B × C)1	D	(B × C)2	
24	3	2	1	3	3	1	3	2	0.576
25	3	3	2	1	1	3	2	2	0.595
26	3	3	2	1	2	1	3	3	0.326
27	3	3	2	1	3	2	1	1	0.211
T_1	4.204	8.698	7.371	5.394	7.756	5.645	5.856	5.950	
T_2	6.087	5.932	4.492	5.702	5.510	6.047	5.836	5.607	
T_3	6.988	2.649	5.416	6.183	4.013	5.587	5.587	5.722	

under electric field force are more easily adsorbed on the leaf surface, but there are limitations with this effect. On the one hand, the charge of the charged droplets decays due to the effect of distance; on the other hand, due to the influence of the thin canopy, more charged droplets are adsorbed by the leaves on the outside of the canopy. Accordingly, the amount of droplets entering the inside canopy will decrease. Hence, air assistance is required to help disturb the surface canopy and increase the chances of charged droplets reaching the inner canopy.

3.3.2 Effect of spraying parameters and canopy characteristics on droplet deposition of abaxial leaf

The results of abaxial droplet deposition are shown in Table 6.

ANOVA was performed on the experiment results in Table 6. The results of the ANOVA are shown in Table 7.

From the above results, F_A, F_B, F_D, F_{A*D}, F_{B*D} exceed the critical value. This suggests that air pressure, spray distance, charge voltage, the interaction terms air pressure × charge voltage and spray distance × charge voltage all have a significant effect on droplet deposition of leaf abaxial. The degree of influence of each factor on the adhesion effect on the abaxial leaf is in the order of air pressure, spray distance, air pressure × charge voltage, spray distance × charge voltage, and charge voltage. During the spraying, the droplets move with the direction of the spray and are more likely to attach to the surface of the adaxial leaf with relatively little deposition on the abaxial surface of the leaf. The attachment of the charge droplets on the abaxial leaf is mainly due to the perturbation of the airflow and the electric field force on the charged droplets together. The interaction between factors was more significant in the droplet deposition experiment on the abaxial leaf.

According to the above results: $T_{A3} > T_{A2} > T_{A1}$, $T_{B3} < T_{B2} < T_{B1}$, $T_{C3} < T_{C2} < T_{C1}$, $T_{D2} > T_{D3} > T_{D1}$. It can be seen that droplet deposition of the abaxial leaf increased with increasing air pressure and decreased with increasing spray distance and leaf area index. When the charge voltage is taken as 2,500 V, there is maximum droplet deposition on the abaxial leaf, which is higher than that of the case without charging. When the air pressure increases from 0.5 to 1.5 bar, we got a maximum deposition of 0.045 μl/cm^2. This is due to the increased air pressure improving droplet delivery efficiency and penetration, while increased disturbance of leaves makes it easier for droplets to reach the inside canopy. Furthermore, the increase in air pressure improves the atomization and charging effect of liquid droplets. The CMR of the charge droplets is higher and easier to be adsorbed on the abaxial leaf by electric field forces under the condition of constant charge voltage. Additionally, the velocity of the charged droplets decreased when they reach the canopy as the spray distance increased from 0.2 to 1 m, which is more difficult for the droplets to reach the inside canopy. At the same time, the charge of the droplets decreases as the distance increases, and the CMR of the droplet decreases after reaching the inside canopy as the spraying distance increases leading to a decrease in droplet deposition on the abaxial leaves.

We suggest that there is an interaction among the factors of air pressure, charge voltage, and spray distance. For example, comparing the results of experiment groups 15 and 16, at the same spray distance of 0.6 m, the deposition at a voltage of 2,500 was 0.037 μl/cm^2, which is much greater than the deposition at a

TABLE 5 Analysis of variance of penetration experiment results.

Variance term	Sum of squared deviations	Degrees of freedom	F-value	$F_{0.95}$ (df_j, df_e)
A	0.44847	2	186.94	4.103
B	2.03777	2	849.42	4.103
C	0.788745	2	328.78	4.103
D	0.005011	2	2.09	4.103
A×B	0.515344	4	107.41	3.478
B×C	0.02076	4	4.33	3.478

10.3389/fpls.2024.1309088

TABLE 6 Results of orthogonal experiments for droplet deposition on abaxial leaf.

Numbers	Factors								Droplet deposition (μl/cm^2)
	B	D	(B × D)1	(B × D)2	A	(A × D)1	C	(A × D)2	
1	1	1	1	1	1	1	1	1	0.015
2	1	1	1	1	2	2	2	2	0.018
3	1	1	1	1	3	3	3	3	0.019
4	1	2	2	2	1	2	2	3	0.012
5	1	2	2	2	2	3	3	1	0.017
6	1	2	2	2	3	1	1	2	0.045
7	1	3	3	3	1	3	3	2	0.010
8	1	3	3	3	2	1	1	3	0.028
9	1	3	3	3	3	2	2	1	0.032
10	2	1	1	3	1	1	2	1	0.011
11	2	1	2	3	2	2	3	2	0.014
12	2	1	3	3	3	3	1	3	0.016
13	2	2	1	1	1	2	3	3	0.008
14	2	2	2	1	2	3	1	1	0.015
15	2	2	3	1	3	1	2	2	0.037
16	2	3	1	2	1	3	1	2	0.008
17	2	3	2	2	2	1	2	3	0.020
18	2	3	3	2	3	2	3	1	0.027
19	3	1	3	2	1	1	3	1	0.006
20	3	1	3	2	2	2	1	2	0.013
21	3	1	3	2	3	3	2	3	0.013
22	3	2	1	3	1	2	1	3	0.007
23	3	2	1	3	2	3	2	1	0.009
24	3	2	1	3	3	1	3	2	0.020
25	3	3	2	1	1	3	2	2	0.005
26	3	3	2	1	2	1	3	3	0.012
27	3	3	2	1	3	2	1	1	0.014
T_1	0.196	0.125	0.115	0.143	0.082	0.194	0.161	0.146	
T_2	0.156	0.170	0.154	0.161	0.146	0.145	0.157	0.170	
T_3	0.099	0.156	0.182	0.147	0.223	0.112	0.133	0.135	

voltage of 5,000 V of 0.008 μl/cm^2. On the one hand, factors affecting the charging effect include the morphology of charged droplets at the nozzle exit, in addition to the charge voltage, electrode shape, and size (Patel et al., 2015). Specifically, when the air pressure is low, the atomization effect is not good, the droplet size is large, and the charging effect is not ideal; when the air pressure is increased and the droplet size becomes smaller, the charging effect of the droplets becomes better. Therefore, there is an interaction between air pressure and charged voltage on the charging effect, and this interaction is also reflected in the adhesion effect on the abaxial leaf. On the other hand, the effect of charged voltage on the charging effect is not linear; with the increase in voltage, the CMR increases before it reaches a peak and then gradually decreases, which is due to the arc discharge phenomenon generated by a high voltage (Zhou et al., 2018). Moreover, there is also an interaction between charge voltage and spray distance due to the different charging effects. When the spray distance is close, there is less charge decay of the charged droplets. Therefore, when the spraying distance is close, the charge voltage has a significant effect on the deposition of the abaxial leaf, and

TABLE 7 Analysis of variance of droplet deposition experiment on abaxial leaf.

Variance term	Sum of squared deviations	Degrees of freedom	F-value	$F_{0.95}$ (df_j, df_e)
A	0.0011080	2	40.03	4.103
B	0.0005280	2	19.07	4.103
C	0.0000509	2	1.84	4.103
D	0.0001180	2	4.26	4.103
A×D	0.0004492	4	8.11	3.478
B×D	0.0002718	4	4.91	3.478

when the spraying distance is far, the adjustment of the charge voltage does not produce a significant change in the deposition effect.

In summary, to improve the deposition efficiency, the CMR should not only be increased by increasing the voltage but also the interactive effects of other spraying parameters and canopy characteristics on deposition should be considered. This study can provide recommendations for the specific application and implementation of electrostatic spraying in agricultural application. According to the results and analysis, the significance of the effect of each factor on droplet penetration, in descending order, is as follows: spray distance, leaf area index, air pressure, and air pressure × spray distance. Since charge voltage has no significant effect on droplet penetration, temporarily setting the charge voltage as 0 V, the optimal solution is obtained as $A_3B_1D_1$ (air pressure 1.5 bar, spray distance 0.2 m, charge voltage 0 V). The significance of the effect of each factor on abaxial leaf deposition, in descending order, is as follows: air pressure, spray distance, air pressure × charge voltage, spray distance × charge voltage, and charge voltage. Obviously, air pressure and spray distance are still the priority. In view of the fact that there is some significant effect of charge voltage on the deposition of abaxial leaves, however, the deposition effect with a 2,500-V charge voltage is better than that of 5,000 V at an air pressure of 1.5 bar. By combining the above analysis and results, the final optimal solution is obtained as $A_3B_1D_2$ (air pressure 1.5 bar, spray distance 0.2 m, charge voltage 2,500 V).

This improved air-assisted electrostatic nozzle in this study does not have a particularly higher CMR compared to the advanced air-induced air-assisted electrostatic nozzle designed by Patel, whose droplets are electrified to more than 10 mC/kg CMR by a charging voltage less than 2.5 kV at a liquid flow of 150 ml/min (Patel et al., 2017). However, in actual orchard spraying operations, we need to avoid excessive consumption of compressed gas during multi-nozzle orchard spraying as well as the requirements of high air pressure on the supporting gas supply equipment. Furthermore, our improved air-assisted electrostatic nozzle only requires a maximum air pressure of 1.5 bar, which is only under half of the air pressure compared to the electrostatic nozzle of Patel. With the same 2,500-V charge voltage, our improved air-assisted electrostatic nozzle can have 1.5 mC/kg of CMR at an air pressure of 1.5 bar, one adaxial droplet deposition of 0.941 μl/cm^2, and another abaxial droplet deposition of 0.045 μl/cm^2 under the above conduction, which are not less than the droplet deposition using the nozzle of Patel (with maximum adaxial droplet deposition of 0.83 μl/cm^2 and maximum abaxial droplet deposition of 0.125 μl/cm^2). We will conduct further field experiments to validate our equipment and improve our nozzle.

4 Conclusions

In this article, an improved air-assisted electrostatic nozzle with induction charging was designed, and an air-assisted electrostatic spraying system was built to conduct the spraying performance experiment of the nozzle. The objective of this study is to obtain the appropriate operating parameters of the electrostatic spraying system combination that maximizes chargeability and uniform droplet distribution and enhances droplet deposition in electrostatic pesticide application through exploring the general regulations of the effect of different operating parameters on the spraying performance. Furthermore, we designed a multi-factor orthogonal experiment and analyzed the impact mechanisms on droplet deposition and penetration characteristics under different operating parameters and canopy characteristics conditions.

The results of the spraying performance experiment proved that the improved air-assisted electrostatic nozzle has good atomization and charging effects. The spraying system has good atomization effect of droplets under the condition of air pressure of 0.5–1.5 bar. An excellent CMR (1.97 mC/kg) is achieved for efficient working of the electrostatic spraying processes with a charging voltage of 4,000 V. The CMR increased by 127.8% from 0.86 to 1.97 mC/kg as the charge voltage increases from 1,000 to 4,000 V at an air pressure of 1.0 bar and a flow rate of 200 ml/min. For the electrostatic nozzle, “the higher the charging voltage, the better the charging effect” does not apply. It is impractical to increase the CMR by increasing the charge voltage alone. It will increase the electrical power consumption and costs, which are not beneficial to agricultural pesticide application.

The electrostatic charging could affect the secondary atomization of the liquid droplets, especially for large droplets over 100 μm, which creates more fine droplets and leads to a significant reduction in VMD. When the air pressure is 1.0 bar, RS tends to be close to 1 under the action of electrostatic forces. Furthermore, the excessive air pressure can also lead to increasing gas power consumption, which can increase agricultural costs and discourage the design and development of spraying equipment. Considering all the above situation, for optimal droplet penetration and abaxial leaf deposition, option $A_3B_1D_2$ is recommended.

These studies can provide technical references for the optimization of operating parameters of electrostatic spraying systems. The appropriate operation parameters could improve the pesticide droplet deposition and the penetration, thereby achieving a good control effect of pests and diseases. It can also guide the farmers to spray pesticides better reducing the pesticide usage and improving the pesticide utilization efficiency.

Data availability statement

The original contributions presented in the study are included in the article/supplementary material. Further inquiries can be directed to the corresponding author.

Author contributions

HZ: Conceptualization, Data curation, Formal analysis, Writing – original draft. MO: Conceptualization, Writing – review & editing. XD: Writing – review & editing. WZ: Data curation, Formal analysis, Writing – original draft. SD: Writing – original draft. WJ: Conceptualization, Writing – review & editing.

Funding

The author(s) declare financial support was received for the research, authorship, and/or publication of this article. This research was funded by the Project of Faculty of Agricultural Equipment of Jiangsu University (No. NZXB20210101), Jiangsu Province, and Education Ministry Co-sponsored Synergistic Innovation Center of Modern Agricultural Equipment (XTCX1003).

Acknowledgments

The authors thank the Faculty of Agricultural Engineering of Jiangsu University for its facilities and support.

Conflict of interest

The authors declare that the research was conducted in the absence of any commercial or financial relationships that could be construed as a potential conflict of interest.

Publisher's note

References

Ahmad, F., Qui, B., Dong, X., Ma, J., and Chandio, F. A. (2020). Effect of operational parameters of UAV sprayer on spray deposition pattern in target and off-target zones during outer field weed control application. *Comput. Electron. Agric.* 172, 105350. doi: 10.1016/j.compag.2020.105350

Appah, S., Jia, W., Ou, M., Wang, P., and Gong, C. (2019b). Investigation of optimum applied voltage, liquid flow pressure, and spraying height for pesticide application by induction charging. *Appl. Eng. Agric.* 355, 795–804. doi: 10.13031/aea.13358

Appah, S., Wang, P., Ou, M. X., Gong, C., and Jia, W. D. (2019a). Review of electrostatic system parameters, charged droplets characteristics and substrate impact behavior from pesticides spraying. *Int. J. Agric. Biol. Eng.* 122, 1–9. doi: 10.25165/j.ijabe.20191202.4673

Bowen, H. D., Splinter, W. E., and Carleton, W. M. (1964). Theoretical implications of electrical fields on deposition of charged particles. *Trans. ASAE* 71, 0075–0082. doi: 10.13031/2013.40700

Chambers, J. E., Greim, H., Kendall, R. J., Segner, H., Sharpe, R. M., and Van Der Kraak, G. (2014). Human and ecological risk assessment of a crop protection chemical: a case study with the azole fungicide epoxiconazole. *Crit. Rev. Toxicol.* 442, 176–210. doi: 10.3109/10408444.2013.855163

Esehaghbeygi, A., Tadayyon, A., and Besharati, S. (2010). Comparison of electrostatic and spinning-discs spray nozzles on wheat weeds control. *J. Am. Sci.* 612, 529–533. doi: 10.7537/marsjas061210.61

Ferguson, J. C., Chechetto, R. G., Hewitt, A. J., Chauhan, B. S., Adkins, S. W., Kruger, G. R., et al. (2016). Assessing the deposition and canopy penetration of nozzles with different spray qualities in an oat (Avena sativa L.) canopy. *Crop Prot.* 81, 14–19. doi: 10.1016/j.cropro.2015.11.013

Gan-Mor, S., Ronen, B., and Ohaliav, K. (2014). The effect of air velocity and proximity on the charging of sprays from conventional hydraulic nozzles. *Biosyst. Eng.* 121, 200–208. doi: 10.1016/j.biosystemseng.2014.03.004

Hoffmann, W. C., and Hewitt, A. J. (2005). Comparison of three imaging systems for water-sensitive papers. *Appl. Eng. Agric.* 21, 961–964. doi: 10.13031/2013.20026

Hoffmann, W. C., Walker, T. W., Smith, V. L., Martin, D. E., and Fritz, B. K. (2007). Droplet-size characterization of handheld atomization equipment typically used in vector control. *J. Am. Mosq. Control Assoc.* 233, 315–320. doi: 10.2987/8756-971X(2007)23[315:DCOHAE]2.0.CO;2

Lan, Y. B., Zhang, H. Y., and Wen, S. (2018). Analysis and experiment on atomization characteristics and spray deposition of electrostatic nozzle. *Trans. Chin. Soc. Agric. Machinery* 494, 131–141. doi: 10.6041/j.issn.1000-1298.2018.04.015

Law, S. E. (1983). Electrostatic pesticide spraying: concepts and practice. *IEEE Trans. Industry Appl.* 192, 160–168. doi: 10.1109/TIA.1983.4504176

Law, S. E. (2001). Agricultural electrostatic spray application: a review of significant research and development during the 20th century. *J. Electrostatics* 51-52, 25–42. doi: 10.1016/S0304-38860100040-7

Law, S. E., and Bowen, H. D. (1966). Charging liquid spray by electrostatic induction. *Transaction ASAE* 94, 501–506. doi: 10.13031/2013.40016

Law, S. E., and Thompson, S. A. (1996). Electroclamping forces for controlling bulk particulate flow: charge relaxation effects. *J. Electrostatics.* 371, 79–93. doi: 10.1016/0304-3886(96)00003-4

Li, X., He, X. K., and Zhong, C. S. (2007). Effect of different spray factors on charged droplet deposit using response surface methodology. *High Voltage Eng.* 332, 32–36. doi: 10.3969/j.issn.1003-6520.2007.02.007

Liao, J., Luo, X., Wang, P., Zhou, Z., O'Donnell, C. C., Zang, Y., et al. (2020). Analysis of the influence of different parameters on droplet characteristics and droplet size classification categories for air induction nozzle. *Agronomy* 10, 256. doi: 10.3390/agronomy10020256

Martini, A. T., Avila, L. A., Camargo, E. R., Helgueira, D. B., Bastiani, M. O., and Loeck, A. E. (2016). Pesticide drift from aircraft applications with conical nozzles and electrostatic system. *Ciec. Rural* 469, 1678–1682. doi: 10.1590/0103-8478cr20151386

Maski, D., and Durairaj, D. (2010). Effects of charging voltage, application speed, target height, and orientation upon charged spray deposition on leaf abaxial and adaxial surfaces. *Crop Prot.* 292, 134–141. doi: 10.1016/j.cropro.2009.10.006

Pascuzzi, S., and Cerruto, E. (2015). Spray deposition in "tendone" vineyards when using a pneumatic electrostatic sprayer. *Crop Prot.* 68, 1–11. doi: 10.1016/j.cropro.2014.11.006

Patel, M. K. (2016). Technological improvements in electrostatic spraying and its impact to agriculture during the last decade and future research perspectives - A review. *Eng. Agriculture Environ. Food* 91, 92–100. doi: 10.1016/j.eaef.2015.09.006

Patel, M. K., Ghanshyam, C., and Kapur, P. (2013). Characterization of electrode material for electrostatic spray charging: Theoretical and engineering practices. *J. Electrostatics* 711, 55–60. doi: 10.1016/j.elstat.2012.11.019

Patel, M. K., Khanchi, A., Chauhan, A., Kumar, A., Akkireddi, S. R. K., Jangra, A., et al. (2022). Real-time measurement of droplet size and its distribution of an air-induced air-assisted electrostatic nozzle. *J. Electrostatics* 115, 103665. doi: 10.1016/j.elstat.2021.103665

Patel, M. K., Kundu, M., Sahoo, H. K., and Nayak, M. K. (2016b). Enhanced performance of an air-assisted electrostatic nozzle: Role of electrode material and its dimensional considerations in spray charging. *Eng. Agriculture Environ. Food* 94, 332–338. doi: 10.1016/j.eaef.2016.05.002

Patel, M. K., Praveen, B., Sahoo, H. K., Patel, B., Kumar, A., Singh, M., et al. (2017). An advance air-induced air-assisted electrostatic nozzle with enhanced performance. *Comput. Electron. Agric.* 135, 280–288. doi: 10.1016/j.compag.2017.02.010

Patel, M. K., Sahoo, H. K., Nayak, M. K., and Ghanshyam, C. (2016a). Plausibility of variable coverage high range spraying: Experimental studies of an externally air-assisted electrostatic nozzle. *Comput. Electron. Agric.* 127, 641–651. doi: 10.1016/j.compag.2016.07.021

Patel, M. K., Shamrma, T., Nayak, M. K., and Ghanshyam, C. (2015). Computational modeling and experimental evaluation of the effects of electrode geometry and deposition target on electrostatic spraying processes. *Int. J. Comput. Appl.* 1242, 10–15. doi: 10.5120/ijca2015905358

Ru, Y., Liu, Y. Y., Qu, R. J., and Patel, M. K. (2020). Experimental study on spraying performance of biological pesticides in aerial rotary cage nozzle. *Int. J. Agric. Biol. Eng.* 136, 1–6. doi: 10.25165/j.ijabe.20201306.5511

Shang, Q. Q., Zhang, Y. Q., Sun, Z. W., Zheng, J. D., Zhao, B. G., and Pan, Y. C. (2004). Study on droplet deposition and penetrability in tree crown by the wind tunnel. *J. Nanjing Forestry Univ. (Natural Sci. Edition)* 4705, 45–48. doi: 10.3969/j.jssn.1000-2006.2004.05.011

Shrimpton, J. S., and Laoonual, Y. (2006). Dynamics of electrically charged transient evaporating sprays. *Int. J. Numerical Methods Eng.* 678, 1063–1081. doi: 10.1002/nme.1647

Wang, S., Li, X., Zeng, A., Song, J., Xu, T., Lv, X., et al. (2022). Effects of adjuvants on spraying characteristics and control efficacy in unmanned aerial application. *Agriculture* 12, 138. doi: 10.3390/agriculture12020138

Wu, C. D., Shi, Y. N., Zhang, B., and Jiang, C. F. (2009). Target backside deposition characteristics of air-assisted electrostatic spraying. *J. Drainage Irrigation Machinery Eng.* 274, 242–246. doi: 10.3969/j.issn.1674—8530.2009.04.009

Yule, A. J., Shrimpton, J. S., Watkins, A. P., Balachandran, W., and Hu, D. (1995). Electrostatically atomized hydrocarbon sprays. *Fuel* 747, 1094–1103. doi: 10.1016/0016-2361(95)00037-6

Zhou, H., Jia, W., Li, Y., and Ou, M. (2021). Method for estimating canopy thickness using ultrasonic sensor technology. *Agriculture* 11, 1011. doi: 10.3390/agriculture11101011

Zhou, L. F., Zhang, L., and Ding, W. M. (2015). Droplet coverage response surface models and influencing factors of air-assisted electrostatic spray. *Trans. Chin. Soc. Agric. Eng. (Transactions CSAE)* 31, 52–59. doi: 10.11975/j.issn.1002-6819.2015.z2.008

Zhou, L. F., Zhang, L., Xue, X. Y., and Chen, C. (2018). Research progress and application status of electrostatic pesticide spray technology. *Trans. Chin. Soc. Agric. Eng. (Transactions CSAE).* 3418, 1–11. doi: 10.11975/j.issn.1002-6819.2018.18.001

Zhou, R. Q., Zhang, H. H., Zheng, J. Q., Zhou, H. P., Tang, Y. S., and Wang, D. (2019). Study on parameters of mobile spraying to droplet penetration targeting forestry pest and disease control. *J. Cent. South Univ. Forestry Technol.* 3907, 114–122. doi: 10.14067/j.cnki.1673-923x.2019.07.016

Zhu, H., Salyani, M., and Fox, R. D. (2011). A portable scanning system for evaluation of spray deposit distribution. *Comput. Electron. Agric.* 761, 38–43. doi: 10.1016/j.compag.2011.01.003

Zhu, H. P., Xian, F. S., and Gao, L. R. (1989). Summary of research on electrostatic spraying technique theory and its application. *Trans. Chin. Soc. Agric. Machinery* 202, 53–59. Available at: https://kns.cnki.net/kcms/detail/detail.aspx?FileName=NYJX198902007&DbName=CJFQ1989.

Frontiers in
Plant Science

Cultivates the science of plant biology and its applications

The most cited plant science journal, which advances our understanding of plant biology for sustainable food security, functional ecosystems and human health.

Discover the latest Research Topics

See more →

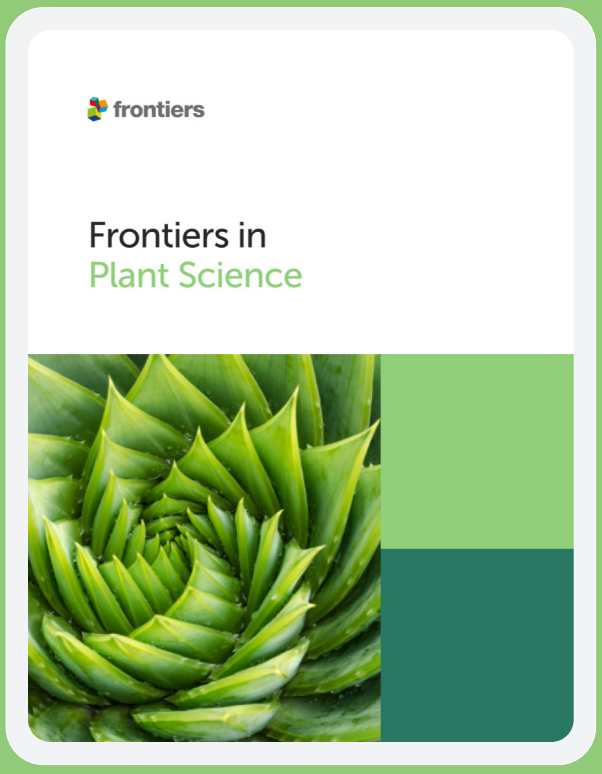

Frontiers

Avenue du Tribunal-Fédéral 34
1005 Lausanne, Switzerland
frontiersin.org

Contact us

+41 (0)21 510 17 00
frontiersin.org/about/contact